

Doctoral Dissertation

Doctoral Program in Urban and Regional Development (33rd Cycle)

Water, carbon and energy fluxes on grasslands of Western Alps: methodological issues, experimental data, hydrological modelling and atmospheric boundary layer phenomena

Davide Gisolo

* * * * * *

Supervisors

Prof. Stefano Ferraris, Supervisor

Prof. Davide Canone, Co-Supervisor

Doctoral Examination Committee:

Prof. Andrea Pitacco, Referee, Università di Padova

Prof. Riccardo Rigon, Referee, Università di Trento

Prof. Giacomo Bertoldi, Eurac Research, Bolzano

Prof. Claudio Cassardo, Università di Torino

Prof. Davide Poggi, Politecnico di Torino

Politecnico di Torino

2021

I hereby declare that, the contents and organisation of this dissertation constitute my own original work and does not compromise in any way the rights of third parties, including those relating to the security of personal data.

……..

Davide Gisolo
Turin, 2021

Summary

The research aims at improving the knowledge about ecohydrological and micrometeorological processes of Alpine unmanaged grasslands. The focus is on land (soil) and biosphere-atmosphere interactions principally regarding exchanges of energy (heat), water vapour and carbon dioxide, also known as fluxes. Those fluxes depend on three main topics addressed in this Thesis: i) the meteorological and micrometeorological properties of the area (e.g. available energy, wind regime, air temperature, air humidity, vapour pressure deficit, precipitation); ii) the biomass and vegetation types and distribution; iii) soil properties, soil water movement and availability. Energy and mass fluxes (included evapotranspiration), micrometeorological and soil properties are experimentally evaluated at three mountain sites. For fluxes evaluation, the eddy covariance technique is used, whereas available models are used to evaluate the sites flux footprint. Particular attention is devoted to evapotranspiration analysis and quantification, using collected data at experimental sites and of modelling approaches.

The innovation of the research project relies on the selected ecosystem: few works have focused the attention on mountain regions exploring, also in complex terrains such as slopes, unmanaged grasslands on multiple years and sites. The study is important, since abandoned or unmanaged grasslands are also experiencing shrubs encroachment which alters the ecosystem.

The use of data collected in various years and of modelling approaches gives useful insights since the study area (North-West Italian Alps) is characterised by a high spatial variability (altitudes range from 500 m a.s.l. to more than 4000 m in few kilometres) and by a high meteorological interannual variability. This last point is also due to the relative proximity to the Mediterranean Sea. Besides, it is not

common to use and compare data collected at sites with very different topography in a relatively small area.

Chapters 1 and 2 are, respectively, the general Introduction and Theoretical framework description. Chapter 3 introduces the description of experimental sites.

Chapter 4 investigates what is the quality of the collected data at the eddy covariance experimental stations. Detailed quality control is used, and each important quality test is analysed separately. The objective is to assess what percentage of good quality data exists for the acquired data sets and to quantify the energy balance closure at the sites. The overall available data outreached 60% and the energy balance closure ranged between 60 and 70% at the most complex experimental site and reached values greater than 80% at the second, less complex site.

Chapter 5 explores micrometeorological characteristics of three eddy covariance Alpine sites and deals with two possible causes of energy imbalance: firstly, the net radiation misrepresentation (hence, its correction according to the turbulent fluxes footprint). Secondly, the presence of low-frequency atmospheric structures (vortices) may cause turbulent fluxes underestimations, and phase differences between the vertical wind velocity and scalars such as temperature, water vapour and carbon dioxide.

The net radiation correction was implemented and improvements greater than 5% were found. Low-frequency, structures were detected at one measurement site, as well as the aforementioned phase differences, and both of them contribute to underestimating the turbulent fluxes.

Chapter 6 investigates the evapotranspiration interannual variability and the roles of soil conditions and meteorologically different hydrological years and growing seasons (in terms of precipitation, humidity and air temperature) on evapotranspiration. The first part of the analysis is devoted to understanding whether the aforementioned interannual variability is high and whether years with very different water availability and temperatures can be used as multiple "scenarios" that mimic the climate change ones. The role of evapotranspiration drivers and their interannual variability are also explored. In the second part of the analysis, the impact of two different land covers (i.e. grass and shrubs) on evapotranspiration is assessed.

Results highlight a high interannual variability with precipitation and temperature changes respectively beyond 100 mm and of about 1°C between growing seasons in different years.

The latent heat flux dominates over the sensible heat flux also in dry growing seasons and it always shows a bimodality due to the lack of precipitation in prolonged periods.

A morning inflexion of the same flux was found, and it is likely related to the downslope to upslope wind regime change.

The interannual variability was also found in periods of 15-days comparing different growing seasons, and also in ET drivers, with global radiation, net radiation and VPD being the main drivers. VPD dominated over net radiation in growing seasons with frequent cloudy conditions. The cumulative evapotranspiration showed interannual differences up to more than 100 mm.

The land cover had high impacts on evapotranspiration. Shrubland would be characterised by evapotranspiration more than 110 mm greater than a grassland in a single growing season. At one measurement site, (characterised by a mix of shrubs and grass), the modelled ET agrees with the measured one. Exceptions were found in "meteorologically extreme" years.

Chapter 7 deals with evapotranspiration modelling with a novel, original hydrological model designed by LABFLUX Team, used and temporally validated by the Author of this Thesis which is composed of two modules, namely, the meteorological and the soil ones. The model requires meteorological data as inputs, whereas the soil water module is a simple "bucket model" with multiple layers. The hydrological model operates with literature formulae and parameters, hence it does not require a classical calibration. The model is tested on a wide area in Valle d'Aosta Region (Italy) and it is validated both temporally (using two eddy covariance stations) and spatially (using a well-known model, called METRIC). Results highlight a rather good agreement with measures and with the METRIC model outputs. Hence, even a simple modelling approach leads to an acceptable ET evaluation

Chapter 8 deals with nine fast-melting snowfall events at one site. The aim is to characterise the events from the micrometeorological point of view, quantify the role of longwave on snowmelt and the role of snowmelt on energy balance residuals explanation and quantify the water balance closure and its components (snowmelt and sublimation).

Results highlight that as soon as the snow starts melting, the first sunny day, there is a strong LE increase, and when the snow has vanished, H flux tends to increase as well. Besides, the friction velocity is only weakly dependent on snow presence.

Longwave radiation is important especially on cloudy nights and, also during daytime, incoming longwave radiation is always at least 20% of the solar radiation. During the nighttime, the longwave inputs can lead to snowmelt. This finding was also confirmed at a second measurement site.

The snowmelt can explain a highly variable fraction of energy residuals, up to 80%, and using the soil moisture probes to detect snowmelt might be a rather interesting choice when no other available data sources exist.

The water balance is nearly closed in almost all the events and snowmelt is the most important term of the snow water equivalent (SWE) balance, while sublimation accounts for a maximum of 35% of SWE. Snowmelt and sublimation terms are comparable with previous studies, also in sites with higher wind speeds.

Chapter 9 introduces the concept of meandering, which is an oscillating behaviour of the wind flow (and also of scalars) and it typically occurs when the flow evolves into quasi-2D structures. Empirical formulae (elaborated for flat and homogeneous terrains) were applied in a complex terrain context to fit the autocorrelation functions and the spectra of wind speed and temperature. Their performance was evaluated, and they were used to identify the hours characterised by meandering. Results show that the formulae can be used, although with care. Only a few hours (3% of the total) were characterised by "complete meandering", that is when the autocorrelation functions of u, v and T oscillate, and all of them occurred in low wind speed conditions (< 1.5 m s^{-1}). No direct relationship between meandering and atmospheric stability was found, even if no complete meandering occurred in stable hours. Besides, frequently, complete meandering occurred in cloudy conditions.

Meandering conditions might be revealed by adequate indexes. Several options were tested at one measurement site. The friction velocity and the ratio of the squares of vertical and horizontal wind speed components were found as good meandering indices.

When meandering (either complete or not) occurs, the sensible heat flux is lower if compared to non-meandering hours. Sensible heat flux uncertainty is also affected by meandering, with higher values in meandering and almost meandering hours. This finding could be implemented in data quality control where suspect meandering conditions occur.

Concluding, the overall conclusions and perspectives are presented.

Keywords: Eddy-covariance, turbulent fluxes, energy and mass balances, air-land interactions, eco-hydrology

Acknowledgement

I would like to thank first of all my Supervisor and Co-supervisor for the patience and for having supported me and my research. I am very grateful to Dr Ivan Bevilacqua for the endless hours of cooperation for the analyses of Chapters 5 and 6. I also would like to thank Dr Maurizio Previati for his appreciated scientific support, and all the remaining members of the Labflux team (past and present) for having accompanied me on this journey.

Thanks to Dr Ivana Stiperski for the useful advices given for the development of Chapter 4.

Sincere thanks to the Environmental Protection Agency of Valle d'Aosta (ARPA VdA) for having provided and shared their meteorological and micrometeorological data. In particular, thanks to Dr Marta Galvagno, who helped to analyse and interpret eddy covariance data of Chapter 5.

I would like to thank the Ufficio Neve e Valanghe of Regione Valle d'Aosta for having provided and shared their snow data.

I am also grateful to Justus van Ramshorst, Dr Lukas Siebicke and Prof. Alexander Knohl for their scientific support for the development of Chapter 6.

Thanks to all the Labflux Team with whom the hydrological model illustrated in Chapter 7 has been developed.

I thank Dr Luca Mortarini of ISAC-CNR in Turin for the software and scientific support in the development of Chapter 9.

Contents

List of Tables

List of Figures

Chapter 1

Introduction

All the ecosystems are extremely important for human societies. We can define "ecosystem" as the combination of two components: one biotic (living) and one abiotic (non-living). These two components interact nonlinearly and include all the interactions between the atmosphere, soil, organic components and autotrophic and heterotrophic living beings (together with what they produce and consume, also within the food chain).

De Groot et al. (2002) describes several functions related to regulation, habitat, production and information. The first includes the ability of the ecosystem to regulate essential ecological processes and to support life. Services for human needs are given by clean air and availability of water and soil. The second is linked to the ecosystems acting as the system where flora and fauna can survive and breed. The services are intended here as the conservation of biological and genetic diversity.
Production functions, in particular, allow the conversion of water, carbon and nutrients to carbohydrate molecules by means of photosynthesis and nutrient uptake. Food, raw materials and energy resources are obtained from this important function. Information functions are related to the reference system to be compared with those created or altered by humans. Natural ecosystems contribute to maintain healthy human beings and provide material for reflection, recreation, and other intellectual activities.

Considering micrometeorological and climate analyses, the production functions, all interconnected, may be the most important, and they include gas and climate regulations.

In this Thesis, a particular ecosystem – that is, the Alpine grasslands – is analysed from physical and ecohydrological point of view with a particular reference to water vapour and carbon dioxide fluxes, including also micrometeorological and meteorological studies.
Studying grasslands is important because grasslands cover almost one fifth of the World's land surface (Hall and Scurlock, 1991) and, more precisely, the percentage

oscillates from 31 to 43% excluded Antarctica (Gibson, 2009). Besides, as mentioned earlier, one third of the European land surfaces (Velthof et al., 2014). Valle d'Aosta has a total area of 3,260 km^2 and mountain grasslands cover about 1,230 km^2, about 40% of the entire regional area (Figure 1.1).

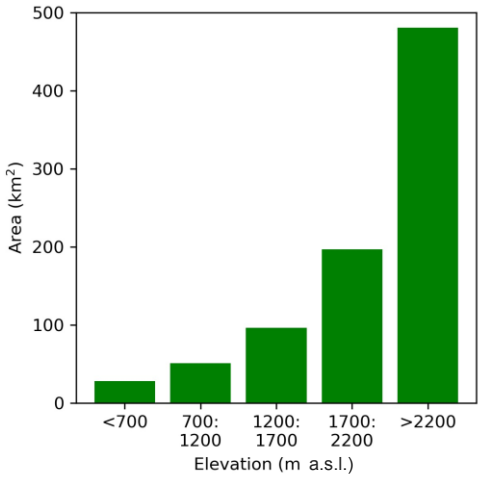

Figure 1.1. Distribution of grasslands in Aosta Valley.

The monitoring of mountain areas is one of the most challenging research fields in the land and atmospheric sciences, because of the terrain complexity. Improved knowledge about those regions, is therefore very important because they play a key role in the water availability (they are considered the "water towers of the World") and because of their rich ecosystem. Furthermore, in the recent past, anthropogenic activities and effects, such as land and cover changes (i.e. tree line shift, ecosystems being colonised by new species, Gehrig-Fasel et al., 2007 and climate change have caused threats to ecosystems (in their functions, involved processes and integrity). Land abandonment, new urban areas, pollution, carbon dioxide and temperature increases are among the most important factors of ecosystems alterations (Figure 1.2). Increased knowledge about how the ecosystems work and may evolve helps their conservation, restoration and management: mitigation and resilience are two important concepts for the future, given the several services provided by ecosystems. This is also one of the research topics of Ecopotential, an H-2020 funded European Project. The climate change is particularly evident in mountain areas, which are hot spots experiencing an enhanced warming with altitude or elevation-dependent warming, EDW (Ceppi et al., 2010; Beniston et al., 1997). The EDW, which is occurring in most of the mountainous regions of the world (Rangwala et al., 2012; Palazzi et al., 2016), has negative consequences for the cryosphere (Giaccone et al., 2015), the hydrological cycle, water resource availability and distribution. Several causes might impact the EDW and among these, there is the water vapour enhanced greenhouse warming (Philipona, 2013; MRI, 2015). Seasonal spatial patterns and temporal trends highlight a certain variability of temperatures in time and space, but all models agree in highlighting this phenomenon (Heinrich et al., 2013b). As annual average, a total increase of 1.5°C is expected in the first half of the 21st century (+0.25°C per decade). A further

acceleration is forecasted in the second half of the century (Gobiet et al., 2014) with an expected annual average warming at the end of the century at about 3.3°C (+0.36°C per decade). This will seriously influence the Alpine Region and, more in general, all mountains areas (e.g. Palazzi et al., 2016; Rottler et al., 2018). Impacts are already evident. It is changing i) the physical environment (e.g. increased thaw of permafrost regions, snow-cover reduction at mid elevation, increased frequency of drought and water scarcity - e.g. Haeberli and Beniston, 1998; Vanham, 2012; Gobiet et al., 2014; Beniston and Stoffel, 2014), ii) the biodiversity and dynamic evolutions of Alpine ecosystem (e.g. distribution and abundance of biotic communities, seasonal cycles and phenology modifications – Alexander et al., 2015; Rogora et al., 2018; Asse et al., 2018), and iii) its socio-economic implications (e.g. winter tourism and ski industry, hydropower generation, natural hazards, agriculture and irrigation, drinking water, ecosystem services – Gaudard et al., 2014; Maran et al., 2014; Einhorn et al., 2015; Fuhrer et al., 2014; Delpla et al., 2009; Schirpke et al., 2017).

The aforementioned ecosystem changes are better detectable in natural environments because of less disturbances directly induced by direct human activities such as grazing on managed terrains. All these modifications affect also the water, carbon and energy balances.

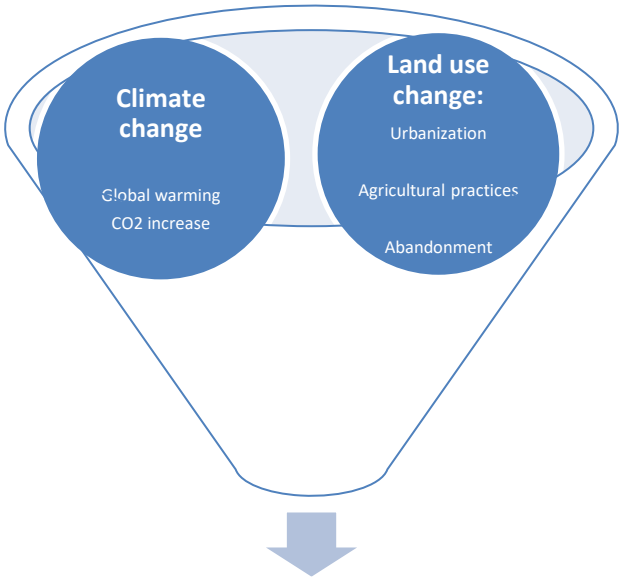

Figure 1.2. Land use changes and climate change affect the ecosystems.

To understand the complex processes involved in the Alpine ecosystems it is important to measure the exchanged fluxes of water, carbon dioxide and energy between the soil surface and atmosphere. This is still a scientific challenge because

in several situations, the environmental conditions are difficult, and several theoretical requirements or expectations are no more met. The problem of complex canopy and orography is clearly involved in the aforementioned mountainous regions, which are common in the World. In Italy, for example, hilly and mountainous regions are a highly representative part of the entire National territory.

Local energy, water and carbon fluxes can be modelled, but a more straightforward approach is to actually measure them. One of the most used techniques is the so-called “eddy covariance”, which allows a relatively direct estimate of fluxes.

Plus, a good understanding of the complex phenomena and processes which occur between the soil and the atmosphere is important for many reasons: the first is studying the eddy-covariance technique performance and then, the properties of the boundary layer and of mass and energy exchanges between the soil and the atmosphere (including radiative and non-radiative fluxes and other related quantities) in a complex environment. The second reason is to improve the estimation of fluxes (here the water and carbon ones are considered): this is important for the computation of energy and mass balances even in wintertime with snow on the soil. Indeed, snow plays an important role in the Alpine water cycle, since it provides, in mountainous areas, a water storage that lasts until summer.

Improving the evapotranspiration estimate computed from the latent heat flux leads to a better evaluation of the water balance and of the aquifer recharge. Multiple information allows to better define the water and carbon cycles at the catchment scale (or other scales).

To perform all the previous analyses, data collected at three eddy covariance stations (all beyond 1,700 m a.s.l.) in Valle d’Aosta Region are used. In addition, modelling tools are used with a focus on evapotranspiration at the site and at a regional scale.

Chapter 2

Theoretical framework

This Chapter aims at providing the general framework about eddy covariance technique (which is widely used to estimate energy and matter fluxes in this Thesis) and biogeochemical cycles. Emphasis is spent on turbulence theory and computing techniques to determine evapotranspiration, carbon dioxide and heat fluxes, as well as to illustrate the important concept of flux footprint, which will be more deeply addressed in Chapter 5.

2.1 Atmospheric boundary layer, turbulence and atmospheric motions

The atmospheric boundary layer (ABL) is the lowest part of the troposphere, which interacts with the soil and its surface. Because of this interaction, the air motion (and the energy and mass transport) is frequently turbulent. In this Thesis, a particular region of the atmospheric boundary layer is considered. It is called atmospheric surface layer (ASL) and it is the lowest part (about 10%) of the ABL. Within this region, the air is directly affected by the Earth's surface. Hence, the air flows are mainly subject to surface friction, interactions with obstacles and surface roughness and vertical gradients. In this layer, the air motions are almost insensitive to Earth's rotation, and the existing vertical gradients (included the shear stresses) can be considered almost constant.

Turbulence is an important part of atmospheric motions, but there is no specific and precise definition of what it is (Davidson, 2004). Considering a boundary layer, an important index of turbulence is the Reynolds number $Re = \frac{u\,d}{\upsilon}$ (where u is the velocity scale, d is the height of the layer and υ is the viscosity term). This number comes from the fact that the equations of fluid mechanics (the Navier-Stokes equation for instance) can be written nondimensionally

In a boundary layer (such as the ABL), a moving fluid can make a transition: starting from a laminar flow (if the fluid is Newtonian), in which the viscous and dynamic forces are of similar magnitude, there is then a region of transition to turbulence, in which the system begins to show chaotic fluctuations form and structures such as vortices and eddies appear. For Re >> 1, there is the full development of turbulence: it is still identifiable a mean steady motion of the fluid, but chaotic trajectories of its particles exist.

Considering the turbulent motion, we should spend some word about the different scales in turbulence, the energy cascade and the spectral properties.

2.1.1. Energy cascade and different scales

When we consider turbulence several hypotheses are made, but we want to know how to mathematically write the existent turbulent fluctuations. Every turbulent variable can be expressed as the sum of the average motion plus a stochastic deviation from the average, which is the turbulent one. So, turbulence can be seen as a stochastic process describing the chaotic motion of fluid particles: if we denote a generic process {Xt} which has the associated variable *a* (it can be a vector, a component of a vector or a scalar). The variable is written as in Eq. 2.1

$$a(x,t) = \bar{a}(x) + a'(x,t) \tag{2.1}$$

where the term $a(x,t)$ is instantaneous, $\bar{a}$ is the average value over any time window, and a' describes turbulent fluctuations

At any instant, *a'* can be seen as a chaotic collection of eddies at different temporal and spatial scales. The largest ones have sizes comparable with the characteristic geometric length (here denoted with *d*) scale of the mean flow.

Large eddies, due to the mean flow instabilities and less prone to viscous forces which are here negligible, tend to break because of inertial instabilities and new smaller vortices form. The lifetime of a vortex is very limited, and it is usually of the order of the "turn-over" time that scales with $\frac{d}{u}$, where *u* is the mean flow speed used as a scale of velocity. At the beginning, the formation of eddies and their splitting is governed by inertial forces and there is also the turbulent kinetic energy (TKE) transfer between the scales. TKE is defined as in Eq. 2.2.

$$TKE = 0.5\,(\sigma_u^2 + \sigma_v^2 + \sigma_w^2) \tag{2.2}$$

where $\sigma_u^2,\ \sigma_v^2, \sigma_w^2$ are the wind speed variances.

In turbulence studies, a very important topic is related to the spectrum of turbulence: eddies at various temporal scales can be analysed in the Fourier space throughout the Fourier transform. Usually, using time series it is useful to determine the autocorrelation of the signal.

If we consider the spectrum of the turbulent variable – for instance the wind speed – we should see sources of turbulence, a peak of spectral energy density and then a "Kolmogorov decay" having a slope of -5/3 in the inertial subrange, a region

in which the net energy associated with eddies, is in equilibrium with the net energy transferred to smaller eddies (so the energy flux is constant) . The shear stress is small, thus the dissipation of TKE is low.

Then, as the eddies become smaller and smaller, a greater amount of TKE is lost. The cascade is stopped when $Re \sim 1$: in this case, the energy is dissipated by the system. If we call l and η the largest and smallest length scales and u and v the velocities associated with the two respective previous scales, one can find that the smallest scale, known as the Kolmogorov scale, can be expressed using $\eta \sim l\,(Re)^{-\frac{3}{4}}$ which is usually less than 1 mm, while v scales as $v \sim u(Re)^{-\frac{1}{4}}$.

2.2 The eddy covariance technique

The eddy-covariance technique used in this Thesis to measure turbulent exchanges between soil and atmosphere, is a micrometeorological method which allows measures of momentum, mass and energy vertical turbulent fluxes (for a more detailed description see Arya, 1988; Stull, 1988; Foken, 2008a; Aubinet, Vesala and Papale, 2012). Fluxes at different time scales can be also computed. The technique is widely used because it is relatively simple to be applied and does not require any initial information about the vertical profile of the variables of interest. Plus, other approaches suggested for heterogeneous surfaces and for model validation (e.g. scintillometry, Vendrame et al., 2020) are not suitable in natural, not easily accessible sites, also given that the scintillometers are not easily installed.

The eddy covariance estimations are done by direct measurements of wind speed and air temperature, provided by sonic anemometers, and gas concentration provided by gas analysers. Several works have been done using this technique for many purposes: micrometeorological analyses on boundary layer structure and properties (Stiperski and Rotach.,2016), transport of pollutants or scalars and energy (Hiller et al., 2008, Feigenwinter et al., 2012; Vendrame et al., 2019), ecohydrological (e.g. Marks et al., 2008; Reba et al., 2012; Chang et al., 2013; Cammalleri et al., 2013) and ecological applications (e.g. Hammerle et al., 2007; Galvagno et al. 2017; Collalti et al., 2016).

The conservation equation of a scalar is the starting point of eddy covariance technique. The equation can be integrated within a control volume $V=2L \times 2L \times h_m$ to obtain Eq. 2.3.

$$\frac{1}{4L^2}\int_{-L}^{L}\int_{-L}^{L}\int_{0}^{h_m}\overline{So}\;dzdxdy \qquad \text{(2.3)}$$

V

$$= \frac{1}{4L^2}\int_{-L}^{L}\int_{-L}^{L}\int_{0}^{h_m}(\overline{\rho_d}\frac{\partial\bar{S}}{\partial t} + \overline{u\rho_d}\frac{\partial\bar{S}}{\partial x} + \overline{v\,\rho_d}\frac{\partial\bar{S}}{\partial y} + \overline{w\rho_d}\frac{\partial\bar{S}}{\partial z}$$

I II

$$+ \frac{\partial\overline{\rho_d}\overline{u'S'}}{\partial x} + \frac{\partial\overline{\rho_d}\overline{v'S'}}{\partial z} + \frac{\partial\overline{\rho_d}\overline{w'S'}}{\partial z})\;dzdxdy$$

III IV

So is the source/sink term, S is the scalar concentration, $\overline{u'S'}$, $\overline{v'S'}$, $\overline{w'S'}$ are the covariances between each wind speed component (*u, v,* w)and the scalar *S*, ρ_d is the dry air density.

Term I is the scalar storage, Term II is the scalar advection (3D), Terms III and IV represent the turbulent transport of scalar *S* and term V represents the source/sink of *S*. ρ_d is the dry air density, *S* is the scalar, *u, v, w* are the three wind speed components, *L* is one dimension of the control volume *V* and *h* is the measurement height.

To apply the eddy-covariance theory some assumptions have to be made:

1) Steady-state of the mean flow
2) Terrains flat and homogeneous
3) Validity of the Boussinesq approximation: air density fluctuations are negligible or, if not, Webb corrections have to be applied (Webb et al., 1980)
4) The turbulence has to be developed
5) The wind speed has to be symmetrical along the direction of the mean wind (isotropy property)

The total scalar flux can be represented as in Eq. 2.4, which is a simplified version of Eq. 2.3.

$$Fs = \int_{0}^{h_m}\overline{\rho_d}\frac{\partial\bar{S}}{\partial t}dz + \int_{0}^{h_m}\overline{w\rho_d}\frac{\partial\bar{S}}{\partial z}dz + \overline{\rho_d}\overline{w'S'} \qquad \text{(2.4)}$$

V I II IV

Term V is the scalar total flux. Term I is the scalar storage between 0 and the mast height. Term II is the vertical advection and term IV is the vertical turbulent flux at the control volume top and it is what can be actually measured at a single point.

Most common simplifications (Aubinet, 2012) imply that the horizontal gradients are small if compared to other terms. Besides, the measured turbulent motions should represent the entire measurement volume. These hypotheses, together with the assumptions earlier enumerated and anemometer coordinate

rotation techniques allow to account only for term IV (that is the only measured divergence, with one measurement level).

As a first approximation, one can write that $Fs = \overline{\rho_d}\overline{w'S'}$, also because the advection estimate is not trivial, and, as already mentioned, at a single point the advection cannot be actually measured.

The term $\overline{w'S'}$ is a covariance, hence it is statistically defined as in Eq. 2.5.

$$\overline{w'S'} = \frac{1}{N-1}\sum_{k=1}^{N}[(w_k - \overline{w_k})\,(S_k - \overline{S_k})] \tag{2.5}$$

2.2.1 Description of the eddy covariance assumptions

The steady-state assumption can be considered valid if temporal averages not beyond 1 hour are considered. To test the assumption, some test has been proposed (see for example Hammerle et al., 2007; Aubinet, Vesala and Papale, 2012): Usually the fluxes averaged over 5 minute and over 30 or 60 minutes are determined and their absolute difference is computed. This value is then divided by the flux averaged on the current timescale (e.g. 30 or 60 minutes), as in Eq. 2.6

$$\Delta_{stationarity} = \frac{\left|\overline{w'S'}_5 - \overline{w'S'}_{30}\right|}{\overline{w'S'}_{30}} \tag{2.6}$$

If this value exceeds an imposed threshold, the datum may be regarded as non-stationary. Other tests are introduced by Foken and Wichura (1996) and by Vickers and Mahrt (1997).

There are several methods to improve the flux steadiness (Moncrieff et al., 2004): among them, there are the block average, the linear detrending and recursive filters such as the moving average or the moving median. It has to be noted that the only method which satisfies the Reynolds averaging is the first one. The choice of the method depends on what is the goal and on the site characteristics.

We are working on the hypothesis that convective structure does not vary in time and space when crossing the sensors (frozen eddy or frozen convection assumption, made firstly by Taylor in 1938). One of the most recent flagging policy in data quality was introduced by Mauder and Foken in 2004 in the CarboEurope framework. It is based on a three-level flagging (2 = low quality; 1 = medium quality, to be used only in long-term analyses; 0= high-quality data) using the steady-state and the integral turbulence tests on the data. The integral turbulence test (ITC) can give an estimation of the conditions of a well-mixed boundary layer and therefore the conditions of sufficient turbulence. In particular, the Monin-Obukhov similarity theory is here used and improved by the studies by Foken et al. (1991), Johansson et al. (2001) and Thomas and Foken (2002): in general, a good index of the turbulence magnitude is the flux variance similarity, so the ratio

between the standard deviation of the variable of interest divided by the turbulent flux of that variable (Eqs. 2.7 and 2.8):

$$\frac{\sigma_{u,v,w}}{u^*} = c * \left(\frac{z}{L}\right)^a \tag{2.7}$$

$$\frac{\sigma_T}{T} = c * \left(\frac{z}{L}\right)^a \tag{2.8}$$

These are general formulations, but with varying atmospheric stability, the above parameters *a* and *c* vary and other studies proposed formulas that should be used for the wind speed components in the cases of neutral and unstable cases (Panofsky et al., 1977) and in case of slightly unstable and stable stratification (Thomas and Foken, 2002, Foken et al., 1997).

Usually, these ratios can be expressed as a function of the stability parameter z/L and of the Coriolis parameter, *f*. So, the ITC can be defined as in Eq. 2.9.

$$ITC = \left| \frac{\left(\frac{\sigma_X}{X^*}\right)_{model} - \left(\frac{\sigma_X}{X^*}\right)_{measured}}{\left(\frac{\sigma_X}{X^*}\right)_{model}} \right| \tag{2.9}$$

If the test parameter ITC is less than 30%, a well-developed turbulence can be assumed.

According to the two tests results, an overall flagging 0 -1-2 can be developed, as was already mentioned.

Flat and homogeneous terrains would be theoretically required, for eddy covariance use, but several works (Hammerle et al., 2007; Hiller et al., 2008) have demonstrated that even if we consider neither flat nor homogeneous terrains, provided that we make quality controls on data, the resultant fluxes are similar from a quality point of view to those obtained in classical conditions of the theory applicability and are reliable.

The Boussinesq approximation is considered valid in a wide range of conditions and cases, while the fully-developed turbulence should be tested using, for instance, the standard deviation of the wind speed vertical component in extremely stable weather conditions, else the friction velocity can be used. The friction velocity (u^*) is a generalised velocity scale which is defined as the shear stress divided by the air density, and it can be also defined as in Eq. 2.10.

$$u^* = \left(\overline{u'w'}^2 + \overline{v'w'}^2\right)^{\frac{1}{4}} \tag{2.10}$$

where $\overline{u'w'}$ and $\overline{v'w'}$ are components of the stress tensor τ and are covariances of between the wind speed components *u* and *w* and *v* and *w*.

The fifth hypothesis, together with the second, allows assuming that the average vertical wind speed and the cross-correlation between wind speed components are close to zero. This property can be obtained also in complex terrain using some streamwise alignment choice (e.g. either double rotation or planar fit techniques).

If these hypotheses are verified, the covariances averaged on a time interval, between vertical wind speed component, normal to a plane and the scalar quantity or other velocity components represent the kinematic flux of the quantity across the plane surface (Kaimal and Finnigan, 1994).

2.2.2 Averaging period choice

One important step prior to beginning computations is the choice of the averaging period (T_A)on which flux calculations have to be done. The steadiness of the mean flow has to be satisfied and, if the observer wants to perform turbulence studies, all the high-frequency contributions to the signal shall be included but eddies at larger scales (both spatial and temporal) should be removed. Usually, the existence of an integral time scale $T = \int \rho(\tau) d\tau$, with $\rho(\tau)$ being the autocorrelation function.

There are several approaches to estimate the averaging period (T_A): for example, Lumley and Panofsky (1964) suggested an empirical formula. Recently the application of the ogive function (Lee, Massman and Law, 2004; Foken et al., 2004) has been proposed: the ogive and the cospectrum (the real part of cross-spectrum of a variable) share the same information, because each point of the ogive represents the integral under the spectral density curve between the highest and the selected frequency of interest. When the ogive curve reaches its asymptotical value, then this means that the observer has sampled for a time long enough.

Another very useful technique is the so-called multiresolution flux decomposition, MRD (Howell and Mahrt, 1995; Vickers and Mahrt, 2003). Without entering in too many details, the decomposition finds its basis in the averaging the time series using several averaging lengths (they can be spatial or temporal). Using time series averaged with many averaging lengths is equal to observing data at different resolutions. If we look at the differences between data at two different temporal resolutions, we will obtain a multiresolution cospectrum value. Usually, multiresolution cospectra start with a value near to 0 and after some time return to 0. The time at which there is the second zero crossing is considered a good averaging time. (Stiperski and Calaf, 2017). See Chapter 4 and Appendix A for further details.

2.2.3 Filtering data and identification of turbulent conditions

The measured data are raw and shall be treated before further analyses. Several approaches and algorithms are aiming at the elimination of unphysical values and outliers, which could lead to wrong results, and at the assessment on the data quality, analysing skewness and kurtosis of time series principally (Vickers and Mahrt, 1997; Mauder et al., 2013; Massman, Lee and Law, 2004; Foken, 2004). Outliers can be excluded and in the present work the algorithm introduced by Mauder et al., 2013 will be used. Another important issue is the malfunctioning of instruments due to technical failures, very bad weather conditions (heavy rain or snowfall, the formation of water droplets on the sensors) or other causes.

Time lags between measured time series could also be important especially if the instruments are very far the one from the other.

2.2.4 Streamwise alignments

Very often, eddy covariance set-up is not located in ideal conditions, so it is also necessary to use a streamwise alignment if the wind flow has a non-zero vertical component and a cross-correlation between the three wind components on average. This effect is more apparent over complex land (for example in mountain valleys, McMillen, 1988). Thus, a reference frame change is needed to nullify the vertical wind component (and also one horizontal to obtain all the information on one component). The streamwise alignment allows finding a new system orientation along the main (mean) flow direction. There are two main methods to do the mentioned alignment: the double (or triple) rotation (Foken, 2004) and the planar fit (Foken, 2004; Lee, Massman and Law, 2004; Wilczak et al., 2001).

Double and third rotation

Each anemometer has its own reference frame and so, to perform the aforementioned alignment a rotation matrix has to be found and applied to the original wind speed vector. A new reference frame is found together with a new wind velocity vector. Depending on the chosen time averaging, the rotation can be applied for each time interval. The double rotation yields a vector with nullified cross-wind and vertical wind speeds. It is possible to perform a third rotation around the new x-axis (with a further rotation matrix applied to the double-rotated data). This allows eliminating the covariances between cross-wind and vertical wind speeds. However, the third rotation is no more recommended (Aubinet et al., 2000; Foken, 2004).

Planar fit

Starting from the instrument reference system and provided that the instruments are not moved from their position for at least two weeks, firstly we have to find a period of interest of at least one or two weeks, assuming that the instruments were not moved at all. Then, using the mean velocity components in the old reference frame, the linear regression $\overline{w_1} = b_0 + b_1\overline{u_1} + b_2\overline{v_1}$ has to be performed to define the mean streamline plane. The regression coefficients are used to determine pitch, roll and yaw angles and so a rotation matrix. The velocity vector is therefore expressed using the new reference system through a projection of the old vector in the new coordinate system (Wilczak et al., 2001; Van Dijk et al., 2004). The planar fit can also be applied without the velocity bias (so with b_0 = 0) or sector-wise by identifying several wind direction sectors and performing for each sector a linear regression. However, in very complex terrains is difficult to use the planar fit technique, since the wind flow may not be planar. The sectorwise planar fit might be more useful, but it requires a multi-directional wind rose. Besides, the planar fit technique requires a constant position of the anemometer, which may not be satisfied also due to the pole oscillations in locations with high wind speed.

2.2.5 Spectral and WPL corrections

It is known that the turbulence energy spectrum shows all the frequencies. The problem is that sometimes we only want to analyse a particular part of the spectrum (i.e. the turbulent one). Besides, instruments have a limited sampling rate and there are set-up issues: support structures, the distance between sonic anemometer(s) and gas analyser(s)): this suggests that we cannot make measurements at time scales lower than the sampling resolution, which acts as a low-pass filter on the data. The averaging period itself can be identified as a high-pass filter. Aliasing and leakage problems on time series might also arise. Because of these problems, spectral corrections are usually applied. Several techniques are commonly used (e.g. Moncrieff et al., 1997; Moncrieff et al., 2004).

Until the 1980s, the eddy-covariance technique was used assuming negligible air density fluctuations, but usually, in the real world, this is not true, especially for non-vertical wind speeds. In the paper by Webb et al., 1980, a procedure to correct turbulent fluxes according to density fluctuations was introduced. This correction is nowadays recommended for heat fluxes, but it is not necessary for the carbon dioxide flux (Aubinet et al., 2000).

2.3 Flux footprint

Ideally, flux measurements, in particular eddy-covariance ones, should be made on relatively flat and homogeneous terrains, which are rarely found. In non-ideal conditions, to better understand what we are measuring and what is the source area of the measured fluxes, the knowledge of the footprint is very useful.

The site footprint is defined as the area upwind the sensors which contribute to the measured quantities (energy, mass) with both sources and sinks contributing to the measuring point (Aubinet et al., 2012). There are mathematical functions representing the flux footprint. They put in relation the measured signal with the spatial distribution of every source or sink that can be found in a certain area near the sensors. The flux measured in a point is expressed as in Eq. 2.11:

$$F(x) = \iiint f(\vec{x}, \overrightarrow{x'}) Q(\overrightarrow{x'}) d\overrightarrow{x'} \tag{2.11}$$

where $F(x)$ is the measured quantity, generally a flux, $\vec{x}$ is a three-dimensional vector, Q is the emission/sink rate in the considered volume. This is a general formulation, which, depending on the footprint function and applying discrete integration schemes, yields more or less complex functions that allow expressing the desired flux. The simplest footprint description is one-dimensional, along the wind flow direction. A 2D approach can be used to describe the lateral diffusion which is often assumed Gaussian.

In several models, the footprint function and therefore the fluxes functional forms, depend on the stability regimes (Aubinet et al., 2012). There are two main branches of models: on one hand, models using analytical functions (analytical models): here there is a strong dependence on the turbulence regime and therefore on the atmospheric stability. On the other hand, models using stochastic approaches and large eddy simulations (Lagrangian stochastic models). Analytical models derived from Lagrangian model outputs are also possible (e.g. Hsieh et al., 2000). Although the latter models can be used in any turbulence regime, the turbulence field shall be defined and they are not uniquely defined, in the sense that several stochastic models satisfy a particular regime. Boundary layer models can also be used for footprint computation purposes, but parameterisation schemes about the turbulence closure are needed.

Depending on the type of land cover, the wanted degree of complexity and purposes, there are several choices already available. Among the most recent analytical models, there are the ones proposed by Baldocchi et al. (1997) and Klaasen and Sogachev (2006) for forests. Hsieh et al. (2000), Kormann and Meixner (2001) and Kljun et al. (2002) proposed models mainly for flat terrains. Sogachev and Lloyd. (2004) proposed an approach for a non-flat topography, Vesala et al. (2008) proposed a footprint estimate in complex urban areas. These are, as many others, diffusion models which assume a homogeneous and flat

surface. They take usually into account the upwind contribution, but the lateral diffusion can be considered as well, for example using a Gaussian formulation (Detto et al., 2006). Kljun et al. (2015) proposed a 2D model that is still characterised by a simple approach, but it has a deeper level of detail and it is valid for a wider range of stability classes. In addition, it does not require a strict application of MOST scaling.

When the terrain is non-homogeneous, usually complex approaches are proposed and closure model approaches are usually adopted. Therefore, equations of mass conservation and momentum, as well as the TKE and scalars are written and then numerically solved, with a computing effort. A good footprint estimate allows better identification of possible flux sources and sinks and also to reconstruct the net radiation over a small domain around the measurement site, also by means of a digital elevation model and a global radiation model. The approach is useful for a better estimation of the net radiation, weighted by means of the footprint.

The flux footprint is important to understand what area contributes to the measured fluxes at the station, but also for other purposes. Among them, we find the correction of net radiation. One of the problems related to eddy covariance is the well-known energy imbalance. Although it is true that turbulent fluxes might be underestimated, another problem, as pointed out by Wohlfahrt et al. (2016) is that usually, horizontally measured net radiation should be corrected according to slope and aspect if flux measurements are taken on a slope. Furthermore, shortwave radiation components and also net radiation are measured at one single point (the eddy covariance tower). However, especially in complex terrains with slopes and also changing aspect, and with fluxes that come from the area surrounding the station, it might be useful to reconstruct the net radiation on the area that coincides with the footprint itself. Indeed, net radiation is among the most important components of the radiative energy balance. Insights of footprint modelling and corrections will be illustrated in Chapter 5.

2.4 Ecosystems and biogeochemical cycles

There are many biogeochemical cycles. Among the most studied, we find the water cycle and the carbon cycle. The first one is related to all the processes involved in water transfer between land surface (biosphere, lithosphere, cryosphere) and atmosphere. Within the water cycle (Figure 2.1) we find evaporation from land, rivers, lakes and oceans; transpiration from vegetation, sublimation from ice and snow; runoff on land and infiltration of water in the soil (and therefore soil moisture); precipitation; water transport in the atmosphere and atmospheric moisture.

The carbon cycle (Figure 2.2) is related to the carbon transfer, again between land surface and atmosphere. The main component of this cycle is carbon dioxide, which is one of the most important greenhouse gases. Nowadays, carbon is emitted

by human activities (land use included), vegetation respiration, outgassing from water bodies, volcanoes. Sinks of carbon are plants throughout photosynthesis; ocean, lake and sea uptake; land sink; rock weathering; fossil fuel reservoirs; marine sediments formation; carbon exchanges happen also in permafrost areas and through atmosphere and ocean exchanges. It can be noted that the modern carbon cycle includes also human emissions (both carbon dioxide and soot, being part of smog), which are nowadays non-negligible.

Climate change is evident (IPCC AR5, 2014) and it is also altering the aforementioned natural cycles involving feedbacks, such as carbon cycle and water vapour feedbacks (both positive: the higher the temperature is, the more carbon dioxide and water vapour will be held in the atmosphere because of atmosphere dilatation and increased emission from land). Other feedbacks include the cloud and ice-albedo ones. While it is difficult to predict the cloud evolution in the future (there is uncertainty about whether there will be severe changes in either low or high clouds and this could change the feedback's sign. Low clouds tend to cool Earth's surface because they capture shortwave radiation, high clouds absorb more infrared radiation thus increasing the temperature of the lower atmosphere and Earth's surface), it is certain that the ice-albedo feedback is positive. Shorter snow seasons (e.g. Klein et al., 2016) and ice loss due to Summer melting increase exposed rocks area, thus increasing the fraction of solar radiation absorbed by the surface, increasing, in return, temperature.

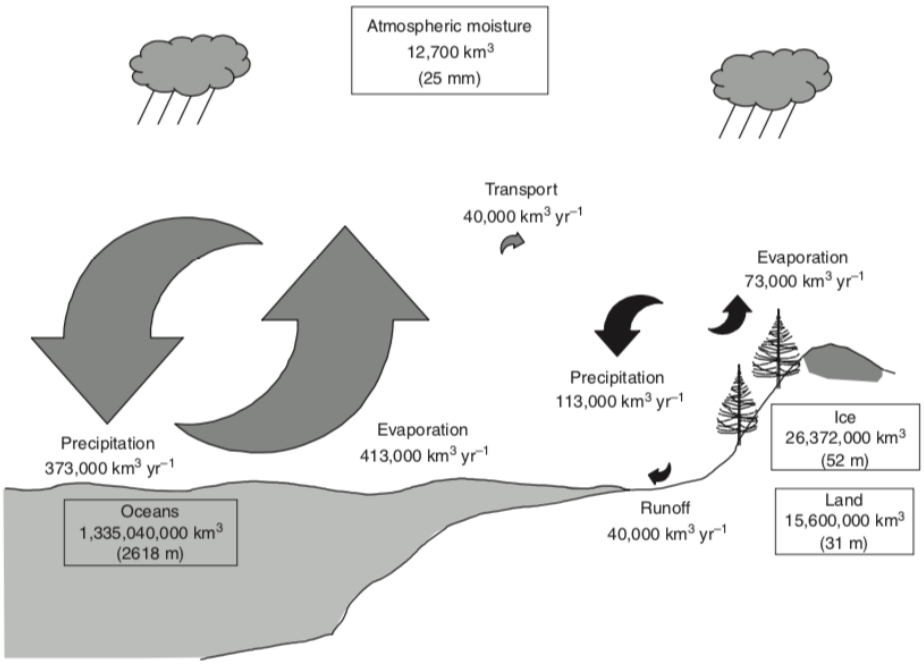

Figure 2.1. Water cycle cycle components. (From Bonan, Ecological Climatology, Third Edition, 2016).

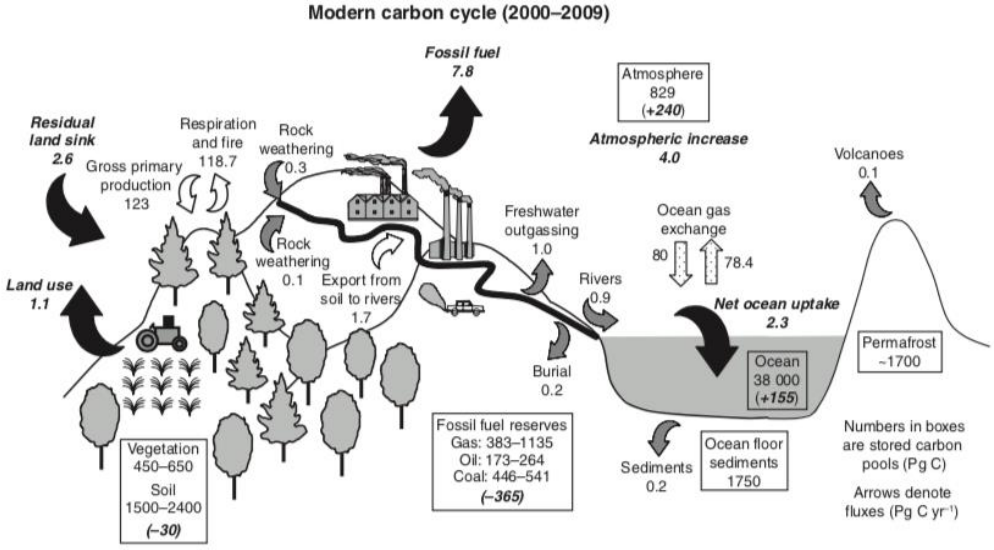

Figure 2.2. Carbon cycle and its components. (From Bonan, Ecological Climatology, Third Edition, 2016).

Chapter 3

Experimental sites

The measurement sites used for this Thesis are located in the Cogne Valley and at Pian del Nivolet, both in the Gran Paradiso National Park. A third station, used in Chapter 5, is managed by the Valle d'Aosta Regional Authority (ARPA VdA), and it is described by Galvagno et al. (2017). The stations aim at monitoring the radiative (latent and sensible heat fluxes) and non-radiative fluxes (ground flux, carbon dioxide and water vapour fluxes). Both the stations are located on natural grasslands, since it is still a poorly explored type of terrain, at least using the eddy covariance technique for the atmospheric part, as will be also described in Chapter 6.

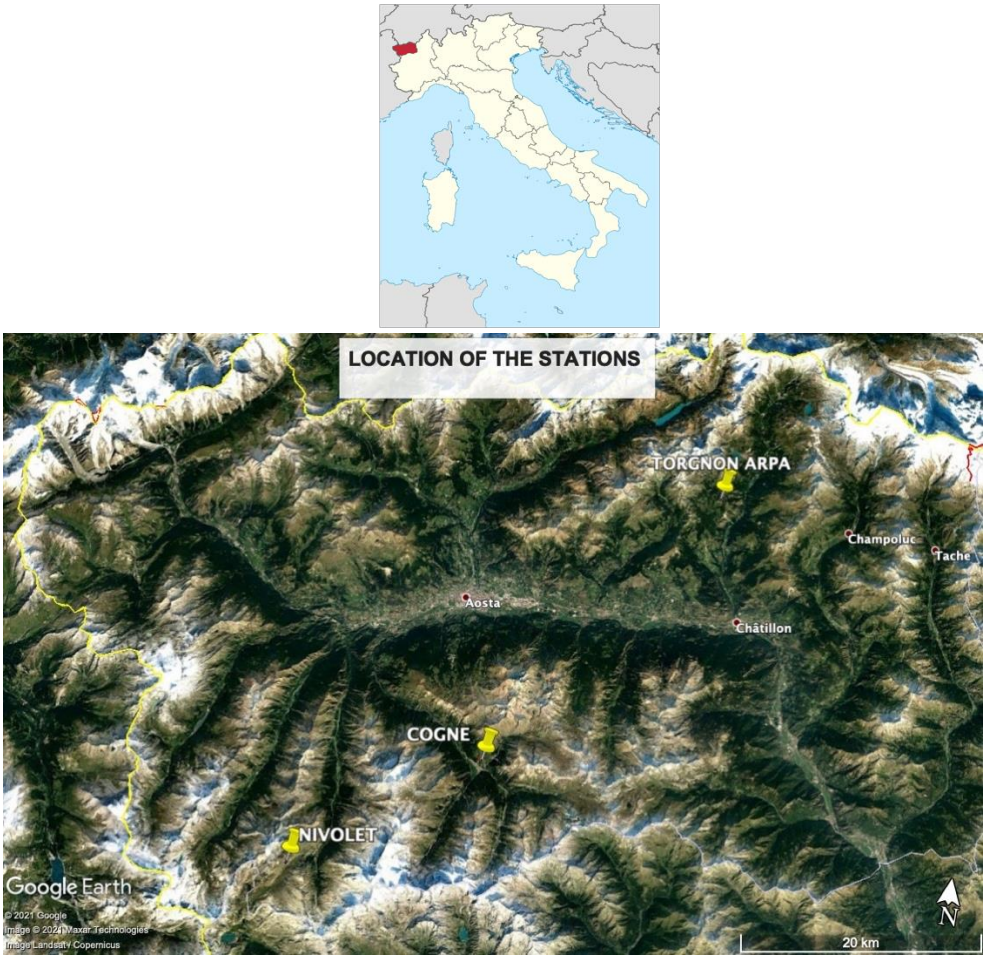

Figure 3.1. Location of the eddy covariance sites in Valle d'Aosta Region. For completeness, the Torgnon site is also shown.

Figure 3.2. The Nivolet experimental site for water vapour, carbon dioxide and soil properties measurements.

The stations (In Figure 3.1 is shown their location in Valle d'Aosta Region, Italy, while in Figure 3.2 the Nivolet site set up is shown), are mainly characterised by one sonic anemometer to measure the wind speed, an open path infrared gas analyser to measure water vapour and carbon dioxide content in the atmosphere, and a thermohygrometer. Two probes measure the ground heat flux at two different depths and two additional probes using the time-domain reflectometry technology measure the soil water content.

The first measurement site is located in Cogne (45.615 N, 7.3585 E), Valle d'Aosta, Italy. The station is at 1730 m. a.s.l. on a steep 150 m long slope of 28°, in a small lateral valley with South-South East aspect. The vegetation is characterised by herbaceous species (mostly Festuca, with a canopy height of about 0.3 m) and shrub (buckthorn bushes, *Lycium, Eleagnus Rhamnoides*, with a typical height ranging from 0.8 m to 1 m) This vegetation is typical for abandoned pastures at high altitudes, making this site is representative for a wide amount of areas in the Alps.

The soil depth ranges from 0.4 to 1.5 m and consists of a sandy loam texture with some gravel (≈73% sand, 22% loam and about 5% of clay). The measured soil bulk density is $1.4 * 10^3$ kg m^{-3}. Finally, the measurement site is located on unmanaged land, next to a very small creek (East of the station) and no irrigation has been done for at least four decades.

The region is characterised by climatic continental conditions with cold winters and hot summers; precipitation occurs mainly in spring and autumn, with an average of 650 mm per year. The average annual temperature is about 4°C. The experimental site is characterized by large amounts of incident solar radiation due to its aspect and distance from the other side of the valley. This can result in large daytime turbulent fluxes and enhanced daily temperature variations. The site is one of the few characterised by abandoned grassland with shrubs encroachment.

At a distance of 150 m from the site, there is a Regional Authority meteorological station with standard hourly measurements of air temperature,

relative humidity, atmospheric pressure, wind speed and direction, global radiation, insolation, and precipitation (measured by a heated automated rain gauge).

In Tables 3.1 and 3.2, the measurement instruments and probes are listed.

Table 3.1. Meteorological measured variables and sensors

Wind speed components *u,v,w (m s^{-1})* and sonic temperature *Ts (°C)*	CO_2 concentration *(mg m^{-3})*, water vapour concentration *(g m^{-3})*	Longwave *(LWin,LWout)* and shortwave *(SWin, SWout)* radiation *(W m^{-2})*	Net radiation *Rn (W m^{-2})*	Precipitation *P (mm)*	Snow depth h_{snow} *(m)*	Air temperature and relative humidity *Tair (°C)* *RH (-)*
Campbell Scientific CSAT 3	LiCor LI-7500A	Hukseflux NR01 radiometer 4 components	Kipp&Zonen NR-LITE	manual rain gauge	Campbell Scientific SR50AT	Vaisala HMP 145
Horizontally displaced 2010-2011 at 2m height; Slope parallel October 2011- at 1.80 m height		Slope parallel 2015-	Horizontally displaced 2010-			

Table 3.2. Soil and soil surface measured variables and sensors.

Ground heat flux *G (W m^{-2})*	Soil temperature *Tsoil (°C)*	Surface temperature *Tsurf (°C)*	Volumetric soil water content θ (m^3m^{-3})
Hukseflux HFP01SC	Campbell Scientific TCAV probes	IRTS-P Infrared sensor	Campbell Scientific CS616
2 probes at -8 cm	2 probes at -8 cm		2010-2015 -10 cm 2015- -20 cm -40 cm

The Nivolet site activity was partially financed by Ecopotential, a European-funded H2020 project focusing on the monitoring of protected areas and the second site, installed in Autumn 2017 was installed on a 2° slope on a steep ridge (> 20°) with a South-South East aspect near Nivolet Pass in Aosta Valley at an altitude of 2,600 m a.s.l. (Latitude: 45.520N; 7.172E). The area surrounding the station is almost flat and it is characterised by a typical Alpine grassland, made mainly of

Alpine clover (*Trifolium alpinum*), Fescue (*Festuca)*, lowbush blueberry (*Vaccinium angustifolium*) and Gentiana (*Gentiana iutea, Gentiana* sect. *ciminalis, Gentiana acaulis*). The Nivolet site site is characterised by a long-lasting snow layer (generally from November to the first two weeks of June). The mean annual temperature is 1.4°C and the annual precipitation is about 1260 mm.

In Tables 3.3 and 3.4, the measured variables, instruments and probes are listed.

Table 3.3. Meteorological measured variables and sensors

Wind speed components *u,v,w* ($m\ s^{-1}$) and sonic temperature *Tsonic (°C)*	CO_2 concentration ($mg\ m^{-3}$), water vapour concentration ($g\ m^{-3}$)	Longwave *(LWin,LWout)* and shortwave *(SWin, SWout)* radiation ($W\ m^{-2}$)	Precipitation *P (mm)*	Snow depth h_{snow} *(m)*	Air temperature and relative humidity *Tair (°C) RH (-)*
Campbell Scientific CSAT 3	LiCor LI-7500A	Hukseflux NR01 radiometer 4 components	manual rain gauge	Campbell Scientific SR50AT	Vaisala HMP 155
Horizontally displaced at 4.6m height October 2017-	October 2017-	October 2017-	October 2017-	October 2017-	October 2017-

Table 3.4. Soil and soil surface measured variables and sensors.

Ground heat flux *G* ($W\ m^{-2}$)	Soil temperature *Tsoil (°C)*	Surface temperature *Tsurf (°C)*	Volumetric soil water content $\theta\ (m^3m^{-3})$	Matric Potential $\psi\ (kPa)$	Soil temperature *Tsoil (°C)*
two probes Hukseflux HFP01SC at -8 cm from 1 August 2019	Campbell Scientific TCAV probes at -8 cm from 1 August 2019	IRTS-P Infrared sensor October 2017-	Decagon EC5 August 2018-	Decagon MPS-6 January 2019-	Campbell Scientific T107 January 2019-
2 probes at -8 cm	2 probes at -8 cm		-10 cm -20 cm -40 cm	-10 cm -20 cm -40 cm	-10 cm -20 cm -40 cm

Chapter 4

Eddy covariance data processing, quality control and surface energy balance

This Chapter is devoted to understanding if the data collected at the eddy covariance sites described in Chapter 3 and located in complex terrains, can be reliable and to what extent they are characterised by good quality. The analyses in this Chapter were performed by the Author of the Thesis. The only part that uses an external source is the one about the multi-resolution decomposition algorithm, for which the Author thanks Dr Ivana Stiperski, who provided the software code for the analysis. Experimental data starting from 2017 onwards were mainly managed by the Author thanks to the LABFLUX Team support.

4.1 Introduction

As it has been illustrated in Chapter 1, the study of air-land interactions in the mountains is challenging because of the complex orography. Tall canopies and sloping terrains make the turbulence structure more complex. Terrains not homogeneous and flag produce irregularities in the streamline flow, and add divergence of advective fluxes. Plus, the air flow is affected by valleys, slopes, and obstacles.
One of the first studies dealing with eddy covariance technique in non-ideal terrains was described by McMillen et al. (1988). They found that, with an appropriate set of data processing combination (time lag removal, coordinate rotation and "detrending" techniques, the computation of turbulent transfer of energy and mass is possible even in complex sites.

Lee (1998) described a method to consider the vertical advection for CO_2 measurements in complex terrain, making possible further studies on advection in such terrains.

Geissbühler et al. (2000) stressed the importance of measuring energy and mass fluxes in the mountains, as well as the need of methods to cope with measurement errors due to flow distortion related to topographic and surface non-homogeneities, were stressed. The surface normal orientation of instruments was proposed, as this choice was considered more reliable than the horizontally mounted setup, due to

lower flow distortion. However, results given by Geissbühler et al. (2000) showed negligible difference between the means and variances of measurements collected from horizontally and slope-normal mounted instruments. Geissbühler et al. (2000) concluded that the evaluation of fluxes in complex terrain might be less delicate than expected. (See also Finnigan, 2008 and Sun, 2007).

Baldocchi et al. (2000) studied and applied the Lee (1998) correction on an undulating terrain with a tall forest. They concluded that the proposed correction was useful but some improvement was needed.

Turnipseed et al. (2003) also described the possibility of using the eddy covariance on slopes, and remarked that EC method is among the most reliable and accurate. The local effects of canopy and topography and of the local flow on the turbulent structures were explored, concluding that they were similar to simpler conditions and that eddy covariance can have good reliability during unstable or neutral atmospheric conditions on slopes. The site was located on a gentle slope of about 5° to 7° and the quality control was performed on integral turbulence conditions, without many other considerations, yielding good results. Hammerle et al. (2007), performed an analysis on carbon dioxide, sensible and latent heat flux data collected in two sites, one located on a flat terrain, and the other located on a 24° slope. They compared two sites, one on almost flat terrain and one on a slope and concluded that the technique can be used adequately. Hiller et al. (2008) measured water vapour and carbon dioxide fluxes on a complex terrain to investigate the applicability of the eddy covariance on an inhomogeneous terrain and the energy imbalance. Furthermore, they evaluated if the carbon dioxide flux measurements are reliable. In that paper, an 82% energy balance closure was obtained, and they concluded that the eddy covariance measurements were applicable to their mountain site. Etzold et al. (2010) found that sloping sites may have the possibility to simplify the advection measurements to a two-dimensional geometry measurement because the wind field has 2D characteristics. This condition is due to the local wind systems (slope or valley winds). It was also shown that the advection on a steep slope (of 24°) is comparable to the advection existing in less steep slopes or even over flat terrains. Other two recent works investigated advection over complex terrain. Feigenwinter et al. (2010) used data collected at South-exposed steep Alpine slope with a up/downslope wind regime. They showed that taking into account the advection would reduce annual estimates of CO_2 uptake. Siebicke et al. (2012) used several approaches to evaluate advection and concluded that the advective contribution was low during daytime but higher at night and in transition evening hours. Besides, Galvagno et al. (2017) showed that in complex terrain the role of advection might be important especially for nighttime measurements of carbon dioxide. The addressed topic, however, is difficult to be estimated in several conditions especially in sites where short experimental campaigns (where at least one EC setup has to be moved at different distances) for advection estimate are not well suitable.

Other works were based on the slope-dependency of the similarity scaling, and deviations from the usual Monin-Obukhov Similarity Theory (MOST) found in

complex terrains: Nadeau et al. (2012) studied the similarity scaling on a steep slope and found that, as is also pointed out by Sfyri et al. (2018), it is site-dependent and differs from the MOST scaling, which was developed for a flat and homogeneous terrain. To investigate slope flows and small-scale physics occurring close to the surface (namely the evening transition of slope flows on clear-sky summer days), Nadeau et al. (2013) deployed two turbulence towers (single and multi-leveled measurement) and several meteorological stations (two weather stations, five surface temperature measurement stations and a tethered balloon system) along a transect on a steep mountain west-faced slope in the Swiss Alps from 1900 to 2200 m a.s.l. They found that the timing and the dynamics of the evening transition of slope flows (from convective to katabatic) is mostly controlled by the local radiation balance, a "shadowing front" occurs and propagates along the slope. About 1.5 h after the sunset is required to reach a quasi-equilibrium for the katabatic flow.

The existing literature indicates that eddy covariance measurements in complex terrain are possible, but suggests to develop and implement a reliable site-dependent quality control.

4.1.1 Data processing

Coordinate rotation has to be applied when advective fluxes are considered non-negligible and the mean vertical wind speed is not zero (Foken, 2008a), as also illustrated in Chapter 2. Finnigan (2004), described two reference systems, namely the Cartesian and the streamlines coordinate systems and found that in steep topography the advantages of using the streamlines are reduced and the results given by the two approaches are similar.

The question, whether to use the double rotation or the planar fit (described in Chapter 2), depends mainly the local topography. Shimizu et al. (2015) used a novel approach considering a fixed coordinate system, whereas during nighttime they used the sector-wise planar fit.

Hammerle et al. (2007), Wohlfahrt et al. (2008) and Mauder et al. (2013) used the simple planar fit. Etzold et al. (2010) used the double rotation, even though they worked on a slope. Yuan et al. (2011) modified the planar fit technique to take into account the dependence of the regression coefficients on wind direction and introduced a sector-wise fit.

Gerdel et al. (2015), again operating on a slope, used the double rotation. Oldroyd et al. (2016), introduced a new approach to optimize the sectorwise planar fit (SPF), suggesting it in case of measurements on slopes. However, Stiperski and Rotach (2016) found that the processing and post-processing choices, as well as the quality controls were site-dependent and were essential for a defensible analysis which relies on the eddy covariance technique. The double rotation was found to be most suitable in general for energy and mass balance purposes.

Another issue is related to the flux corrections needed to take into account humidity effects on sensible heat flux (Schotanus et al., 1983) and air density fluctuations (Webb et al., 1980, then revised by van Djik et al., 2004). The latter correction is also known as WPL and, although it does not comply with Reynolds decomposition, it is still used (Masseroni et al., 2013).
Stiperski and Rotach (2016) tested multiple data processing algorithms, concluding that they are site-dependent, although for "budgeting" purposes, the double rotation yielded the best results.

4.1.2 Quality controls on fluxes

Foken and Wichura (1996) introduced the first system of quality flagging based on steady state and developed-turbulence tests, while Vickers and Mahrt (1997) developed a powerful set of quality controls for data screening on single raw variables, which helps the identification of either a possible instrument malfunction or bad meteorological conditions.

Geissbühler et al. (2000) used a data quality assessment based on Foken and Wichura (1996): the standard deviation of the vertical wind speed, normalized by friction velocity u^* – defined as in Eq. 2.9 - was used, but large variations of the stability parameter were found under stable conditions. In the same paper, a test using the bulk drag coefficient was proposed, but it depended on the sensor height normalised by the roughness length, which can be variable in inhomogeneous terrains.

Foken et al. (2004) elaborated a quality flagging system based on Foken and Wichura (1996) with nine classes of quality (0 being the highest rank and 9 the lowest one). Mauder and Foken (2004), in their report for the CarboEurope standard, elaborated a 0-1-2 flagging system based on the aforementioned papers by Foken et al. (2004) and Foken and Wichura (1996). Papale et al. (2006) introduced some concepts about the impact of several choices on data quality on the total data set and on the available carbon dioxide flux (more in detail, on the Net Ecosystem Exchange).

In Hammerle et al. (2007), data quality control was carried out using mainly the steady state, the integral turbulence characteristics and u^* filtering tests. They did not find great differences between fluxes determined on the flat terrain and those estimated on the slope, but their quality control did not include the Vickers and Mahrt tests. Wohlfahrt et al. (2008) introduced the following procedure: screening for unphysical values (but only for carbon dioxide), elimination of data about CO_2 mixing ratio and pressure having the coefficient of variation outside a determined range, the Foken and Wichura tests and the evaluation of the maximum footprint function. At the end, a u^* filter was adopted. Hiller et al. (2008) showed that the flux data quality on turbulence theoretical requirements can be used even in complex terrain, although it was pointed out that some of the hypothesis on which the original eddy covariance theory was introduced are not met. The data quality

was focused on the work by Foken and Wichura (1996), but several other crosschecks were made. Göckede et al. (2008) used the flagging scheme of Foken et al. (2004) and implemented it with a footprint filter. In that paper, no u* threshold was used. Mauder et al. (2013) introduced a detailed quality control, but in complex terrains it is not easy to define and compute stochastic errors and a footprint. Stiperski and Rotach (2016) used some of the statistical tests described by Vickers and Mahrt (1997) on raw high frequency time series, namely the skewness and kurtosis on temperature and wind components, but the quality was not assessed in terms of the turbulence and steady state theoretical requirements because it was not necessary for their site. Sfyri et al. (2018) used the same quality control as Stiperski and Rotach (2016).

Concluding, the theoretical issues and quality control are an important step of eddy covariance post-processing, to ensure that the measures are reliable and can be used for ecological and hydrological studies and for modelling purposes. Several approaches exist, but the procedures are site-dependent.

4.1.3 Surface energy balance closure

According to several works among which we find Foken et al. (2006b); Foken (2008), Hiller et al. (2008); Masseroni et al. (2014), and also more recent papers (e.g. Eshonkulov et al., 2019 a,b), the energy balance is an open issue, but during the last decades progresses have been made. Aubinet et al. (2000) and Wilson and Baldocchi (2000) have shown that the turbulent fluxes of energy are consistently underestimated. From several sites within the "FLUXNET" network it has been found that surface turbulent energy fluxes are frequently underestimated by about 10-30% relative to the measured incoming energy R_n (Wilson et al., 2002). This underestimation occurs because the fluxes carry also non-turbulent information which is usually neglected.

A discrepancy in the energy balance closure was even detected, although in smaller percentages, on simpler flat surfaces with uniform and low vegetation (Twine et al., 2000). Leuning et al. (2012) found that a possible explanation to underestimation of turbulent fluxes is related to strong advective fluxes which only slightly affect measures and there are detectable at 30-minutes time scale only if very high humidity and temperature gradients exist. A part of the imbalance can be explained by incorrect estimates of the energy stored in air and biomass below the measurement height (e.g. Eshonkulov et al., 2019a), but also by incorrect net radiation estimates due to horizontal measures of net radiation (e.g. Wohlfahrt et al., 2016). However, for relatively simple land cover configurations (e.g. grasslands and crops) the canopy and air storages term, determined using infrared temperature, can be small if the anemometer is close to the ground and no tall vegetation exists (Leuning et al., 2012). Hammerle et al. (2007) analysed the energy balance during the growing season at two grassland sites in the Alps. One site was situated on a

slope with an average inclination of 24° and exposed to northeast, the other was situated on a flat terrain. They concluded that EC measurements made above a mountain slope were of similar quality as fluxes measured over a flat terrain. Hiller et al. (2008) measured turbulent heat and CO_2 fluxes using the eddy covariance method on a slope with an inclination of 25° in the Swiss Alps. They did not find any indication that the eddy covariance method does not work on complex terrain and suggested to look for sites having prevailing winds along the contour lines of the terrain.

4.1.4 Carbon dioxide

Carbon dioxide is among the most important greenhouse gases, together with water vapour and methane. In addition, it is directly involved in the carbon cycle in which vegetation and water bodies play a key role in sequestrating it. Carbon dioxide regulation in atmosphere depends therefore on the plant type and, more widely, on land use (management). Changes in environmental conditions such as temperature shifts, modifications of precipitation patterns, land cover alterations can affect the amount of carbon dioxide and feedbacks can occur: if there is for example a temperature increase, new vegetation species can colonise a soil. This can lead, depending on the plant species, to more (or less) carbon sequestration. Since mountains are facing evident effect of climate change, carbon dioxide monitoring can provide useful information, together with information on vapour pressure deficit, air humidity, evapotranspiration, sensible heat transfer and soil properties. Carbon dioxide has an impact over the vapour pressure deficit and on water use efficiency (WUE), which depends on gross primary production (GPP), namely the gross uptake of CO_2 by photosynthesis. Therefore, ultimately, carbon dioxide flux is strongly connected with evapotranspiration, since *ET* depends also on WUE and VPD (and on water availability and plant type). Carbon dioxide flux is directly measured by micrometeorological approaches (e.g. Aubinet, Vesala and Papale, 2012). The Net Ecosystem Exchange (NEE) is given by $NEE = F_c^{EC} + F_{storage}$. Hence, as a first approximation, NEE is given by the eddy covariance-measured carbon dioxide flux.

4.2 Methodology

Local meteorological conditions were explored by means of the “Metvurst” R package (Appendix F; Appelhans, 2013), here adapted to process 30-minute data. In particular, the data were classified according to the time and the wind directions. The wind directions were split into 36 sectors and then a contingency table giving the distribution frequencies about the occurrence of a particular wind direction for

each half hour period was computed. By doing so, the contourplot of the wind direction frequencies was obtained. At the end, the temperature time series was plotted as a colormap against the wind direction, for each half hour from 00:00 to 23:30. Then, for each wind direction sector and each half hour, the mean temperature value was computed and subsequently plotted as a colour-map.

A wind speed classification was introduced. In the literature, the Low-Wind Speed (LWS) conditions have been set when the horizontal wind speed fell under 1.5 m/s (Mortarini et al., 2013). The dataset was split into two main wind speed classes, with the aforementioned threshold.

4.2.1 High-frequency data and 30-minute step computation

EC data were sampled at 10 Hz and then, after being checked for data loss, these measurements were averaged over 30-minute periods, using the EddyPro software (versions 6.2.1 and 7.0.1). It was decided to use this averaging period because it allowed consideration of almost all the turbulent scales. This choice was also based on the use of multi-resolution decomposition technique (MRD, e.g. Howell and Mahrt, 1995; Vickers and Mahrt, 2003; Appendix A). The MRD technique relies on the orthogonal decomposition of a variable (e.g. a flux) using different averaging lengths of time series. The covariances are in this case locally converted in cospectra and decomposed into moving averaging windows of different widths (i.e. the multiresolution decomposition), and the peak in multiresolution cospectra depends likely on the width of the main flux events. See Appendix A shows further details.

A similar approach to that suggested by Stiperski and Calaf (2017) was used, except for the quality requirement on critical Richardson number below 0.25. One month of data collected at Cogne (June 2016) was despiked as illustrated by Mauder et al. (2013) to eliminate the outliers. Check for physical data plausibility was performed, but no wind direction filter was adopted, since the ITC (test on turbulence) proposed by Mauder and Foken (2004) was used, and at this stage, the objective was to understand whether 30-minute averages were acceptable, but no particular study on turbulence requiring more quality control was performed. Then, streamwise alignment with double rotation was applied, after a linear detrending. A study of double rotation and planar fit techniques, together with rotation angles for eddy fluxes calculation is shown in Appendix B. Four atmospheric stability classes were selected using the atmospheric stability parameter $\frac{z}{L}$, where z is the measurement height and L is the Monin-Obukhov length, defined as $L = -\frac{u^{*3}\overline{\theta_v}}{k\, g\, (\overline{w'\theta_v'})}$, where $\overline{\theta_v}$ is the mean virtual potential temperature, $(\overline{w'\theta_v'})$ is the surface virtual potential temperature flux (a sort of sensible heat flux), k is the Von Karman constant (0.41), and g is the gravitational acceleration.

The stability classes were: unstable ($\frac{Z}{L} < -0.5$), weakly unstable ($-0.5 \leq \frac{Z}{L} < -0.01$), weakly stable ($0.1 < \frac{Z}{L} \leq 0.5$) and stable ($\frac{Z}{L} \geq 0.5$). The multi-resolution heat flux was obtained for each stability class, and highlighted that the 30-minutes averaging was appropriate, since the multiresolution flux decomposition of sensible heat flux showed values around 0 at about 1800 s (Figure 4.1), hence the loss if information is minimal. It is reasonable to think that this averaging period is appropriate also for Nivolet site, since at that site the wind speed and turbulent motions are enhanced with respect to Cogne site.

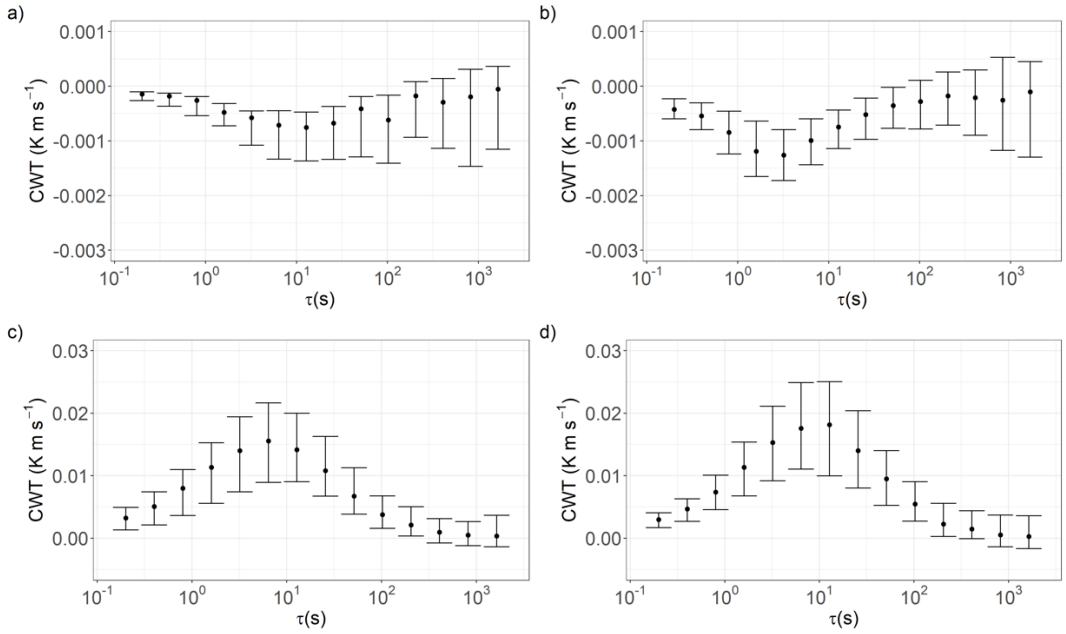

Figure 4.1. Multi-resolution flux decomposition of sensible heat flux (CWT) for: a) stable; b) weakly stable; c) weakly unstable and d) unstable atmospheric conditions. For stable and weakly stable condition, only nighttime data were considered; for weakly unstable and unstable conditions, only daytime data were considered.

When global radiation exceeded 10 W m^{-2}, daytime started. The high frequency data were divided into 30-minute windows and were checked for instrumental malfunction (identified through the CSAT3 diagnostics). In Figure 4.2, a scheme of the Methodology is shown. Initially, the entire data set was considered (both night and daytime). Point 6 in Figure 4.2 was not used.

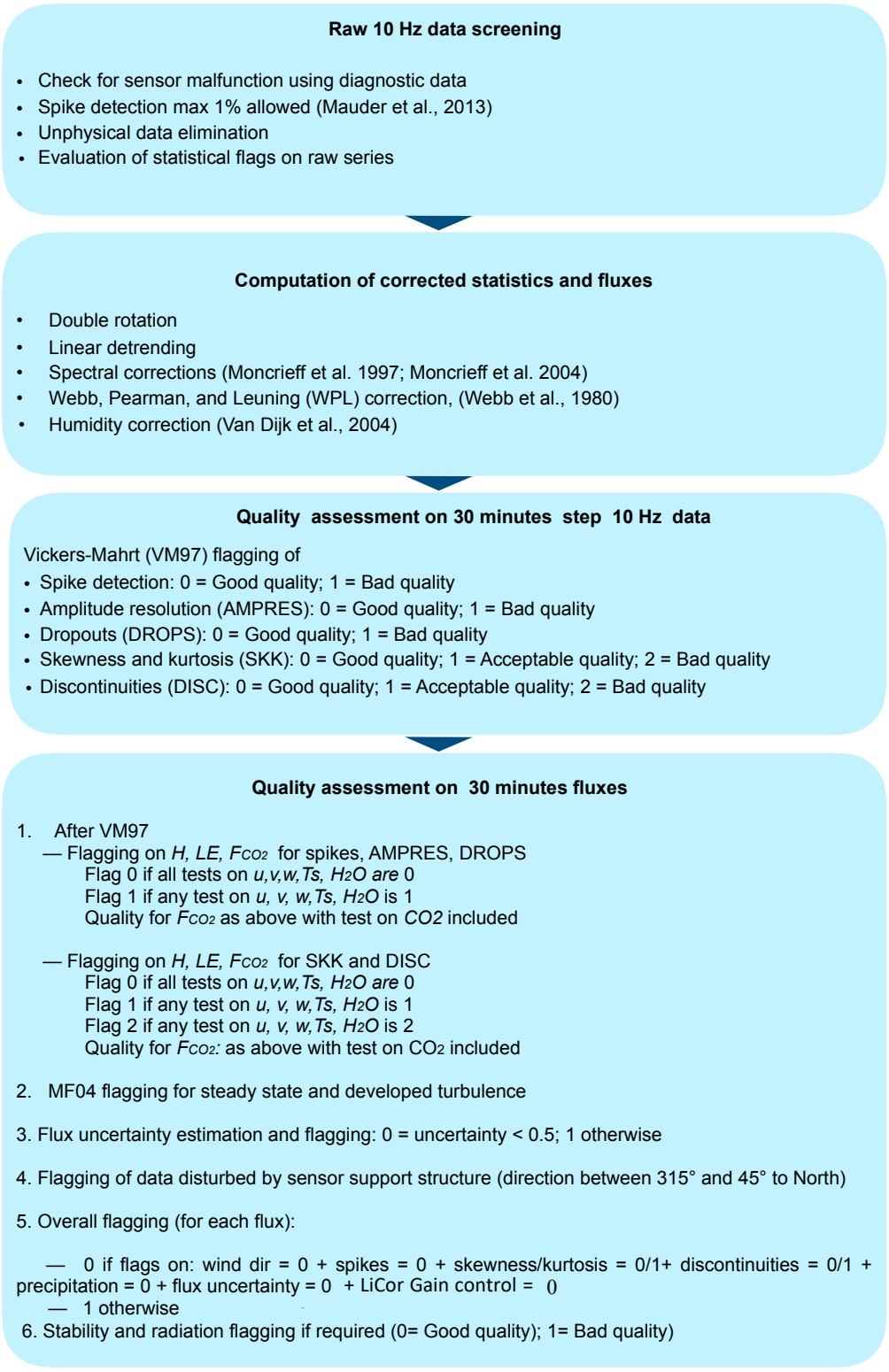

Figure 4.2. Scheme of the methodology adopted. VM97 refers to Vickers and Mahrt (1997) procedure, while MF04 refers to Mauder and Foken (2004) quality control flagging.

Possible unphysical values were identified and discarded. In Table 4.1, the instrumental plausibility ranges are shown. Each test was performed separately, assigning a quality flag for each raw variable (u, v, w, T_s, CO_2 and H_2O vapour).

Table 4.1. Range of physical plausible data for the sites.

u ($m\ s^{-1}$)		*v* ($m\ s^{-1}$)		*w* ($m\ s^{-1}$)		*Ts* (°C)		CO_2 ($\mu mol\ m^{-3}$)		H_2O ($mmol\ m^{-3}$)	
min	max	min	max	min	max	min	max	min	max	min	max
-30	+30	-30	+30	-5	+5	-40	+50	7	30	0	1800

On what follows, other quality tests are shown. The term "hard-flag" refers to data with very likely bad quality. The term "soft-flag" refers to data with still acceptable quality according to a single quality test.

Spikes and unphysical values detection on raw data

In the case of extremely weak variance (i.e. stable conditions and very weak winds) or technical failures, fluctuations in variables may be below the amplitude resolution of the system. A set of discrete frequency distributions was computed on 1000 data points overlapping windows. For each position of the window, 100 bins were considered with a 7σ range of variation taken into account and, when the percentage of empty bins exceeded 70%, the time series (of wind speed, sonic temperature, water vapour or carbon dioxide) was hard flagged. The amplitude resolution test was no longer considered, because it had a negligible impact on the data. The test had a 0-1 flagging system (where 0 corresponded to good quality and 1 to bad quality).

Dropouts

Dropouts are locations in which the time series values fall and settle to a nearly constant value. This may be representative of recording problems or other technical issues. Using the same procedure described by Vickers and Mahrt (1997), the extreme values were defined as smaller than the 10^{th} or greater than the 90^{th} percentiles of the distribution. The dropouts were revealed with the following choices: for each variable, the variation range was determined. Then, it was divided into *n* bins which were categorised as "central" or "extreme" bins. The percentile setting the threshold which divided the two categories was the 10^{th} percentile. The percentage of accepted central dropouts was 10%, whereas the accepted number of extreme dropouts was 6%. The drop-outs test was no more considered, because it had a negligible impact on the data. The test had a 0-1 flagging system (where 0 corresponded to good quality and 1 to bad quality).

Skewness and kurtosis test

Enhanced skewness and kurtosis values could indicate problems in the raw time series, for example, due to technical failures. As reported by Vickers and Mahrt, if the skewness of the selected time series was outside the range (-2,2) or the kurtosis was outside the range (1,8), the record was hard flagged, while if the two moments were outside the range (-1,1) and (2,5) respectively, the record was soft flagged. This was repeated for every variable. The skewness and kurtosis test had a three-value flag for each variable: 0 (good), 1 (acceptable quality), and 2 (bad quality).

Discontinuity test

Discontinuities in time series are defined as semi-permanent changes in the series. They can be detected using the same procedure implemented by Vickers and Mahrt (1997). The Haar wavelet transform (Mahrt, 1991) was used and then it was normalised by the smaller value of the standard deviation for the entire record and one-fourth the range for the total record with the same threshold values for the hard and soft flagging. In particular, the hard flag was used when the value of the normalised transform was greater than 3 and soft-flagged if the value was 2. The skewness and kurtosis test had a three-value flag for each variable: 0 (good), 1 (acceptable quality), and 2 (bad quality).

4.2.2 Averages, variances, covariances, fluxes and tests on theoretical requirements for eddy covariance

To compute fluxes, the EddyPro software procedure was used. At first, the raw variables were despiked (Mauder et al., 2013). Second, unphysical values were removed (see Table 1 for details). Crosswind correction of sonic temperature was already performed by the Campbell CSAT3 software. Due to the features of the site and to a change in the anemometer orientation in July 2017 (98° with respect to the old position), it was chosen to use double rotation for the entire analysis. Then the time lag correction using the covariance maximisation technique following Fan et al. (1990) was applied. Linear detrending on the variables was used as well. Covariances and uncorrected fluxes, variances and other variables of interest, such as the friction velocity u^* (Eq. 2.9), the mean wind speed components and the stability parameter were computed. The fluxes were adjusted, and corrected values were achieved using a step-by-step approach: spectral corrections of fluxes by Moncrieff et al. (2004) and Moncrieff et al. (1997). Humidity correction of the

sensible heat flux according to Schotanus et al. (1983) and the van Dijk et al. (2004) revised formulation; Webb-Pearman-Leuning (WPL) correction (Webb et al. 1980). Note that the final carbon dioxide flux was computed after the sensible and latent heat fluxes correction.

The Mauder and Foken flagging policy (Mauder and Foken, 2004) was used to assess two of the most important conditions so that the eddy covariance holds: the flow steady state (as illustrated in Chapter 2, Eq. 2.5) and the integral turbulence characteristic, which indicates whether there is sufficient air turbulence (ITC, Chapter 2, Eq. 2.8). The tests were introduced by Foken and Wichura (1996). The steady-state assumption can be considered valid if temporal averages less than 1 hour are considered. To verify the assumption, usually the fluxes, averaged over 5 minutes and over 30 minutes, were determined and their absolute difference was computed. This value was then divided by the flux averaged on the current timescale, i.e. 30 minutes (Hammerle et al., 2007; Aubinet, Vesala and Papale, 2012).

If $\Delta_{stationarity}$ exceeded a threshold (i.e. 30%, Foken and Wichura, 1996), the data was considered non-stationary.

In general, a good index of the turbulence magnitude is the flux variance similarity, calculated as the ratio between the standard deviation of the variable of interest divided by the turbulent flux of that variable. To compute this index, the Monin-Obukhov similarity theory was here used in its improved formulation given by Foken et al. (1991); Foken et al. (1997) and Thomas and Foken (2002).

Usually, the aforementioned ratios can be expressed as a function of the stability parameter ζ and of the Coriolis parameter, f, here neglected.

The Mauder and Foken flagging policy was introduced in 2004 in the CarboEurope framework. It is based on a three-level flagging (2 = bad quality; 1 = acceptable quality, to be used in long-term analyses; 0 = good quality data) using the steady state and the integral turbulence tests on the data. The integral turbulence test (ITC) is able to give an estimation of the conditions of a well-mixed boundary layer and therefore the conditions of sufficient turbulence. The test can be performed for each kind of flux (H, LE and F_C).

4.2.3 Post-processing quality control

In this Section, the quality control procedure is completed: the flags obtained in the previous Sections are used to produce a quantitative assessment on the data and fluxes quality (for each test and then by merging every test to yield an overall flag, further integrated by other analyses).

The quality control was devoted to three purposes:

1) For each of the six raw variables (*u, v, w* – the anemometer wind speed components; *Ts* – the sonic temperature; H_2O – water vapour concentration; CO_2 – carbon dioxide concentration), to find the percentage of data associated with each flag.

2) For the three analysed fluxes, to understand which is the percentage of data associated with each flag.

30-minute outliers' identification and description of the quality tests on 30-minute data

The procedure for flagging was structured as follows: first, for the data screening tests, the purpose was to evaluate the percentage of data associated with each flag. Second, the missing fluxes periods were identified. Third, the 30-minute outliers of fluxes were found by means of a simple moving median filter. Then, a flag system for fluxes (H, LE and F_C) was created, and it was derived from the tests, performed on each 30-minute step, on the separate, six raw variables (u, v, w, T_s, CO_2 and H_2O vapour). For H and LE, the checked variables are u, v, w, T_s and H_2O vapour, while for F_C, the control on CO_2 was added to the other tested variables.

Spikes and outliers, amplitude resolution and drop-outs

The flag was "0" if all the raw variables of interest passed the test. It was "1", if at least one variable did not pass the test. Since the spikes detection test on data was not evident (only 8 values were hard-flagged for carbon dioxide flux and 2 for *LE*), the test was included in the overall flagging, but it was not analysed separately. Because of small number of the hard-flagged records after the first despiking on raw, 10 Hz data, they were included in the computation of the outliers detected after the moving median filter. Therefore, the half hour periods characterised by spikes related to the 10 Hz data and then also by spikes on the 30-minute fluxes were discarded, but the total amount of spikes was computed including both the high-frequency and the low-frequency, 30-minute data spikes.

Skewness and kurtosis and discontinuity tests

For skewness and kurtosis and discontinuities tests, the flag on fluxes was "0" if all the raw variables of interest passed the test. It was "1" if at least one variable was soft-flagged and it was 2 if at least one variable was hard-flagged.

Test on eddy covariance theoretical requirements

The Mauder and Foken (2004) flagging policy was already performed on fluxes and was used to obtain a quantitative assessment on the amount of flux data which met the activated turbulence and steady-state theoretical fulfilments.

Flux uncertainty

Random uncertainty was estimated by means of the Finkelstein and Sims (2001) method. However, since the estimation process is determined itself by uncertainties, a simpler approach implemented in the quality control was used.

The flux uncertainty involved in the quality assessment was estimated by means of the formulas introduced by Wyngaard et al. (1971). The same technique was used and suggested by Stiperski and Rotach (2016). The variances formulae are reported in Eq. 4.1 for the scalars. The formula of sensible heat flux uncertainty was adapted to be used also for waver vapour (hence, *LE*) and carbon dioxide fluxes.

$$a_{wT}^2 = \frac{z}{1800}\left(\frac{\overline{(w'T')^2}}{\overline{(w'T')}^2} - 1\right)$$

$$a_{wH_2O}^2 = \frac{z}{1800}\left(\frac{\overline{(w'H_2O')^2}}{\overline{(w'H_2O')}^2} - 1\right) \tag{4.1}$$

$$a_{CO_2}^2 = \frac{z}{1800}\left(\frac{\overline{(w'CO_2')^2}}{\overline{(w'CO_2')}^2} - 1\right)$$

where a_{nm} is the uncertainty on the covariance and *U* is the mean wind speed at the height *z=2 m.*

Half-hour periods with an error on covariances greater than 0.5 were again hard-flagged.

Overall flag and friction velocity

Disturbed data due to the anemometer geometry were hard flagged (“1”). The wind sector from 315° to 45° was considered for hard flagging (“1”). For the one-month field campaign in July 2017, the new disturbed wind sector was between 45° and 135°. At the end, an overall flag including precipitation information was found combining the previous tests: it was considered “0” (acceptable quality), if the data passed the following requirements on fluxes: wind direction (“0”), spikes (“0”), skewness and kurtosis (“0 or 1”), discontinuities (“0 or 1”) and Mauder and Foken (“0 or 1”) tests passed, no missing sensible heat flux data, latent heat flux data and vice versa, absence of precipitation, flux uncertainty (“0”).

The general site meteorological data were investigated at a 30-minute temporal resolution, to assess prevailing winds and average wind speeds, mean temperatures and average meteorological conditions for each JJAS (June-to-September) period. Half hour samples with low net radiation or with precipitation different from zero were identified as well. The cumulative precipitation for each one of the three summertime periods was determined. No significant snowfall was present.

The wind speed impact on data was evaluated computing how many flagged data for unreliability were found in the two wind speed classes.

For the friction velocity test, u^* was computed, using the complete formulation given in Eq. 2.9.

The hard-flagged momentum flux according to the Mauder and Foken flagging policy was discarded. Therefore, the stability parameter and the u* were discarded as well. A detailed discussion on the atmospheric stability and wind speed dependencies is beyond the purposes of this paper, but it is important to correctly evaluate the impact of stable or deeply unstable and/or low wind speed conditions.

The friction velocity estimation depends on the momentum flux so, several works questioned whether to use it or not to identify low-turbulence periods, in particular during night-time (Papale et al., 2006; Acevedo et al., 2009). A u^* filtering was explored fixing a threshold value of 0.075 m s^{-1} (Hiller et al., 2008) applied on the already filtered 30-minute data.

Since daytime data and only fluxes passing the Mauder and Foken tests were selected, it was chosen not to use the u^* filtering, although its effects will be explored after the final flagging (see the following section).

Evaluation of the quality tests results

To quantify the impact of each test, of the overall flag and of the other tests (friction velocity, stability and global radiation Rg), the percentages of fluxes with the related flag were computed, excluding the missing data and the outliers. Missing data and outliers' percentages were evaluated separately on the total amount of data.

To evaluate the impact of the tests and of the flagging policy on the measured fluxes, cumulative fluxes were estimated multiplying the fluxes by 1800 s (each half hour time step) and then cumulating the values for each month, to obtain the cumulative flux. This helped to understand what was effectively measured at the site. An evaluation of unavailable data and outliers' impact was performed: for 25 days blocks, the median value of the quantity (namely the fluxes each 30 minutes) was computed and used as a first guess for the estimation of the lost cumulative flux for H, LE and F_{CO_2}. The outliers' identification was considered substituting the related 30-minute fluxes with values estimated through the reference values of the block moving median (having a 221 half-hours window). This procedure was repeated for each one of the performed tests. The unavailable data contribution was also estimated, even in terms of impact on the cumulative fluxes by computing the value of the median of 25 days of data around the gaps and filling those gaps with the median values.

4.2.4 Analyses with the quality-controlled dataset

The mean daytime ($Rg > 10\ W\ m^{-2}$) cycles were computed to understand if a general pattern on the data behaviour could be found. The expectations should be: positive fluxes for H and LE, while the carbon dioxide flux should be almost always negative because of the vegetation activity. The daytime data as previously described were used. The variability was expressed in terms of the standard deviation of flux data for each half-hour.

The energy balance

The energy balance at the land surface can be expressed as in Eq. 4.2:

$$H + LE = R_n - G - S \tag{4.2}$$

where H is the sensible heat flux, LE is the latent heat flux (both these fluxes are estimated by eddy covariance in this Thesis), R_n is the net radiation, $G_0 = G - S$ is the ground heat flux at the soil surface. The net radiation was measured by a horizontally-displaced net radiometer in 2014. The horizontally measured values were corrected using a linear regression between slope-parallel measures in 2015, 2016 and 2017 and the horizontal measures in the same years. The slope obtained by the regression was then applied to correct the 2014 data.

The ground heat flux estimation is not trivial. The heat moves across the soil according to a diffusion equation. Let us consider a volume of soil, a cylinder of area A and depth z, having two levels: z and $z + \Delta z$. The heat conduction equation can be written as in Eq. 4.3.

$$\frac{\partial}{\partial t}(\rho c T) = -\frac{\partial}{\partial z} G \tag{4.3}$$

where ρ is the soil density, c is its heat capacity, T is its temperature and G is the soil heat flux.

If the sensors are located under the surface, the heat flux they measure shall be corrected introducing the heat storage of the above layers by means of an empirical or analytical approach. The analytical point of view tends to better describe the underlying physical processes occurring in the soil. Therefore, if there is the possibility to estimate the soil temperature gradient at the surface and the soil-thermal conductivity, the corrected value for G_0 (soil heat flux at the soil's surface) can be derived. It can be developed an entirely analytical model that allows computing the G and G_0 terms using the soil conductivity, the temperature gradient and the propagation of heat (and the signal temperature) across the soil, with a

discrete trigonometric Fourier series. In this case, the soil temperature signal follows the partial differential equation (Eq. 4.4).

$$\frac{\partial}{\partial t}T = -\frac{\partial}{\partial z}\left(\frac{k}{\rho c}\frac{\partial T}{\partial z}\right) = \frac{\partial}{\partial z}\left(\alpha_h \frac{\partial T}{\partial z}\right) \tag{4.4}$$

where α_h is $\frac{k}{\rho c}$.

Eq. 4.4 can be solved in the phase space, thus considering the signal decomposed in Fourier series. The solution of the previous equation can be expressed with a function $T(z,t) = \bar{T}(z) + \sum_{n=1}^{inf} T_{z,n}\sin(n\omega t + \phi_n(z))$, where $\bar{T}(z)$ is the daily average soil temperature, $T_{z,n}$ is the amplitude of the harmonics and $\phi_n(z)$ is their phase; *n* is the harmonic number. ω is the daily radial frequency.

Therefore, *G* in Eq. 2.10 can be written in the following terms (Eq. 4.5):

$$G(z,t) = -k\,\frac{\partial \bar{T}(z)}{\partial z} - \sqrt{2}\sum_{n=1}^{inf}\frac{T_{z,n}}{\mathrm{D_n}}\exp\left(-\frac{z}{D_n}\right)\sin\left(n\omega t + \phi_n(z) + \frac{\pi}{4}\right) \tag{4.5}$$

where the term $\mathrm{D_n}$ is the soil thermal diffusivity.

The ground heat flux at the interface between soil and atmosphere can be written as in Eq. 4.6.

$$G(0,t) = -k\,\frac{\partial \bar{T}(z)}{\partial z} - \sqrt{2}\,\sum_{n=1}^{inf}\frac{T_{z,n}}{\mathrm{D_n}}\sin(n\omega t + \phi_{n,0}(z) + \pi/4) \tag{4.6}$$

The *G* value was measured by two soil heat flux plates (HFP01, Campbell Scientific). The average of the two measures was then computed and used.

The final step is to evaluate the rate of change of the storage heat (Eq. 4.7).

$$S(t) = \int_{z1}^{z2} c\,T(z,t)dz \tag{4.7}$$

where c is the volumetric soil thermal capacity. Knowing the functional form of $T(x,t)$, the rate of change of the heat storage can be derived. z_1 and z_2 are the two levels between the depth at which the probe is located and the soil surface.

If this information is not available, the classical approach can be used, even if the correction of *G* is not simple (e.g. Heusinkveld et al., 2004). Usually, the rate of change is summed to the heat flux measured by the probes in the soil. This should be done, because the instruments are located at a certain depth in the soil, so they are not able to well reproduce the flux at the surface (Eq. 4.8)

$$G_0 = G_z + S(t) \tag{4.8}$$

where G_0 (W m^{-2}) is the surface ground heat flux, G_z (W m^{-2}) is the heat flux as measured by the probes at a certain depth. $S(t)$ (W m^{-2}) is the rate of change of the heat storage term.

The 30-minute ground heat flux (G) was measured whereas the storage heat flux term was estimated with a simpler approach than the one mentioned above, as illustrated in Eq. 4.9 expressed in W m^{-2} (German, 2000; Campbell Scientific, 2016).

$$S_{soil}(t) = \frac{\Delta T_s \, C_s \, d}{\Delta t} \tag{4.9}$$

where ΔT_s (°K) is the soil temperature variation in time at each time step (measured by the HFP01 probes, Campbell Scientific), C_s (J m^{-3}K^{-1}) is the soil heat capacity, d (m) is the soil depth at the site and t is the time step (here 1800 s), Eq. 4.10.

$$C_s = \rho_b \, C_d + \theta_v \, \rho_w \, C_w \tag{4.10}$$

$\rho_b = 1.4 * 10^3$ (kg m^{-3}) is the soil bulk density, C_d is dry soil heat capacity (840 J kg^{-1} K^{-1} Hanks and Ashcroft, 1980), θ_v is volumetric soil water content, ρ_w is water density, C_w is the water heat capacity, assumed equal to 4185 J kg^{-1} K^{-1}.

The canopy storage term in W m^{-2}, is estimated following Wohlfahrt et al. (2016), Eq. 4.11:

$$S_{canopy} = \frac{\Delta T_{surface}}{\Delta t}(C_w m_w + C_0 m_0) \tag{4.11}$$

where $\frac{\Delta T_{surface}}{\Delta t}$ is the rate of change in surface infrared temperature, $C_w = 4190$ J kg^{-1} K^{-1}is the water heat capacity, $m_w = 0.38$ kg m^{-2} is the organic water mass , $C_0 =$ 1920 J kg^{-1} K^{-1} is the dry organic heat capacity and $m_0 = 0.30$ kg m^{-2} is the dry organic matter mass.

The overall storage term was estimated as $S = S_{soil} + S_{canopy}$

The energy balance closure was computed as the slope of the regression line of *H+LE* versus *Rn-G-S*. Hence, the slope is dimensionless. The linear regression was obtained via the reduced major axis (RMA) technique using the "lmodel2" R package (see Appendix F for further information).

4.3 Results

4.3.1 Site characterisation

The four June-to-September (JJAS) growing periods showed different meteorological conditions. The 2014 growing season (July in particular) was characterised by more precipitation than the other two JJAS periods, in particular in July 2014. This can be seen in Figure 4.3, where both the total amount of precipitation in the three growing seasons and the cumulative precipitation for the months from May to September 2014, 2016 and 2017 are shown. May is here included because it helps understand the conditions prior to the period examined. The cumulative precipitation of the May to September periods of 2014, 2016 and 2017 were 332, 290 and 236 mm respectively. The monthly precipitation peaked in July 2014 at 152.0 mm, while the minimum was in September 2017 at just 6.0 mm. The mean daily rainfall per day. was respectively 0.09 mm, 0.061 mm and 0.062 mm for 2014, 2016 and 2017, respectively. The average precipitation on the entire analysed period was 0.07 mm d^{-1}.

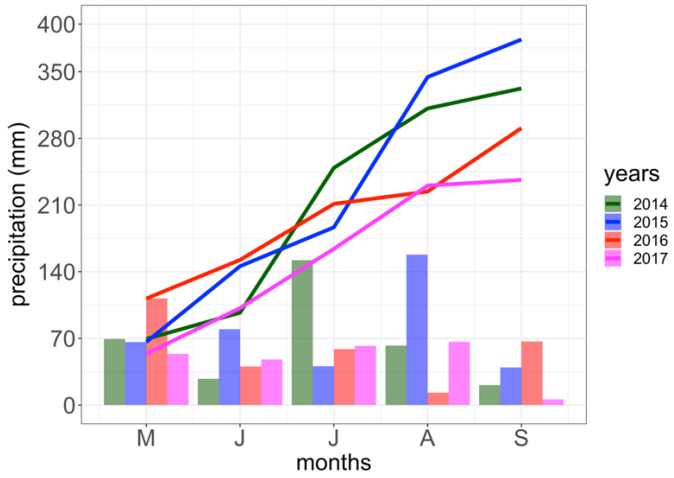

Figure 4.3. Monthly (May to September) cumulative precipitation in the years 2014, 2015, 2016 and 2017.

Temperatures measurement results showed a clear difference between day and night. The 2014 JJAS period showed a mean daily maximum temperature of 19.0°C and a mean daily minimum of 7.3°C, with an average value for the period of 12.0°C. JJAS 2016 was characterised by a mean maximum temperature of 22.3 °C, a mean minimum value of 7.5°C and a full period average of 13.9 °C. In 2017, the three average temperature values were 22.2°C, 7.3 °C and 13.6 °C respectively.

Since the site is located in a small valley, the wind flow is channelled upslope and downslope most (69.4%) of the time. Daytime hours, except in few cases, are characterised by up-slope winds (that is, the wind coming from South-South-East). In Figure 4.4, the left panels show the wind direction frequencies and the air temperature contour plots for the three June-to-September periods. The panels on

the right show the daily mean wind speed. The upslope and downslope wind regime throughout the day can be seen clearly, with more intense, warm winds up-slope during daytime and downslope winds during nighttime, when, cold air flows towards the bottom of the valley. Average temperatures range on average from about 5 to 24 °C. The predominance of low-wind conditions can be noted in each JJAS period.

On the total amount of data (both daytime and nighttime, the latter being not considered in this paper), the low-wind speed conditions prevail, with $U \leq 1.5\ m\ s^{-1}$ prevail (more than 92% of the time and 62% for daytime-only data).

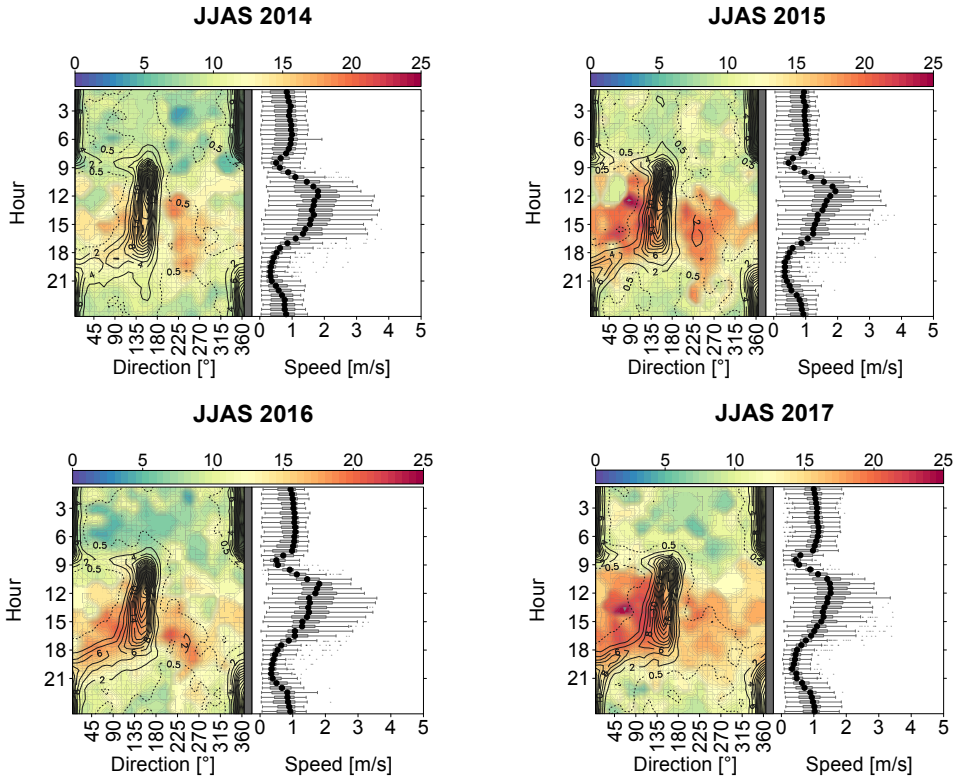

Figure 4.4. Average temperature and wind direction probability contour maps as a function of wind direction and hour of the day (left) and wind speed versus hour of the day (right) for the 2014, 2015, 2016 and 2017 growing seasons. The colour scale of temperature is reported above each panel.

Growing season mean air temperature in 2014 was around 1.3°C lower compared to the other three years (Figure 4.5). Mean air temperature during the growing seasons (JJAS) of 2014-2017 varied between 12 °C (2014) and 13.4 °C (2016) (Figure 4.5, upper panel). Cumulative precipitation during of the four growing seasons varied between 179 mm (2016) and 317.6 mm (2015), as illustrated in Figure 4.5, lower panel). To better understand what the starting point of water income was, we also evaluated the precipitation occurred in May. In that month, cumulative precipitation was 69.4, 66.2, 111.8 and 53.8 mm, respectively for 2014, 2015, 2016 and 2017.

Summarised, there is one wet and cold growing season (2014), one warmer and wet (2015) and two consecutive growing seasons with less precipitation and also with warm conditions. However, if annual values are considered, there were three wet years (696, 757, 640 and 624 mm respectively for 2014, 2015, 2016 and 2017). The higher average annual temperature was found in 2015 (+6.5°) if compared to the other three years which experienced average temperatures ranging from 5.7 to 5.9°C. Average soil temperature in growing seasons was 13.2, 14.3, 13.7 and 14.7°C, respectively for the four growing seasons. The highest values were found in 2015 and 2017.

At the eddy covariance site, the wind is channelled, and it is characterised by an up/downslope regime. Therefore, a relatively local wind flow exists, and mesoscale contaminations are negligible. At the Regional Authority standard site, located 150 m West of the eddy covariance station, instead, the contributions from mesoscale main valley are important and this indicates that the location choice in a complex area plays a key role for eddy covariance measures. (Figure 4.6 - done with Openair R-Package, Carslaw and Ropkins, 2012, Appendix F).

The wind rose structure in the growing seasons is almost the same.

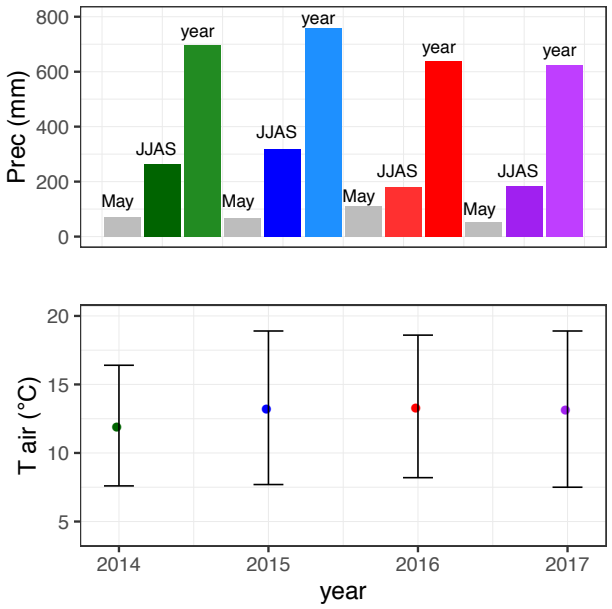

Figure 4.5. Cumulative precipitation for the whole hydrological year, growing seasons and May (upper panel); Mean air temperature for the four growing seasons (lower panel). Error bars in the lower panels indicate one standard deviation.

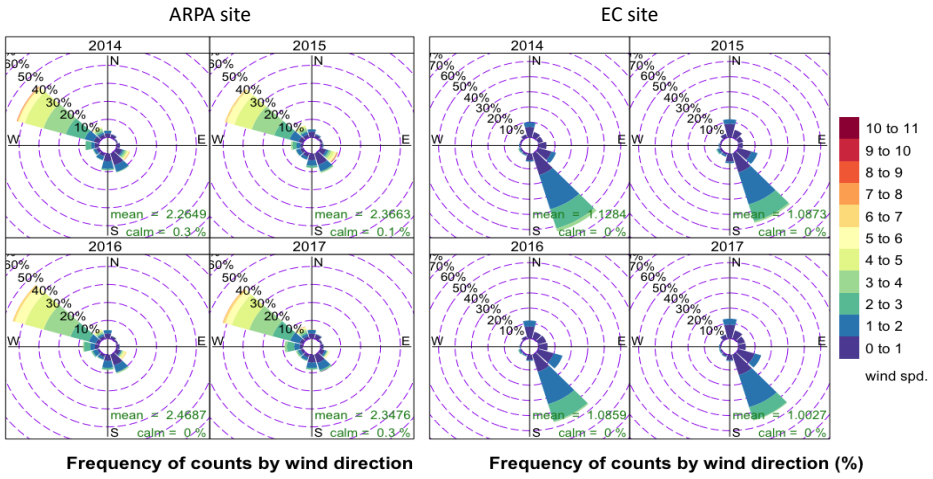

Figure 4.6. Daytime wind rose for the Regional Authority meteorological station (left) and wind rose at the Cogne eddy covariance site (right).

4.3.2 High frequency data and 30-minute step computations

Spikes and unphysical values detection on raw data and 30-minute flux time series despiking

Hard-flagged, high frequency data in every 30-minute window were rare: for the wind speed components and the sonic temperature, no record exceeded the 1% of accepted spikes. The carbon dioxide concentration time series showed only 8 hard-flagged periods, while the water vapour concentration had only two hard-flagged, 30-minute periods. Therefore, both the percentage of hard-flagged data and the amount of cumulative fluxes related to them was reduced. Over the twelve months of data, only the gas concentrations had some unphysical values. Technical problems were detected during July and August 2017, when around 12% of data was discarded.

The number of 30-minute missing data (defined as the periods with more than 10 % of 10 Hz data gaps and after the removal of 10 Hz spikes on single variables and unphysical data)

is shown in Table 4.2. The percentages refer to the flux data after the first despiking procedure leading to the exclusion of few half hour periods and after the second procedure for the outliers' elimination on the half hourly fluxes. The impact on missing data is also presented as a percentage.

The occurrence of missing data is low, except for 2017, where there was an increase due to instrumental malfunctioning. Data classified as outliers are, generally, higher in 2014 than in the other two years, probably because of the higher number of rainfall events.

Table 4.2. Percentages of data flagged as missing data for the 30-minute flux data. The percentages are computed on the full dataset.

		2014	2015	2016	2017
H	Missing data (%)	4.2	17.8	0	9.1
LE	Missing data (%)	9.0	23.8	3.9	21.4
F_c	Missing data (%)	4.3	19.8	1.5	19.8

Amplitude resolution test

Possible resolution problems were detected in only nine time periods for water vapour, but the carbon dioxide measures were not affected by the problem. In addition, the previous despiking and data processing already eliminated the data located in the hard-flagged periods. So, the final impact is not significant.

Dropouts test

Using the threshold values suggested by Vickers and Mahrt (1997) significant drop-outs were not detected in the raw time series. Therefore, this test was not considered when the final quality-corrected database was produced for further analyses.

Skewness and kurtosis test

Table 4.3 shows, for the six single variables, the percentages of data for each quality class after the skewness and kurtosis test. The amount of acceptable data is high, in particular for the wind speed components, with respect to carbon dioxide and water vapour concentrations. Overall, the number of acceptable data is always high (more than 80% for each variable). However, while for the wind speed above 80% of data is 0-flagged, for the other variables that percentage drops. This effect may be due to some measurement problem related to the gas analyser but only in 16.5% of cases for carbon dioxide and in 17.9% of cases for water vapour.

Table 4.3. The percentages of 0, 1 and 2 flags, on half hour data, of the variables u, v, w, T_s, CO_2 and H_2O after the skewness and kurtosis test.

	2014			2015			2016			2017		
flag	u	v	w	u	v	w	u	v	w	u	v	w
0 (%)	95.6	93.1	81.7	95.7	92.9	83.0	96.0	93.2	81.1	94.8	93.7	84.3
1 (%)	3.7	6.2	17.6	3.4	6.4	16.0	3.3	6.1	19.1	4.3	5.5	14.2
2(%)	0.7	0.7	0.8	0.9	0.9	1.1	0.6	0.6	0.7	0.8	0.8	1.4
	T_s	CO_2	H_2O	T_s	CO_2	H_2O	T_s	CO_2	H_2O	T_s	CO_2	H_2O
0 (%)	77.5	65.3	70.3	76.1	64.8	65.7	72.9	66.1	66.5	75.3	69.0	69.3
1 (%)	21.5	29.8	23.1	22.6	30.4	25.7	26.0	29.3	27.9	23.2	27.4	27.5
2 (%)	1.1	4.9	6.5	1.4	4.8	9.6	1.1	4.6	5.5	1.5	4.5	4.2

Table 4.4 shows the percentages of fluxes single data assigned to a certain flag. The same information is also shown in Figure 4.7. The data described here had been already despiked. The quality assigned to the fluxes is high, but the effect of the selected flagging policy implies an increased quantity of intermediate quality fluxes. Again, this is not a real problem, since reliable data include both the 0 and the 1-flagged fluxes. The sensible and the latent heat fluxes show similar percentages for each quality class and the total number of reliable fluxes is beyond 95%. The carbon dioxide flux shows a slightly different conditions, because there are less 0-flagged data and more 1-flagged data, with respect to the other two fluxes.

Table 4.4. The percentages of 0, 1 and 2 flags, on half hour data, of the fluxes after the skewness and kurtosis test. Flag "0+1" indicates the number of data actually passing the test (data flagged as 0 or 1).

	flag	2014	2015	2016	2017
H	0 (%)	46.8	43.5	42.4	49.2
	1 (%)	49.2	50.7	54.5	49.9
	2 (%)	4	5.8	3.1	2.8
	0 + 1 (%)	96	94.2	96.9	97.1
LE	0 (%)	47.8	45.7	43.5	48
	1 (%)	49.1	51.1	54.4	49.8
	2 (%)	3.1	3.3	2.2	2.2
	0 + 1 (%)	96.9	96.8	97.9	97.8
F_c	0 (%)	39.3	39.1	37.7	41
	1 (%)	57.2	57.9	59.9	56.1
	2 (%)	3.4	3.9	2.4	2.9
	0 + 1 (%)	96.5	96	97.6	97.1

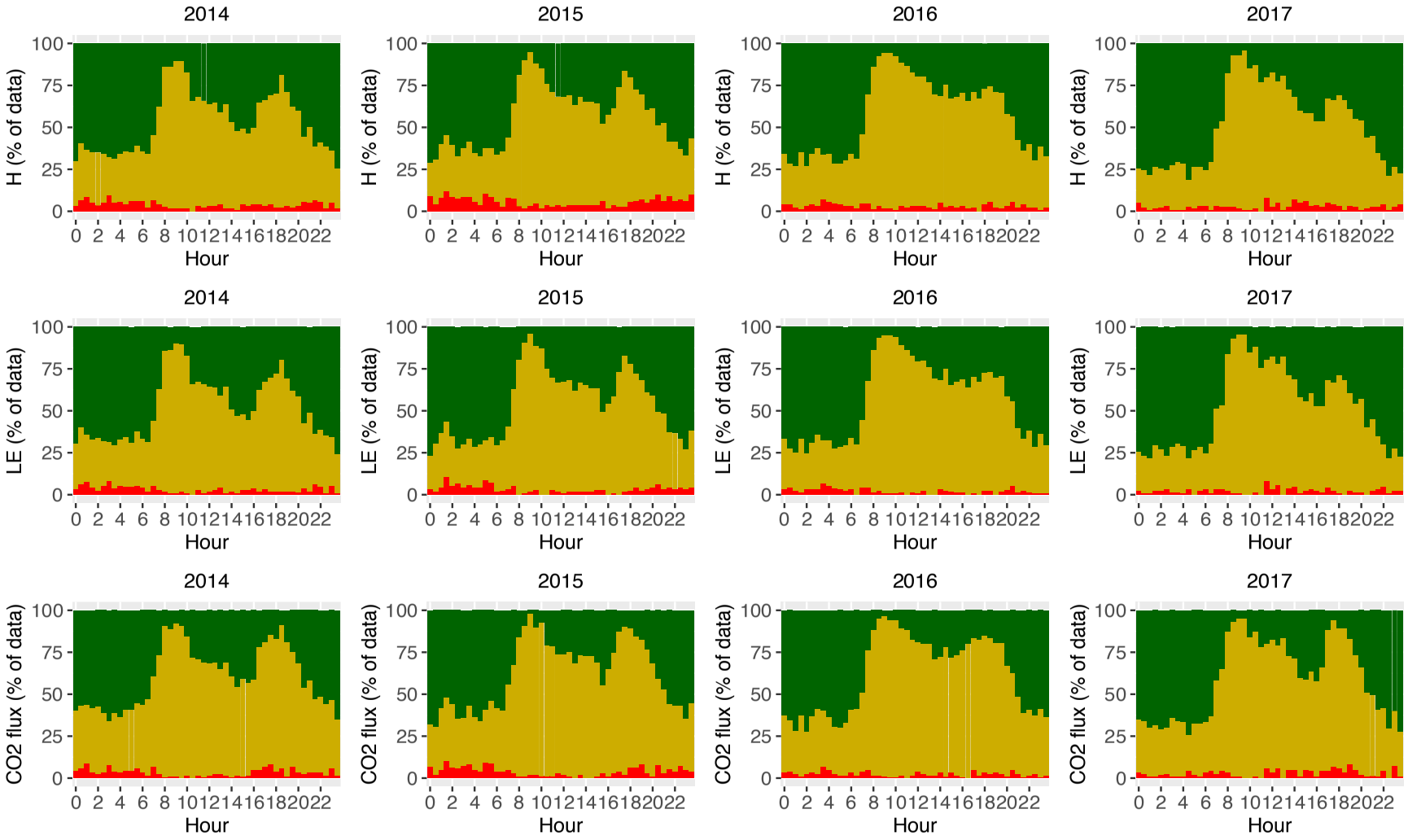

Figure 4.7. Skewness and kurtosis quality control: percentages of half hour period. In green, good quality data, in yellow medium quality data, in red bad quality data.

Discontinuity test

When considering the six variables (u, v, w, T, H_2O *and* CO_2), the high-quality data according to the discontinuity test are the majority. In Table 4.5, the percentages of data falling in each of the three quality classes are shown. For each variable, more than 85% of the data was 0-flagged. The low-quality data often are due to rainfall. For example, 42.9% and 55.5% of carbon dioxide and water vapour measures with inadequate quality occurred during rainfall periods. These events are generally highlighted by this test. In Table 4.6, the percentages of flux data (also represented in Figure 4.8), classified again according to a 0-1-2 system after the discontinuities test, are shown. The percentages refer to each one of the four growing seasons for each cumulative flux and the percentages related to the flags are computed without considering the fluxes interpreted as outliers or missing values. The number of acceptable data is high (all above 90% except water vapour in 2014).

Table 4.5. The percentages of 0, 1 and 2 flags, on half hour data, of the variables u, v, w, T_s, CO_2 and H_2O after the discontinuity test.

	2014			2015			2016			2017		
flag	*u*	*v*	*w*	*u*	*v*	*w*	*u*	*v*	*w*	*u*	*v*	*w*
0 (%)	99	99.4	99.3	99.8	99.1	99	99.2	99.4	99.4	99.1	99.3	99.0
1 (%)	0.5	0.1	0	0.4	0.1	0.1	0.3	0	0	0.2	0.0	0.2
2 (%)	0.5	0.5	0.7	0.8	0.8	0.9	0.5	0.6	0.6	0.7	0.7	1.3
	T_s	CO_2	H_2O	T_s	CO_2	H_2O	T_s	CO_2	H_2O	T_s	CO_2	H_2O
0 (%)	99.4	92.5	89.5	99.2	89.3	86.7	99.5	94	93.4	99.3	95.7	95.0
1 (%)	0.1	2.4	2.5	0	1.7	3	0.1	1.2	1.6	0.0	0.8	1.0
2 (%)	0.5	5.1	9.1	0.8	9.9	10.3	0.5	4.8	5	4.1	3.4	0.7

Table 4.6. The percentages of 0, 1 and 2 flags, on half hour data, of the fluxes after the discontinuity test. Flag "0+1" indicates the number of data actually passing the test (data flagged as 0 or 1).

	flag	2014	2015	2016	2017
H	0 (%)	89.6	86.2	92.8	93.7
	1 (%)	3.1	3.4	2.0	1.4
	2 (%)	9.3	10.4	5.3	5.0
	0 + 1 (%)	91.7	89.6	94.8	95.1
LE	0 (%)	91.1	92.0	95.6	95.4
	1 (%)	2.9	3.3	1.8	1.4
	2 (%)	6.0	4.7	2.6	3.2
	0 + 1(%)	94.0	95.3	97.4	96.8
F_c	0 (%)	86.9	86.2	92.6	93.1
	1 (%)	5.1	5.0	2.8	2.3

2 (%)	7.9	9.7	4.6	4.5
0 + 1 (%)	92.0	91.2	95.4	95.4

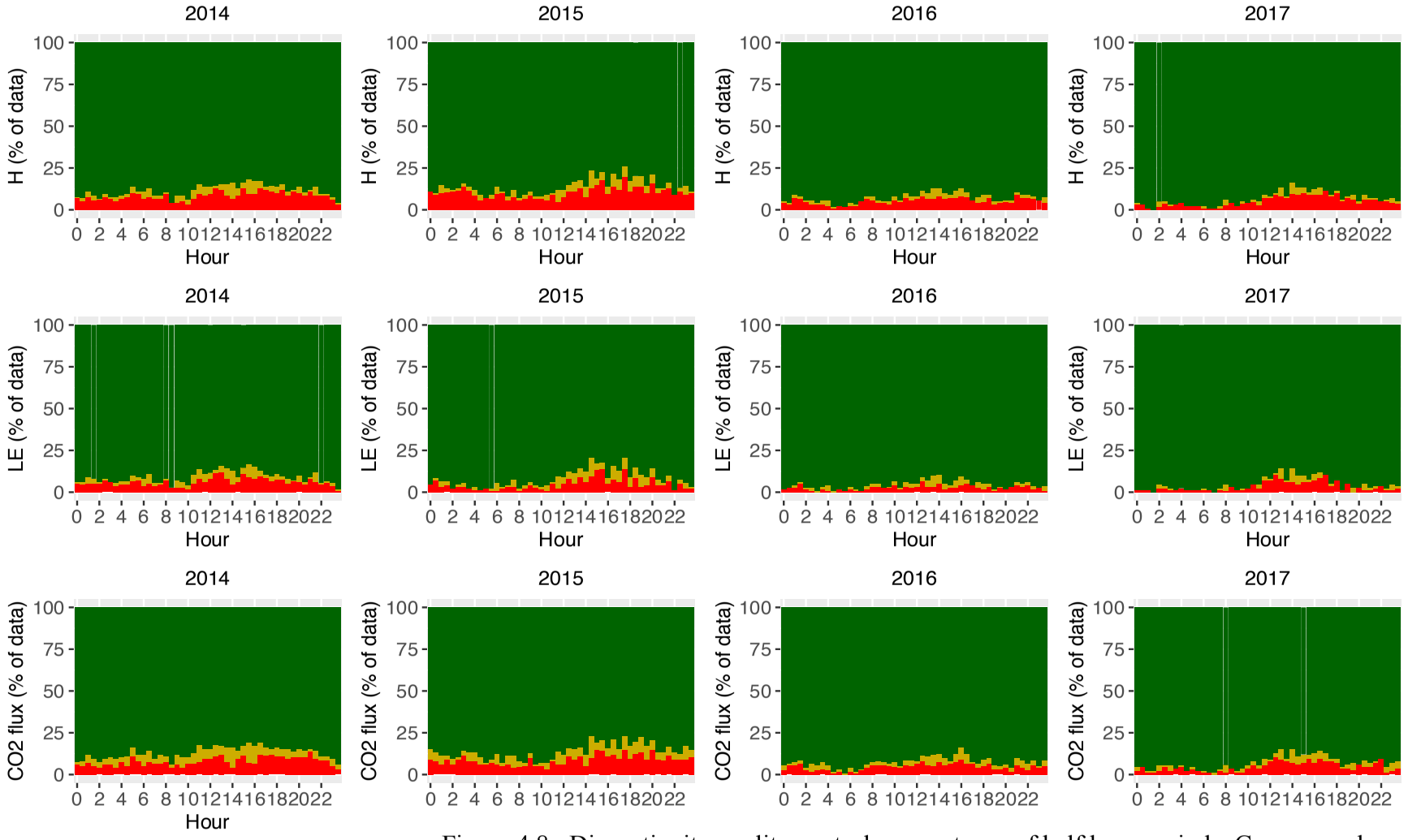

Figure 4.8. Discontinuity quality control: percentages of half hour periods. Green: good quality; yellow: medium quality; red: bad quality.

Tests on theoretical requirements for eddy covariance

In Table 4.7, the percentages of fluxes falling into one of the three quality classes according to the test of Mauder and Foken (2004), are shown. Outliers and missing values are not considered when the percentages are computed. In Figure 4.9, the percentages of flagged-data according to 0-1-2 scheme are shown. Results show a high percentage of acceptable data.

Table 4.7. The percentages of 0, 1 and 2 flags, on half hour flux data, of the fluxes after the Muader and Foken (2004) test. Flag "0+1" indicates the number of data actually passing the test (data flagged as 0 or 1).

	flag	2014	2015	2016	2017
H	0 (%)	46.2	49.0	52.1	52.9
	1 (%)	33.9	37.8	35.1	33.7
	2 (%)	19.8	19.8	12.8	13.4
	0 + 1 (%)	80.1	86.8	87.2	86.6
LE	0 (%)	42.8	42.8	44.3	45.7
	1 (%)	41.6	41.6	40.3	39.2
	2 (%)	15.6	15.6	15.4	15.1
	0 + 1 (%)	84.4	84.4	84.6	84.9
F_c	0 (%)	40.8	40.8	43.0	44.7
	1 (%)	39.0	39.0	40.0	37.7
	2 (%)	21.2	21.2	16.9	17.6
	0 + 1 (%)	79.8	79.8	83.0	82.4

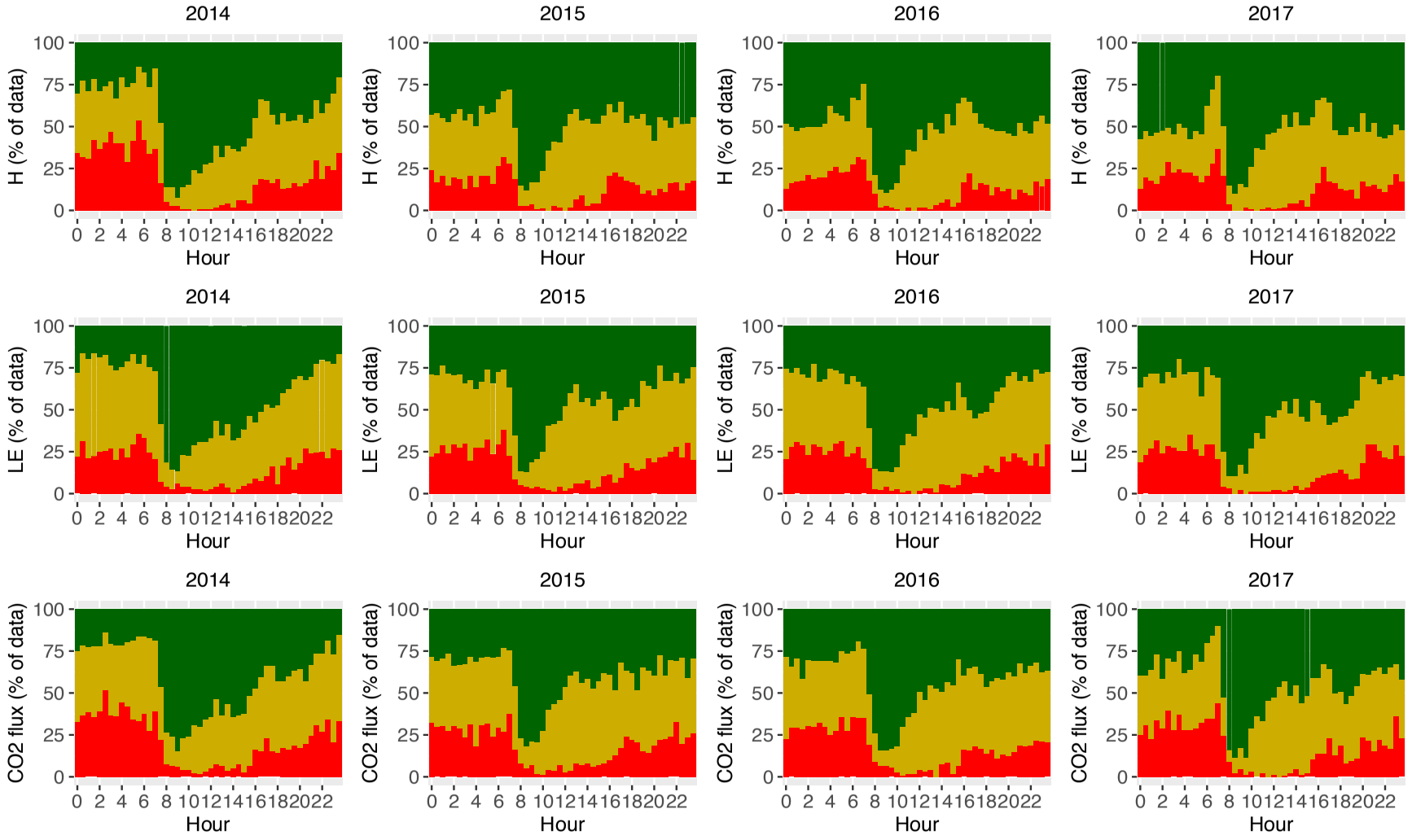

Figure 4.9. Mauder and Foken quality control: percentages of half hours within each flag value. Green: good quality; yellow: intermediate quality; red: bad quality.

Uncertainty and overall flag

The overall flag included each control previously aforementioned, plus the hard-flag on periods characterised by rainfall events and the identification of periods with a high flux uncertainty. On the total amount of available data (after the post-processing computations), 84.7%, 73.7% and 72.6% of flux data were characterised by acceptable uncertainty (below 50% of the flux), respectively for sensible heat, latent heat and carbon dioxide fluxes

In Figure 4.10, the quality control effect with the overall flagging system on data availability is shown.

It seems that the proposed quality-flagging system allows finding the majority of suspect data and it was found that the low wind speed (LWS) condition does not necessarily imply a low-quality data about single variables or fluxes, but the flagging system was already acceptable and no further wind speed filtering was adopted.

As can be noted, the choice of the u* threshold and, more generally, of the u*-based quality check has a relatively low impact on data availability.

In Table 4.8, the percentages related to the amount of the data passing the overall test procedure is shown. The 0-flagged flux data are beyond 40% for the sensible and the latent heat. Carbon dioxide can experience lower high-quality data amount. However, if the computation is performed on daytime-only data, the percentages increase up to more than 55% for the analysed fluxes. In Figure 4.10, the result of overall quality control is shown. Again, most of daytime data has an acceptable quality, whereas it decreases at nighttime, as expected because of reduced turbulence and usually weak wind flow. Nighttime data were also filtered according to friction velocity threshold following Papale et al. (2006).

Table 4.8. The percentages of 0, 1 and 2 flags (half hour data) of the fluxes after the overall flag and the friction velocity control. NAs are not included in the computation.

	flag	2014	2015	2016	2017
H	0 (%)	45.0	46.8	57.5	53.6
	flag 0 + flag u* 0 (%)	44.8	46.6	56.1	53.1
LE	0 (%)	47.4	50.5	59.8	62.6
	ag 0 + flag u* 0 (%)	46.4	50.3	59.3	62.1
F_c	0 (%)	39.1	40.9	51.4	54.2
	flag 0 + flag *u** 0 (%)	39.4	40.7	50.2	53.7

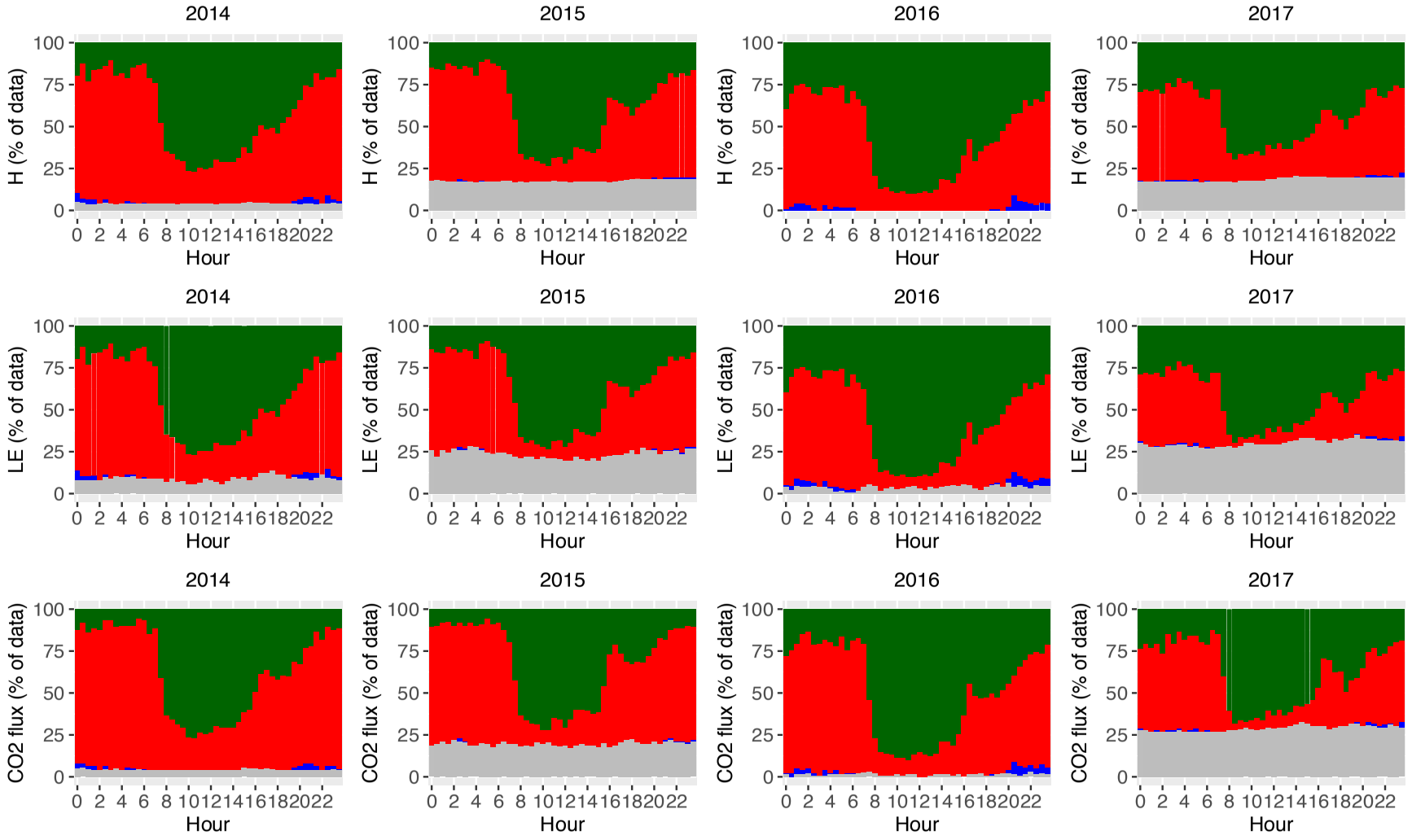

Figure 4.10. Overall flag and friction velocity flag. Percentages of half hour periods. Green: data that passed the overall flag quality control without friction velocity test. Red: bad quality data. Blue: good quality data that did not pass friction velocity test. Grey: missing data.

The quality control impact can be evaluated also in terms of flux amount that might be discarded. Figure 4.11 shows this effect and it can be noted that most of daytime fluxes is caught even with a strict quality control. Instead, it is pointed out that during nighttime, there could be problems for estimating carbon dioxide release due to vegetation respiration, because the bad quality fluxes can be of the same order of magnitude, near or outreach 0-flagged data (Figure 4.12).

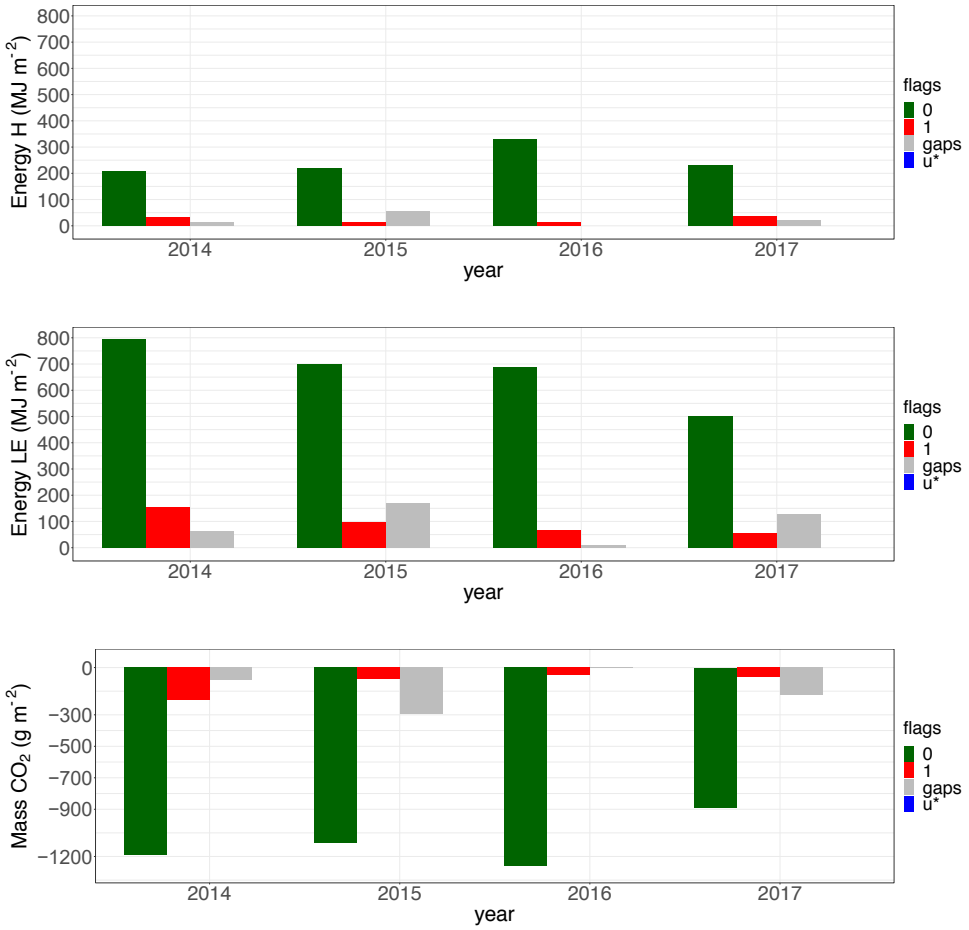

Figure 4.11. Cumulative daytime fluxes according to quality flags.

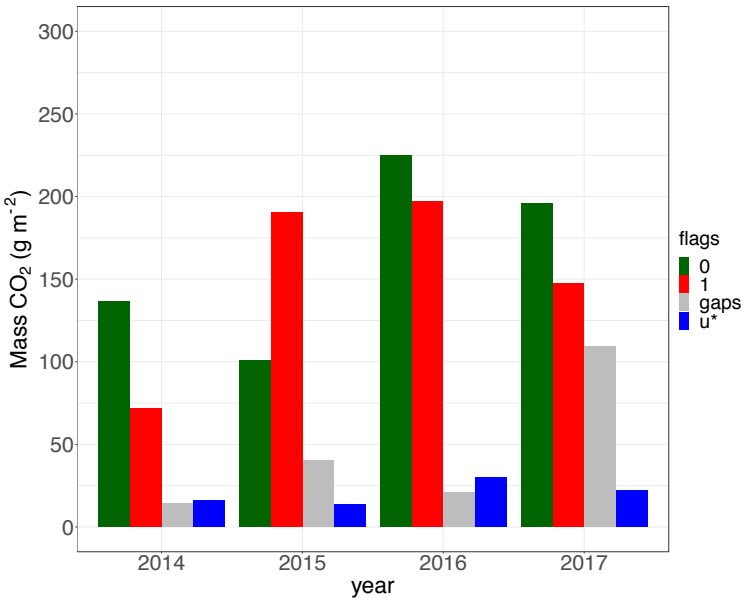

Figure 4.12. Cumulative carbon dioxide flux according to quality flags during nighttime.

4.3.3 Energy balance and mean diurnal cycles

To produce an overall assessment over the quality of collected data, one instrument is the energy balance closure evaluation. The results about ranged major axis (RMA) regression technique using lmodel2 R Package (Legendre, 2018) are shown here for the four growing seasons between 2014 and 2017. Figure 4.13 represents the data points and respective regression lines compared to the 1:1 lines to understand the divergence from ideal closure. Table 4.9 shows, in numbers, what is illustrated in Figure 4.13. The two wet growing seasons are characterised by an enhanced energy closure than the other two dry growing seasons (the difference is around 12%). This difference is likely due to latent heat flux injection which is higher when moister conditions occur. Values of energy balance closure are within the range of previous works FLUXNET sites (e.g. Wilson et al., 2002; Hammerle et al., 2007; Hiller et al., 2008). The closure is not very high, but the Cogne site is very complex from a topographic point of view.

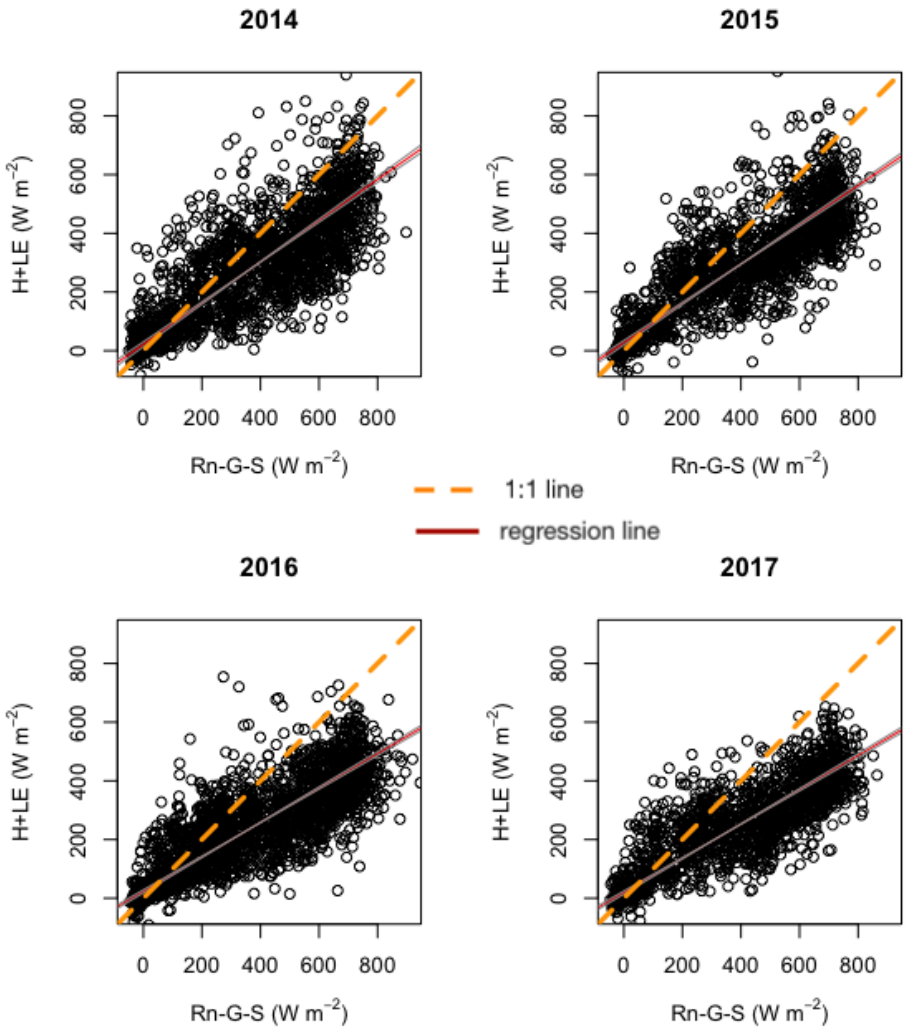

Figure 4.13. Ranged Major Axis (RMA) regression to estimate energy balance closure.

Table 4.9. Slope and intercept after the regression RMA. All the regressions are significant (p-value < 0.05)

	Slope	Interc	R^2
2014	0.71 (0.69 - 0.74)	16.0 (7.4 – 24.5)	0.65, n=1966
2015	0.68 (0.66 – 0.70)	22.7 (15.1 – 30.3)	0.71, n=1784
2016	0.59 (0.57 – 0.60)	23.3 (19.1 – 29.4)	0.72, n=2463
2017	0.58 (0.57 – 0.60)	19.8 (13.6 – 24.0)	0.76, n=1835

The daytime values of the storage term, S, oscillate between -100 and +200 W m^{-2} but, on average, the maximum value fluctuates around +100 W m^{-2}. The values are similar to those reported by Hiller et al. (2008).

In Figure 4.14, the mean daytime cycles for the analysed heat fluxes are shown for the temporal range 7:00 – 18:00. As was already shown the latent heat can be higher than the sensible one, in particular when dealing with wet growing seasons, such as the 2014 one. Even in 2016 and 2017, the latent heat flux tends to be higher with respect to the sensible heat flux. The standard deviation of LE is greater than the sensible heat flux one. However, with the 2014 exception, the LE values are in general included in the $\pm 1\ \sigma$ bars of H. This is not verified at 16:00 hours.

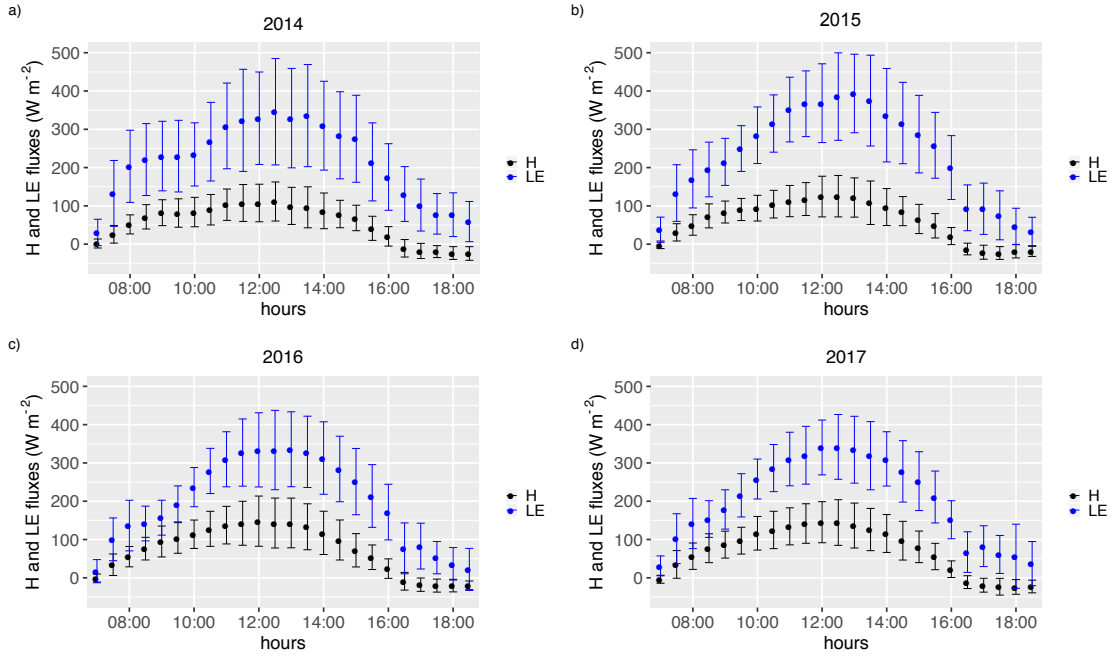

Figure 4.14. H and LE daytime fluxes for the four growing seasons (2014, 2015, 2016 and 2017). Error bars indicate one standard deviation.

As it has been previously observed, the monthly carbon dioxide cumulative daytime fluxes, at least in the 0-flagged amount of data, are negative, indicating that the ecosystem is sequestrating carbon dioxide from the atmosphere during daytime. The same information can be derived from Figure 4.15 where the mean daytime cycle for carbon dioxide flux is shown for the four growing seasons (2014, 2015, 2016 and 2017). Mean values around -10 $\mu mol\ m^{-2}s^{-1}$ were found in the three years. Those values are comparable to those found by Hiller et al. (2008) and by Etzold et al. (2010) during daytime. The standard deviation of the carbon dioxide flux is reduced in 2017 growing season, if compared to the other two seasons. The mean values are, in the three years, of the same magnitude.

Considering nighttime and daytime carbon dioxide flux data, their sums over the period 1st June – 13th September is -179, -182, -146 and -92 g C. In the dry

growing season 2017, the sequestrated carbon was half the value in 2015 (wet growing season).

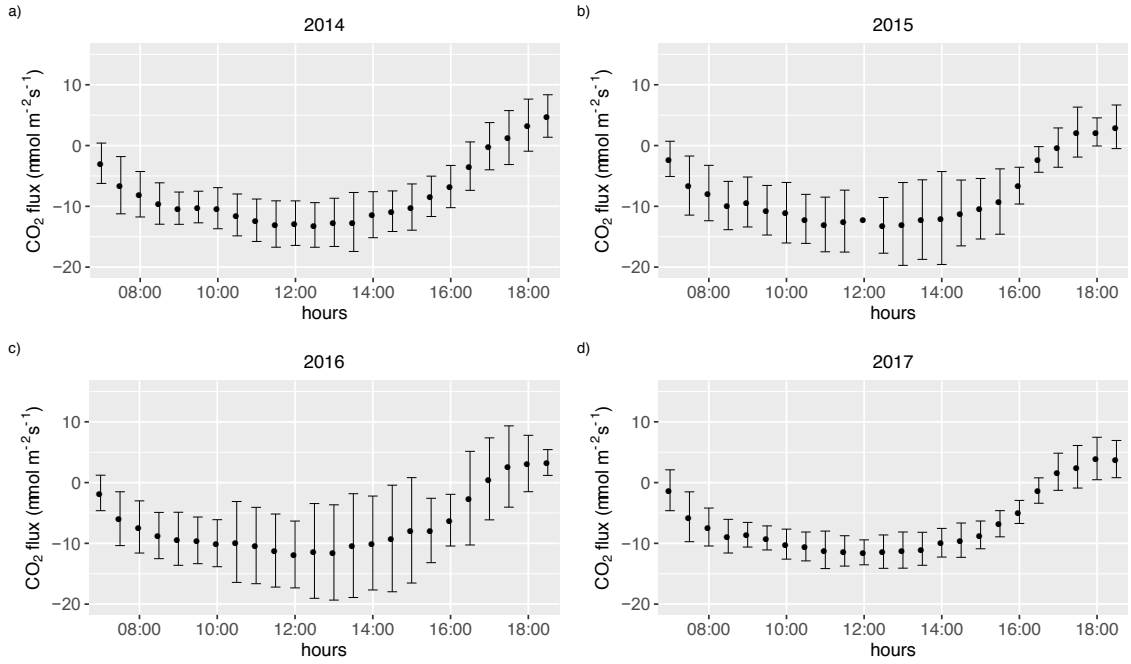

Figure 4.15. Fc (carbon dioxide) daytime flux for the four growing seasons. Error bars indicate one standard deviation.

4.4 Data quality control at the Nivolet site

Nivolet site is located on a flat plateau on a slope at about 2,600 m a.s.l. Its main objective is the monitoring of a high-elevation grassland site. The quality controls on eddy covariance data are the same as the ones performed for the Cogne site. Figure 4.16 shows the wind rose on the June-to-September (JJAS) 2018 at Nivolet, showing that cross-wind contaminations occur at the site and an average wind speed equal to 2.2 m s^{-1}. Average air temperature on JJAS 2018 was 9°C, whereas the yearly (2018) value was 1.4°C. Cumulative precipitation over JJAS 2018 period was 284 mm and the yearly (2018) value was 1262 mm.

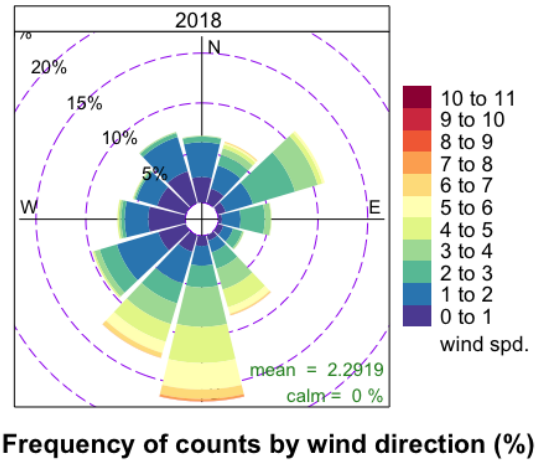

Figure 4.16. Wind rose for the JJAS 2018 period at Nivolet.

Spikes, unphysical values, missing values

The 30-minute periods characterised by either more than 10% of 10 Hz missing data or more than 1% of spikes or unphysical values were accounted for "missing data" (Table 4.10). Due to gas analyser instrumental malfunctioning, the percentage of missing flux data is beyond 15%.

Table 4.10. Percentages of data flagged as missing data for the 30-minute fluxes. The percentages are computed on the full dataset.

		2018
H	Missing data (%)	1.0
LE	Missing data (%)	21.6
F_c	Missing data (%)	17.1

Skewness and kurtosis

The result of skewness and kurtosis test shows that most of data is not affected by large deviations from the acceptable values of these two statistical parameters caused by possible instrumental errors or droplets on gas analyser optical path. Table 4.11 shows the test results, whereas Figure 4.17 shows graphically the percentages.

Table 4.11. Percentages of data flagged for skewness and kurtosis.

	flag	2018
H	0 (%)	60.8
	1 (%)	29.4
	2 (%)	9.7
	0 + 1 (%)	90.2
LE	0 (%)	62.2
	1 (%)	33.4
	2 (%)	4.4
	0 + 1 (%)	95.6
F_c	0 (%)	53.3
	1 (%)	41.1
	2 (%)	5.6
	0 + 1 (%)	94.4

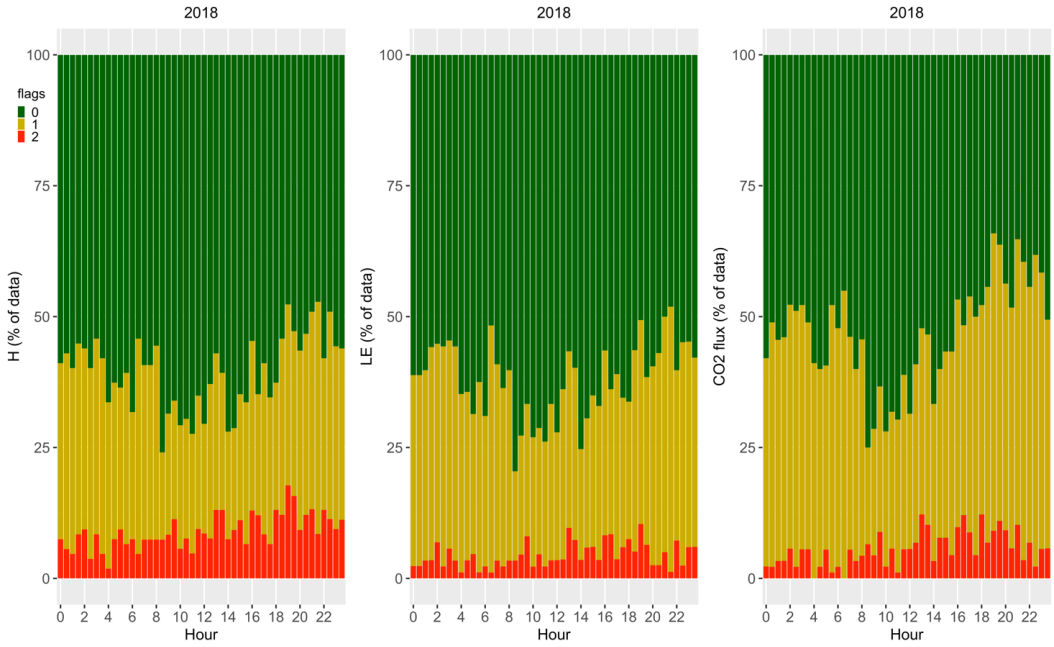

Figure 4.17. Percentages of data flagged for according to skewness and kurtosis test. Green: good quality data; yellow: medium quality data; red: bad quality data.

Discontinuities

Table 4.12 shows that the amount of data likely not affected by discontinuity problems is high, with more than 90% of acceptable data. Figure 4.18 shows graphically the results from the previous table.

Table 4.12. Percentages of flux data flagged for discontinuities.

	flag	2018
H	0 (%)	84.3
	1 (%)	5.8
	2 (%)	9.9
	0 + 1 (%)	90.1
LE	0 (%)	90.7
	1 (%)	5.3
	2 (%)	4.0
	0 + 1 (%)	96.0
F_c	0 (%)	86.1
	1 (%)	6.4
	2 (%)	7.5
	0 + 1 (%)	92.5

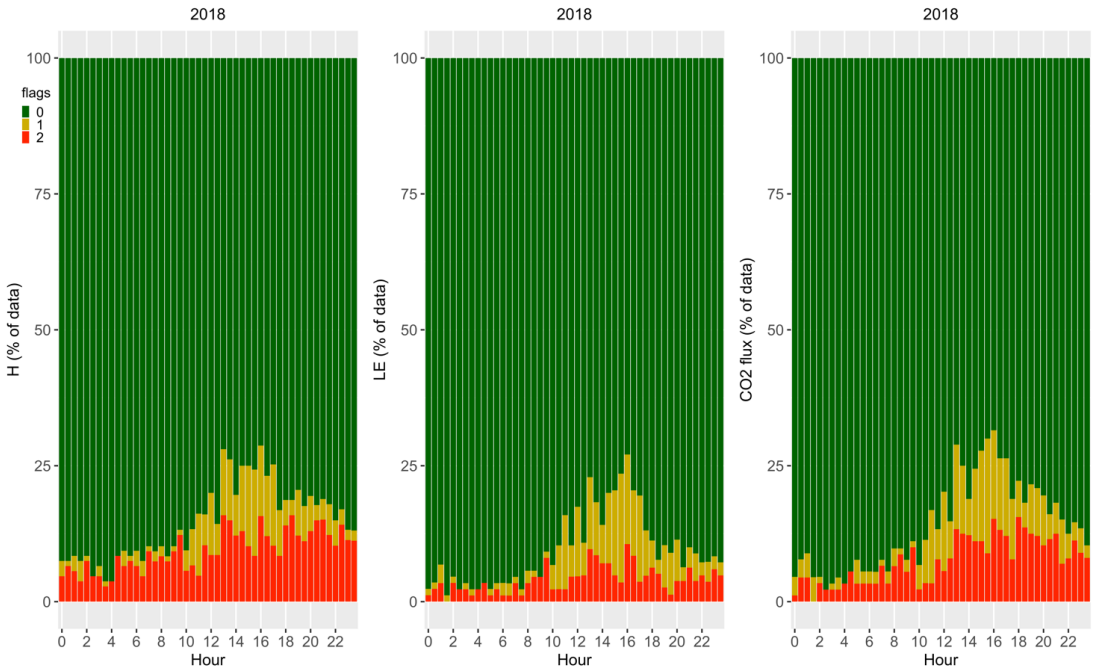

Figure 4.18. Percentages of flux data flagged for discontinuities. Green: good quality data; yellow: medium quality data; red: bad quality data.

Mauder and Foken tests on steady state and turbulence

The usual recommendations for data quality control for steady state and developed turbulence conditions require that the fluxes are flagged either 0 or 1 if they are used for long-term analyses or for mass balance purposes. Therefore, fluxes

flagged with “0” and “1” are considered acceptable. Concluding, after this test, less than 20% of flux data are discarded (Table 4.13 and Figure 4.19).

Table 4.13. Percentages of flux data flagged according to Mauder and Foken (2004) test on eddy covariance theoretical requirements.

	flag	2018
H	0 (%)	50.5
	1 (%)	39.2
	2 (%)	11.3
	0 + 1 (%)	89.7
LE	0 (%)	43.3
	1 (%)	40.2
	2 (%)	16.5
	0 + 1 (%)	83.5
F_c	0 (%)	50.2
	1 (%)	37.8
	2 (%)	12.0

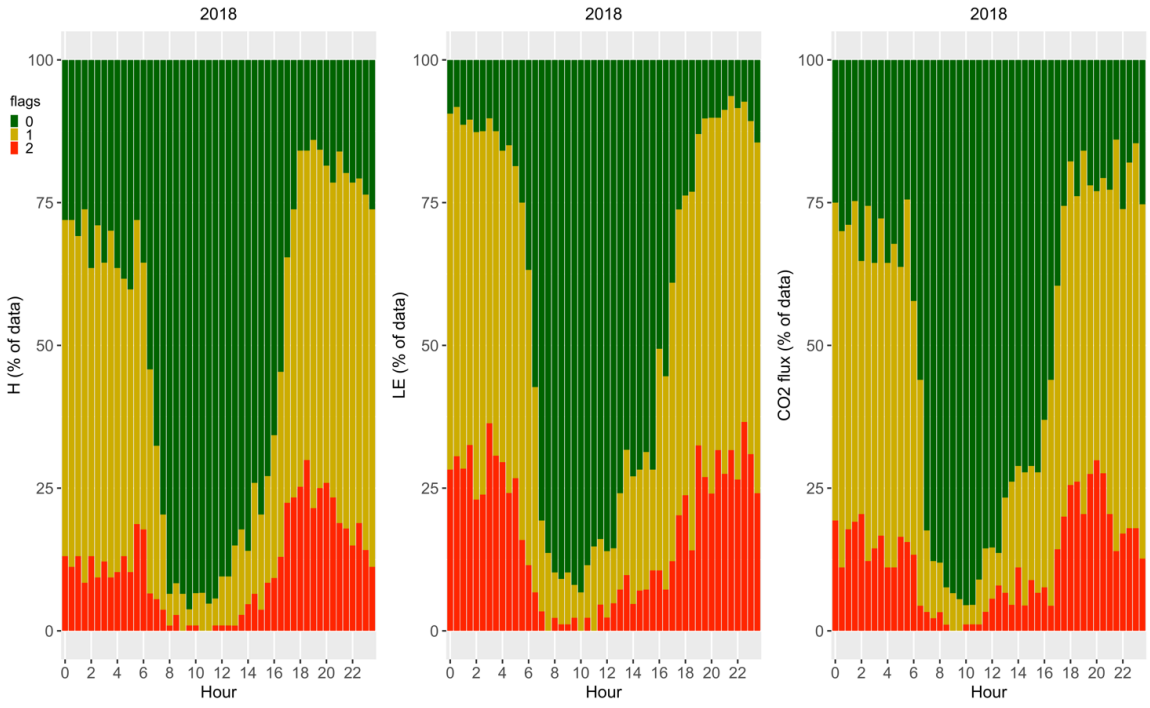

Figure 4.19. Percentages of flux data flagged according to Mauder and Foken (2004) test on eddy covariance theoretical requirements. Green: good quality data; yellow: medium quality data; red: bad quality data.

Flux uncertainties, overall flag, friction velocity

Flux uncertainties were generally low. 94.5%, 90.3% and 93.2% of flux data, respectively for sensible heat, latent heat and carbon dioxide fluxes, met the requirements for a random uncertainty lower than 50% of the considered flux. The overall flag included all the previous tests plus the LiCor gain control. The friction velocity check was introduced for nighttime data, for which a threshold of 0.09 m s^{-1} was found, and only when the Mauder and Foken test failed or was not available. Table 4.14 shows the amount of good quality data after the overall flag and after the combination between that flagging scheme plus the friction velocity test. Good quality data amount is beyond 40% in the worst case. Figure 4.20 shows the percentage of data 0-flagged, 0-flagged but hard-flagged for friction velocity, 1-flagged (discarded) and missing data.

Table 4.14. Percentages of flux data 0-flagged after all the tests.

	flag	2018
H	0 (%)	43.4
	flag 0 + flag u* 0 (%)	41.9
LE	0 (%)	60.6
	flag 0 + flag u* 0 (%)	59.5
F_c	0 (%)	53.5
	flag 0 + flag *u** 0 (%)	51.6

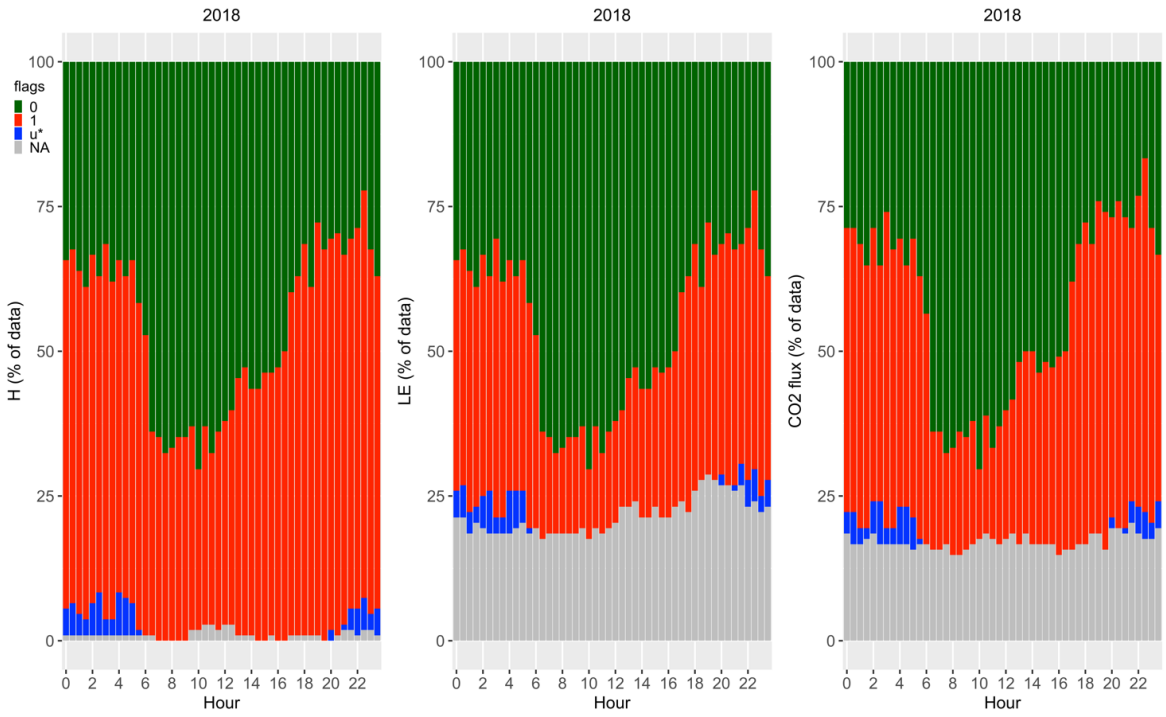

Figure 4.20. Overall flag, missing data and friction velocity flag. Green: data passing the overall flagging system without test on low friction velocity; red: bad quality data; blue: data passing the overall flag but not the friction velocity test. Grey: missing data.

The quality control impact can be evaluated also in terms of flux amount that might be discarded. Figure 4.21 shows this effect and it can be noted that most of daytime fluxes is caught even with a strict quality control. Instead, it is pointed out that during nighttime, there could be problems, although reduced with respect to Cogne site, for estimating carbon dioxide release due to vegetation respiration, because the bad quality fluxes can be significantly high, although lower than good quality data (Figure 4.22).

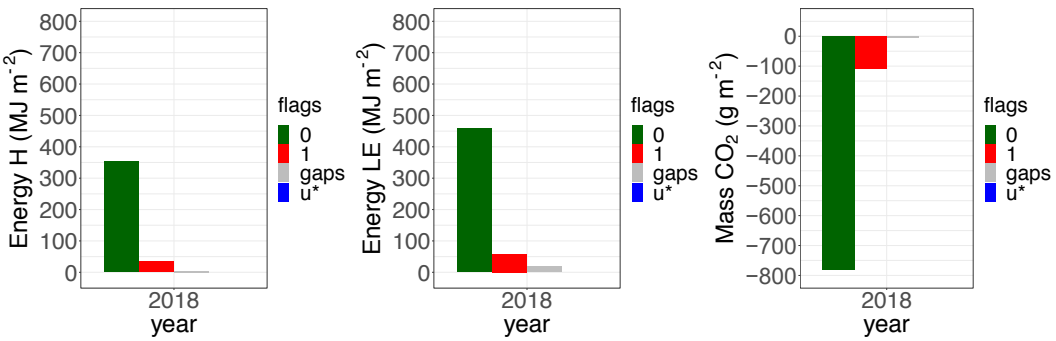

Figure 4.21. Cumulative daytime flux data after overall flagging and after friction velocity flagging.

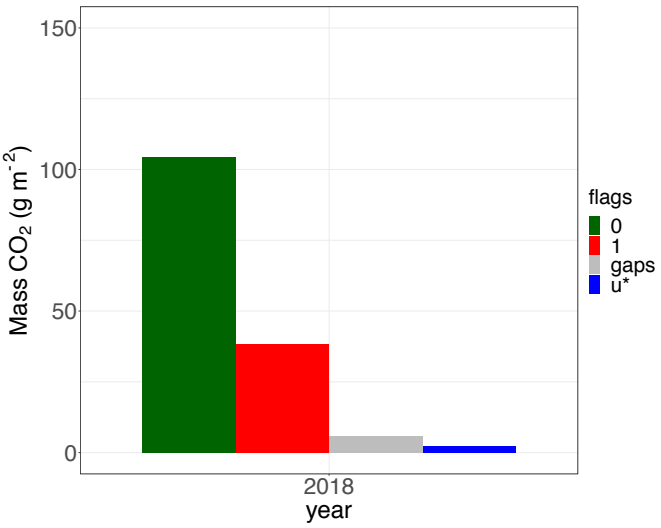

Figure 4.22. Cumulative carbon dioxide flux data according to quality flag during nighttime.

Energy balance

The energy balance at Nivolet site was higher than at Cogne. This was likely due to a decrease topographic complexity which enhance the fluxes measured by eddy covariance technique. Indeed, the regression line between the turbulent fluxes and $R_n - G_0$, (where $G_0 = 0.05\ Rn$ is the ground heat flux at the interface between the soil and the atmosphere), performed with the ranged major axis regression technique, suggested that the energy balance closure reached up to 78%. (Figure 4.23 and Table 4.15), thus more comparable with literature results with respect to the Cogne site outcomes. At both sites, the energy balance closure was comparable to several FLUXNET sites (Wilson et al., 2002) and with other publications (e.g. Vendrame et al., 2020, report closures from 64 to 79%).

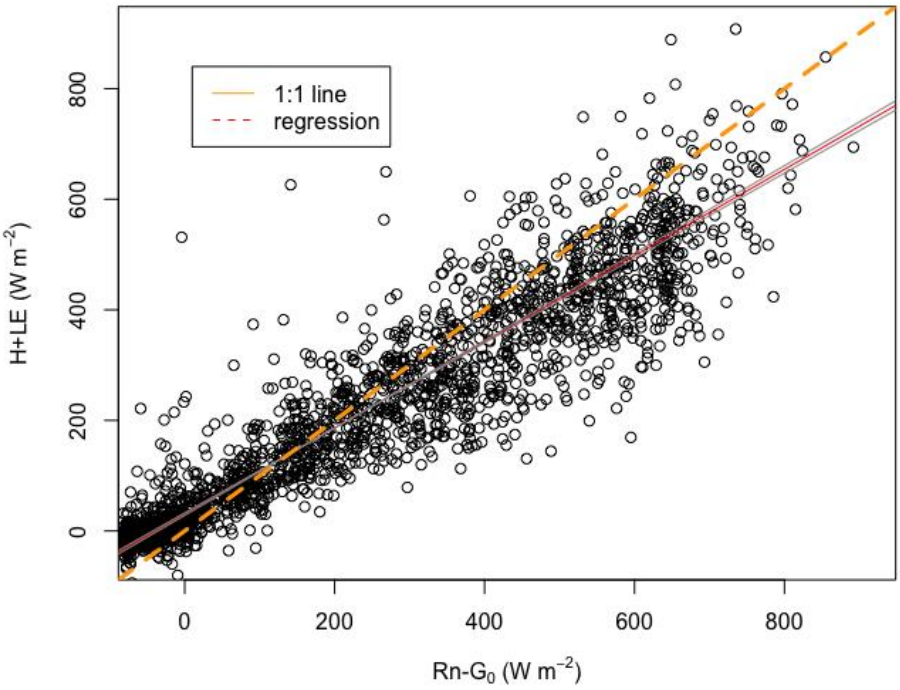

Figure 4.23. Ranged Major Axis (RMA) regression to estimate energy balance closure.

Table 4.15. Slope and intercept of the regression line. The regression is significant (p-value < 0.05).

Slope	Interc	R^2
0.78 (0.77 - 0.79)	30.4 (28.1– 32.6)	0.88, n=2460

4.5 Final remarks

A data quality analysis was on the two eddy covariance sites. The reliability of measured fluxes was also evaluated.

The Vickers and Mahrt (1997) quality control tests seem to identify many problems of the original time series. In particular, the skewness and kurtosis test, as well as the discontinuities test are able to discard the most unreliable data. They have the highest impact on the available energy and mass, if compared to the results obtained using the other statistical tests used. The dropouts and the amplitude resolution tests have a negligible impact on the analysis. The number of data that pass each one of the two tests is significant and this is an important result, if one considers the strict requirements to pass the tests.

The turbulence theoretical fulfilments are explored by means of the Mauder

and Foken (2004) policy. This algorithm is a useful tool for the assessments on developed turbulence and the steadiness of the fluxes. It is apparent that the high and medium quality data are the majority for the three summer periods. In site conditions with weak winds and eddies which may not be developed even during daytime, the Mauder and Foken test should be used, although the test on the developed turbulence conditions relies on scaling relationships which are based on the Monin-Obukhov Similarity Theory. Since it is not rigorously applicable in complex terrains, the test on turbulence should be considered as an index on how much the actual conditions deviate from the ideal ones in which the MOST is valid. Even after the aforementioned tests, some unreliable data was still found. Therefore, further manual filtering actions (based on radiation and atmospheric stability) were carried out on the dataset. This final quality control eliminated a further tranche of unacceptable data.

The daytime sensible and latent heat flux cycles show that, on average, $LE > H$. The daytime mean carbon dioxide flux cycle shows that the local ecosystem can be classified as a sink (during the daytime hours). For the high-elevation grassland site, on average the sensible heat flux is higher than the latent heat one because of reduced vegetation activity. For the Cogne site the average balance closure was higher than 55%, whereas a better closure was obtained for the Nivolet site (78%). At the latter site, as it will be shown in the next chapter, there is an increased importance of sensible heat flux if compared to Cogne.

Chapter 5

Inter-comparison of three eddy covariance sites: topography, fluxes, footprints and energy imbalance issues

In this Chapter, three eddy covariance sites are compared analysing the meteorological and ecosystem differences, to understand whether a link with morphology can be found and to explore possible energy imbalance sources. In addition, two mainstream footprint models (namely, the Hsieh et al., 2000 and Kljun et al., 2015 models) are used to correct the net radiation according to the procedure suggested by Wohlfahrt et al. (2016), in order to understand whether there are topographic effects that may play a key role in the footprint modelling and whether the energy balance always improves, and with which model the performances are improved. Indeed, Wohlfahrt et al. (2016) proposed that it is possible to increase the energy balance closure by correcting net radiation considering the flux footprint, because, the turbulent fluxes are representative of the mass and energy transport from within the footprint. However, usually, the net radiation is measured at the scale of some meters.

Finally, phase differences between vertical wind speed and scalars, including carbon dioxide (not studied in previous works), are searched at every site and analysed, since they are another possible cause of energy imbalance, according to Gao et al. (2017). This last analysis aims at understanding if the phase differences can be detected also on complex terrain and which is their magnitude, since they affect the energy balance.

This Chapter has been developed thanks to the cooperation with the Environmental Protection Agency of Valle d'Aosta, which provided the Torgnon site data and helped with the data analysis. The Author performed most of the analyses and the modelling part (with the kind help of Dr Ivan Bevilacqua for the data visualisation).

5.1 Introduction

The study of energy, water and carbon dioxide fluxes measured at different eddy covariance sites in a mountain region is important since it shows how the local ecosystem responds to topographic and meteorological forcings. This is especially true if sites are located at different altitudes, are characterised by different topography and canopy cover. Indeed, local topography, soil and canopy properties have an impact on the energy balance components, evapotranspiration and carbon dioxide net ecosystem exchange and also on flux footprint evaluation.

Some study about sites inter-comparison in mountainous areas has been performed (Hammerle et al., 2007; Stiperski and Rotach, 2016). In Austria, the i-Box project (e.g. Stiperski et al., 2012) aims at developing the knowledge about boundary layer properties in complex terrain, but most of studies are focused on turbulence structure instead of being focused on problems that are more related to ecosystem investigations problems that arise using eddy covariance technique, such as the energy balance non-closure. Plus, usually, when eddy covariance sites in complex areas are compared, they are spatially close.

One study about the role of topography was addressed in a small Tunisian valley (Zitouna-Chebbi et al., 2012). However, in that paper, the wind regime was externally driven (no diurnal cycle of wind direction, that is, anabatic/katabatic winds, occurred). They performed an analysis more devoted to the viability of eddy covariance and related data processing in sloping topography and found an energy balance of 0.64 and 0.73, respectively for downward and upward wind flow.

Studies on sites comparison at altitudes beyond 1,600 m a.s.l. with non-grazed grasslands are, nowadays, still rare. Those ecosystems are still poorly studied in the Alps, at least by means of eddy covariance systems and, as it will be discussed in detail in Chapter 6, meadows are an important ecosystem, especially if they are abandoned, since land cover changes occur, adding an impact over exchanged fluxes (e.g. van den Bergh et al., 2018). As it was already described in Chapter 4, past studies demonstrated that, provided a good data quality analysis, the eddy covariance technique can be used also on complex terrain (e.g. Hammerle et al., 2007; Hiller et al., 2008), and non-turbulent transport such as advection can occur but it is smaller than expected (Etzold et al., 2010), but it might be still important especially for carbon dioxide budget purposes (Galvagno et al., 2017).

The footprint estimate is an important objective, when one deals with eddy covariance sites, since it allows the understanding of the area which contributes to the measured fluxes. As already described in Chapter 2, several modelling approaches exist (e.g. Leclerc, 2014) and include analytical models, Lagrangian models, Higher-order closure models, large-eddy simulations and combinations of the above methods.

Analytical models are based on either an exact or an approximate solution of the advection-diffusion equation and include also the description of vertical diffusion. These models are computationally not so expensive, but they are not able

to well reproduce the scalar diffusion in many cases, also because they neglect the height dependence of eddies diffusivity and do not take into correct account the effect of atmospheric stability.

In this footprint models category, the Horst and Weil (1992) and Kormann and Meixner (2001) models are included.

Lagrangian models derive from the Lagrangian approach, describing how the particles of fluid are diffused. To elaborate a Lagrangian stochastic model, a large computing resource is needed. This drawback can be partly solved using an analytical model obtained from a Lagrangian model output (e.g. Hsieh et al., 2000). Another example of Lagrangian-derived modelling is given by Kljun et al. (2002; 2004). Among the other Lagrangian models, which are more complex to implement and derive, there is the Leclerc and Thurtell (1990) model.

The third modelling approach is related to higher-order closure models. It derives from the fact that the Navier-Stokes equation contains nonlinear terms and it is not solvable analytically (until these days). Hence, assumptions and simplifications have to be made. Considering the turbulent flow description, one finds that there is a system of differential equations with more unknowns than equations, and assumptions, called closure techniques, have to be made to determine the unknown parameters (also called moments). The closure order is related to the highest order of parameters that is computed using the prognostic equations. The moments of the following orders have to be determined, but they are functions of higher-order moments. As a consequence, these moments have to be parameterised with some approach, such as the zero-order, half order, first order, second order or third order closures (Stull, 1988).

Higher-order models describe a change in scalar fluxes in two merging fields with different scalar and aerodynamic properties. An example of footprint model is SCADIS (e.g. Sogachev and Leclerc, 2011).

Large-eddy simulation models allow the determination of footprints without externally-derived turbulence statistics, but they may be time-consuming and require complex simulations. An example is given by Leclerc et al. (1997).

There is a relatively new class of footprint models which is a breed of the previously enumerated types. Typically, one can find LES-driven Lagrangian models (e.g. Prabha et al., 2008), LES-embedded Lagrangian models (Steinfeld et al., 2008), and higher-order closure driven Lagrangian approaches (e.g. Hsieh and Katul, 2009).

The selection of the flux footprint model is not trivial. Mostly used footprint models, also for eddy covariance studies, include: the model introduced by Hsieh et al. (2000), a simple analytical model, then extended for 2D applications by Detto et al. (2006); Kormann and Meixner 1D model (Korman and Meixner, 2001), Kljun model (Kljun et al., 2002; Kljun et al., 2015) and Hsieh and Katul (2009) 2D model for heterogeneous surfaces, which is not trivially implementable in highly complex and steep terrains.

The most complex models, such as the Lagrangian ones, are not easy to run, they are computationally expensive and they are not easy to implement in complex

environments, from an experimental point of view. In addition, they often have limitations in certain atmospheric conditions. Analytical models such as the one proposed by Kormann and Meixner (2001) are simple but limited to a range of boundary layer conditions, narrower than the conditions usually met and they are not suitable for the entire stability range, including neutral conditions.

The parameterisations (mixed analytical-Lagrangian) suggested by Horst and Weil (1992) or Hsieh et al. (2000) are relatively simple but they are limited to certain turbulence scaling domain. Originally, as already mentioned, the latter model was 1D. The 2D formulation, using a gaussian cross-wind function, was proposed by Detto et al. (2006). The Hsieh and Katul model is, however, used in several works, such as Wohlfahrt et al. (2016), and it is a common choice because of its simplicity, also in the post-processing phase of eddy covariance data.

The recent model proposed by Kljun et al. (2002; 2004a; 2004b; 2015) is more suitable for a wider range of stability classes. However, there are some requirements and limitations on the friction velocity threshold and assumptions (indeed common in footprint modelling) on horizontal flow homogeneity.

All the aforementioned models were implemented and validated, but not frequently used in highly complex and steep terrains.

One important issue about the use of eddy covariance technique is the well-known energy balance non-closure, as illustrated in Chapter 4. Its causes are still debated (e.g. Foken et al., 2006b ; Foken, 2008a; Foken, 2008b; Lee et al., 2004; Leuning et al., 2012), although it is clear that it involves, at different degrees of importance, all the terms.

The first issue is related to the non-estimation or misrepresentation of the heat stored within the canopy, and the non-estimation or underestimation of the heat stored between the soil surface and the height of the eddy covariance system (anemometer and gas analyser), although, especially the air scalar storage can be small, especially in grasslands (Leuning et al., 2012). Besides, their estimation, if only one level of measurements is available is an approximation, especially for latent heat.

The second issue is related to net radiation measure: an eddy covariance site measures turbulent energy and mass fluxes that come from within the footprint area. Recently, a novel approach has been proposed to partially overcome the net radiation problem (Wohlfahrt et al., 2016). The starting point is the consideration that an eddy covariance system measures turbulent fluxes originated from within the upwind area nearby the station (this area is known as the flux footprint). Hence, also the net radiation should be corrected and "redistributed" on the whole site (turbulent) flux footprint, since the net radiation has a footprint of about 10 m (Mauder et al., 2020). This approach, however, needs the calculation of the flux footprint, which is not trivial. Most sites have only one tower, hence fluid dynamics studies for a real calculation of the footprint are not feasible. Hence, models have to be used, at least to provide an estimate of the footprint extent.

The third issue is related, as also illustrated in Chapter 2, to the *H*, *LE* (and *Fc*) underestimation. The possible causes for this effect are here recalled: air flow in non-steady-state conditions; advection (e.g. Etzold et al., 2010; Gao et al., 2016; Galvagno et al., 2017; Moderow et al., 2021); post-processing choices such as the averaging period (e.g. Charuchittipan et al., 2014), the detrending technique before computing covariances, the coordinate rotation choice (e.g. Stiperski and Rotach, 2016). Plus, the fluxes are also affected by systematic and random errors.

Random errors are difficult to be estimated because they require the calculation of the integral turbulence scale (ITS) and the guess about the maximum correlation period between the variables used to compute the covariances.

Another possible source of imbalance is related to not adequate sampling of low-frequency eddies (large eddies, Wilson et al., 2002; Foken, 2008a; Russell et al., 2015), associated with mesoscale motions. Typically, spatially small structures are associated with high-frequency turbulent motions and are called small eddies, whereas larger (including mesoscale) structures are related with lower frequency turbulent motions and they are called large eddies. It is nowadays known that among the possible causes of energy imbalance, large eddies might lead to turbulent fluxes underestimations (Foken et al., 2011) due to the finite time-averaging of relatively large, convective structures (Kanda et al., 2004). Plus, the phase difference (in both small and large eddies) between vertical velocity and temperature and water vapour produces a decrease of turbulent fluxes (sensible and latent heat fluxes, Gao et al., 2017). In particularly complex areas, this phenomenon can be amplified due to orographic lift, cold pools and advection. It should be pointed out that the phase differences are an intrinsic property of turbulence (Gao et al., 2017). Hence, they can be considered but they do not need corrections.

5.2 Materials and Methods

5.2.1 Data analysis and flux footprints

Three sites were used for this work: Cogne, Nivolet and Torgnon. The first two sites have already been described in Chapter 3. The third site (45.84°N, 7.58° E) is managed by the Aosta Valley Regional Environmental Protection Agency (ARPA VdA, Regional Authority). A description of the site is given by Galvagno et al. (2017).

Three datasets, each consisting of seventy days between the 1st June 2016 and 8th August 2016 for Cogne and Torgnon and between 1st June 2018 and 8th August 2018 for the Nivolet and Torgnon stations, were used.

The raw data were processed using the EddyPro 6.2.1 software. The Cogne and Nivolet datasets were treated following the same procedure indicated in Chapter 4, whereas the Torgnon data had already been processed by ARPA Valle d'Aosta using the post-processing illustrated in Galvagno et al. (2017), which included planar fit rotation and correction of spectral losses as in Moore (1986). The required quality control was less strict than the other sites, since the Torgnon site is on a more homogeneous terrain and the time series are characterised by less problems. The quality control included the Foken and Wichura (1996) tests. Mean diurnal cycles of wind speed, stability parameter, sensible and latent heat fluxes, net ecosystem exchange, friction velocity, global radiation and wind direction were computed. As seen in Chapter 2, Section 2.3, the footprint modelling is important. A Lagrangian footprint model approach is one of the most natural to represent the motion of particles. Using models with relatively simple parameterisations is important as the first step on complex terrains. Therefore, two widely used Lagrangian footprint models were adopted: namely the Hsieh et al. (2000) model, then refined by Detto et al. (2006), and the model described by Kljun et al. (2015). The climatological flux footprints for the whole period were estimated for each site using only the Kljun et al. (2015) formulation. In addition, a particular analysis on the footprint modelling usage for net radiation correction was performed on the following clear sky days: 22nd June 2016 for the Cogne and Torgnon sites; 27th June 2018 for the Nivolet and Torgnon sites.

The Hsieh model can be applied in a wide range of stability classes and it was obtained from a combination of Lagrangian stochastic model and dimensional analysis. However, it assumes MOST theory to be valid. The footprint function is defined as in Eq. 5.1:

$$f(x, z_m) = \frac{1}{k^2 x^2} D z_u^p |L|^{1-p} e^{-\frac{1}{k^2 x} D z_u^p |L|^{1-p}} \quad (5.1)$$

where x is the along-wind coordinate, k is the von Karman constant (0.41); D and P are constant parameters depending on the atmospheric stability class:

$\frac{z_u}{L} < 0.04$: Unstable
$|\frac{z_u}{L}| < 0.04$: Near neutral and neutral
$\frac{z_u}{L} > 0.04$: Stable

$D = 0.28; P = 0.59$, unstable
$D = 0.97; P = 1$, near neutral and neutral
$D = 2.44; P = 1.33$, stable

L is Monin-Obukhov length and $z_u = z_m (\ln\left(\frac{z_m}{z_0}\right) - 1 + \frac{z_0}{z_m})$. z_m is the measurement height of the tower station, and z_0 is the roughness length.

To implement the 2D information (the original model was only 1D), the modification suggested by Detto et al. (2008) was used. In that work, the lateral diffusion is assumed to be Gaussian and therefore, as in Eq. 5.2:

$$D(x,y) = \frac{1}{\sqrt{2\pi}\sigma_y} e^{-\frac{1}{2}(\frac{y}{\sigma_y})} \tag{5.2}$$

where $\sigma_y = \frac{a_1 z_{0m}\, \sigma_v}{u^*} \left(\frac{x}{z_{0m}}\right)^{p1}$

$a_1 = 0.3; p1 = 0.86$ are similarity parameters, z_{0_m} is the momentum roughness length, u^* is the friction velocity x is the along-wind coordinate.

The Kljun model is based on LPDM model (Rotach et al., 1996), a Lagrangian model. A wide range of atmospheric stability classes is considered and approximates a skewed probability density function of the *w* (vertical) velocity component, and it models the footprint with a backward algorithm. The model is based on the convective boundary layer scheme proposed by Baerentsen and Berkowicz (1984). The footprint model is based on a scaled crosswind dispersion and a crosswind integrated footprint function. Hence, the overall function can be written as in Eq. 5.4.

$$f(x,y) = \overline{f^y(x)} \frac{1}{\sqrt{2\,\pi}\sigma_y} e^{-\frac{y^2}{2\sigma_y^2}} = \overline{f^y(x)}\, D_y \tag{5.4}$$

where $\overline{f^y(x)}$ is the crosswind integrated footprint function and D_y is the lateral dispersion term. $\overline{f^y(x)}$ can be written non-dimensionally as

$$F^y = f^y z_m \left(1 - \frac{z_m}{h}\right)^{-1} \left(\ln\left(\frac{z_m}{z_0}\right) - \Psi_m\right) \tag{5.5}$$

where x is the along-wind coordinate, z_m is the measurement height, h is the boundary layer height, z_0 is the roughness length and

$$\Psi_m = \begin{cases} -\frac{\frac{5}{3}\, z_m}{L} & L > 0 \\ \ln\left(\frac{1+\chi}{2}\right)^2 + 2\ln\left(\frac{1+\chi}{2}\right) & \\ -2\tan^{-1}(\chi) + \frac{\pi}{2}, & L < 0 \end{cases} \tag{5.6}$$

Equation (5.5) can also be rewritten using a fit (see Kljun et al., 2015) and retrieving the best fit parameters *a, b, c* and *d*:

$$F^{y} = a\left(\hat{X}^{*} - d\right)^{b} e^{-\frac{c}{\hat{X}^{*}-d}} \tag{5.7}$$

This is a more complex approach, that was used to estimate the climatological footprints for the analysed periods and also to produce daily footprints to be compared with the outcomes of the Hsieh model.
The two footprint models were implemented using a 2 x 2 m grid to be comparable with the digital elevation model and the solar radiation model resolution described in the following Section.

5.2.2 Solar model and net radiation reconstruction

To evaluate the energy balance closure, the EBR method was adopted. This method is given by the computation of the ratio

$$EBR = \sum \frac{H + LE}{R_n - G_o} \tag{5.8}$$

where the sum is done on the daytime hours, G_0 is the ground heat flux at the air-land surface interface.

A possible, recent procedure to improve the closure was tested for the three sites in single clear sky days, following the procedure proposed by Wohlfahrt et al. (2016). That approach allows reconstructing the solar radiation using a digital elevation model (DEM) and single-point measurements of longwave radiation. The used DEM, retrieved from Valle d'Aosta Region Geoportal, the Regional geographical data repository, has a resolution of 2 x 2 m and takes into account the slope and aspect of the terrain. To reconstruct the global radiation and shortwave incoming radiation fields for the three sites pixel by pixel, the SAGA-GIS Module for potential incoming solar radiation (e.g, Hofierka and Suri, 2002; Boehner and Antonic, 2009) was used. The model set-up illustrated in Table 5.1 was used.

The sky view factor and solar geometry were computed using the SAGA-GIS tool referred to as "Module Sky View Factor" (Boehner and Antonic, 2009; Hantzschel et al., 2005), whereas the shading was computed within a built-in function of the model.

The global radiation field within an area comparable to the footprint was reconstructed using the aforementioned solar radiation model. The values were validated against measured data and they were used to derive the correction for net radiation. This choice was based on the fact that several approaches to correct measured global radiation according to slope and aspect require either the measure or the estimate of the fraction of diffuse radiation (e.g. Ham, 2005; Wohlfahrt et al.,

2016). This estimate is based on models (e.g. the Gompertz function). These models have to be optimised for each site and to perform such optimisations, nearby stations data have to be used (such as photosynthetically active radiation or solar radiation). However, in highly complex terrains stations sufficiently near the eddy covariance site are often not available (as for this analysis). Another approach corrects the global radiation using only data about solar declination, azimuth, zenith, aspect and slope (Kondratiev et al., 1978). However, all these methods are based on a single-point measurement that is corrected for each pixel aspect, slope and, more in general, for geometrical factors. For single pixels or a small group of pixels, this is acceptable, but for several dozens of pixels (i.e. the extension of the flux footprint), it might cause problems due to different shading from surrounding mountains. As a consequence, it was chosen to use a model that reconstructs the global radiation pixel by pixel.

To produce an assessment on the model validation, the global radiation modelled values were compared to measurements of incoming shortwave radiation at the three sites: Cogne (where the radiometer is parallel to the slope), Torgnon, which is on almost flat terrain and Nivolet after the correction of measurements for the slope and aspect – following the procedure described by Kondratiev et al. (1978) - of the area surrounding the station. (The station is on flat terrain, but the surroundings have a slope of about 11°). The correction was applied to measured data which are related only to the station surroundings, hence it was acceptable to use it.

The net radiation was then determined for each pixel at the three stations, with the formula

$$R_n = R_{g_s}(1 - \alpha) + LW_{in} - LW_{out} \tag{5.9}$$

where R_{g_s} is the reconstructed modelled global radiation, α is the albedo (assumed equal to 0.23), LW_{in} is the longwave incoming radiation and LW_{out} is the outgoing longwave radiation. Both these values are single point measures, as it has been demonstrated that these two components are not strongly dependent on aspect and slope.

Table 5.1. The solar radiation model set-up.

Latitude	derived from DEM
Solar constant	1367 W m^{-2}
Atmospheric effects	lumped atmospheric transmittance 60%
Shadow	“fat” (the whole cell’s shadow is traced)

The lumped approach for atmospheric effects assumes a homogeneous and cloudless atmosphere. The direct beam follows the Beer's Law. The transmission coefficient was empirically chosen equal to 0.6.

Two different approaches were used, considering the two models: the Hsieh model operated at 30-minutes time scale. Therefore, also the global radiation model was run with that time step.

To use the Kljun footprint model, data were instead aggregated at 1 hour. To run the model, the local boundary layer was estimated from the ERA5 reanalysis repository (https://cds.climate.copernicus.eu/) having a 0.25°x0.25° grid.

The net radiation was weighted using the footprint functions found before, using

$$R_{n_s} = \frac{\sum f(x,y)\, R_n(x,y)}{\sum f(x,y)} \tag{5.10}$$

where $f(x,y)$ and $R_n(x,y)$ are the footprint function and the net radiation respectively, pixel by pixel. The summation is intended over all the pixels included within the footprint domain. After the correction using the two alternative procedures explained earlier, the energy balance ratio was again computed.

5.2.3 Large and small eddies contributions to energy imbalance

Possible effects of large and small eddy contributions on surface energy imbalance were investigated using the approach of Gao et al. (2017). However, they used data collected on flat and homogeneous sites, whereas, in this Chapter, data from topographically complex sites are used.

It is nowadays known that the phase difference between vertical velocity and water vapour produces a decrease of latent heat flux (Gao et al., 2017). This difference can characterise the variations in large, low-frequency and also small, high-frequency structures (eddies). Possible cause for the phase difference include large eddies having the same characteristics of small eddies and disturbing the atmospheric surface layer, and downward large eddies carrying warm and moist air. In the latter case, the vortices (eddies) contribute negatively to the sensible and latent heat fluxes (Gao et al., 2017).

The phase difference implies also time lags between the time series of vertical wind speed and scalars. Furthermore, in particularly complex areas, this phenomenon can be amplified due to orographic lift, cold pools and advection.

For each 30 minutes period (one run) and after the quality control, the fluctuations *w'*, H_2O' and CO_2' were computed and then the Ensemble Empirical Mode Decomposition (EEMD, e.g. Wu and Huang, 2009) was applied. EEMD was

used to detect and separate large from small eddies, defined as the structures below and above the frequency of 0.02 Hz, respectively.
Every signal can be in principle decomposed, by means of EEMD in two components, as illustrated in Eq. 5.11.

$$x(t) = r(t) + \sum_{i=1}^{n} CM_{i,x}(t) \tag{5.11}$$

where the first term is called "residual", and the second term is a set of oscillatory components which are amplitude-frequency modulated (a set of intrinsic mode functions, IMF). The EEMD algorithm was used on 30 minutes data for the fluctuations of *w, T,* H_2O, and CO_2.

The EEMD technique is based on adding, iteratively, various white noise time series to the signal. The added noise is different for each trial, hence the IMFs in N different trials are not correlated.

1) For each trial, a white noise is added to the signal
2) The signal, now contaminated with noise, is decomposed as illustrated in Eq. 5.11
3) The first two steps are iterated for N trials varying the white noise added to the signal
4) The final, average IMF of the EEMD is computed by averaging the total IMF related to the N trials

Each of the components associated with the second term of Eq. 5.11 are related to a particular frequency and to a particular range of eddy structures. A threshold can be set to divide large from small eddies, usually 0.02 Hz. Following Gao et al. (2017), that threshold was used. Hence, components with frequencies lower than 0.02 Hz were considered large eddies (namely, the components from 1 to 8 in the summation term). Components having frequencies greater than 0.02 Hz were considered small eddies (namely, the components from 9 to 14). On the 30-minutes periods, the turbulent fluctuations were computed using the block average approach after the despiking process and the double rotation.

Then, the Hilbert transform was defined as

$$\hat{x}(t) = \frac{1}{\pi} CP \int_{-\infty}^{+\infty} \frac{x(\tau)}{t-\tau} d\tau \tag{5.12}$$

where $\hat{x}(t)$ is the Hilbert transform of signal $x(t)$ the signal, $x(\tau)$ is the signal at time τ, *CP* is a Cauchy principle value integral. The Hilbert transform was computed for both the signals. An analytic signal was derived and it is represented by $s^x(t) = x(t) + i\hat{x}(t)$. The same is valid for a second signal $y(t)$.

Then, the Hilbert cross spectrum was derived. Given the two signals (large and small eddies), it is defined as $HCSP(t) = s(t)^{x^*}\, s^y(t)$, where $*$ indicates complex conjugation,

The phase difference between signals $x(t)$ and $y(t)$ was then estimated with Eq. 5.13.

$$\Phi_{diff}(t) = \text{atan}\left(\frac{Im\big(HSCP(t)\big)}{Re\big(HCSP(t)\big)}\right) \tag{5.13}$$

In this analysis, the phase differences are meant to be between turbulent fluctuations, that is, w' and T', w' and H_2O' and w' and $CO_2{}'$ for both the large (denoted with *l* subscript) and small (denoted with *s* subscript) eddies.

The EEMD and Hilbert Transform were applied using, respectively, the "hht" R packages (see Appendix F)

5.3 Results and discussion

5.3.1 Micrometeorological analysis of the three sites

In Figure 5.1 and 5.2, the wind direction, wind speed, global radiation, stability parameter and friction velocity are shown. All three sites are characterised by a high of solar radiation, but they differ in wind regime. In particular, Cogne and Torgnon have more channelled winds than Nivolet site. This is particularly true for Cogne. The Nivolet site, instead, has a more variable regime with lateral (up/downvalley) contaminations.

Among the most notable characteristics of the sites, the atmospheric stability parameter shows that the Cogne site has the most unstable conditions during the daytime, especially if compared to Torgnon. Therefore, even if wind speed and $u*$ are low if compared to the other sites, the fluxes are still quite well measured. The highest friction velocity values were found for the Nivolet site, which is the most exposed to higher speed winds and also to up/downvalley winds.

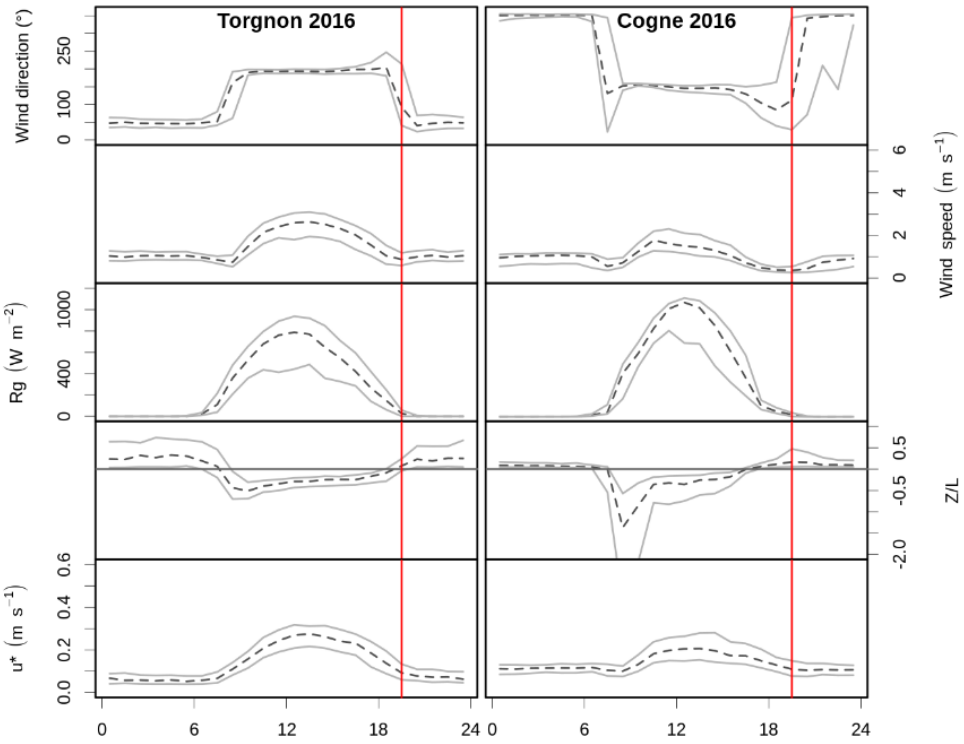

Figure 5.1. Wind direction, wind speed, global radiation, Monin-Obukhov stability parameter and friction velocity for the period 1st June – 8th August 2016. The red line indicates sunset.

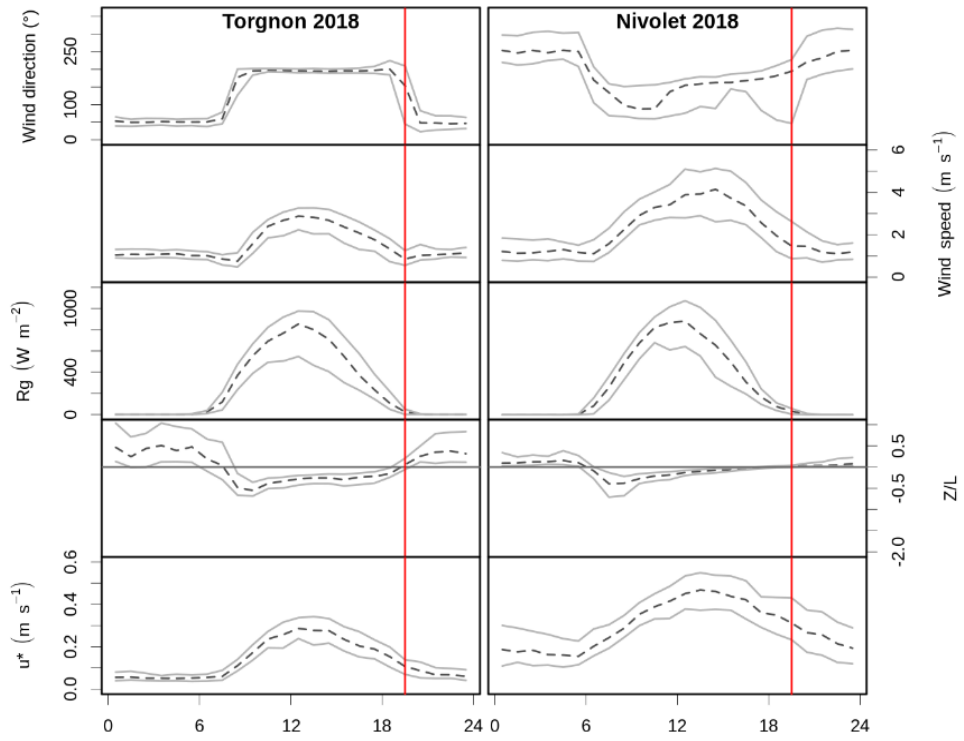

Figure 5.2. Wind direction, wind speed, global radiation, Monin-Obukhov stability parameter and friction velocity for the period 1st June -8th August 2018. The red line indicates sunset.

In Figure 5.3 and 5.4, the sensible heat, the latent heat flux and the net ecosystem exchange (NEE) are shown for the sites. The latent heat flux is notably higher than sensible heat flux at the two lower altitude sites (Cogne and Torgnon), whereas at the Nivolet site the opposite condition occurs, because of a reduced canopy activity (in both photosynthesis and respiration).

A major ability for carbon sequestration is found at the lowest site (Cogne). Interestingly, the two sites of Torgnon and Nivolet show similar NEE values and share even an analogous curve shape, with a minimum localised around 10 a.m., whereas Cogne shows a negative peak shifted at around midday. The deeper peak can be explained by the fact that the Cogne site is located at a lower altitude if compared to the other two sites. The peak shift could be induced by the saturation of photosynthesis response to light in the central hours of the day. The saturation occurs later likely because the site is characterised by a mixture of grass and shrubs, while at the other two sites there is only grass, which is more sensitive to dry periods. The mixed land cover at Cogne may compensate the photosynthesis saturation which occurs at high radiation (Tramontana et al., 2020).

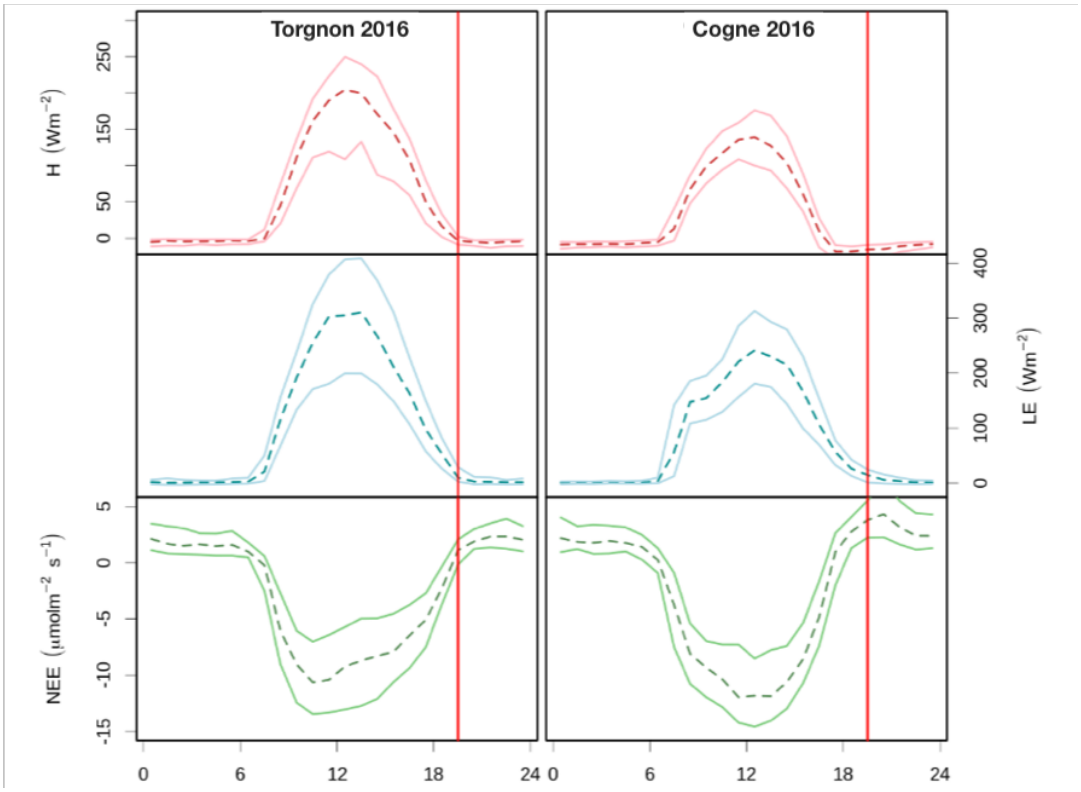

Figure 5.3. Mean diurnal course of sensible heat flux, latent heat flux and net ecosystem exchange for Torgnon and Cogne 2016 growing season. The red line indicates the local sunset.

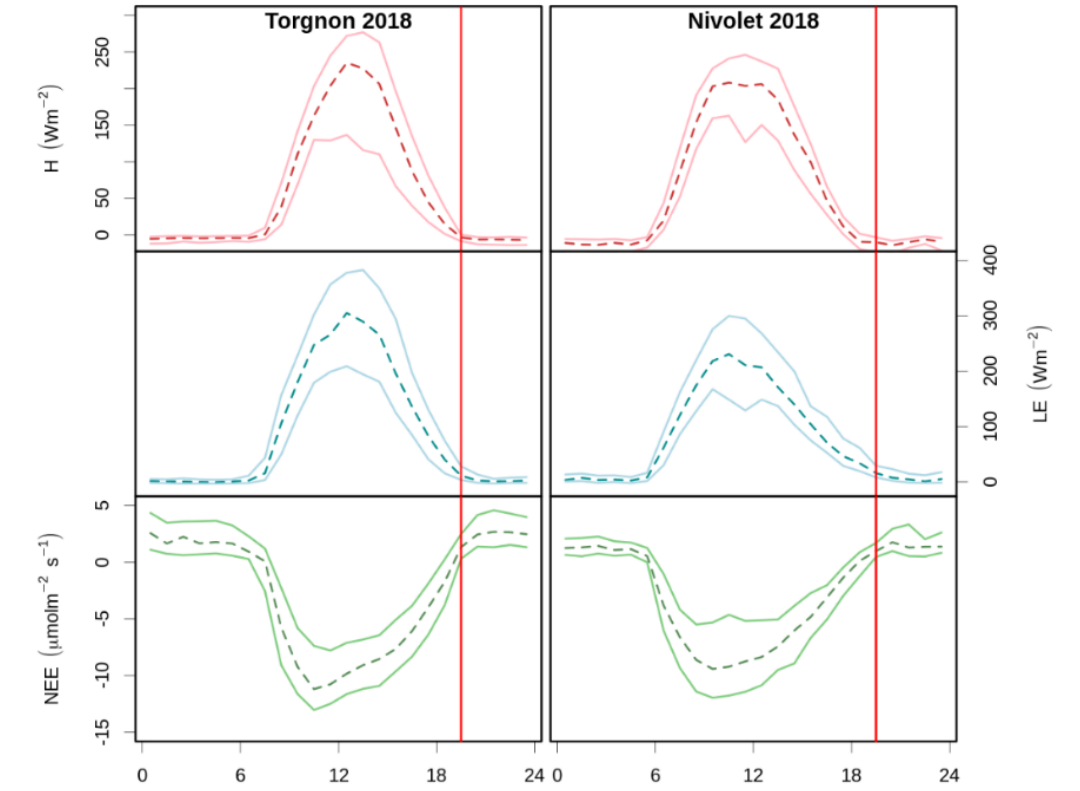

Figure 5.4. Mean diurnal course of sensible heat flux, latent heat flux and net ecosystem exchange for Torgnon and Nivolet 2018 growing season. The red line indicates the local sunset.

An interesting feature is found especially in the turbulent fluxes measured at Cogne, and it will be better explored in Chapter 6. The latent heat flux and, less evidently, the sensible heat1 and the carbon dioxide fluxes show a morning inflexion (between 9:00 and 10:00, Figure 5.3) on their mean diurnal course determined for the period 1st June – 8th August which is not found at the other two sites (Figures 5.3 and 5.4). This inflexion might be caused by topography-induced wind regimes. Indeed, the wind flow changes from downslope (katabatic wind) to upslope (anabatic wind) in the morning, regularly between 7:00 and 9:00. Prior to the stabilisation at around 150° (at around 10:00-10:30), on average, in the first part of the morning, the wind flow comes mainly from a direction near 100° (see also Figure 5.5) and, therefore, it transports heat (hence, influencing also latent heat) from a slope near the station that is exposed to sunlight earlier. This warms the air reaching the station. However, at about 10:00 in the morning, the flow comes from 150° (bottom of the valley, where the air is still cold). This colder air arrives to the station and likely causes the same morning inflexion also on the air temperature (Figure 5.5). The inflexion is not evident (Figure 5.5) on the mean cycle of carbon dioxide or water vapour (which is not an interesting quantity because of its variability and absence of diurnal cycle, hence it is not shown), but, it is instead found for the covariances $\overline{w'T'}$, $\overline{w'H_2O'}$, and $\overline{w'CO_2'}$ (Figure 5.5). The wind regime change has, therefore, effects on fluxes also because the flux footprint changes orientation. The transport towards the station is not immediate and there is the inertia of the system, hence the effects are measured with a time lag. A further analysis on the mentioned inflexion will also be done in Chapter 6.

More spatial information about possible sources and sinks of water vapour and carbon dioxide can be retrieved from the colour maps shown in Figure 5.6. Sources are identified during daytime for sensible and latent heat, whereas carbon dioxide is sequestrated due to photosynthetic activity. This response exists in all case studies. However, the CO_2 emitted at night at the highest elevation site is lower if compared to the other two sites, due to reduced respiration caused by lower temperatures. Especially at the Cogne site, the spots of fluxes (either negative or positive) are more coupled with local topographically induced wind regime if compared to the other site with a defined night-time and daytime regime (Torgnon). Probably this fact can be explained by the Cogne site location: in a small lateral valley with less influence from mesoscale systems, therefore with the weak or non-existent lateral wind. Besides, at Cogne and Torgnon, the sources and sinks of heat, water vapour and carbon dioxide are very well localised with respect to Nivolet.

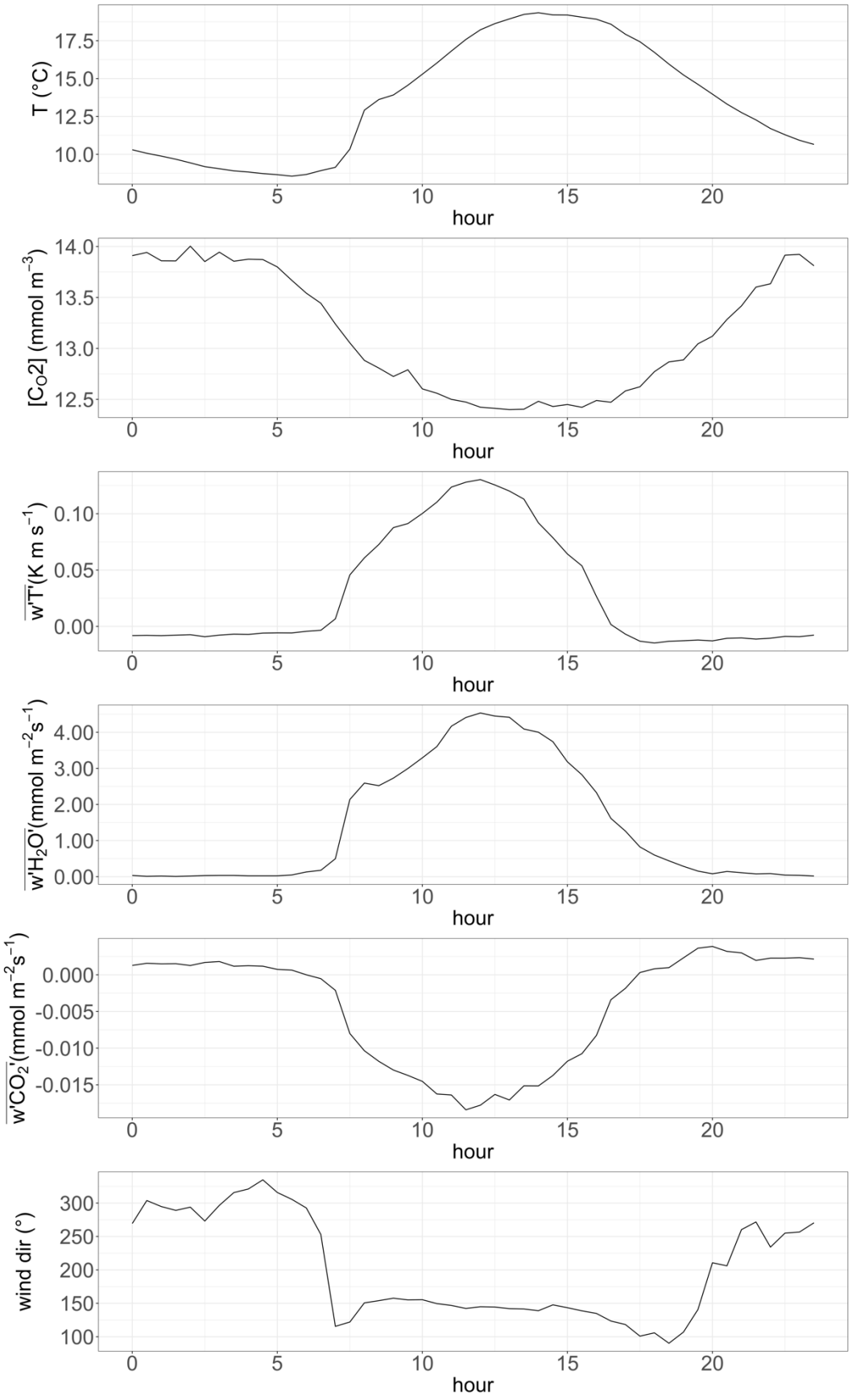

Figure 5.5. Mean diurnal cycles of temperature, concentration of carbon dioxide, covariances of scalars and wind direction at Cogne (1 June – 8 August 2016).

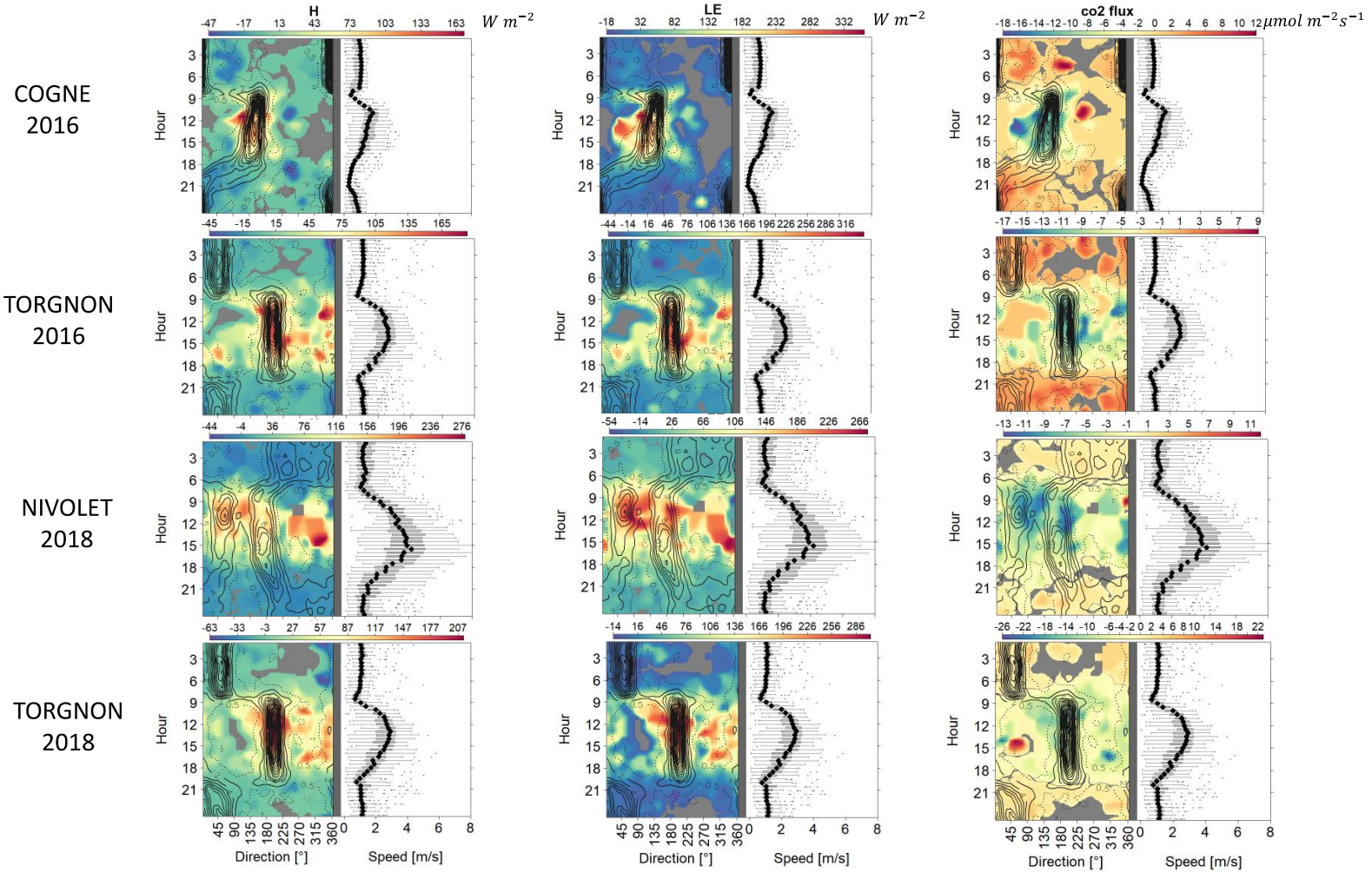

Figure 5.6.Average fluxes and wind direction probability contour maps as a function of wind direction and hour of the day (left) and wind speed vs hour of the day (right)

The climatological footprints for the three sites were confirmed by the analysis of the wind roses and highlighted that Cogne is the site with the smallest footprint (2765 m^2 at 80%, Figure 5.7). This may indicate that, if advection existed, its contribution might not be extremely important because most of the time, the energy and mass transport in a non-turbulent motion does not come far away from the site. The Torgnon footprint (Figure 5.8, footprint at 80% of contribution) was characterised by a footprint three times greater than Cogne (9618 and 8775 m^2 in 2016 and 2018, respectively, with little differences in the footprint shape). The Nivolet site (Figure 5.9, footprint at 80% of contribution) had the largest and most complex footprint (47096 m^2), it was not an ellipsoid such as at the other two sites, and it included contributions of the along-valley (crosswind) transect. It should be noted that at Nivolet the measurement height is 4.6 m and not 2 m and that the site experienced the highest wind speed values. The Torgnon flux footprint is an ellipsoid such as the one found for Cogne, and it is almost constant throughout the years.

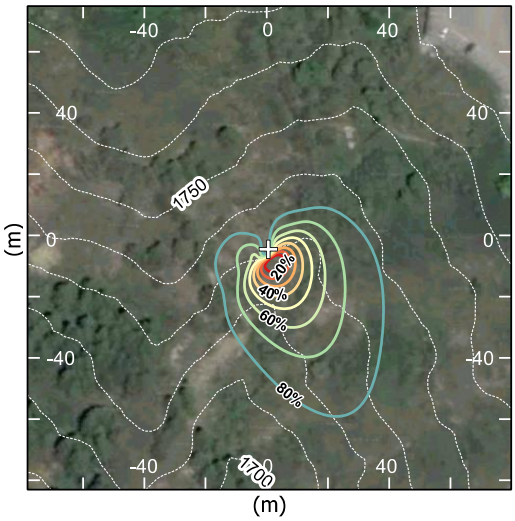

Figure 5.7. Climatological footprint at Cogne for the period 1st June – 8th August 2016.

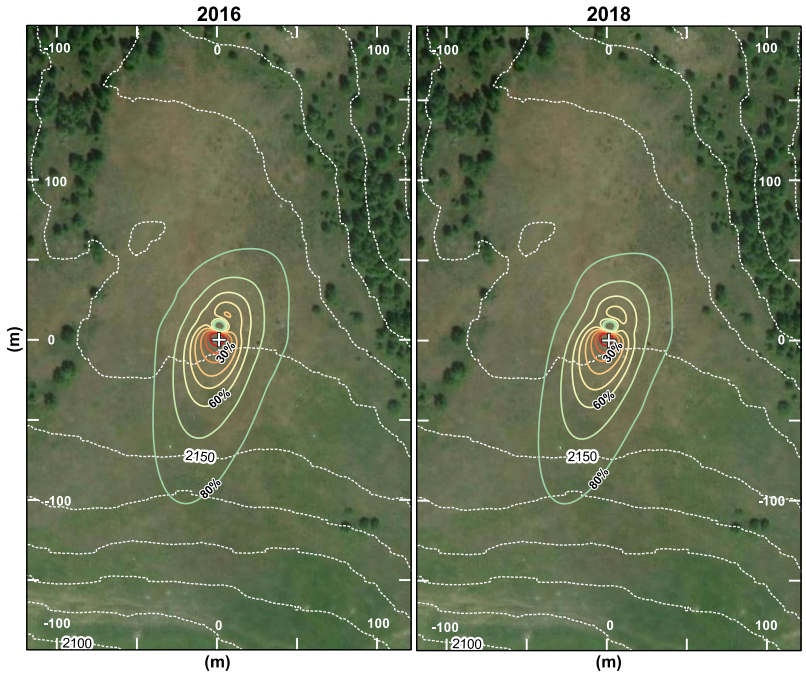

Figure 5.8. Climatological footprint at Torgnon for the period 1st June – 8th August 2016 and 2018.

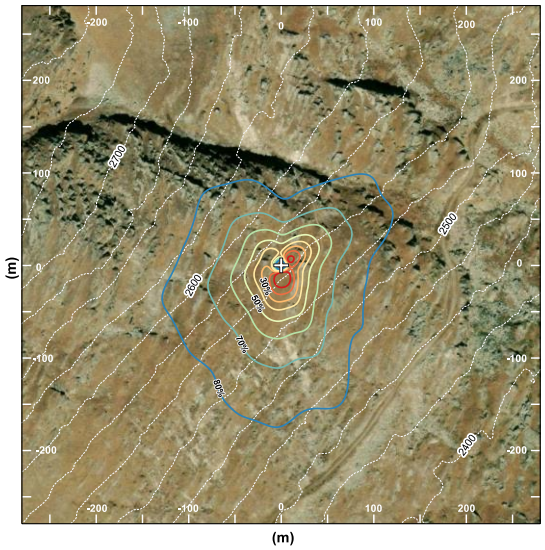

Figure 5.9. Climatological footprint at Nivolet for the period 1st June – 8th August 2018.

The evaluation of energy balance closure on the whole period 1st June – 8th August was performed on daytime data at every site. Results highlight that at Torgnon there is the highest energy balance closure (beyond 95%). At Nivolet, the closure is around 65% and at Cogne is 57% (Table 5.2). The energy balance closure at Torgnon and Nivolet sites is comparable with previous findings (FLUXNET sites, Wilson et al., 2002), especially if in complex terrain (Hiller et al., 2008, with an overall closure of 0.74 on a flat terrace on a slope, similarly to Nivolet site). At the Cogne site, the closure is lower than at the other sites and lower than the findings

of Hiller et al. (2008). However, it is still within the range of FLUXNET sites and of what was reported by Xin et al. (2018). They investigated 10 mountain stations data in the Tibetan plateau, and found closures ranging from 0.57 to 0.99.

Table 5.2. Linear regression values of the energy balance closure at the Cogne, Nivolet and Torgnon eddy covariance sites.

Site	Slope	Interc	R^2
Cogne	0.571 (0.538-0.610)	35.8 (19.9-51.7)	0.53 (n=1005)
Nivolet	0.822 (0.766 – 0.883)	76.9 (56.2-97.4)	0.42 (n=1049)
Torgnon 2016	0.980 (0.937-1.016)	-0.6 (-12 - 10.9)	0.82 (n=543)
Torgnon 2018	0.981 (0.935 – 1.028)	-7.1 (-23.4 - -5.4)	0.77 (n=521)

5.3.2 Net radiation correction and energy balance closure

Global and net radiation reconstruction

In this Section, a detailed solar and net radiation reconstruction is performed to understand whether the energy balance closure improves. The analysis is performed on single clear sky days.

The modelled global radiation, reconstructed pixel by pixel employing the "Module potential incoming solar radiation" included in the SAGA-GIS environment (e.g. Hofierka and Suri, 2002) was close to the measured values at the three sites, considering the pixel assigned to the station. Results (Figure 5.10) indicate an acceptable agreement between modelled and measured values for the three sites of Cogne, Nivolet and Torgnon. The model is actually able to satisfactorily reproduce global radiation at the three sites. For the Cogne site, the RMSE between modelled and observed global radiation is 46 W m^{-2}. At Torgnon, RMSE values of 19.6 W m^{-2} and 19.5 W m^{-2} are found, respectively for 22nd June 2016 and 27th June 2018. The Nivolet site shows a RMSE equal to 75.6 W m^{-2}. The best performance is obtained at Torgnon. Relatively high values at Cogne and Nivolet can be imputed to topography complexity and because the DEM pixel at Cogne may include global radiation contributions that are not well represented by single-point measures.

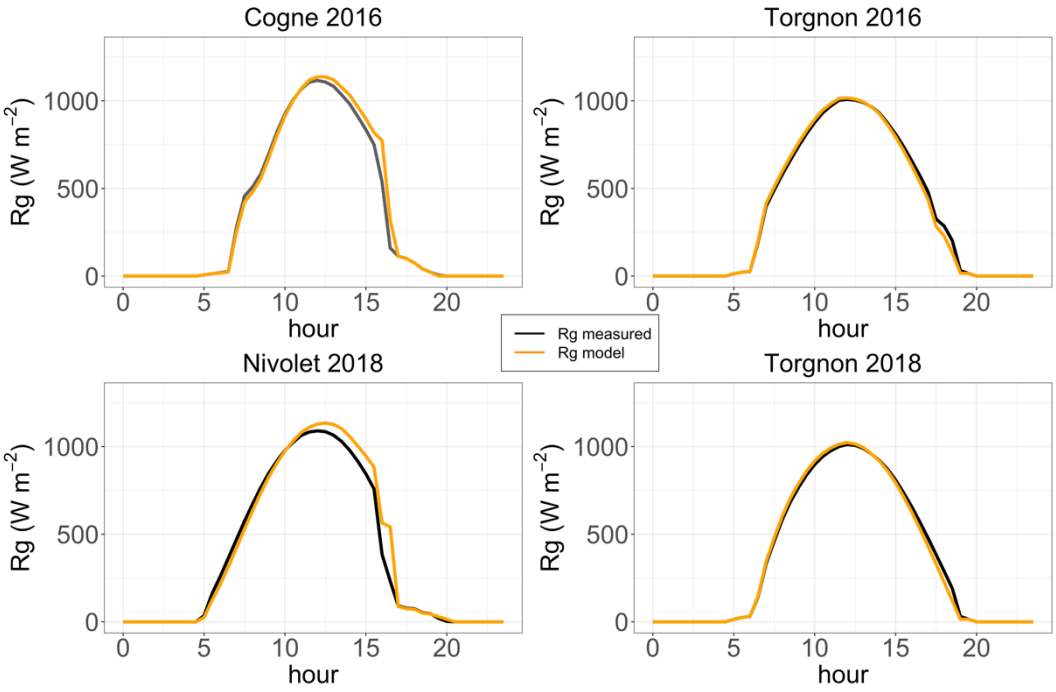

Figure 5.10. Measured and modelled global radiation for 22nd June 2016 at Cogne and Torgnon and for 27th June 2018 at Nivolet and Torgnon.

Once the global radiation is reconstructed over the domain, it can be used to estimate net radiation, which will be then corrected according to the actual footprint area using Eq. 5.9, hence using only the pixels included within the footprint.

The footprint models used for this analysis are the Hsieh et al. (2000) model, improved by Detto et al. (2006) and the Kljun et al. (2015) model, hereafter also referred, respectively, as "Hsieh model" and "Kljun model". The first model has an along-wind distance 10-15 m greater than the second model, whereas similar cross-wind distances are found. During daytime hours (i.e. in the range 8:00 – 16:00) the along-wind footprint direction at Cogne is almost constant, as at Torgnon.

The footprint models' performance on net radiation reconstruction can be evaluated for both the models looking at the shape of the net radiation diurnal course. At the Torgnon and Nivolet sites, the two footprint models allow a reasonable net radiation correction without any topographic forcing (Figures 5.11 and 5.12), as net radiation reaches the maximum value around midday and then begins to decrease in the afternoon, as also shown by the turbulent fluxes. Between the two models no particular difference is found. The two mentioned sites are characterised by a less complex topography, if compared to the Cogne site. This site is located on a steep slope in a narrow lateral valley and the two footprint models, likely, yield a misrepresented footprint. The modelled footprint has a main direction (along-wind) which does not correspond to the "real" direction heavily influenced by topography. Therefore, the actual area contributing to measured fluxes is not well represented. When compared with measured net radiation and, above all, with turbulent fluxes, the reconstructed net radiation does not follow the

typical diurnal course with a peak in the central hours and a decrease in the afternoon. This outcome is probably because the modelled footprint extends towards the opposite slope (still hit by sun rays) of the narrow valley.

Likely, for topographically complex, concave and steep sites, the along-wind direction of the footprint should be corrected according to local topography. Both the Hsieh and Kljun models need this correction for the Cogne site. Figures 5.11 and 5.12 show two possible and *a priori* reasonably corrected along-wind directions, that is, 169° (the site aspect) and 210° (the average aspect of the valley side where the station is located). This forcing is constant along the day, and this choice is based on the almost constant wind direction measured at the site, so even if with a forcing, the footprint orientation is not heavily changed.

Results highlight that, to obtain a reliable and acceptable net radiation reconstruction, the 210° direction should be taken.

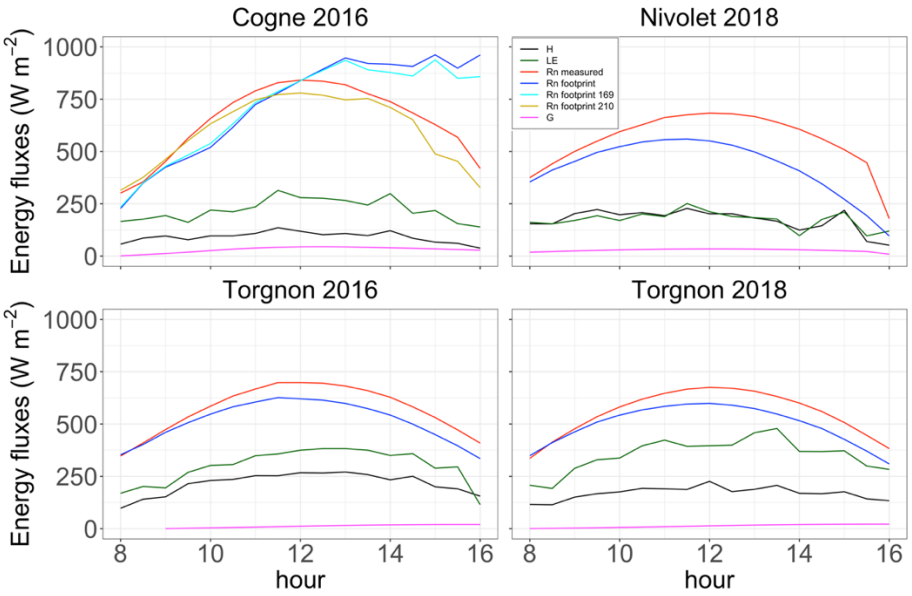

Figure 5.11. Net radiation reconstruction and energy balance ratio improvement using the Hsieh and Katul model.

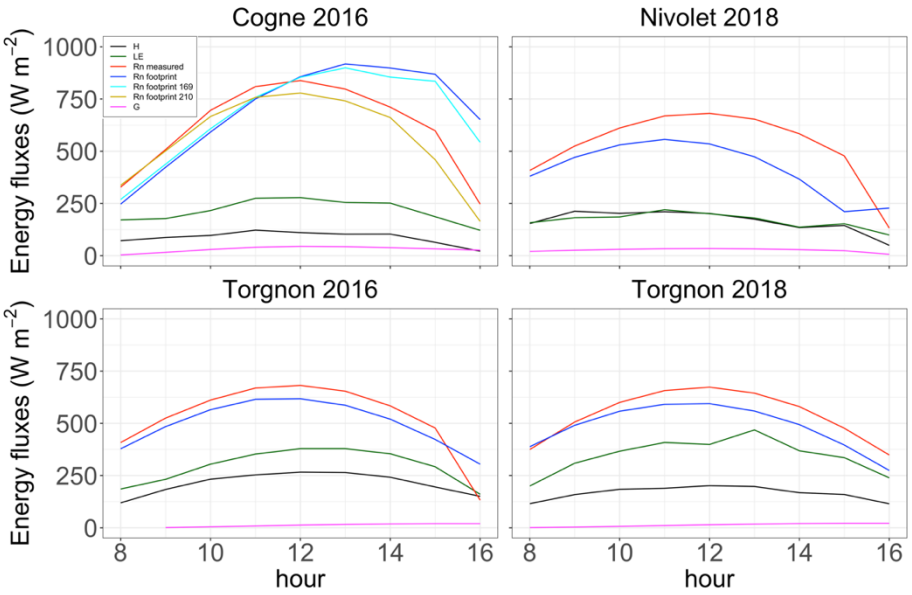

Figure 5.12. Net radiation reconstruction and energy balance ratio improvement using the Kljun model.

Energy balance closure improvement

The effect of footprint model choice and of along-wind direction shifting at Cogne are also found when the energy balance ratio (EBR) is used to evaluate the energy balance closure at the sites on single days.

The EBR is improved, independently from the footprint model and without any correction, at the Torgnon and Nivolet sites (Table 5.3). Using the Hsieh model at Torgnon, an improvement of +13% on both days (22nd June 2016 and 27th June 2018) is found. The Kljun model instead yields +6.0% and +13.0% on the two mentioned days. It should be noted that, at the Torgnon site, the net radiation reconstruction is not strictly required, because the energy balance closure is very high already without the correction.

At Nivolet, similar EBR improvements are found using the two models (+27.8% and +28.2%). A slightly higher EBR is, therefore, found with the Kljun model.

At the Cogne site, if no along-wind direction correction, or if the 169° forcing is used, the EBR does not improve. With the the 210° forcing, instead, the energy balance closure improves of almost 7% at Cogne using the Hsieh formulation and +10% using the Kljun formulation (Table 5.3). The net radiation correction is more effective at the Nivolet site likely because it is characterised by the widest footprint, which shows both up/downslope and up/downvalley winds, and the new global radiation takes into account the enhanced area contributing to measured fluxes

With the appropriate choice of topography forcing at the steepest site (Cogne), the energy balance closure is improved at every site, and the improvements are comparable with the findings illustrated by Wohlfahrt et al. (2016) for a wider period that is, around up to 10% at the Cogne and Torgnon sites. At Nivolet, this improvement is around two times this value.

Table 5.3. Energy balance closure improvement at the three sites using the two different footprint models.

Site	Date	EBR change (Hsieh not corrected)	EBR change (Hsieh forced 169°)	EBR change (Hsieh forced 210°)	EBR change (Kljun not corrected)	Kljun Cogne forced (169°)	Kljun Cogne forced (210°)
Cogne	22/06/16	-17.4%	-14.8%	+6.8%	-11.8%	-9.4%	+10.2%
Nivolet	27/06/18	+27.8%	-	-	+28.2%	-	-
Torgnon	22/06/16	+13.0%	-	-	+6.1%	-	-
	27/06/18	+13.2%	-	-	+13.0%	-	-

5.3.3 Large and small eddies

Some clear sky day (namely, 22nd June 2016 for Cogne and Torgnon sites and 27th June 2018 for Torgnon and Nivolet sites) were selected because of acceptable $\frac{z}{L}$ daytime values, high net radiation available and developed turbulence. The comparison, in those days, of large and small eddy contributions of sensible and latent heat fluxes (Figure 5.13) suggests that, in the analysed days, the large eddies do not seem to show a great contribution at the site in all daytime hours, even during the late afternoon. Indeed, low frequency contributions (large eddies), although not negligible, are lower than high frequency ones (small eddies). It is interesting to note that the small eddies contribution is always higher than the one given by large eddies, and that the large eddies usually show greater oscillations than small ones, as also noted by Gao et al. (2017). This is especially true for two sites (Cogne and Torgnon). This is likely due to the lower wind speed and air turbulence if compared to Nivolet site.

At the Cogne and Torgnon sites, the large eddy latent heat flux is predominant over the large eddy sensible heat flux, whereas at the Nivolet site, there is the opposite situation.

The problem of closing the energy balance is reflected also in the computation of the carbon dioxide flux (NEE). In particular, occurring underestimations of turbulent fluxes *H* and *LE* might suggest that also *Fc* is underestimated due to the eddy covariance system inability to adequately sample low-frequency motions

(large eddies). At the three sites, the higher ability to sequestrate carbon dioxide during daytime hours is associated with small eddies for all the sites (Figure 5.14). Large eddies, instead, cause an underestimation of *Fc* (carbon dioxide flux). This outcome is also found by Gao et al. (2019) for a semi-arid sagebrush area.

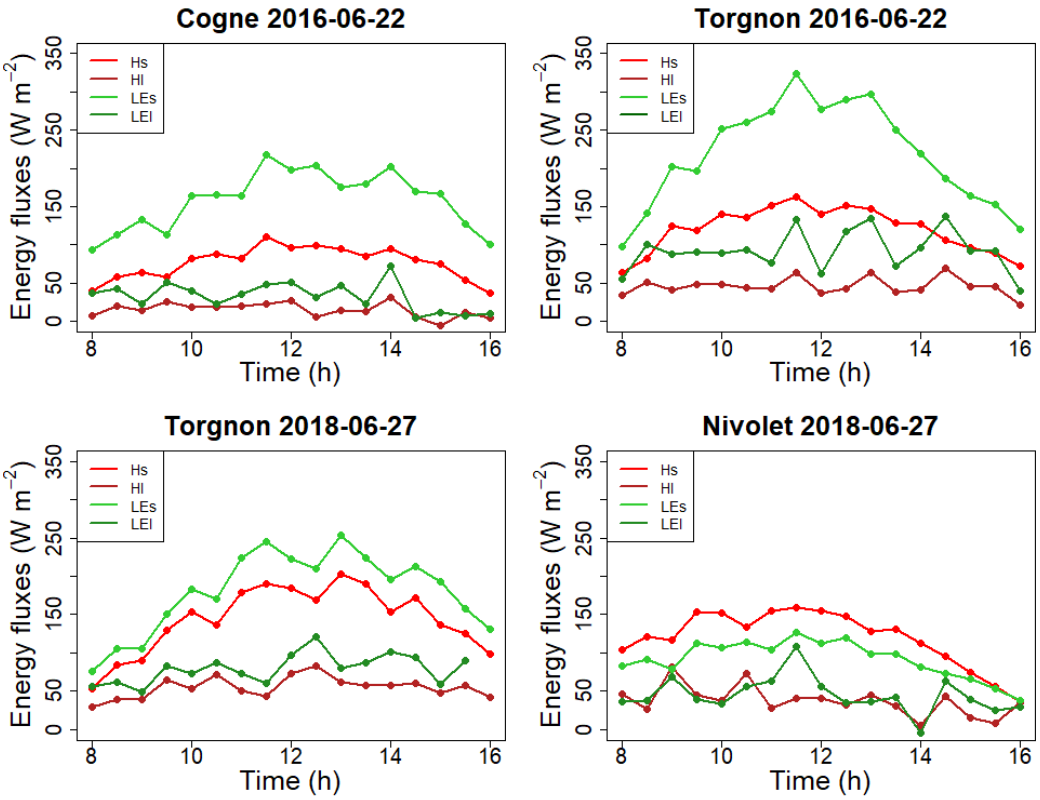

Figure 5.13. Latent and sensible heat flux small and large eddies contributions for the three sites.

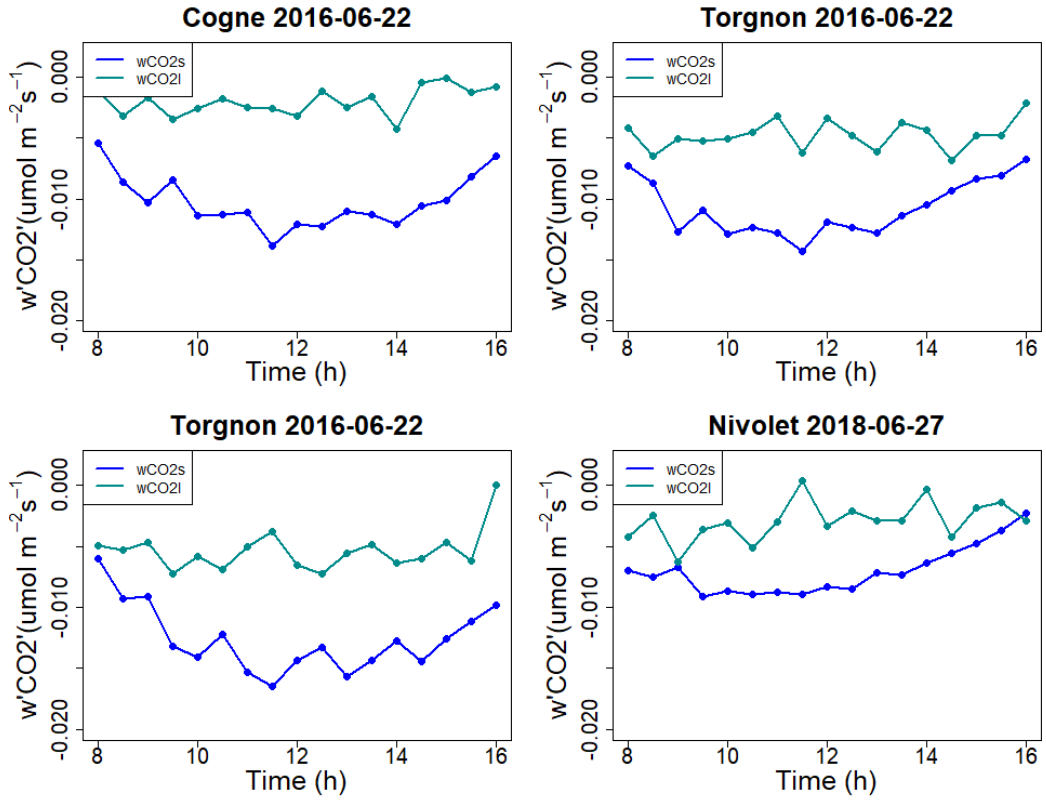

Figure 5.14. covariance w' CO_2' (carbon dioxide flux) small and large eddies contributions for the three sites.

Furthermore, the phase differences between vertical velocity *w* and the scalar CO_2 range from 25° to 45°, and similar values are found at all the Alpine sites analysed in this Chapter.

Besides, at the Nivolet site, a high contribution of small eddies is found, but the overall ability to sequestrate carbon dioxide is lower if compared to the other two sites, because the canopy activity is reduced.

Large and small eddies have their own Hilbert phase differences between vertical wind speed and scalars fluctuations. For large eddies, between w_l' and T_l' or $w_l'$and H_2O_l', or w_l' and CO_{2_l}'. For small eddies, between w_s' and T_s' or $w_s'$and H_2O_s', or w_s' and CO_{2_s}'. The phase differences are non-zero and show values ranging from 30° to 55°, with greater values in the central hours of the day (Figure 5.15). Phase differences related to large eddies have more constant values (around 40° along the day, Figure 5.16) and also an enhanced variability, if compared to small eddies. The phase differences exist also in complex terrain, they are comparable with the values found by Gao et al. (2017), and they may affect the turbulent fluxes and, hence, the energy balance closure.

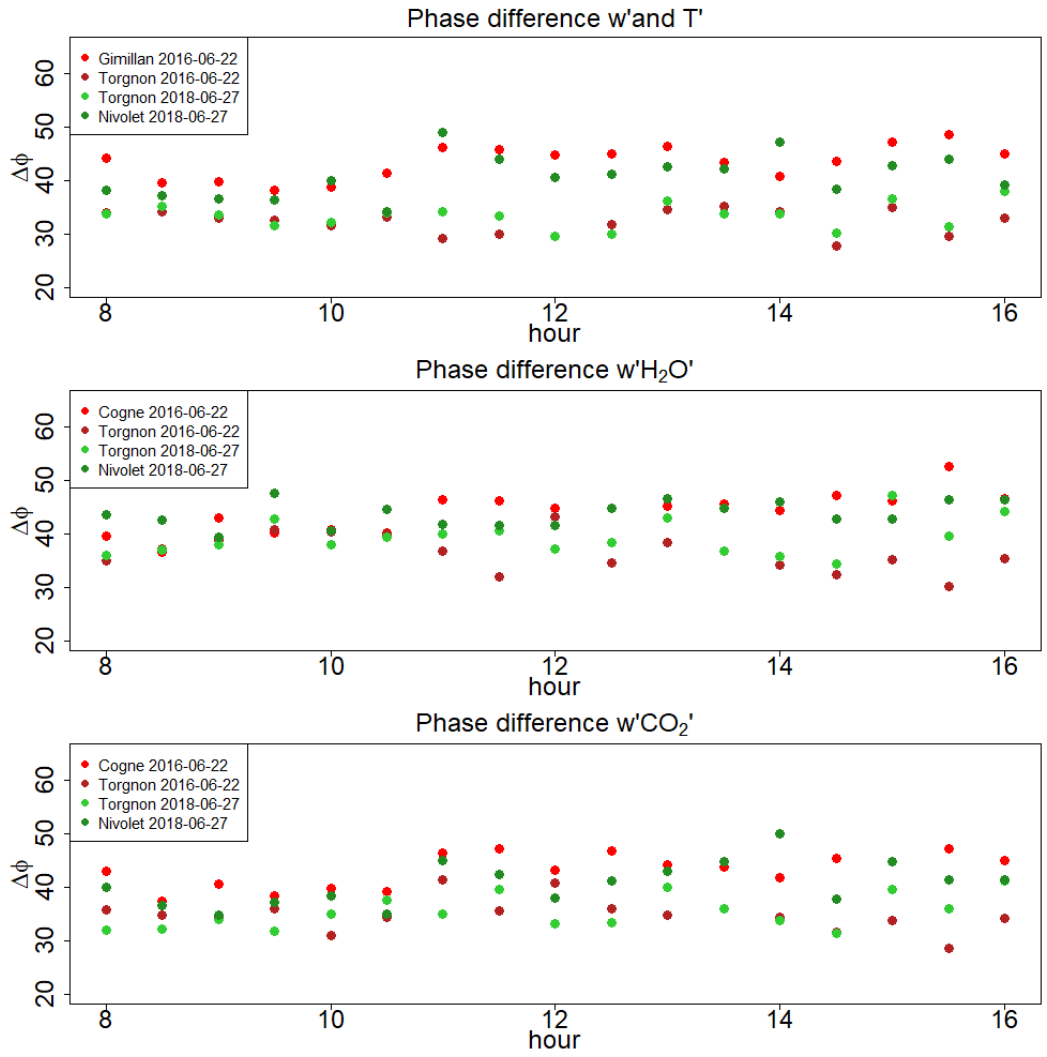

Figure 5.15. Phase difference between low frequency (large eddies) w' and, respectively, T', H_2O' and CO_2'.

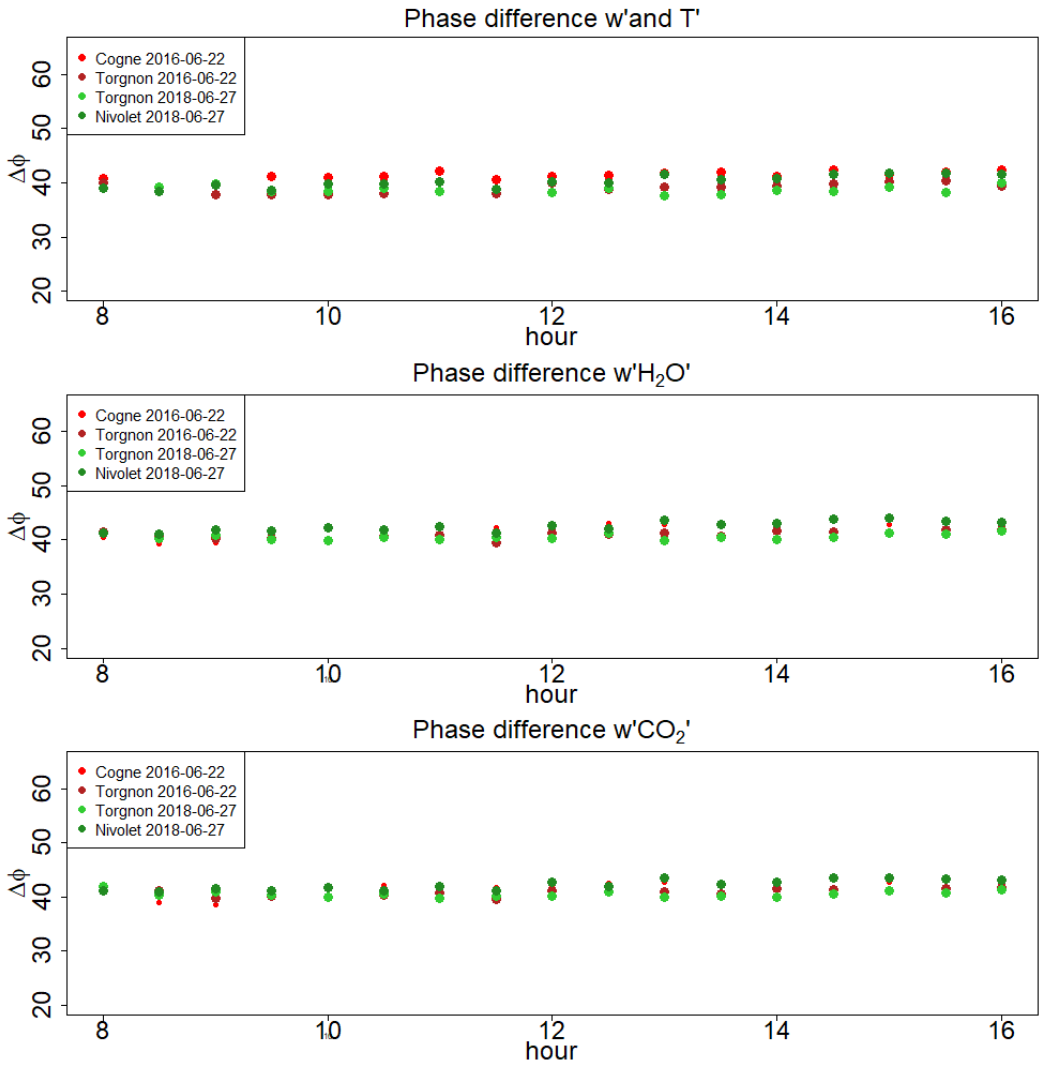

Figure 5.16. Phase difference between low frequency (large eddies) w' and, respectively, T', H_2O' and CO_2'.

5.4 Final Remarks

In this Chapter, three eddy covariance stations on natural grasslands (Cogne, 1,700 m a.s.l. on a steep slope in a narrow valley on a convex location; Torgnon, at 2,100 m a.s.l. on a 5° slope and Nivolet, at 2,600 m a.s.l. on an almost flat ridge of a slope with an inclination of about 30°) were used. Collected data ranged from 1st June to 8th August 2016 for Cogne and Torgnon and from 1st June to 8th August 2018 again for Torgnon and for Nivolet.

The aim was to investigate the meteorological, canopy and topography-induced differences existing between the sites. This analysis included the evaluation turbulent fluxes differences among the three sites, the evaluation of energy balance closure, and the energy balance closure improvement by means of the net radiation

correction according to the flux footprint of the sites, estimated with the Hsieh and the Kljun models. Finally, the properties of the turbulent structures called “small eddies” and “large eddies” were investigated.

Using the whole data set between 1st June to 8th August, mean diurnal cycles of micrometeorological variables and turbulent fluxes were obtained. Results suggest that the two sites located in more concave terrain have few cross-wind contaminations and are mainly characterised by up and downslope winds. The third site, located at a higher elevation and on a convex ridge, is more exposed to up and downvalley winds and it experiences higher wind speed and friction velocity values, if compared to the other sites, and a more complex wind regime.

The lower-elevation sites show a predominance of the latent heat flux over the sensible heat flux. while the highest-elevation site is characterised by an opposite behaviour. This might be caused by a less-active vegetation due to higher altitude and lower air temperature. The Net Ecosystem Exchange highlights an enhanced ability to sequestrate carbon dioxide at the sites below the tree line, where the canopy photosynthesis and respiration experience a higher activity with respect to the highest-elevation site. The maximum carbon dioxide sequestration occurs later in the morning at Cogne probably because the canopy reaches later the saturation of photosynthesis reaction to light. This effect might be explained by the presence of a grassland encroached by shrubs.

At Cogne, all the turbulent fluxes and air temperature show a morning inflexion on the mean diurnal course. This is likely caused by the wind regime change from downslope to upslope in a site where the wind is strongly channelled and no or negligible contaminations from up/downvalley winds exist. The morning inflexion is not found at the other two sites.

Where channelled winds exist, sources and sinks of heat and carbon dioxide are more easily localised. Also, the climatological footprints, estimated with the Kljun model, highlight the up/downslope regime when channelled winds exist, whereas at the site with a more variable wind rose, the footprint highlights the contaminations from other directions, including up and downvalley contributions. The site with the highest wind speed (Nivolet) is characterised by the greatest footprint (around 47000 m^2), followed by the other two sites (between 2000 and 9000 m^2).

The differences between the three sites were also analysed with the energy balance closure. On the period 1st June – 8th August, the balance closure was beyond 95% at Torgnon, about 82% at Nivolet. and 57% at Cogne. Hence, the site with the steepest slope has also the lowest energy balance closure.

The net radiation was corrected using the estimated flux footprint estimated with two models: the first one is the Hsieh 2D model, the second one is the Kljun 2D model. The net radiation reconstruction was performed at the three sites on single, clear sky days (namely, 22nd June 2016 and 27th June 2018). The reconstruction was successful at two sites (Torgnon and Nivolet), whereas at Cogne, the along-wind direction of both footprint models needed to be shifted with a topography forcing, that is, towards the aspect of the entire hydrographic right of

the small valley. With this forcing, the net radiation correction was successful. At the three sites, the energy balance closure improves significantly. The site with the highest closure increase is Nivolet (beyond +27%), followed by Torgnon (between +6 and +13%), and Cogne (between +6 and +10%). Generally, the Kljun model yields the best results, with only one exception (Torgnon, 22nd June 2016).

Another possible source of energy imbalance is related to low frequency turbulent structures and to phase differences between vertical velocity and scalars such as water vapour and carbon dioxide in the vortices known as "eddies".

Eddies can be divided into either low frequency, large scale or high frequency, small scale turbulent structures (respectively: large and small eddies). Large and small eddies were detected also at the analysed sites, hence in complex terrain. Small eddies prevail over large eddies at all sites, but at Nivolet the small eddy sensible heat flux was greater than the small eddy latent heat flux, coherently with the observations on the mean diurnal cycles, where H was higher than LE. At the other two sites, an opposite behaviour is found. Small eddies prevail at every site also for carbon dioxide flux, because most of carbon dioxide sequestration is related to small vortices. A reduced small eddy carbon dioxide flux is found at the Nivolet site, coherently with the observations of NEE over a wider period, showing reduced photosynthetic activity at that site, which is the highest one.

The aforementioned phase differences were detected at the three sites and were comparable with literature findings. Phase differences between vertical velocity and carbon dioxide are comparable with other scalars (namely, air temperature and water vapour).

Problems about energy balance non-closure still remain due to the uncertainties related to non-turbulent transport leading to H and LE fluxes underestimation, to the choice of footprint model to correct net radiation, and phase differences between vertical velocity and scalars fluctuations, which are an intrinsic turbulence property. Future research may be oriented towards the estimate of advection in highly complex terrain and to the improvement of footprint models using a set of topography forcings and its validation in field campaigns.

Chapter 6

Evapotranspiration analysis of an abandoned Alpine pasture at the Cogne site

This Chapter can be divided in two parts. In the first one (experimental), the objectives are: to study the growing season interannual variability of an abandoned steep grassland in terms of sensible heat flux and evapotranspiration; to quantify the evapotranspiration drivers and their variability in different growing seasons; to quantify the cumulative evapotranspiration in the four growing seasons.
The second part uses a hydrological modelling approach and it is devoted to understanding if land cover changes (from grass to shrub) may affect evapotranspiration in a small area. Differences between modelled grass and shrub configurations will be illustrated for soil water content and evapotranspiration and the evapotranspiration from the two modelled land cover scenarios will also be averaged. Evapotranspiration and soil water content modelled data will be compared with observations. For this Chapter, the sole Cogne experimental site is used.
The whole experimental data analysis was performed by the Author of the Thesis, whereas the modelling part was done in cooperation with Dr Ivan Bevilacqua and the LABFLUX Team.

6.1 Introduction

Evapotranspiration plays a key role in the water budget, it links ecosystem functioning, carbon and climate feedbacks, agricultural management, and water resources (Fisher et al., 2017). It is a complex process depending on many factors: water availability, energy availability, wind speed, humidity gradient, physical attributes of the vegetation (stress included), and soil characteristics. The evapotranspiration is considered the most difficult water budget component to estimate (Lettenmaier and Famiglietti, 2006) and it is responsible for positive feedbacks on temperature and greenhouse gases in the coupled system land-atmosphere. Evapotranspiration, which is a key component of the water cycle, is mainly driven by temperature, precipitation, soil moisture and canopy phenology (Konzelmann et al., 1997).

The atmospheric demand for water vapour depends on the difference between water vapour pressure and its saturation value and this difference is known as the vapour pressure deficit (VPD). Two important limitations for evapotranspiration are if the coupled atmosphere-soil system is in either water-limited regime (when water availability is low) or in the energy-limited regime (when there is enough soil moisture and the evapotranspiration limitation is related to net radiation). Some studies found that dry years significantly impacted evapotranspiration in semi-arid grasslands (Rajan et al., 2015), while other studies concluded that even in years with limited water input, interannual variability between dry and wet years was low, the canopy did not experience water stress and evapotranspiration was not strongly reduced due to water limitation (Wieser et al., 2008).

Within the climate change context, temperatures rise, and land cover changes are expected, leading to evapotranspiration alterations, which will affect the water cycle. As already mentioned, climate change is particularly evident in mountain areas, which are hot spots experiencing the elevation-dependent warming (EDW). Plus, Rottler et al. (2018) found strongest warmings in spring and summer and that annual temperatures are increasing with different rates depending on altitude, where the range between 900 and 1900 m experienced the second highest warming rate (0.31 °C/decade, from annual average temperature values), compared to 0.35°C/decade at lower altitudes (200-800 m a.s.l.). Because of the warming effects, it is important to carry on hydrological studies on sites at these altitudes. Next to the expected increase in temperature, possible changes in precipitation patterns could cause more frequent drought periods (Spinoni et al., 2018). In addition, an increased intensity of summer heat waves could lead to increased evapotranspiration, altering the water cycle and causing possible amplification of summer drought as a positive feedback in return (Teuling et al., 2013).

At the same time, there are land cover changes, which are difficult to detect in managed systems due to the disturbance of natural processes, such as grazing. Therefore, the analysis is performed on an abandoned grassland, where no direct human activity is no longer present. In this area, the land cover can change if new species colonise the terrain. The first species which typically colonise such areas are shrubs (with a process called encroachment), as in situ observations and past research have shown in several areas in the World (Maestre et al., 2009). Encroachment is happening also in the Alps (Tasser et al. 2005; Gellrich et al. 2007) and it is affected also by topography, with enhanced colonisation along steep slopes (Komac et al., 2011) and it leads also to increased evapotranspiration and reduced runoff (Van der Bergh et al., 2018). In addition, in the past century, land abandonment increased by 34% in all the Alps (Baur et al., 2007). However, analyses on shrub encroachment have not yet been shown for a system in the Western Alps using eddy covariance data.

While studying these effects, local scales are preferable to global scales analyses, because the real, specific ecosystem is more well-represented.

To evaluate local scale climate and land change effects, long-term campaigns are useful, but they are rare in mountainous regions. If instead land-surface models are used, they need validation and climate models outputs (properly downscaled). It is difficult to determine the set of parameters and initial values and to make spin-ups for complex and unmanaged areas. A simpler method is to use multi-annual analysis on fluxes and meteorological variability using measured data and hydrological simulations. The last approach can be used even in complex mountainous regions, because less input data is required. An example of multi-annual analysis involves interannual variability of evapotranspiration (wet/dry, warm/cold). That variability can be seen as an approximation of expected climate variations. This analysis is still characterised by a debate, because it might be significant (Wever et al., 2002; Ryu et al., 2008) or maybe not in other areas (Hammerle et al., 2007; Wieser et al., 2008). Other studies (e.g. Abera et al., 2017) suggest that the highest variability is found for precipitation and not for evapotranspiration. This does not mean that it does not exist, but that a high meteorological variability is required to observe differences and not all Alpine sites may experience it. This is why Italian Western Alps are very interesting: they show a developed meteorological inter-annual variability mainly caused by high-elevation mountains quite near the Mediterranean Sea. They are a barrier which implies that meteorological phenomena occurring in Central and Northern Europe may not have effects on the other side of Alps. The 2015 European drought (Haslinger and Blöschl, 2017; van Lanen et al., 2016; Ionita et al., 2017) had no or little impact over the Italian Alpine area, at least in his western part, while 2016 and 2017 summers were dry. The year 2017 was characterised by heat waves and an average decrease in precipitation of more than 30% with respect to 1971-2000 average (Desiato et al., ISPRA report, 2018) but no drought was experienced elsewhere in Europe. All these conditions make hydrological studies in this part of the Alps very interesting, because if very different meteorological conditions exist, this will represent a sort of difference in climate scenarios (e.g. more or less rainfall, higher or lower temperature from one year to another)

As it was illustrated in Chapter 4, there are many techniques to monitor evapotranspiration and sensible heat flux. The eddy covariance (EC) technique is one of them (e.g. Foken et al., 2008). In the past 20 years several studies demonstrated that it can be used also on slopes (Geissbühler et al., 2000; Turnipseed et al. (2003) Hammerle et al., 2007; Hiller et al., 2008), provided there is proper quality control and post-processing (Stiperski and Rotach, 2016).

However, in complex morphologies, it is not common to find long-term measurements, especially devoted to hydrological studies. To the authors' knowledge, in Europe, studies on grasslands beyond 1,500 m a.s.l. are rare. Only 14 sites are available in this altitude range (Table 6.1, Figure 6.2). Five stations are on flat and homogeneous terrain and all of them are built on managed areas, Three are on a managed meadow and on a slope classified as "strong" (> 10%; for two Austrian sites on a mountain side, the slope is beyond 50%) and one, again on managed pasture, on a 5% slope. Only one site (Stubai abandoned meadow,

Carbomont Project, Tenhunen et al., 2009) is on a natural grassland abandoned and afforested on a strong (> 50%) slope.

Table 6.1. Stations on Alpine grasslands beyond 1,500 m a.s.l. and below 2,300 m a.s.l. (hence, below the tree line) and with more than two years of available data. EC means eddy covariance. Slopes are classified as follows: <2%: gentle slope; <5%: medium slope; <10%: significant slope; > 10%: strong slope.

Site	Altitude	Terrain	Land use	EC	Reference
AT-Sta	1970	strong slope	abandoned grassland	no	Tenhunen et al. (2009); Meyer et al. (2012)
AT-Stm	1770	strong slope	managed meadow	yes	Hammerle et al. (2007)
AT-Stp	1850	strong slope	pasture	no	Tenhunen et al. (2009); Meyer et al. (2012)
CH-Aws	1978	flat	pasture	yes	Michna et al. (2013)
CH-Dsc	1590	flat	pasture	yes	Merbold et al. (2013)
CH-Frk	2100	strong slope	pasture	yes	Scholz et al. (2018)
ES-Cst	1900	gentle slope	pasture	yes	Ibanez et al. (2020)
ES-Vda	1770	gentle slope	managed meadow	yes	Wisskirchen et al. (2013); Chang et al. (2013
FR-Clt	2000	signif.slope	pasture	no	Leitinger et al. (2015)
IT-Mal	2000	gentle slope	pasture	yes	Valentini and Miglietta (2015)
IT-Mbo	1550	flat	pasture	yes	Marcolla et al. (2011)
IT-Mtm	1500	strong slope	managed meadow	yes	Castelli et al. (2018)
IT-Mtp	1500	strong slope	pasture	yes	Castelli et al. (2018)
IT-Tor	2150	gentle slope	unmanaged meadow	yes	Galvagno et al. (2017)

Only two sites are on real abandoned grassland between 1,500 and 2,200 (tree line altitude) m a.s.l.: Torgnon eddy covariance site (the only one in Western Alps but not being colonised by shrubs but abandoned about only 10 years ago (Galvagno et al., 2017) and the Stubai abandoned meadow on a steep mountain slope (Tenhunen et al., 2009; Meyer et al., 2012), colonised by shrubs but without eddy covariance measurements. Both sites have been mainly used for carbon dioxide studies, although recently, two papers involved the Torgnon site: the first was devoted to determine crop coefficients for unmanaged areas (Corbari et al. 2017) and the second was focused on ecophysiological responses depending on precipitation variability at different latitudes, in Italy (Conte et al. 2019).

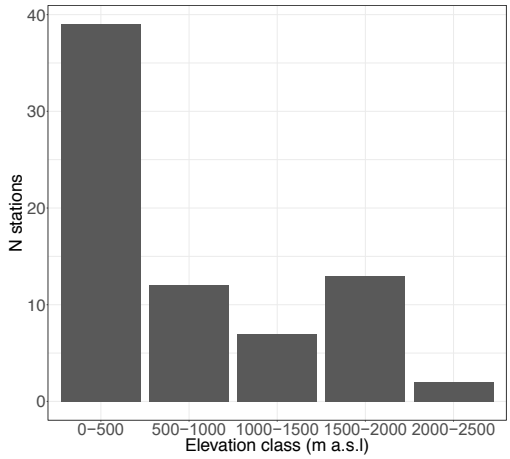

Figure 6.1. Number of grassland stations in Europe compared against elevation classes.

Nowadays, no hydrological study based on eddy covariance measurements has been carried out on a steep slope characterised by a grassland abandoned more than 40 years ago and being colonised by shrubs in the last few years. To this end, the four growing seasons between 2014 and 2017 illustrated in Chapter 4, and characterised by different meteorological and soil conditions were used. In Chapter 4, the data reliability was shown, whereas Chapter 5 revealed interesting topographical features at the Cogne site.

6.2 Methodology

6.2.1 Soil water balance components

The water cycle is closed and can be expressed, at a daily scale, as in Eq. 6.1.

$$P + I - Perc - ET \pm \Delta S = 0 \quad (6.1)$$

where P is the precipitation, I is the irrigation, ET is the actual or potential evapotranspiration and ΔS is the change in soil water content; $Perc$ is the term describing the percolation of water towards deeper soil layers. It also considers the infiltration. Here the subsurface flow and the capillary rise are not considered. The subsurface flow would exist, but it is very difficult to evaluate it. Evaluating correctly the evapotranspiration is fundamental to obtain better water balances. To properly evaluate the previous balance, as well as the energy one, the knowledge about soil properties (texture, chemical composition) and variables (soil water content, matric potential, heat propagation, number of layers) is required. Figure 6.2 shows graphically the balance, with the wilting point being the soil water content at -15 kPa of hydraulic head, when the plants are no more able to extract water from the soil, and field capacity being the soil water content in the soil after the excess water has drained away. RAW is the readily available water, the water easily extracted from the soil by vegetation, root depletion is the depth at which the roots can extract water, TAW is the total available water.

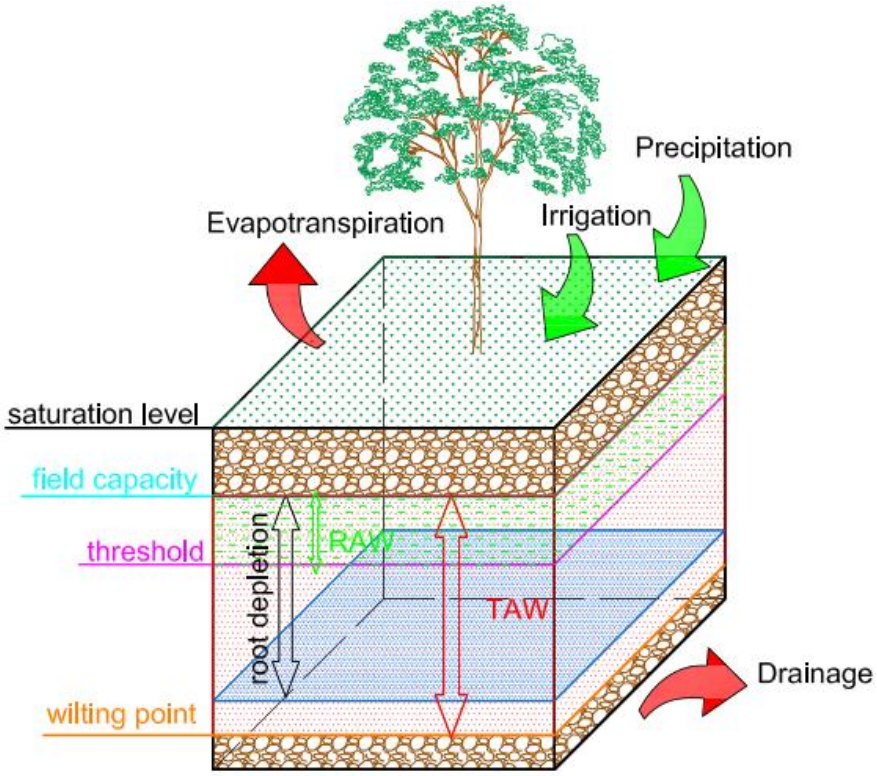

Figure 6.2. Hydrological balance components.

The eddy covariance data of four growing seasons (June to September 2014, 2015, 2016 and 2017 at the Cogne site) were used for this study. The same data processing and quality control adopted in Chapter 4 was used. The only difference was related to wind direction filtering. To avoid an excessive data loss, it was hypothesised that the turbulence test by Mauder and Foken (2004), together with the tests on single variables suggested by Vickers and Mahrt (1997) should be able to discard those episodes of extremely low turbulence.

The half-hourly eddy covariance fluxes were gap filled using the REddyProc R package (Wutzler et al., 2018; see also Appendix F). The mean diurnal sampling (MDS) algorithm was used, as described in Reichstein et al. (2005), which partially modified the algorithm introduced by Falge et al. (2001). The gap filled data set was then aggregated at the hourly scale. Evapotranspiration was then derived from latent heat flux.

6.2.2 Flux footprint and latent heat flux spatial variability

The spatial interannual variability was explored using the footprint estimate and comparing latent heat flux against wind direction. The footprint estimate is devoted to understanding whether the site shows similar source areas in different years. For each of the four growing seasons, the footprint climatology was computed as follows. Data were aggregated at the hourly scale and then, for each time step (i.e. 60 minutes after the aggregation), the single site footprint was computed using a two-dimensional parameterisation for flux footprint prediction (Kljun et al., 2015). To obtain the footprint climatology, footprints were aggregated following Kljun et al. (2015). The Kljun model uses the available data on roughness length, measurement height, mean wind speed, wind direction, wind velocity lateral standard deviation and friction velocity. Friction velocity was computed using Eq. 4.1.

The boundary layer height required to run the Kljun model was estimated using ERA5 reanalyses on hourly data on the 0.25°x0.25° grid cell nearest to the site. The data were downloaded from the Copernicus repository https://cds.climate.copernicus.eu/.

6.2.3 Flux partitioning interannual variability

The dry spell duration was used as another parameter to assess local interannual variability of hydrological cycle. A dry day was identified when the amount of daily precipitation was below 1 mm (Baiamonte et al., 2018). The averaged dry spell duration per year was computed as the average number of days with precipitation below 1 mm.

Flux partitioning was explored in terms of the amount of sensible and latent heat flux percentage related to the available energy (net radiation) and using evaporative fraction ($EF = \frac{LE}{H+LE}$) and Bowen ratio ($B = \frac{H}{LE}$) indices.

In particular, the evaporative fraction compared to soil water content should allow to understand whether the system is in water limited or energy limited regime,

since below the critical soil water content, a decrease of EF could be found (Bonan, 2016). Besides, the EF analysis can reveal also if the wilting point is reached (when actual evapotranspiration is near zero). The two indices allowed a better quantification of which one of the two fluxes was dominant and if there was a change in flux partitioning due to different soil conditions. The evaporative fraction, Bowen ratio, average precipitation, air temperature and vapour pressure deficit were also computed as averages on groups of 15 days, to identify patterns that might be smoothened at larger temporal scales.

Vapour Pressure Deficit (VPD) was also calculated using the relative humidity measurements and computing the saturation vapour pressure as suggested by Lowe (1977) and its comparison with hour of the day, relative humidity and air temperature were analysed.

6.2.4 Measured evapotranspiration interannual variability

The derived different evapotranspiration variables (with evapotranspiration being in equivalent millimetres) were called ETa_{Obs} and ETa_{Obs_g}, respectively for evapotranspiration and gap filled evapotranspiration time series.

The derived two evapotranspiration values (with evapotranspiration being in equivalent millimetres) were called ETa_{Obs} and ETa_{Obs_g}, respectively for evapotranspiration and gap filled evapotranspiration time series.

To assess if the ecosystem is either water limited or energy limited, a comparison between measured actual evapotranspiration (ETa_{Obs}) and potential evapotranspiration (Penman-Monteith-derived formula, as illustrated in Eq. 6.2, ET_0) is performed. The steps for its computation are shown in Appendix C.

$$ETo = \frac{1}{\lambda}\frac{\Delta(R_n - G_0) + \rho_a c_p \frac{e_s - e_a}{r_a}}{\Delta + \gamma(1 + \frac{r_s}{r_a})} \quad (6.2)$$

where Δ (kPa °C^{-1}) is the slope of the curve in Clausius-Clapeyron equation, R_n is the net radiation (W m^{-2}), G_0(W m^{-2}) is the ground heat flux at the surface, γ is the psychrometric constant, ρ_a(kg m^{-3}) is the mean air density at constant pressure; c_p (J kg^{-1}K^{-1}) the specific heat of the air; r_a (s m^{-1}) is the aerodynamic resistance, r_s (s m^{-1}) is the bulk surface resistance, λ (MJ kg^{-1}) is the latent heat of evaporation for water.

The higher the difference between ETa and ET_0 is, the closer the ecosystem is to water stress. By doing so, comparisons between different growing seasons were more suitable for comparison. When no cumulative values were analysed, the complete time series were used.

6.2.5 Modelling actual evapotranspiration: land cover change impact

The hydrological model Hydrus 1D, version 4.17 (e.g. Simunek et al., 2012) was used to model water balance components at the Cogne site (see Chapter 3). The results were compared against observations to validate the model on a single point. For measurements and model outputs comparison purpose and water balance components evaluation, the hourly eddy covariance data were used and then also aggregated at a daily scale. Two main simulations were carried out: one with only grass (fescue) and one with a land cover characterised by Alpine shrubs.

The potential evapotranspiration (ET_0) was modelled using Penman-Monteith FAO 56 formula. The soil column was simulated considering the properties of local soil (vegetation, soil texture, bulk density, bedrock depth). A more detailed description can be found in Raffelli et al. (2017). The finite elements mesh was constructed dividing the soil column into 101 nodes equally distributed. The soil column was divided into four layers (0-10 cm, 10-20 cm, 20-40 cm and 40 cm to bottom, that, depending on the simulation, was at 100, 150 or 200 cm). For water infiltration, the Richards equation was used.

The model was set up with the specifications given by Schaap et al. (2001) and they are shown in Table 2. For the root water uptake and other crop parameters (Feddes et al., 1978), the grass values were taken from Peters et al. (2017), whereas the shrub parameters were taken from Minacapilli et al. (2009). Root depth for grass was assumed equal to 30 cm, whereas the root depth for shrubs was assumed equal to 1.5 m (maximum). Between 0 and 40 cm of soil depth, the model was fed with measured values. For deeper soil horizon, a constant value of 0.11 $m^3\ m^{-3}$ was selected. These choices were supported by experimental evidences, by a good agreement between soil water content measures and modelled values (within the 0-40 cm soil layer). In addition, they minimised the mean absolute deviation of evapotranspiration between measured and modelled values.

Table 6.2. Soil parameters in the HYDRUS 1D model set up. θ_r: residual soil water content, θ_s: saturation soil water content; α, n, K_s, l: Van Genuchten water retention curve parameters estimated with ROSETTA model (Schaap et al., 2001).

Soil type	θ_r ($m^3\ m^{-3}$)	θ_s ($m^3\ m^{-3}$)	α (cm^{-1})	n (-)	K_s ($cm\ h^{-1}$)	l (-)
Sandy loam	0.024	0.380	0.021	1.53	70.1	0.5

First, the modelled soil water content was compared against the measured one. For 2015, 2016 and 2017 measurements in two depths (20 and 40 cm) were available and therefore both modelled shrubs and grassland soil moistures were computed within a 20 and 40 cm horizon. For the 2014 growing season, the comparison was made between 10 cm depth measured soil water content and a

simulated soil horizon within that depth. Second, the model *actual evapotranspiration* hereafter called ETa_{Sim} was compared to the observations, using two configurations for the observed evapotranspiration time series: ET from eddy covariance (called ETa_{Obs}) and gap filled ET from eddy covariance (called ETa_{Obs_g}). Temporal comparisons between modelled and observed ETa together with other information (soil water content, VPD, precipitation) helped to find differences between modelled shrub and grass simulated evapotranspiration, to better understand which one was closer to observations and in what conditions the two model setups were closer or they differed more evidently (also with observations).

6.3 Results

6.3.1 Flux footprint and latent heat flux spatial variability

In Figure 6.3, the footprint climatology for the 2014, 2015, 2016 and 2017 growing seasons is shown. The site footprint is almost constant throughout the years, making the comparison of different years possible. Furthermore, the footprint is limited to the site surroundings, in agreement with what is usually expected if the anemometer and gas analyser are placed at 2 m above the ground. The contour lines describe up to 80% of the total flux contribution and reach about 30-40 m from the station along the main wind direction.

In figure 6.4, the left coloured panels show the wind direction frequencies (for both daytime and nighttime) and the latent heat flux colour map for the four June-to-September periods, between 6:00 and 20:00, when most of evapotranspiration occurs. The right white panels show the mean wind speed along the day, together with standard deviation of values for each hour. It is interesting to note the difference between daytime and nighttime wind regime, with daytime flow coming mainly from South-South East, the wind being upslope. This regime is preserved in all the four growing seasons. The map allows to identify possible sources and sinks of water vapour. The main source of water vapour is located to the station's South-East, where a moist area with some shrubs exists. To the South-West and West there is instead a drier area, which has been recently colonised by shrubs. The potential sources of water vapour and, therefore, of latent heat during wet growing seasons were less active or non-existent in dry growing seasons. This suggests that the small creek might have negligible or no direct effect on fluxes, because the water discharge is almost constant throughout the growing seasons.

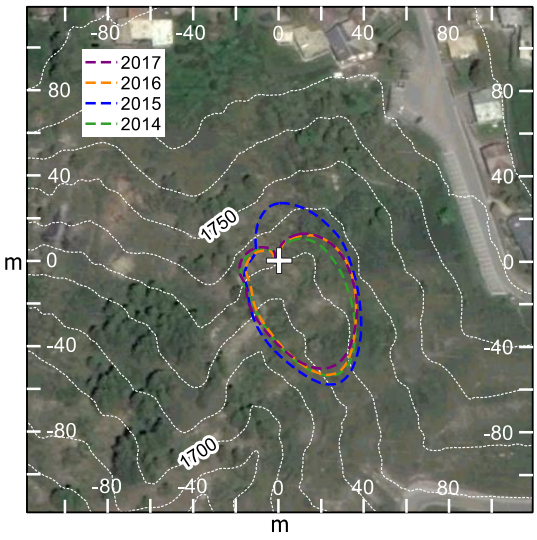

Figure 6.3. Footprint climatology for the Cogne eddy covariance site in the four growing seasons (2014, 2015, 2016 and 2017). The contour lines reach up to 80% of flux contribution.

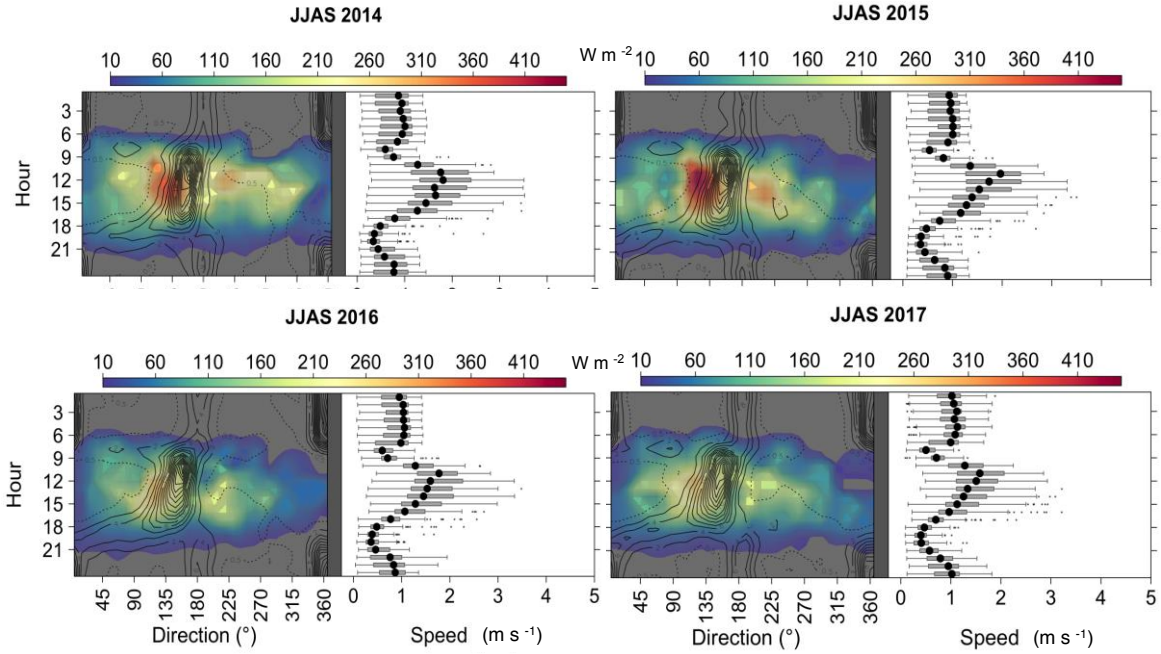

Figure 6.4. Mean latent heat flux and wind frequency contour maps as a function of wind direction and hour of the day (left) and wind speed versus hour of the day (right), for the 2014, 2015, 2016 and 2017 growing seasons. The colour scale of LE is reported above each panel and wind direction contour lines are shown for both nighttime and daytime to highlight the changing wind regime.

6.3.2 Micrometeorological and soil interannual variability

The four growing seasons were characterised by different meteorological conditions. There are two wet growing seasons (2014 and 2015) and two dry growing seasons (2016 and 2017). This distinction is supported by several indicators: on the hydrological year by average dry spell (as defined by Baiamonte et al., 2018) and amount of precipitation; on the growing season by average dry spell, number of dry days, amount of precipitation, average temperature, relative humidity and *LE/Rn* ratio. The interannual difference will also be shown and confirmed by other analyses later in this Chapter.

In Table 6.3, the average dry spell and amount of precipitation are shown for the hydrological year. In the same table, the average dry spell, total number of days without rain, amount of precipitation (*P*) and relative humidity (RH) are illustrated for the growing season. These variables partially allow the identification of two wet (2014, 2015) and two dry (2016, 2017) growing seasons.

Table 6.3. Variables of hydrological interest. The average shallow soil water content is within the first 15 cm of soil.

	Hydrological year				Growing season			
	Dry spell avg.	Prec	Dry spell avg.	n. dry days	P	RH	SWC	LE/Rn
2014	4.2	696	3.7	86	263	67.1	0.09	0.62
2015	6.8	757	6.2	92	317.6	64.0	0.09	0.53
2016	6.3	640	6.1	95	179	58.6	0.07	0.42
2017	7.9	624	5.9	91	182.6	57.4	0.06	0.43

With the two periods in mind (hydrological year and growing season), the wettest conditions occurred likely in 2014, whereas the driest conditions occurred in 2017.This might be also confirmed by the *LE/Rn* ratio (Table 6.3), which decreases in 2016 and 2017 growing seasons.

In the 2014 growing season, cumulative daytime net radiation was about 1701 MJ m^{-2} against 1829, 1811 and 1697 MJ m^{-2} respectively for 2014, 2015, 2016 and 2017. In all four growing seasons, the soil water content was apparently enough to provide water for evapotranspiration, also because of the shrubs' presence.

LE and soil water content bimodality

The interannual variability emerges also in frequency density distributions of latent heat flux and soil water content (Figure 6.5). The two wet years have higher mean values of latent heat flux frequency density (Figure 6.5, upper panel), if compared to drier growing seasons. The distributions, although still bimodal, and with a higher peak on the left, are different in their higher values. The two drier growing seasons are evident because the soil water content frequency density (Figure 6.5, lower panel) is lower if compared to 2014 and 2015.

The bimodality is found in each growing season for *LE*, with a less developed second peak in 2016 (a dry growing season), related to higher soil water content.

The *LE* bimodality may be related to two distinct regimes: the first one occurs during the either morning or sunset wind flow regime transition, between 5:00 – 8:00 and 17:00 – 20:00, when there is *LE* release, but the values are low because of low radiation forcing. The second occurs when the ecosystem is fully activated (i.e. locally between 8:00 and 17:00). The site is located on a South-East slope, hence as soon as the sun has risen, the latent heat flux increases greatly and rapidly. The sharp decrease in the evening, happens because the sun sets quickly due to mountain shadowing. The morning condition determines the distributions bimodality, with one peak around 20 W m^{-2} and the other between 100 and 200 W m^{-2}. This bimodality is found plotting the frequency density distributions of hours within the range 5:00-7:00 and 17:00-20:00 and then comparing the results with the range 08:00-16:00 (histograms in the background represent the distributions in the two time-ranges for 2015).

The bimodality found at Cogne differs from other studies, where it was pointed out either a dependence on agriculture management (Jiménez et al., 2018) or soil moisture changed conditions (Anav et al., 2010).

Soil water content showed bimodality especially in 2015. This can be explained with the lack of precipitation in prolonged periods, whereas 2014, 2016 and 2017 experienced more frequent rainfall even if very different in magnitude. The ecosystem appears to be more water-stressed in 2017 also because of low water input during the months before the growing seasons. The average water content in 2017 growing season was the lowest, as well as the hydrologic year total. The bimodality is also visible in the lower panel of Figure 6.5: the histograms of two wet periods in 2015 (DOY 164-184; 224-253) are almost superimposed and are well separated from the histogram related to a dry period (DOY 185-223). It seems that, from experimental data, the bimodality is given by the transition between wet and dry periods. Other studies showed the bimodality of soil water content and attempted to explore the causes of the phenomenon. D'Odorico and Porporato (2004) explained it by a "state-dependence in the timing of the forcing of the terrestrial water balance is found to be able to generate bimodality in the probability distribution of soil water content" and again, the positive feedback between soil moisture and precipitation timing may produce two states in (summer) soil moisture

dynamics. Teuling et al. (2005) found again wet and dry modes influence, and that there was a switch between a wet state at the beginning of the growing season followed by a dry state. They showed, contrarily to the previous paper, that the bimodality (transition from wet to dry modes) can *also* arise from the soil moisture-precipitation feedback, but not necessarily. The transition is instead governed by the ratio of the maximum precipitation deficit and the water, actually available for transpiration, between θ_{fc} (at field capacity) and θ_c (the critical soil moisture). In climates such as the Alpine one, where there is a winter precipitation surplus, no bimodality for the soil water content in the growing season is found if the aforementioned ratio is lower than 1. The bimodality would be induced by seasonality of meteorological conditions combined with the nonlinear soil moisture response. However, merging all the four growing seasons together, only a very weak bimodality emerges (Figure 6.5, lower panel), differently from D'Odorico and Porporato (2004) and Teuling et al. (2005), where multiple growing seasons over about twenty years were used. The bimodality emerges in growing seasons with strong wet to dry transitions. In addition, a bimodality was also found considering all the data (black histogram, Figure 6.5, lower panel), in agreement with the aforementioned studies.

Future investigations could be devoted to understanding whether the bimodality causes identified by the aforementioned studies can be actually valid for the Cogne site.

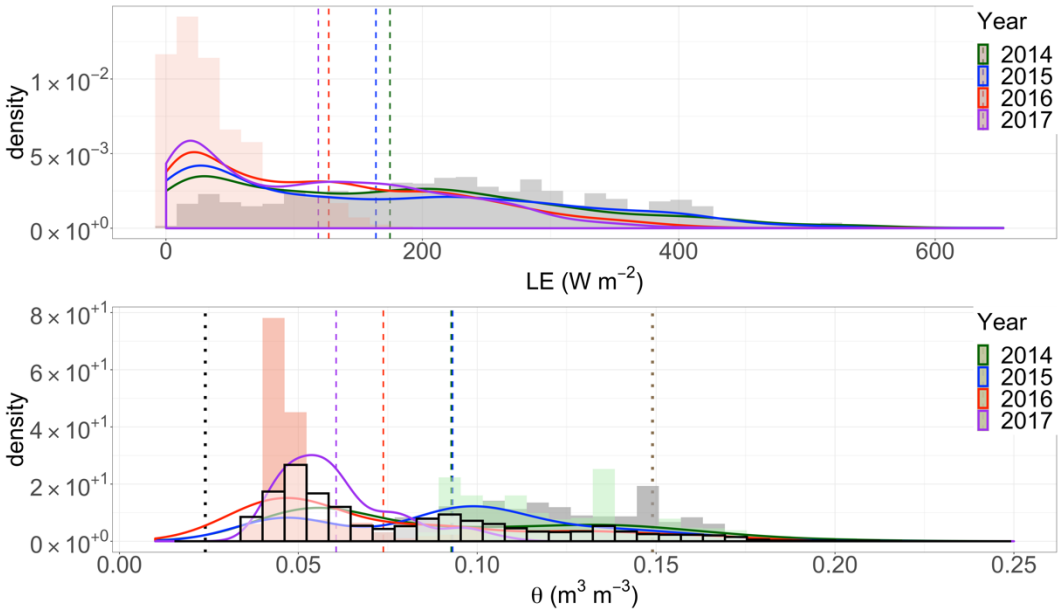

Figure 6.5. Frequency density distributions for LE (upper panel) and for soil water content between 0.1 and 0.2 m (lower panel). Dotted lines in lower panel represent wilting point (black, 0.024 m^3 m^{-3}) and field capacity (brown, 0.15 m^3 m^{-3}). The dashed lines in the two panels represent the means of the distributions, whereas the black histogram includes data from all the growing seasons.

Using a t-test, statistically significant (p value < 0.05) differences between distributions means were found between dry and wet growing seasons. Namely,

2014 and 2015 latent heat flux (*LE*) values differ, on average, significantly from 2016 and 2017 ones. This suggests again that the interannual variability might be significant at our site. In addition, the two wet growing seasons are still characterised by statistically significant differences between *LE* means, whereas between the dry growing seasons non-significant differences were found.

For soil water content, significant differences between mean values were found between the two wet and the two dry growing seasons. Another significant difference in mean was found between 2016 and 2017, therefore in two dry seasons, whereas very similar means existed in 2014 and 2015. No statistical difference was found between 2014 and 2015 (p-value > 0.05). Indeed, the two means are very similar, and the modes difference is also low (between 0.05 and 0.10 m^3 m^{-3}. Besides, the highest peaks of the soil water content distributions are found at the lowest mode (0.05 – 0.06 m^3 m^{-3}), likely because of the soil texture: shortly after a rainfall event, the upper part of the soil dries rapidly. The wilting point is around 0.024 m^3m^{-3} (at -15 kPa of hydraulic head) in agreement with Raffelli et al. (2017), as also estimated by water retention curves using HYDRUS 1D model providing the soil texture experimentally obtained at Cogne. The field capacity, never actually reached, is at 0.15 m^3m^{-3} (value of water retention curve at -33 kPa of hydraulic head)

Mean diurnal cycles of micrometeorological variables and daily hydrological variables

The mean diurnal cycles of daytime temperature and *LE* flux show also, for all growing seasons, a morning inflexion (Figure 6.6). The inflexion was also found in the diurnal cycle of *H* but not for *Rn*, on average (Figure 6.7). The inflexion is likely caused by the wind flow regime change from downslope to upslope in the morning. In the first hours after the wind direction shift, the transported air is still cold, hence there are lower sensible and latent heat fluxes. A similar inflexion can be found in Rotach et al. (2008), where turbulence exchange mechanisms and boundary layer properties were explored in highly complex terrain.

Besides, the *LE* flux mean diurnal cycle in wet growing seasons shows higher values than in dry growing seasons, with differences up to about 100 W m^{-2} in the central hours of the day. The *LE* range between $\pm 1\sigma$ is always near 100 W m^{-2} (89.9 W m^{-2} in 2017 and 130.1 W m^{-2} in 2015). The temperature difference between 2014 and the other growing seasons is also visible in the mean diurnal cycle of temperature, since in 2014, mean temperature can be about 2°C lower than in other growing seasons around midday.

The net radiation and the sensible heat flux *H* (Figure 6.7) are characterised by a mean diurnal cycle similar to *LE*. However, for the net radiation the inflexion is on average not found. This may suggest that the inflexion formation is due to wind flow regime changes. The net radiation shows the second highest variability after *LE* (up to around 70 W m^{-2}), with 2014 being the year with lowest values due to

frequent cloudy days and rainfall. For *H*, the interannual differences in the central hours of the day are lower if compared to *LE* (no more than 40 W m^{-2}), and the cycle variability ($\pm 1\sigma$) is lower than the one found for *LE* (maximum 69.8 W m^{-2} in 2017 growing season).

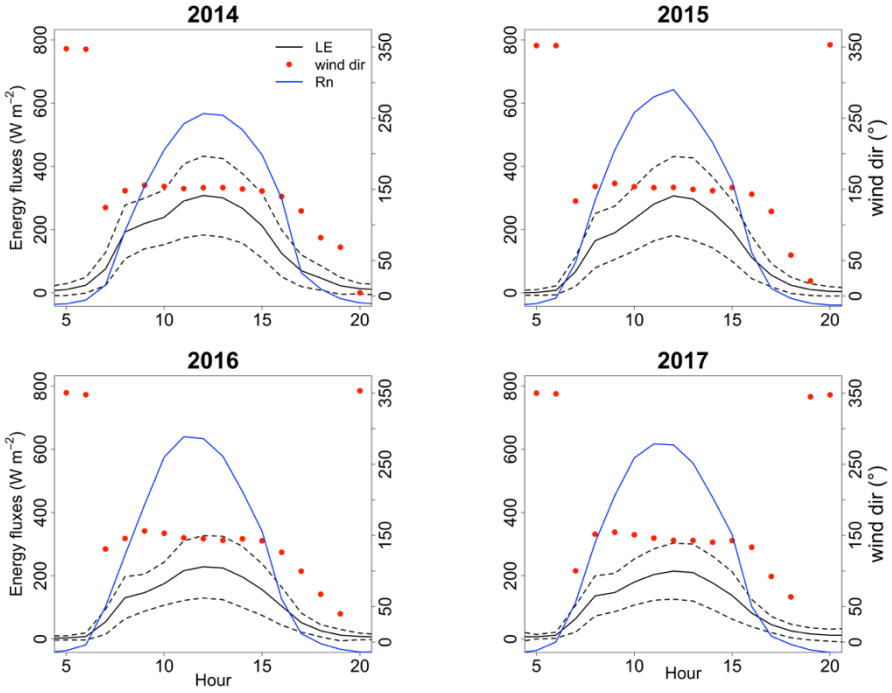

Figure 6.6**.** Mean diurnal cycles of daytime latent heat flux, net radiation and wind direction for the four growing seasons. Dashed lines represent the range of one standard deviation from mean values for each hour.

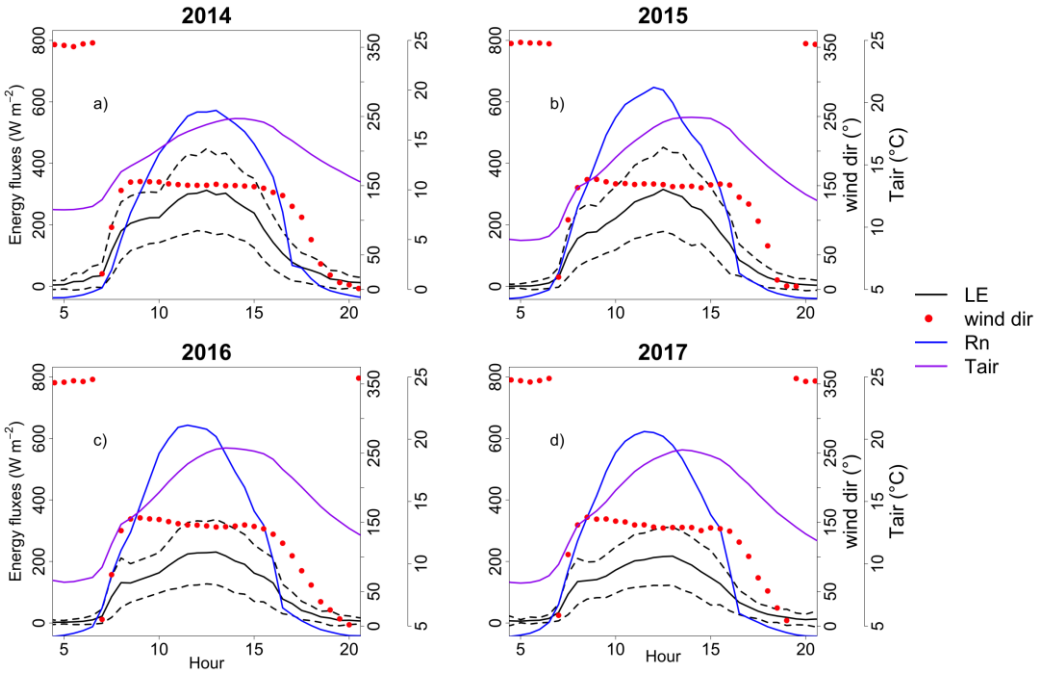

Figure 6.7. Mean diurnal cycles of daytime sensible heat flux, net radiation and wind direction for the four growing seasons. Dashed lines represent the range of one standard deviation from mean values for each hour.

Usually, within the temperatures rise context, the VPD (hence, the water vapour atmospheric demand) will also increase and this is found in Figure 6.8. This occurs because with higher temperature values, the atmosphere expands and, according to the Clausius Clapeyron Law, can contain more water. In addition, the two variables, temperature and VPD, are highly correlated, R=0.86 (not shown). Enhanced differences of temperature and water availability between growing seasons, can be seen as different climate scenarios.

The 2014 growing season experienced lower temperature if compared to the other three growing seasons and also lower VPD values, because of the moist air (the peak value in 2014 is almost 500 Pa lower than the 2017 one). The growing season 2015 was warm but wet. Hence, given a higher temperature on average, the VPD reached higher values than 2014. The 2015 VPD was also lower than in 2016 and 2017 one. The warm and relatively dry growing seasons experienced high VPD (low RH) and high temperatures. Generally, enhanced evapotranspiration would be expected, but this could not always happen because there are cases where the evapotranspiration is water-limited, therefore the evapotranspiration was likely limited by stomatal closure.

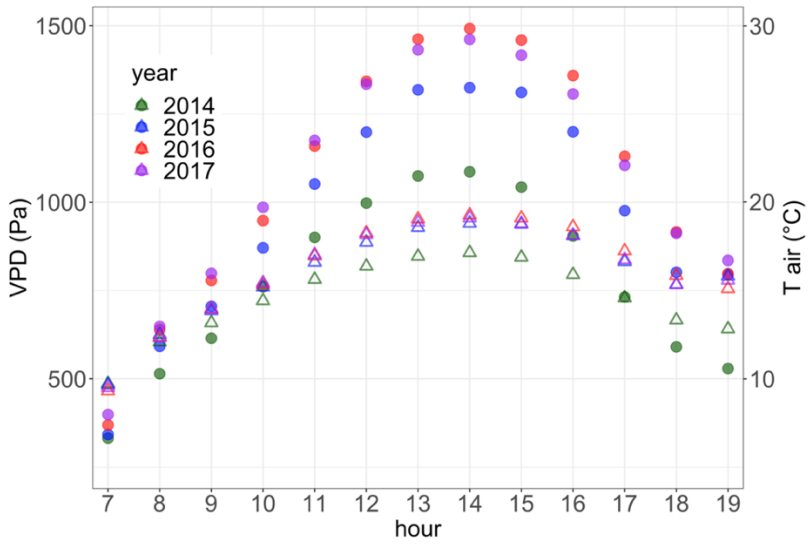

Figure 6.8. Vapour pressure deficit (VPD, dots) and air temperature (triangles) during the daytime hours between 7:00 and 19:00 from 2014 to 2017 growing seasons.

The *LE* (and, hence, *ET*) shows a dependence on VPD and air temperature. However, the relationship is non-linear and the three variables do not follow a normal distribution (Shapiro-Walk test, p-value < 0.05). Therefore, the correlation was explored in terms of Spearman correlation coefficient (Table 6.4), keeping in mind that also VPD is temperature-driven. The values of correlation suggest that *LE* is well correlated with both VPD and air temperature with a predominance of *T air*. While correlation between *LE* and *VPD* decreases in dry growing seasons, the correlation with temperature is almost insensitive to changes. This might be explained by the dependence of VPD on air humidity.

Table 6.4. Spearman's correlation coefficient between LE and VPD and T_{air}. All values are significant (p-value < 0.05).

ρ	*VPD*	*T air*
LE	0.70	0.67
	0.62	0.69
	0.60	0.68
	0.59	0.68

Exploring the relationship between EF and soil water content (Figure 6.9) allows to better identify when evapotranspiration is limited by either energy or water availability.

The regression curves were computed using the loess filter provided in the "stats" R-package (Appendix F) following the approach of Cleveland et al. (1992). In the present study, low soil water content values appear to be reached, but even

in dry and hot growing seasons the system does not reach the wilting point, whereas the estimated field capacity can be reached. Interestingly, in 2014 EF shows a tendency to increase with water content, whereas in the three other growing seasons this trend is not met. This trend absence does not, however, necessarily indicate a water-limited regime. In addition, there are cases where the EF is high, but a low soil water content is found. The explanation could be an increase of temperature, a relatively high VPD and a sufficient amount of deep-water storage. Indeed, the measured soil water content is in a horizon within 40 cm from the surface out (the soil water content can be low). This layer can dry but in the horizon underneath there is still water. Since the land cover is a mix of grass and shrubs, the EF can be high because shrubs are able to use water of deep soil layers, well below 40 cm. This aspect will be analysed in the modelling part of this Chapter. Further details on the *ET* drivers will be detailed in Section 6.3.3.

The two Panels of Figure 6.9 show that, in addition, EF at midday can also be used instead of considering the EF over other daytime "central" hours (Crago and Brutsaert, 1996), that is, in this study, between 08:00 and 15:00. This is also suggested by Table 6.5 outcomes. Besides, Figure 6.9 shows that the evapotranspiration is rarely water-limited and that a weak correlation between EF and the shallow soil water content exists.

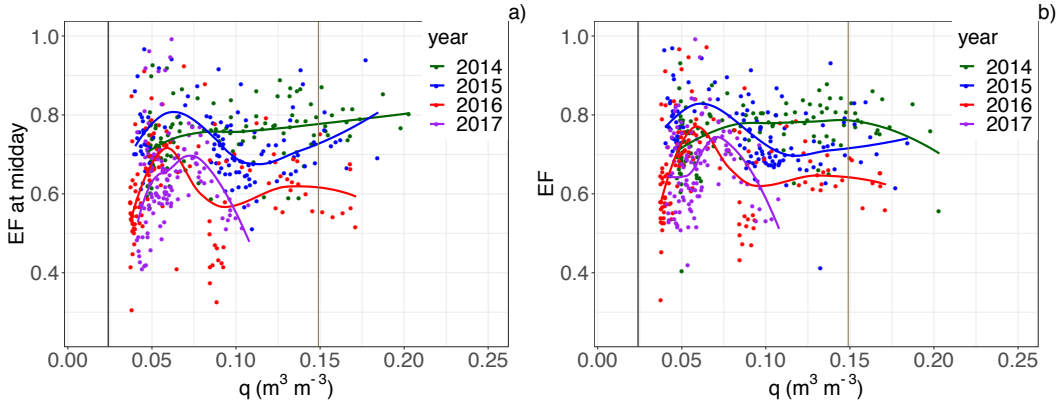

Figure 6.9. Evaporative fraction (EF) at midday (Panel a) and as an average of the hours between 8:00 and 15:00 each day (Panel b) versus soil water content (between 0.1 and 0.2 m) with fitted curves. In black: line indicating the wilting point.

Table 6.5. RMSE of EF versus soil water content fit.

EF midday				**EF central hours**			
2014	2015	2016	2017	2014	2015	2016	2017
0.10	0.11	0.12	0.38	0.11	0.11	0.10	0.39

At a daily scale, the evaporative fraction is higher in 2014 and 2015 than in other growing seasons (Figure 6.10).

Average values are 0.75, 0.75, 0.63 and 0.62, respectively for 2014, 2015, 2016 and 2017. Despite the variability, dry growing seasons experience lower

evaporative fraction, as expected. In addition, despite a high initial soil water content in 2016 (caused by the high precipitation amount occurred in May), the evaporative fraction seems not particularly affected, likely because the infiltrated water due to rainfall was stored in the deep layers and it was still not extracted by vegetation.

The actual evapotranspiration is very frequently very close to *ETo* (potential evapotranspiration) only in 2014 (a wet year with high soil water content even in the 10 cm horizon) and the two values differ on average about 0.40 mm. The difference increases in 2015, 2016 and 2017, with 1 mm, 1.78 mm and 1.66 mm (Figure 6.11) and this difference is also due to decreased precipitation frequency in 2015 and decreased frequency and amount in 2016 and 2017. Figure 6.11 illustrates also a frequently water-limited evapotranspiration, with 2014 exception (it was characterised likely by the wettest conditions). The water-limited conditions are apparently in contrast with Figure 6.9. This behaviour (and the weak correlation between EF and soil water content showed in Figure 6.10) can be explained by the fact that the evapotranspiration could be mainly driven by deeper soil water content because shrubs can extract and use water from below 30-40 cm. Sometimes, $ETo > ETa$. This indicates solely that the potential evapotranspiration is evaluated by means of a model, which is clearly not the truth. In addition, the actual evapotranspiration is a value derived from measures and not from a model, and it is influenced by the contributes of the whole flux footprint.

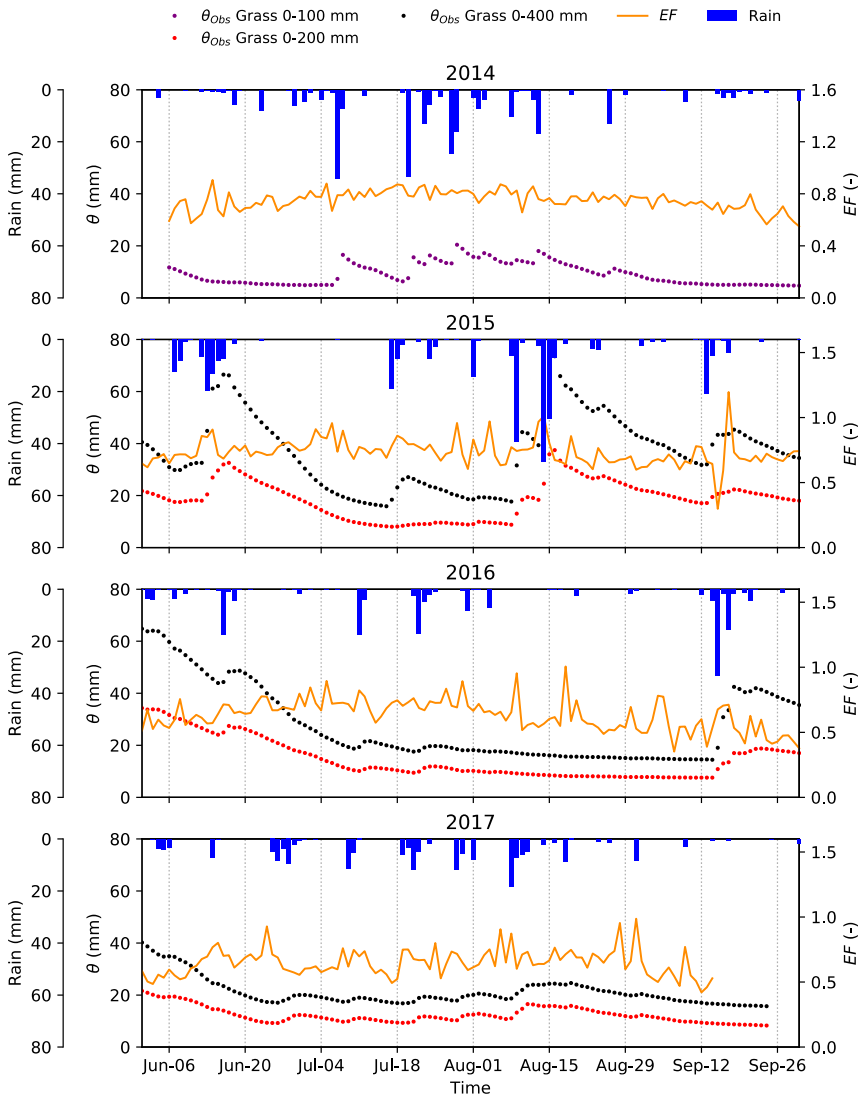

Figure 6.10. Precipitation bars, evaporative fraction at midday and measured soil water content between 10 and 20 cm of depth. The soil water content was related to the soil horizon and converted into equivalent millimetres multiplying the volumetric water content by the soil depth of each layer (10 or 20 cm). In the plot all measures are reported in millimetres to have an easier comparison.

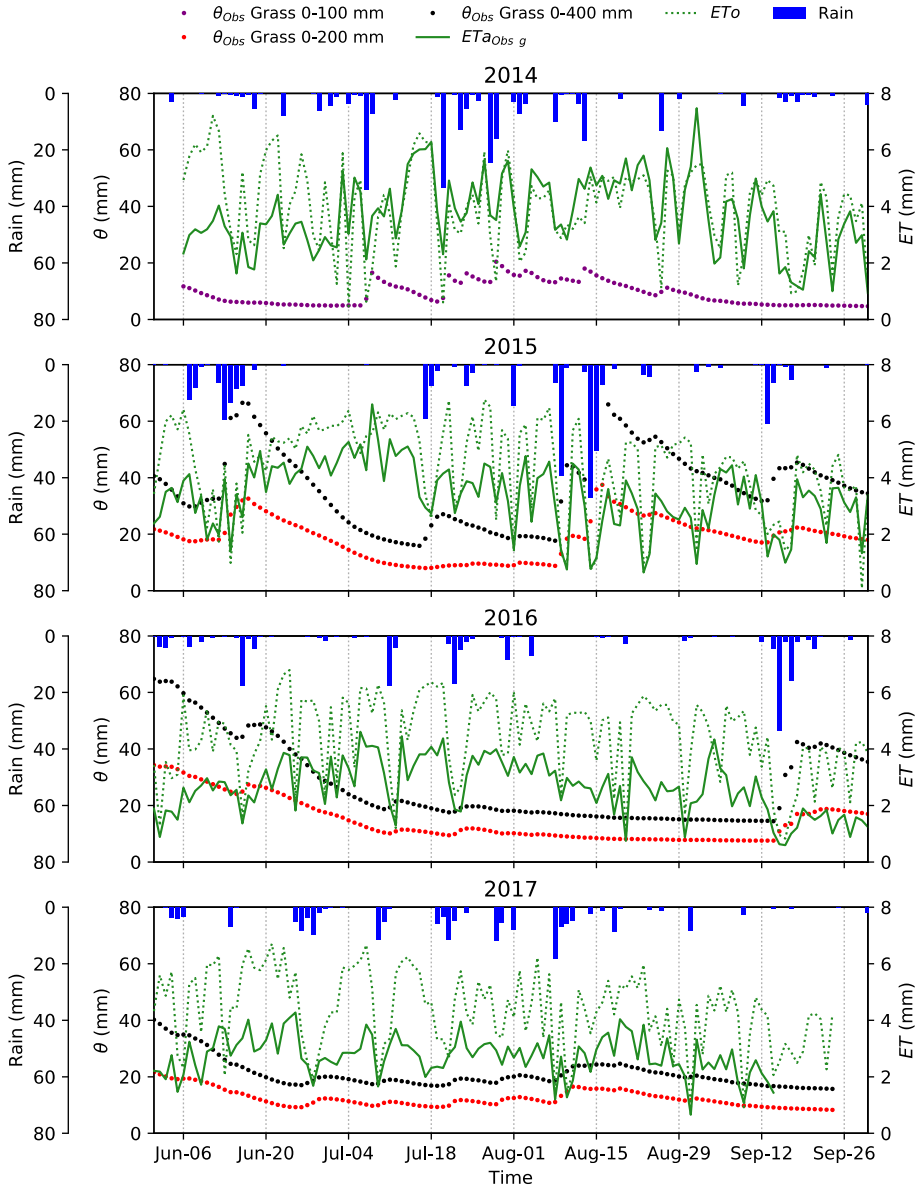

Figure 6.11. Daily precipitation bars, potential and actual evapotranspiration and measured soil water content expressed in millimetres at 10 or 20 cm depth. The soil water content was related to the soil horizon and converted into equivalent millimetres multiplying the volumetric water content by the soil depth of each layer (10 or 20 cm). In the plot, all measures are reported in millimetres to have an easier comparison.

15-days analysis of micrometeorological variables

The interannual variability can be also noted looking micrometeorological variables on 15-days periods as illustrated in Figure 6.12.

In the boxplots, median and mean values are shown for periods of 15 days. Again, *LE* shows a high variability, which is reflected in the different values in the four growing seasons, of Bowen ratio and evaporative fraction.

A high Bowen ratio and a relatively low evaporative fraction (Figure 6.8, Panels *a* and *b*) can be usually found in warm and dry growing seasons if compared to wet growing seasons. In particular, the decreasing trend from 2014 to 2017 can be found in all periods except the 15th June – 30th June one. In that case, there is a little interannual difference of B, EF and *ET* probably because of similar precipitation amount for 2014, 2016 and 2017. The 2015 period between the second part of June and the first 15 days of July experienced a reduced precipitation amount, but it should be considered that in the previous period (1st – 15th June 2015) the average precipitation per day was high (about 5 mm), therefore it contributed, at least partially, to the evapotranspiration of the period between 16th June and 15th July.

The latent heat flux covers up to 60% of the total energy and it is therefore dominant over the sensible heat flux (Figure 6.8, panel *a*). This predominance is attenuated in dry periods, since the EF shows a negative trend (with a complementary Bowen ratio increase, Figure 6.8, panel *b*). The EF values, in the same period of the growing season, but in different years, can decrease from about 0.80 to 0.65.

An enhanced variability, between wet and dry growing seasons, of B and EF was found in September.

Frequently, when EF decreases, VPD and T increase (Figure 6.8, panels *c* and *d*). When high amount of precipitation occurs (panel *e*), a consequent low number of dry days is found (panel *f*) and there is a lower cumulative net radiation (panel *g*). In particular, the period between 1st July – 15th July 2015 is characterised by a cumulative net radiation 80 MJ m^{-2} higher than in the same period in 2014. The evapotranspiration (panel *h*) is characterised by interannual differences up to 10-15 mm, when in the same periods but different years less precipitation and drier soil conditions occur. Indeed, the evapotranspiration can be higher in dry periods than in moister conditions because of higher VPD.

When there is a dramatic decrease of precipitation after a wetter period (e.g. 1st July – 15th July 2015), the *ET* increases more than in other periods when moister conditions occur but a reduced VPD exists. (Indeed, when precipitation occurs, the high initial air relative humidity and relatively low net radiation reduce further evapotranspiration).

Evapotranspiration changes could be mainly due to land cover change and they could not happen because of severe peaks of VPD induced by higher temperatures. Indeed, in Figure 6.8, Panels *c)* and *h)* show that when *ET* is reduced, VPD is not

always characterised by a decline. In addition, in some case, periods with enhanced VPD do not experience high *ET* if compared to periods with lower VPD (e.g. the fourth group of days, namely between 16th July and 30th July in Figure 6.8). These findings, together with the lowering EF across different years when VPD increases are coherent with what was remarked by Massmann et al. (2019): depending on the environment and plant strategies (i.e. stomata closure or opening), *ET (*and EF) can be reduced even if VPD increases because the plants retain water, if water supply is reduced. A marked difference was noticed between wet and dry growing seasons for evaporative fraction, Bowen ratio and VPD (higher in dry growing seasons). Differences were detected in six over eight 15-days periods for average rain per day, and the highest peaks in panel e) are found for 2015. Excluded periods were 16th – 30th June and 1st – 15th September. Air temperature and VPD highlighted also interannual differences in five periods (1st-15th June, 1st -15th July, 16th -30th July, 16th -30th August, 1st – 15th September). A great *ET* difference was also noticed in three over eight periods of 15 days (1st – 15th July; 1st – 15th September; 16th – 30th September).

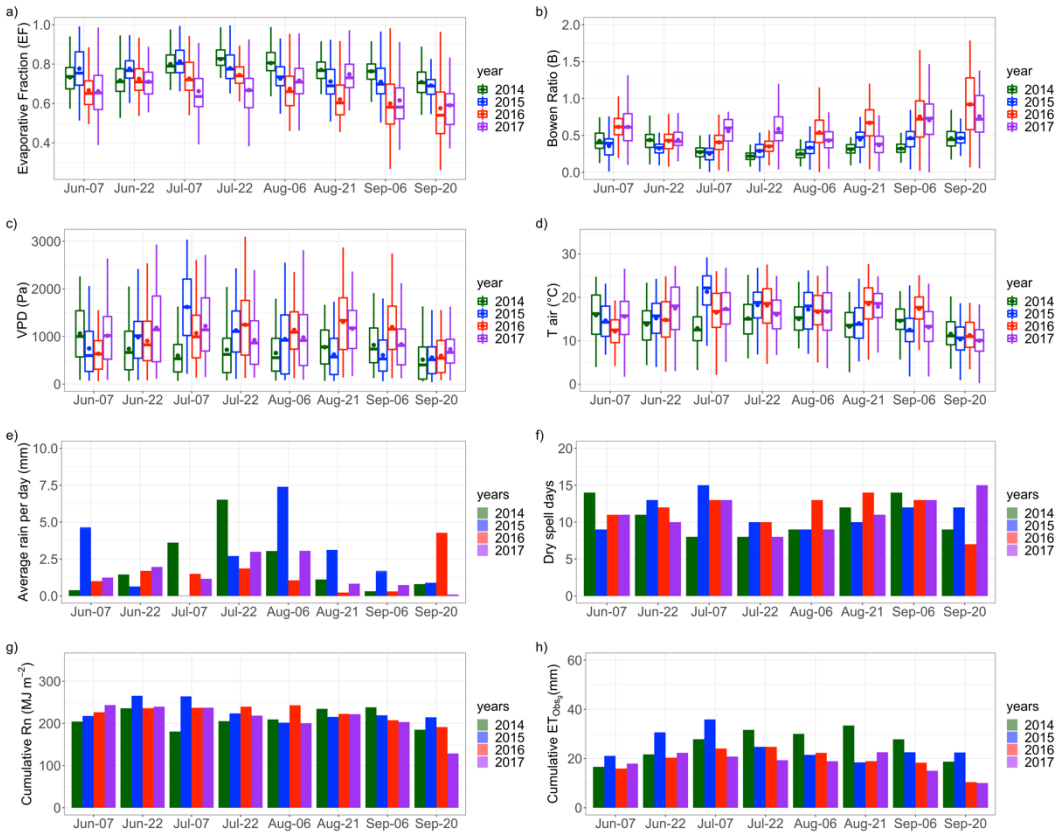

Figure 6.12. Two-week averages (dots) and medians (boxplot horizontal lines) of evaporative fraction (EF, panel a), Bowen ratio (B, panel b), vapour pressure deficit (VPD, panel c), air temperature (T air, panel d). Two-weeks average precipitation per day (panel e), number of dry days for each 15-days period, cumulative net radiation and measured gap filled evapotranspiration ($ETa_{Obs\ g}$, panel f). The boxplots from Panel a) to Panel d) show the minimum data point, the 1st quartile

(25th percentile), mean value instead of median, 2nd quartile (75th percentile) and maximum.

6.3.3 Interannual variability of measured evapotranspiration and its drivers at the daily scale

General overview of the drivers

The results of previous Sections, highlight a high interannual variability, also quantifiable with the coefficient of variation of ET and precipitation P. The *ET* coefficient of variation was 16.4%, compared to 7.1% found by Wieser et al. (2008), whereas the *P* coefficient of variation was 8.8%, compared to 16.4% in that paper, where the ecosystems were Alpine grassland but not encroached by shrubs.

The growing season evapotranspiration ranged from 44.9% to 56.5% of hydrologic year cumulative precipitation, respectively in 2014 and 2017. These findings suggest an enhanced interannual variability at Cogne site if compared to the Austrian one.

Given this variability, it is important to evaluate how the *ET* drivers (global and net radiation, VPD and others such as air temperature, wind speed, soil moisture and precipitation) respond to the changes occurring in different growing seasons.

The relationship between evapotranspiration and global radiation is very similar to the one with net radiation (R=0.63). The VPD, shows the second highest correlation coefficient after net radiation (R=0.57 considering the natural logarithm of VPD). A correlation also exists between *ET* and air temperature, in particular with maximum temperature (R=0.50), whereas lower values exist between evapotranspiration and mean and minimum temperature (R=0.39 and R=0.14, respectively). Wind speed also might play a key role (R=0.47), together with ground heat flux at the surface (R=0.42). More unclear relationships exist with soil water content and precipitation, as will be shown later.

In the following paragraphs, the analysis for each mentioned variable is performed, in decreasing order of significance, and it is performed on each growing season.

Evapotranspiration, global and net radiation

If single growing seasons are considered, the evapotranspiration shows high correlation coefficients with global radiation (R=0.62 0.80, 0.76 and 0.69). There is a linear relationship also between the evapotranspiration and the net radiation, with values of R = 0.58, 0.80, 0.72 and 0.67.

Analysing the relationship between evapotranspiration and global and net radiation (Figure 6.13, panels a) and b)), the fraction of variability explained by the radiation values is illustrated in Table 6.6.

Table 6.6. Regression R^2 values for global and net radiation. All regressions are significant ($p < 0.05$).

	Rg	*Rn*
Year	R^2	R^2
2014	0.38	0.41
2015	0.68	0.66
2016	0.57	0.54
2017	0.48	0.45

A dramatic increase is found in warm growing seasons. However, it should be noted that in 2017 there is again a reduction of correlation between ET and both global and net radiation. This effect might be explained by the decreased average dry spell in 2014 and 2017 if compared to the other two years (3.4 and 4.9 days against 6.2 and 6.1 days). In 2014 and 2017 growing seasons, the higher occurrence of cloudy conditions and rainfall likely affected the relationship of radiation with evapotranspiration.

Evapotranspiration and VPD

The relationship between *ET* and VPD (Figure 6.13, panel c)) is interesting because it involves also canopy physiological processes and it is more complex than the other examined relationships. Indeed, as it was noted by Wieser et al. (2008), the relationship with the VPD might be fitted by a logarithmic model, as also verified here ad shown in Panel c) of Figure 6.13.

A second order polynomial fit was also used, with similar results, as shown in Table 6.7. However, as it was pointed out by Narula et al. (1979), the regression with ordinary polynomials has some drawback, because the tests on significance are not independent and the estimates of polynomial parameters depend on the polynomial degree. Hence, the choice of orthogonal polynomials is preferable. The best reasonable polynomial was a second order one. As can be observed in Table 6.6, the two models (namely, polynomial and logarithmic) have very similar performances and explain almost the same amount of variance. The polynomial model has a slight improved performance only in 2014. For these reasons, the choice of either the first model or the second model has a low importance. Hence, the simplest model (the logarithmic one) was chosen, also to compare results with previous studies.

Table 6.7. Regression results for both the polynomial and logarithmic models.

		RMSE	R^2	dof
2014	polynomial	0.90	0.45	119
	logarithmic	0.94	0.42	120
2015	polynomial	0.63	0.70	119
	logarithmic	0.63	0.70	120
2016	polynomial	0.60	0.60	119
	logarithmic	0.61	0.58	120
2017	polynomial	0.45	0.59	103
	logarithmic	0.45	0.59	104

In Figure 6.13, it can also be noted that, in JJAS 2014, the highest VPD values were lower than in other growing seasons (likely because of lower temperature), suggesting a reduced atmospheric demand of water vapour partially overcome by the high-water availability.

The daily evapotranspiration values showed that the *ET* decreases (and the difference between *ETa* and *ETo* increases) in dry growing seasons if compared to wet periods (2014 and 2015), even with relatively high values of VPD, thus showing a soil water-limited regime. The regression output shows that VPD explains a higher ET fraction of variability than either net radiation or global radiation), respectively in 2014, 2015, 2016 and 2017 (all regressions are significant). The lower R^2 value in 2014 might be explained by the lowest dry spell period (thus, an enhanced rainfall frequency).

The R^2 values for net radiation and VPD were lower than other studies (e.g. Wieser et al., 2008, on Alpine grasslands, but could reach values much higher than the findings of Detsch et al., 2007 – maximum: 0.46 on Kilimanjaro grasslands). In our case, is not clear whether more importance should be assigned to precipitation, or if the data are noisier. In particular, when precipitation occurs more frequently (JJAS 2014), it might play an enhanced role on *ET* dynamics (and its variance).

The VPD explains the highest fraction of variance than any other variable in three over four growing seasons (namely, 2014, 2016 and 2017), whereas the global radiation explains the highest fraction of variance in 2015. The high VPD importance might indicate that the air moisture conditions play a more important role than available radiation, wind speed and air temperature at Cogne, if compared to other sites (e.g. Wieser et al., 2008, where the net radiation is the most important predictor for evapotranspiration). This finding is interesting because the Cogne site is characterised by a mix of shrubs (despite being water-stress resistant they can be classified as anisohydric according to Tang et al., 2018) and grass (tall fescue can be considered also anisohydric, according to Martre, 2001). A recent study by Konings et al. (2017) showed that anisohydric grasslands are at least three times

more sensitive to VPD than isohydric ones. This might explain why VPD is very important at our site.

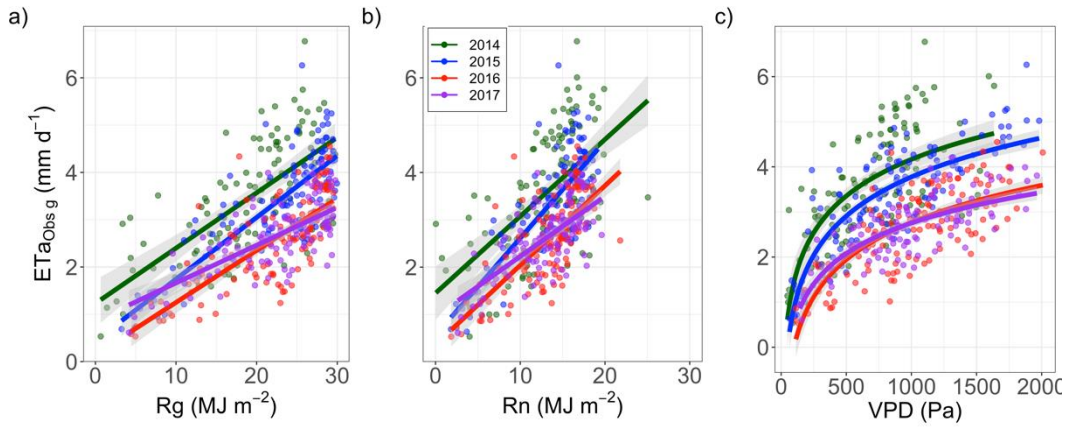

Figure 6.13. Daily measured evapotranspiration versus global radiation (panel a), net radiation (panel b) and vapour pressure deficit (panel c). The fitted regressions are all significant (p-value < 0.05) and they are linear in the first two cases and logarithmic for VPD.

Evapotranspiration, air temperature, wind speed, ground heat flux and soil water content

As already mentioned, ET is related to other variables, including wind speed, maximum air temperature and ground heat flux at the surface and soil water content (at 10 cm depth in 2014 or 20 cm depth in the following years). Instead, the mean and minimum air temperature were weakly correlated with ET, hence they were not considered for this analysis.

The R^2 values of the regressions between ET and each of the aforementioned variables are shown in Table 6.8. The regressions are shown in Figure 6.14. Wind speed, maximum air temperature and G_0 are still good ET predictors, and G_0 could be more important than wind speed and it has values within the range of what was found by Detsch et al. (2017). In particular, ET increases with θ only in 2014, when the wettest soil conditions occurred in the growing season (Table 6.8, Figure 6.14, panel d). The relationship between ET and θ is the weakest.

Table 6.8. Regression R^2 values for wind speed, maximum air temperature and soil water content between 10 and 20 cm. All regressions are significant ($p < 0.05$) with the reported exception in 2017 for soil water content.

	U	*Tair max*	*G0*	θ
year	R^2	R^2	R^2	R^2
2014	0.17	0.36	0.38	0.18
2015	0.24	0.46	0.55	0.10
2016	0.22	0.49	0.37	0.03
2017	0.15	0.45	0.30	~0 (*p > 0.05)*

The four variables have a minor direct impact on ET if compared to *Rg, Rn* and VPD. Soil water content is the least impacting variable over ET, at least at a daily scale, since the soil has a relatively high inertia.

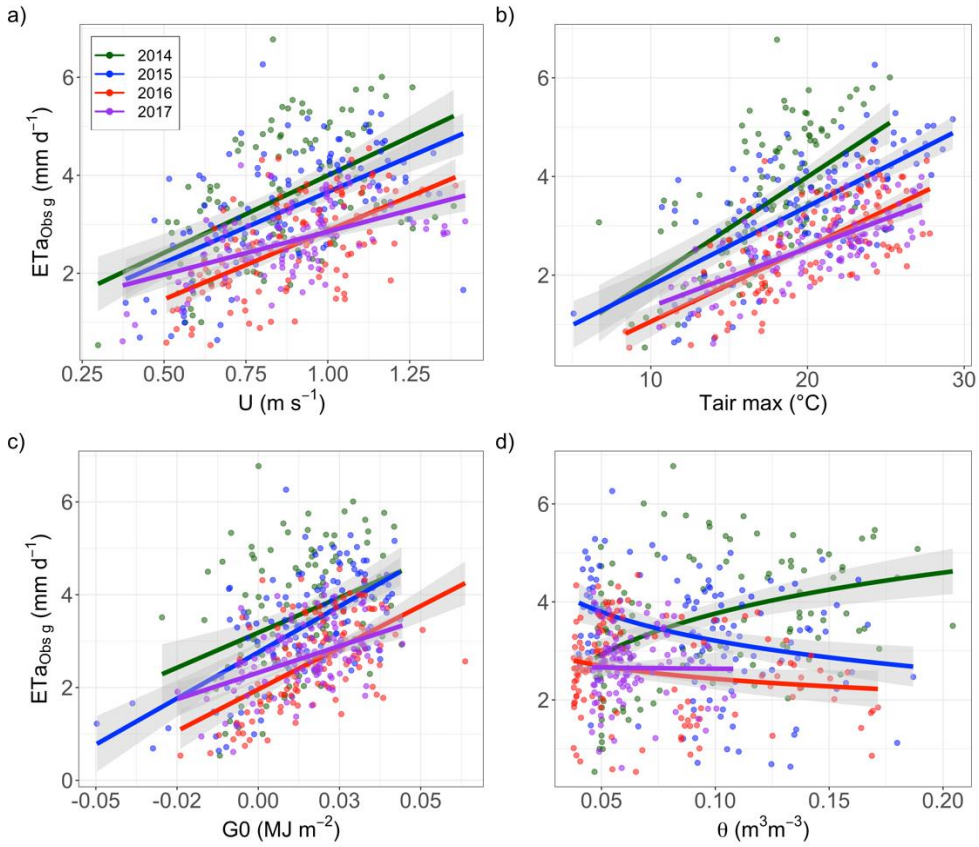

Figure 6.14. Daily measured evapotranspiration versus mean wind speed (panel a), maximum air temperature (panel b) and ground heat flux at the surface (panel c) and soil water content between 10 and 20 cm of depth (panel d). The fitted regressions are all significant (p-value < 0.05) with the 2017 regression for soil water content.

Evapotranspiration, precipitation and soil water content: a deeper insight

It is not trivial to quantify the relationship between *ET* and *P* or between *ET* and soil moisture, because of the time lag existing between the two variables. That lag is due to slow processes occurring in the soil. However, some exploration of their interaction is useful to understand *ET* dynamics on scales longer than the daily one.

At a site as Cogne, where high precipitation pattern changes exist between different years, the evapotranspiration (and its variability) might show a higher sensitivity to precipitation temporal variability, which is, however, lower at Cogne if compared to Eastern Alps sites, at least in the analysed years. It should be noted, however, that Wieser et al. (2008) considered six years, while at Cogne four years were analysed. The curve of cumulative *ET* versus the cumulative *P* (Figure 6.15)

shows that evapotranspiration increases in moist growing seasons and that, interestingly, the data collected at Cogne appear on the same curve as the data shown in the aforementioned paper, even if in different contexts, and in different years.

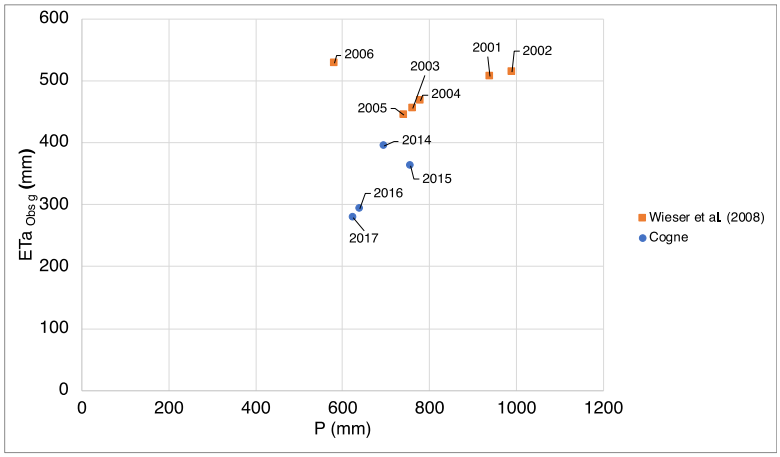

Figure 6.15. Measured evapotranspiration versus precipitation for Cogne and Neustift (Wieser et al., 2008) sites.

To obtain further information about the impact of precipitation over evapotranspiration, the relationship between *ET* and *P* can be analysed considering sums over periods of 15, 26, 35 and 52 days (Figure 6.16), because relatively long periods might partially overcome the soil inertia. In the figure, the evapotranspiration is divided by the number of days for each selected period.

Data, included regression results, indicate that with different groups of days there is a positive trend between the two variables, although the relationship is weak because it is related to an autoregressive process which involves soil water dynamics. Due to very weak trends, several figures are represented, to show what is the difference found between growing seasons.

First, the data are fitted with a linear model. The resultant RMSE is 0.70, 0.59, 0.53 and 0.48 mm, respectively for the 15, 26, 35 and 52-days periods. The highest R^2 is associated with 35 and 52 days (R^2=0.18), whereas the lowest value is found for 15-days periods (R^2 almost 0), likely because soil dynamics involves processes longer than 15 days.

None of the regressions is statistically significant, but it can be noted that the maximum values of ET are slightly higher than the average *ETo* (mean of the four growing seasons, 4.25 mm).

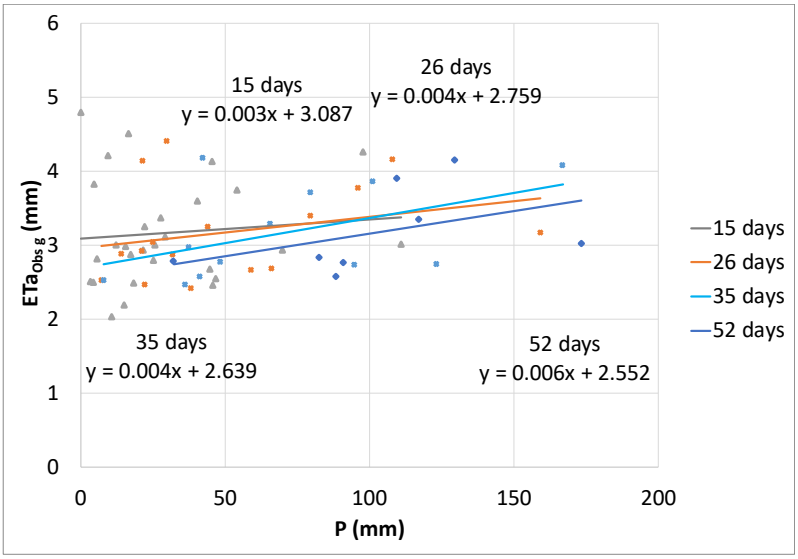

Figure 6.16. Measured evapotranspiration divided by number of days for each group of 14, 26, 35 and 52 days versus precipitation.

Figure 6.17 shows that the data might be also fitted using a nonlinear approach, with a modified logistic function

$ET = \frac{2n}{(e^{-kP}+1)-n}$, with ET being the evapotranspiration and P being the precipitation.

The nonlinear fit yields residual standard errors equal to 1.82, 1.17, 0.84 and 0.65 mm, suggesting an improved performance for a high number of grouped days (35 and 52 days). This is a similarity with the linear regressions, for which the residual standard error decreases towards high numbers of grouped days. The logistic function highlights a trend similar to a Budyko curve, with the two components, namely the water and energy-limited regimes. The RMSE, however, is higher than in the linear model case.

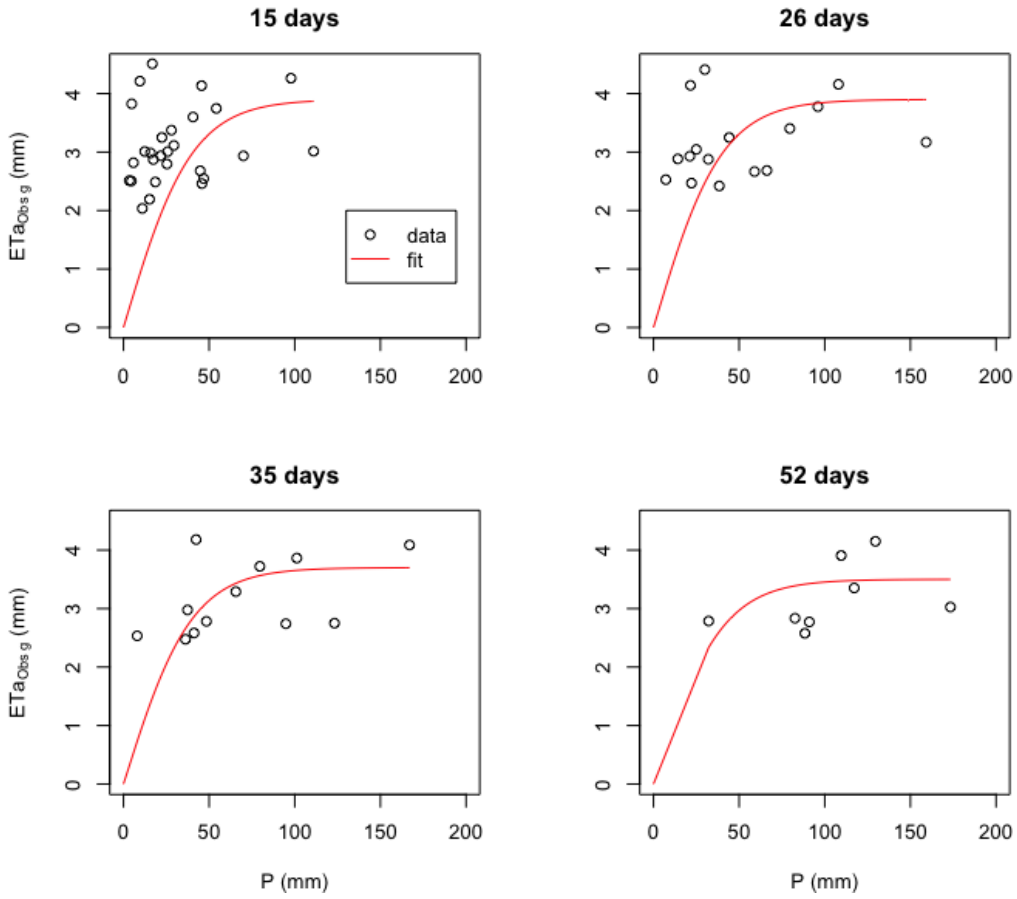

Figure 6.17. Measured evapotranspiration divided by number of days for each group of 15, 26, 35 and 52 days versus precipitation. Nonlinear fit of data using a modified logistic function. The regression parameter is significant.

For each growing season, the selection of 15, 26, 35 and 52 days cumulative *ETa* divided by the number of days and *P* allows to identify different data patterns among the years (Figure 6.18). Generally, the different years show, for every group of days, point on different regions of the plane – that is, different clusters - in particular 2014, 2015 and 2016-2017 (which show instead similar behaviours).

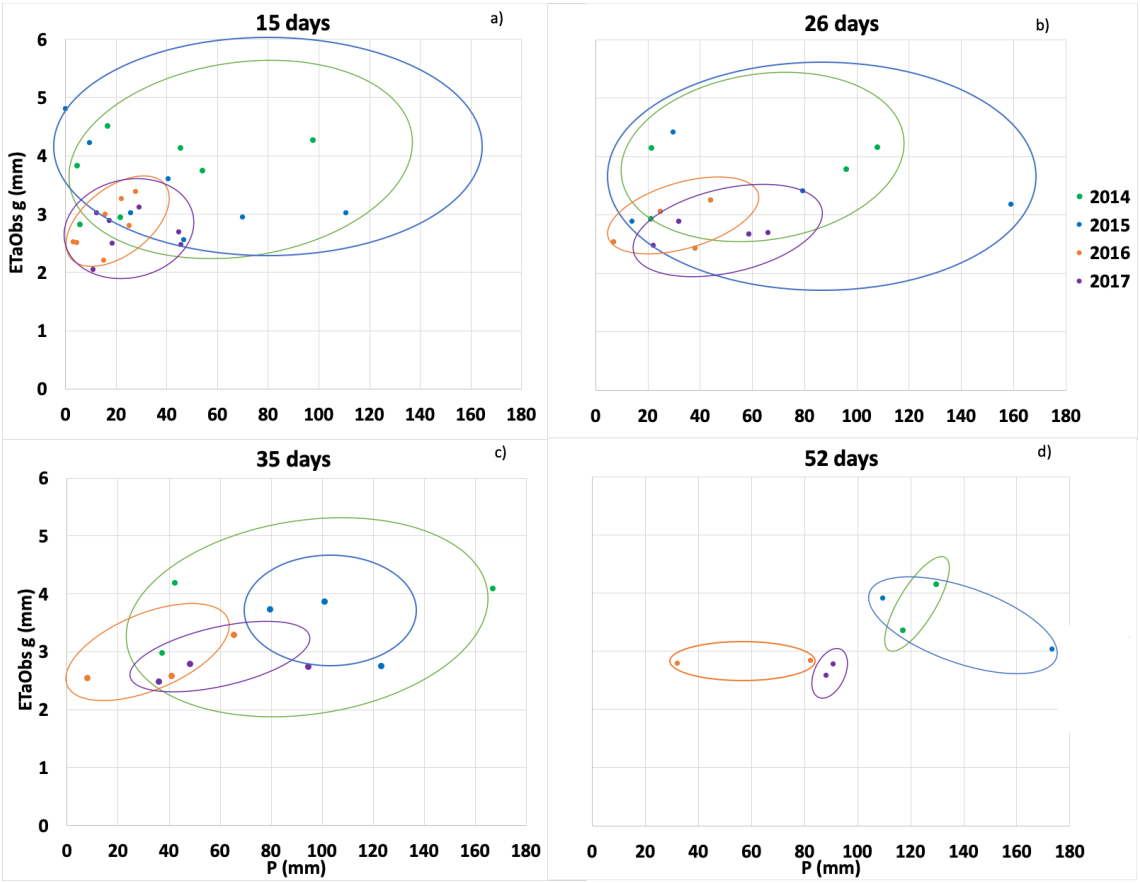

Figure 6.18. Measured evapotranspiration divided by the number of days for the 15, 26, 35 and 52-days group versus precipitation in the same group of days. Ellipses highlight the different regions in which the data lay in different years.

If cumulative evapotranspiration on each group of days (14, 26, 35 and 52 days) is plotted against the average soil water content (mean of the two soil moisture measures at 200 and 400 mm of depth) as in Figure 6.19, the fitted data from 15, 26 and 35 days show an almost horizontal line, indicating no or little direct dependence on soil moisture, whereas the *ET* versus precipitation showed a more positive trend. Only the 52-days period shows a clearly positive slope (and it is the

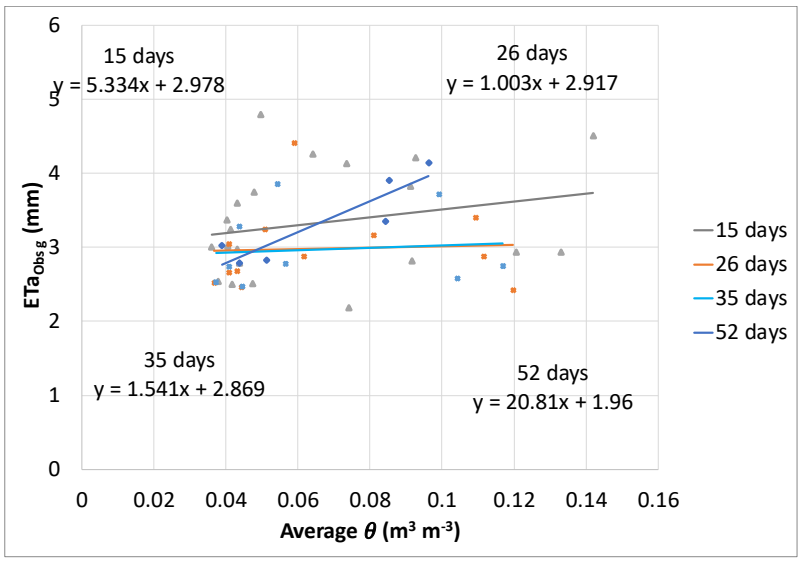

Figure 6.19. Measured evapotranspiration divided by number of days for each group of 15, 26, 35 and 52 days versus average of the measured soil moisture between 20 and 40 cm of depth.

Mean, median and cumulative values of evapotranspiration

The period 1st June – 13th September was used to determine cumulative evapotranspiration and, when specified, also averages were compute considering that interval. This option was considered since in 2017 technical issues caused data loss after that date and was applied to every growing season to allow meaningful comparisons.

The 2014 growing season experienced the highest peaks of evapotranspiration (3.7 mm) and also a higher variability of evapotranspiration even if compared to 2015 (with 3.4 mm of average evapotranspiration). The average evapotranspiration was equal to 2.9 and 2.8 mm per day in 2016 and 2017, respectively (Figure 6.20, upper panel).

There is also an evident interannual difference, in cumulative values (Figure 6.23, lower panel): 246.8 mm, 304 mm, 114.8 mm and 179.4 mm of precipitation and 393.6 mm, 361.8 mm, 294.2 mm and 279.9 mm of evapotranspiration, for 2014, 2015, 2016 and 2017 growing seasons, with an evident gap between wet and dry growing seasons, but also between seasons classified as wet or dry. In addition, if the 2014 growing season (coldest one, with -1.9°C and -1.8°C of difference with respectively 2015, 2016 and 2017) is compared to the others, evapotranspiration deficits are found, even with 2015 (-31.8 mm, -99.4 mm, -113.6 mm). The fact that the precipitation was lower than evapotranspiration can be explained considering that previous precipitation (namely in the late Spring) contributes to the water storage and to the growing season evapotranspiration, but it is not reported here. Plus, the precipitation measures from the ARPA VdA rain gauge were also confirmed by the measures collected by the manual rain gauge at the station.

The evapotranspiration values found in this study are comparable to the findings of Gao et al. (2019), which found 350 mm between in the June to September period at their meadow in the Qilian Mountains.

The reasons for the 2014 evapotranspiration being the highest (although precipitation in 2015 growing season was higher than in the previous one) are: i) lower temperature and, consequently, lower water stress; ii) frequent rainfall events (dry spell: 3.7 days versus 6.2 days and 28 against 26 rainy days between 2014 and 2015); iii) The amount of precipitation between April and May was 20 mm higher in 2014, if compared to 2015 (not shown); iv) a sufficient amount of rainfall during the hydrologic year and also during the growing season. Enhanced dry spell in 2015 was also associated with high temperatures but their effect was reduced by high precipitation amount and number of rainy days.

Despite the average temperature differences are very low (< 0.1°C), such as between 2015 growing season and the following two – 2016 and 2017 – the *ETa* deficit can be greater than 60 mm (67.6 mm and 81.8 mm). Also, a deficit of 14.3 mm existed between the two dry growing seasons. The dramatic decrease of evapotranspiration in 2016 is explained by a combination of strongly enhanced dry spell (7.1 days), only 18 days with precipitation and low precipitation amount (114.8 mm), whereas the decrease in 2017 is explained mainly by low precipitation, low soil water content amount and higher temperature, because the dry spell (4.9 days) and the number of rainy days (29 days) were comparable to the ones found in wet growing seasons. The 2016 growing season experienced a higher cumulative evapotranspiration than in 2017 (which was wetter) likely because of rainfall events in August. As mentioned in Section 6.3.2, the ecosystem in 2016 and 2017 was water-limited. Therefore, even with high temperature and high VPD (causing an enhanced wate vapour demand in atmosphere), the actual evapotranspiration was strongly reduced. Thus, changes in precipitation amount and in air temperature might be very important.

Mastrotheodoros et al. (2020) showed that in a climate change scenario, the average *ETa* increase is 45 mm (maximum: 100 mm) with a temperature rise of +3°C. In our analysis, even with lower temperature differences (below 2°C but in contiguous years), the evapotranspiration can vary significantly and show values similar to those described in the mentioned paper. However, the evapotranspiration is not automatically enhanced because of water-limitation mechanisms and vegetation stress. If more frequent dry and hot growing seasons such as those in 2016 and 2017 are expected, the *ETa* might not increase, at least locally, also because of plant strategies, as previously described.

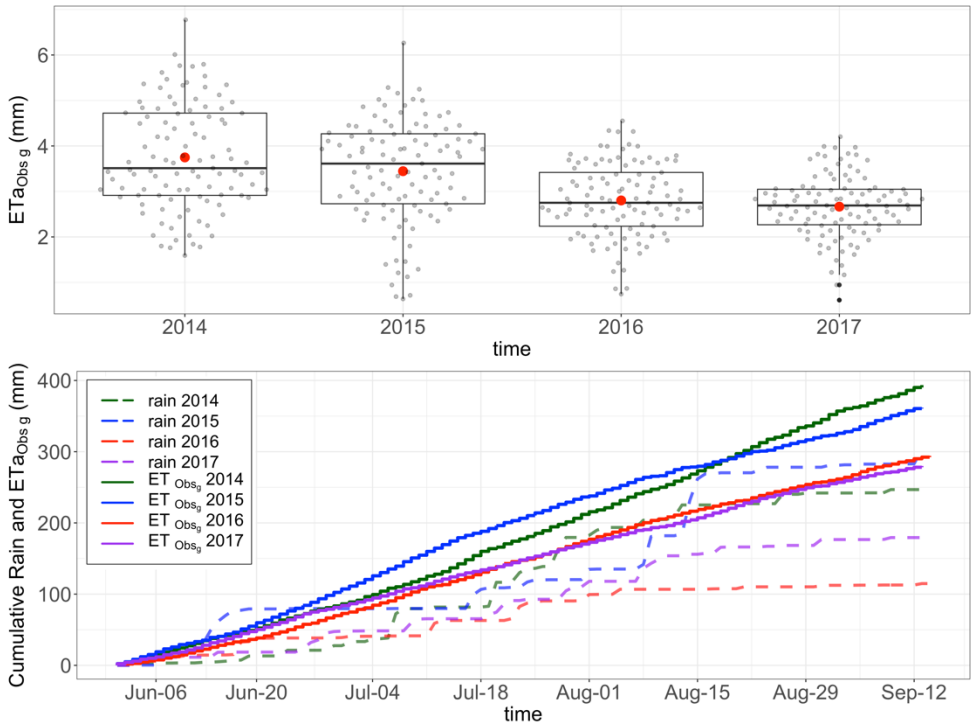

Figure 6.20. Upper panel: average daily measured evapotranspiration for each growing season. Lower panel: cumulative rainfall and measured evapotranspiration for the growing seasons in each year.

6.3.4 Modelling actual evapotranspiration

Model parameters and set-up

Modelling tools are useful to perform simulations of actual evapotranspiration with different land covers and also with changing atmospheric and soil conditions. It is important to investigate what would happen if all the land cover was characterised by grass and make comparisons using only shrubs, to find whether there are significant changes in evapotranspiration caused by shrub encroachment.

The two land cover configurations were used to compute a weighted mean (Eq. 6.1)

$$ET_{a_{Sim\ avg}} = w\ ET_{a_{Sim\ grass}} + (1 - w) ET_{a_{Sim\ shrub}} \quad (6.1)$$

with the weight *w* being as in Eq. 6.2.

$$arg\{w \in [0,1]\} \mid \min\left(\sum \left|ET_{Obs} - ET_{a_{Sim}}\right|\right)\} \tag{6.2}$$

The optimal weight value was 0.41 considering all the growing seasons, therefore shrubs accounted for 41% of the land cover.

Once the weight had been found, several model configurations (Table 6.9 and Figure 6.21) were examined to obtain results closer to observations. For each the configuration, the evapotranspiration from grass and shrub and their weighted average were computed. Within the soil horizon 0 – 0.4 m, soil moisture data were used. Below that depth, a guessed initial value was used. From previous analyses, the soil depth at Cogne was 1.5 m. However, the hypothesis of a soil depth down to 2 m was also tested. At the bottom of soil column, three hypotheses were considered: a) constant deep water content at the bottom node; b) no flux boundary condition at the bottom (water is not lost across the boundary); c) free drainage boundary condition supposing that the water table lies below the domain of interest (gradient of pressure heat is zero, that is, water can be lost at the bottom node). In cases b) and c), an initial deep soil water content was assumed. The deviations from measures were examined computing the mean absolute deviation (MAD) for each analysed model configuration

$$MAD = \frac{1}{n}\sum |ET_{Sim} - ET_{Obs}| \tag{6.3}$$

The model is very sensitive to either initial or constant deep soil water content, if comparisons are made varying either soil or root depth. The deviations differ very little if only the soil depth or the root depth are modified. However, overall, there is a slight worse performance of simulations in the 2 m case, whereas root depth does not change severely the MAD values. Previous measure campaigns showed that the Cogne soil depth is maximum 1.5 m and this value appears reasonable. Therefore, for this analysis that value was considered, also because the model performances improved with respect to other configurations. *Eleagnus Rhamnoides* root system can reach the water table (Turekhanova, 1995) and also MAD data seem to support this finding. Therefore, a maximum of 1.5 m for root depth was chosen. Reasonable values for deep water content did not exceed 0.13 $m^3 m^{-3}$, because with higher values, unrealistic simulated water content and evapotranspiration were found. The choice which minimised the deviations was 0.11 $m^3 m^{-3}$.

Table 6.9. Soil and root depths, initial or constant deep soil water content and boundary condition at soil column bottom.

Constant deep SWC			No flux			Free drainage		
z soil (m)	z root (m)	SWC (m^3 m^{-3})	z soil (m)	z root (m)	SWC (m^3 m^{-3})	z soil (m)	z root (m)	SWC (m^3 m^{-3})
	1.3	0.10		1.3	0.10		1.3	0.10
		0.11			0.12			0.12
		0.12	1.5		0.15	1.5		0.15
		0.13			0.20			0.20
1.5		0.15						
		0.20		1.5	0.10		1.5	0.10
					0.12			0.12
	1.5	0.10			0.15			0.15
		0.11			0.20			0.20
		0.12						
		0.13		1.3	0.10		1.3	0.10
		0.15			0.12			0.12
		0.20			0.15			0.15
					0.20			0.20
	1.3	0.10						
		0.12		1.5	0.10		1.5	0.10
		0.15			0.12			0.12
		0.20	2		0.15	2		0.15
					0.20			0.20
	1.5	0.10						
		0.12		1.8	0.10		1.8	0.10
2		0.15			0.12			0.12
		0.20			0.15			0.15
					0.20			0.20
	1.8	0.10						
		0.12		2	0.10		2	0.10
		0.15			0.12			0.12
		0.20			0.15			0.15
					0.20			0.20
	2	0.10						
		0.12						
		0.15						
		0.20						

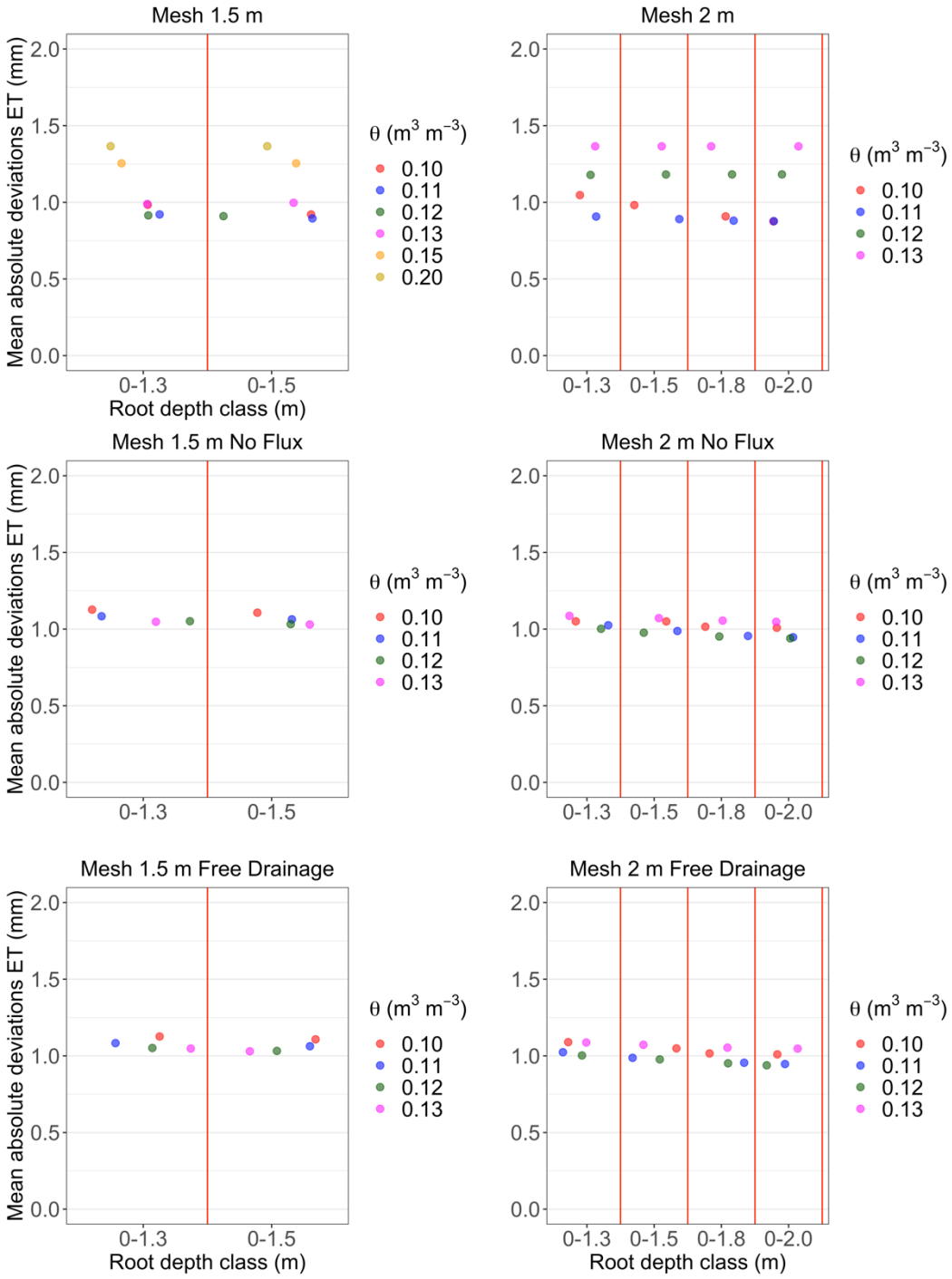

Figure 6.21. Mean absolute deviations of evapotranspiration compared against root depth classes for all the considered cases. "Mesh" refers to the constructed soil column finite elements mesh (grid).

Different land cover impacts on evapotranspiration

The comparison between measured evapotranspiration and model outputs contributes to understand which one of the simulated land covers is closer to reality (at the site there is, nowadays, a combination of shrubs and grass).

Figure 6.22 shows the modelled and observed volumetric water content, reconstructing the soil profile down to 40 cm of depth. The comparison indicates that there is an acceptable agreement between modelled versus observed water content. However, differences exist especially because the model appears to be more sensitive to occurring rainfall than observations. A high agreement is found in 2014 within the 0-10 cm (0-100 mm) soil horizon, with slight differences between simulated grass and shrub land cover. Between 2015 and 2016, the best agreement between measures within the 0-400 and 0-200 mm (the 0-100 mm horizon was not available) horizon and simulations in the same horizon is obtained if shrubs are considered, in particular after relatively intense rainfall events, at the beginning of the season if earlier precipitation occurred or when prolonged dry periods occur (i.e. June-July 2014 and August 2016). Especially in the middle part of the growing season, the reconstructed soil water content is usually higher than the measured one at the same profile depth. The model had a higher sensitivity to precipitation than measures.

The last growing season (2017) shows again the model enhanced sensitivity to precipitation which is not captured by measurements. The modelled soil water content appears overestimated for both the land covers in particular after 20th June and especially in the 0-40 cm horizon.

The agreement of measured and modelled shrub data during drought periods can be explained with the fact that shrubs are characterised by an enhanced evapotranspiration if compared to grass, therefore the water content tends to decrease.

These findings indicate that, likely, the shrubs are already significant, as also shown in Figure 6.23, where the ETa_{Sim} is compared against measured evapotranspiration. With few exceptions there is an agreement between model simulations with shrubs and observations, but it changes across years. This can be seen also in Table 6.10, where regression results are shown. The slopes are lower in the grass case, if compared to shrubland. Plus, the regressions show a great variability. In addition, the residual standard error for each regression is always below 1.5 mm for both shrub and grass evapotranspiration compared to measured ones and it is always lower in the shrub case, with the lowest values in 2015 and 2017. Also, the R^2 is always higher for the shrub land cover, while in three over four growing seasons also RMSE is lower for the shrub case, if compared to grass. This suggests that shrub contribution is non-negligible. However, if the weighted mean of shrub and grass evapotranspiration is computed, grass is still contributing up to 58% of the total. Considering the evapotranspiration that has been used later in this paper (the gap filled one), RMSE shows negligible variations when gap filled *ETa* time series is used. Slight increases (or stationary values) are found in 2015 and 2017 for shrubs and in 2015, 2016 and 2017 for grass, although R^2 is very low in the latter land cover case.

R^2 values of the regression between eddy covariance data and shrubs *ETa* are similar to the findings of Ochoa-Sanchez et al. (2019), despite they use other

hydrological models. Only the case of HBV-light model shows, in their paper, a higher R^2 (0.77).

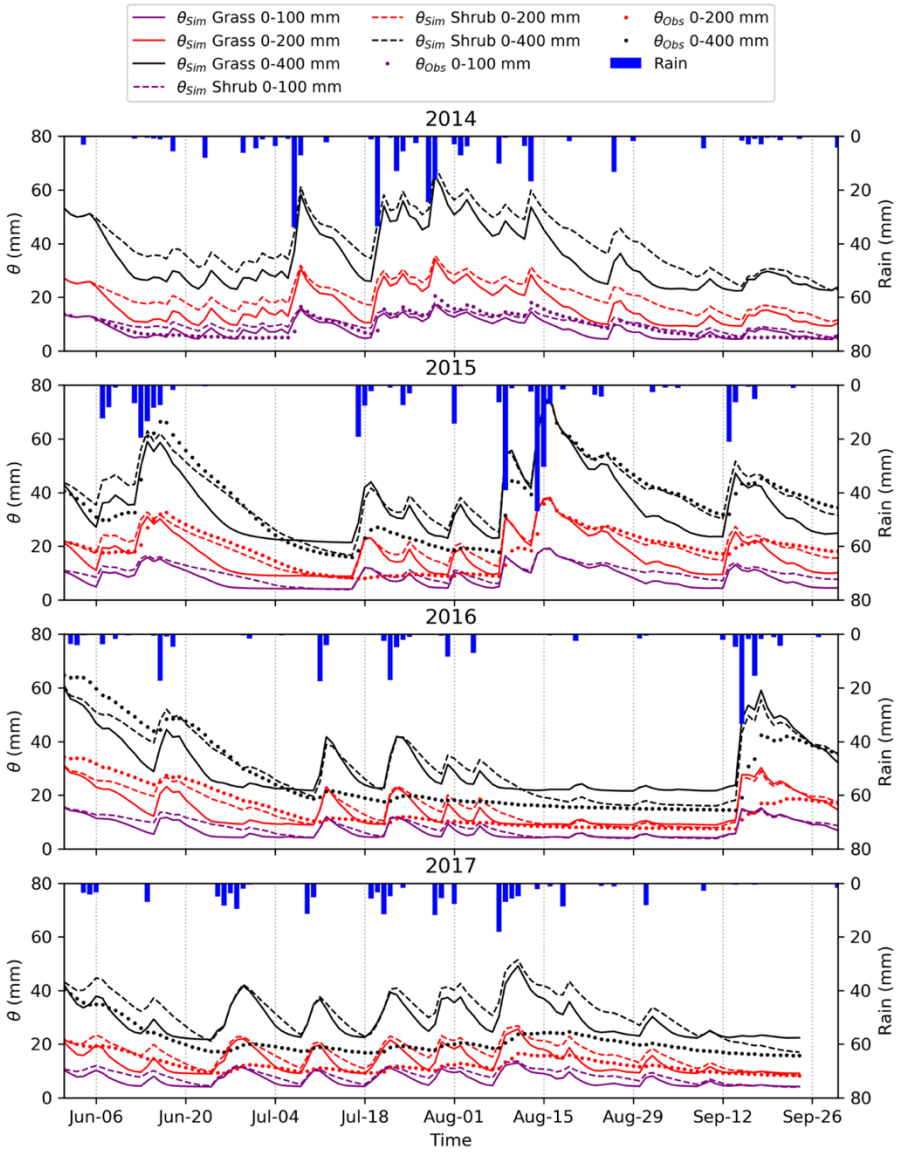

Figure 6.22**.** Daily modelled water content compared with measured soil water content. To have a better comparison, the profile from 0 to 400 mm is shown, because the probes were positioned at 100, 200, and 400 mm depth. Therefore, the simulated soil profile has here the same depth. The soil water content was related to the soil horizon and converted into equivalent millimetres multiplying the volumetric water content by the soil depth of each layer (10 or 20 cm). All measures are reported in millimetres to have an easier comparison.

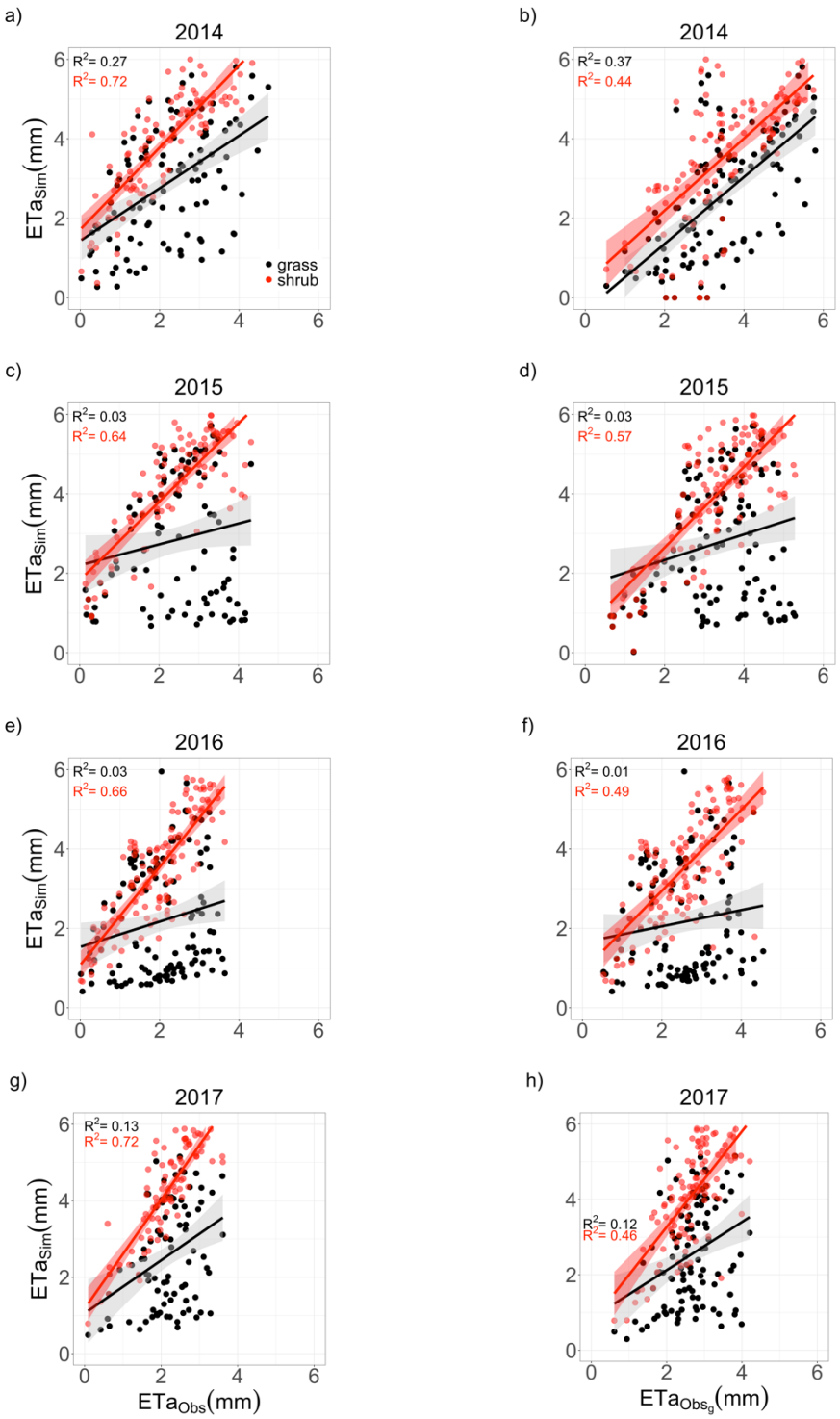

Figure 6.23. Modelled versus observed daily actual evapotranspiration and regression lines for the four growing seasons and for two different land covers (black dots and lines: grass; red dots and lines: shrubs). ETa_{sim} is the modelled evapotranspiration, whereas ETa_{Obs} is the eddy covariance evapotranspiration, and ETa_{Obs_g} is the eddy covariance gap filled evapotranspiration. Shaded areas are the slope standard error.

Table 6.10. Parameters for the grass modelled daily *ETa* versus measured *ETa* regressions. The fifth column indicates which Panel of figure 6.14 is related to the illustrated values. Green rows report gap filled *ETa* measured data.

slope (confidence interval)	R^2	p-value	RMSE (mm)	Panel	land cover
0.66 (0.45-0.87)	0.27	0.00	1.21	a	grass 2014
1.08 (0.95-1.21)	0.71	0.00	0.76	a	shrub 2014
0.76 (0.59-0.94)	0.38	0.00	1.22	b	grass 2014
0.92 (0.74-1.10)	0.45	0.00	1.27	b	shrub 2014
0.26 (-0.02 – 0.55)	0.02	0.07	1.55	c	grass 2015
1.00 (0.84-1.15)	0.64	0.07	0.83	c	shrub 2015
0.27 (0.03-0.51)	0.03	0.03	1.52	d	grass 2015
0.99 (0.81-1.11)	0.58	0.00	0.97	d	shrub 2015
0.32 (0.04-0.60)	0.03	0.02	1.37	e	grass 2016
1.29 (1.12-1.45)	0.66	0.02	0.83	e	shrub 2016
0.20 (-0.06-0.47)	0.01	0.14	1.39	f	grass 2016
1.07 (0.87-1.27)	0.49	0.00	1.00	f	shrub 2016
0.69 (0.31-1.07)	0.12	0.00	1.25	g	grass 2017
1.44 (1.25-1.64)	0.72	0.00	0.65	g	shrub 2017
0.64 (0.29-0.99)	0.12	0.00	1.25	h	grass 2017
1.30 (1.03-1.57)	0.48	0.00	0.96	h	shrub 2017

Figure 6.24 shows the amount of daily precipitation, the reference ET_0 Penman-Monteith FAO 56, the modelled actual evapotranspiration form both grassland and shrubs and the measured evapotranspiration. There is an agreement between measured and observed, although it can be noted again that, especially from 2015 onwards, there is a better agreement between the ETa_{Obs} time series and the ETa_{Sim} supposing a land cover characterised by shrubs, especially when drought periods occur, whereas the measured time series oscillations are also captured by the model. The growing season with closer values between shrub and grass is 2014, while already in 2015 discrepancies can be noted. The comparison between *ETo* and *ETa* allows to conclude that the ecosystem was frequently near stress conditions not only in the dry growing seasons but also in wet 2015 growing season, which experienced a wide period without rainfall between the end of June and the first week of July. In addition, especially in wet growing seasons, the shrubs are in saturated conditions, hence their evapotranspiration was closer to *ETo*.

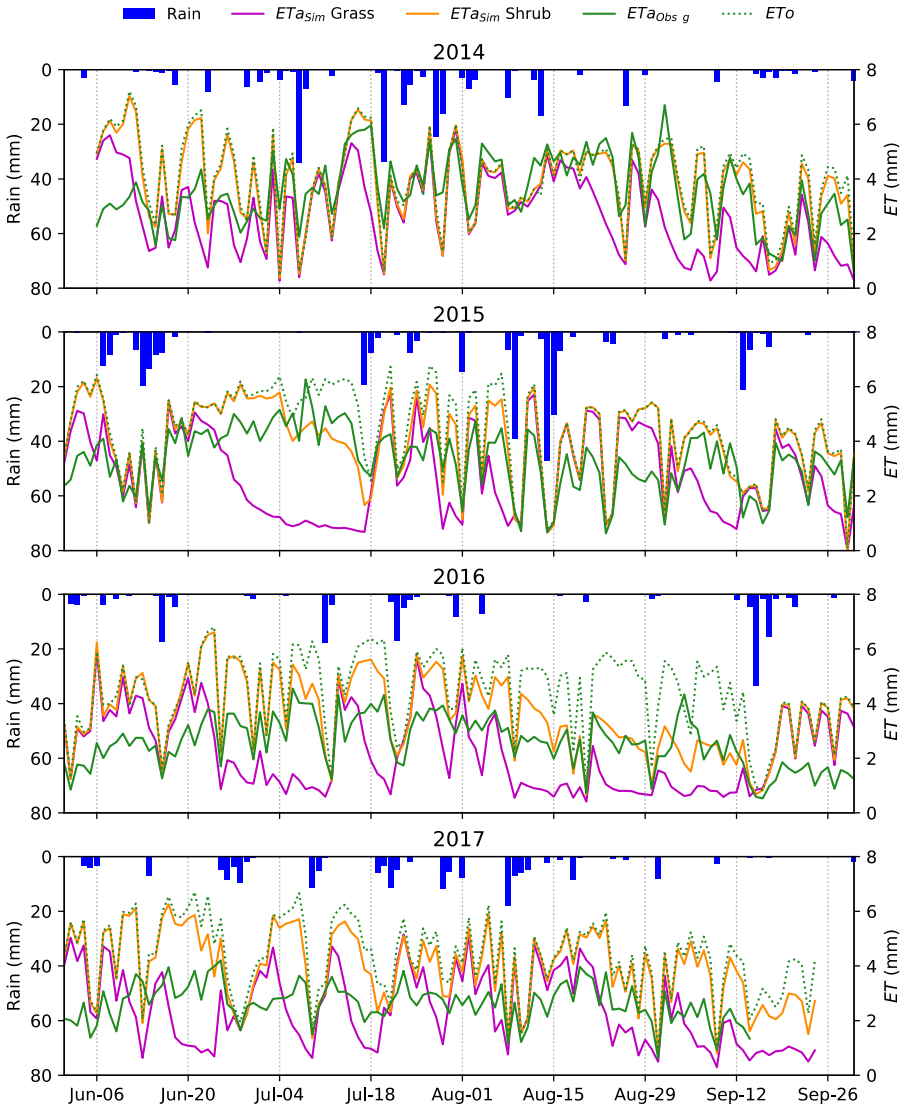

Figure 6.24. Daily modelled (for both shrubs and grassland) evapotranspiration and potential evapotranspiration (FAO 56 Penman-Monteith), measured evapotranspiration and precipitation for the four growing seasons. ETa_{Sim} is the modelled evapotranspiration, whereas ETa_{Obs} is the observed gap filled ET. In the plot, all measures are reported in millimetres to have an easier comparison.

The shrubs root system extends in the deeper soil horizon, till the bedrock. This allows a stronger water uptake than the one related to grass, so it is expected to find an enhanced evapotranspiration. It is interesting to evaluate its magnitude at the daily and growing season scales. Plus, especially in wet growing seasons, the shrubs roots can extract water from moister deep soil layers. This implies an increased *ETa* which is also closer to *ETo*. Wegehenkel and Beyrich (2014) used Hydrus-1D model to simulate evapotranspiration over grassland. They found that in periods with dry soil conditions, the model tends to underestimate evapotranspiration if compared to eddy covariance one. In this study, we found the same behaviour for both shrub and grass land covers, in particular in 2015 and 2016 growing seasons,

where prolonged dry periods are found. This might be due to the model difficulty to correctly represent the local heterogeneous water reservoir in those conditions. In the present case, the different behaviour between the model and the measured data in the grass configuration is due to the unrealistic choice of a grass-only land cover, making clear that shrubs are already playing an important role in the local water cycle, as also noted considering the weight associated with the shrubs (42% of modelled *ETa*).

The correlation between model and measures improves for shrubs and generally in dry growing seasons. The mean absolute deviation (MAD, Table 6.11) between model and gap filled measurements is almost always lower for shrubs than for grass with 2017 exception, probably because the model is more sensitive than observations to occurring rainfall in that year. In addition, MAD is higher in dry growing seasons, with the exception of MAD between grass evapotranspiration and measures in 2017. This is likely due to the model overestimation of soil water content in that year.

These findings suggest that the ability of Hydrus model to catch evapotranspiration fluctuations is greater in the shrub case in three over four growing seasons, especially in wet ones, whereas the results given in Table 4 indicate that the correlation between simulations and measures increases in dry growing seasons, especially for shrubs.

Table 6.11. Mean absolute deviation (MAD) between daily modelled shrub and grass evapotranspiration and the measured values for the four growing seasons.

year	shrub-measured (mm day^{-1})	grass-measured (mm day^{-1})
2014	0.96	1.22
2015	0.95	1.41
2016	1.12	1.43
2017	1.45	1.07

The weighted average of simulated grass and shrubs evapotranspiration gives the best results, so it was plotted as a function of time. The results are shown in Figure 6.25. The two growing seasons with a closer agreement between measures and model output are found in 2015 and 2016, despite a prolonged dry period in 2015, where the model tends to underestimate evapotranspiration, likely because an underestimated deep soil water content. In 2014, instead, the model underestimates the evapotranspiration, while in 2017 overestimates it probably because of less exact assumptions on deep soil water content due to the fact that the model ignores the precipitation occurred earlier in Spring.

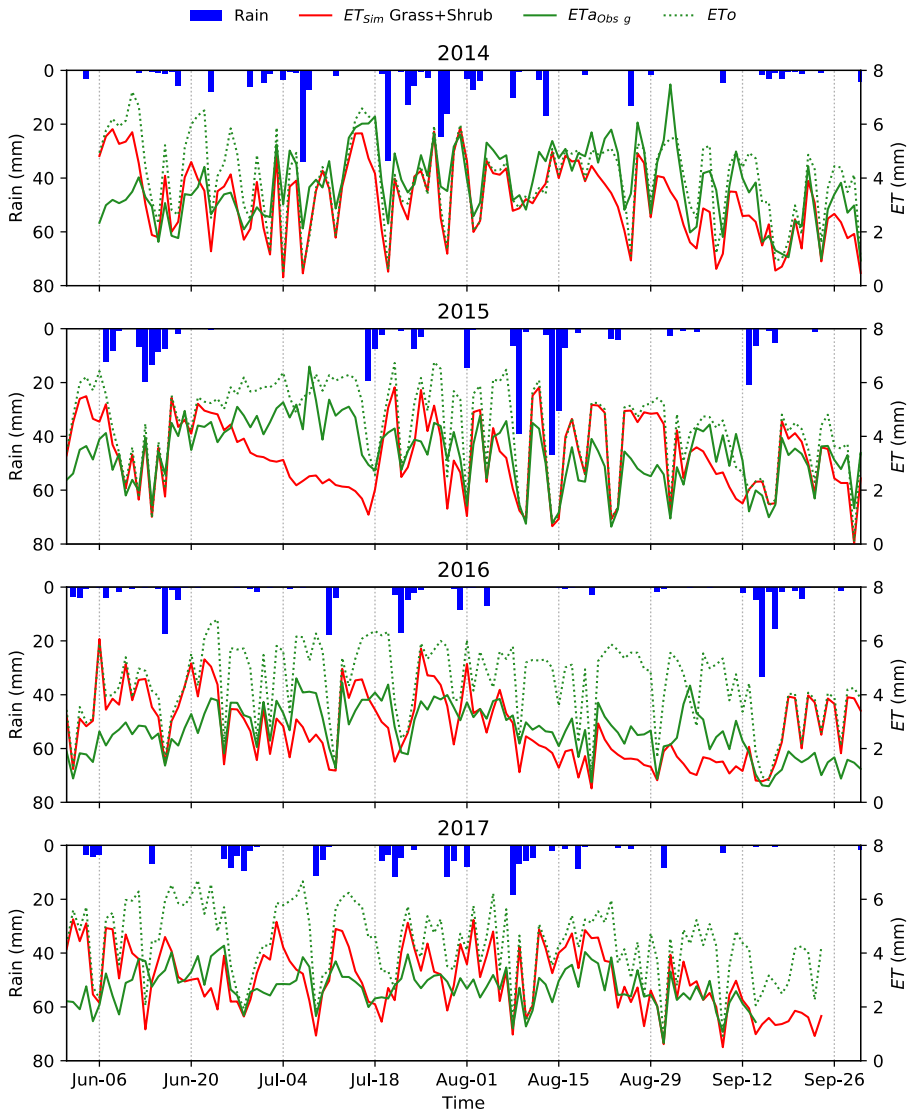

Figure 6.25. Daily modelled evapotranspiration (weighted average of simulated grass and shrub) and potential evapotranspiration (FAO 56 Penman-Monteith), measured evapotranspiration and precipitation for the four growing seasons. ETa_{Sim} is the modelled evapotranspiration, whereas ETa_{Obs} is the observed gap filled ET. All measures are reported in millimetres to have an easier comparison.

More information can be retrieved from *ETa* differences and comparison with VPD (VPD is known to affect differently the exchanged water vapour, depending on whether shrubs or grass are considered). It has been already stated that modelled shrub evapotranspiration is generally closer to measured one, but it is important to identify whether there are particular conditions when this is happening, looking at VPD and soil water content. Figure 6.26 shows that, where the difference between shrub and grass evapotranspiration rises when VPD also increases (drier conditions). In those conditions, the difference between observed and modelled values is lower if evapotranspiration from shrubs is considered. In addition, the difference between modelled values is always positive, suggesting that in any

condition the shrubs are characterised, at the daily scale, by a higher evapotranspiration (and water uptake) than grass. Plus, this difference increases when VPD also increases (Figure 6.26, panels a), b), c), d), e), f), g), h)). In addition, the *ETa* oscillations are well captured by the model for the simulations with the two land cover types, but the model appears more sensitive to precipitation than reality, as already observed for modelled soil water content (e.g. in 2017, panels d) and l)). The gap between measured and shrubs modelled evapotranspiration is on average closer to 0 (in absolute value) than the grassland case, but it can be locally positive and high if long dry periods occur (Panels a), b), c), d), i), j), k), l)), whereas the differences with modelled grassland evapotranspiration are more frequently significantly nonzero (Panels a), b), c) and d)). In wet periods, instead, the differences are low (e.g. Panels a) and i)).

Furthermore, the bias between eddy covariance evapotranspiration and modelled shrubs *ETa* tends towards negative values, indicating that shrubs would have an enhanced evapotranspiration if compared to the existing condition with a mix of species. Positive biases between the measured and weighted mean of modelled evapotranspiration values are found especially in wet years, mainly because the grass evapotranspiration is very low of compared to measures.

If one imagines drawing the difference between observed and the modelled weighted mean of *ETa*, values close to 0 would be found and some positive biases would exist in wet growing seasons because the grass evapotranspiration is very low. In dry growing seasons, (especially in 2017) the simulated grass is in stress and shrubs are instead able to use deep soil water because of the deeper root system (the upper layers, between 0 and 40 cm have a scarcer water availability), therefore the bias can be negative. This behaviour is expected, but it is interesting to note the magnitude of the difference between the two vegetation scenarios (values up to almost 5 mm day^{-1}).

The effects of shrubs are also visible on cumulative values. To assess temporally the differences in the cumulative evapotranspiration over an extended time period, the sums were computed over the 1st June– 13th September, to show the evolution of cumulative evapotranspiration estimated by the model. Figure 6.27 illustrates what would happen if the land cover were characterised either by grass or shrubs, whereas Figure 6.28 shows the cumulative evapotranspiration resulting from a weighted average between shrub and grass *ETa* compared with observations.

From the analysis of cumulative evapotranspiration (from 1st June to 13th September) is evident that also the cumulative *ETa* from a shrubland would be characterised by a far higher evapotranspiration than a grassland, especially in dry growing seasons (Figure 6.27). This confirms the observations described in van den Bergh et al. (2018). If compared to grassland, a shrubland would have emitted +111.2 mm, +142.2 mm, +172.3 mm and +165.1 mm of evapotranspiration, respectively for 2014, 2015, 2016, 2017, thus having a major impact in dry growing seasons. There is a generally acceptable agreement with observations, if a mixed land cover is considered (hence using the weighted mean of the two simulated evapotranspiration values, from shrubs and grass, Figure 6.28). Considering the

period 1st June – 13th September of each year and the weighted average of modelled evapotranspiration, Figure 6.29 shows that the two growing seasons with the highest agreement with EC evapotranspiration were 2015 and 2016 (bias between modelled and observed was respectively -6.9 mm and -2.5 mm). In 2014, the bias between modelled and observed was more negative (-51.9 mm), whereas in 2017 the bias was strongly positive (+57.3 mm). This fact is likely due to a model underestimation of deep soil water content in 2014 and a model overestimation of deep soil water content in 2017. The lowest *ETo* value is found in 2014, while in the three following growing seasons the cumulative values increase. In the other three growing seasons, the difference between measured *ETa* and *ETo* increases (especially in the two dry seasons). For the modelled values, a distinction between the weighted average and the two *ETa* from shrubs and from grass is done. Shrubs *ETa* is always closer to *ETo*, particularly in 2014. This is due to the deep root system which allows a higher evapotranspiration than from grass. Again, the behaviour is expected since it is within the model set up, but it is coherent with previous studies (e.g. van den Bergh et al., 2018) and it interesting to estimate the magnitude of the growing seasons modelled *ETa* also compared with experimental data. The model decreased performance in 2014 and 2017 might be explained by an underestimation of deep soil water reservoir in 2014 (the hydrological year was characterised by 696 mm of rain and experienced the lowest dry spell, 4.2 days , hence the highest rainfall occurrence) and an overestimation of the soil water reservoir in 2017. The rainfall amount on the hydrological year 2017 was the lowest (624 mm against 696, 757 and 640 mm, respectively in 2014, 2015 and 2016) and the average dry spell was the highest (7.9 days against 4.2, 6.8 and 6.3 days). Hence, also at the beginning of the growing season, the deep soil water was probably lower than hypothesised.

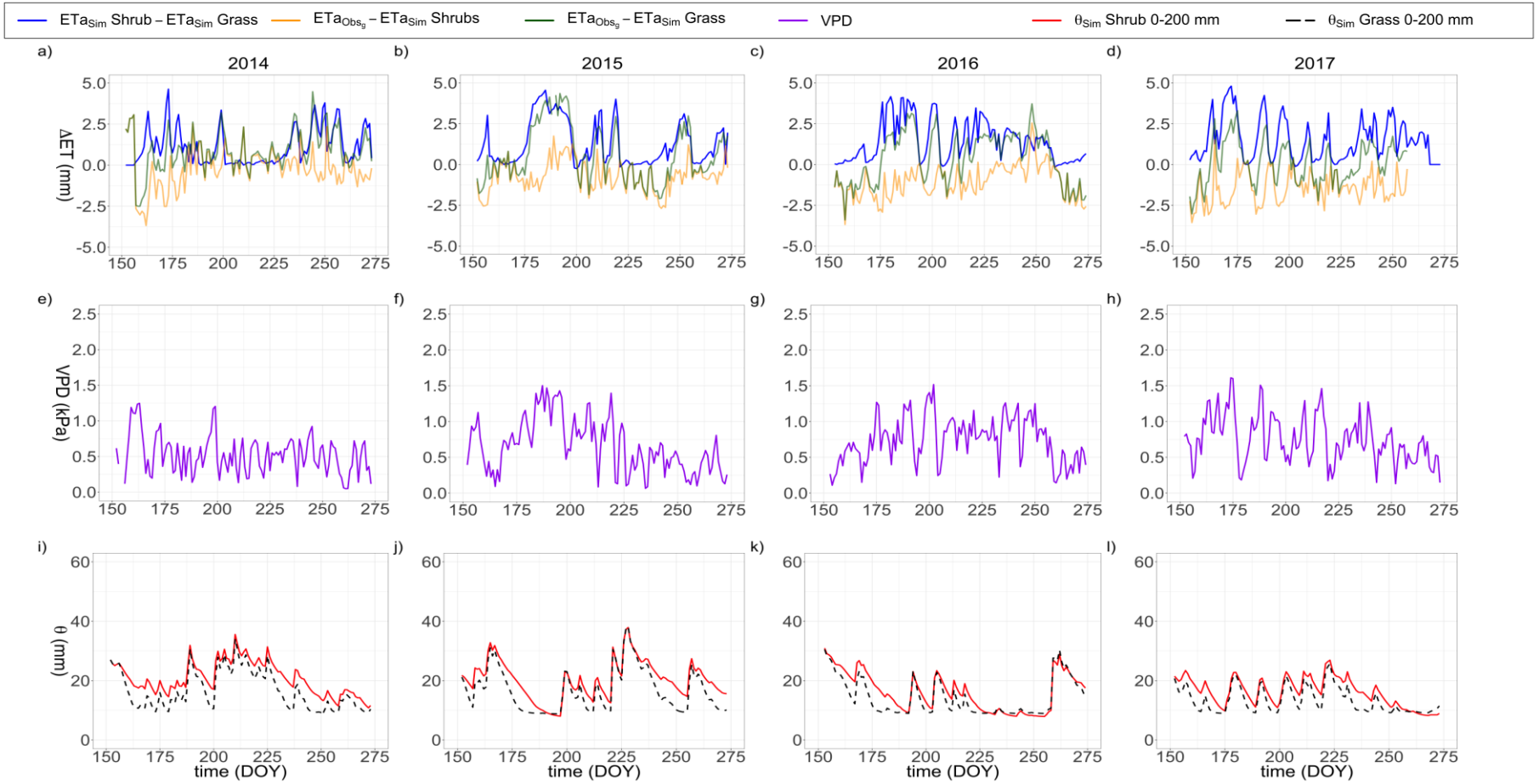

Figure 6.26. Difference between the two modelled values of evapotranspiration, the difference between observed and modelled evapotranspiration (Panels a), b), c) and d)), the VPD (Panels (e), f), g), h)) and modelled 30 cm soil moisture for shrub and grass (Panels i), j), k), l)) are plotted for the four growing seasons. To make the figure more readable, here the dates are expressed as Julian days (DOY, day of year).

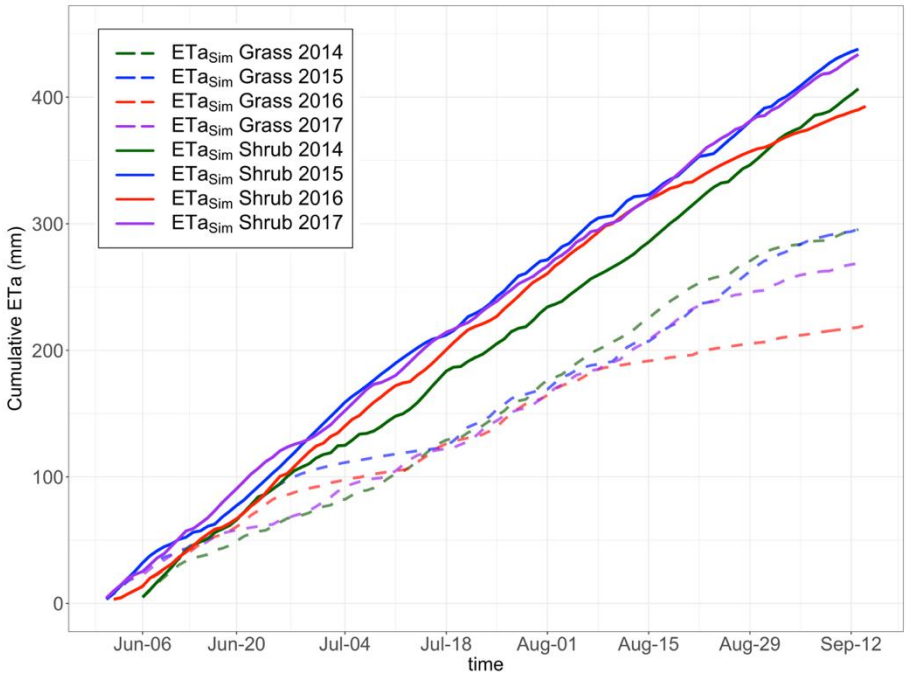

Figure 6.27. Cumulative evapotranspiration from modelled grassland and modelled shrubland evapotranspiration.

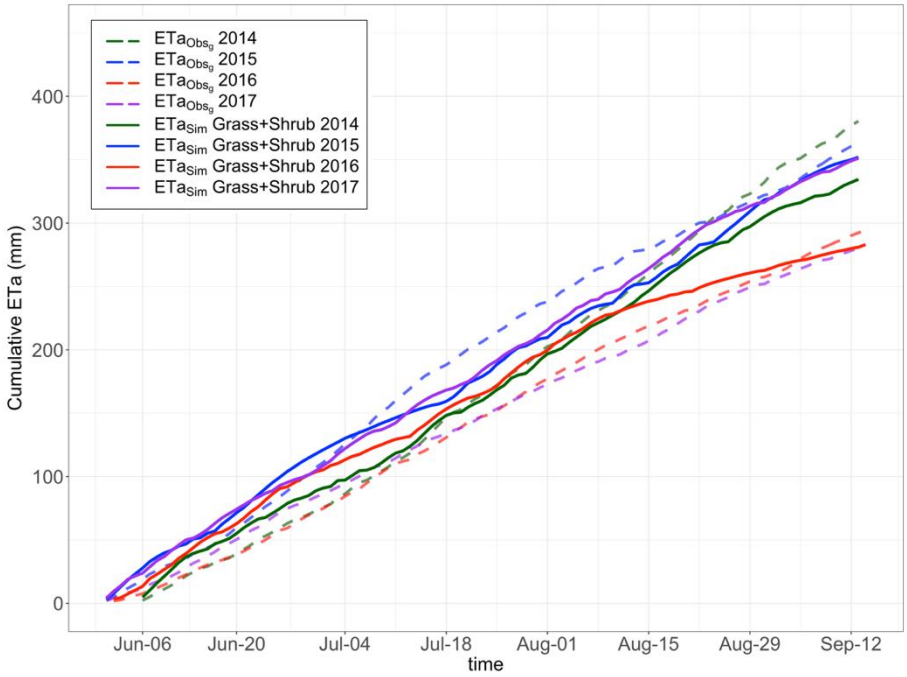

Figure 6.28. Cumulative evapotranspiration from observations (dashed lines) and from weighed average between grass and shrub simulated land covers.

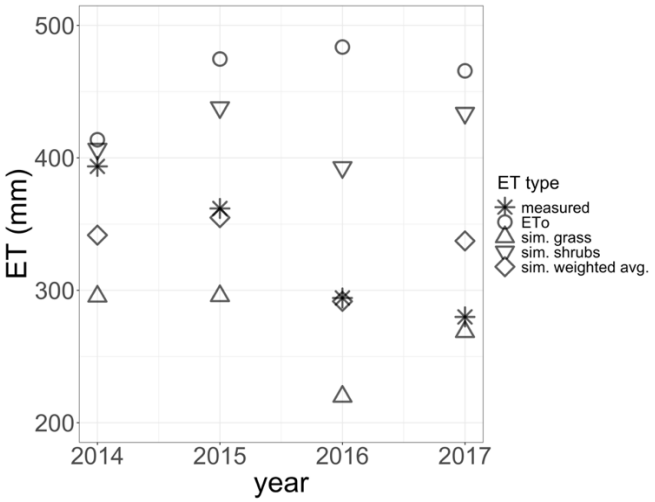

Figure 6.29. Cumulative evapotranspiration values of the four growing seasons from measures and from simulated grassland, shrubland and the weighted modelled evapotranspiration of shrub and grass.

6.4 Final Remarks

In this Chapter, a twofold analysis was performed. First, the interannual variability of evapotranspiration and, second, the ecohydrological impacts of shrubs and grass coexistence on a steep abandoned pasture were analysed. Experimental data include eddy covariance-derived sensible heat flux and evapotranspiration, soil moisture and meteorological data. For the analysis, two wet growing seasons (2014, cold and wet; 2015, warm and wet) and two dry growing seasons (2016 and 2017, warm and dry) were selected.

Results show that the site flux footprint is almost constant throughout the years. Also, the wind flow regime is stable with an average constant direction of the upslope flow during daytime. The spatial variability of latent heat flux (*LE*) indicates that the location of source areas is almost constant, but a reduction of the spots is reduced in dry growing seasons.

The eddy covariance flux data yield an energy balance closure ranging from 60% (2016, 2017) to 70% (2014, 2015). This is an overall good result, considering the high terrain complexity of the site. Besides, the *LE* flux is predominant over *H,* but the ecosystem can reach water stress conditions. This occurs also in a warm and wet growing season.

The frequency distributions of *LE* flux and soil water content showed a bimodality, more apparent for the energy flux and with different patterns in the four growing seasons. Statistically significant differences in *LE* means and soil moisture means were found between dry and wet growing seasons. The four years were also different considering the occurred precipitation and the mean temperature.

Interannual difference can exceed 100 mm, whereas mean air temperature can differ more than 1.5°C. The 2014 growing season was the coldest (-1.9°C if compared to 2015 and -1.8°C if compared to 2016 and 2017).

The *LE* (and *ETa*) mean diurnal cycle showed reduced peaks in dry growing seasons and an inflexion (reduction) of *LE* in the morning transition between downslope to upslope wind regime.

The interannual meteorological variability was also analysed with 15-days averaged data of evaporative fraction (EF), Bowen ratio (B), air temperature and vapour pressure deficit, and with 15-days cumulative precipitation, dry days and evapotranspiration (*ETa*).

LE is higher than *H* in dry growing seasons, and a marked difference between wet and dry growing seasons for evaporative fraction, Bowen ratio and VPD (higher in dry growing seasons) was found. Differences were detected in most of 15-days period for air temperature and average rain per day. A great *ETa* difference was found in three over eight periods of 15 days. In the month of September, the two 15-days periods showed enhanced differences especially for EF, Bowen ratio and, hence, for *ETa.*

The evapotranspiration was frequently water-limited in three growing seasons and the relationship of EF with shallow soil water content suggests the probable non-negligible effect of deeper roots of shrubs. Besides, EF at midday was representative for the daytime hours.

The most important drivers of *ETa* were, in order of importance, VPD and global and net radiation. Hence, VPD was the most important driver, likely due to anisohydric land cover.

The *ETa* showed a high interannual variability, well-represented by the coefficient of variation (16.4%). In 2014 the highest *ETa* value was found (394 mm), together with the highest shallow soil water content. In the following three growing seasons (2014, 2016 and 2017), the cumulative evapotranspiration was respectively 362, 294 and 280 mm.

The high *ETa* differences between dry and wet years are found even if the mean temperature values are close to the 2015 growing season, mainly because of differences in precipitation amounts between the whole hydrological years (up to 133 mm comparing 2017 with 2015).

The *ETa* in 2015 was 32 mm lower than in the previous year, despite the lower RH and higher temperature. This was likely caused by a combination of events: a prolonged dry period without precipitation from late June to the half of July and another dry period (with very limited rainfall) from late August to the half of September. The two dry growing seasons were characterised by a severe decrease of cumulative evapotranspiration (-99 mm in 2016 and -114 mm in 2017, if compared to 2014), and they also experienced lower precipitation amounts (263, 317, 179 and 183 mm in the four growing seasons). The impact of the most important micrometeorological variables on *ETa* was studied also at the daily scale, showing the major role of global radiation, net radiation and vapour pressure deficit with respect to wind speed, air temperature and precipitation.

The interannual *ETa* differences are located within the range of variability found for climate change-induced variations (up to around 100 mm) as simulated in other studies for the Alps in a +3°C temperature increase scenario. The analysis performed in this Chapter, however, highlights *ETa* variations of the same magnitude but in contiguous years and with lower temperature increases (around +1.5°C). In addition, the *ETa* is reduced in warm growing seasons instead of being higher because a lower rainfall occurs, with consequent reduction of the vegetation activity, shrubs included.

The impact of land cover changes was studied using HYDRUS 1D simulations. The model allowed to evaluate the contribution of shallow (grass) and deeper (shrubs) roots to evapotranspiration. Two model parameters were optimised minimising the mean absolute deviation between observed and modelled evapotranspiration: lower boundary condition deep soil water content (at 1.5 m, assumed constant) and shrubs root depth. The optimised parameters were 0.11 m^3 m^{-3} and 1.5 m. The modelled shrubs evapotranspiration was generally higher than the grass one: the difference was between +111 mm in 2014 and + 172 mm in 2016 and it was more correlated with measured eddy covariance evapotranspiration in all years ($R^2 > 0.4$ for shrubs and $R^2 < 0.1$ for grass). Only 2014 was an exception with a comparable R^2 for grass, probably because of higher shallow soil moisture (also due to lower air temperature).

The best fit simulated evapotranspiration was derived using a weighted mean with optimised weight equal to 42% for shrubs and 58% for grass. When dry days occur, the difference between shrub and grass evapotranspiration is enhanced, as well as the difference between weighted mean simulated and eddy covariance measured *ETa*.

If the coexistence of grass and shrubs is considered, in 2015 and 2016 growing seasons the modelled evapotranspiration is closer to observations (small biases of -7 and -2 mm, respectively). Larger bases (-52 mm and +57 mm) arise instead in growing seasons of meteorologically more extreme hydrological years 2014 and 2017. The 2014 growing season was characterised by the lowest mean temperature and the most frequent rainfall frequency (also in the whole hydrological year), thus an increases water annual reservoir existed but was underestimated by the model. The year 2017 experienced the driest conditions and the soil water content within the deep soil horizon probably was lower than the constant value assumed for the four growing seasons. Hence, the water reservoir is overestimated at the beginning of the growing season.

These errors highlight also the difficulty to set up the model parameters when significant deviations from “standard meteorological conditions” exist.

Understanding the ecosystem evapotranspiration interannual variability and the impact of land cover on *ETa* is important because shrubs will very likely colonise almost entirely the area and other abandoned grasslands will be encroached by shrubs, also because of more frequent dry and hot growing seasons.

Chapter 7

Regional Modelling of evapotranspiration

This Chapter deals with the modelling of evapotranspiration using an approach without calibration of parameters and at the regional scale for Alpine natural grasslands (CaLIbrationless soil water Model for actual Evapotranspiration of Mountain Grasslands - CLIME-MG). The model is described and validated temporally using data from two eddy covariance stations. A spatial analysis is performed comparing the model outcomes with a well-known model (METRIC). Contrarily to HYDRUS model used in Chapter 6, CLIME-MG is more suitable for a study at the regional scale. The CLIME-MG model was developed and partially validated by LABFLUX Team between 2014 and 2016, and the Author completed the validation on the Cogne site, run the model again and performed the validation on the second experimental site (Nivolet). Plus, the spatial comparison between CLIME-MG and METRIC (implemented earlier in 2015), already partially performed by LABFLUX Team, was completed.

7.1 Introduction

The Alps are experiencing an enhanced warming rate, that is about two times larger than the northern hemispheric mean (Auer et al., 2007), with the process starting from the beginning of 20th Century. This acceleration towards higher temperatures has been cited in Chapters 1 and 6, and it is known as "elevation-dependent warming" – EDW – and it is studied since the end of 1990s, and further acceleration of warming is expected along the 21st Century.

Besides, grasslands, as already mentioned in Chapters 1 and 6, are a very important ecosystem whose extent is non negligible, and evapotranspiration estimate is difficult. Because of its importance in a wide range of disciplines and contexts, a number of different solutions have been developed to either measure or estimate evapotranspiration (e.g. Wang and Dickinson, 2012), adopting both analytical and empirical approaches together with direct or indirect methods.

On the one hand there is the category of the experimental surveys at the field scale which rely on various approaches, namely: hydrological approaches (e.g. weighing lysimeters, a point scale method– Evett et al., 2012, Previati et al., 2020; soil water balance – Chen et al., 2008, Raffelli et al., 2017); micrometeorological approaches (e.g. eddy covariance – Wever et al., 2002, Gu et al., 2008, Ochoa-Sanchez et al., 2019); aerodynamic methods (Ortega-Farias et al., 1996); energy

balance and Bowen ratio – Malek and Bingham, 1993); plant physiology law-based approaches (e.g. sap flow method – Granier, 1987; chambers systems – Reicosky et al., 1983); and optical-based approaches (e.g. scintillometry - Hemakumara et al., 2003).

On the other hand, there are non-field campaign related methods. The first category includes methods that use meteorological variables; the second category include proper hydrological models with atmospheric and soil modules; the third category includes remote sensing-based estimations. The first category uses meteorological variables to estimate potential evapotranspiration including temperature-based models (e.g. Thornthwaite, 1948; Hargreaves and Samani, 1982); solar-radiation based models (e.g. Priestley and Taylor, 1972), and "mixed" models which are based on energy/mass balance principles (e.g. Penman, 1948; FAO Penman-Monteith, Allen et al., 1998).

The second category includes either parametric models or physically-based, mathematical models. The parametric (empirical) models attempt to describe all the components of the hydrological cycle. They are made of interconnected reservoirs representing ideally the elements in a catchment. The reservoirs are recharged by precipitation, infiltration and percolation and can be voided by runoff, evapotranspiration, drainage and other processes. Among the empirical models, there are MODE-ACM model (Guo et al., 2014) and IHACRES (e.g. Jakeman et al., 1990) or the model suggested by Romano et al. (2011). Physically-based models try to mathematically represent the hydrological processes using physical principia. They are the most advanced available models, and include GEOtop (Rigon et al., 2006); HYDRUS (e.g. Simunek et al., 2008); SWAT (e.g. Easton et al., 2010), and TOPMODEL (e.g. Nourani et al., 2011). More generally, models can be divided into two main categories: bucket models (e.g. Romano et al., 2011); distributed models (HBV model, Bergström, 1976; PDM model, Moore, 1985); lumped models (e.g. SWAT model).

The third category can be divided in three main clusters. Methods demanding remote sensed atmospheric and radiation variables (e.g. Venturini et al., 2008). Methods based on remote sensed vegetation indexes such as NDVI (where surface losses depend mainly from the transpiration intensity – e-g- Cleugh et al., 2007). Methods based on remote sensed surface temperatures, such as thermal infrared domain (i.e. contextual pixel models, based on the simultaneous presence of hot and dry and cold and wet pixels within the satellite image domain – e-g- S-SEBI, - Roerink et al., 2000; TTME – Moran et al., 1994; SEBAL – Bastiaansen et al., 1998, and METRIC – Allen et al., 2007). There are also single pixel models, solving the surface energy budget for each pixel, independently from the others – e.g. TSEB (Norman et al., 1995; Chirouze et al., 2013) and SEBS (e.g. Su, 2002).

Notwithstanding the great number of existing approaches, the uncertainties and the local applicability is subject to continuous studies and updates with hundreds of contributions. For a more comprehensive overview, several reviews are available (e.g. Wang and Dickinson, 2012).

Alpine regions are characterised by complex environmental and terrain conditions which limit accessibility and make the realization of surveys and studies particularly challenging. Hence, those regions suffer of a limited quantity and quality of information as well as modelling tools for both characterising actual conditions, making forecasts and elaborate scenarios (especially at local scale). However, climate change studies in mountain areas require a higher resolution for ET models, with high spatial and temporal resolution (Gürtz et al., 2005), to account for the local terrain and ecosystem complexity but without the possibility to rely on the data that are usually requested. Lumped hydrological models do not require large amount of input data, but they are based on input/output relationships that are only valid for the specific region or basin considered for the study.

Distributed "physically-based" models account explicitly for soil variation within watersheds, but they often require parameter values which are not commonly available, and cannot be realistically obtained (Baveye and Labac, 2015). Pedotransfer functions can be used to derive some parameter values from more easily measured variables (van Looy et al., 2017). However, at high altitudes it is difficult to even evaluate simple soil characteristics. Also, pedotransfer functions may provide reasonable approximations as long as the model is used within the particular set of soils for which specific functions have been developed (e.g., Wösten et al., 1990). However, this is frequently not the case for abandoned soils in heterogeneous terrains.

Satellite observations together with the above mentioned remote sensed based approaches are usually designed for routine applications over large areas, hence they are characterised by coarse resolutions in space and/or in time (depending on the orbital characteristics of the sensor platform and sensor characteristics (e.g. Landsat images have a temporal resolution of 16 days and a spatial resolution of 30 m – USGS, 2019). Furthermore, all of these methods are subject to calibration procedures which are not often easy-to-apply and user-friendly.

In this context, some insight can be found in the following works. Rogowski (1972), in his article on soil spatial variability, identified criteria according to which the soils in a watershed could be considered uniform, i.e., to determine when their heterogeneity could be ignored. Also, Bouma (1989) stated that pedological differences in soils do not necessarily imply different hydrological properties.

More recently, McDonnell et al. (2007) have pointed out the need to figure out a way to include heterogeneity or the consequence of heterogeneity into models but without requiring potentially unavailable data. One way to do this, according to these authors and also according to Jury (1982), is not to concentrate one's efforts on a detailed characterisation of the heterogeneity of the system, but to focus instead on the "properties that emerge with increasing scales, and on their resulting hydrological effects" (Baveye and Labac, 2015). Some studies (e.g. Basu et al, 2010) found out a quite spatially homogeneous capacity of soil to retain water at the watershed scale.

Among the several variables that need to be modelled, one finds the soil depth, whose estimation is not trivial. Direct measures are rare, especially in mountainous

areas. Besides, the soil depth is strongly spatially variable. The spatial variability limits the applicability of surveys for hydrological purposes (Tesfa et al., 2009). Statistical models have been proposed to estimate indirectly the soil depth, but they require calibration and a high number of observations (Tesfa et al., 2009).

The need to have a realistic but simple hydrological model that can be used in a regional modelling is here translated into a simple soil water model (CLIME-MG) which does not require calibration of parameters. Starting from the hypothesis that much of the spatial and temporal variability of *ETa* in high altitude areas can be mainly related to aspect/slope of the land in conjunction with land cover and meteorological forcing (which are typically temporally and spatially highly variable in the mountains), the objective of this work was to present and validate a new soil water model (i.e. CLIME-MG).

CLIME-MG allows mapping the actual evapotranspiration (*ETa*) and, hence, the water balance. CLIME-MG can be thought as an empirical distributed model and it is made of a meteorological module that aims at reconstructing the meteorological field variables over a specified domain, including the dew estimation on the canopy, and of a soil bucket 2D module with a part that aims at the reconstruction of the soil depth with a physically-based approach. The goal is to model evapotranspiration without calibrating parameters, using only the information from a DTM, meteorological inputs, simple formulas and depth. The outcome is to understand whether the results are reasonable.

7.2 Methodology: the CLIME-MG model structure

The presented model is composed by two modules: the meteorological module and the soil-water-balance module. The meteorological module elaborates meteorological data to compute the potential evapotranspiration *(ETo)* with the here recalled Penman-Monteith formula and following the Allen et al. (1998) approach as in Chapter 6, starting from Eq. 7.1:

$$ETo = \frac{1}{\lambda}\frac{\Delta(R_n - G_0) + \rho_a c_p \frac{e_s - e_a}{r_a}}{\Delta + \gamma(1 + \frac{r_s}{r_a})} \tag{7.1}$$

where Δ is the slope of the Clausius-Clapeyron relation, R_n is the net radiation, G_0 is the soil heat flux at the surface, $VPD = e_s - e_a$ is the vapour pressure deficit, ρ_a is the air density, c_p is the specific heat at constant pressure, r_a and r_s are respectively the aerodynamic and the surface resistances estimated using FAO56 relationships, γ is the psychrometric constant and λ is the latent heat of vaporisation.

The soil-water balance module (SWB-module), as will be better illustrated in Section 7.2.2 computes the soil-water balance to estimate the vegetation stress coefficient, K_s, and thus the fraction of water vapour transferred to the atmosphere (and, therefore, the ratio ETa/ETo).

7.2.1 Meteorological module

Hourly time-step standard weather data (such as temperature, humidity, wind and precipitation) were mapped using known formulas obtained from literature, as detailed in the following. Atmospheric pressure and global solar radiation were also used but they are less spatially variable.

When empirical formulas were adopted for estimating variables, parameters belonging to published look-up-tables were used (i.e. most of them are reported in the FAO 56 volume). The required initial conditions about meteorological conditions are taken from meteorological stations on 1 June (2016 and 2018). The meteorological field is reconstructed on the whole domain using the approaches illustrated in the following paragraphs.

Radiation

To compute the net radiation on the domain, all the four solar radiation components were reconstructed taking into consideration the shading effect. To this end, and to compute the hours of shading, a model using the DTM topographic information was implemented using TopoToolbox software (Schwanghart and Scherler, 2014, see Appendix D) in Matlab environment and containing a set of Matlab functions for topographic analysis. The hourly SW_{in} was mapped over the whole domain starting from data collected by a representative local station corrected for shading and sloping effects in order to obtain a SW_{in} on a horizontal surface.

Before local sunrise and after local sunset, SW_{in} radiation was reconstructed by multiplying the clearness index CI (i.e. the ratio between the $SW_{in}$and the Top of Atmosphere incoming short wave radiation SW_{TOA}), computed at the local sunrise and local sunset respectively, by the SW_{TOA}, of the shaded hours.

Beam (SW_b) and diffuse (SW_d) radiation, were separately estimated according to:

$$SW_{in} = SW_b + SW_d \tag{7.2}$$

The beam radiation incident on a sloping surface, SW_b, is a function of the zenith angle and illumination angle (Iqbal, 1983; Twidell and Weir 1986; Aguilar et al., 2010).

SW_b was calculated as suggested by Chung and Yun (2004)

$$SW_b = SW_{in}\tau^{1/\sin(d)} \quad (7.3)$$

where d is the atmospheric thickness as a function of the sun elevation on the horizon. A Rayleigh sky condition and an isotropic sky radiation was also assumed (so SW_d was only affected by the sky view factor: $SVF = \cos^2\left(\frac{\beta}{2}\right)$ with β being the pixel slope, following Chung and Yun, 2004). A value of $\tau = 0.8$ was used following Chung and Yun (2004), assuming Rayleigh sky condition. The actual diffuse radiation collected by a surface with slope SW_d was hence calculated using Eq. 7.4:

$$SW_{d,\beta} = SW_d\, SVF \quad (7.4)$$

Outgoing radiation was computed as $SW_o = SW_{in}$. For grasslands, typical values of albedo vary between 0.15 and 0.23 (Brutsaert, 2005). In the model the albedo was set to $\alpha = 0.17$. LW_{in} and LW_o were computed with the Stefan-Boltzmann law.

For LW_{in}, $T = T_a$ and the emissivity was parameterised as in Eq. 7.5 (Brutsaert, 2005)

$$\epsilon = a\left(\frac{e_a}{T_a}\right)^b = 0.99 \quad (7.5)$$

For LW_o, the surface temperature was estimated with a linear relationship with T_a, as reported by Gallo et al. (2011) and Jin and Mullens (2014):

$$LW_0 = \epsilon\sigma(c_0 + c_1 T_a)^4 \quad (7.6)$$

The soil surface temperature is given by $T_s = c_o + c_1 T_a$, where T_a is the air temperature. A discrimination between night (*SWin* < 50 W m^{-2}) and day (*SWin* > 50 W m^{-2}) was used. Averaged values for daytime during clear and cloudy conditions were taken from Gallo et al. (2011): $c_0 = -2.075\,°C$ and $c_1 = 1.075$. At night, the situation was supposed to be different. Following the findings of Jin and Mullens (2014), we assumed this difference as a constant during the night-time hours. Therefore, $T_s = T_a - 1.5$. This approximation relies on the absence of strong fluctuations of the two temperatures during night-time.

For incoming long-wave radiation, the coefficients introduced by Brutsaert (2005) were used, namely $a = 1.24$, and $b = \frac{1}{7}$.

Temperature

In complex terrains, temperature is primarily affected by solar irradiance. Therefore, elevation and topography play an important role in the spatial distribution of the air temperature. Solar irradiance, in turn, is governed by shading due to the surrounding mountains (Chung and Yun, 2004). Hence, two different approaches were followed for mapping daytime and nighttime temperatures. For daytime temperatures (T_{day}), identified when the lapse rate of potential temperature was lower than the lapse rate of "standard temperature", a multi-linear regression was adopted:

$$T_{day}(z, SW_{anom}) = a_0 + a_1 z + a_2 SW_{anom} \quad (7.7)$$

where SW_{anom} is the anomaly of incoming shortwave radiation to the mean spatial SW_{in} and $a_2 \geq 0$.

For nighttime, after sunset, temperature inversion occurs in a stable atmosphere. Hence, it was simpler to reconstruct the potential temperature (θ), with vertical profile in free atmosphere approximated by the formula (from Stull, 1988):

$$\theta(z) = a_0 - a_1 e^{-z/a_2} \quad (7.8)$$

To this purpose, Whiteman et al. (2004) and Massaro et al. (2015) observed that the pseudo-vertical profile of the near-surface air temperature along valley slopes is representative of the vertical profile of temperature in free atmosphere. Therefore, it was possible to solve a statistical regression with Equation 8, computing the best fit parameters using the DTM height as an input.

Humidity

For the Clausius-Clapeyron law, the water vapour content in the air increases exponentially with the temperature; since T_a decreases approximately linearly with the altitude, H_a decreases with height with an exponential behaviour. Linear regression with observed variables was used to map H_a over the domain:

$$\log H_a = c_0 + c_1 z \quad (7.9)$$

Once the absolute humidity was reconstructed on the domain, it was possible to compute the saturation and actual water pressures (Foken and Nappo, 2008).

Dew deposition and ground heat flux

In mountainous areas, nocturnal dew deposition can give a remarkable contribution to the water budget (Jacobs et al., 2006). Evaporation or dew formation can be estimated, in nighttime hours, with a re-written Penman-Monteith equation (Eq. 7.10, as in Garratt et al., 1992; Jacobs et al., 2006)

$$\lambda LE = \frac{\Delta}{\Delta + \gamma}(R_n - G) + \frac{\gamma}{\Delta + \gamma}\frac{\rho_a \lambda (e_s - e_a)}{r_a} \tag{7.10}$$

The proposed model includes also a routine for the hourly ($\Delta t = 1h$) dew estimation, according to the following relations:

$$\begin{array}{ll} D = \lambda LE\ \Delta t & \text{if } E \leq 0 \\ D = 0 & \text{if } E > 0 \end{array} \tag{7.11}$$

The ground heat flux can be estimated as a fraction of net radiation R_n (Moran et al., 1994). Assuming a homogeneous 30-cm height vegetation cover on the entire domain, G can be estimated with a good approximation (as verified by the measured data at Cogne site) as

$$G = 0.05\ R_n \tag{7.12}$$

Wind, precipitation and pressure fields

Wind and rainfall fields are characterised by spatial and temporal significant intermittence, especially in mountain areas (Rebora et al., 2006). In the model, a constant value of wind speed for the entire domain was used, averaging the measured data at the stations because the temporal variability is significant, and the spatial variability estimation is very difficult in the mountain contexts.

For precipitation, at each point was assigned the rainfall amount measured at the nearest station, identified by a Voronoi partitioning of the domain.

The CLIME-MG model is hydrostatic, and the air density was assumed constant throughout the domain, also because the pressure values do not play a major role in *ETa* estimate.

7.2.2 Soil water balance (SWB) module

As climatology is heavily affected by topography in mountain areas (Fridley, 2009), a high-resolution DTM is the main input for the model. In addition, an original, multiple-layer soil model is here presented, merging available literature formulations for soil depth reconstruction, water percolation, runoff and evapotranspiration for the water-balance evaluation.

Soil depth

Soil depth is estimated with a process-based approach built on the local high-resolution topography (provided by the DTM) and some empirical parameters (Dietrich et al., 1995). This mode assumes a net sediment transport vector, q_{soil}, downslope of soil converted from bedrock by biogenic and climate processes at a rate proportional to the gradient (i.e. $q_{soil} = -K\nabla z$). The mass conservation equation can be written as the balance between the local rate of bedrock-soil production, $f(z_s)$, and the divergence of the transport vector:

$$K\nabla^2 z = \frac{\delta z_s}{\delta t} - \frac{\rho_{rock}}{\rho_{soil}} f(z_s) \tag{7.13}$$

In the model, $f(z_s)$ is assumed to decrease exponentially. This hypothesis was suggested by Dietrich et al. (1995) and Heimsath et al. (1999).

$$f(z_s) = P_0 e^{-m/z_s} \tag{7.14}$$

Values of the empirical parameters for the implementation of the soil-depth model in Eq. (13) were chosen from literature and theoretical considerations. For our purposes, as described in Dietrich et al. (1995), the mean value of $K = 50\ cm^2/yr$ was adopted, and ρ_r/ρ_s was set to 1.7. Pixels with exposed bedrock ($z_s = 0$, following the land-cover map) were considered in order to estimate P_0. A lower limit for P_0 was also estimated. m was determined by fitting $f(z_s)$ between $f(0) = P_0$ and $f(100) = 0.01P_0$. The model start was set to 15000 years before 2014 with 100 years of time step. Since the model is not sensitive to the initial soil depth, a 0.30 m initial depth was assumed.

According to the aforementioned explanations, values of $P_0 = 0.009\ cm\ yr^{-1}$, and $m = 0.045\ cm^{-1}$ were computed. Measured soil depths at Cogne (by means of an electrical resistivity tomography - Raffelli et al., 2017) and in Valnontey (by simple steel rods vertical insertion) were compared with modelled values. At Cogne, there was an underestimation of actual soil depth (down to -1,5 m compared

with 0.84 m estimated by the soil depth model. At Valnontey, the values were more comparable (0.67 m from the soil depth model compared with 0.60 m measured).

Soil water balance

A soil model was designed for describing soil moisture evolution during time, starting from the water balance equation in Eq. 6.1. Following Ritchie (1998), the soil vertical profile z_s of each pixel was partitioned in several communicating layers with incremental thickness, starting from 50 mm the shallower, followed by, respectively, two 100 mm, one 300 mm, and three deeper layers 500 mm thick (Figure 7.1).

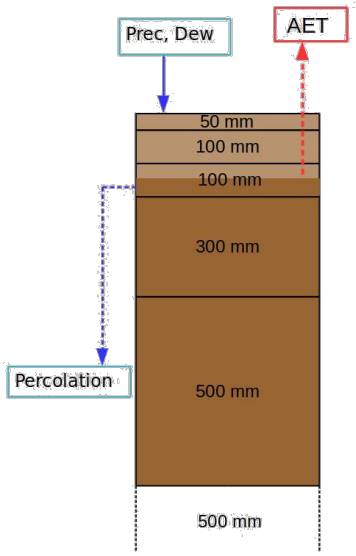

Figure 7.1. Soil model scheme. Each layer is represented as a bucket of different increasing capacity, depending on depth and actual porosity. Water comes from the surfaces and moves downward when layers are full. *ETa* also dries starting from the surface and it reaches deeper layers when the shallower are empty.

According with observations, all the inputs entered into the system from the soil surface with a higher variability in the superficial layers, and a smoother behaviour in depth. The considered external positive inputs were precipitation and dew. The *ETa* was the negative term of the balance and affected the first non-empty layer from the surface. Each layer was approximated as a bucket for which the Total Available Water (TAW) was considered the maximum amount of storable water, computed as in Eq. 7.15:

$$TAW = \rho_s \, z_l \tag{7.15}$$

where ρ_s (the porosity) was set to 0.2 (Terzaghi et al., 1996), whereas z_l is the layer depth. The porosity value was chosen because the mountainous soils of the analysed

area are coarse, sandy loam with some gravel. Hence, the model porosity is maintained low.

Deep percolation ($perc$) occurred when the maximum storable capacity was achieved and, therefore, the exceeding water moved outside the lowest layer. Water percolation from the deepest layer was assumed lost by the system.

The water-balance was computed in each layer (l) as a sum of positive and negative fluxes (Allen et al., 1998) considering the water availability, $0 \leq W_l \leq TAW$ and the root depletion D_r as in Eq. 7.16:

$$W_l(t) = W_l(t-1) + D_r(t) + P(t) + D(t) - ETa(t) \quad l = 1$$

$$W_l(t) = W_l(t-1) - D_r(t) + perc(t) - ETa(t) \quad l = 2 \ldots . n \tag{7.16}$$

Runoff and capillary rise were not included in the work, as well as the lateral flow, which is supposed a negligible term, also to maintain the model as simple as possible.

As shown by Tromp-Van Meerveld and McDonnell (2006), at the end of the snow-melt season (i.e., April or May in the Alps), the soil water content is not affected by topography and it is approximately constant along the vertical soil profile with initial values corresponding to $W_l(t = 0) = 0.7\ TAW$ for each layer, whereas term $D_r(t = 0) = 0.3\ TAW$ again for each layer. Precipitation and percolation were considered 0 at *t=0*. Hence, the model initial condition includes a soil at field capacity, with almost null root depletion.

The model computes *ETa* by using (Eq.7.17, Allen et al., 1998):

$$ETa_{CLIME} = K_s\ K_c\ ETo \tag{7.17}$$

Look-up tables with estimated vegetation coefficient already exist especially for crops (Allen et al., 1998), and pastures. Alpine grasslands were reasonably considered as extensive pastures with $K_c = 0.7$.

K_s was estimated for each soil layer according to Allen et al., (1998). The depletion fraction (root zone depletion) for extensive pastures was also adopted. The model computes the stress coefficient for each pixel with a weighted average of the $K_s$coefficient associated with each layer (Eq. 7.18):

$$K_s = \sum_{i}^{n} \frac{K_{s_i}}{w_i} n \quad \text{where} \quad \mathrm{w_i} = \frac{\mathrm{z_{l_i}}}{\sum \mathrm{z_l}} \tag{7.18}$$

In the model, the area defined as grasslands was derived using the land cover map and was assumed to have homogeneous and full-covered grass (therefore evaporation from bare soil was not included in the *ETa* computation).

7.3 Study Site and Datasets

The studied area (Figure 7.2) is located in North-Western Italy in the Aosta Valley Region (45. 462 N - 45.670 N; 7.145 E - 7.518 E) and it covers about 600 km^2 Grasslands are here located in a range between 1500 m and 4061 m (height of the Gran Paradiso peak), and the spatial domain presents a very complex morphology.

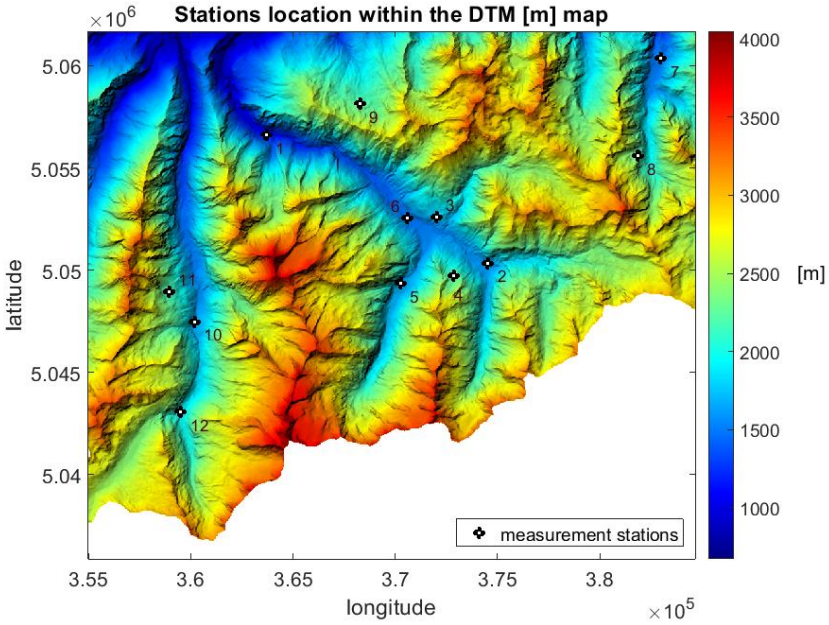

Figure 7.2. Automatic Weather Stations (AWS) location within the DTM domain.

Concerning the databases, a 10 m resolution DTM is aggregated at 30 m to superimpose the Landsat satellite images, needed for the spatial validation. The land cover map, provided by ARPA VdA, with a spatial resolution of 30 m, is used to select grasslands in the domain.

Meteorological data are retrieved from the 11 Automatic Weather Stations (AWSs) managed by the Centro Funzionale Regione Valle d'Aosta and the Aosta Valley Regional Environmental Protection Agency (ARPA VdA) in the considered domain. The available meteorological variables of each station are shown in Table 7.1. Data are provided with 30 minutes time-step, then aggregated at 1 hour in this work. The period studied lasts from June 1st to August 31st for the 2014 and 2015 years.

Table 7.1. AWS non eddy covariance variables.

	n	Elevation [m]	T_a [°C]	RH [%]	U [$m\ s^{-1}$]	P [mm]	SW_{in} [W m^{-2}]
Aymavilles	1	1139	no	no	no	yes	no
Lillaz	2	1613	yes	no	no	yes	no
Cogne	3	1785	yes	yes	yes	yes	yes
Gran Crot	4	2279	yes	no	yes	yes	no
Valnontey	5	1682	yes	no	no	yes	no
Cretaz	6	1470	yes	no	no	no	no
Clavalité	7	1531	yes	yes	yes	yes	no
Lavodilec	8	2250	yes	no	no	yes	no
Gressan	9	2280	yes	yes	yes	yes	no
Eaux Rousses	10	1651	yes	no	no	yes	no
Orvieille	11	2170	yes	no	no	yes	no
Pont	12	1951	yes	no	yes	yes	yes

7.3.1 Model validation

Temporal Validation

The eddy covariance data from the research measurement station of Cogne and Nivolet stations were used. Torgnon site data were not used since the site is not included in the area investigated by means of CLIME-MG. In particular, growing season 2014 and 2015 eddy covariance evapotranspiration from Cogne and 2018 growing season measured evapotranspiration from Nivolet site are considered.

Collected data allow the actual evapotranspiration estimation by means of the eddy covariance technique. Radiative components (namely, net radiation, incoming shortwave radiation, SW_{in}, ground and storage heat fluxes, longwave radiation) are measured with the NR01 Hukseflux four components radiometer. Measures of soil water content at different soil depths and of latent heat flux (therefore, evapotranspiration) were compared to the modelled values. The turbulent fluxes (sensible heat and latent heat flux) were processed using the EddyPro 6.2.1 software

(developed by LI-COR, see Fratini and Mauder, 2014). The data processing description is given in Chapter 4.

For the *ETa* comparison between measured and modelled data, the root mean square error (RMSE), the normalised root mean square error ($NRMSE = \frac{RMSE}{\overline{obs}}$), the RMSE-observations standard deviation ratio ($RSR = \frac{RMSE}{\sigma_{obs}}$) and the correlation coefficient (R) were used. The same statistical metrics were used for the comparison between measured and modelled soil water content between 0 and 55 cm of depth.

Comparison between CLIME-MG and METRIC model

METRIC (Mapping EvapoTranspiration at high Resolution with Internalized Calibration) is a model proposed by Allen et al. (2007). It maps *ETa* by means of satellite-based data and images processing, and it uses the same principles of the SEBAL model (Bastiaansen et al., 2005). METRIC is based on the radiative energy balance closure assumption. Furthermore, the storage term is assumed negligible.

The computation is performed at an hourly temporal scale, in the sense that through the model it is possible to obtain an instantaneous (time at which the satellite passes on the domain) *ETa* value. The daily cumulative *ETa* is computed following Allen et al. (2007). Further information about METRIC is given in Appendix D.

For the spatial validation, another normalisation of RMSE was used. More in detail the normalised root mean square error of evapotranspiration was computed with the following formula:

$NRMSE = \frac{RMSE}{\overline{ET_{CLIME}}}$, where $\overline{ET_{CLIME}}$ is the spatial average over all pixels of CLIME evapotranspiration. Also, the correlation coefficient was used.

Table 7.2 shows the average environmental conditions occurred at the four dates. In particular, one day (13 July 2015) was characterised by very dry soil conditions, high temperatures and low relative humidity.

Table 7.2. Environmental and meteorological main data recorded by the Cogne monitoring station during the four selected days.

Date	**Air Temperature** *[°C]*			**Rn Avg** (24 h) *[W m^{-2}]*	**Rn Avg** (daytime) *[W m^{-2}]*	**RH Avg** [%]	**Vol. soil moisture** [-]
	Min	*Max*	*Avg*				
27/08/2014	6.5	20.1	12.4	179.8	389.1	53.7	0.11
27/06/2015	10.2	22.5	16.4	195.7	401.3	45.2	0.11
13/07/2015	11.4	25.5	18.1	187.1	344.3	39.5	0.04

30/08/2015	9.9	22.9	15.7	188.2	409.0	64.6	0.12

7.4 Results

The proposed model performances are evaluated as follows: first, the soil water balance (SWB) module is temporally validated using observed meteorological data: *ETa* and soil water content outputs are compared against the measured data collected at the eddy-covariance site located in the research site in Aosta Valley. Finally, the model outputs are compared against METRIC outputs which were obtained from satellite images analysis.

7.4.1 Temporal validation

Among the several variables that are modelled in the meteorological module, a particular attention should be used with the net radiation. Prior to focus on evapotranspiration, the comparison between modelled and measured net radiation in 2015 is shown (Figure 7.3). The correlation coefficient is high (R=0.96), and the RMSE is 79.8 W m^{-2}. The two variables are then well correlated.

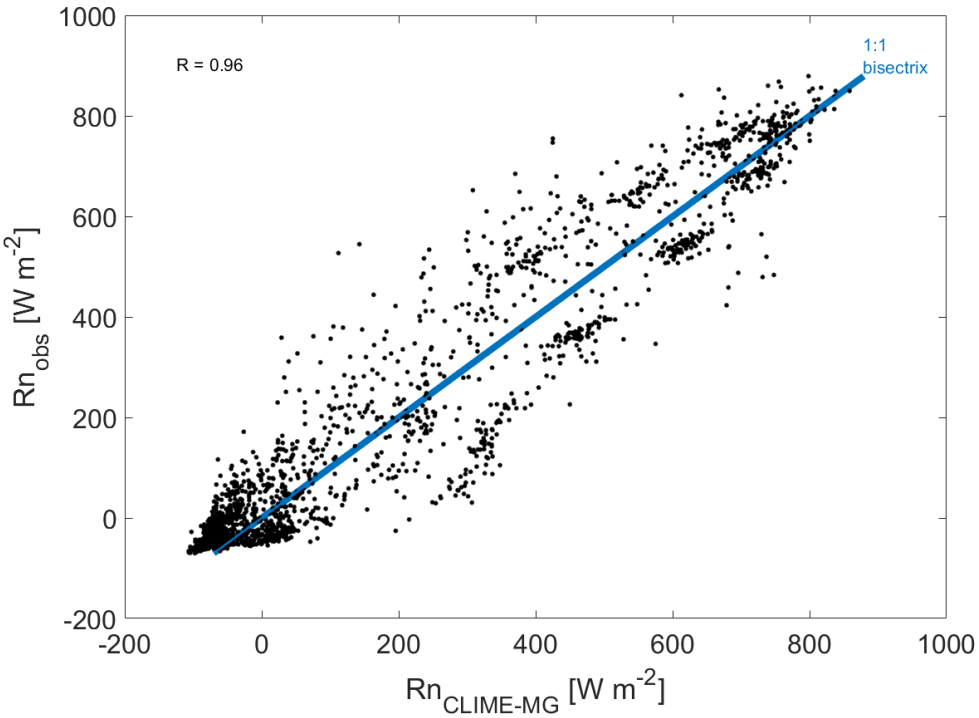

Figure 7.3. Net radiation observed versus modelled values (2015). Hourly values.

In Table 7.3, statistical parameters of the model performances compared with the observed data are shown, both for hourly and daily values at Cogne and Nivolet sites. Generally, modelled hourly data are characterised by a lower *RMSE* and *RSR* with respect to daily data and the correlation coefficient, is lower for the hourly case. The normalised root mean square error (RMSE normalised with the mean) - *NRMSE* – indicates a decrease for daily values but this occurs because the daily values are higher than hourly ones. Hourly RMSE values at Cogne and at Nivolet are respectively higher and within the range of the findings illustrated by Bottazzi et al. (2021) for the modelled *ETa* with GEOframe Prospero, Penman Monteith and Priestley-Taylor models at the Torgnon site.

In Figures 7.4 and 7.5, the daily-cumulative time series of measured and modelled evapotranspiration are displayed for, respectively, Cogne and Nivolet sites; rainfall events are highlighted in grey. A greater agreement between model and observations is found at Nivolet. The influence of the initial values of the soil moisture is lost after an intense rainfall event or a long-lasting drought. During the analysed period one of these conditions occurred within few days. Without considering the initial initialization period (about 15 days), the outputs show in both sites, good agreement with eddy covariance data, especially in wetter periods with recurring rain events. Besides, during prolonged dry periods, as also observed by Wegehenkel and Beyrich (2014), which used HYDRUS 1D for their simulations, measured and modelled *ETa* data have a significant bias, with an evident underestimation of the modelled values. This behaviour can be partially due to the dynamics of comparison between data simulated at a point scale and values measured with large footprint areas. It is interesting to note that a similar behaviour was found by Wegehenkel and Beyrich (2014) for a grass-covered boundary layer field in North-Eastern Germany. CLIME-MG has a lower performance in dry conditions, contrarily to GEOframe-Prospero model (Bottazzi et al., 2021).

Table 7.3. Normalised root mean square error (NRMSE), Root mean squared error (RMSE), RMSE-observations standard deviation ratio (RSR, a second normalized RMSE) and correlation coefficient between measured *ETa* and modelled data.

Site		CLIME VS EDDY			
		RMSE	NRMSE	RSR	R
Cogne	2014 hourly	0.108 mm h^{-1}	0.667	0.293	0.91
	2015 hourly	0.082 mm h^{-1}	0.546	0.230	0.92
	2014 daily	1.46 mm d^{-1}	0.379	1.25	0.81
	2015 daily	1.01 mm d^{-1}	0.281	0.86	0.78
Nivolet	2018 hourly	0.049 mm h^{-1}	0.425	0.034	0.94
	2018 daily	0.43 mm d^{-1}	0.146	0.725	0.86

The performances of the SWB-module appear satisfactory considering that it runs without calibration parameters. The RSR values, more indicated for comparison purposes, are higher for hourly values than daily ones at Cogne, whereas an opposite situation is met at the Nivolet site. The daily error values are higher than in other studies (e.g. Ochoa-Sanchez et al., 2019, where three hydrological models evapotranspiration outputs were compared with eddy covariance measures), but it should be pointed out that they used a different RMSE normalisation, with RMSE being normalised according to the difference between maximum and minimum *ETa* values. The correlation coefficient (for daily values) is instead comparable with the mentioned study.

This is noted considering that the correlation between modelled and observed actual evapotranspiration at the two experimental sites is relatively high: *R=0.91* and *R=0.81* in 2014; *R=0.92* and *R=0.78* in 2015 at Cogne, whereas at Nivolet site *R=0.94* and *R=0.86* in 2018. The model error consequently tends to increase from hourly to daily values. This is very likely caused by hourly underestimations that, cumulated over an entire day, might yield to enhanced underestimation of actual evapotranspiration values.

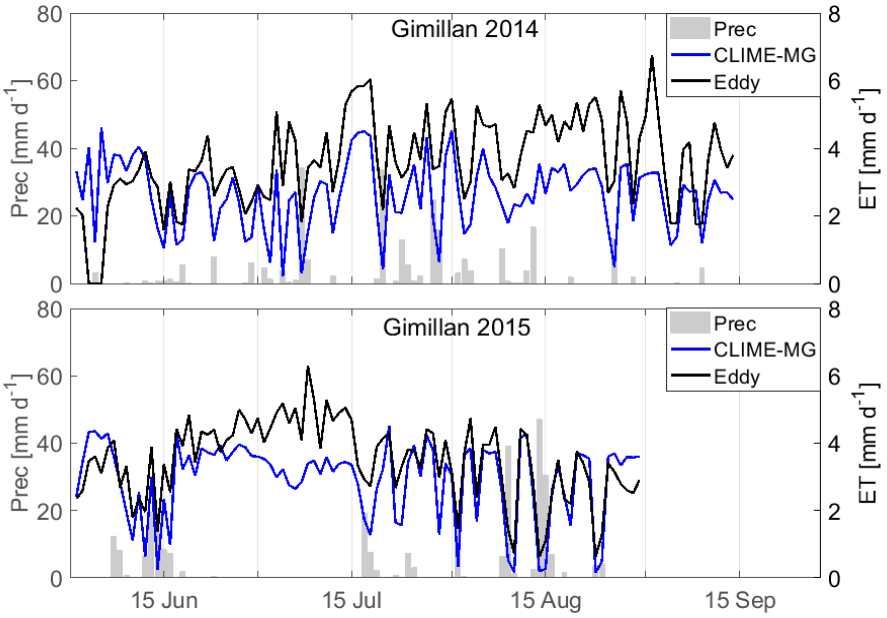

Figure 7.4. Growing seasons in 2014 – 2015: time series comparison between daily *ETa* data (observed – blue line, measured by the eddy covariance system – dashed, and modelled by CLIME – black line). Cumulative rainfall data are shown in grey.

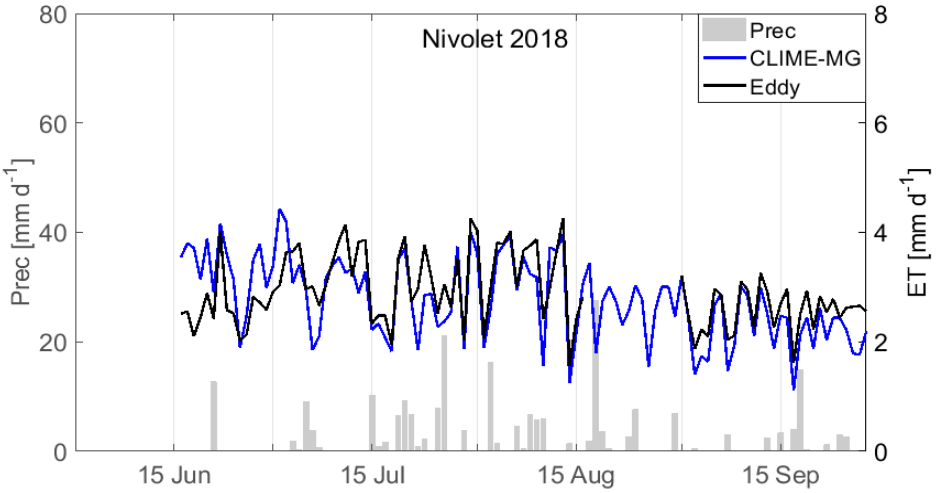

Figure 7.5. Nivolet site 2018 growing season: time series comparison between daily *ETa* data (observed – blue line, measured by the eddy covariance system – dashed,and modelled by CLIME – black line). Cumulative rainfall data are shown in grey.

In Figure 7.6 and Figure 7.7, the proposed model and the measured time series of soil moisture are compared, for Cogne 2014 and 2015 growing seasons and for the 2019 Nivolet growing season. Soil moisture data for 2014 are available only for the last month of the season. For the Nivolet modelled soil moisture validation, the 2019 soil moisture data were chosen, since in 2018 there were few measurements available. The beginning of the growing season for both 2018 and 2019 was set to 15th of June, because before that date, the soil is still partially covered by snow.

At the Cogne site, the mean measured value of soil water content between 20 and 40 cm is shown and the water content in the layer between 0 and 55 cm is therefore also reconstructed. This measured water content is compared with the mean modelled value between the surface and 55 cm of depth. It is evident a similar behaviour. However, modelled data show a bias likely because the real soil conditions are not well represented, in particular the soil porosity spatial and temporal variability. Additional problems might include problems in estimating the initial conditions of the soil (the model was run on the hypothesis that the initial condition is a soil at field capacity and almost null root depletion and RAW close to TAW, but this assumption might not be always true)

This bias is less evident at Nivolet site, likely because of a lower spatial variability of porosity and, in addition, initial conditions are more easily obtained, because at the beginning of June the terrain is still covered by at least 0.5 to 1 m of snow. This might explain why both the *RMSE* and the *NRMSE* are one order of magnitude lower at Nivolet site with respect to Cogne (Table 7.4). The RMSE values at Cogne are higher than in other studies (Silva Ursulino et al., 2019, where the measured soil water content was compared with Hydrus 1D model outcomes), but they are lower if compared to other hydrological modelling works, such as Wegehenkel and Beyrich (2014), where they find RMSE values between 0.02 and 0.09 $m^3 m^{-3}$.

The RMSE at Nivolet is instead very well comparable with the results of Silva Ursulino et al. (2019) for their basin (RMSE=0.012 and 0.020 m^3 m^{-3}) and slightly lower than the results found by Wegehenkel and Beyerich (2014).

The R values of soil moisture validation are higher at Cogne than at Nivolet. Besides, if converted to R^2, they are also comparable with Motovilov et al. (1999), which validated ECOMAG model (Motovilov et al., 1999) within the NOPEX area (e.g. Halldin et al., 1995). At Cogne and Nivolet site, the R^2 values of soil moisture validation ranged between 0.67 and 0.97, whereas Motovilov et al. (1999) found values between 0.52 and 0.87. It should be noted that, overall, CLIME-MG can yield results comparable (or even better) with respect to other studies that used models requiring parameters optimisation.

The aforementioned results illustrate that, despite the relatively simple structure of CLIME-MG, the soil moisture behaviour is appropriately captured even if there is a systematic overestimation of the soil water content.

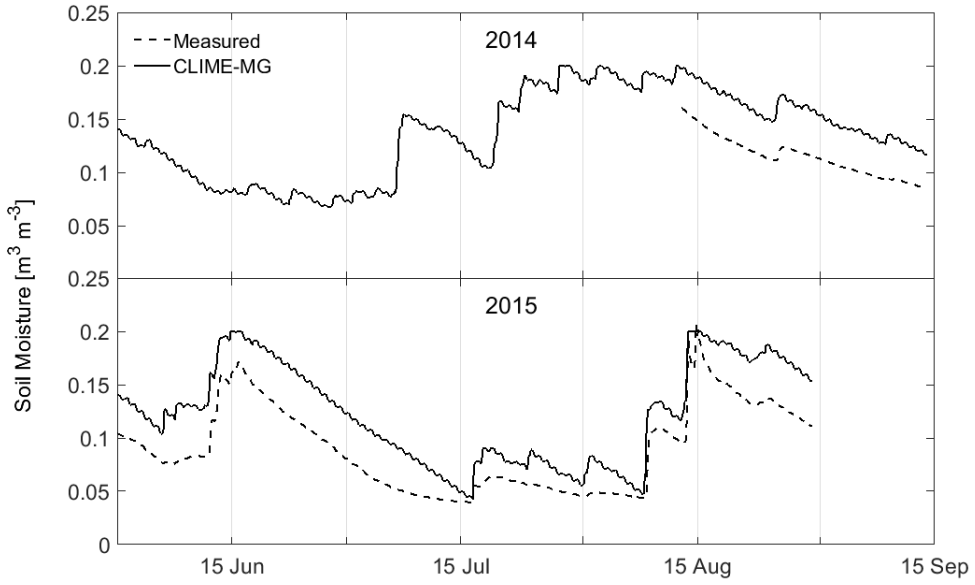

Figure 7.6. Modelled and measured (weighted average of the two soil moisture probes) soil water content for eddy covariance Cogne site, in 2014 and 2015.

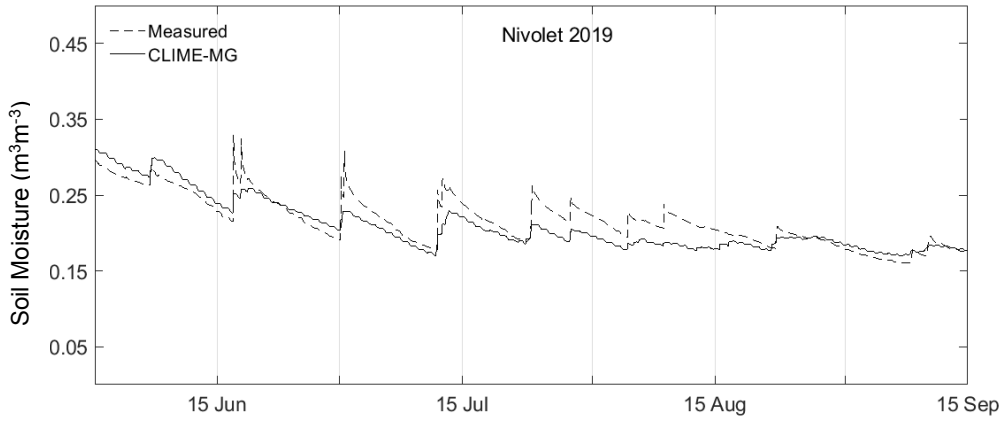

Figure 7.7. Modelled and measured (weighted average of the three soil moisture probes) soil water content for eddy covariance Nivolet site.

Table 7.4. Statistical analysis of modelled versus measured soil water content between 0 and 55 cm of depth for Cogne and Nivolet sites. Root mean squared error (RMSE), Normalised root mean square error (NRMSE), RMSE-observations standard deviation ratio (RSR, a second normalized RMSE) and correlation coefficient between measured *ETa* and modelled data.

Site		RMSE ($m^3\ m^{-3}$)	NRMSE	RSR	R
Cogne	2014	0.024	0.205	0.294	0.986
	2015	0.034	0.371	0.230	0.973
Nivolet	2018	0.019	0.088	0.047	0.820

7.4.2 Spatial validation

In this section, CLIME-MG and METRIC outputs are compared to evaluate the performance of our model over the whole geographical domain. Figures 7.7 and 7.8 show, for both models, the hourly and daily differences between the two models for four dates, pixel by pixel. Although in 27th June 2015 the meteorological conditions were not optimal, in what follows this date is also used.

Generally, lower biases between hourly METRIC and CLIME-MG data exist at the hourly scale, with respect to daily values, where more extreme (either positive or negative) differences exist. Indeed, for hourly values, the biases between the two models are around 0 (between -0.5 and +0.5 mm h^{-1}), whereas for daily values, biases can reach $\pm$ 1 mm d^{-1} with some lower or higher value. This has an impact on cumulative *ETa* over an entire growing season, for example. For two over four dates (namely, 27th August 2014 and 27th June 2015) CLIME, if compared to METRIC, tended to overestimate evapotranspiration in almost all the grassland areas, whereas in the other two dates, strong overestimates were more alternated

with enhanced underestimates. This might be due to the fact that METRIC is more limited in temporal variability because it is bounded to satellite data.

If differences between *ETa* in each pixel compared to the spatial average are computed for both CLIME and METRIC (e.g. 30th August 2015), usually the biases between pixel values and the values averaged on the whole domain are negative or near zero, with few exceptions for hourly values. For daily cumulative values, instead, there are more extreme differences, especially for METRIC, which seems to be more sensitive to spatial changes, whereas CLIME is characterised by smoother differences. These characteristics were also found in the other three available dates. CLIME-MG and METRIC show a general agreement in localising maximum and minimum *ETa* areas. The frequency distributions show a general agreement between CLIME-MG and METRIC *ETa* values (Figure 7.10), and the integrals differ but not extremely. METRIC tends to show lower peaks and larger frequency distribution than CLIME-MG . METRIC shows a greater spatial variability, that implies values covering a wider range for both hourly and daily values. Generally, however, the frequency distribution peak values of the two models are close in each figure

The $K_c\,ETo$ distributions are reported in order to show the maximum theoretical limit of *ETa* for grasslands. Those distributions identify two main dry episodes: 27th June and especially, 13th July, when the actual evapotranspiration was very low if compared to potential evapotranspiration, thus indicating very dry soil conditions (this extreme condition likely caused the difference in models outcomes for that date). Statistical measures are also reported in Tables from 7.5 to 7.8. On 27 June 2015, daily values of CLIME-MG of *ETa c*can be higher than $K_c\ ETo$. This is caused by the fact that $K_c\ ETo$ is given by another model, it is not the "real world" and that, if it always worked well, there would not be a need to develop other models.

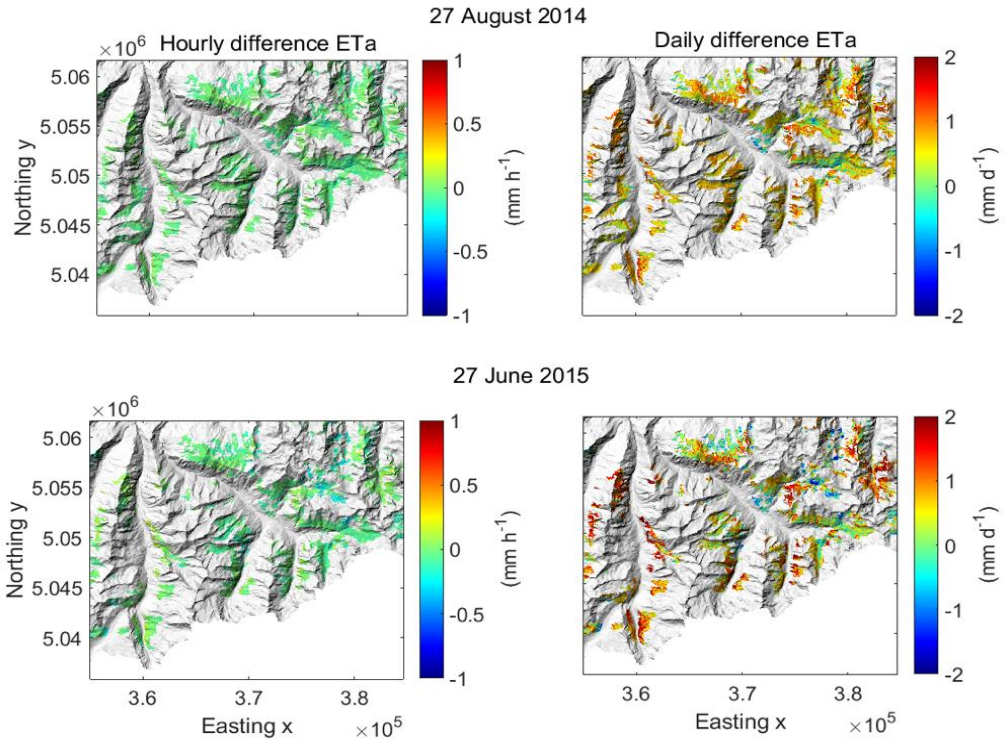

Figure 7.8. Difference ($ETa_{CLIME\text{-}MG} - ETa_{METRIC}$) between CLIME-MG and METRIC modelled evapotranspiration for both hourly and daily values for 27^{h} August 2014 and 27th June 2015. Grey areas are pixels without grassland.

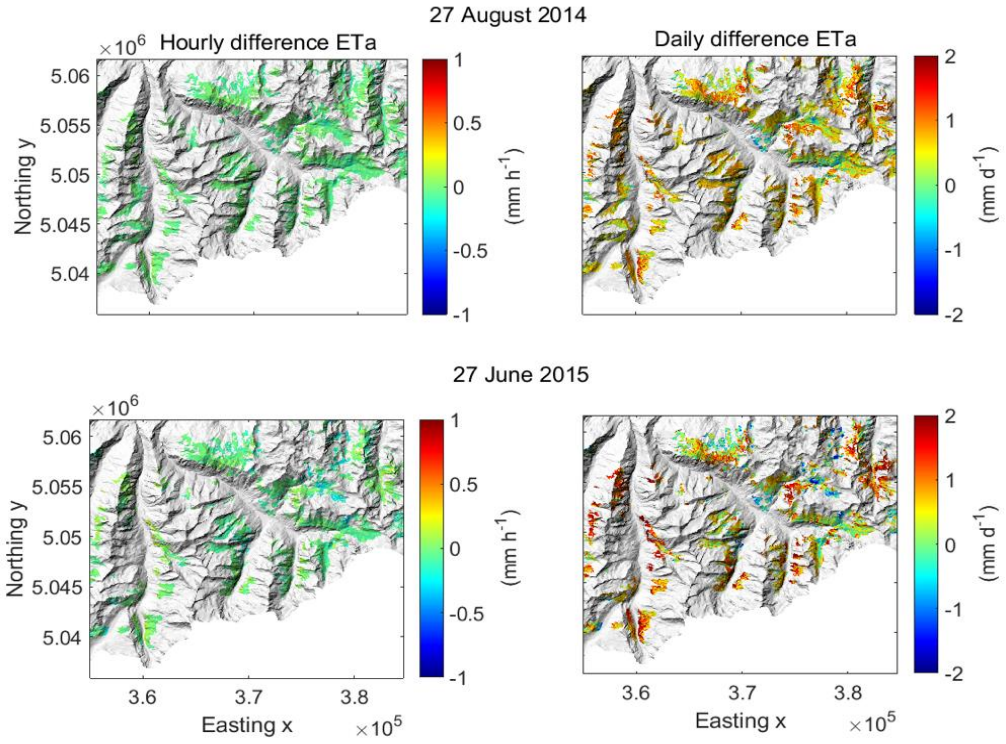

Figure 7.9. Difference ($ETa_{CLIME\text{-}MG} - ETa_{METRIC}$) between CLIME-MG and METRIC modelled evapotranspiration for both hourly and daily values for 13th July 2015 and 30th August 2015. Grey areas are pixels without grassland.

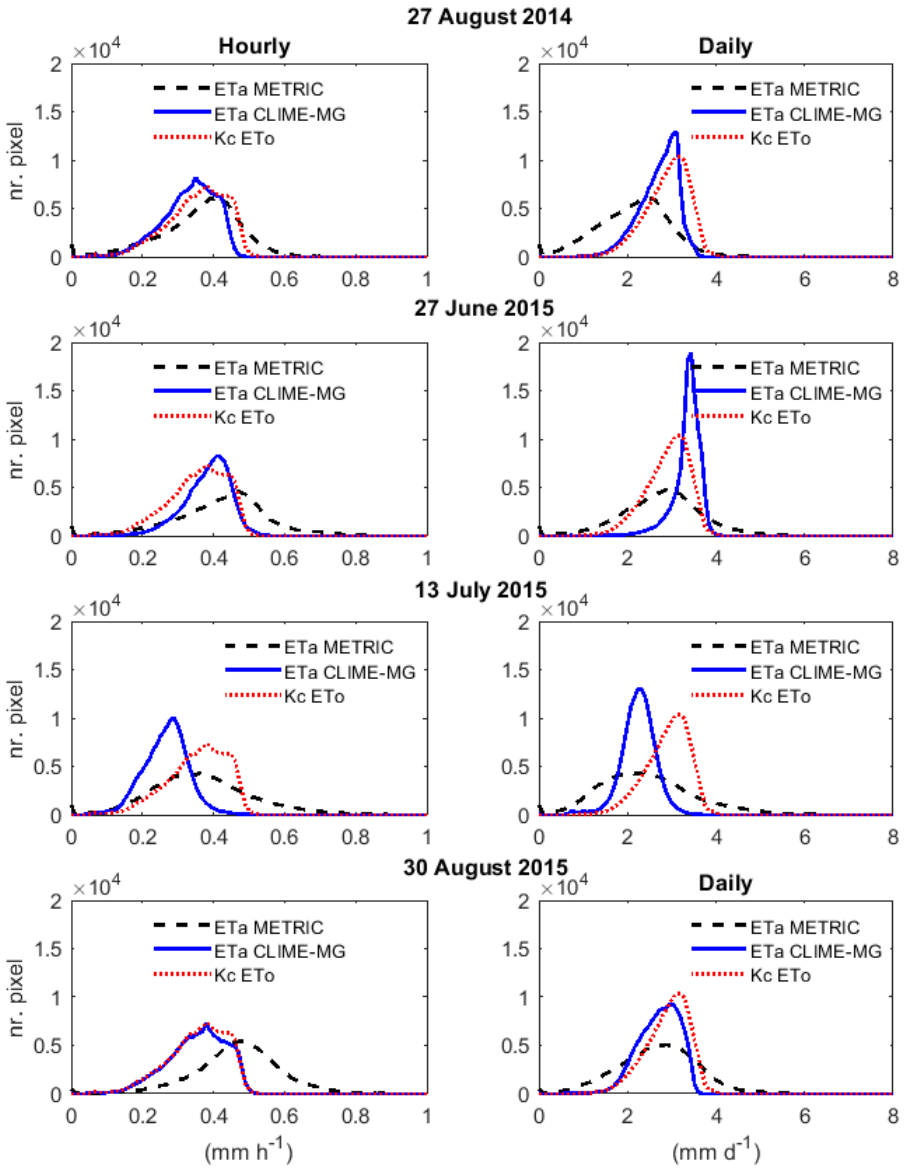

Figure 7.10. Spatial frequency distributions of evapotranspiration for four different cases, namely 27th August 2014, 27th June 2015, 13th July 2015 and 30th August 2015. Red dotted line: $K_c\,ETo$; blue soild line: CLIME-MG actual evapotranspiration ($ETa_{\,CLIME\text{-}MG}$); black dashed line: METRIC actual evapotranspiration ($ETa_{\,METRIC}$).

Table 7.5. Statistical measures for 27 August 2014. Hourly mean *ETa* values are expressed in mm h^{-1}, daily values in mm d^{-1}.

		mean	variance	skewness	kurtosis	mode	zeros
HOURLY	*ETa* CLIME	0.332	0.005	-0.66	0.26	0.35	45
	ETa METRIC	0.362	0.013	-0.65	0.61	0.41	1248
	$K_c\ ETo$	0.354	0.007	-0.65	0.10	0.38	0
DAILY	*ETa* CLIME	2.71	0.19	-0.83	0.84	3.12	44
	ETa METRIC	2.13	0.64	-0.17	0.22	2.40	1248
	$K_c\ ETo$	2.90	0.24	-0.66	0.32	3.20	0

Table 7.6. Statistical measures for 27 June 2015. Hourly *ETa* mean values are expressed in mm h^{-1}, daily values in mm d^{-1}.

		mean	variance	skewness	kurtosis	mode	zeros
HOURLY	*ETa* CLIME	0.381	0.005	-0.92	1.60	0.41	41
	ETa METRIC	0.420	0.018	-0.38	0.69	0.47	946
	$K_c\ ETo$	0.463	0.007	-0.78	0.71	0.51	0
DAILY	*ETa* CLIME	3.34	0.11	-2.31	11.11	3.44	38
	ETa METRIC	2.76	0.82	-0.20	0.51	2.88	946
	$K_c\ ETo$	4.10	0.20	-0.54	1.15	4.24	0

Table 7.7. Statistical measures for 13 July 2015, hourly *ETa* mean values are expressed in mm h^{-1} daily values in mm d^{-1}.

		mean	variance	skewness	kurtosis	mode	zeros
HOURLY	*ETa* CLIME	0.266	0.004	-0.14	0.61	0.29	47
	ETa METRIC	0.367	0.020	0.38	0.49	0.36	959
	$K_c\ ETo$	0.489	0.009	-0.93	0.80	0.55	0
DAILY	*ETa* CLIME	2.25	0.15	-0.51	1.97	2.24	44
	ETa METRIC	2.44	1.11	0.48	0.30	2.00	959
	$K_c\ ETo$	4.16	0.21	-0.81	1.32	4.40	0

Table 7.8. Statistical measures for 30 August 2015, hourly *ETa* mean values are expressed in mm h^{-1}, daily values in mm d^{-1}.

		mean	variance	skewness	kurtosis	mode	zeros
HOURLY	*ETa* CLIME	0.353	0.007	-0.60	0.13	0.38	44
	ETa METRIC	0.466	0.015	-0.39	1.17	0.47	526
	$K_c\ ETo$	0.409	0.010	-0.61	-0.05	0.44	0
DAILY	*ETa* CLIME	2.71	0.21	-0.60	0.42	2.96	43
	ETa METRIC	2.68	0.81	-0.06	0.23	2.88	526
	$K_c\ ETo$	3.16	0.31	-0.67	0.23	3.44	0

The hourly mean *ETa* values show greater values for METRIC than CLIME-MG, while the daily mean values show the opposite, with the exception of 13th July 2015. Considering the standard deviation, there is the confirmation of the different variability between the two models. METRIC shows hourly standard deviations which range from two to five times greater than CLIME-MG ones. The METRIC daily standard deviations show values about four times greater than CLIME-MG, with the exception of 27th June 2015 and 13th July 2015, presenting a 1:7 ratio. The analysis of skewness and kurtosis shows an agreement between the two models distributions, confirming the likeness in modelling *ETa*: Furthermore, skewness is negative for all the outputs produced but the METRIC 13 July 2015 distributions, hence the left tail of the distributions is longer. This means that a greater part of the pixels, i.e. the grasslands, is concentrated on the right of the figure, and so in correspondence of high values of *ETa*. The kurtosis is almost always positive, meaning that the distributions are generally more peaked than the normal distribution. In two cases, namely the 27 June and 13 July 2015, the kurtosis of hourly CLIME-MG evapotranspiration frequency distribution is higher than the METRIC one. There is not a clear pattern between daily and hourly *ETa* values, but generally the daily *ETa* frequency distribution peaks are higher than the corresponding hourly ones. (So, a greater number of pixels is involved). The daily *ETa* variance is usually higher than the hourly variance values.

To assess the general agreement between CLIME-MG and METRIC, the spatial correlation is calculated over the whole domain and it is shown in Table 7.9. Acceptable outcomes are found: the lower correlation coefficients are around 0.5, whilst the highest one reaches the value of 0.90. It is also clear that the hourly actual evapotranspiration simulations present a better correlation than the daily comparison. Looking at the *NRMSE* and correlation coefficient values together, CLIME-MG and METRIC show closer results on 27 August 2014, while it seems

that there is less agreement the 13 July 2015, when the drought period affected the domain. Ten smaller areas (also referred as tiles) are then considered, in order to check if the proximity to the AWS (where inputs are measured) could affect the outputs, and so if CLIME-MG is self-consistent even in areas where AWS are farther.

Table 7.9. Correlation coefficient R and normalised root mean square error (NRMSE) between CLIME-MG and METRIC in the four days.

	R		NRMSE	
	Hourly	Daily	Hourly	Daily
2014 Aug 27	0.90	0.89	0.08	0.11
2015 Jun 27	0.82	0.66	0.09	0.10
2015 Jul 13	0.49	0.48	0.24	0.17
2015 Aug 30	0.75	0.85	0.16	0.08

The domain is extended for 26 km in latitude and 30 km in longitude, while the small areas are 1800 m side squares. The tiles areas within which an AWS is located, as shown in Figure 7.10, are the ones identified by *a, b, c*. In addition to these, the *d* and *e* tiles are located in proximity of at least one AWS.

Considering only the four dates with optimal meteorological conditions and without significant clouds over the domain (27th August 2014; 27th June 2015; 13th July 2015 and 30th August 2015), figure 7.11 shows the spatial correlation coefficient *R* and the normalised root mean square error *NRMSE* computed between the hourly evapotranspiration values of CLIME-MG and METRIC over the areas identified by the tiles, for four cases. The statistical measures show that the outputs are not significantly affected by the proximity of the stations (the measures of c tile for the 27 June 2015 are omitted due to the presence of clouds over that area).

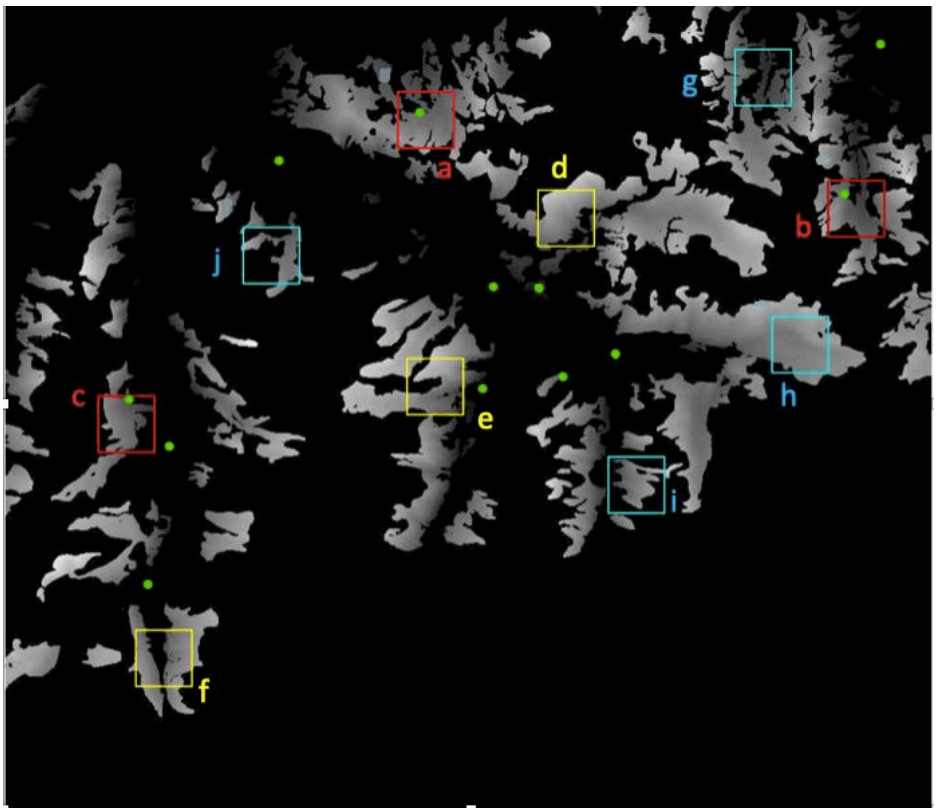

Figure 7.11. Tiles show the small areas analysed. Green dots show the AWS locations.

The weather stations are not uniformly spatially distributed (also by elevation), as shown in Table 7.1. Therefore, it is useful to test CLIME-MG consistency also at altitudes where no measurement stations are available. The maximum elevation for the used AWS network is below 2300 m, while the studied grasslands can reach 3300 m. Figure 7.12 shows statistical measures of this analysis. The correlation and the normalized RMSE between the two models decrease with elevation in two over four considered cases. This suggests that the models are less correlated when high-elevation grasslands are considered, probably because METRIC was designed to operate at lower altitudes with cultivated areas. However, the *NRMSE* is low, indicating also that, although less correlated, the *ETa* estimates are more similar with increased elevation. In addition, even in this test, the presence or not of AWS does not affect CLIME-MG outputs.

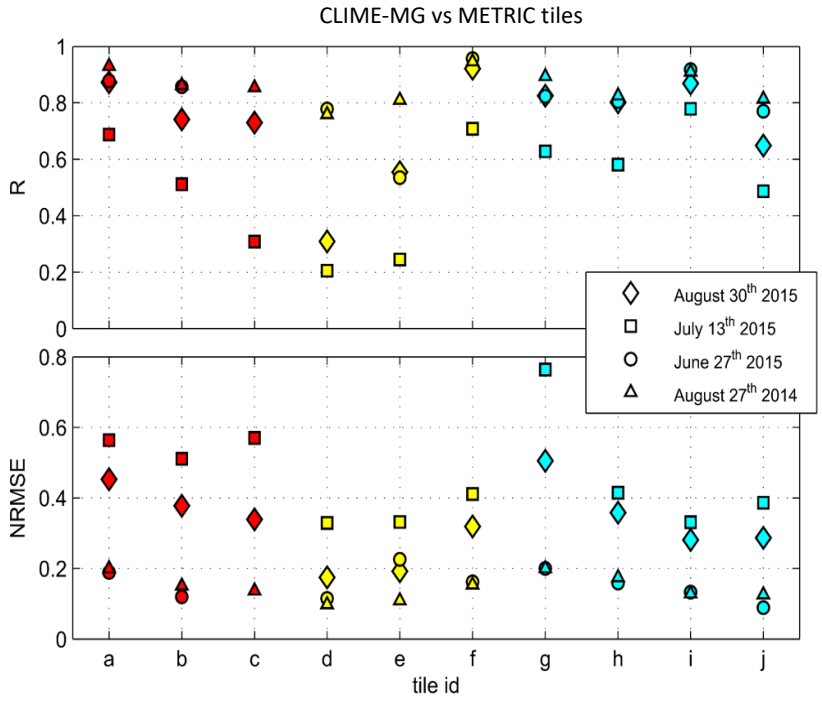

Figure 7.12. Correlation coefficient R and normalised root mean square error (NRMSE) between CLIME-MG model and METRIC for hourly evapotranspiration values. Statistical parameters are shown according to tiles.

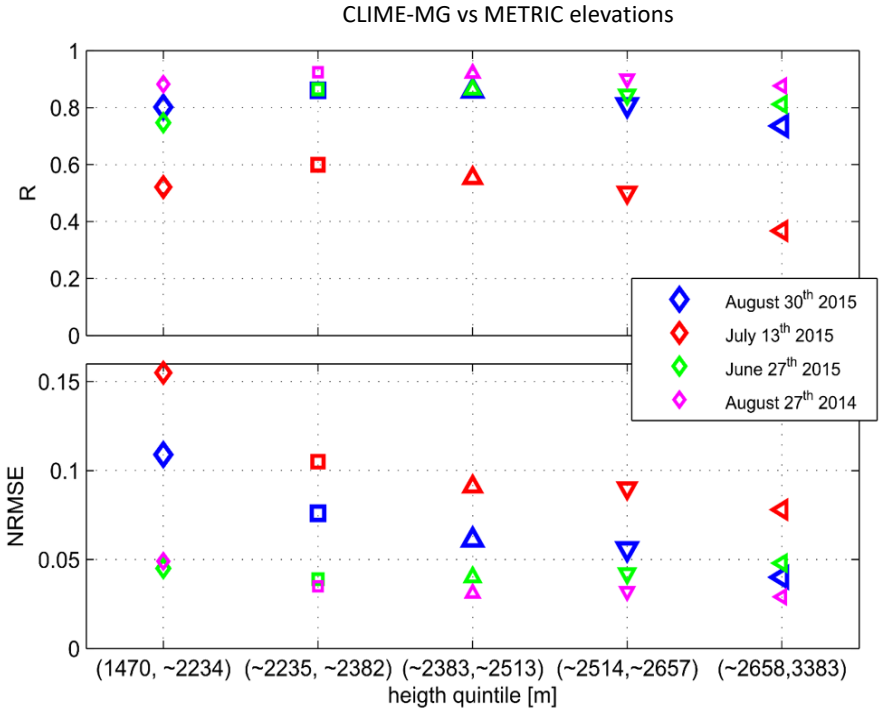

Figure 7.13. Correlation coefficient (R) and normalised root mean square error (NRMSE) between CLIME-MG model and METRIC four hourly actual evapotranspiration values. Statistical values are shown according to elevation ranges.

The differences between CLIME-MG model and METRIC are sensitive to altitude, aspect, soil depth and slope at hourly and daily (Figures 7.14 – 7.15) scales. At both the hourly and daily scales, the strongest impact on the difference between the two models is found for elevation and slope classes. In particular, the bias tends to be negative for low altitudes and then moves towards 0 and positive values in 13th July and 30th August 2015 (for which the most important NRMSE reduction is also found, see Figure 7.15). Mostly positive biases exist in the other two cases with weaker variations which can be found looking again at R and especially at NRMSE (slight changes with height).

For the aspect, the difference between CLIME and METRIC is reduced on slopes with South aspect. Thus, slope angle, aspect and also elevation seem to play a key role in modelling evapotranspiration, at least on mountain grasslands.

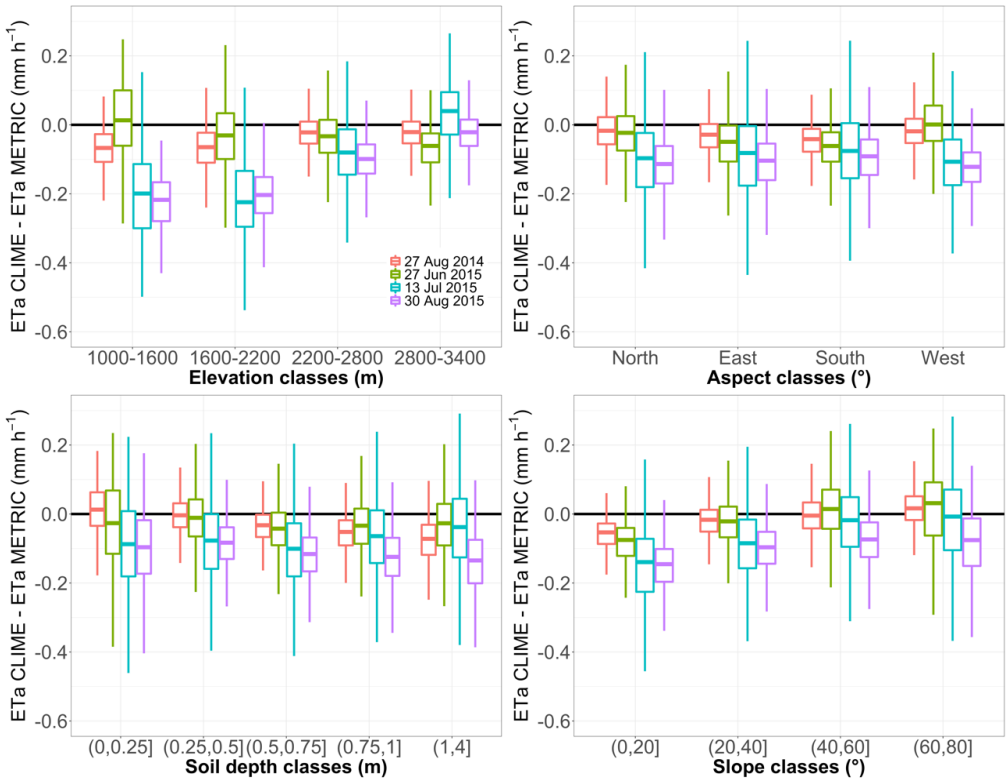

Figure 7.14. Boxplots of difference between CLIME and METRIC hourly *ETa* according to elevation, aspect, soil depth and slope classes.

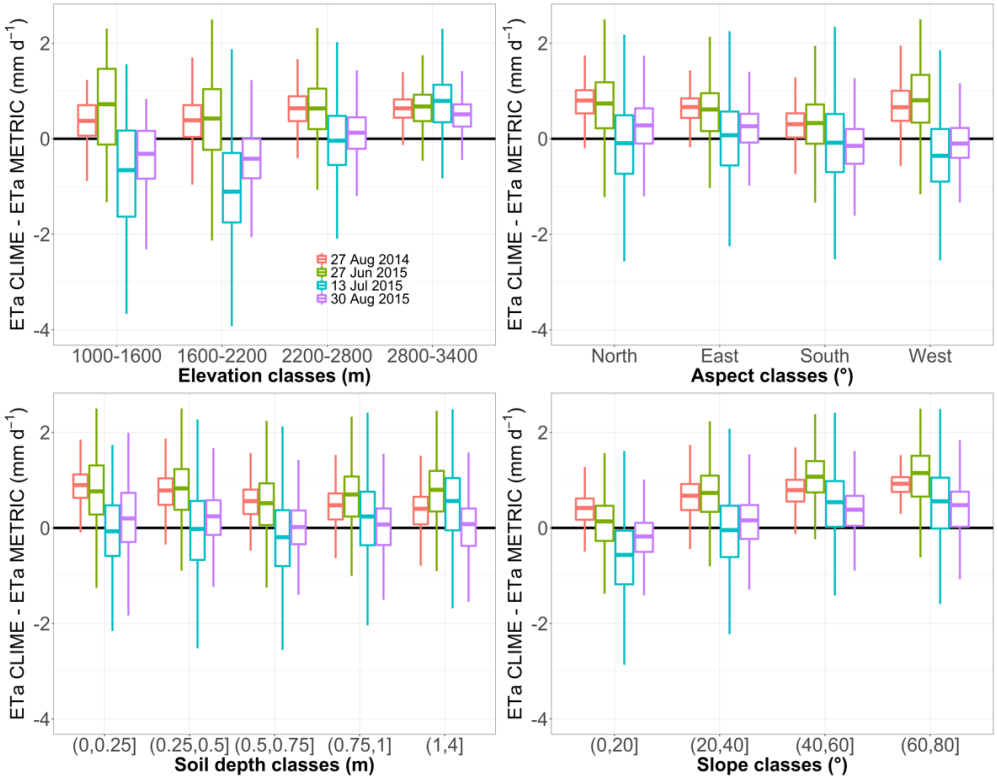

Figure 7.15. Boxplots of differences between CLIME and METRIC daily *ETa* according to elevation, aspect, soil depth and slope classes.

7.5 Final Remarks

Alpine regions are characterised by complex terrains and meteorological conditions and limited accessibility, suffer of a limited quantity and quality of information and of modelling tools for both characterising actual conditions and producing forecasts.

In this Chapter, a simple model based only on standard weather data for mapping actual evapotranspiration *(ETa)* fields has been described, the Calibrationless Soil Water Model for Estimating Actual Evapotranspiration of Mountain Grasslands (CLIME-MG). The model is designed for grassland areas with complex orography and its main feature is the absence of calibration parameters. The retrieval of parameters calibrated according to the researcher's needs and environmental conditions can be considerably difficult in complex topographies, because of non-standard soils, lack of experimental data and difficulty to set up field campaigns especially in the mountains. In addition, controlled experiments are almost impossible to carry on. Indeed, in many occasions, correct calibrations require laboratory experiments, and several models are designed to work especially on cultivated areas or at least on crops with known vegetation species. This is not often the case in the mountains.

The model is composed by two main modules, one modelling meteorological fields and computing the potential evapotranspiration *(ETo)*. The second module is devoted to model the soil water transfer and it computes the vegetation stress coefficient by estimating the soil moisture with an original model of soil water balance. In addition to the weather data, the model requires a DTM and a land cover map as inputs, because orography and land cover heavily affect the micro-climate conditions in mountain regions and the shading effect is not negligible. In the model development, the spatial and temporal variability of *ETa* in mountain grasslands was also related to the aspect and slope of the land, together with the meteorological components, which show a variability also in both time and space.

The model was validated with a time series of *ETa*, measured with two eddy covariance stations, showing good performances (correlation coefficients and root mean square errors comparable with other studies using models requiring parameters optimisation). Moreover, CLIME-MG outputs were compared with the METRIC model evapotranspiration outputs, namely the *ETa* estimation based on satellite images and an independent modelling approach. METRIC is among the most used hydrological models, therefore a spatial comparison of the performances of the two models yielded the information on how much CLIME-MG differed from an acknowledge and well-known approach.

The comparison results showed a good spatial correlation, even if topography plays a great influence on the grassland actual evapotranspiration process. In addition, a comparison focused on particular areas proved the homogeneous performance of CLIME-MG with respect to local elevation and distance from a meteorological station. By contrast, differences in the spatial variability, higher for METRIC than for CLIME-MG, were revealed. METRIC model tends to

overestimate the spatial variability (it shows a high number of points with null *ETa* and also many with an unexpected high *ETa*), probably because it was designed for cultivated areas. Within the four days of best weather conditions, the results highlighted an acceptable correlation between CLIME-MG and the reference model (METRIC). A slight decrease of correlation was found with increasing elevation of pixels in two over four cases, with a decrease also in NRMSE. The CLIME-MG model performed better than the simpler $Kc\ PET$ distribution in the case of a drought day.

The model proved to be performing for mountain grassland *ETa* modelling. Further studies will be essential to confirm the robustness of the proposed approach. Future improvements could aim at a dynamic crop coefficient estimation and an adaption for different land covers and uses.

Chapter 8

Energy and mass fluxes over melting snow

This Chapter analyses water cycle components in the Alpine cold season, from October to April. The analyses are focused on nine snowfall events occurred at the Cogne site (on a South-facing slope, with negligible wind-blown snow) and on the consequent fast snowmelt (1 to 4 days). The analysis is devoted to i) characterise the events from a micrometeorological point of view and in different seasons; ii) quantify the role of longwave radiation on snowmelt also during daytime and compare the longwave contribution with the shortwave one; iii) Quantify the energy balance closure and its temporal evolution; iv) quantify the percentage of energy residuals explained by snowmelt estimated using soil water content increase detected by time domain reflectometry probe, quantify snow sublimation and evaluate the snow water equivalent balance closure. The analyses of this Chapter were performed jointly between the Author and the LABFLUX Team.

8.1 Introduction

The snowmelt energy flux components control the location of source waters and the effects of climate on Winter ecological processes (e.g. Jones et al., 2001; Campbell et al., 2005), soil water content stock (e.g. Hayashi et al., 2003; Previati et al., 2011), streams flow (e.g. Armstrong and Brun, 2008; Jepsen et al., 2012), avalanche formation (e.g. Brun et al., 1989; Bartelt and Lehning, 2002; Lehning at al., 2002a, 2002b; Lehning et al., 2004; Ceaglio et al., 2017), and hydro electrical generation (e.g. Schaefli et al., 2007).

It is important to carry out studies on possible formation of avalanches, because they constitute a danger for mountaineers, for inhabitants of areas at risk and for users of infrastructures, such as roads. Analyses of snowpack energy and mass balances are important, since they affect the way the ice crystals form connections between each other, and the formation of snow layers. For example, there are processes that imply a weakening of those connections, thus making a snow layer weaker than in previous conditions.

One condition is related to snow that melted and then froze again. If this layer is covered by fresh snow, the younger layer could be unstable. The second condition is called snow wetting and it may occur because of either further snowfalls or rain

or because of a positive energy balance of the snowpack (therefore, snow begins to melt). If the energy balance becomes positive, three phases occur. In the first one, the temperature increases without any melting. A second phase, isothermal, takes place when the snow temperature is around 0°C. The temperature no more increases, and the phase transition begins. The third phase occurs when, also due to other external contributions (such as rain on the snow, high radiation input, high soil temperature), the snow melts. The liquid water can also infiltrate in deep layers through percolation and if the snow liquid water amount increases, then the snow grains can increase their dimensions, thus causing a weakening of the layer.

Within the snowmelt process, therefore, the sensible heat flux plays a key role, together with the radiative components (net radiation, shortwave and longwave radiation). The transport of sublimated water vapour is instead accounted considering water vapour flux and latent heat flux.

Sunny slopes with a South or near South aspect have a very different snowpack with respect to North aspect. Much more incoming heat occurs and snow melts faster. This explains why it is more frequent to find snow melted and then frozen again and crusts that can originate weak snow layers. Studying the impact of energy balance components on snow and how energy and mass balance change when melting processes occurs, might be able to deepen the knowledge about avalanche formation.

Especially on sunny alpine slopes, the energy, snow (and water) mass balances can show strong temporal variability, and surface temperatures have oscillations of about 20 Celsius degrees in a few hours or minutes (Nadeau et al., 2013).

Within the climate change context, higher temperatures would imply a shortened snow seasons, with earlier snowmelt (around 5.8 days per decade in the Swiss Alps, Klein et al., 2016). It increases

radiation absorption and starts a positive feedback, the snow-albedo one, which in turn will affect again the snow depth and snow cover season duration, as well as net radiation (Pépin et al., 2015: Diffenbaugh et al., 2005, Lopez-Moreno et al., 2013). Despite these high interests, data from Alpine and Subalpine environments are rare, mainly because of the measurement difficulties. Today, as already described in previous Chapters, the eddy covariance (EC) is the most used technique to measure the turbulent fluxes of energy in the lowest layer of the atmosphere, but its use in mountain areas is difficult especially out of the growing season, due to the severe weather conditions, together with the complex morphology leading to non-ideal location (e.g. Reba et al., 2009; Reba et al., 2012). A method for analysing the scalar turbulent fluxes measured by eddy covariance is the Energy Balance Closure (Wilson et al. 2002). This is a formulation of the first law of thermodynamics, and it requires that the sum of the latent (*LE*) and sensible (*H*) heat fluxes equals the sum of all other energy fluxes and time change of energy storage, as shown in Eq. 8.1a:

$$\delta = \frac{dE}{dt} = LWin - LWout + SWin - SWout - H - LE - G - S - A - Qr \quad (8.1a)$$

where $\frac{dE}{dt}$ is the net change rate of snowpack internal energy, LW_{in}, LW_{out}, SW_{in} and SW_{out} are, respectively, incoming and outgoing longwave radiation, and incoming and outgoing shortwave radiation, H is sensible heat flux, LE is the latent heat flux, G is the ground heat flux in the soil, S is the rate of change of thermal energy stored in the layer above the heat flux sensor. A is the rate of change of heat storage (air and biomass) between the soil surface and the level of EC, usually negligible if sensors are close to the ground. Qr includes all potential sources and sinks of the system (such as the energy carried as sensible or latent heat by either precipitation or blowing snow, usually negligible). Qr includes also potential errors of underestimations of turbulent energy fluxes are also included, if the eddy covariance system is used. The net change of snowpack internal energy is, instead, given by (at least) two terms (Eq. 8.1b): one related to the thermal content, and the second related to the material phase.

$$\frac{dE}{dt} = Q_{melt} + \frac{dU}{dt} \tag{8.1b}$$

where $Q_{melt} = \lambda_{melt} R_t$ and $\frac{dU}{dt} = \int_0^{h_{snow}} \frac{d}{dt}\left(\rho_{snow}(t,z) c_{p_{ice}} T_{snow}(t,z)\right) dz$

Q_{melt} represents the melting or freezing (phase change) of the snowpack, where: λ_{melt} is the latent heat of fusion of ice, R_t is the net rate of freezing and melting. Term $\frac{dU}{dt}$ represents the warming or the cooling of the snowpack and includes the snow density profile $\rho_{snow}(t,z)$ and the snow temperature profile, $T_{snow}(t,z)$; $c_{p_{ice}}$ is the specific heat capacity of ice. The integral is written supposing that the temporal scale is not sufficient to vary significantly the snow depth. Hence the integral extrema can be thought constant in time. Pomeroy et al. (2006), in their work on tundra shrubland, use only the melt term included in term (a) of Eq. 8.1b, and here this approach is adopted, although discussions can be made on the other terms.

As it was shown in Chapter 4, the eddy covariance technique (EC) can be used in mountainous areas, but the energy balance closure is still an open issue on complex terrains. The eddy covariance technique has been used on snow-covered ground of varying complexity. The first applications over snow were conducted at homogeneous sites such as frozen lakes or flat glaciers (e.g. Hicks and Martin, 1972; Andreas et al., 1979). Some studies have focused on the sublimation of the snowpack and the effects that the vegetative cover may have on it (e.g. Nakai et al. 1999) while others investigated the interaction between vegetation and soil (e.g. Pomeroy et al., 2003; Turnipseed et al. 2003) and surface hoar dynamics (Stössel et al., 2010). Mott et al. (2013) evaluated the micrometeorological processes related to the snow ablation in an Alpine catchment and they found that radiation dominates the snow ablation early in the season, while the advection contribution becomes

important late in the season. They assumed the existence of a stable boundary layer above a patchy snow cover that exerts a dominant control on the timing and magnitude of snow ablation.

Few studies analysed the energy and mass balances components in a snow-covered site. Reba et al. (2009) performed a three years measurement in a wind-exposed mountain site, with mainly sagebrush as a vegetation. They concluded that EC was applicable, provided corrections of fluxes in post-processing phase, such as spike removal and minor 10 Hz data gap filling, wind direction filtering, air density correction, sensor heating correction and coordinate rotation. Strasser et al. (2008) performed a study in an Alpine catchment, finding that snowmelt is the most important term in mass balance.

MacDonald et al. (2010) studied and modelled the role of snow sublimation on a mountain top, north-facing and south-facing slopes (being around 20°), highlighting the role of wind blowing on sublimation at their sites, which pose a problem in snowpack modelling.

Chen et al. (2011) studied the energy balance partition before, during and after the snowfalls on a flat meadow in Eastern Mongolia and they concluded that a diurnal cycle existed in the energy balance. A diurnal partitioning of net radiation into *LE* was found when the snow had melted, whereas during snowmelt, the net radiation was mainly partitioned into *H*.

Saitoh et al. (2011) evaluated the closure of energy balance over a temperate forest on steep slope (21°) in a snowfall-dominated region over a three-year period. Their experimental site had a north-northeast aspect. They concluded that the energy balance closure over a slope was of similar degree of accuracy as those over a flat topography.

Reba et al. (2012) found that the sublimation rate is around 0.39 mm day^{-1} at their exposed site on a gentle slope, and that it covers a wide range of percentage on maximum snow accumulation.

Helgason and Pomeroy (2012) investigated the internal energy of snow-cover during a snow melting period and they found that relatively large energy imbalances were caused by longwave radiation losses (higher during daytime) being not balanced by downward turbulent fluxes, solar radiation (during daytime) or conductive heat of the ground. They also found that eddy covariance random errors were not able to explain all the imbalance and that, very likely, the underestimation was above all related to the sensible heat flux.

Sexstone et al. (2016) compared several methods to estimate sublimation. In their study a mountain site was included. The energy balance closure ranged between 0.60 and 0.71.
Plus, they found sublimation rates of 0.60 to 0.80 mm day^{-1}.

In addition, in mountainous environment and in the snow period, longwave radiation can provide to snow as much energy as, or greater energy than shortwave radiation and it might be comparable with other energy balance components (Plüss and Ohmura, 1997). Longwave incoming radiation can come from the sky (clouds included). Therefore, evaluating the impact of longwave radiation on turbulent

fluxes and the snow cover is important. If the snowpack is heated by LW radiation, it can begin to melt well before the solar radiation is available, thus accelerating the melting process.

8.2 Methodology

The study focuses on nine events for Cogne site and one snowmelt period at Nivolet site, and it attributes a part of the residual of the imbalance in the energy closure to the energy used for melting the snow accumulation. In addition, it explores how the radiation components (in particular longwave ones) can affect the turbulent fluxes, the energy imbalance and the snow layer. The study analyses also what would be the potential contribution if all the energy imbalance was used for snow melt. The analysed periods are shown in Table 8.1.

Table 8.1. List of the snowfall events. SWE numbers with "*" were measured in-situ. Values with "**" were reconstructed. LW stands for longwave radiation; SW stands for shortwave (solar) radiation. [1]: data property of Ufficio Neve e Valanghe – Regione Autonoma Valle d'Aosta.

Event	Site	Period	LW-SW measures	Snow depth (m)	Snow density (kg m^{-3})	SWE (mm)
Oct. 2010 (1)	Cogne	24/10-28/10	N/A	N/A	N/A	12.5*
Mar.2011 (2)		03/03 –07/03	N/A	N/A	N/A	16.5*
Mar.2011 (3)		15/03-21/03	N/A	N/A	N/A	27.5*
Apr. 2012 (4)		14/04 – 20/04	N/A	N/A	N/A	25.0*
Nov.2012 (5)		31/10 – 03/11	N/A	N/A	N/A	7.2*
Nov.2012 (6)		10/11-15/11	N/A	N/A	N/A	28.0*
Feb. 2015 (7)		05/02-14/02	yes	0.27	54[1]	14.6**
Mar.2015 (8)		15/03-19/03	yes	0.23	70[1]	16.1**
Apr.2017 (9)		01/04 – 06/04	yes	0.21	100[1]	21.0**
Late Spring 2019	Nivolet	15/05-15/06	yes	1.5	N/A	N/A

The snow water equivalent values used in this Chapter come from *in situ* measurements after the analysed events. Where these measurements are not available, values of snow density measured at the Valnontey Regione VDA site are used and multiplied by snow depth measured at Cogne by the infrared sensor SR50AT (Campbell Scientific, Logan, USA).

The two stations located at Cogne and Pian del Nivolet were used. For Cogne, the data set starting from 2010 to 2017 was used, including two different configurations of sensors: (a) horizontally leveled at a height of 1.80 m above the

ground (from September 2010 to October 2011) and (b) slope-normal at a height of 2 m from October 2011 to 2017.

The turbulent fluxes of energy (latent heat, *LE* and sensible heat, *H*) were calculated using measured covariances of fluctuations in vertical wind speed component and specific humidity and temperature, respectively (Lee, Massman and Law al., 2004):

$$\begin{aligned} LE &= \lambda\rho(\overline{w'q'}) \\ H &= \rho C_p(\overline{w'T'}) \end{aligned} \tag{8.2}$$

where λ is the latent heat of vaporization (J kg^{-1}), ρ the density of dry air, (kg m^{-3}), w the vertical wind speed, (m s^{-1}), q the specific humidity, (kg kg^{-1}), C_p the specific heat capacity of dry air (1013 J $kg^{-1}K^{-1}$), T the sonic temperature (°C). Primed quantities refer to fluctuations around mean values.

For the Cogne site, 10 Hz data were processed with EddyPro 6.2.1. software and aggregated at 30-minute time scale. Spikes in the 10 Hz time series were identified through the algorithm described by Mauder et al. (2013) and the consequent gaps were filled through linear interpolation only if a maximum of 1% of missing data existed. Turbulent flux data were determined after linear detrending of original time series (e.g. Foken, 2008a), double rotation (e.g. Kaimal and Finnigan, 1994) of anemometer axes, linear detrending, application of the correction for air density fluctuations (WPL, Webb et al., 1980) and for humidity effects (Schotanus et al., 1983).

The eddy covariance data related to the second station (Nivolet), also sampled at 10 Hz, were again processed with EddyPro but with its 7.0 version and aggregated at 30 minutes after a first despiking of 10 Hz time series using the algorithm described by Mauder et al. (2013). The turbulent fluctuations were computed starting from the mean removal using block average (e.g. Lee, Massman and Law, 2004). The anemometer coordinate system was rotated using the simple planar fit (Wilczak et al., 2001). WPL and air humidity corrections were also applied. Nivolet data were used for comparison between turbulent fluxes, net radiation and other radiation components (longwave and shortwave ones).

At both sites, a quality control was performed. Since only few days were available for each event, the implemented quality control was less demanding with respect to Chapter 4. This choice allowed to avoid a severe data loss. The quality control involved a visual inspection of time series. In addition, for each half hour period, the following flux data filtering was implemented:

1) *H* and *LE* fluxes in half hours with at least one hard-flagged variable for skewness and/or kurtosis among *u, v, w, H_2O* were discarded. The flagging system used the same boundaries as shown by Vickers and Mahrt (1997)
2) *H* and *LE* fluxes in half hours with more than 1% of spikes in the 10 Hz time series of *u, v, w,* or *H_2O* were discarded.

3) *H* and *LE* fluxes in half hours with either hard-flagged CSAT3 or LiCor gain control were discarded
4) Half hours with precipitation > 0.2 mm were discarded
5) Turbulent fluxes with failed stationarity and integral turbulence tests as described by Mauder and Foken (2004) were also filtered.

All fluxes were computed normally to the surface. The ground heat flux at 8 cm depth *G* was obtained directly from the average of these two heat flux plates. Slope-normal sensible heat flux *H*, the latent heat flux *LE* and the ground heat flux *G* are defined as positive away from the surface, while the net incoming radiation R_n is positive toward the surface. *G* term cannot be measured at the surface of the soil and therefore the storage contribution of the shallow soil has to be computed (e.g. Chen et al., 2011).

The soil heat storage variation was computed as described in Chapter 4 (Campbell Scientific, Inc., 1990; German, 2000).

To evaluate the net and global radiation over an inclined surface an adjustment of shortwave radiation and of the net radiation (when measured with horizontally leveled sensors between 2010 and 2014) was necessary. This has been done differently if compared to previous Chapters, following the procedure proposed by Kondratiev et al. (1978). This choice was made because in this Chapter, single events of few days are considered. Hence, the correction using linear regression as in Chapter 4 could be less reliable.

The zenith and the azimuth angles of the sun are necessary to estimate the solar radiation on sloping surfaces and they were calculated with the Solar Position Algorithm developed by the NREL (National Renewable Energy Laboratory-U.S Department of Energy). The mountain slope inclination is around 26°. For the cases with only horizontally measured net radiation and no shortwave or longwave radiation (at the eddy covariance site), the nearby horizontal measures of global radiation collected at ARPA Gimillan site on flat terrain were used. Those data were corrected for slope, zenith and azimuth using Eq. 8.4a.

$$SW_{in_{corr}} = \frac{SW_{in_{hor}} \cos(i)}{\cos(\xi)} \tag{8.4a}$$

where $\cos(i) = \cos(\alpha)\cos(\xi) + \text{sen}(\alpha) sen(\xi) \cos(\psi - \psi_s)$. α is the slope angle; ξ is the zenith angle; ψ is the Azimuth angle and ψ_s is the slope aspect.

Wohlfahrt et al. (2016) suggested that the longwave radiation is not strongly directional, hence either slope-parallel or horizontal measurements are not significantly different, so, no particular correction was required. Only the shortwave direct downward component was adjusted for the angle of the slope. The procedure has then been validated with the installation in 2014 of a four-component radiometer, previously installed horizontal, and then slope parallel and the outgoing shortwave radiation did not differ significantly between the two configurations.

The slope-parallel net radiation was then evaluated as in Eq. 8.4b.

$$R_n = R_{n_{hor}} + \Delta SW_{in} \tag{8.4b}$$

where $\Delta SW_{in} = SW_{in_{corr}} - SW_{in_{hor}}$

8.2.1 Energy and water balances

Longwave radiation

From 2015 onwards at Cogne and for late Spring 2019 for Nivolet site, an analysis on longwave and shortwave radiation compared to turbulent fluxes was carried out. This helped the understanding of the role of the radiation components on both sensible and latent heat fluxes. The shortwave and longwave were acquired with a four-components radiometer (NR01, Huskeflux, Netherlands). Collected data were: shortwave and longwave infrared incoming and outgoing radiation.
Data were used at Cogne only during three snowfall events (and following days), namely, February 2015, March 2015 and April 2017, whereas a continuous data set was obtained for Late Spring 2019 at Nivolet. The measures were checked for spikes and for unphysical values.

Relationship between energy residuals and snowmelt

The energy balance equation is usually represented by Eq. 8.5a

$$H + LE = R_n - G - S - \delta \tag{8.5a}$$

where δ is the residual term due to measurement errors or non-estimated terms and, when snowpack exists, to net change of internal energy of the snowpack, which includes the two terms shown in Eq. 8.1b.

For this work, we are interested in positive residuals (i.e. those actively contributing to snowmelt). Over a snowpack, the energy balance can be written as:

$$\delta = Q_{melt} + \frac{dU}{dt} + A + Qr \cong \lambda_{melt} M + \frac{dU}{dt} + A + Q_r \tag{8.5b}$$

Term A could be important under the shrubs, but its estimate is not trivial. Terms A and Q_r can be merged into term ϵ, which includes all the other potential sources and sinks of energy and also turbulent fluxes miscalculations. The rate of snowmelt is indicated as M, λ_{melt} is the latent heat of fusion ($3.34*10^5$ J kg^{-1}).

Q_{melt} can be also described as the excess of energy that can no longer warm the snow (because of the 0°C temperature constraint) and is used for phase change and melting. Once the snowpack reaches the isothermal conditions, especially in the first sunny day, the hypothesis is that one of the main energy imbalance causes is related to the snowmelt process, whose effects are not captured by eddy covariance technique. The contribution of snowmelt was assessed through the ratio $Q_{melt}\ /\delta$.

Water and snow balances

To describe the snowmelt process, it is also necessary to consider its mass balance (Eq.9.6a) and the soil water balance (Eq. 8.6b).

$$M = P - ES \tag{8.6a}$$

$$P(snow) - E \pm \Delta S = 0 \tag{8.6b}$$

In Eq. 8.6a, M is the melt term; P=SWE is the snow precipitation volume; E is the sublimation term. The blowing snow-related term is considered negligible. In Eq. 8.6b, ΔS is the water storage in the soil (including also percolation from the soil surface. The runoff is negligible at Cogne.

These interconnected balances are used to: i) test whether the choice of using soil water content increase (soil water storage) as an estimate of the melt term is reliable; ii) quantify the closure of the water balance. For each event, the day and time of probable water balance closure was identified when the soil water content began to decrease monotonically after having reached one (or more) peaks and also using information from measured surface temperature, soil temperature and, when available, albedo. These three variables allow to identify whether the soil is still covered by snow, if probable patchy conditions exist or whether no snow is left on the soil.

Daily cumulative values of soil water increase and sublimation were computed starting from the first detected soil moisture increase or, if sublimation occurred earlier, from the hour of first available sublimation data after the snowfall.

8.3 Results

8.3.1 Micrometeorological and soil conditions

The nine events identified at Cogne were characterised by a sufficient amount of snowfall greater than 10 mm of snow water equivalent (SWE). They cover all the cold season, from October to April and they included either one or two snowfall days followed immediately or almost immediately by sunny days which contribute to a fast melting process. Table 8.2 shows the main meteorological and soil variables. A relatively wide range of soil and air temperature is covered. The table will also be helpful later on, when discussing the snowmelt relation with energy balance residuals and also the water balance. The surface temperature is among the indicators of snow presence, along with net radiation and, if available, albedo. Indeed, as soon as the snow vanishes, the surface temperature increases, as also shown in Table 8.2. There can be a sudden and temporally limited increase of soil water content, thus not always the daily averaged soil water content increases. Usually there is instead an increase in daytime averages of turbulent fluxes and also of radiative fluxes (net radiation, ground heat flux) the days after the snowfall, when the snowpack begins to melt until it vanishes (Table 8.3). The estimated sensible heat storage between the soil (or the snow) surface and the sonic anemometer is negligible (always within the range between -10 and +10 W m^{-2}), so it will not be discussed.

Table 8.2. Daily average, minimum and maximum values of air, surface and soil temperatures, daily average soil water content and wind speed for all the events at Cogne.

Event	Date	$T\,air$ (°C)			$T\,surface$ (W m^{-2})			$T\,soil$ (°C)			θ (m^3 m^{-3})	U (m s^{-1})
		AVG	MIN	MAX	AVG	MIN	MAX	AVG	MIN	MAX	AVG	AVG
1	26/10/2010	0.9	-2.1	4.5	-1.7	-7.3	8.2	5.6	3.8	9.3	0.14	1.02
	27/10/2010	3.1	-2.4	8.7	3.9	-5.2	23.1	6.2	1.5	11.5	0.16	1.29
2	04/03/2011	-3.3	-5.9	0.6	-3.1	-8.0	2.0	1.4	0.9	1.8	0.15	0.93
	05/03/2011	-1.5	-7.0	3.9	-3.0	-10.7	6.0	1.7	-0.1	3.2	0.17	1.20
	06/03/2011	1.0	-4.4	8.5	2.4	-7.0	22.0	3.2	-1.4	8.2	0.17	1.40
	07/03/2011	-3.4	-6.0	-0.1	1.5	-7.6	17.6	3.0	-0.6	6.6	0.16	1.33
3	16/03/2011	2.3	-3.8	5.0	1.2	0.4	1.9	2.2	1.9	2.8	0.17	0.57
	17/03/2011	3.9	0.8	6.7	1.5	-1.5	3.3	1.9	1.5	2.2	0.17	0.57
	18/03/2011	3.6	-2.3	10.9	3.2	-5.1	20.8	3.7	0.2	8.7	0.18	1.04
	19/03/2011	1.8	-1.6	7.5	3.0	-3.9	18.1	3.6	1.7	6.4	0.17	1.01
	20/03/2011	0.6	-4.3	7.2	4.3	-6.2	25.3	4.1	0.1	8.5	0.16	1.54
	21/03/2011	-0.8	-5.3	5.5	2.8	-7.4	24.2	3.8	0.2	8.1	0.15	1.56
4	14/04/2012	2.4	-2.0	5.9	3.4	0.9	10.3	5.9	5.0	7.5	0.13	0.82
	15/04/2012	2.7	0.1	8.1	1.2	0.4	1.9	4.4	3.8	5.1	0.14	0.50
	16/04/2012	2.8	-1.2	6.7	1.6	-0.8	3.3	3.8	3.5	4.1	0.16	0.56
	17/04/2012	2.2	-0.7	6.9	5.2	-2.8	19.0	6.2	3.0	10.2	0.17	1.21
	18/04/2012	1.8	-1.2	7.1	4.9	-3.3	21.9	6.2	3.7	10.0	0.15	1.20
	19/04/2012	-0.4	-2.5	2.9	3.3	-3.4	14.2	5.4	3.5	7.7	0.15	1.06
	20/04/2012	1.0	-2.4	6.5	4.2	-3.5	18.3	6.3	4.0	9.7	0.15	0.99
5	01/11/2012	1.6	-2.2	7.0	-0.2	-3.8	5.7	4.8	3.1	7.3	0.09	0.51
	02/11/2012	2.3	0.1	6.9	3.7	0.5	14.3	6.5	4.3	10.5	0.12	0.74
	03/11/2012	2.6	0.1	6.9	3.9	-1.0	15.6	7.0	4.0	10.6	0.11	0.92
6	11/11/2012	-	-	-	-	-	-	-	-	-	-	
	12/11/2012	2.0	-1.2	7.4	-0.1	-3.3	7.0	4.6	3.1	6.8	0.14	1.09
	13/11/2012	1.4	-2.3	7.5	1.0	-4.6	14.4	5.1	2.0	9.1	0.14	1.23
	14/11/2012	1.6	-2.1	8.0	2.6	-3.6	18.0	5.5	2.3	9.6	0.13	1.22
	15/11/2012	3.1	-0.7	9.6	4.1	-2.6	20.9	5.9	2.6	10.2	0.13	1.39
7	07/02/2015	-2.9	-6.4	6.3	-4.4	-8.4	0.6	0.2	-0.2	0.5	0.11	1.58
	08/02/2015	-0.1	-6.6	10.1	-4.1	-9.3	3.2	0.1	-0.6	0.5	0.11	0.90
	09/02/2015	0.4	-7.2	11.1	-3.6	-9.8	3.5	0.2	-0.6	0.7	0.11	1.23
	10/02/2015	3.3	-3.6	15.1	-1.3	-6.3	6.2	0.2	-0.7	0.9	0.12	1.18
	11/02/2015	2.2	-3.5	13.0	-0.8	-5.9	8.1	0.2	-0.7	0.9	0.13	1.24
	12/02/2015	0.6	-4.1	10.1	-0.5	-6.0	11.0	0.4	-0.7	1.5	0.14	1.23
	13/02/2015	-2.2	-5.4	4.1	-0.4	-6.4	10.2	0.6	-0.4	1.6	0.14	0.92
	14/02/2015	-3.8	-4.8	-1.1	-1.3	-3.1	2.8	0.4	0.3	0.7	0.14	0.59
8	16/03/2015	-1.5	-3.5	2.9	-0.9	-1.9	1.0	2.3	2.1	2.4	0.14	0.40
	17/03/2015	-0.1	-2.6	5.1	0.5	-1.4	2.2	2.2	2.1	2.3	0.14	0.57
	18/03/2015	3.7	-4.6	12.5	1.4	-5.6	12.5	4.6	1.2	4.3	0.17	0.93
	19/03/2015	4.2	-1.9	13.2	6.4	-3.0	26.0	3.6	0.6	6.2	0.18	1.57
9	03/04/2017	3.9	-1.4	9.2	2.7	-1.7	8.0	3.7	2.8	4.6	0.19	0.40
	04/04/2017	5.0	-0.5	11.1	7.3	-2.4	24.3	4.6	2.0	6.7	0.20	0.57
	05/04/2017	3.8	1.7	8.1	7.0	-0.7	24.7	4.9	3.7	6.6	0.19	0.93
	06/04/2017	6.0	0.2	13.6	10.1	-2.5	33.0	5.2	2.3	7.9	0.18	1.57

Table 8.3. Daily average and maximum values for net radiation, ground heat flux at the soil surface; daytime averages of sensible and latent heat fluxes at Cogne.

Ev.	Date	Rn ($\mathrm{W\ m^{-2}}$)	Rn ($\mathrm{W\ m^{-2}}$)	G_0 ($\mathrm{W\ m^{-2}}$)	G_0 ($\mathrm{W\ m^{-2}}$)	H ($\mathrm{W\ m^{-2}}$)	LE ($\mathrm{W\ m^{-2}}$)
		AVG	MAX	AVG	MAX	AVG	AVG
1	26/10/2010	62.9	476.3	-3.9	98.3	42.5	56.0
	27/10/2010	121.2	637.1	-4.2	125.2	42.3	42.7
2	04/03/2011	49.0	389.1	-4.3	28.5	-3.3	9.4
	05/03/2011	100.6	517.2	-1.8	67.8	-11.8	38.3
	06/03/2011	140.8	665.6	9.1	172.7	11.3	50.6
	07/03/2011	164.5	768.4	2.4	138.3	53.4	18.6
3	16/03/2011	5.0	116.8	-5.0	10.1		
	17/03/2011	37.1	385.9	-2.9	20.0	-9.4	14.4
	18/03/2011	151.6	730.8	11.5	172.7	6.4	56.0
	19/03/2011	96.7	672.8	0.0	155.1	20.1	41.9
	20/03/2011	151.5	645.3	7.4	136.9	46.8	28.0
	21/03/2011	146.9	542.6	3.4	129.4	54.3	28.4
4	14/04/2012	47.6	338.8	-5.5	34.8	28.2	40.0
	15/04/2012	-0.9	74.9	-8.6	-1.9	-	-
	16/04/2012	50.0	274.3	-4.9	6.8	10.3	25.5
	17/04/2012	170.4	760.5	5.5	127.6	51.9	61.9
	18/04/2012	124.6	639.9	-2.3	122.6	63.7	35.6
	19/04/2012	101.0	489.3	-3.7	71.8	54.2	22.2
	20/04/2012	133.3	564.7	-1.2	91.2	51.4	50.3
5	01/11/2012	77.7	480.0	0.5	62.6	23.1	40.5
	02/11/2012	89.4	612.3	1.1	101.7	52.9	71.3
	03/11/2012	102.7	538.1	2.0	108.5	37.8	21.9
6	11/11/2012	-	-	-	-	-	-
	12/11/2012	59.0	423.4	-4.7	50.3	22.8	57.7
	13/11/2012	79.4	487.5	-1.2	109.2	62.4	64.7
	14/11/2012	76.7	509.3	-0.9	97.2	39.9	23.0
	15/11/2012	72.5	498.2	-0.6	112.0	47.2	27.4
7	07/02/2015	3.5	264.2	-3.0	15.6	-0.8	6.4
	08/02/2015	17.4	317.4	-3.5	20.8	7.9	71.0
	09/02/2015	41.5	390.8	-3.5	17.2	28.1	63.0
	10/02/2015	59.0	474.1	-3.5	19.3	71.8	85.7
	11/02/2015	77.5	543.6	-3.6	18.5	47.2	63.8
	12/02/2015	90.8	587.5	-2.0	52.5	40.0	31.0
	13/02/2015	77.4	519.4	-1.8	29.5	23.6	21.3
	14/02/2015	39.3	175.4	-3.8	2.5	24.0	20.7
8	16/03/2015	17.9	64.8	-3.4	3.9	3.2	29.2
	17/03/2015	18.9	113.2	-3.0	3.2	-0.9	5.7
	18/03/2015	104.6	615.3	0.3	53.1	21.1	40.4
	19/03/2015	140.6	691.2	6.6	99.7	94.7	57.5
9	03/04/2017	109.3	528.6	-4.4	26.1	12.6	48.6
	04/04/2017	166.5	914.0	6.9	76.3	38.7	48.6
	05/04/2017	115.6	731.6	-0.6	63.9	55.8	33.1
	06/04/2017	175.0	772.6	4.4	90.7	109.9	39.9

From this point onwards, the Events will be separated into Autumn and Winter cases (October to February) and Spring cases (March to April).

Taking into account the correction related to slope facing and the shading generated by nearby mountains, the net radiation highlighted a late-morning appearance characterised by high ray incidence on the slope. At Cogne, the maximum values recorded in clear-sky conditions during autumn days were near 400 W m^{-2}, while in early spring times, values reached and exceeded the 600 W m^{-2} (generating also some modest lift-winds during the midday). The average daily values after the snowfalls range between 3.5 W m^{-2} (7th February 2015) and 170.4 W m^{-2} on 17th April 2012.

In different seasons, no particular difference was found between daily daytime averages of sensible and latent heat fluxes (Figures 8.1 and 8.2). Besides, the tendency for *H* and *LE* is to increase when the melting process is occurring (with a more evident trend in Spring events, while in Autumn there is a less sharp increase followed by a plateau region). Daily average values of $R_n - G - S$ tend instead to be lower in Autumn/Winter with respect to Spring, because available net radiation is reduced due to daytime shortening (Figure 8.3). It should be pointed out that the average values could suffer from an excessive smoothing, hence it is still useful to maintain the distinction between Autumn/Winter events and Spring events.

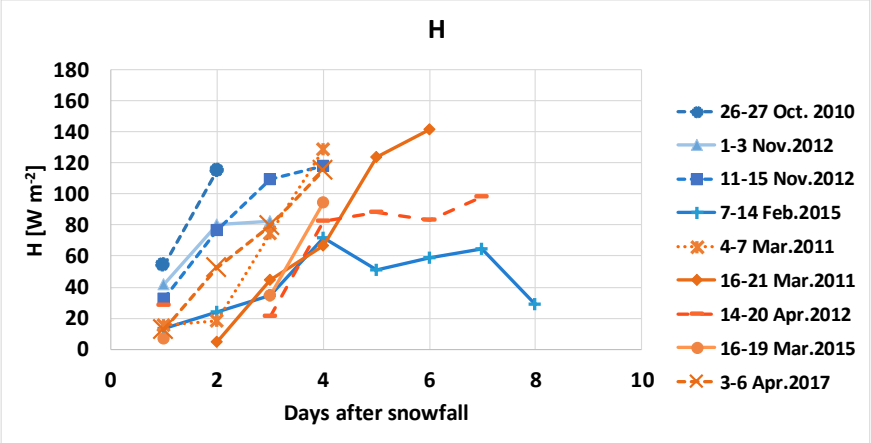

Figure 8.1. Daily averages of sensible heat flux for all the days of the snowfall events.

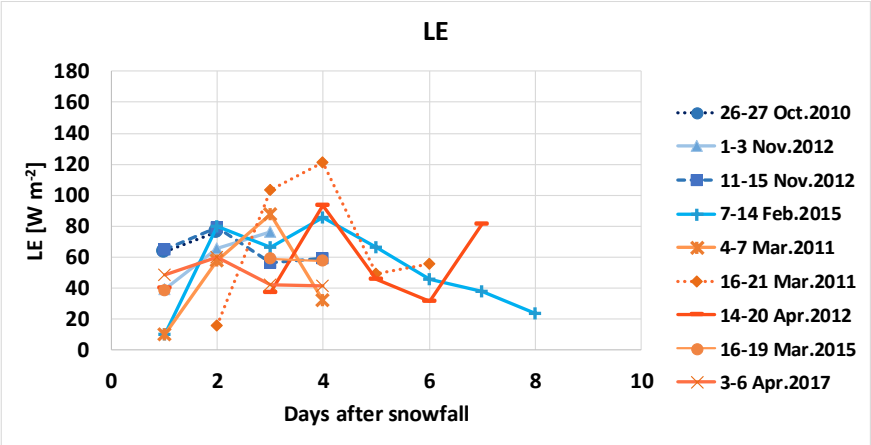

Figure 8.2. Daily averages of latent heat flux for all the days of the snowfall events.

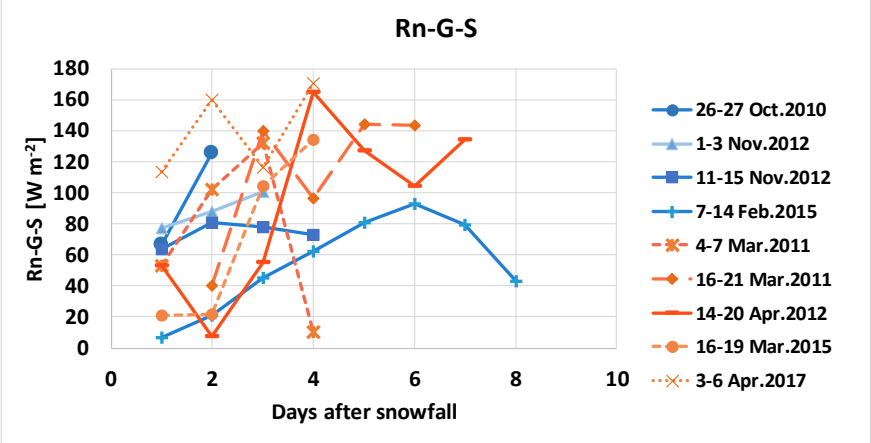

Figure 8.3. Daily averages Rn-G-S term for all the days of the snowfall events.

In presence of snow cover, the sensible heat flux should usually remain close to zero, because the snowpack has a low thermal conductivity and absorbed incident radiation over snow (also due to high snow reflectance) is also low. Hence, the snowpack temperature increase is also relatively low. As observed in the monitored events, as soon as the snowmelt gradually exposes soil portions around the station, the sensible heat flux increases day by day up to a condition without snow (Figures E1 to E9 in Appendix E, panel *a*). In discontinuous snow covers, the presence of uncovered zones can cause *H* flux increases even before the end of the snowfall event, when the radiation hits the slope. Values up to around 200 W m^{-2} can be found. The sensible heat flux can therefore be important for snowmelt process and consequent water infiltration and it can be higher than latent heat flux at the end of the melting process up to more than 100 W m^{-2} in the single half hour periods.

The latent heat is related to the production of vapour produced mainly through sublimation. The melting process, instead, is not detected by the EC system. The energy required to melt the snow represents a non-negligible amount that can lead

to significant underestimation of energy balance closure as explained in more detail below.

Together with the energy fluxes, when the snow starts to melt (in sunny days), the air, surface and soil temperatures begin to show the typical diurnal cycle with a peak in the central hours of the day, and enhanced differences between daytime and nighttime values occur.

As soon as the snow cover begins to melt, the soil insulation due to snow layer decreases. Hence, larger diurnal variations of surface and soil temperatures (Figures E1 – E9, panel *b*) are found, with peaks, around midday. For surface temperature, the variations are higher if compared to soil temperature at 8 cm of depth and also higher in Spring (up to +30°C) than either Autumn or Winter (where the diurnal variation oscillates around a maximum of +15°C). The soil temperature shows diurnal variations below 10°C all along the cold season from October to April. February 2015 shows a frozen soil, hence even if the snow cover partially melts, the soil temperature does not show particular variations along the day. Since the air temperature is not particularly low if compared to other events, the low soil temperature could be caused by persistent patchy conditions. This means that where the soil moisture probes (and soil heat flux plates) are installed, there is still snow, but in other areas the snow has melted. In panel *b* of Figures E1 to E9, the thermohygrometer temperatures are also reported (where available), in case the sonic temperature shows unreliable values such as during snowfalls, such as during the snowfalls of events 3 (Figure E6, night between 16th and 17th March 2011), 4 (Figure E7, night between 16th and 17th April 2012) and 9 (Figure E9, from the afternoon of 2nd April to the morning of 3rd April 2017).

The wind speed (Panel *c* of Figures from E1 to E9) oscillates between calm and maximum values of about 3 m s^{-1}. Especially the wind speed shows well developed diurnal cycles in Spring events, whereas a strongly reduced amplitude was found in Autumn and Winter events, with the exception of the period 1st – 3rd November 2012, where a diurnal cycle was recognisable (Figure 8.6), as soon as the snowpack starts to melt. In Spring cases, it is easier to find peaks of wind speed of about 3 m s^{-1}, and up to 4 m s^{-1}, whereas this does not happen in Autumn and Winter.

The friction velocity (panel *d* , Figures E1 – E9) has values very frequently below 0.4 m s^{-1}, but evidently, the amount of turbulence is still sufficient to allow eddy covariance measurements (the flux data shown were filtered also according to Mauder and Foken, 2004 tests). The u^* shows bell-shaped cycles with peaks in the central hours of the day (i.e. around midday) and lower values during transition hours and nighttime. This diurnal cycle is attenuated if the meteorological conditions are not optimal, especially in Winter and Autumn, and it seems not strongly dependent upon the snow presence. This may be due to the relatively thin snow layers. Besides, the u* values are within the range of previous studies (e.g. Chen et al., 2011, found values ranging from 0.11 to 0.24 m s^{-1} at a more "ideal", snow-covered site if compared to Cogne).

8.3.2 Longwave radiation

Longwave radiation can be as important as shortwave radiation when the latter is low. Another cause is related to complex topography because the longwave emission from mountains slopes can be input in other points of a valley. For instance, the Cogne and Nivolet sites are potentially in this condition, because the stations are located on a slope surrounded by other slopes.

To investigate this aspect, two events in 2015 (February and March, Figures 8.4 and 8.5), one event in Spring 2017 (April, Figure 8.6) and one melting season (15th May – 15th June 2019, Figure 8.6) at Nivolet were used to explore the behaviour of the turbulent fluxes and of longwave radiation. Sudden increases of incoming longwave radiation could lead to accelerated melting even during nighttime or before dawn, when sublimation likely does not occur, and sensible heat flux is considered negligible or it is negative.

In cases when the melting process occurs also during nighttime or during transition hours, likely the incoming longwave radiation plays a key role, because the net longwave radiation can also be positive (Figures 8.4 and 8.5, Spring events), whereas this does not occur in colder conditions, such as in February 2015 (Figure 8.6).

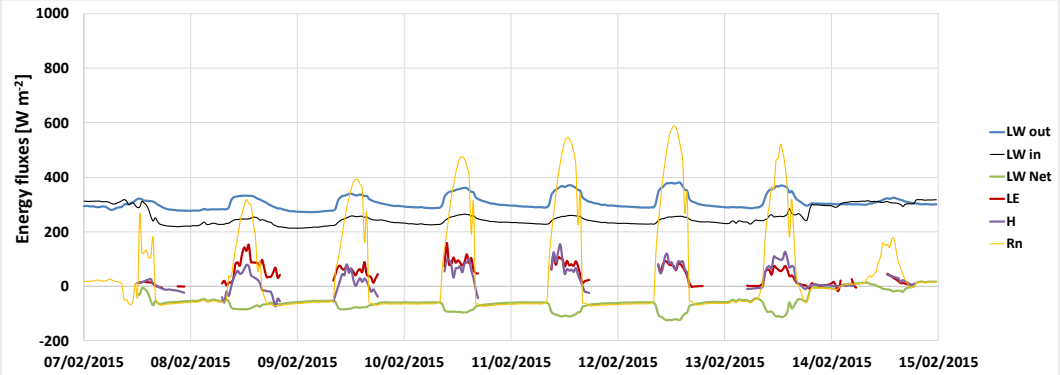

Figure 8.4. Incoming and outgoing longwave radiation, latent and sensible heat fluxes and net radiation for the Event in February 2015. The outgoing longwave radiation (negative) has the positive sign for comparison.

The net longwave radiation is often negative, suggesting that the outgoing term is greater than the incoming one, as also noted by Helgason and Pomeroy (2012) for their site. There are cases when the net longwave radiation is 0 or positive, up to 10 W m^{-2}, especially during nighttime (16-17th March 2015; 2-3rd April 2017, Figures 8.5 and 8.6, respectively). This indicates an outcast sky and a warming snowpack. Hence, the melting process occurs already during the snowfall and, sometimes, in nocturnal hours.

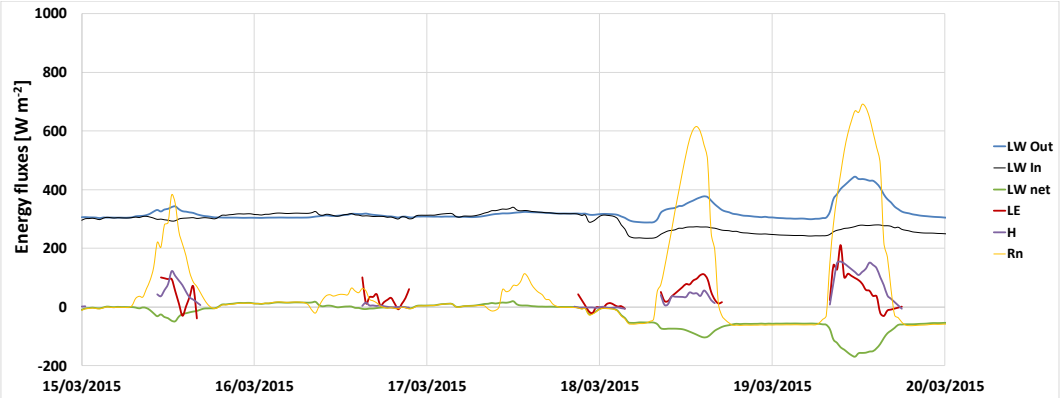

Figure 8.5. Incoming and outgoing longwave radiation, latent and sensible heat fluxes and net radiation for the Event in March 2015. The outgoing longwave radiation (negative) has the positive sign for comparison.

During daytime, the sign of turbulent fluxes is usually positive, indicating an upward flux, as the outgoing longwave radiation (OLR). The net longwave radiation can decrease down to more than -100 W m^{-2}.

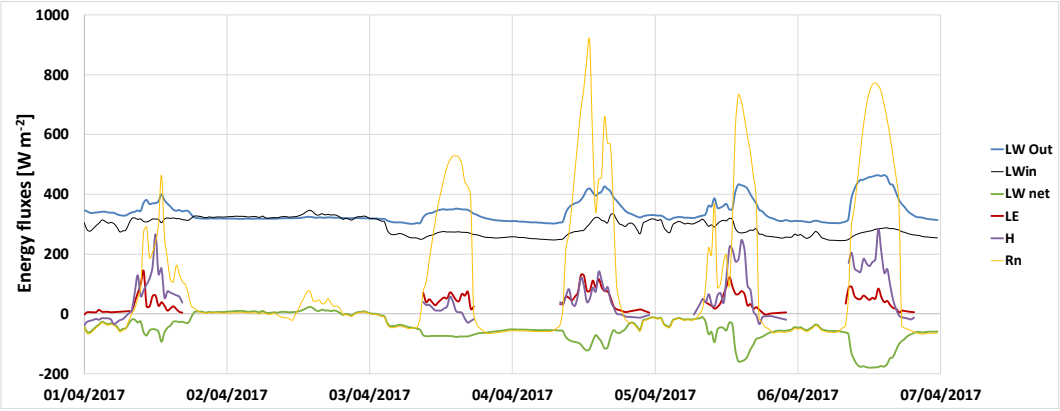

Figure 8.6. Incoming and outgoing longwave radiation, latent and sensible heat fluxes and net radiation for the snowfall Event in February 2015. The outgoing longwave radiation (negative) has the positive sign for comparison.

During nighttime, the turbulent fluxes are not able to compensate the negative net radiation (that is, the longwave losses, since the shortwave radiation is either non-existent or negligible). The nighttime net longwave radiation oscillates between -50 and +10 W m^{-2}, hence the losses are limited, if compared to daytime hours. The outgoing longwave radiation is almost constant throughout the events, but the daily cycle amplitude increases when the snow cover vanishes. The incoming longwave radiation is usually between 50 and 100 W m^{-2} lower than OLR. Hence, the net LW radiation is negative and on the first sunny day after the snowfall the net LW radiation is already negative, with more negative peaks the following

days. At Cogne, the net longwave radiation has negative average values (-57.1, -34.1 and -49.1 W m^{-2} for February 2015, March 2015 and April 2017).

At the Nivolet site, the longwave radiation (Figure 8.7) is also high, especially at night and during cloudy sky as at the other site, and turbulent fluxes do not seem to balance the usually negative net longwave radiation during nighttime, while they outreach it during daytime hours.

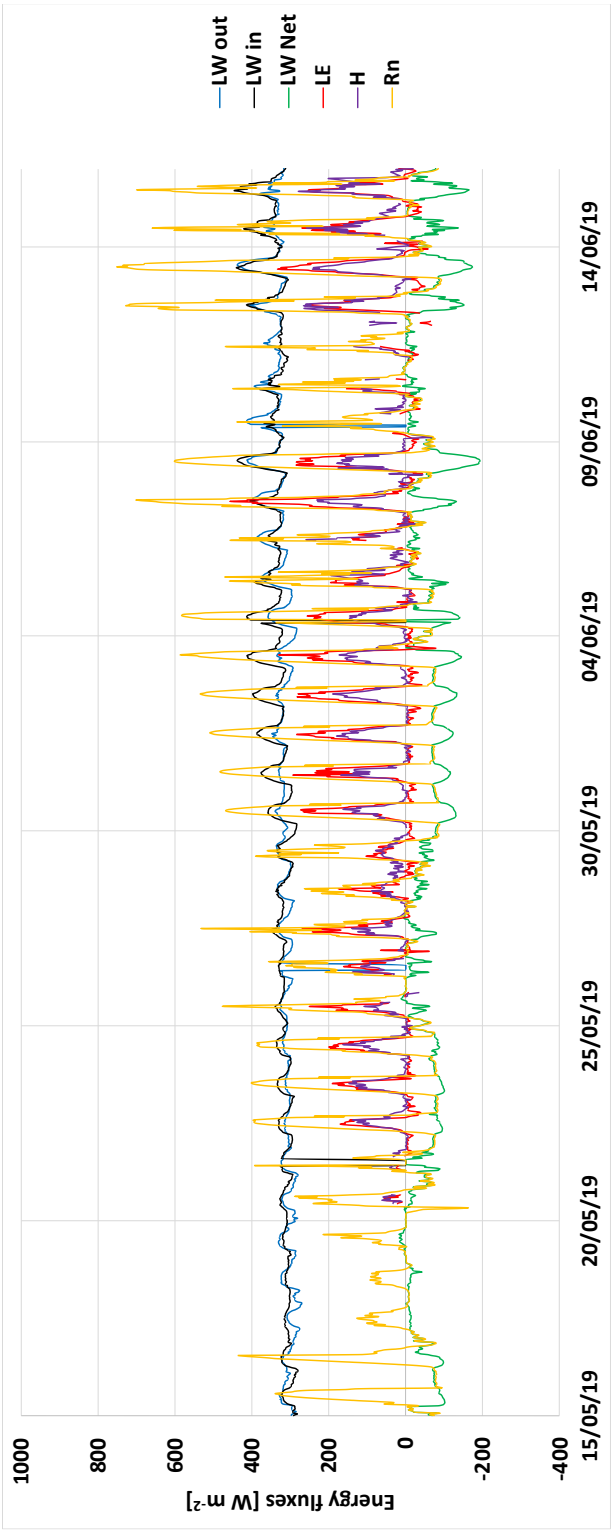

Figure 8.7. Longwave outgoing radiation, net longwave radiation, turbulent fluxes and net radiation.

Although the site has a less complex morphology than the Cogne site, the incoming longwave radiation plays a similar role at the two sites. The net longwave radiation measured at Nivolet shows values close to those measured at the Cogne site (the average value is – 51 W m^{-2}). This suggests that the system made of ground plus snowpack loses energy and that the two sites show quite similar behaviours of the longwave radiation (both incoming and outgoing).

At the two sites, very often net longwave radiation can reach down to -200 W m^{-2}, especially during daytime hours and when the snowpack is no more complete. Indeed, with a complete snow cover, lower negative values occur, likely because the snowpack absorbs more longwave radiation than bare soil or than the canopy.

The incoming longwave radiation can be as important as - or greater than - the shortwave radiation in cloudy days (Figure 8.8). Sometimes, *LWin* can be more than one time *SWin* also during daytime hours, when the sky is covered by clouds (Figure 8.8, 16-17th March 2015 and 2nd April 2017). During central hours of the day (between 9:00 and 15:00), the incoming longwave radiation oscillates between 20 and 50% of *SWin* at Cogne, whereas at Nivolet (Figure 8.9), this ratio is always greater than 30% and at the beginning of June it can reach up to 40% of *SWin* at midday. This can also (but not only) be explained by the different periods in the year chosen for the two sites.

In transition hours, the incoming longwave radiation can be more than 100 times the incoming shortwave radiation, but this is trivial, since the solar forcing is low (not shown in Figure 8.8 and Figure 8.9). At Nivolet site, the outcomes are similar to Cogne. The importance of incoming longwave radiation is enhanced with respect to flat sites, because the Cogne site is affected also by the longwave radiation reflected from the surrounding slopes, in agreement with Sicart et al. (2006).

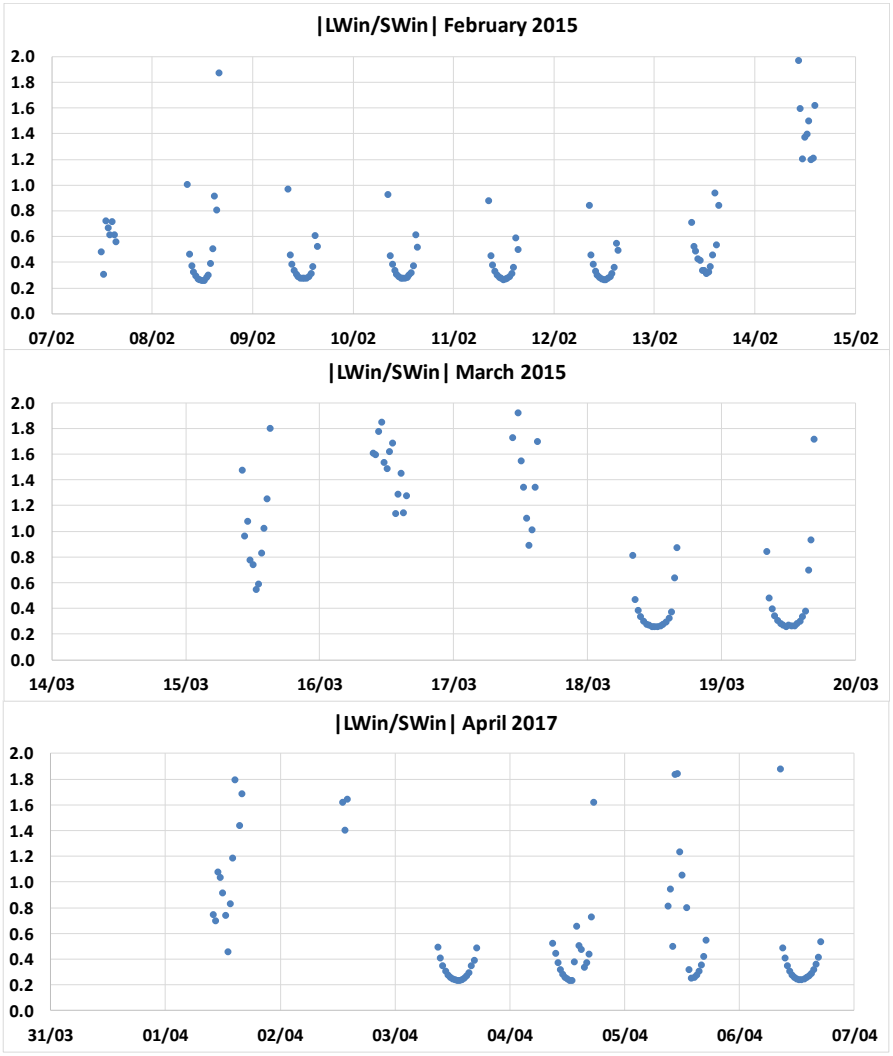

Figure 8.8. LW_{in}/SW_{in} ratio in three monitored events at Cogne site.

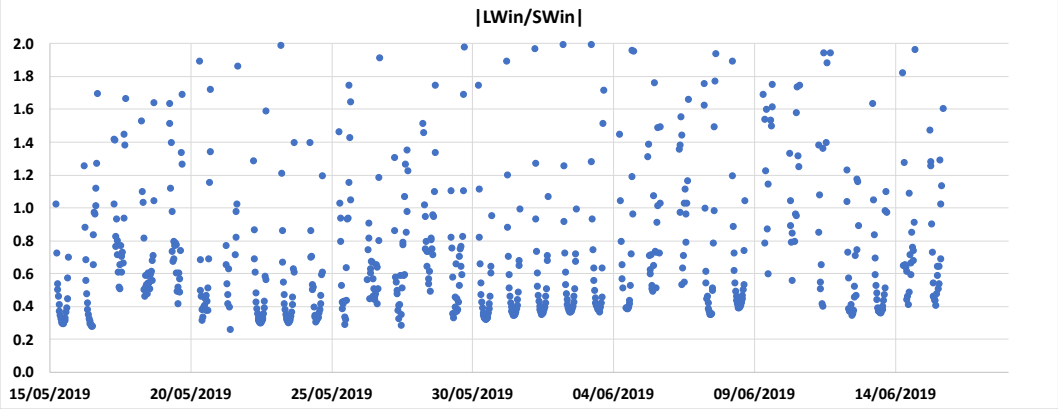

Figure 8.9. Incoming longwave/shortwave radiation ratiofor the 2019 melting season at Nivolet.

8.3.3 Relation between energy balance residuals and snowmelt

From a theoretical point of view (Eq. 8.1), the variation of snowpack internal energy should be calculated as the residual from all the other terms of Eq. 8.5a. However, in practice, there are high uncertainties in the canopy storage (within the shrubs) estimate, in internal energy change evaluation, and in the calculation of turbulent fluxes, which are usually underestimated (e.g. Lee, Massman and Law, 2004). Hence, only a variable part of the energy imbalance can be explained by the estimated energy required for snowmelt.

Usually, efforts are made to compute directly the internal energy change of snow, which includes the melting (phase transition) term and the term associated with the snowpack temperature gradient (e.g. Armstrong and Brun, 2008).

At Cogne, the first term, also called Q_{melt} in Eq. 8.5b, was evaluated using the soil water increase measured by the TDR probe, starting from the consideration that the energy required to melt the snow can be converted into equivalent millimetres of water. This choice potentially allows the estimate of snowmelt when continuous snow density and snow depth measures are not available. Other studies (e.g. Helgason and Pomeroy, 2012; Sexstone et al., 2016) focus on the snowpack temperature change because at their site little or no melting/refreezing occurred. This assumption is not valid at Cogne.

Figure 8.10 shows the fraction of explained residuals, that is, how much Q_{melt} explains δ. This fraction is always below 100%, with the exception of November 2012 (between 10th and 17th November). The percentage of explained residuals increases the first sunny day immediately after the snowfall and, mainly, when the shortwave radiation increases, as in February 2015 or in March 2015. High explanation percentages are found in October 2010, with 55%; event from 1st to 3rd November 2012 (46%); April 2012 (62%); March 2015 (79%); event April 2017 (53%). In events of 4th – 7th March 2011 and 15th – 21st March 2015, the fraction of explained residuals is below 40%. The percentage falls below 10% in the event 7 (February 2015) mainly because of frozen soil which does not allow a reliable measure of percolated water in the soil given by the TDR probes.

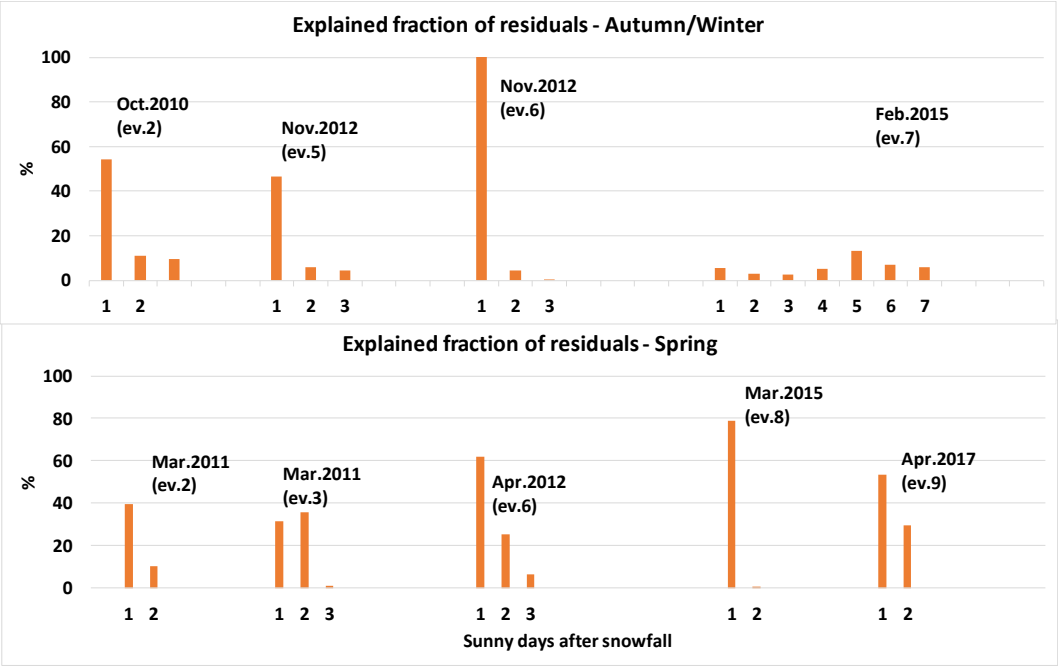

Figure 8.10. Estimated fraction of explained energy residuals by snowmelt.

8.3.4 Water balance

In Table 8.4 and in Figures 8.11 to 8.19 the water balance at the end of each snowmelt period is illustrated. For completeness, the figures illustrate the water balance over each event, also in the days beyond the identified day and time of closure (when the soil water content begins to decrease monotonically, soil temperature has a wide daily range and albedo is low. The purpose is to show the small soil water content increases occurring after the snow has almost entirely vanished, as it will be discussed later. Table 8.4 illustrates also the events where the sublimation term more nearly balanced the SWE a few days before the supposed ending of the event.

In three cases the residuals are higher than 2 mm, an arbitrary threshold. This occurs in events of March 2015 and April 2017. The sign of water balance residuals is positive. The negative residual (-2.7 mm) in February 2015 is the only significantly negative one. It is caused instead by frozen soil (soil temperature around 0 on average, as shown in Table 8.1) that does not allow a rapid water infiltration in the soil. Hence, the transient is slow, and the water balance is fulfilled only if more than 8 days are considered. However, this choice was not possible, since a new snowfall event occurred at the end of the 8th day (14th February 2015).

The results show a good closure of the balance, with low residuals. This suggests that, for the analysed event (eventually excluding the events with a constantly frozen soil), the snowmelt can be approximated with soil water storage increase detected by time domain reflectometry soil moisture probes.

As illustrated in Table 8.5, the sublimation accounts for a variable contribution on snow water equivalent. The table shows the contributions of both snowmelt and sublimation terms in a reduced range of days, when the water balance is nearest to closure.

In Autumn and Winter events, sublimation contribution on SWE percentages range from 2.3% (event 6, 12th -15th November 2012) to 34.2% (7th – 14th February 2015). In Spring events, contributions oscillate between 5.6% (15th – 19th March 2015) and 19.3% (15th – 21st March 2011). In all the events, the snowmelt is the most important term of the balance, with more than 70% of contribution. The only exception is found in February 2015 and it is likely due to frozen soil.

Table 8.4. Water balance for each snowfall event. The values in parentheses represent, when occurring, the sums over a shorter temporal range (reduced number of days), when the (SWE) water balance reaches the closest point to closure (at the end of the last 24h period).

	Ev.	**Dates**	**SWC (mm)**	**sublimation + θ increase (mm)**	**Cum. energy residuals (mm)**	**Day of water balance closure**
Autumn Winter	**1**	25/10-28/10/10	12.5	14.2 (12.8)	43.7 (30.4)	27/10
	5	31/10-03/11/12	7.2	8.2 (7.0)	38.8 (22.4)	2/11
	6	10/11-15/11/12	28.0	33.5 (28.2)	45.7 (16.0)	12/11
	7	7/02-14/02/15	14.6	11.9	101.0	14/02
Spring	**2**	3/03-07/03/11	16.5	17.2 (16.8)	82.1 (66.8)	7/03 morning
	3	15/03-21/03/11	27.5	28.0	96.2	21/03
	4	14/04-20/04/12	25.0	26.1	98.2	20/04
	8	15/03-20/03/15	16.1	21.0 (20.0)	53.6 (29.6)	18/03
	9	01/04-06/04/17	21.0	25.6 (23.6)	118.4 (60.8)	4/04

Table 8.5. Snow water equivalent (SWE), cumulative snowmelt and sublimation and their relative contribution for each event. The contributions are shown for the period from the snowfall end until the supposed water balance closure.

Ev.	Dates	SWE (mm)	cum. snowmelt (mm)	cum. sublimation (mm)	% snowmelt	% sublimation
1	26-27/10/10	12.5	11.4	1.5	91.2	12.0
5	01-02/11/12	7.2	5.5	1.5	76.4	20.8
6	12-13/11/12	28.0	27.5	0.6	98.3	2.3
7	07-14/02/15	14.6	6.9	5.0	47.3	34.2
2	03-07/03/11	16.5	13.8	3.0	83.6	18.2
3	15-21/03/11	27.5	23.2	5.3	84.4	19.3
4	14-20/04/12	25.0	20.2	5.0	80.8	20.0
8	15-19/03/15	16.1	19.2	1.8	119.2	11.1
9	02-04/04/17	21.0	22.1	1.5	105.7	7.1

A visual inspection of the water balance and of the total energy balance residuals (in millimetres) can be done for each event, as follows. The energy balance residuals were converted in equivalent millimetres of melted snow with the formula give in Eq. 9.7.

$$\delta(mm) = \delta(W\ m^{-2})1800\ s\frac{1}{\lambda_{fus}} \tag{9.7}$$

where λ_{fus}= 334000 J kg^{-1}. Eq. 8.7, yields residuals expressed in kg m^{-2} (or equivalent millimetres of water). For the following analysis, only positive residuals were considered. Hence, in some periods the cumulative value can remain constant.

Autumn and Winter events

The Autumn case represented in Figure 8.11 (24th – 28th October 2010) shows that most of the snow melts during the first day, which is characterised by further residuals despite a lower net radiation. The highest melting rate occurred the day after the last snowfall. The following days show higher net radiation and lower

residuals: it is consistent with soil portions progressively uncovered by snow (confirmed also by both the sensible heat flux and the soil surface temperature diurnal progressive increasing). However, the evolution of the soil water content emphasizes the existence of patchy snow that melts in the following days. During the melting period the topsoil temperature remain always over the freezing conditions, while the soil surface temperature and the air temperature alternate freezing (nighttime) and thawing (daytime) conditions. The water balance is almost closed.

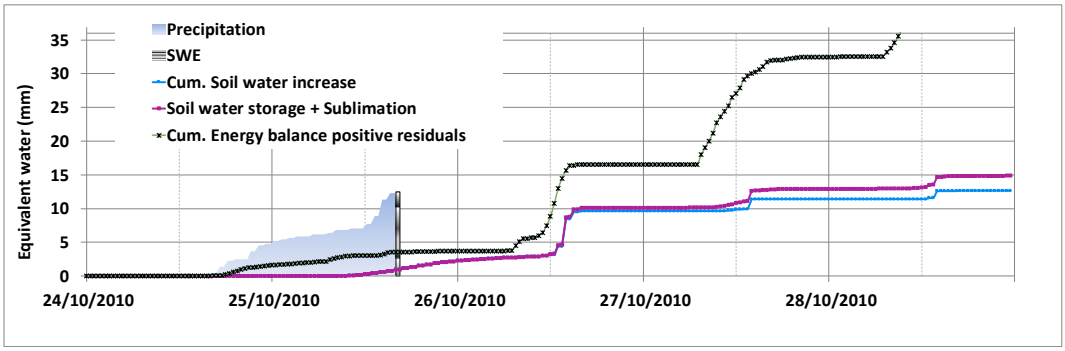

Figure 8.11. Snow water equivalent, cumulative measured soil water increase and soil water increase + sublimation and cumulative residuals of energy balance equation for the Event in October 2010.

The Autumn case in Figure 8.12 highlights that the balance is almost closed, and that the residuals of energy balance sharply increase on 1st November. Already on 1st November, most of the snow cover melted, because the soil temperature diurnal cycle experienced an enhanced amplitude (Figure E2, panel *b*). The cumulative energy residuals are high the first day after the snowfall.

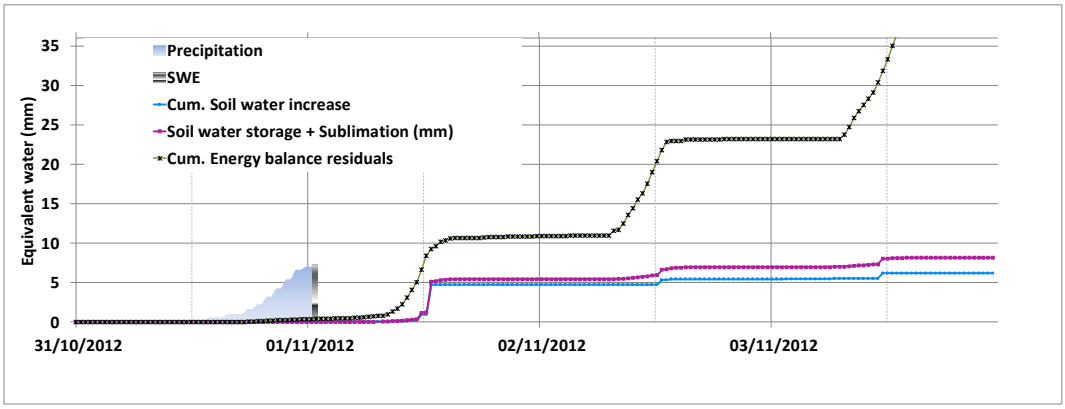

Figure 8.12. Snow water equivalent, cumulative measured soil water increase and soil water increase + sublimation and cumulative residuals of energy balance equation for the event 31st October – 20th March 2011.

Another Autumn case (November 2012, Figure 8.13) shows that the water balance is closed, but the cumulative residuals of energy imbalance are lower than SWE and soil water content increase, especially the first sunny day after the snowfall (12 November 2012). This phenomenon can be explained by rain on snow

on 11th November, as it will also be discussed in the Discussion section. In addition, the wind speed is not characterised by daytime peaks as in other cases (Figure E3), and the friction velocity does remains low (below 0.3 m s^{-1}), hence there could be a higher underestimation of turbulent fluxes. The greatest contribution is given by water percolation.

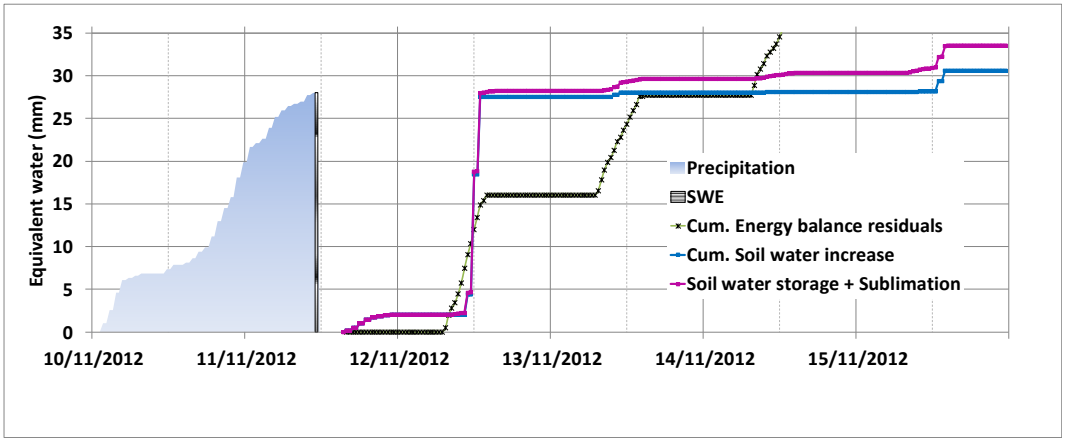

Figure 8.13. Snow water equivalent, cumulative measured soil water increase and soil water increase + sublimation and cumulative residuals of energy balance equation for the event 10th November – 13th November 2012.

The Winter event in February 2015 (Figure 8.14) shows that the water balance is not fully closed. The loss of information can be explained by the single-point measures and by the frozen soil which, as already mentioned, slows the water percolation in the soil. The cumulative energy residuals (in millimetres) show a steep growth the days after the snowfall.

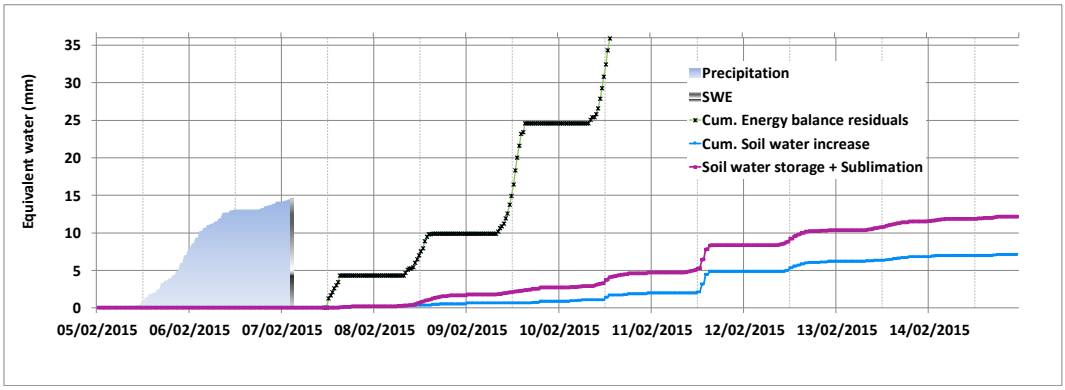

Figure 8.14. Snow water equivalent, cumulative measured soil water increase and soil water increase + sublimation and cumulative residuals of energy balance equation for the event in from 5th to 14th February 2015.

Spring events

The Spring event illustrated in Figure 8.15 highlights that the residuals of the energy balance can increase sharply the first sunny day or even before the end of

the snowfall. Besides, the turbulent fluxes are low until 4th March, when the turbulent fluxes data are complete along the daytime hours. However, until 5th March, the main contribution is given by snowmelt. Then, the sublimation term begins to increase, and it actively contributes to the water balance. The cumulative energy residuals are characterised by a steep increase even before the end of the snowfall. This is mainly driven by positive net radiation values also in the night between 3rd and 4th March, as also noticeable in Figure E5.

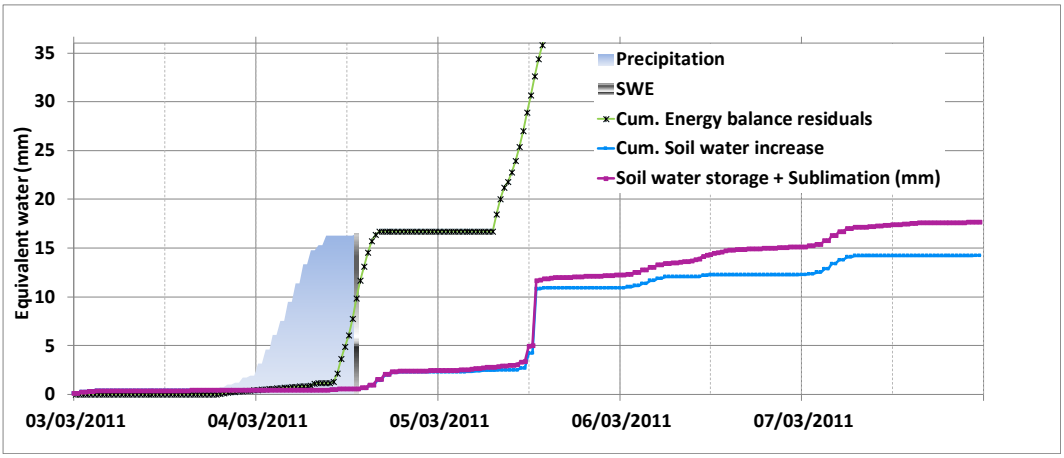

Figure 8.15. Snow water equivalent, cumulative measured soil water increase and soil water increase + sublimation and cumulative residuals of energy balance equation for the event 4th – 7th March 2011.

The Spring event, represented in Figure 8.16, shows that most of the snow melts during the first sunny day (18/03/2011 - characterised by high energy residuals), but part of the snowmelt occurred both during the snowfall, and during the first day (cloudy day) after the snowfall. This phenomenon can be mainly related three factors: the soil temperature with values higher than 0°C (non-freezing conditions, Figure E6, panel *b*); the presence of continuity at the soil-snow interface; longwave radiation contribution especially in cloudy conditions. In March 2011 (event 3), as in other cases, the days following the snowfall highlight higher net radiation but lower residuals, and the existence of patchy snow conditions with the residual snow slowly melting. During the melting period the topsoil temperature remain always over the freezing conditions, while the soil surface temperature and the air temperature alternate freezing (night-time) and thawing (daytime) conditions.

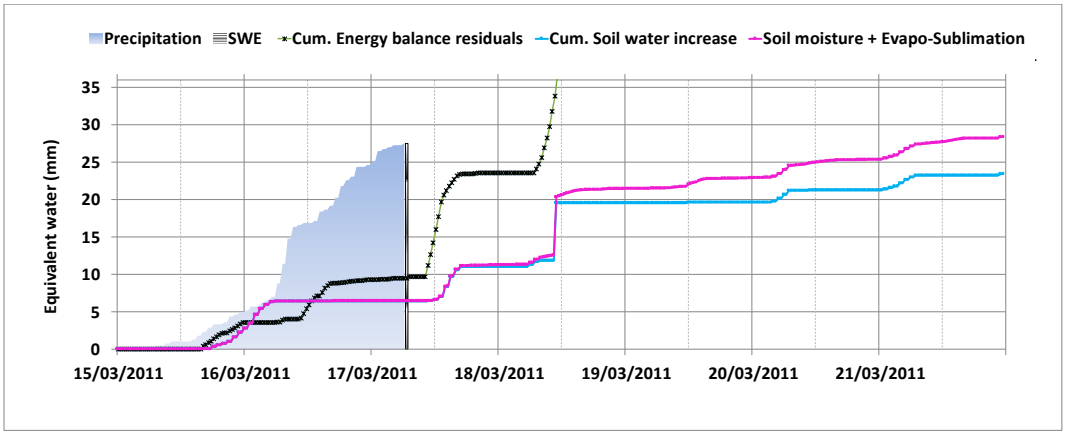

Figure 8.16. Snow water equivalent, cumulative measured soil water increase and soil water increase + sublimation and cumulative residuals of energy balance equation for the event 15th March – 20th March 2011.

The April 2012 event (Figure 8.17) was characterised by two snowfalls. The first one occurred during the night of 14th April. During the daytime hours of 14th April, part of this snow cover melted and sublimated. Hence, the residuals of the energy balance begin to increase that day. The following night, a new snowfall occurred, and it continued until the early afternoon of 15th April. That day, the turbulent fluxes were not available, but they can be assumed low since the air temperature and radiative forcing were low. On the contrary, the soil temperature was above 0°C and the snow melted. This process was captured by the TDR (time domain reflectometry) soil water probes. The melting process can be assumed as the main contribution to water balance.

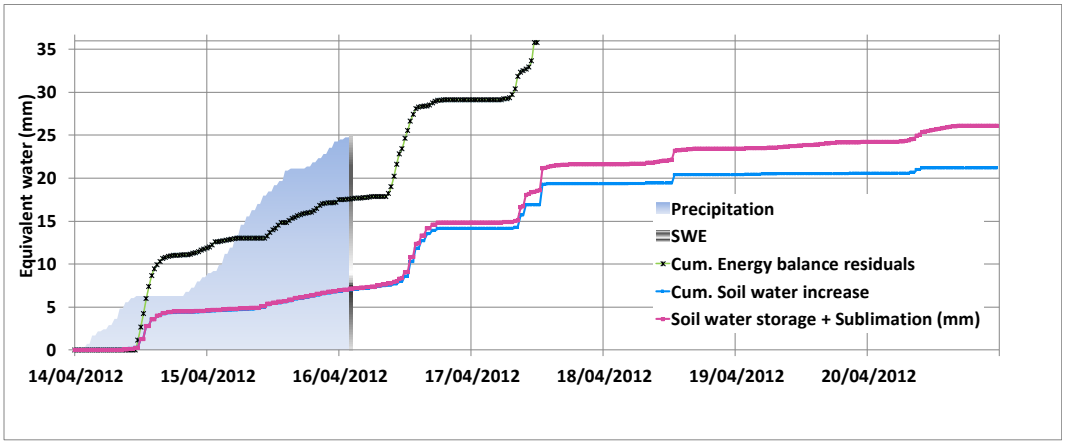

Figure 8.17. Snow water equivalent, cumulative measured soil water increase and soil water increase + sublimation and cumulative residuals of energy balance equation for the event 14th – 20th April 2012.

The March 2015 event (Figure 8.18) shows that, until the first sunny day after the snowfall (18th March), the contribution of sublimation is low, and also the soil moisture increase is low. The soil and surface temperatures are at near 0°C (Figure E8), hence a very limited snowmelt and water percolation) occur. The residuals are,

however, still high well before the clear sky day, but the little explanatory power of energy required to melt the snow compared to the energy residuals was proven to be low.

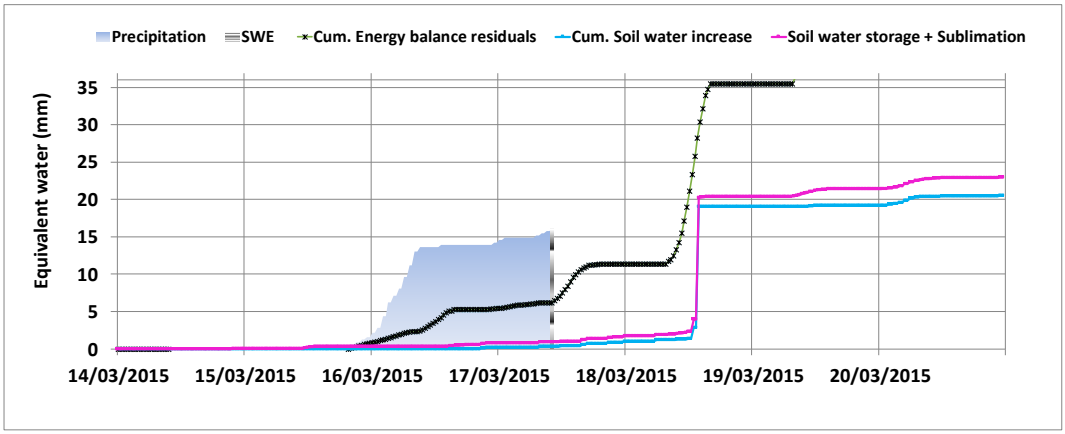

Figure 8.18. Snow water equivalent, cumulative measured soil water increase and soil water increase + sublimation and cumulative residuals of energy balance equation for the event 15th march – 19th March 2015.

The April 2017 Spring event (Figure 8.19), was characterised by an intense snowmelt the first sunny day. So, almost all the snow had melted on 4th April, when the soil and surface temperatures begin to show an increased amplitude of the diurnal cycle, and the energy residuals were already really high, while the water balance was almost closed. The soil water storage increases already during the last precipitation period, and in the days between 3rd and 4th April.

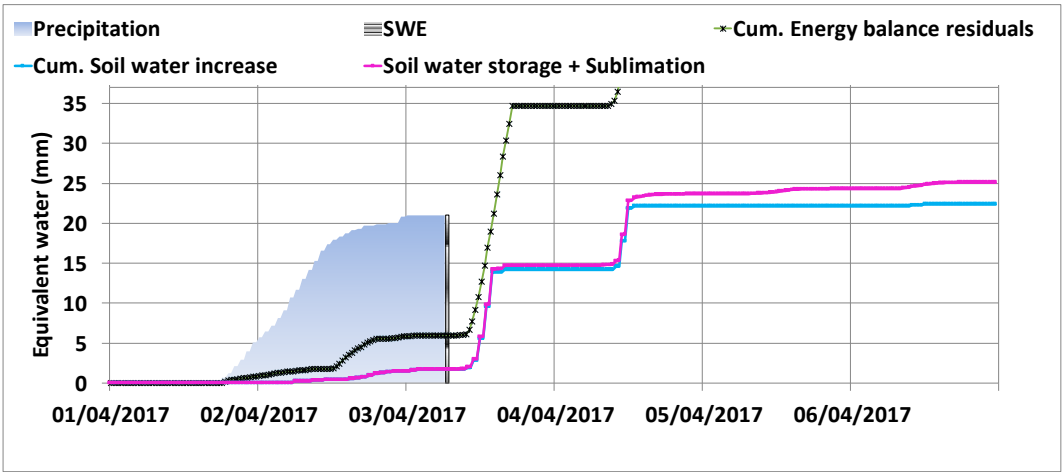

Figure 8.19. Snow water equivalent, cumulative measured soil water increase and soil water increase + sublimation and cumulative residuals of energy balance equation for the event from 1st to 6th April 2017.

8.4 Discussion of results

8.4.1 Micrometeorological and soil conditions

The fast snowmelt events identified at Cogne show high net radiation peaks (greater than 700 W m^{-2} as on 18th March 2011, Figure E6), higher than at other sites, where maximum values are around or less 400 W m^{-2} (Datt et al., 2008 – Himalayan mountain site ; Pomeroy et al., 2006 – tundra shrubland; Chen et al., 2011 – snow-covered meadow). This occurs because of the site aspect (South), and it gives the maximum contribution to the snowmelt intensity. The ground heat flux at the soil surface, G_0 has daily averages oscillating between -5 W m^{-2} and +11.5 W m^{-2}. Half-hourly maximum values can be greater than 150 W m^{-2} (19th March 2011, Figure 8.9). Both Rn and G_0 daily values increase as soon as the snowpack melts (Table 8.3). Daily averages of G_0 are within the range found by Chen et al. (2011), but the maximum, daily average values are lower at Cogne (maximum daily averages are about +12 W m^{-2}, lower if compared to about 40 W m^{-2} in the aforementioned paper).

Turbulent fluxes can reach values greater than some other studies. Half-hourly *H* maximum values can be greater than 300 W m^{-2}, while *LE* values can be up to 250 W m^{-2} (Figures B1-B9). The values are comparable with previous findings (Pomeroy et al., 2006; Chen et al., 2011), but they are higher than the findings of Datt et al. (2008), where the turbulent fluxes are included between -20 and +30 W m^{-2}. Low values were also found by Helgason and Pomeroy (2012) at their flat, snow-covered site. It might be argued that the Cogne site aspect make easier to have high radiative forcing. Hence, this partially compensates the flux underestimation due to non-ideal terrain and turbulent fluxes can be comparable with several sites having less complex terrains, and with stronger winds (Reba et al., 2012, measured an average of 5 m s^{-1} at their exposed site, while at Cogne, the average wind speed is 1 m s^{-1}).

Considering all the data (daytime and nighttime), the daily average *LE* flux in each event is within the range between 6 W m^{-2} (17th March 2015) and 86 W m^{-2} (10th February 2015). These values are generally within the range of previous studies (Datt et al., 2008; Chen et al., 2011). However, no negative value is found at Cogne, contrarily to Datt et al. (which found negative values in colder conditions in January).

The daily average *H* flux oscillates between -12 W m^{-2} (5th March 2011) and 110 W m^{-2} (6th April 2017, when the snow has melted). Hence, daily *H* flux can be occasionally negative (when the solar forcing is low because of cloudy sky), with values comparable to those found by Helgason and Pomeroy (2012), but particularly sunny days when most of the snow has melted, show values higher than the maximum daily averages found by Datt et al. (2008) and Chen et al. (2011). At

Cogne, the snow melting and the snow melted phases are very fast (few days). The first sunny day after the snowfall, *LE* increases due to sublimation process. Increases of *H* are also found, and in six over nine events (four in Spring – on 7th March and 21st March 2011; 20th April 2012; 19th March 2015 and 6th April 2017 - and two in Autumn – 3rd November and 15th November 2012), at the end of the event $H > LE$. Besides, the last days of the events the turbulent fluxes are always greater than 20 W m^{-2}. The findings of Datt et al. (2008) revealed instead fluxes close to 0 at the end of the snowmelt season, whereas according to Chen et al. (2011), in the snow melting and snow melted periods, *LE* increases up to more than 100 W m^{-2} while *H* tends to decrease. It has to be highlighted that, at Cogne, the snowmelt process is very fast, there is not a unique cold season snowpack and a maximum of 7 days is considered for each event at Cogne. Hence, the temporal variability is different from studies where long-lasting snow exists.

The average values of energy fluxes *Rn, G+S, H* and *LE* are shown in Table 8.6 on, respectively, the whole Autumn/Winter, Spring and overall periods (that is, considering all the days of all the events). *Rn* averages are close to the value found by Datt et al. (2011), which was 83 W m^{-2}. The term *G+S* is instead within the range of the findings of Chen et al. (2011), that is around 0 W m^{-2}.

The average turbulent fluxes for each of the mentioned periods are higher than the findings of a mountain, snow-covered site (Datt et al., 2008 found average turbulent fluxes near 0 in the whole local snowmelt period) but similar to the findings of Chen et al. (2011). Plus, *LE* averages are also higher than values reported by Plüss and Mazzoni (1994) with -4 W m^{-2} at a high Alpine site, on 16 days. Few differences can be noticed between Autumn/Winter and Spring events for *LE* and *H*.

Table 8.6. Daily averages of energy fluxes for Autumn/Winter, Spring and all the events at Cogne.

LE (W m^{-2})			H (W m^{-2})			Rn (W m^{-2})			G_0=G+S (W m^{-2})		
A/W	Spring	All	A/W	Spring	All	A/W	Spring	All	A/W	Spring	All
45.1	35.8	39.8	36.0	33.1	34.3	68	101	87	-2.2	0.2	-0.7

Other variables which define the environmental conditions are the surface, air and soil temperatures, as well as the initial soil water content (just before the snowfall occurs).

The daily average surface and air temperatures measured at Cogne are within the range of mountain sites in the cold season (from -4°C to 3°C; from -4°C to 6°C, Table 8.2), comparable with the values found in other studies (Datt et al. 2008; Helgason and Pomeroy, 2012).

The mean soil temperature daily values oscillate from 0°C (7th February 2015) to 7°C (3rd November 2012). Very frequently, values greater than 0°C can be found, and peaks of 4 up to 7°C (such as on 3rd November 2012) are common. Besides, during the snowmelt process the average soil temperatures are usually greater than 0°C. Only in February 2015 event we find average values constantly below 0°C. The average soil temperature over all the events, is 3.6°C, far greater than negative temperatures found by Chen et al. (2011).
The average initial soil water content is 0.15 m^3 m^{-3}, with higher values in Spring with respect to Autumn and Winter, as will be discussed in Section 8.4.3.

8.4.2 Longwave radiation

The longwave radiation contributes to the snowmelt. *LWin* and *LWout* values at Cogne and Nivolet ranged between 200 and 450 W m^{-2}, with scarce differences between seasons and sites, as illustrated in Figures from 8.4 to 8.7. in Section 8.3.2. The LW values are in agreement with Sicart et al. (2006) and Helgason and Pomeroy (2012), which analysed, respectively, two snowmelt seasons (April – May) and one Winter month (February). The average net longwave (on all the hours of all the events, and on transition hours), the average shortwave radiation (on all the hours of all the events), and the average incoming longwave radiation in transition hours are illustrated in Table 8.7.

The net longwave radiation values are in agreement with the ones reported by Datt et al. (2008) and Helgason and Pomeroy (2012), which report, respectively, -33 W m^{-2} in the cold season from 13 January to 13 April 2005 and -30.8 W m^{-2} in February 2007. Both the studies were done on almost terrains covered by snow. During transition hours (i.e. between 5:00 and 8:00 and 16:00 to 20:00), the average longwave incoming radiation (*LWin*), represents a non-negligible contribution, confirming that longwave irradiance can be important in the local energy balance over snow, as noticed by Plüss and Ohmura (1996). However, the upward (outgoing) longwave radiation is, most of the time, higher than the downward (incoming) longwave radiation flux at Cogne and Nivolet. Hence, the average net longwave radiation, also in transition hours, is negative.

During nighttime, the turbulent fluxes were low and, most of the time, they did not balance longwave losses (Table 8.7). The role of longwave radiation on snowmelt occurs rarely and only with cloudy sky conditions (Figures 8.4-8.7; Figures 8.8 and 8.9).

Table 8.7. Average net longwave radiation (overall, in transition hours and nighttime), average incoming longwave radiation in transition hours, average net shortwave radiation and average sums of H + LE fluxes for three events at Cogne and for the snowmelt period at Nivolet. Negative sign implies heat loss from the snowpack.

	Cogne			Nivolet
	7-14/02/2015	16-19/03/2015	2-6/04/2017	15th May – 15th June 2019
Net LW (W m^{-2})	-57.1	-34.3	-52.7	-48.7
Net LW (W m^{-2}) (transition hours)	-46.6	-28.1	-46.1	-46.2
Net LW nighttime	-17.0	-12.6	-39.8	-46.6
LWin (W m^{-2}) (transition hours)	249.3	287.9	278.1	299.9
Net SW (W m^{-2})	111.0	123.3	169.9	186.1
H+LE nighttime	~0	-7.8	+4.6	+6.3

The findings at both Cogne and Nivolet sites highlighted that the longwave incoming radiation is always at least 20% of shortwave radiation in the analysed events at Cogne and also within the 2019 snowmelt period at Nivolet (Figures 8.8 and 8.9), with high percentages, beyond 60-70% on cloudy days, despite the average net shortwave radiation is always beyond +100 W m^{-2} (Table 8.7). This is another confirmation of the importance of longwave radiation on snowmelt.

8.4.3 Explained energy residuals and snowmelt

A highly variable part of energy imbalance can be explained by the energy required for snowmelt. The ratio $R_e = Q_{melt}/\delta$ illustrates how much the measured snowmelt (by means of time-domain reflectometry soil moisture probe) can explain the total energy residuals.

Typically, for a South-facing site such as Cogne, the maximum value of R_e is found on the first sunny day after the snowfall. R_e has a high variability among

events (from less than 10% to about 80% of total energy residuals). The ratio is also plotted as a function of net radiation, longwave radiation, soil and air temperature, SWE and the soil water content before infiltration occurs. This allows exploring the possible causes of this variability (Figure 8.20, with R_e of the first sunny day after the snowfall).

Let us group again the events into two categories: Autumn and Winter events and Spring events. For each category - longwave radiation excluded - the average value of the variables shown in Figure 8.20 is computed. In Spring events, the surface temperature (T_{surf}, Figure 8.20, panel *b*), air temperature (T_{air} Figure 8.20, panel *c*), net radiation (R_n Figure 8.20, panel *e*), incoming longwave radiation (*LWin*, Figure 8.20, panel *f*) and snow water equivalent (SWE Figure 8.20, panel *g*) are higher than in Autumn/Winter events. In particular, respectively, the following clear differences are found: 54 W m^{-2}, 30 W m^{-2}, around 2°C for air and surface temperature, 5.7 mm and 0.04 m^3m^{-3}.

An opposite tendency is found for soil temperature (T_{soil}, Figure 8.20, panel *a*) and relative humidity (RH, Figure 8.20, panel *d*). T_{soil} and RH are, respectively, around 1°C and 8% lower in Spring events than in Autumn/Winter events. Besides, single values of net radiation, longwave incoming radiation, air temperature, SWE and initial soil water content in Spring events reach higher values if compared to Autumn/Winter events. In addition, R_e increases only with RH and longwave radiation, whereas no clear dependence exists with the other variables. The lowest R_e, also visible in Figure 8.20 (it is the lowest point in all the panels), is the one related to event 7 (February 2015) and it can be explained considering that the soil is almost frozen (as shown in Figure E4). Little snowmelt is detected, day by day, by the TDR probe. However, high energy residuals exist. In this case, likely, the TDR probe did not operate in optimal conditions due to low soil temperatures and a higher number of days is required to observe the melted snow percolation.
In the two events in March 2011, the relatively low explanatory power could be due to TDR probe not measuring all the percolation, despite relatively high soil temperature which potentially allow the water infiltration.

Besides, in most of events (all Autumn and Winter events plus the event 3rd – 7th March 2011), the friction velocity is always low (around or below 0.2 m s^{-1}). This might be a further source of turbulent fluxes underestimation due to advection. However, no direct relationship on cumulative residuals was found (Figure 8.21).

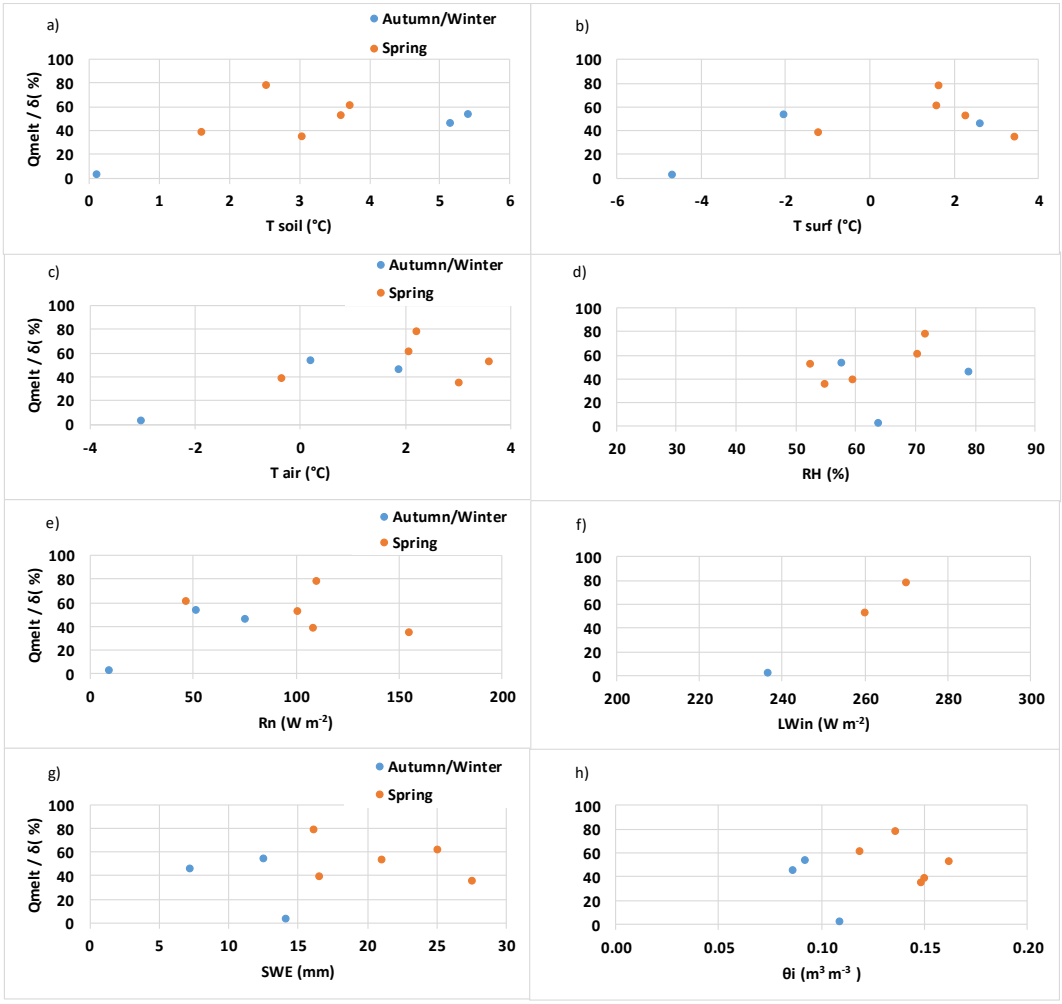

Figure 8.20. Ratio Q_{melt}/δ of the first sunny day of snowmelt in each event versus meteorological and soil variables. Panel a): soil temperature; panel b):ground (or snow, when applicable) surface temperature; panel c): air temperature; panel d): relative humidity; panel e): net radiation; panel f): longwave incoming (downward) radiation; panel g): snow water equivalent; panel h): soil water content before snowmelt occurrence.

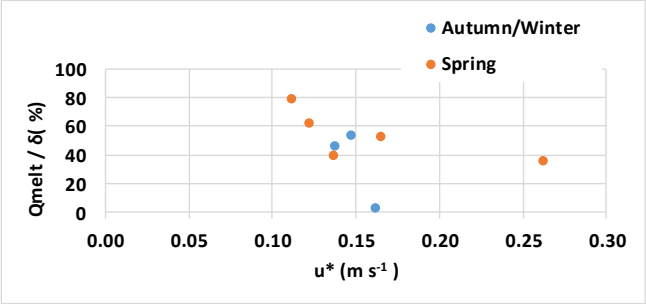

Figure 8.21. Ratio Q_{melt}/δ versus friction velocity for the first sunny day of snowmelt in each event.

As can be noticed, the term Q_{melt}/δ does not fully explain the melting. This suggests that there are other additional contributions to the unexplained percentage of R_e in all the events. These contributions may include the impossibility to correctly evaluate the heat stored or released within the snowpack and the heat stored within the shrubs and in the grass (also due to respiration, not always negligible, according to Eshonkulov et al., 2019a). The heat storage terms might change in different seasons and may not be negligible (especially the term related to heat stored under the shrubs, which have an average height of 1 m, and under the compacted tall grass). Plus, advection may have an impact on the turbulent fluxes underestimation.

The soil contribution (included in computations) instead might not be so high. The snowpack stands as an insulating layer that prevents the soil to absorb new energy; also, the presence of a discontinuity in the snow-soil contact can strongly reduce any exchange flux and diurnal variation of soil and surface temperatures. This discontinuity could be mainly caused by physical obstacles (e.g. residues of vegetation). The above-mentioned insulation layer is dynamic over time and space because the residual vegetation layer modifies its shape from Autumn to Spring due to snow weight and biological degradation. In Autumn, there is much more insulating air than in Spring. Once that the snow-melt process begins to expose some small portions of the soil surface, some proximity interactions between snowpack and those boundary layers can further accelerate the snowmelt processes (Mott et al., 2013). While the soil heat storage is considered in the computations, the vegetation heat storage is not. However, Wohlfahrt et al. (2016) found summer values mostly within the range $\pm$ 5 W m^{-2} at their mountain site (although no data are available for senescence season). Other minor terms (air heat storage and atmospheric moisture change) can be considered negligible, in cases of eddy covariance set-up installed close to the ground (2-5 m), as noticed by Foken (2008b) and Eshonkulov et al. (2019a).

Also, the rain on snow (during the snowfall) might increase the soil water content measure. In Autumn event 11th – 15th November 2012, the first day after the snowfall is sufficiently sunny, but the soil water increase is much higher than energy balance residuals expressed in millimetres (27.5 mm versus 16.0 mm), and

the main soil water increase occurs during daytime hours. The micrometeorological and soil conditions did not allow any conclusion, since they were comparable with the other events in Autumn. One possible explanation is given by the air temperature. At the beginning of the event, (10th November, 02:00) the temperature was around 1°C, then it rapidly decreased. We can suppose that the event started as rain and then turned to snow. On 10th November between 12:00 and 17:00, and on 11th November between 9:00 and 11:00 (end of the event), the air temperature was above 0°C, with frequent values greater than 0.5°C, up to 2.8°C at 11:00. In the aforementioned periods, precipitation occurred, but it was likely rain. As it was pointed out by Strasser et al. (2008), this might explain why the total snowmelt is greater than SWE is the period 11th – 13th November 2011.

Similar conditions (probable rain on snow) occur also in April 2017, especially on 2nd April, when the measured air temperature is higher than 0.5°C during the daytime precipitation. Sonic temperature value was not considered because of unrealistic values likely due to snow deposition on the anemometer. Hence, the snowmelt started before the end of snowfall. However, the soil water content increase was not very high as in November 2012. This might be explained again by soil temperature, which was about 2°C lower in April 2017, also in the first sunny day.

8.4.4 Water (SWE) balance

As described in Section 8.2.1, the water balance has the snow water equivalent (SWE) as the input. The water storage increase is related to snowmelt, and the sublimation term is the same for the two balances.

In each event at Cogne, the positive residuals of energy imbalance, if cumulated (Table 8.5), tend to sharply increase as soon as either a non-outcast or sunny day occurs. In the second event of November 2012 (Figure 8.13), the residuals for each half-hour period are lower than in the other events. As already discussed, this might be due mainly to soil water content overestimation.

The water balance is nearly closed in all the events, as illustrated in Table 8.5, whereas other studies show a high imbalance (around 180 mm in an Alpine catchment, Strasser et al., 2008; between 70 mm and 327 mm at two Himalayan sites, according to Stigter et al., 2021). The water balance residuals at Cogne range from 0.3 mm (October 2010) to 3.9 mm (April 2017), and the average non-closure of 1.4 mm.

The snowmelt can occur already during the snowfall, as already noticed. This phenomenon is found in events 1 (25th - 28th October 2010, Figure 8.11), 3 (14th – 21th March 2011, Figure 8.15), 4 (April 2012, Figure 8.17) and 9 (1st – 6th April 2017, Figure 8.19), and it is mainly due to high soil temperatures. On 2nd April 2017, the positive net longwave radiation might also partially explain the early snowmelt already during the snowfall.

In the events of October 2010, November 2012 and April 2017, a very fast snowmelt occurs, since the day following the snowfall, most of the snow has vanished and the water balance is nearly closed. In March 2015 event, the radiative forcing is low on the first two days after the snowfall (16th March - 17th March). Hence, the snowmelt is limited, and albedo is almost constant (Figure 8.22). The first sunny day, the snowmelt almost entirely follows the behaviour of the other mentioned events (on 18th March), and the albedo strongly decreases such as in April 2017 (Figure 8.22). The rapid melt is due to high solar radiation and soil temperatures on average greater than 4°C, the first sufficiently sunny day.

The remaining events (March 2011, April 2012 and February 2015) highlight a slower process. This can be partially explained by average soil temperatures below 4°C the first available sunny day. February event shows instead a soil almost frozen (soil temperature always around 0°C). Indeed, the albedo decreases more slowly reaching values below 0.4 only after four days (Figure 8.22, blue line). We can hypothesise that patchy conditions occurred: under the radiometer no snow existed, but in the station surrounding some area still covered by snow existed.

Besides, frequently, during the lasting phase of the snow-melting process, small quantities of patchy snow remain on the slopes (e.g. shaded by bushes and protected from direct sunlight); this situation, connected to the micrometeorological conditions, can persist even after the first day and is confirmed by the small increases in soil water content during the second and third day of the monitored events (Figures 8.11 – 8.19).

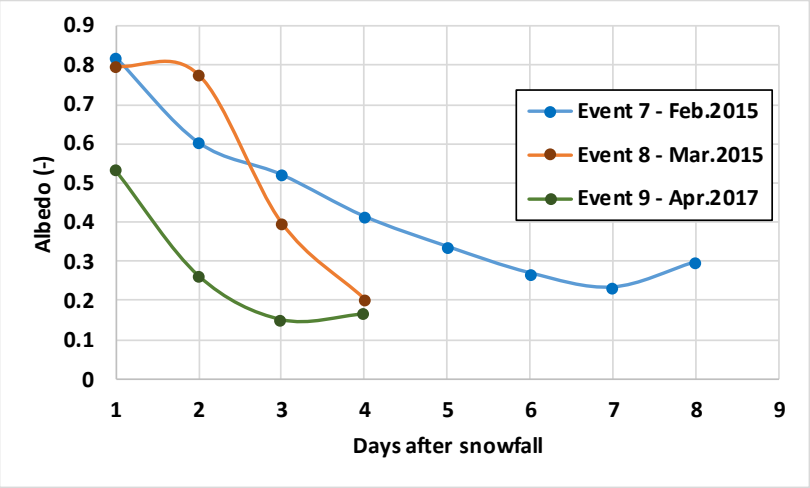

Figure 8.22. Mean daily (daytime) albedo for the events 7, 8 and 9.

Snowmelt and sublimation terms

The values reported in Table 8.5 show that the sublimation term at the Cogne site is important in all the analysed events, and it oscillates between 2% in event 6 (11th November – 15th November 2012) and almost 35% in the event 7 (February 2015).

Snowmelt (indirectly detected as the soil water storage increase) is the most important term in the snow mass balance, with values always beyond 50% and an

average of 87%. These findings are comparable with Strasser et al. (2008), which, analysing an Alpine site with a modelling approach, found that sublimation from ground and canopy accounts for around 20% of snow water equivalent, and snowmelt is the highest term (they found 106% of contribution because of rain on snow). As already discussed, the lowest snowmelt contribution is found when the soil is frozen (event of February 2015). It is worth noting that, at Cogne, the snowmelt contribution is greater than 100% in two events: March 2015 and April 2017. In the first case, the SWE was likely underestimated. In the second case, rain on snow occurred, so the measured soil water increase measured also the infiltrated rain. As already noticed, it was characterised by rain on snow and high soil temperature. The fact that snowmelt contribution is lower than 100%, could be due to either the choice to consider only the first day (when most of the snow melted) or to the spatial variability of the soil moisture measurements. At the event scale, the spatial variability of the soil water content is greater than on a seasonal scale.

The daily average melt rates at Cogne are 5.7, 2.7, 27.5 and 1 mm day^{-1} in Autumn and Winter events. In Spring events, one finds 4.7, 12.6, 3.0, 6.8 and 7.4 mm day^{-1}. No particular differences can be noticed in different seasons, with the exception of event in February 2015 (because of frozen soil).

These values are comparable with the findings of Pomeroy et al. (2006) at their sites on tundra shrubland between 1995 and 2001 (average values range from 2.7 to 21.2 mm day^{-1}, yearly values).

Considering all the events, the daily mean sublimation values (0.77 mm day^{-1} - overall; 0.71 mm day^{-1} in Autumn/Winter events; 0.81 mm day^{-1}in Spring events) is compared in the following studies. It is essential to highlight that the Cogne site is on a South-facing aspect slope with weak winds. Considering all the events, the average wind speed is 1.0 m s^{-1}, lower than in studies where blowing snow is important (such as MacDonald et al., 2010, where average wind speed values exceed 2.5 m s^{-1} on a South-facing slope with shrubs). In addition, the snowmelt process is fast. The daily average sublimation (considering all the events or dividing between Autumn/Winter and Spring events) found at Cogne is higher than the daily average value found by Pomeroy et al. (2006), 0.35 mm day^{-1} at a shrub-covered site considering one melting season (April-May 2003), and by Reba et al. (2012), 0.39 mm day^{-1} at a South-facing exposed and complex opening in a forest where blowing snow likely does not occur.

Besides, the results found at Cogne are also comparable with the findings of Sexstone et al. (2016) at their site located on a gentle, East-facing slope characterised by higher wind speed values than Cogne (equal to or greater than 2 m s^{-1}, on average). Reported sublimation values vary between 0.60 and 0.80 mm day^{-1} in the snowmelt period of two winter seasons. In sites where the blowing snow effect is high, considerably higher values are found (e.g. Pomeroy and Essery, 1999, report average values between 1.2 and 1.8 mm day^{-1} at their flat site on a 20 days period). However, it should be pointed out that, on single events at Cogne, the sublimation term can be as high as the values illustrated by Pomeroy and Essery

(1999), since sublimation values can be up to 1.7 mm day^{-1} on 18th March 2011, interestingly with a low average wind speed of 0.9 m s^{-1}. The minimum value is found on 17th March 2011 (0.12 mm day^{-1}, with an average wind speed of 0.6 m s^{-1}), and it is lower than the rate of 0.35 mm day^{-1} found by Pomeroy et al., 2006.

Higher maximum sublimation rates (up to 1.7 mm day^{-1}) are found in Spring events, compared to 1.0 mm day^{-1} in Autumn and Winter, because of a higher radiative forcing. This produce, as already mentioned, a higher average sublimation rate in Spring if compared to Autumn and Winter cases.

8.5 Final remarks

In this Chapter, nine snowfall events from a medium-elevation site on a South-facing slope (Cogne, 1730 m a.s.l.) were analysed. All the events are characterised by a fast melt: in all the events the snow vanishes almost entirely in one to six days.

The characterisation of the events revealed that the sensible heat flux increases when the snowpack melts. An increase of latent heat flux is found above all the first sunny day after the snowfall, and the sensible heat flux tends to increase with vanishing snow. When the snow melts, the soil and surface temperatures begin to show the enhanced amplitude of the diurnal cycle (with values up to 30°C for surface temperature and to 6-7°C for soil temperature at the end of the events), because the insulating effect of the snow layer is reduced and then vanishes. Together with albedo, the surface temperature can be a good indicator of the presence of snow. The wind speed was, on average, 1 m s^{-1} considering all the events, with peaks up to almost 4 m s^{-1} in Spring events (April 2012 event). Lower maximum values were found in Autumn (maximum 3 m s^{-1} in March 2015 event) and Winter (maximum 2.5 m s^{-1} in February 2015 event). The friction velocity is quite low (almost always below 0.4 m s^{-1} with multiple exceptions only in the events at the beginning of March 2011 and of March 2015). Nevertheless, it allows sufficient turbulent conditions since the turbulent flux data pass the developed turbulence quality test. The friction velocity does not show a strong dependence on snow presence, since it does not increase significantly after the snow has vanished.

The role of longwave radiation is important at both sites (Cogne and Nivolet), confirming findings found in other works. Incoming radiation (*LWin*) can be between 20% and 80% of shortwave incoming shortwave radiation (*SWin*) during daytime hours. In particular, the ratio increases dramatically when outcast sky days occur. Average *LWin* ranges between 250 and almost 300 W m^{-2} at the two sites, and the net longwave radiation shows ranges between about -50 and +10 W m^{-2} at the two sites (comparable with findings at similar sites known from literature), except for the March 2015 at Cogne (negative peak of -22 W m^{-2}). During nighttime, the turbulent fluxes are small, and tend not balance longwave losses.

The energy required to melt the snow shows a wide range, on the first sunny day after the snowfall. The ratio between snowmelt and total energy residuals

increases with RH and with longwave incoming radiation, but the correlation evaluation is not trivial because of few data points. No direct relationship was found with friction velocity.

Values between 6% and 80% of the total residuals were found, except for the second event of November 2012 (11^{th} – 15^{th} November), when the percentage is well above 100%. This might be caused by soil temperature greater than 5°C during daytime and by enhanced soil water content increase due to rain falling on snow. Low explanatory power is found when frozen soil conditions occur, such as in February 2015 event, when a limited infiltration occurs. The above-mentioned ratio shows rapidly increases in the days after the snowfall.

The water balance is nearly closed in all the analysed events, with residuals lower than 4 mm. The most important term of SWE balance is snowmelt, with values always beyond 45% and up to more than 90% of snow water equivalent. The sublimation term contributes for maximum 35% (February 2015 event), and its daily values are comparable with other studies.

Further studies could be addressed to better understand the relationship of snowmelt and residuals of energy balance and the causes of its variability, including more snowfall events with different meteorological and soil conditions.

Chapter 9

Low frequency boundary layer phenomena: the meandering

In this Chapter, the air meandering phenomenon is analysed at the Cogne site, which is on a mountain slope. During low-wind speed events, a phenomenon known as "meandering" can occur. Wind direction is no more well-defined, and the wind flow tends to oscillate and create 2D structures which are similar to river meanders. The oscillations can be noted in the autocorrelation functions of (especially horizontal) wind speed components (u, v, w) and temperature (θ), but also for the vertical wind speed, although much less frequently.

The objectives are: i) to understand whether the empirical formulae recently proposed in literature to fit autocorrelation function and spectra of wind speed and temperature can be used for a non-ideal site; ii) to understand if the meandering effect occurs even on a steep, South-faced slope with channelled winds that might obstacle the 2D wind flow motion; iii) to understand if possible relationships exist between meandering occurrence and meteorological conditions; iv) to investigate, for a topographically complex site, possible meandering indicators known in literature; v) to quantify the relationship between meandering and sensible heat flux uncertainty. The analyses performed in this Chapter are all original and performed by the Author using and adapting the already existing model and statistical analysis software kindly provided by ISAC-CNR of Turin (Dr Luca Mortarini).

9.1 Introduction

Within the eddy covariance technique context, systematic problems of data quality and underestimations of measured fluxes occur. This is caused by low wind speeds, mesoscale flows and also by low frequency, non-turbulent motions transporting energy and scalars. At this point it should be also clear that even the flux uncertainties can rise in particular meteorological conditions (e.g. during either stable, weakly stable or neutral atmospheric conditions). These problems contribute to the radiative energy imbalance, which suggests that sensible and latent heat fluxes (therefore, also carbon dioxide flux) are very likely underestimated, thus affecting also further evaluations on components of water and carbon cycles.

Especially sites characterised by low wind speed conditions may experience more deeply these problems. Among the several low frequency processes occurring in the surface layer, we find the meandering, which might affect the measures and also their quality. Meandering phenomenon occurs when, especially with low wind speeds, the wind flow starts to have at least a 2D structure and begins to oscillate, forming structures that are analogous to river meanders. In these conditions, it is therefore not trivial to define a wind direction (Moor et al., 2015) and even the vertical motions are affected.

The meandering phenomenon is also studied for pollutant dispersion modelling, also because it affects the shape of empirical autocorrelation functions (ACF) and they are at the basis of several dispersion models (e.g. Anfossi et al., 2006). Moreover, despite its importance the meandering is still not fully physically understood (Mortarini et al., 2016a) and a number of studies has been devoted to understanding the causes of the phenomenon. Possible causes of meandering can include submeso motions existence of gravity waves, cold-air drainage, solitons, vortex structures with axes that can be either horizontal or vertical (e.g. Mahrt, 2007). Goulart et al. (2007) proposed that meandering could be considered as an intrinsic property of the wind flow and it might arise, in low wind conditions, when Reynolds stresses are low and the bi-dimensional flow approximates geostrophic balance, and it is extinguished when the Reynolds stresses reach larger values. According to this interpretation, generally no particular trigger mechanisms are required to start the process.

Moreover, in the scientific community there is still a not complete agreement on whether the phenomenon has some site-dependency or not. For instance, Joffre and Laurila (1988) and Hanna (1983 and 1990) showed a weak or absent dependence on site's surface properties, but Hoover et al. (2014) showed that, especially in low wind regime, the topography can influence local wind flows. Meandering seems to be independent of meteorological conditions, topography or seasonality in low wind speed regime (Anfossi et al., 2005).

Several studies tried to model the velocity (and temperature) spectra. Among the most important formulations, Pasquill (1974) proposed the formulation given in Eq. 9.1, valid only in high wind speed conditions

$$nS_i(n) = A_i \left(\bar{u}\frac{\epsilon}{n}\right)^{2/3} \tag{9.1}$$

where n is the non-dimensional frequency, S is the spectrum, the index i is the notation for the three wind speed components (u, v, w), ϵ is the rate of turbulent kinetic energy (TKE) dissipation, A_u=0.15; $A_{v,w}$=0.2. Eq. 9.1 does not represent correctly the spectrum at low frequencies.

Kaimal and Finnigan (1994) illustrate a formula which follows the Kolmogorov 2/3 law in the inertial subrange, but it is only valid in stable conditions (Eq. 9.2)

$$\frac{nS_i(n)}{\sigma_i^2} = \frac{A\left(\frac{n}{n_0}\right)}{1 + A\left(\frac{n}{n_0}\right)^{\frac{5}{3}}} \tag{9.2}$$

where σ_i^2 is the wind speed variance; A=0.164 for i= *u, v, w,* θ (temperature); n_0 is the frequency at which the inertial subrange intersects the $\frac{nS(n)}{\sigma_i^2}$ = 1 line. This formula, using the Pasquill formulation and considering that $n_0 = \frac{n_{max}}{3.77}$ illustrates that the spectrum is independent of stability in the inertial subrange, and it is proportional to $n^{2/3}$.

For unstable conditions, several formulations have been proposed.

INSERIRE FORMULE.

Kaimal (1978) proposed a model consisting of a low-frequency term, a high-frequency term and a third term obtained from the first two terms, but only for the wind speed components *u* and *v* (Eqs. 9.3 and 9.4).

$$\frac{nS_u(n)}{u^{*2}\phi_\epsilon^{\frac{2}{3}}} = \begin{cases} 0.4\, f^{\frac{2}{3}}, & \lambda \le 2z \\ 0.4\, f^{-p}, & 0.67z_i \ge \lambda \ge 2z \\ AB\ \dfrac{f}{1 + 3.1\,(Bf)^{\frac{5}{3}}}, & \lambda \ge 0.67z \end{cases} \tag{9.3}$$

$$\frac{nS_v(n)}{u^{*2}\phi_\epsilon^{2/3}} \begin{cases} 0.4\, f^{\frac{2}{3}}, & \lambda \le z \\ 0.4\, f^{-p}, & 0.25z_i \ge \lambda \ge z \\ AB\ \dfrac{f}{1 + 3.1\,(Bf)^{5/3}}, & \lambda \ge 0.25z \end{cases} \tag{9.4}$$

where λ is the wavenumber, z_i is the depth of the convective boundary layer and z is the measurement height above ground. *A, B*, *p, q* are variables as illustrated by Kaimal (1978).

Hojstrup (1981) introduced, for the three wind speed components (Eqs. 9.5, 9.6 and 9.7), a spectrum model made of two terms, one at low-frequency, and one at high frequency following the Kolmogorov 2/3 law.

$$\frac{nS_u(n)}{u^{*2}} = \frac{0.5\, f_i}{1 + 2.2\, f_i^{\frac{5}{3}}}\left(-\frac{z_i}{L}\right)^{2/3} + \frac{105f}{(1+33f)^{5/3}} \tag{9.5}$$

$$\frac{nS_v(n)}{u^{*2}} = \frac{0.32\, f_i}{1 + 1.1\, f_i^{\frac{5}{3}}}\left(-\frac{z_i}{L}\right)^{2/3} + \frac{105f}{(1+33f)^{5/3}} \tag{9.6}$$

$$\frac{nS_w(n)}{u^{*2}} = \frac{32\, fi}{1 + 17\, f_i^{\frac{5}{3}}}\left(-\frac{z}{L}\right)^{2/3} + \frac{2f}{(1+5.3f)^{5/3}} \tag{9.7}$$

Tampieri et al. (2004) considered again a low-frequency, an intermediate frequency and a high-frequency range, which will not be discussed here for brevity.

In recent years, many improvements were done. In particular, Anfossi et al. (2005) computed the autocorrelation functions of horizontal wind components using literature formulae and identified an oscillating pattern and even negative lobes. Trini-Castelli and Falabino (2013) showed that the horizontal wind components (*u* and *v*) standard deviations are very close in low wind speeds regime.

However, to investigate the meandering phenomenon, which involves autocorrelation oscillation and low wind speed in different atmospheric stability classes, a new formulation was proposed by Mortarini et al. (2013). They mathematically defined the meandering after the computation of the so-called meandering parameters and meandering periods, whereas a new empirical formula for fitting spectra even in low wind speed cases was introduced by Mortarini and Anfossi (2015) for horizontal wind components and for vertical velocity and air temperature by Mortarini et al. (2016a), based also on the findings of Anfossi et al. (2005).

The new formulations allowed also to use the meandering (or loop) parameter for identifying meandering, almost meandering or not meandering conditions. Mortarini et al. (2016b) showed that no apparent dependence on stability existed, whereas a marked dependence on wind speed was found. Furthermore, they indicated that a possible parameter that can be used as a meandering index is the ratio of vertical wind speed standard deviation (or variance) over the standard deviation (or variance) of horizontal wind components.

Studies on turbulence and wind flow properties on complex terrain, in particular on mountains slopes were mainly focused on turbulence parameters analysis (Martins et al., 2009), similarity scaling alternative to Monin Obukhov Similarity Theory (MOST) (e.g. Nadeau et al., 2013; Sfyri et al., 2018), fluxes and wind flow during transition hours (Parlange et al., 2013), flux-variance similarity and non-stationarity challenges (Babic et al., 2015) or the methodology to be used in complex terrain (Stiperski and Rotach, 2016). However, no study on meandering phenomenon was carried out using a data set lasting almost 12 months, winter-time included, on a steep slope in the Western Alps. Deeper studies on meandering can

have many important outcomes in modelling pollutants (Giovannini et al., 2020) and also in modelling and understanding the transport of energy, water vapour and carbon dioxide.

9.2 Dataset and Methodology

9.2.1 Data processing

The Cogne site dataset was used. The data from June 2016 to June 2017 were analysed. October 2016 was excluded from further analysis, because of the great data gaps due to technical problems.

The wind speed raw components are referred as: U_x (along the slope) and positive for winds coming from South to North; U_y (cross-wind) positive from West to East; U_z (vertical component), positive upwards. Local meteorological conditions were explored with the "Metvurst" R package (Appelhans, 2013). In particular, the data were classified according to the time and the wind directions.

In what follows, the boundaries for the variables are shown and they are based on expected values, partially based on Aubinet et al. (2012). Data outside these ranges were discarded.

$$Ux = u \in [-30{,}30] \text{ m s}^{-1} ;$$

$$Uy = v \in [-30{,}30] \text{ m s}^{-1} ;$$

$$Uz = w \in [-6.5{,}6.5] \text{ m s}^{-1} ;$$

$$|\theta - \theta_{mean}| < 25°\text{C}$$

where *u, v* are the horizontal wind speed components and *w* is the vertical wind speed; θ is the sonic temperature.

Particular periods of severe meteorological conditions which caused probable malfunctions to the instrumentation or data considered unreliable were excluded from further analysis.

After the first correction on the raw data, the wind speed components were rotated to obtain the alignment to the North. Furthermore, a climatological analysis was performed on the considered period. In particular, contour plots of wind directions and speeds and air temperature were drawn. This was done to better understand the properties of the area, the main flows, the periods of low-wind conditions.

After this preliminary analysis, on a monthly basis, the despiked 10 Hz data were divided into one-hour subsets and the speed data were then corrected using the planar fit technique (Wilczak et al. 2000; Richiardone et al., 2008; Yuan et al., 2010; Nadeau et al., 2013).

9.2.2 Autocorrelation functions and spectra

The hourly series were used to compute the autocorrelation functions and the velocity spectra, which were computed using the fast-fourier transform. Furthermore, the evaluation of spectra was based on the technique explained by Kaimal et al. (1972), Kaimal and Finnigan (1994) and used by Mortarini and Anfossi (2015) and Mortarini et al. (2016a). The formula for fitting the autocorrelation was taken from the works of Frenkiel (1953) and Murgatroyd (1969) – Eq. 9.8

$$R(t) = e^{-pt}\cos(qt) \tag{9.8}$$

where p is the turbulence time scale – related parameter (time of de-correlation), and q is the large-scale disturbances related parameter, or oscillation frequency. p and q (expressed in seconds) were the best-fit parameters of the autocorrelation model fitting the experimentally-obtained autocorrelation. We can then define $m = \frac{q}{p}$ as the loop (or meandering) parameter and $T = \frac{p}{(p^2+q^2)}$ (in seconds) as the Eulerian time scale.

The spectra empirical formula was derived from a modification of Kaimal and Finnigan (1994) approach and practically implemented using a Fast Fourier Transform (FFT). Two different parts (low wind speed and high wind speed – inertial subrange) were merged with a linear combination to obtain a formula that ideally covered most of the frequency range, as shown in Eq. 9.9.

$$F(n,m,T) = a\,F_{LW}(n,m,T) + b\,F_{HW}(n) = \cdots$$

$$= a\frac{4\,[T + 4(1+m^2)n^2\pi^2T^3]}{1 + 8(1-m^2)\,\pi^2n^2T^2 + 16(m^2+1)^2\pi^2n^4T^2} + \; b\frac{A\,\frac{n}{n_0}}{1 + A\left(\frac{n}{n_0}\right)^{5/3}} \tag{9.9}$$

where n is the frequency (Hz), m is the loop parameter, T is the time scale (seconds), $n_{max} = \frac{\sqrt{p^2+q^2}}{2\,\pi}$ is the frequency of the spectrum maximum (the spectrum peak), $n_0 \cong \frac{n_{max}}{3.8}$, and A =0.164. a and b are two fit coefficients. a must guarantee that $\int F(n,m,t)dn = 1$ and it is computed in the form (Eq. 9.10).

$$a = 1 - \int b\, F_{HW}(n) dn \tag{9.10}$$

where

$$b = \frac{1 - 2\left(\frac{n}{n_{max}}\right) + \left(\frac{n}{n_{max}}\right)^2}{1 + \lambda\left(\frac{n}{n_{max}}\right) + \left(\frac{n}{n_{max}}\right)^2} \tag{9.11}$$

where λ is a shape parameter that considers the amount of energy in association with the frequency range between high and low frequencies.

The autocorrelation and spectral modelling was performed following Mortarini and Anfossi (2015), Mortarini et al. (2016a) and using, adapting them, the software tools written with R software and provided by ISAC-CNR. The data analysis was again performed in R environment partially using the software tools provided by Dr Luca Mortarini and getting inspired also by the work of Mortarini et al. (2016b).

9.2.3 Data analysis

Daytime cases were identified if the shortwave radiation was greater than a threshold set to 20 W m^{-2}. Transition times were identified as the hour before and after local dawn and sunset. Cloudy hours were identified in two different ways for daytime and nighttime. At daytime, comparing the shortwave radiation to reference, sunny days. At nighttime, comparing the net radiation and upward longwave radiation to the one of a known, cloud-free day. Furthermore, a clearness index (Aubinet et al., 1994) or the clear sky index (Marty and Philipona, 2000) was used. We decided to use a clear sky index following Marty and Philipona (2000): this method allowed us to roughly reconstruct sky cover even during nighttime, because it uses the longwave radiation. A 0 (clear sky) / 1 (outcast sky) index was built according to the outcomes of the method.

A distinction was also based on stability, to see whether a relationship between meandering and atmospheric stability could be found in a complex area. Stability classes were $\frac{z}{L} < -0.5$, $-0.5 \leq \frac{z}{L} < -0.05$, $-0.05 \leq \frac{z}{L} \leq 0.05$, $0.05 < \frac{z}{L} \leq 0.5$ and $\frac{z}{L} > 0.5$, respectively unstable, weakly unstable, near neutral, weakly stable and stable conditions.

For the stable (mostly nighttime) cases, the hourly *z/L* parameter was computed using the 5-minutes averages to get a more accurate estimate. An additional empirical distinction was made. Surely unstable hours were hypothesised between 10:00 am and 15:00.

An overall dataset was at the end obtained merging the monthly datasets. Due to the anemometer orientation, the data associated with wind directions between 315° and 45° were hard flagged. Hours with rainfall were also discarded. After this quality control, 3572 hourly periods were considered reliable.

The complete meandering cases were identified when, according to Mortarini et al. (2016a), $m_{u,v,\theta} \geq 1$. However, we did not detect any m values equal to 1, at least in the analysed period. When at least one variable oscillated (not necessarily in LWS), the almost-meandering cases were found. Single variable oscillations were analysed as well.

Furthermore, the particular cases of meandering processes with a period inferior to 1 hour were of interest, so meandering periods greater than 3600 s were especially investigated. Hourly periods with meandering periods greater than 3600s were considered only in the computation of meandering, almost meandering and not meandering hours, but were not considered to produce assessments over the fitting performance (and Kolmogorov slope analysis) because they could cause problems in the parameters computation when fitting EAFs and spectra.

The dataset was also analysed using a wind speed classification, with a set threshold of 1.5 m s^{-1}, between low-wind speed hours (LWS) and high-wind speed hours (HWS). Besides, to consider all possible cases, that classification, when specified, is not used.

Meandering and almost-meandering periods were analysed in terms of the aforementioned atmospheric stability, radiation, wind direction and speed, air temperature and ACF and spectral characteristics. The Kolmogorov slope within the inertial subrange was also analysed to understand whether the spectra modelling was able to reproduce. Subsequently, an assessment on the fitting performance on ACF and spectra was done.

9.2.4 Error analysis

Up to these days, no study has been devoted to the understanding of the relationship between meandering and flux uncertainties described by Wyngaard in 1973.

The flux uncertainties of the covariances $u'w'$, $v'w'$, $w'\theta'$ were computed and their classification based on meandering was performed, to understand whether larger errors could be detected in meandering or almost meandering hours.

The statistical non-dimensional uncertainties were computed following Wyngaard et al. (1973), as shown in Eq. 9.6.

$$\begin{aligned} a^2_{w'\theta'} &= \frac{z}{\tau\, U}\left[\frac{\overline{(w'\theta')^2}}{\overline{(w'\theta')}^2} - 1\right] \\ a^2_{u'w'} &= \frac{z}{\tau\, U}\left[\frac{\overline{(u'w')^2}}{(u^*)^4} - 1\right] \\ a^2_{v'w'} &= \frac{z}{\tau\, U}\left[\frac{\overline{(v'w')^2}}{(u^*)^4} - 1\right] \end{aligned} \tag{9.12}$$

where a is the flux uncertainty, z is the measurement height, U is the wind speed module at height z, τ is the averaging time and u^* is the friction velocity. The uncertainty threshold was set at 50% of the flux.

9.3 Results and discussion

From the analysis of contour plots and average wind speed diurnal cycle shown in Figure 9.1 one notices that the wind regime is characterised by an up (anabatic) and down slope (katabatic) regime. The main interest is to catch the upcoming flow which transports latent and sensible heat fluxes and the most important jet comes from South-South East during daytime hours. Warmer air jets occur during daytime and they are originated from areas which surround the station and come mainly from the North-West between November and May, but in Late Autumn and Winter, the warm flows are spread also on a relatively wide wind direction range. In the June-to-September period, the main warm jet flow comes mainly within the North-East to South-East sector. Colder air flows usually come from within the range between North-East to North-West directions. The right panels of the figure show the average diurnal cycle of wind speed. It can be noted that the average wind speed is low, with frequent values below 1.5 m s^{-1}. Maximum average values can reach up to 2 m s^{-1} in Spring and between June and September, whereas between November and February the wind speed is lower than in the other periods (the maximum value is around 1.5 m s^{-1}). Without considering any quality control, the number of hours with wind speed below 1.5 m s^{-1} (LWS – low wind speed conditions) is 85% of the total amount of available hours.

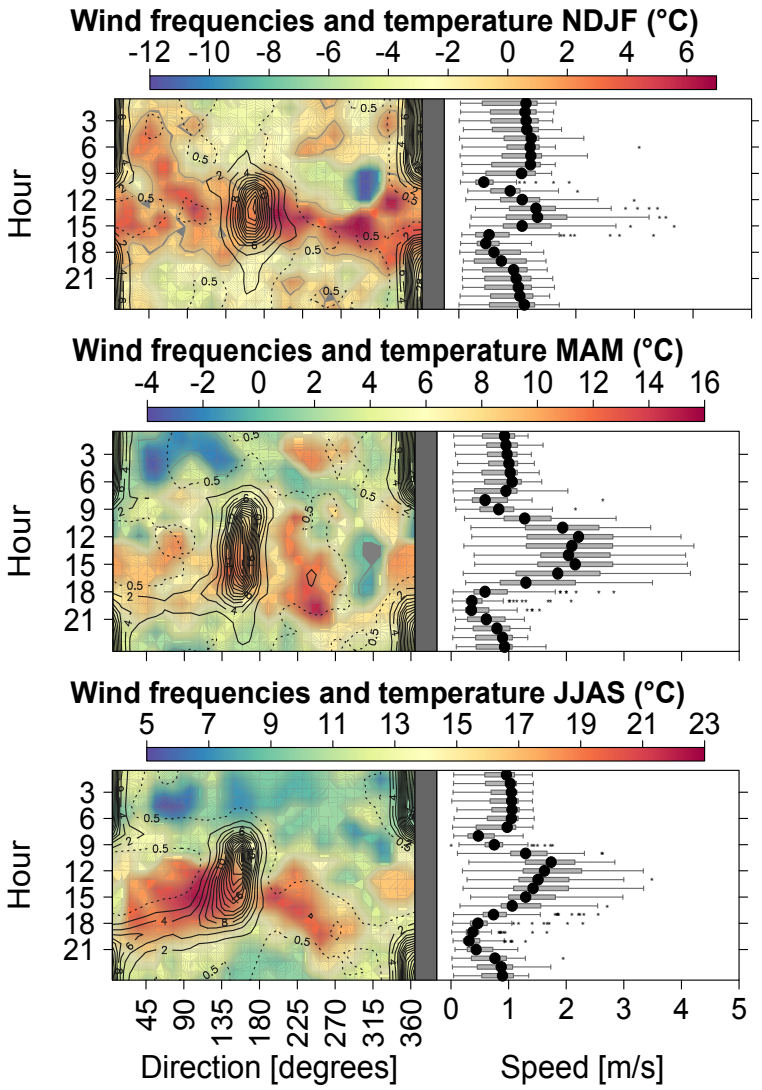

Figure 9.1. Average air temperature and wind direction frequency contour maps as a function of wind direction and hour of the day (left) and wind speed vs. hour of the day (right), for the June-to September (JJAS), November-to-February (NDJF) and March-to-April (MAM) periods. (The colour scale of mean temperature is reported above each figure). Wind direction contour lines are shown for both nighttime and daytime.

9.3.1 Autocorrelation functions, spectra and meandering: fitting data

Let us consider the variables *u, v, w* and θ. The modelled ACF (Eq. 9.1 fitted on data) is able to represent the oscillating behaviour of experimental autocorrelation function (EAF) in 979, 839, 592 and 1170 hours on the total of 8616 hours (11.5%, 9.7%, 6.9% and 13.6%), respectively for *u, v, w* and θ. In addition, when exists, the fitted EAF of *w* is not well captured by the model (Figure 9.2). This is expected, since the meandering is defined as a property of 2D flow (Goulart et al., 2007).

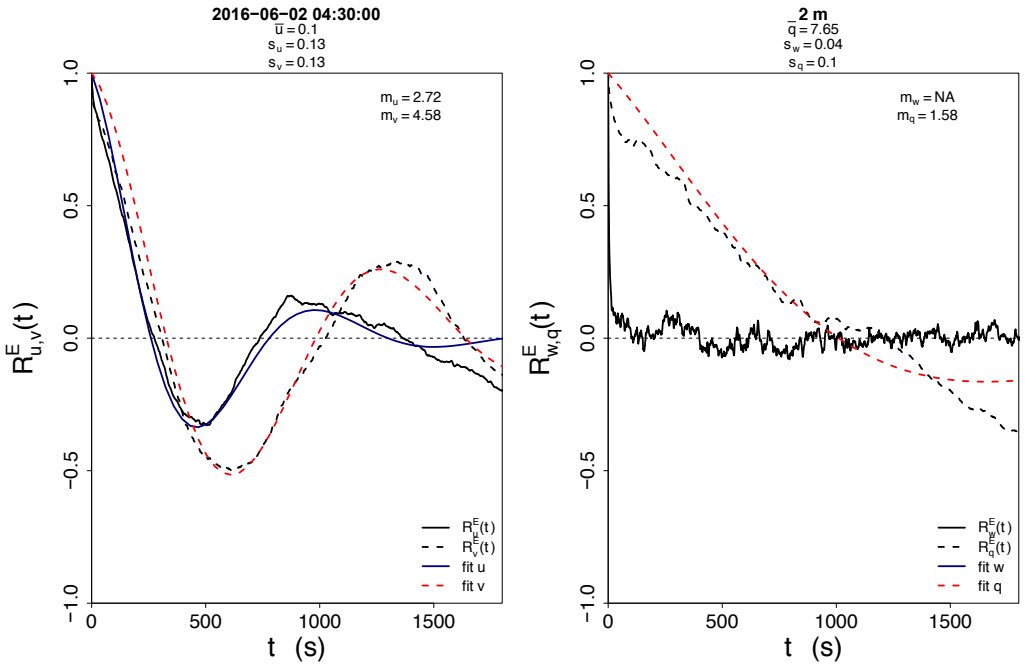

Figure 9.2. Example of w EAF fitted by modelled ACF. 2nd June 2016 04:30 (nighttime, stable). τ is the time, R^E is the autocorrelation function.

In Figures 9.3 and 9.4, the autocorrelation functions and the spectra are respectively shown for a summertime case in a daytime hour: on 16 June 2016 at 10:30 UTC. The *u, v* and θ spectra appear to be satisfactorily approximated by the empirical formulae proposed by Mortarini and Anfossi (2015) and Mortarini et al. (2016). The analysed hour was characterised by low wind speed and low shortwave solar radiation (outcast sky). Furthermore, a typical "complete meandering" situation exists: well defined oscillations in the autocorrelation functions for the horizontal wind speed components and the temperature are identified and, in particular for *u* and θ, well approximated by the empirical formula, while the *v*-component empirical autocorrelation function is able to fit only the first lobe. It can be also noted that even if loop parameters can reach high values ($m_u > 5$), the fit appears still satisfactory and it approximates the spectrum peak.

In Figures 9.5 and 9.6, a wintertime, nighttime case is shown: 26 January 2017, at 21:30. The hour was characterised by a low horizontal wind speed and a relatively high, less negative upward longwave radiation that implied a less negative net radiation, suggesting that the sky was covered by clouds.

Even in this case the fit is successful in representing the ACFs, especially the first lobe. The spectrum is also fitted and, the fitted function is able to represent the Kolmogorov slope and the peak at low frequencies for the two horizontal wind speed components and the air temperature.

The "complete meandering" is evident. The theoretical Kolmogorov's slope was less frequently found during meandering occurrence for the horizontal wind speed components: only 113 and 91 hours were found out of 2381 and 1434 hours,

respectively. Applying the wind direction filter, the vertical wind speed does not show *m* values greater than 1.

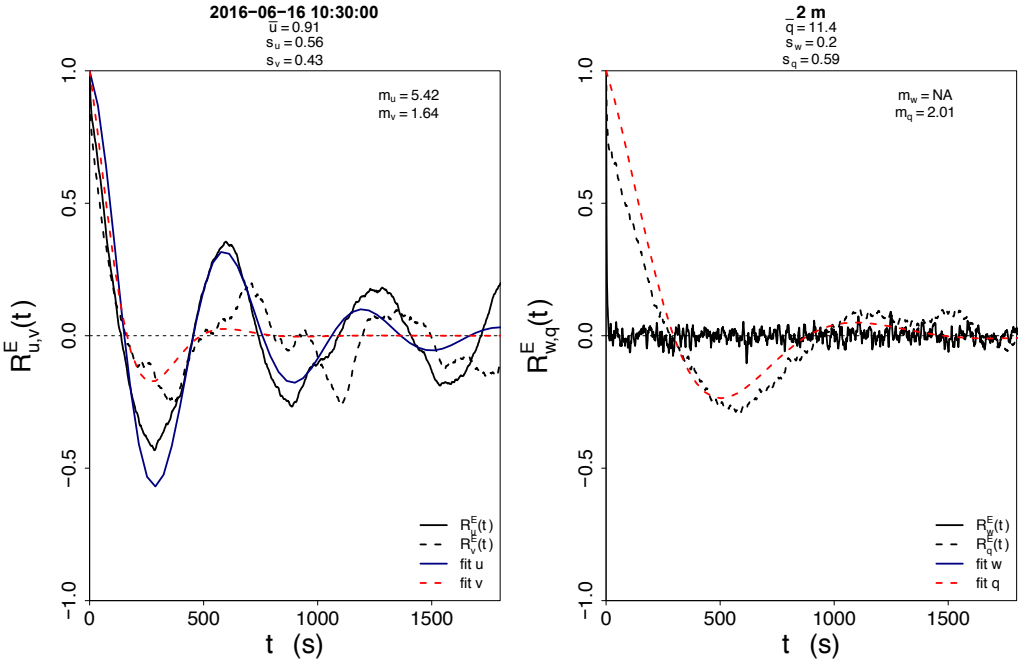

Figure 9.3. 16 June 2016, 10:30: a summertime and daytime unstable example of successfully fitted ACF in a complete meandering hour. and spectra in a complete meandering hour.

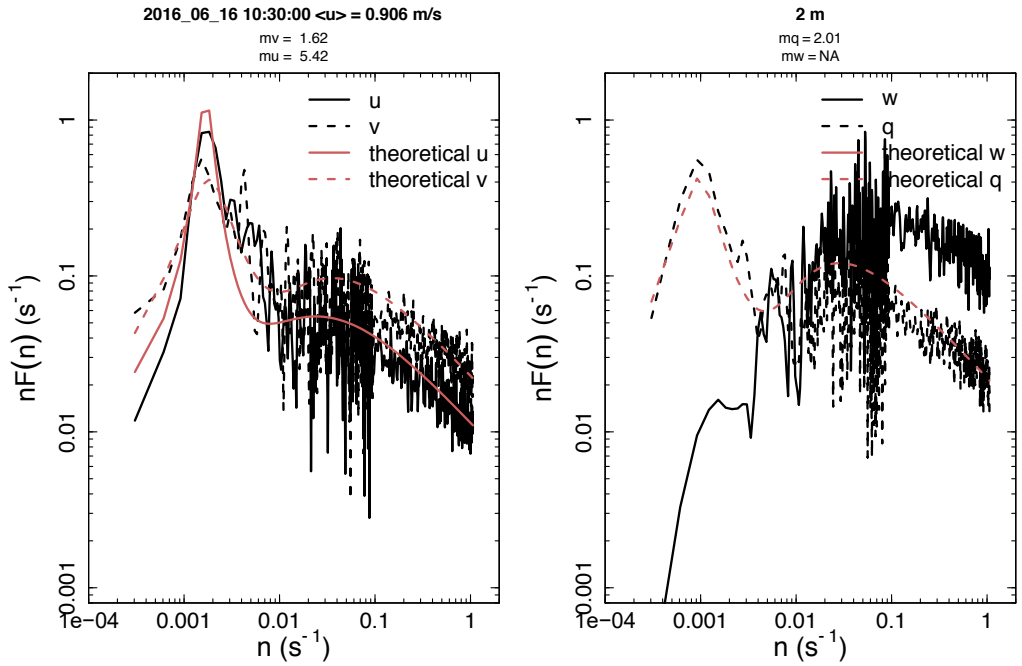

Figure 9.4. 16 June 2016, 10:30: a summertime and daytime unstable example of successfully fitted spectrum for the wind components in a complete meandering hour.

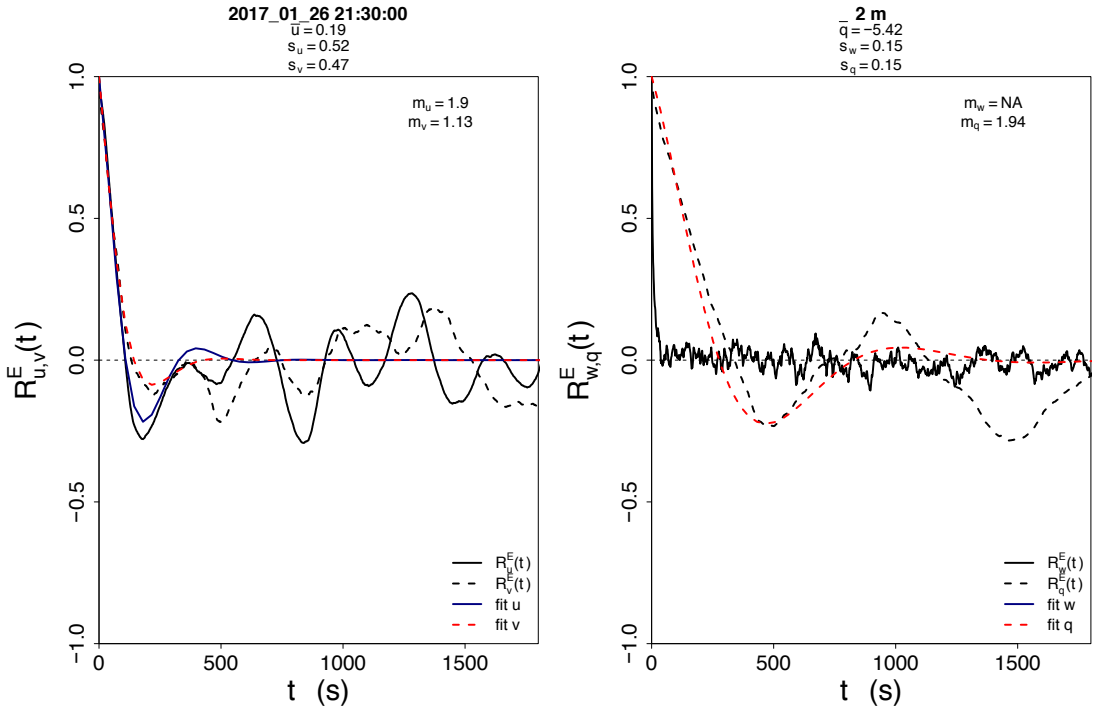

Figure 9.5. 26 January 2017, 21:30: a wintertime and nighttime stable example of successfully fitted ACF in a complete meandering hour.

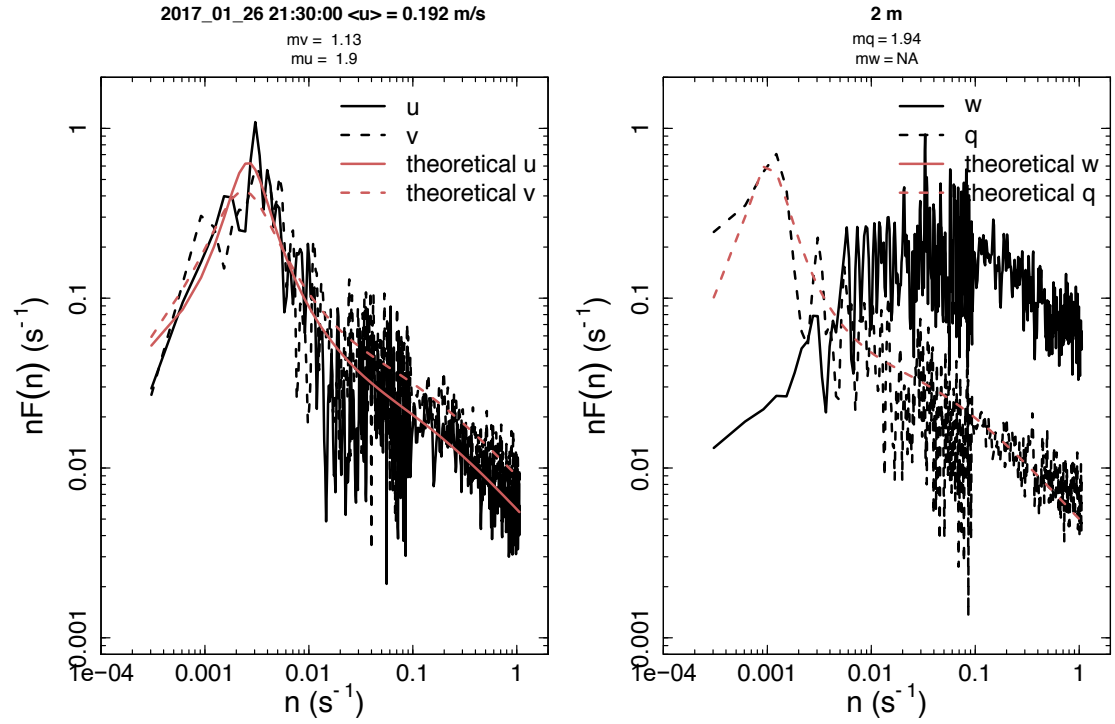

Figure 9.6. 26 January 2017, 21:30: a wintertime and nighttime stable example of successfully fitted spectrum in a complete meandering hour.

The hourly spectra showed an acceptable amount of sub-inertial range slopes near to the theoretical value (-2/3). In particular, the velocity components follow the Kolmogorov slope in 59.3%, 34.5% and 30.0% of the total amount of hours for *u, v* and *w*, respectively. The nighttime meandering cases were more common in wintertime, whereas the daytime hours were more frequently found throughout the dataset.

If one requires that the three components follow, at the same time, the Kolmogorov's slope, then the percentage falls to 12.6% of hours. Figure 9.7 shows the histogram of hours in which the three components follow, at the same time, the Kolmogorov law. An almost bimodal distribution during transition hours (morning and evening) can be noted.

Using the empirical formulae proposed by Mortarini and Anfossi (2015) and Mortarini et al. (2016a), The fit was successful, for ACFs and spectra, in 27.6%, 23.6%, 16.5% and 32.8% of hours, respectively for u, v, w and θ. Sometimes, the fit was also available in HWS conditions. As Table 9.1 shows, for *u* and *v*, on the total number of successful fit, the Kolmogorov behaviour in the inertial subrange were found in a high number of cases, whereas the *w* component was characterised by a lower performance. This suggests that the fit of the spectrum was successful in many hours even if the site is on complex terrain.

Table 9.1. Percentages of hours characterised by fitted spectra and Kolmogorov slope in the inertial subrange

u	*v*	*w*
90.1	81.9	44.1

The fit performance for the vertical wind speed was not high (as already mentioned). As a matter of fact, the *w* component does not show particular ACF oscillations.

The fit performance can depend on loop parameter values. For instance, Mortarini and Anfossi. (2015) found that the fit quality decreases if $m > 2$. In the present study, several hours were characterised by loop parameters greater than 2. However, generally the fitted spectra approximated satisfactorily the spectral peak. For each analysed variable (*u, v, w* and θ), the number of hours with *m* being included in the range from 1 to 2 (Tables 8.2 and Table 9.3) was lower than the case of hours with $m > 2$ (Table 9.4). Interestingly, *w* oscillations occurred only one time for loop parameter between 1 and 2 and 18 times for loop parameter greater than 2. This confirms that *w* oscillations are very rare at Cogne site. This can be explained considering that the measurement height is only 2 m above ground and it is already significant the fact that one can detect such oscillating conditions for the vertical velocity.

Table 9.2. Numbers of hours with m parameters between 1 and 2.

u	v	w	θ
287	263	1	559

Table 9.3. The number of hours characterised by m parameters between 1 and 2. T* constraint was considered.

u	v	w	θ
229	216	1	173

Table 9.4. The number of hours characterised by m parameters greater than 2. T* constraint was considered.

u	v	w	θ
106	79	18	121

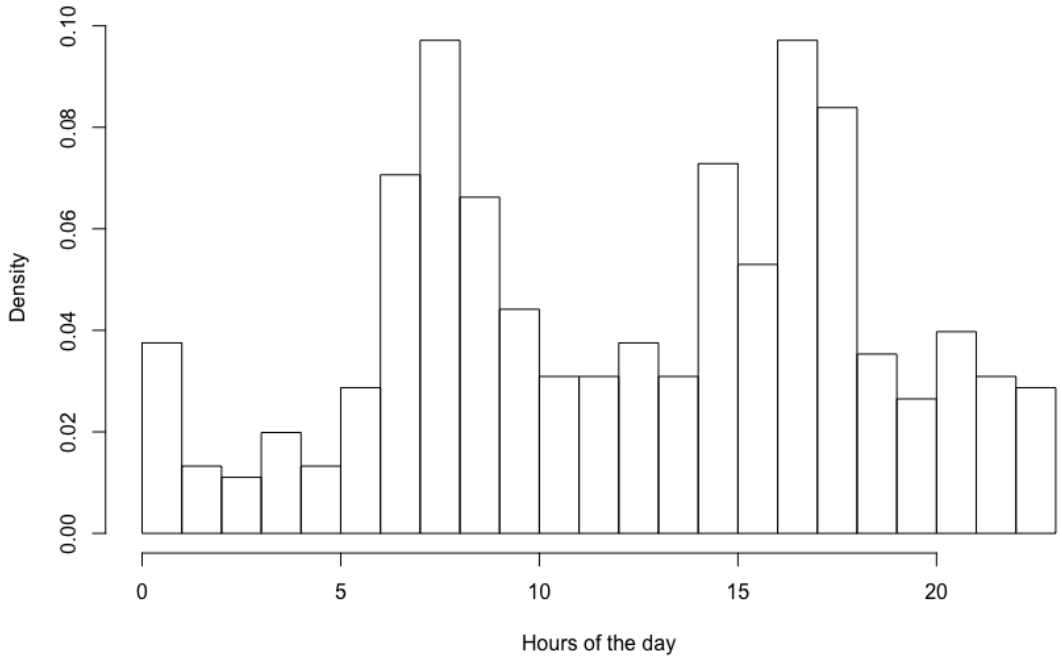

Figure 9.7. Density histogram of hours characterised by the three wind speed components following at the same time the Kolmogorov Law in the inertial subrange. All months are considered.

The oscillation periods (also called meandering periods) varied according to the analysed variable. As was noted by Mortarini et al. (2016a), the temperature and the horizontal speed follow the same equation for EAF, their oscillations should be comparable. In Figure 9.8, the meandering periods boxplots for u and θ are shown, and they are comparable with previous studies, such as Mortarini et al. (2016a): the wind speed has a median oscillation period of 873.1 s, whereas the temperature is characterised by a higher meandering period: 1546.5 s. The two values are therefore different but not so far from each other. Considering only single-variable oscillations and without making distinctions based on complete meandering, we found that the median T^* value was 523.2 s, 477.7 s, 35.1 s and 2215.4 s, respectively for u, v, w and θ. The temperature showed the highest value, whereas the vertical wind speed shows the lowest one. T_θ^* showed the highest variability, while the lowest one was found for T_w^*. The fact that the temperature meandering period is greater than the velocity one might be due to some topographical obstacle that reduces the wind flow meanders.

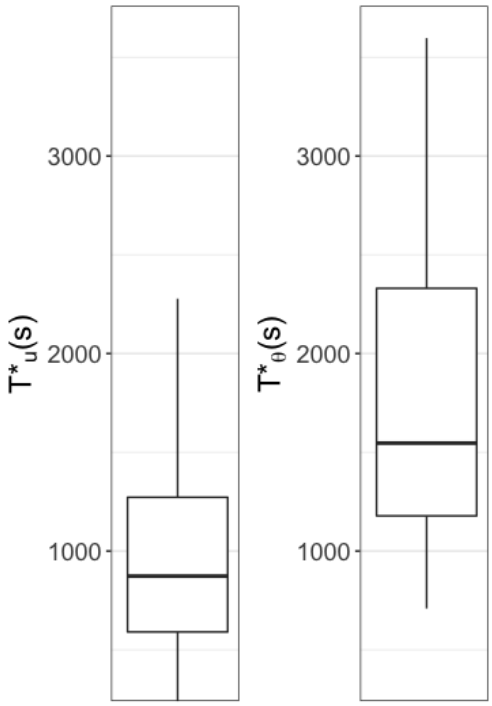

Figure 9.8. Boxplots for the meandering periods lower than 3600 s. The u and θ variables. The boxplot extremes include the 5th and 95th percentiles. The horizontal bar represents the median value. The bars extend towards the minimum and the maximum values ($Q1 - 1.5\ IQR$ and $Q3 + 1.5\ IQR$, where IQR is the Interquartile range, $Q1$ is the 25th percentile and $Q3$ is the 75th percentile).

During the complete meandering hours, there was not a significant oscillation related to the w component and in the cases in which m_w was available, it was lower than 1, indicating no or negligible ACF oscillations. This could imply that no gravity waves were detected.

9.3.2 Meandering on single variables during daytime

Single variable oscillations, considering oscillation periods lower than 3600s, occurred in 222, 161, 18 and 178 hours (imposing, for each variable, $m > 1$ and $T^* < 3600$ s). In non-LWS conditions, u oscillated in 21 hours, whereas v, w and θ showed oscillations in respectively 4, 13 and 15 hours. In those hours, the stability parameter was negative, with neutral conditions occurring in 10 cases, overall.

Therefore, the oscillating phenomenon occurred in unstable and neutral conditions, and also in HWS conditions, even if in the minority of cases. These "high-wind speed" conditions were found in summer, autumn, winter and spring.

406 cases out of 3120 daytime hours happened when at least one variable oscillated. Of these cases, 69 were characterised by HWS conditions. Differently

from the nighttime hours, here the meandering parameter for the temperature was also lower than 1.

The m parameter was sometimes greater than 3, indicating that large scale motions could be significant, but the high parameters were not necessarily related to meandering periods greater than one hour: in fact, discarding periods beyond 3600 s, meandering parameters greater than 3 still exist: 4, 2, 6 and 12 hours showed separate oscillations for the three wind speed components, respectively (we isolated only the hours characterised by single oscillations at a time).

In Figure 9.9, a particular case is shown: the wind speed components do not oscillate, but θ does. In the example, flow came from about 148° (so from the valley bottom), the wind speed was greater than 1.5 m s^{-1} and the meandering parameter for the temperature was 1.97. This case shows that, occasionally, the meandering can occur for scalars also without oscillations of the wind speed component

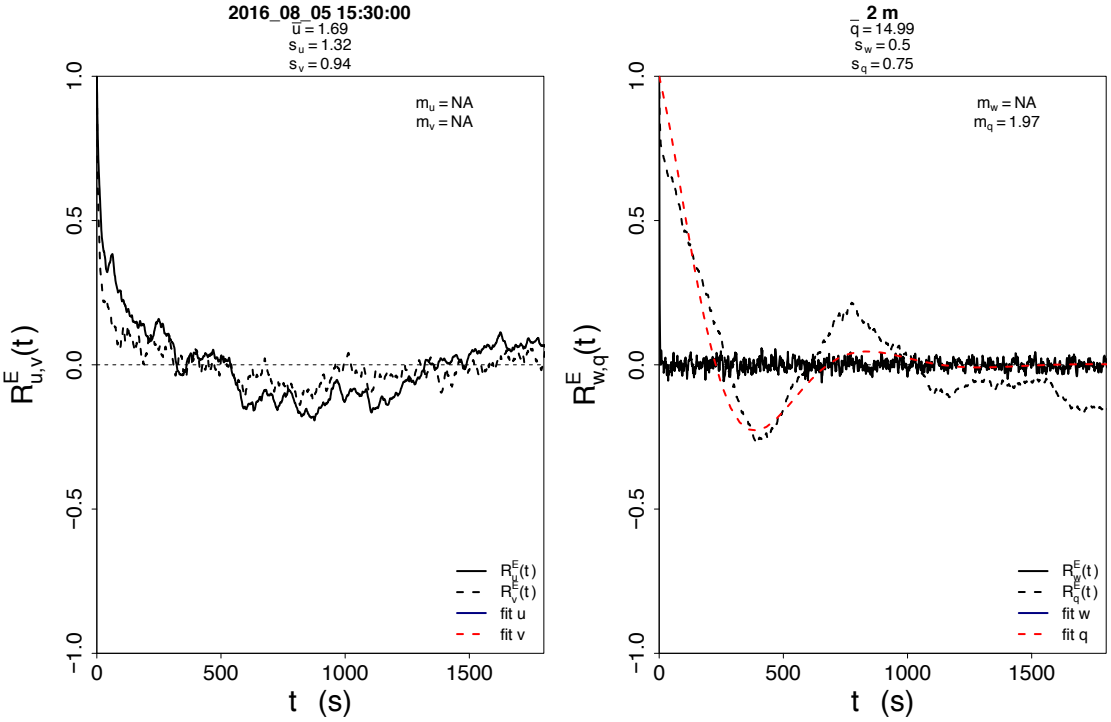

Figure 9.9. Autocorrelation functions and the fitted model, 5th August 2016, 15:30 (unstable).

The meandering, during the daytime, could be locally driven by the solar radiation and net radiation, in particular for the temperature. Furthermore, although there is no clear relation between the occurrence of meandering and the stability parameter, the autocorrelation function minimum negative lobe was more negative when the conditions were weakly stable or neutral. This can be probably explained by means of the low turbulent mixing. Consequently, larger scale motions can be more evident.

A cluster was seen in almost neutral conditions. This behaviour was not found for the wind speed autocorrelation function.

As was already mentioned, 25 hours of complete meandering were found during daytime (this includes transition hours, still characterised by an incoming solar radiation greater than 20 W m^{-2}). 13 cases were associated to transition hours (also in sunny days), while the remaining were characterised by low shortwave incoming radiation (cloudy sky). The winds came from the valley bottom in all the meandering hours. Both the autocorrelation function and the spectrum were well approximated by the empirical formula in many meandering cases. In those situations, the turbulent kinetic energy was lower if compared to the same hour in other days and this is likely due to a cloudy sky and, as was already noticed, meandering conditions generally are typical of either outcast sky or transition hours.

The meandering seems to be independent from the surface albedo and it mainly occurs during outcast days, therefore when there is a lack of radiation. We noticed that the periods when meandering occurred in sunny or almost sunny days, were transition hours (that is, near either dawn or sunset).

In low-wind speed conditions and excluding oscillation periods greater than 3600 s, in 84.8, 61.2 and 77.8 % of cases, the formulae were successfully fitted to the data and were able to satisfactorily represent the Kolmogorov slope.

9.3.3 Meandering on single variables during nighttime

When each variable was considered separately and we isolated the cases in which only one variable oscillated per time, we found 113, 134, 1 and 116 hours, respectively for u, v, w and θ. Oscillations were found only in LWS conditions.

An interesting case is shown in Figure 9.10 and 8.11: no oscillation for other variables but v was found. v was characterised by a strong oscillation which is also well-approximated by the empirical formula. The wind came from South West, meaning that probably higher contribution not coming directly from the katabatic, along slope wind existed. In that day, the sky was at least partially covered by clouds. The meandering period was near the average value.

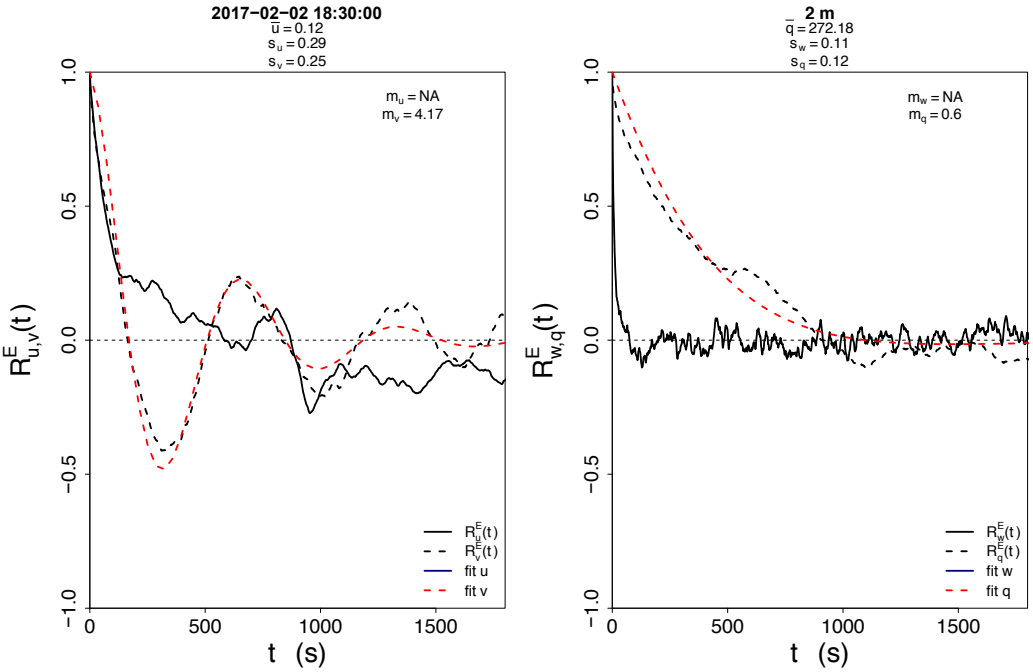

Figure 9.10. Wintertime and transition hour example of successfully fitted ACF in an hour characterised by oscillations of only one variable.

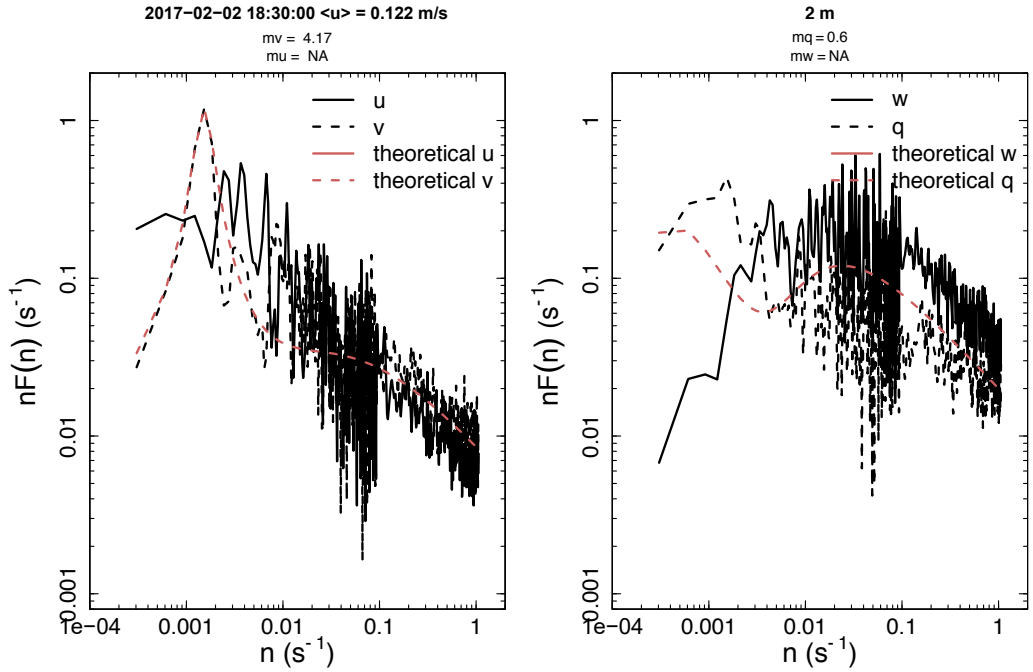

Figure 9.11. Wintertime and transition hour example of successfully fitted spectrum in an hour characterised by oscillations of only one variable.

Out of a total of 467 available, 204 hours were characterised by almost meandering. Besides, 6 hours were characterised by HWS conditions. In those hours, m_θ was always greater than 1, whereas only in one case m_u was greater than 1. No values greater than 1 were found for m_v and m_w.

During nighttime, the meandering hours number was greater with respect to the daytime period, as expected. The complete meandering hours were characterised by several wind directions, ranging from 50 to 300° (stronger wind direction changes happened). Furthermore, the majority of meandering cases took place in cloudy conditions, when the net radiation was less negative, if compared to clear sky hours. Therefore, the phenomenon could be related to the available radiation even during nighttime, when the land surface is characterised by a reduced cooling, confirmed by the surface temperature measurements.

Using the stability parameter computed every five minutes, only one certain unstable case was found, and it is the case shown in Figure 9.1. Despite being unstable according to the new stability parameter definition, the fit was able to successfully approximate the experimental ACF and spectrum. Furthermore, the velocity spectra followed the Kolmogorov -2/3 Law in the inertial subrange.

In low-wind speed conditions and excluding oscillation periods greater than 3600 s, in 84.4, 80.0 and 27.7 % of cases, the formulae were successfully fitted to the data and were able to satisfactorily represent the Kolmogorov slope. The aforementioned cases were found generally at dawn and sunset for u and v: a bimodal distribution of hours was observed. The hours characterised by successful fit for the vertical wind speed showed a monomodal distribution peaked in the morning at about 10 a.m. This could be related to the up/downslope wind regime, which is more evident in the horizontal wind speed components.

9.3.4 Air turbulence, stability and meandering

The complete meandering occurred more frequently in wintertime and autumn (Figure 9.12) and this can be explained in terms of a less developed turbulence. In winter, the air is colder, turbulence is reduced, therefore it is not surprising to find meandering. The second peak noticeable in Figure 9.12 is due to the fact that two June periods were considered (June 2016 and June 2017). The meandering is also more explicable during nighttime or in transition hours, when eddies are developing (morning) or when they are weakening (at sunset). In addition, 57.6% of hours with either meandering or almost meandering hours occur when an outcast sky exists.

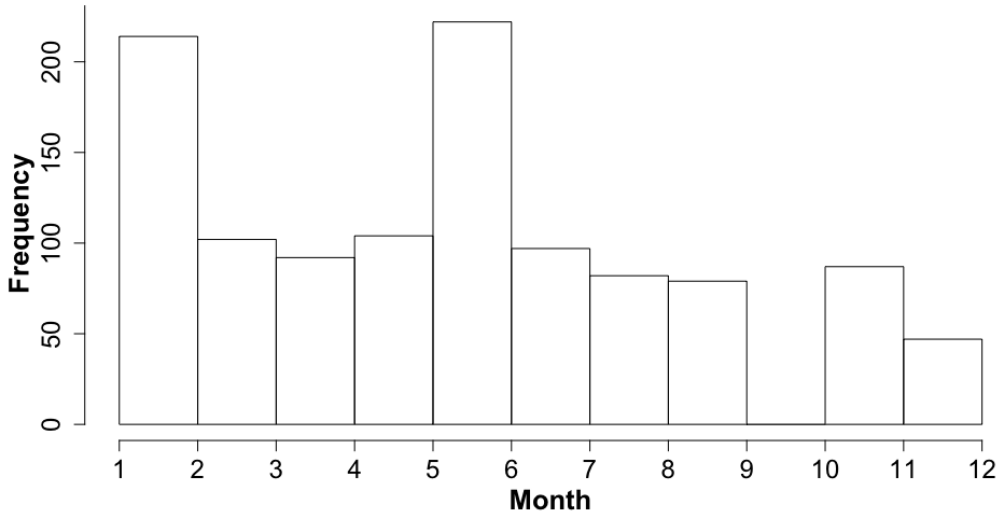

Figure 9.12. Meandering and almost-meandering hours occurrence for each month.

At the Cogne site, low wind speed cases were 69.5% of the total hours. The complete meandering phenomenon was rarely detected. On the total hours amount, 3572, without any constraint on meandering period T^*, 75 hours were identified (Table 9.5). This value can be also compared with the total number of hours with all the meandering parameters m_u, m_v, m_θ non null (221 hours). Hence, 34% of hours is characterised by complete meandering, on the total number of hours where all the three meandering parameters are available. During night-time, 34 hours were identified, whereas 41 hours were identified during daytime. However, the "daytime hours" include also transition hours (i.e. between 5:00-9:00 and 17:00 – 20:00). The transition hours characterised by complete meandering were 44 (59%). Complete meandering was found only in low wind-speed conditions and it was not very frequent (3% of LWS cases), if compared to other sites, where meandering hours oscillate between 9% and 29% of low-wind speed hours, depending on the analysed site (Mortarini et al., 2016b). The results obtained for the Cogne dataset might be affected by a decreased performance of empirical formulae approximating ACFs and spectra. Almost meandering conditions were found in 1051 hours (792 daytime, 259 night-time and 473 during transition hours). Besides, it occurred in 8.5% of high wind speed hours and 38.2% of low wind speed hours (Tables 8.5 and 8.6). Mortarini et al. (2016b) found instead around 50% of LWS hours characterised by almost meandering conditions.

In the majority of hourly periods, non-meandering conditions occurs. The very low complete meandering episodes could be due to orography properties which cause a channelled wind, thus preventing frequent wind flow oscillations. As it was noticed also by Mortarini et al. (2016b), the almost meandering hours are more frequent than meandering hours.

With T^* constraint, all the percentages decreased (Table 9.6). In any case, considering only the hours with non-null meandering parameters for u, v and θ, 34% of hours and 23% of hours were characterised by complete meandering (with respectively, no T^* constraint and with T^* constraint).

Table 9.5. Number of hours with the T* constraint (only data below 3600 s are considered) of high wind speed and low wind speed and percentage of hours, in each class, of meandering, almost meandering and non-meandering hours.

T* constraint	HWS	LWS
Total hours	1090	2482
Percentage of hours	30.5	69.5
Meandering hours	0	50 (2%)
Almost meandering hours	40 (3.7%)	562 (22.6%)
Non meandering hours	1050 (96.3%)	1870 (75.3%)

Table 9.6. Number of hours without the T* constraint of high wind speed and low wind speed and percentage of hours, in each class, of meandering, almost meandering and non-meandering hours.

No T* constraint	HWS	LWS
Total hours	1090	2482
Percentage of hours	30.5	69.5
Meandering hours	0	75 (3%)
Almost meandering hours	93 (8.5%)	958 (38.2%)
Non meandering hours	997 (91.4%)	1449 (58.4%)

Most of the hourly periods was characterised by non-meandering cases. In Figures 9.13 and 9.14, the frequency distribution of, respectively, meandering, almost meandering and non-meandering conditions is shown for daytime and night-time atmospheric stability classes. During daytime, as expected the atmosphere is mostly unstable. The frequency of meandering, although remaining very low, increases reaching the highest value (2.7%) in weakly unstable conditions, whereas almost meandering cases are mostly frequent in stable conditions (65.8%). During night-time, neutral conditions are frequent, but, the meandering conditions occur mainly in the few unstable periods (16.7%). In Figure 9.15, a unique stability parameter is used, independently from daytime or nighttime. Differently from other studies (e.g. Mortarini et al., 2016b), the neutral conditions are not negligible, since their occurrence is comparable with weakly unstable conditions. In addition, the most frequent stability class is the unstable one. Weakly stable and stable conditions are less frequent. Most of meandering occurs during weakly unstable, neutral and weakly stable conditions whereas, surprisingly, complete meandering does not

occur in stable hours. Results confirm that there is not a certain dependence of meandering on stability classes, as suggested by Mortarini and Anfossi (2015), and that meandering occurs also in neutral and unstable conditions, as found by Sharan et al. (2003); Mortarini et al. (2013); Mortarini and Anfossi (2015).

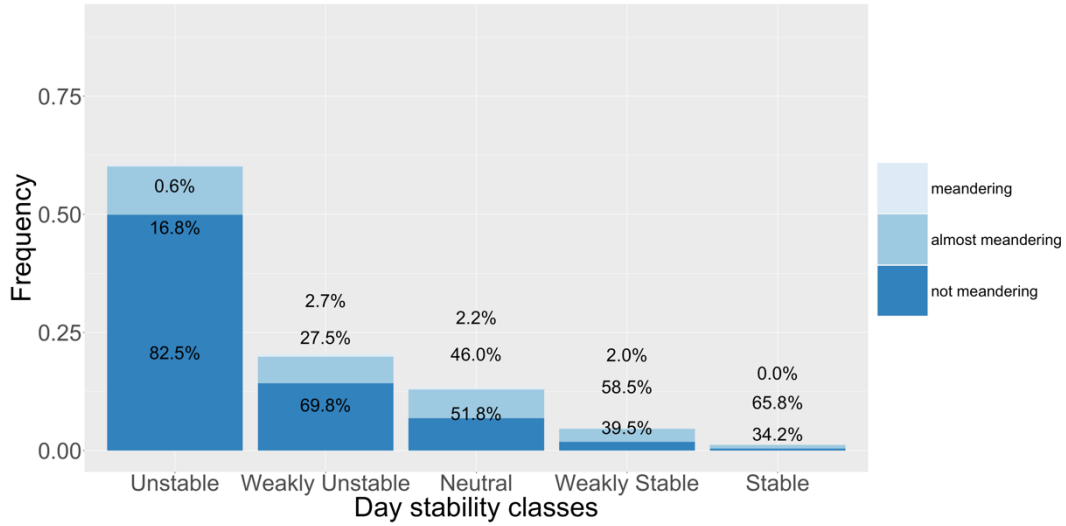

Figure 9.13. Frequency distribution of meandering, almost meandering and not meandering hours versus daytime stability classes. No constraints on T* period are used. Percentages refer to the number of hours characterised by meandering, almost meandering and not meandering.

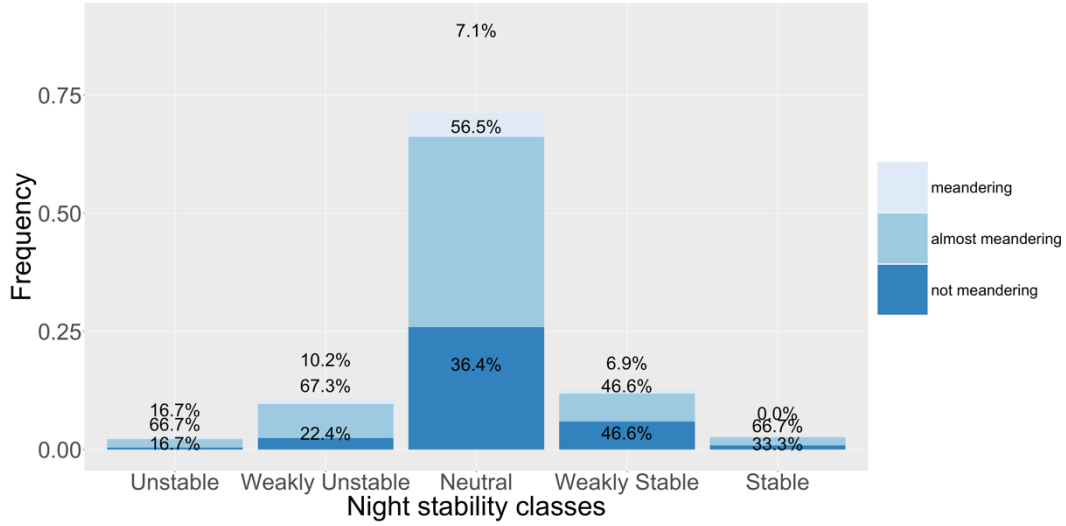

Figure 9.14. Frequency distribution of meandering, almost meandering and not meandering hours versus nighttime stability classes. No constraints on T* period are used. Percentages refer to the number of hours characterised by meandering, almost meandering and not meandering.

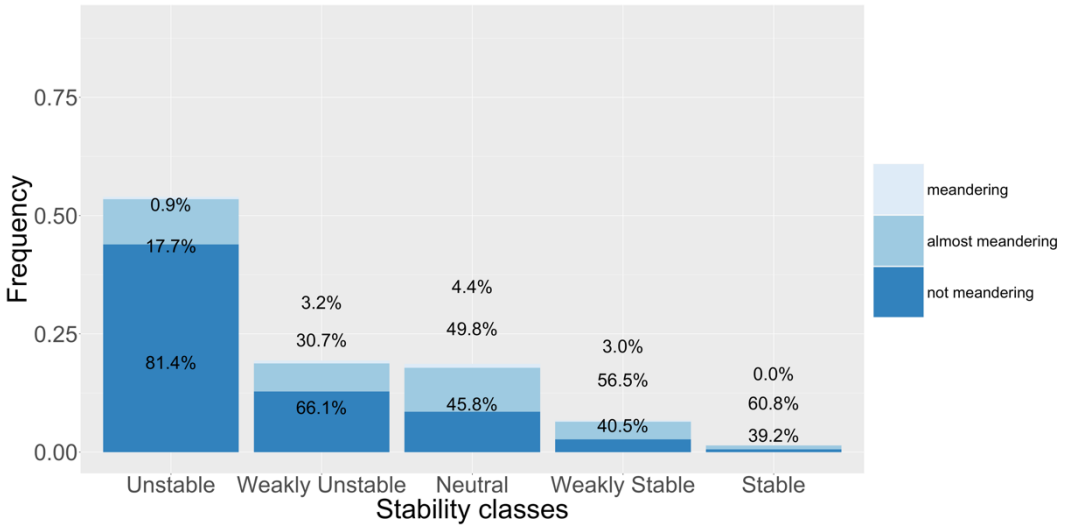

Figure 9.15. Frequency distribution of meandering, almost meandering and not meandering hours versus stability classes, including both daytime and night-time hours. No constraints on T* period are used. Percentages refer to the number of hours characterised by meandering, almost meandering and not meandering.

The analysis on frequency of meandering occurrence in different wind regimes (Figure 9.16) shows that, as was already noticed, complete meandering occurs only below 1.2 m s^{-1}, contrarily to what was detected by Mortarini et al. (2016b), which found some meandering episode till 1.5 m s^{-1}. Almost meandering can instead be found at every wind regime, as illustrated in Tables 8.5 and 8.6.

The wind direction associated with meandering shows a clear pattern around 150°, which is the main daytime wind direction, and also a secondary pattern within the North-North West sector (during nighttime, downslope wind, Figure 9.17)

Since the analysed data are at an hourly scale, meandering periods greater than 3600 s can be excluded from the further analysis. However, until this point it was decided to compute them because they exist. Imposing the 3600 s constraint on the meandering periods of u, v and T, the total amount of hours characterised by meandering is 50 (25 during nighttime), whereas almost meandering is found in 602 hours. Of these, 196 occurred during nighttime and 406 during daytime. The number of cases thus decreases significantly.

No cases with HWS conditions and m parameter greater than 1 for u, v and θ were found. Consequently, the "complete meandering" occurred only in LWS conditions, and definition given by Mortarini et al. (2016a, b) was maintained. All complete meandering hours were characterised by cloudy sky (also confirmed using the clearness index), with only one exception. In the only clear sky hour, the meandering occurred at a transition time (7:30 UTC, when the shortwave radiation was slightly beyond the imposed threshold equal to 20 W m^{-2}).

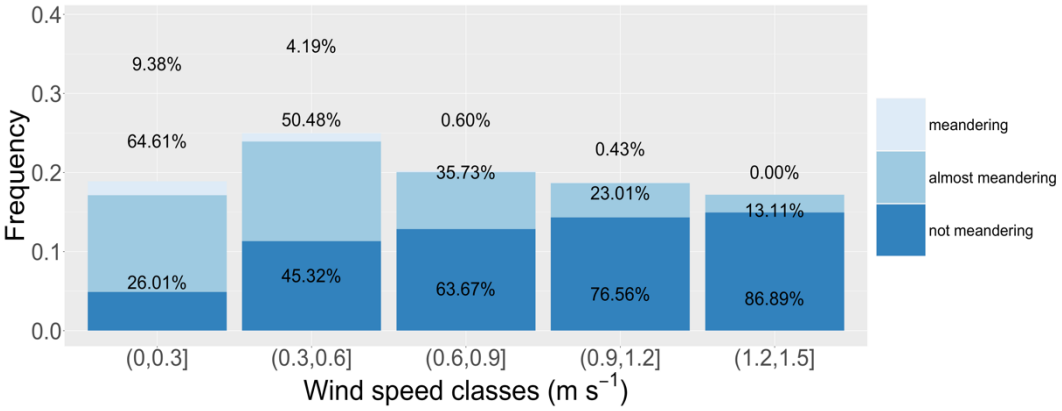

Figure 9.16. Frequency distribution of meandering, almost meandering and not meandering hours versus wind speed classes. No constraints on T* period are used. Percentages refer to the number of hours characterised by meandering, almost meandering and not meandering.

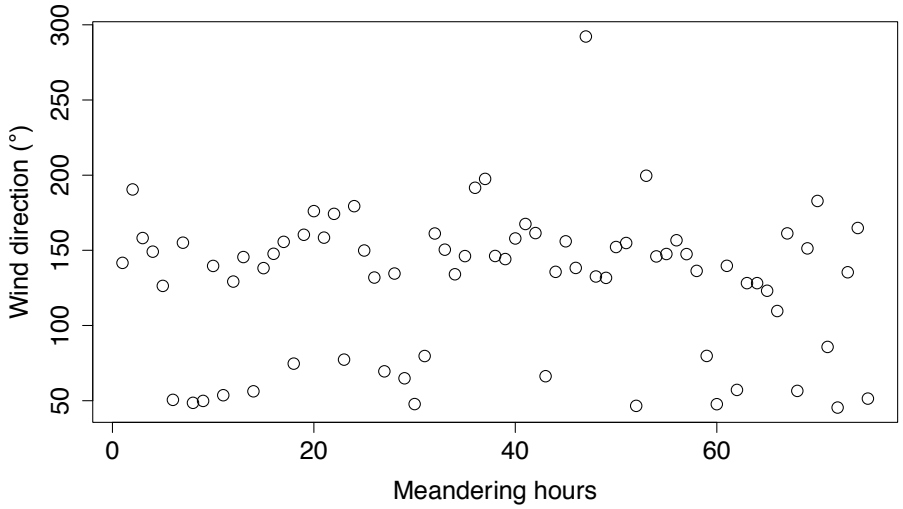

Figure 9.17. Wind direction versus full meandering hours. No T* constraint.

9.3.5 Meandering indicators

The Turbulent Kinetic Energy (TKE), which has been presented in Chapter 2 (Eq. 2.2) is related to the meandering phenomenon, as in the meandering cases it decreases. The TKE distribution is shown in Figure 9.18 for both the meandering and non-meandering cases (where here non-meandering includes also almost meandering hours): lower values are observed during meandering events, meaning that a weaker turbulence exists. A similar result was found introducing the "almost meandering cases".

In past works (i.e. Mortarini et al., 2016b), some index has been proposed to allow a better identification of meandering: Figure 9.19 shows the friction velocity boxplots divided by meandering, almost meandering and not meandering

conditions. It can be noted that the lowest friction velocity median is found in meandering conditions. Thus, friction velocity still appears a good index. Besides, 100% of meandering hours, and 85% of almost meandering hours occur when u^* is below 0.2 m s^{-1}.

Another index that might be useful is the ratio of vertical over horizontal velocity either standard deviation or variances, which are index of turbulence (Figures 9.20 and 9.21). This choice is based on the fact that meandering or almost meandering imply a 2D flow motion, therefore, horizontal wind speed might be larger than the vertical ones. Figure 9.19 shows only the cases of both full meandering and not-meandering cases (included almost meandering), whereas Figure 9.20 shows the same variables but with limited wind speed and with the total classification (meandering, almost meandering and non-meandering).

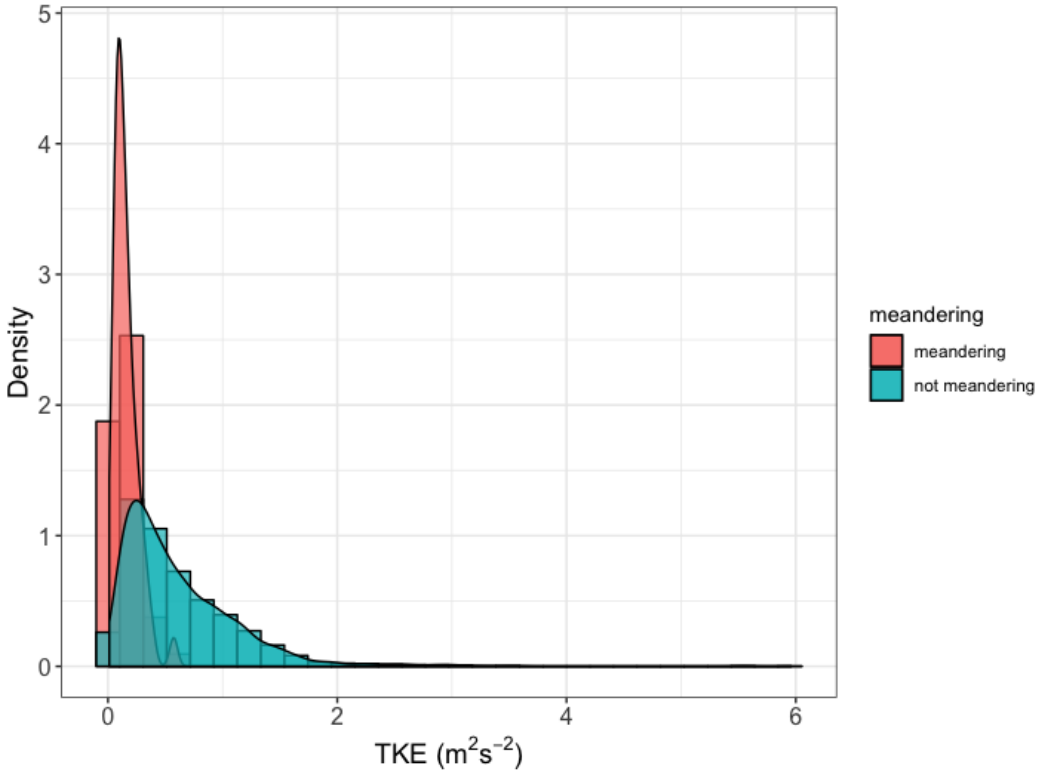

Figure 9.18. Density histograms and curves for the Turbulent Kinetic Energy in meandering and non-meandering cases.

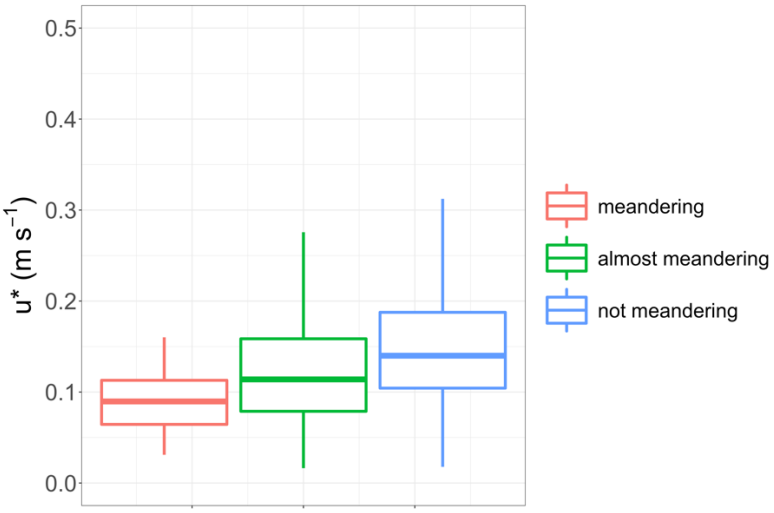

Figure 9.19. Friction velocity boxplots according to meandering, almost meandering and non-meandering cases. No T* constraint.

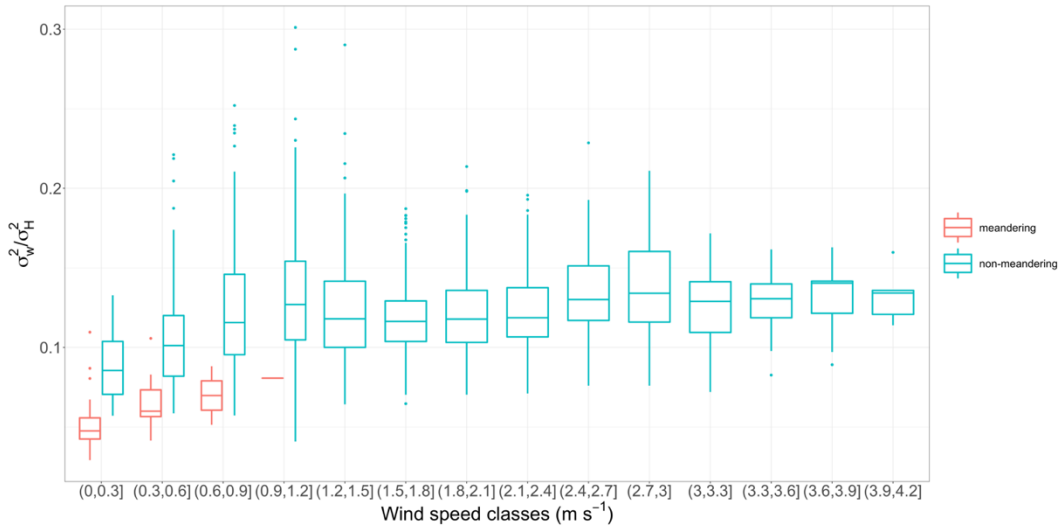

Figure 9.20. Ratio of vertical over horizontal variance of wind velocities for complete meandering and non-meandering cases. No T* constraint.

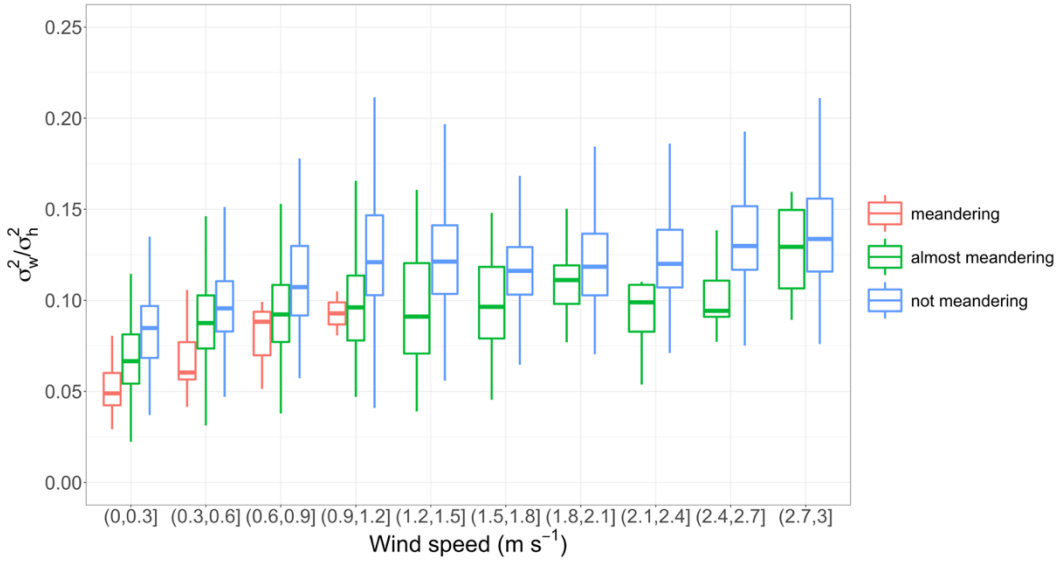

Figure 9.21. Ratio of vertical over horizontal variance of wind velocities for complete meandering, almost meandering and non-meandering cases. No T* constraint.

With the exception of wind speed values greater than 2.5 m s^{-1}, the almost meandering conditions are well identifiable from non-meandering cases. When complete meandering occurs, it is distinguishable because the IQR (inter-quartile range) are separated, even for very low wind speeds, in agreement with other studies in less complex areas, even if the IQR in our case are not extremely separated. This effect is probably caused by up or downward flow being weaker than in other sites, but still sufficient for eddy covariance needs. Moreover, since the Reynolds stress might hinder the meandering occurrence (Oettl et al., 2005; Mortarini et al., 2016), another index that could detect the phenomenon is the ratio of friction velocity over horizontal velocity variance. In the present analysis this index was able to detect differences between the three data categories. However, the interquartile ranges between meandering, almost meandering and non-meandering conditions were not very separated, and the median values were also very close in many wind speed classes. Therefore, the Oettl hypothesis is confirmed also in complex terrain on a slope, but not for very low wind speed (where the difference even between not meandering and meandering conditions is quite low) and in many cases not for almost meandering conditions, with the exception of the wind speed range between 0.3 and 1.2 m s^{-1}. It can also be noted that, another index that has been used for meandering detection (i.e. u^*/σ_h) is not able to well resolve meandering or almost meandering cases with few exceptions (Figure 9.22), as also found by Mortarini et al. 2016b).

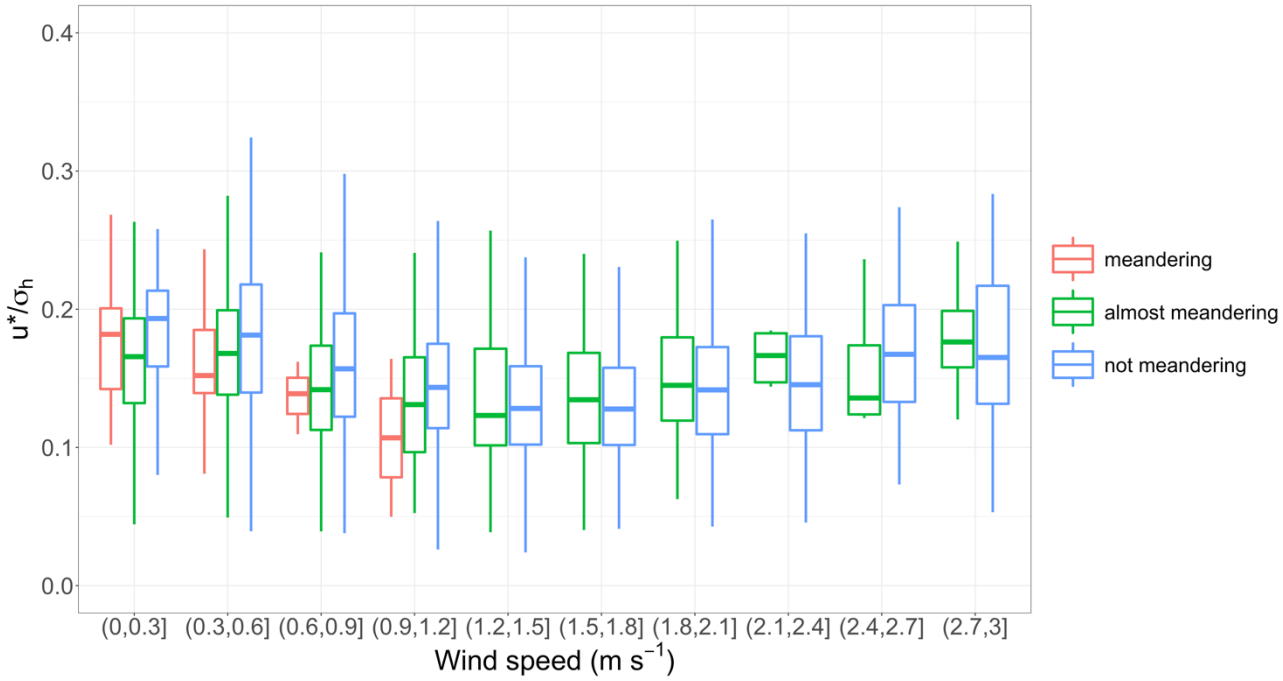

Figure 9.22. Ratio of friction velocity over horizontal velocity standard deviation versus wind speed classes. No T* constraint.

9.3.6 Sensible heat flux and its uncertainty

For ecohydrological and ecological studies, but also for studies over snowpack, one of the important fluxes is the sensible heat flux. Hence, it is important to study it also from the uncertainty point of view, as it was also noted by Stiperski and Rotach (2016). As it can be noted in Figure 9.23, the sensible heat flux is affected by complete meandering conditions mainly at dawn and sunset, whereas almost meandering conditions occur also during daytime and H values associated with almost meandering cases are lower than non-meandering H values. This fact can be explained by the meandering conditions, when the turbulent transport is less efficient. Between the minimum median in non-meandering conditions and the minimum median in almost meandering conditions, there is a difference of about 115 W m^{-2}, showing that even not complete meandering events have an impact on the measures.

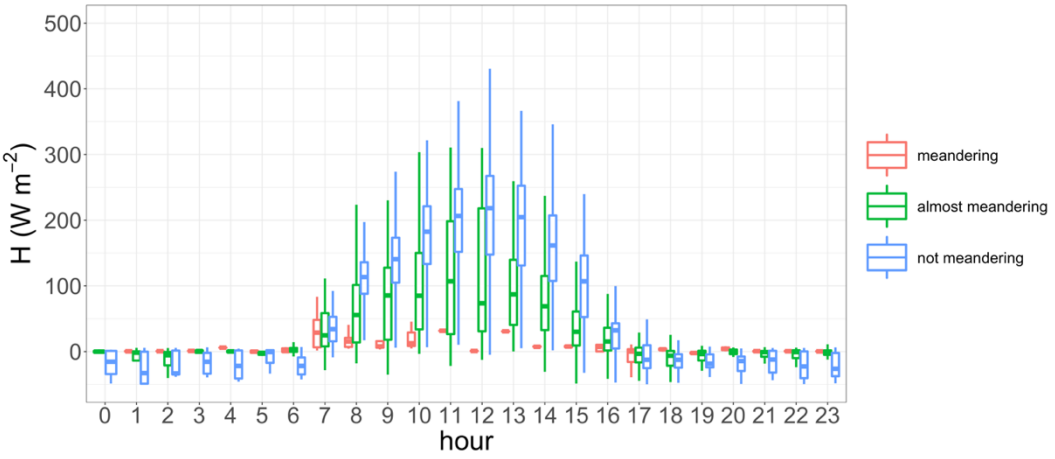

Figure 9.23. Sensible heat flux diurnal cycle according to meandering, almost meandering and non-meandering cases. No T* constraint.

Results indicate that in the meandering and almost meandering cases, one finds not only the largest medians, but also the widest interquartile ranges, if compared to not meandering conditions. Besides, the largest uncertainties occur mainly during nighttime hours (Figure 9.24). This can be explained by lower wind speed and also, on average, diminished air turbulence. However, night-time TKE can show a peak between 2:00 and 4:00. an also shows an enhanced variability and can reach relatively high values comparable to daytime ones. The same behaviour is found for the friction velocity. Peaks in both TKE and friction velocity during nighttime might indicate downslope jet flows. The two phenomena of complete meandering and almost meandering are generally characterised by a higher uncertainty than non-meandering hours. Since the uncertainties are thought to be more significant at night, study on separate stability classes for daytime and night-time is important. The higher uncertainty in meandering and almost meandering hours occurs in all stability classes, during daytime and nighttime (Figures 9.25-9.26), even in unstable conditions. During daytime, there is a net identification of the three cases (i.e. meandering, almost meandering and not meandering) in weakly unstable, neutral and weakly stable classes. At night, the net identification can be found for neutral, weakly stable and stable classes. Considering nighttime hours characterised by neutral, weakly stable and stable hours, the uncertainties are on average greater than unstable or weakly unstable daytime hours. For completeness, all the stability classes were reported for both daytime and night-time hours. However, it should be noted that the classes from neutral to stable during daytime and from weakly unstable to unstable during night, are rare, hence the statistics is not extremely robust.

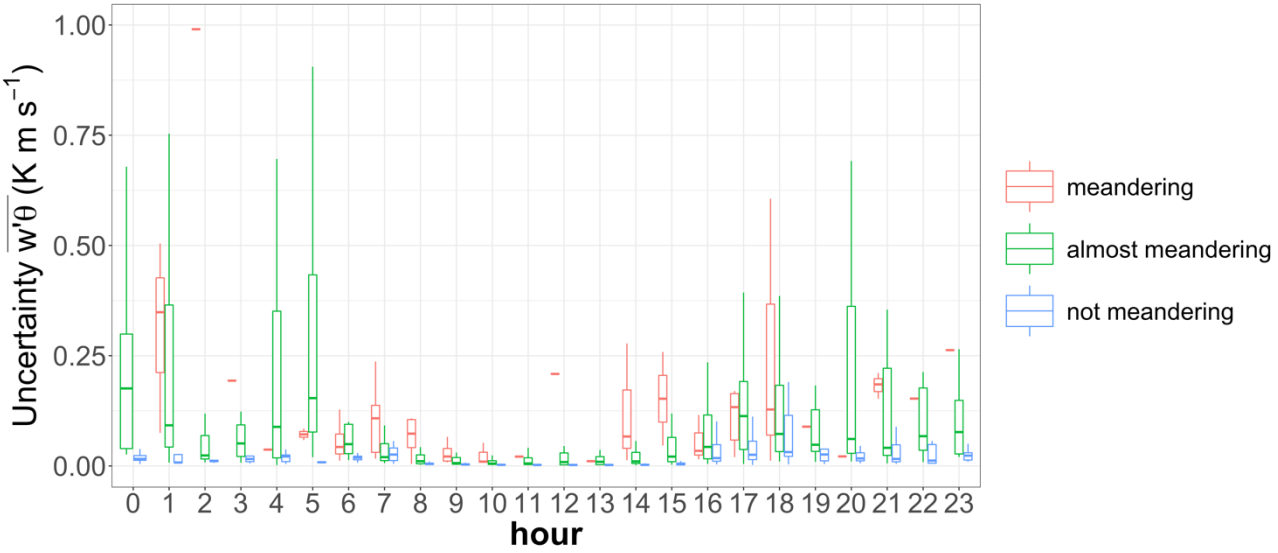

Figure 9.24. $\overline{w'\theta'}$ uncertainty versus hours of the day

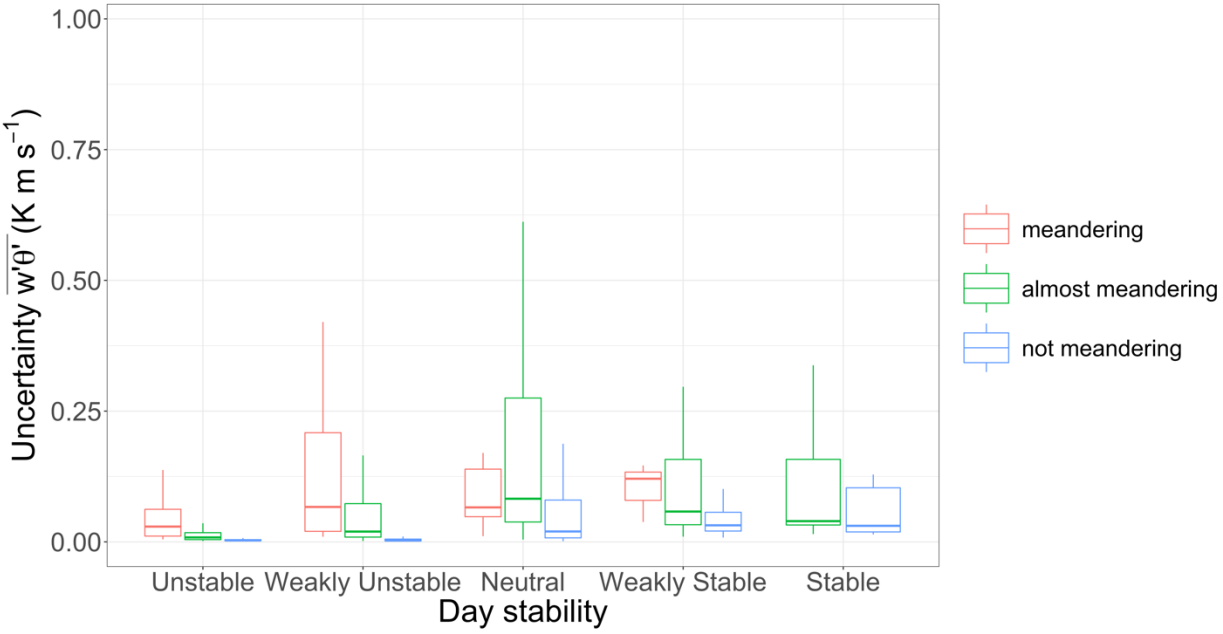

Figure 9.25. $\overline{w'\theta'}$ uncertainty versus daytime stability classes.

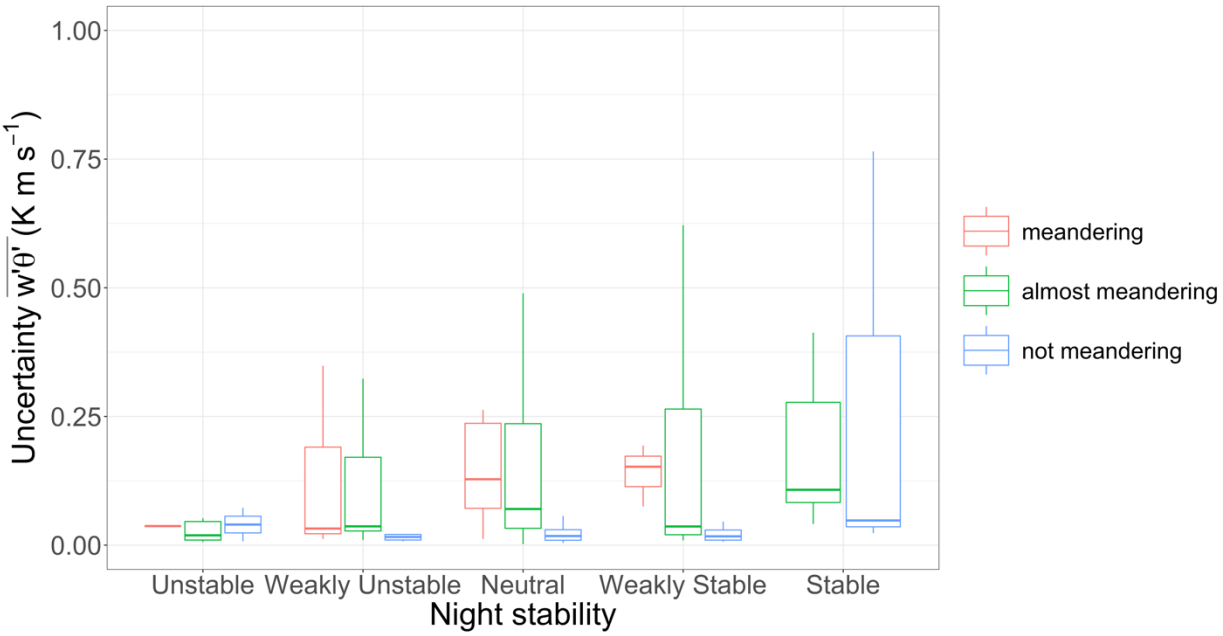

Figure 9.26. $\overline{w'\theta'}$ uncertainty versus nighttime stability classes.

Moreover, it can be noted that most of larger uncertainties are found in low wind speeds, especially below 1.2 m s^{-1} (Figure 9.27). From this analysis, very likely the meandering phenomenon can alter significantly the error associated to flux measurements based on eddy covariance technique. This occurs because the flow becomes at least 2D and it can transport scalars with a non-turbulent motion.

Figure 9.28 illustrates that the highest uncertainty is associated with meandering and almost meandering conditions (around 0.07 and 0.05 K m s^{-1}, respectively for meandering and almost meandering cases), whereas not meandering hours are characterised by low uncertainty (around 0, and also low variability of uncertainty).

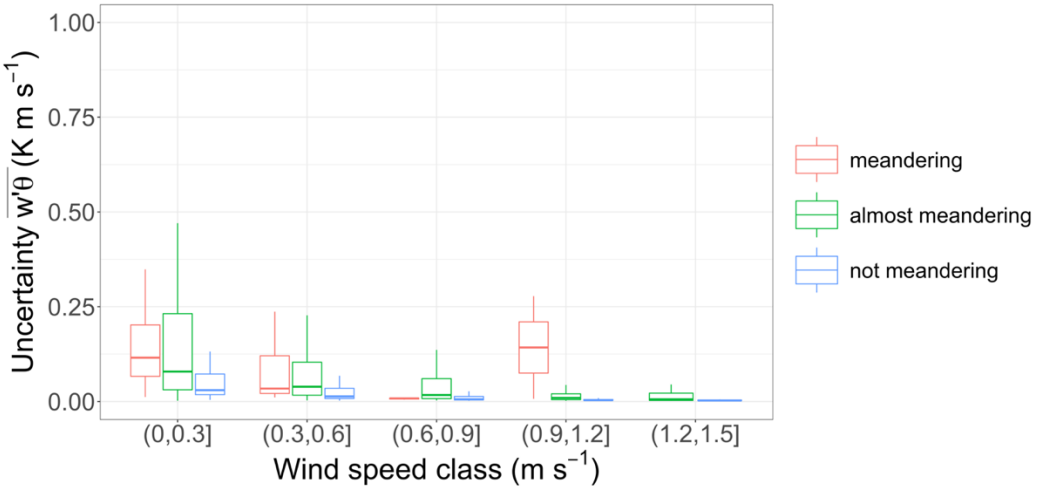

Figure 9.27. $\overline{w'\theta'}$ uncertainty versus wind speed classes.

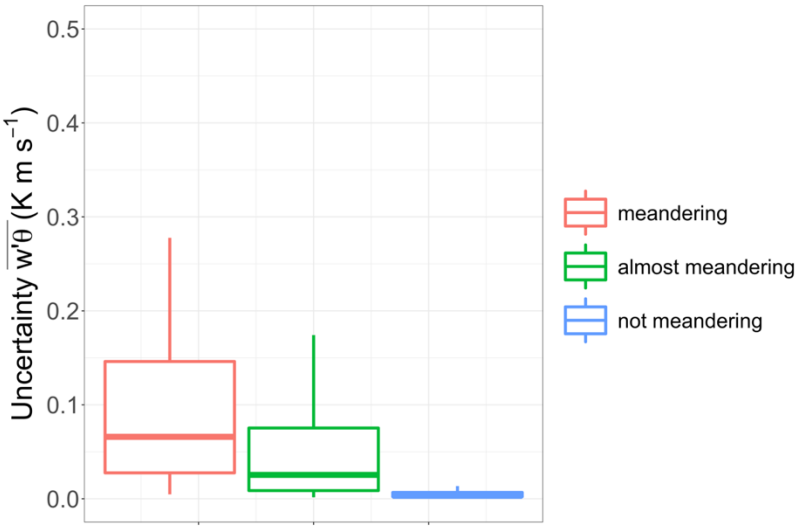

Figure 9.28. $\overline{w'\theta'}$uncertainty divided into meandering, almost meandering and not meandering classes.

9.4 Final Remarks

The meandering phenomenon was explored using one year of collected eddy covariance data on a mountain slope site characterised by frequent low wind speed (LWS) conditions, since beyond 69% of total hours were classified as LWS.
Empirical formulae for the wind speed and temperature ACF and spectra fit in low wind conditions found for flat and homogeneous terrains can be used also in complex sites, even if the performance is not extremely high. The fitting parameters of autocorrelation function and, hence, the meandering parameter, m, were calculated for the wind speed components and the air temperature. The fitting was successful in 27.4, 23.5, 16.6 and 32.8% of available hours, respectively for u, v, w and θ. Fitted spectra complied with Kolmogorov law in the sub-inertial range in more than 80% of hours with found fitting parameters for the horizontal wind speed components, whereas the percentage decreases at 44% for w. Complete meandering (when both the horizontal wind speed and temperature show autocorrelation oscillation) cases were found only in low-wind speed hours in about 3% of cases and especially during night-time hours in the cold season. Almost meandering hours (when at least one variable among u, v and θ (air temperature) were 29% of the total amount of hours and occurred also in high wind speed (HWS) conditions (8.5%), although the main occurrence was verified for LWS conditions (38.2%). The relatively low percentages of hours suggest that the local orography effect could play an important role, also for the meandering occurrence: stations located on steep slopes in a narrow valley may not experience a great number of meandering hours because of topography barrier to large oscillating motions. Complete meandering was in particular observed during transition hours and in wintertime, but some

daytime cases were identified as well. Almost meandering hours occurred usually in the afternoon between 15:00 and 18:00. In about 57.6% of either meandering or almost meandering hours, the sky was covered by clouds (either partially or fully). This causes warmer air and lower heat losses from the ground. The phenomenon could be related to the meteorological conditions (and available solar and net radiations, therefore turbulence intensity given by the turbulent kinetic energy). Considering each variable (u, v, w and θ) separately, the oscillation behaviour was found, even during non-LWS conditions, in particular for the two horizontal wind speed components and the temperature.

No direct, quantitative relationship between the meandering and the stability parameter was found. However, the autocorrelation function minimum negative lobes for the temperature, were mainly reached in almost neutral conditions.

There are several parameters related to meandering. The first one is friction velocity, which increases, on average, in not meandering hours. The lowest values are found for meandering hours, when friction velocity is always below 0.2 m s^{-1}. 85% of almost meandering hours were instead characterised by friction velocity lower than 0.2 m s^{-1}. Two other indices related to meandering were explored. The first one (the ratio of the squares of vertical and horizontal wind speed components) allowed to clearly identify meandering, almost meandering and not meandering cases, whereas the second index (the ratio of friction velocity over the standard deviation of horizontal wind speed components) was not an optimal choice, since it did not yield a clear distinction.

Sensible heat flux during meandering and almost meandering hours was sensibly lower than in non-meandering hours. This suggests that possible underestimations are possible if shorter time periods (i.e. 15 min, 30 min) are used.

Differences were found comparing the uncertainty with stability and wind speed classes and distinguishing between meandering, almost meandering and not meandering cases. Significant uncertainty differences were found especially for neutral, weakly stable and stable conditions at night and for weakly unstable, neutral and weakly stable classes during daytime. For the uncertainty versus wind speed classes, significant differences exist especially for very low wind speeds and for the class between 1 and 1.2 m s^{-1}. The estimated sensible heat flux uncertainty was related to the meandering since its median is higher when either meandering or almost meandering occur.

The score of empirical formulae fitting the data is not very high, although acceptable. Even with this consideration, it is still important to notice that the meandering is not easily detected, despite the usually low wind speeds at the Cogne site. However, when it occurs, it could be not negligible and therefore effects on the measured fluxes could occur. Therefore, a meandering "filter" is potentially useful in a quality control. Further analyses may be oriented towards an improved formulation of the low-wind formulae for the autocorrelation and spectrum approximations and towards a better understanding of how the local topography, the land cover, the sky coverage and in general meteorological conditions can affect the meandering.

Chapter 10

Conclusions

Future climate scenarios require a better understanding of ongoing processes in particularly sensitive areas of the Earth. In addition, providing new data sets as inputs or to validate climate and hydrological models is crucial for their improvement. In the Western Alps, few ecohydrological studies using modelling approaches and eddy covariance data exist, despite the area being characterised by a high meteorological variability. Therefore, every effort that gives contributions to the understanding of poorly studied terrains (either abandoned or natural surfaces without human interference) is needed to answer to questions about land cover changes impacts and how the ecosystem is reacting to ongoing climate change, that poses threats that have to be mitigated. The results obtained in this Thesis are encouraging and several findings could be applied in future data quality control procedures and in eco-hydrological modelling.

In this Thesis, an ecohydrological analysis with air turbulence deepening was carried out for mountain either natural or abandoned grasslands. These areas are sensitive to drought periods, they are not directly affected by human activities, are a still poorly explored ecosystem, but they can cover great areas (about 40% of the Valle d'Aosta Region in Italy, analysed in this study).

The eddy covariance technique was employed to measure turbulent fluxes of heat, evapotranspiration (latent heat flux) and carbon dioxide from unmanaged grasslands. Additional collected data include radiation measurements of shortwave, longwave and net radiation. Soil properties were also evaluated by means of soil temperature, ground heat flux, soil water content and soil surface temperature. Part of the ecohydrological analysis experimental outcomes were also analysed from a modelling point of view.

Eddy covariance data processing, quality control and surface energy balance. It is not sufficient to retrieve data. They should be controlled and validated. This is particularly true for the experimental sites used for this work, since they are located on complex terrains with non-ideal field conditions that, however, represent the reality (flat and totally homogeneous terrains are rare and non-representative of Alpine areas). After a strict quality control procedure on two eddy covariance sites, one on a steep slope, the other on a more homogeneous terrain but at high-elevation, results showed that 61% of the flux data were reliable at the steepest site and about 50% of data were reliable at the second, high-elevation site (on a single growing season). The energy balance closure reached 70% and almost 80%, respectively at the first and at the second site.

Inter-comparison of three eddy covariance sites: topography, fluxes, footprints and energy imbalance issues. Three eddy covariance sites all on unmanaged grasslands were compared to understand the local micrometeorological properties (i.e. wind regime, mean diurnal cycles of temperature, sensible and latent heat fluxes, carbon dioxide flux, atmospheric stability). The energy balance closure was also assessed, finding that the better closure, as expected, is found at the more homogeneous site, but that also in the other two sites the energy balance closure is always, on average, beyond 55%, so in the range of previous studies, even at the steepest and most complex site. Two possible sources of energy imbalance were explored: i) the misrepresentation of net radiation measured at a single point due to the fact that the turbulent fluxes are given by the contribution of a wider area (the flux footprint) and ii) the phase difference on fluxes induced by small and large eddy structures. For the three sites, it was confirmed that with the improved estimate of net radiation using two footprint models, the energy balance closure improves at all sites and that phase differences between vertical velocity and scalars exist and might be important for energy imbalance evaluation and underestimation of turbulent fluxes, confirming previous studies carried out on homogeneous and flat terrains.

Evapotranspiration analysis of an abandoned Alpine pasture at the Cogne site. The analysis of four growing seasons on one site showed that there is a marked interannual variability of meteorological conditions. This variability is also found in fluxes and in particular for evapotranspiration. Evapotranspiration is strongly related to VPD and even it also depends on temperature, as expected, but with little dependence on whether the growing season was wet or not. The cumulative and mean ET values on the wet growing seasons were significantly higher than in dry ones and they outreached precipitation since there is a dependence on past rainfall in Spring. To understand whether the land cover change (grassland versus shrubland) might affect ET, simulations using HYDRUS model were performed. They indicated that the simulated ET in case of shrubland is closer to measures, even if shrubs at the site may account for 42% and it is significantly higher than in the grassland case. This is explained by the deeper roots of shrubs compared to grass, so they can extract more water. The model is able to reconstruct ET fluctuations and that cumulative values, are higher than measured in the shrubs case and dramatically lower in the grassland case. A mix of shrub and grass simulated ET was more in agreement with measures, showing higher discrepancies in more meteorologically extreme years, where it was more difficult to evaluate the correct deep-soil water storage.

Regional modelling of evapotranspiration. A novel modelling approach for mapping evapotranspiration over a wide area (~ 600 km^2) was introduced. The model is called CLIME-MG and it is made of two modules: one meteorological and one of soil water balance. It is a deterministic soil bucket model with parameters

retrieved from literature and, therefore, it does not require any calibration prior to simulations. This is an advantage, since in complex terrains it is often difficult to retrieve sufficient information for a good calibration. Results of temporal validation highlighted a good performance of the simulated soil water content and evapotranspiration, if compared to site measurements with also eddy covariance derived evapotranspiration (correlation coefficient $R > 0.80$). A spatial validation was also performed to compare CLIME-MG outputs with the evapotranspiration estimated by one of the most known models that uses satellite data: METRIC. Results showed a significant correlation between the two models ($R > 0.60$, generally). METRIC is characterised by an enhanced spatial variability with respect to CLIME and it tends to underestimate frequently the evapotranspiration, but the frequency distributions are similar. Also, CLIME is likely independent of the presence of nearby stations whose data are used as model inputs.

Energy and mass fluxes over melting snow. The snow deposition on the ground is able to alter the local radiative energy balance. In addition, the energy required for the snowmelt process is not measured by the eddy covariance system making the energy imbalance to increase. However, it is still not clear whether the energy balance residuals in the days following a snowfall can be still explained by snowmelt, and to what extent. To explore these issues, nine fast melting snowfall events were selected.

Results show that, the first sunny day the latent heat flux (*LE*) sharply increases and that sensible heat flux increases and can outreach *LE* as soon as portions of soil are free from snow. It was confirmed that longwave radiation can give contributions to snowmelt (also using a second dataset collected at high-elevation site) and that the snowmelt (measured by soil water content probes) can explain a variable percentage, up to 80%, of energy balance residuals. For almost all the identified snowfall events, the water balance was almost closed, and snowmelt contribution was greater than sublimation one in the balance equation. The water balance components are within the ranges found in literature.

Low frequency boundary layer phenomena: the meandering. Especially when low wind speed conditions occur, the wind flow can show low frequency processes in the atmosphere and a “meandering” behaviour, therefore with a preferential 2D structure, with oscillations of the horizontal wind speed components. Besides, more rarely, even also the vertical component shows the same oscillating behaviour, which can also affect scalars such as temperature, and the phenomenon is also visible in the autocorrelation function oscillations which lead also to negative values (that is, anti-autocorrelation).

In meandering conditions, it could be difficult to well define the wind direction. Besides, the meandering is important for pollutant and other scalars dispersion (and, therefore, also for the detection of sensible heat flux, carbon dioxide flux and evapotranspiration) because the scalars are transported with a non-turbulent mechanism. This might have implications for eddy covariance measurements

performance and data quality. At one site, the most complex one, 12 months of data were analysed to understand whether the meandering occurred, in what conditions and whether empirical formulae used to approximate the autocorrelation and the velocity and temperature spectra in flat and homogeneous terrains could be applied in complex terrain. Empirical formulae proposed in recent years were fitted to the experimental autocorrelations and spectra. Results highlight that the formulae can be used and they give useful insights on the local boundary layer behaviour, although there is a need, for the future, to consider more deeply the site characteristics if in non-ideal and non-homogeneous topography.

Considering a distinction between complete meandering (*u, v, T* oscillate – that is, all the autocorrelation functions show an oscillating behaviour), almost meandering (at least one variable shows oscillations) and no meandering (no oscillations), the complete meandering was rare (75 hours identified over more than 3000 hours), whereas almost meandering and not meandering conditions were the most frequent conditions. Meandering tended to occur when cloudy sky existed.

Appendix A

Multi-resolution decomposition technique (MRD)

This appendix deepens the concepts of cospectrum and multi-resolution decomposition presented in Chapters 2 and 4.

The geophysical signals can be decomposed on different (temporal) scales. Given a cross-covariance between two random variables a and b ($\overline{a'b'}$), it is possible to evaluate its Fourier spectrum, which is composed of a real part (called cospectrum, $C_{a,b}$) and an imaginary part (called quadrature spectrum). The cospectrum gives information about the averaging time and frequency response for the fluxes estimation. In addition, the fluxes, as already illustrated in Chapter 2, are the integrals of cospectra on the whole frequency domain (from f=0 to ∞):

$$\overline{a'b'} = \int_0^\infty C_{a,b}(f)df \tag{A1}$$

Cospectra of covariances can be interpreted as fluxes decomposed into values computed from moving averages (Howell and Mahrt, 1997). The turbulent fluxes (or, better, the covariances) can be thought as locally decomposed into several "modes". Each mode is an unweighted moving average and it satisfies Reynolds' averaging, unlike Fourier analysis (e.g. Vickers and Mahrt, 2003).
The flux decomposition in different time scales is performed computing time averages on non-overlapping windows with different length.

Considering the time series of vertical velocity w and a scalar S (water vapour, carbon dioxide, temperature), consisting of 2^M points, the steps are the following:

1) Subrecord averages (for the nth segment at scale m) of the time series are computed over a window of 2^m points

$$w_n(2^m) = \frac{1}{2^m} \sum_{i=(n-1)2^m}^{n2^m-1} w_i \tag{A2}$$

The averages are on different scales (that is, segment length), from 1 to 2^M consecutive data points. The number n, integer, refers to the position of the $2^{(M-m)}$ averaging windows of different length of 2^m points (averaging length). Note that

the lowest order mode ($m=M$) corresponds to the largest averaging scale, whereas the highest order mode ($m=0$) corresponds to the shortest averaging timescale.

The same approach is also applied to the scalar variable.

2) The vertical flux is computed as

$$\overline{w'(2^m)S'(2^m)} = \frac{1}{2^M}\sum_{i=0}^{2^M-1}\left(w_i - \overline{w_n}(2^m)\right)(S_i - \overline{S_n}\,(2^m)) \tag{A3}$$

The multiresolution cospectra for two time series, can be written as in Eq. (A3).

$$\begin{aligned}\overline{\delta w(2^m)\delta S(2^m)} &= D_{wS}(m+1)\\ &= \frac{1}{2^{M-m}}\sum_{n=1}^{2^{M-m}}[w_{2n}(2^{m-1}) - \overline{w_n}(2^m)]\ [\overline{S_{2n}}(2^{m-1}) - \overline{S_n}(2^m)]\\ &= \frac{1}{2^{M-m}}\sum_{n=1}^{2^{M-m}}\overline{w_n}(m)\overline{S_n}(m)\end{aligned} \tag{A4}$$

Eq. (A3) shows a multiresolution cospectrum for the averaging length of 2^m points. For each temporal length, a cospectrum is therefore computed. This allows to determine an appropriate averaging period, which is the one found when the flux crosses the zero line in the plot of cospectrum versus time, as illustrated in Chapter 4.

The sum of $D_{wS}(m)$ over scales from 1 to $P<M$ is the average eddy correlation flux computed considering an averaging scale of 2^P points:

$$\sum_{m=1}^{P} D_{wS}(m) = [(w - \overline{w}^P)(S - \bar{S}^P)]$$

The length of the record (2^M points) indicates the time period of the average of the flux.

The total flux of Eq. (A4) over the time span 1 to $P=M$ is given by Eq. (A5).

$$\begin{aligned}\overline{w'(2^M)S'(2^M)} &= \sum_{m=1}^{M} D_{wS}(m) = \sum_{m=1}^{M}\overline{\delta w(2^m)\delta S(2^m)}\\ &= [(w - < w >)(S - < S >)]\end{aligned} \tag{A5}$$

where the symbol < > indicates the average over the whole time series length.

Appendix B

Coordinate rotation

The post-processing requires the use of coordinate rotation technique to align the wind speed measurements with the mean streamlines, as illustrated in Chapter 2 and 4. Two main configurations were tested at Cogne and Nivolet: double rotation and planar fit.

The yaw and pitch angles of the double rotation performed at Cogne and at Nivolet are illustrated in Figures B1 and B2 for half hourly time step.

In the figures, the yaw angles are related to the wind direction regime, whereas the pitch angles reveal that the double rotation is likely reliable at both sites, since the tilt changes are generally not extreme. This may suggest that the double rotation is characterised by a streamwise plane which does not vary severely and without unrealistic tilt (or pitch) angles.

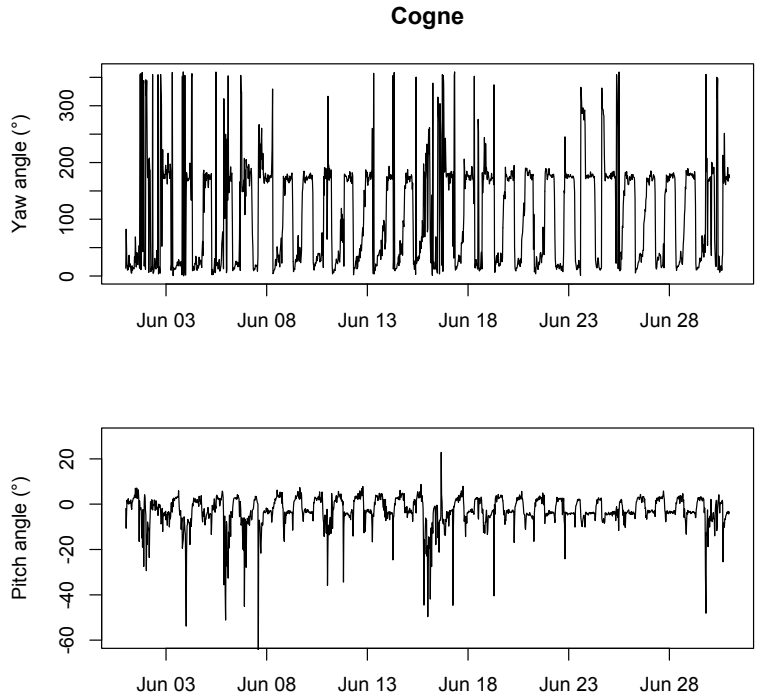

Figure B 1. Yaw and pitch angles after double rotation for Cogne fluxes on the period 1 June – 30 June 2016.

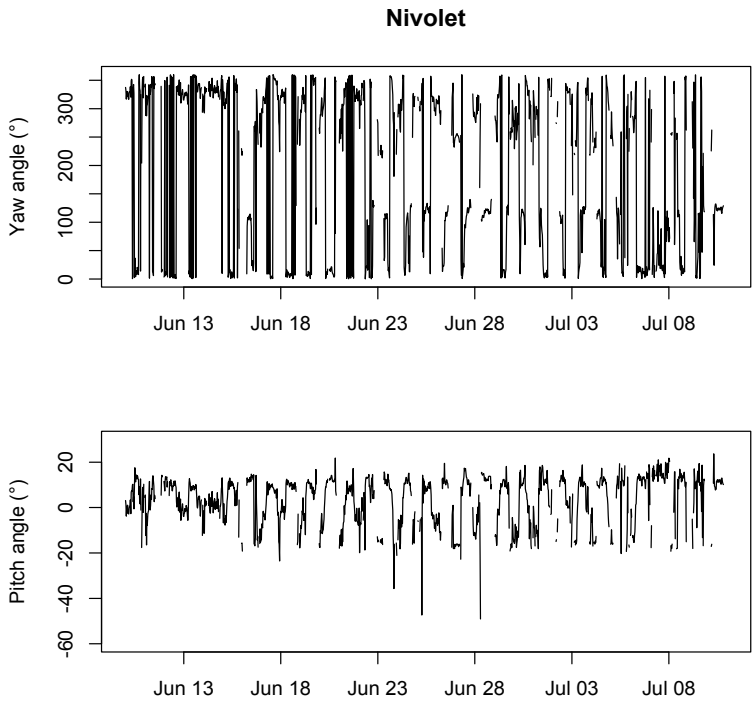

Figure B 2. Yaw and pitch angles after double rotation for Nivolet fluxes on the period 10 June – 10 July 2019.

The planarity of the flow can be tested plotting the tilt angle between the fitted plane obtained from planar fit algorithm and the mean wind speed vector (Figures B3 and B4). If the data lie on the plane, the method can be applied without issues and it is more reliable. The plot is performed dividing the wind direction (obtained from the wind speed vector) in sectors. In this case, in agreement with Golzio et al. (2019), wind direction sectors of 10° were used.

Results suggest that at Cogne, the planar fit can be used but considering a reduction of reliability, because the data lie not exactly on the plane and the sinusoidal form is not fully obtained, indicating possible non-planarities of the wind velocity vector, although not severe. Hence, the PF can be used but with care, and Chapter 9 of the Thesis tested its use at Cogne. At the Nivolet site, there is a higher PF performance and a single PF plane can interpolate appropriately the wind vectors.

Despite the potential use of planar fit, the double rotation was revealed to be more appropriate at both sites but for different reasons. At Cogne, from a theoretical point of view, DR yields better results and, according to Stiperski and Rotach (2016) it gives also higher flux estimates. At Nivolet, the pole oscillations due to more frequent high-wind speed make the PF technique use more complex, because PF technique assumes that the anemometer is not moved at all.

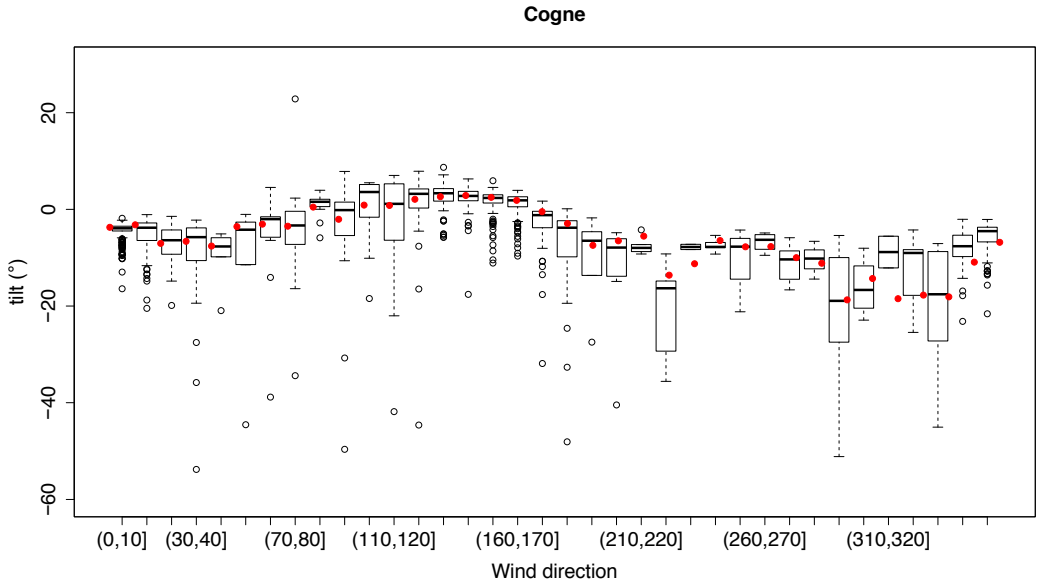

Figure B 3. Distribution, for the Cogne site, of the tilt angle of the 10° sectors for mean velocity vectors above the horizontal plane. The black boxplot represents the measured data, whereas red dots are the medians of the points on the ideal plane. Data from 1 June to 30 June 2016.

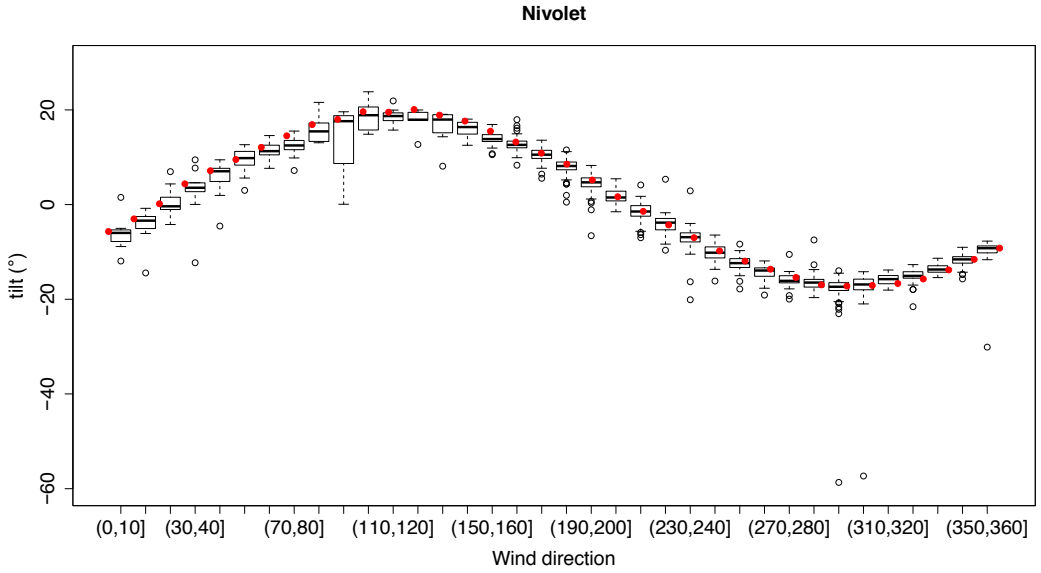

Figure B 4. Distribution, for the Nivolet site, of the tilt angle of the 10° sectors for mean velocity vectors above the horizontal plane. The black boxplot represents the measured data, whereas red dots are the medians of the points on the ideal plane. Data from 1 June to 10 July 2019.

Appendix C

Computing potential evapotranspiration

The Penman-Monteith equation is given by Eq. B1.

$$ET_o = \frac{1}{\lambda}\left(\frac{\Delta(R_n - G_0) + \frac{\rho_a c_p (e_s - e_a)}{r_a}}{\Delta + \gamma\left(1 + \frac{r_s}{r_a}\right)}\right) \quad \text{(B1)}$$

As already explained in Chapter 7, Δ (kPa °C^{-1}) is the slope of the curve in Clausius-Clapeyron equation, R_n is the net radiation (W m^{-2}), G_0(W m^{-2}) is the ground heat flux at the surface, γ is the psychrometric constant, ρ_a(kg m^{-3}) is the mean air density at constant pressure; c_p (J kg^{-1}K^{-1}) the specific heat of the air; r_a (s m^{-1}) is the aerodynamic resistance, r_s (s m^{-1}) is the bulk surface resistance, λ (MJ kg^{-1}) is the latent heat of evaporation for water.

The specific heat of the air and the air density can be expressed as $c_p = \frac{\gamma \epsilon \lambda}{P}$ and $\rho_a = \frac{P}{T_{virt} R}$. $\epsilon = 0.622$ is the ratio molecular weight of water vapour over dry air, P is the air pressure in kPa, $T_{virt} = 1.01(T + 273.5)$, in Kelvin is the virtual temperature, R=0.287 kJ kg^{-1}K^{-1} is the gas constant.

The radiative terms R_n and G_0, and the vapour pressure e_s derive from measures, whereas the other terms need to be estimated with the following formulae:

$$\lambda = 2.500 - 0.00236\, T \quad \text{(B2)}$$

$$\Delta = \frac{2508.3\ \mathrm{e}^{\left(\frac{17.27\, T}{T+237.3}\right)}}{(T + 237.3)^2} \quad \text{(B3)}$$

$$e_s = 6.11\ e^{\frac{17.62\, T}{T+237.3}} \quad \text{(B4)}$$

where T is the measured air temperature.

$$r_a = \frac{\ln\left[\frac{z_m - d}{z_{om}}\right] \ln\left[\frac{z_h - d}{z_{oh}}\right]}{k^2 u} \quad \text{(B5)}$$

$$r_s = \frac{r_i}{LAI_{active}} \quad \text{(B6)}$$

where $z_h = 2\,m$ is the relative humidity measurement height; $z_m = 2\,m$ is the measurement height of wind speed ; z_{om}=0.123 h; h=0.25 m is the canopy height $z_{oh} = 0.1\,z_{om}$; $d = \frac{2}{3}h$ is the zero plane displacement height. k^2 is the square of Von Karman constant (k=*0.41*); u is the average hourly wind speed.

$r_i = 100$ is the bulk stomatal resistance of a well-illuminated leaf; (Allen et al., 1998); An approximation of LAI is given by $LAI = 24\,h$; $LAI_{active} = 0.5\,LAI$

With the required substitutions and multiplying by 3600 s, one finds Eq. B7 for the potential evapotranspiration:

$$ETo = \left(\frac{\Delta(\mathrm{R_n} - G_0)}{\lambda} + \frac{\gamma\ 3600\ \epsilon\ (e_s - e_a)}{r_a\ 1.01\ (T + 273.15)R}\right)\frac{1}{\Delta + \gamma(1 + \frac{r_s}{r_a})}$$

Appendix D

Regional modelling of evapotranspiration

METRIC

The incoming solar radiation computation used within METRIC, shown in Eq. A1, gives the total amount of solar radiation, as direct and diffuse, causing an underestimation over steep sloped areas

$$SW_{in} = \frac{G_{sc}\cos(\theta_{rel})\tau_{sw}}{d^2} \quad \text{(A1)}$$

where G_{sc} is the solar constant (1367 W m^{-2}); θ_{rel} is the solar incidence angle, d^2 is the square of the relative distance between Earth and Sun in astronomical units and τ_{sw} is the broad-band atmospheric transmissivity.

METRIC has been developed for gently sloping areas, this fact leads to some changes for the computation of variables affected by orography, namely, the incident solar radiation. Allen et al. (2007) show a known formula to derive the solar incidence angle pixel by pixel, because that angle is no more equal to the solar zenith.

A significant source of uncertainty of METRIC outputs is related to the sensible heat component because of the internal calibration procedure. The sensible heat is computed as in Eq. A2:

$$H = \rho_{air} c_p \Delta T / r_{ah} \quad \text{(A2)}$$

where ρ_{air} is the air density, c_p is the air specific heat at constant pressure and r_{ah} is the aerodynamic resistance between two near surface heights. The term ΔT is computed with an internal calibration and it is necessary to choose a “hot” pixel and a "cold" pixel, for which the sensible heat is already known or easily computable.

In this paper, the “cold” pixel is set over an Alpine lake located within the domain, hence $ET = ETo$ and ETo is computed using the Priestley-Taylor (PT) equation (with $\alpha = 1$ as the parameter in PT Equation), whose variables are provided in METRIC.

The "hot" pixel is set where *H* is supposed to be maximized, so the goal is to select a pixel with shallow soil depth, facing south, with scarce vegetation and high temperature.

The METRIC model needs the following inputs:

- satellite images from the visible and infrared spectral regions;
- a digital elevation model;
- a weather station measuring vapour pressure and wind speed.

In the present case, Landsat 8 images are used to compute the Top of Atmosphere (TOA) reflectance. The conversion from digital numbers to TOA reflectance is computed according to USGS (2019). The retrieved satellite images have a pixel size of 30 m. This satellite passes every 16 days, but image quality and availability depend on weather conditions, hence for the time period studied, three acquisitions are very good (27 August 2014, 13 July 2015 and 30 August 2015), whereas the fourth acquisition (27 June 2015) is also used but its quality is lower. The passing time is almost constant at about 10:15 UTC.

The other input used in METRIC are a digital elevation model of Aosta valley, that is the same used for the model, and the vapour pressure and the wind speed data measured in Cogne.

TopoToolbox

TopoToolbox is a code written in Matlab (Schwanghart and Scherler, 2014). It is a collection of functions providing utilities for spatial and non-spatial numerical analysis. The tool allows to read a DEM importing it into a Matlab environment. The DEM must have a projected coordinate system (in this case: UTM WGS84) and it is considered as an instance of the object called “GRIDobj”. The DEM contains properties included the gridded data and information on the spatial referencing of the grid. Information such as pixel slope, aspect (its orientation), altitude a.s.l. is included.

Among the TopoToolbox functions, in this Thesis the mainly used algorithms were: i) “sun position” which determines the solar position along the day as a function of local time and geographical position; ii) “castshadow”, which allows also the determination of the shading due to obstacles (i.e. the shadow created by the mountains), with a “1 (true)” on pixels with shadow and “0 (false)” on the others. The shading is computed when the Sun is above the horizon, and it requires the geographical information given by an accurate DEM.

Appendix E

Micrometeorological and soil variables for each snow event

In this Appendix, the turbulent, radiative and non-radiative fluxes, air, surface and soil temperature, wind speed and friction velocity are shown for a better understanding of each snowfall – snowmelt event.

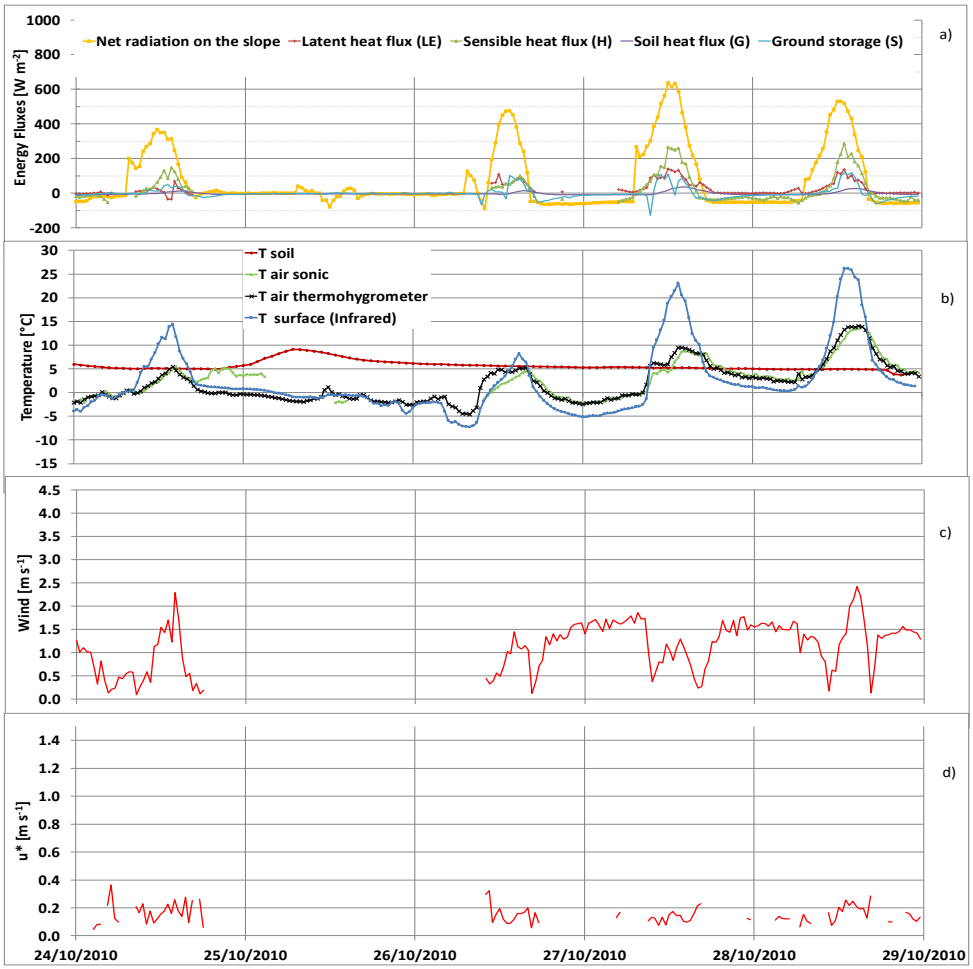

Figure E 1. Event from 24th October to 28th October 2010. Panel a): half hourly values of sensible heat, latent heat fluxes, net radiation, ground heat flux and storage. Panel b): Air (from both sonic anemometer and thermohygrometer), soil and surface (with either snow or not) temperatures. Panel c): Wind speed. Panel d): friction velocity.

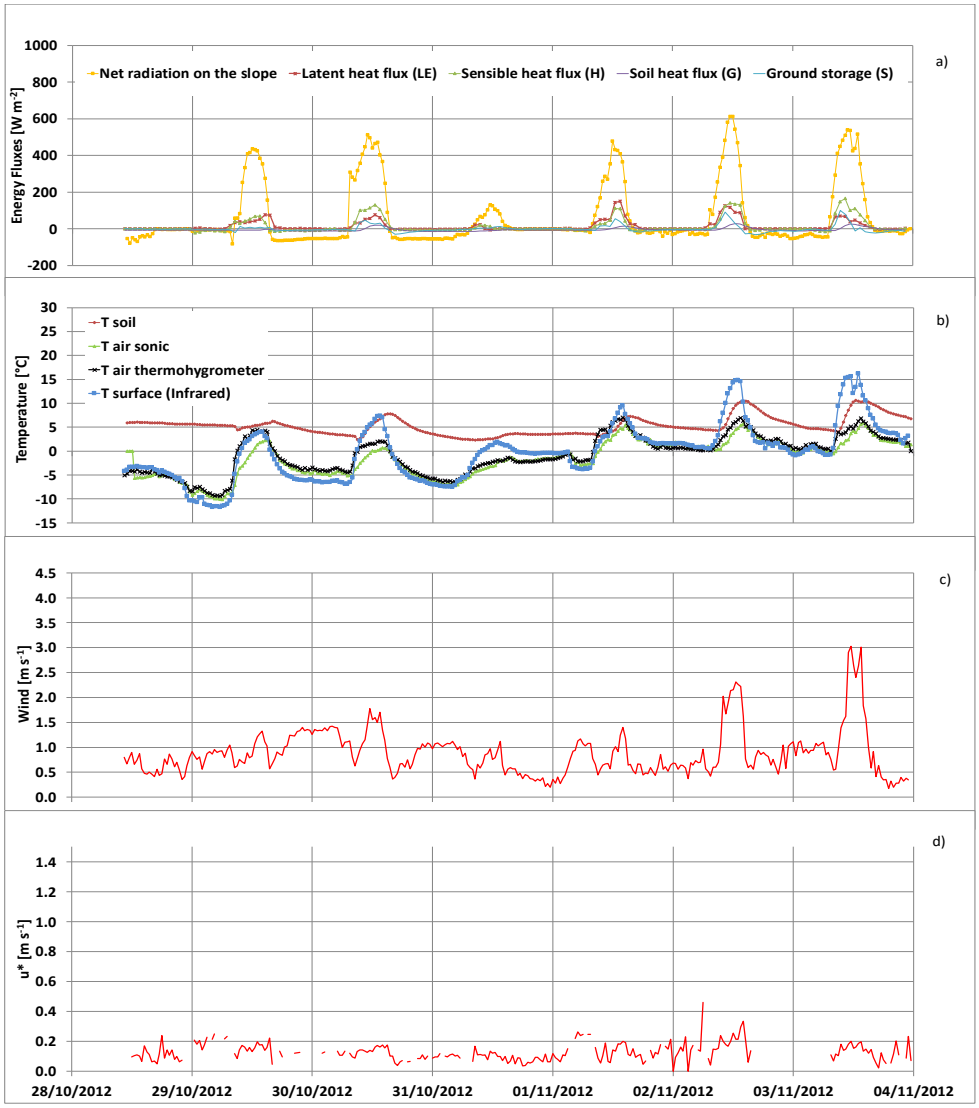

Figure E 2. Event from 31st October to 3rd November 2012. Panel a): 30-minute values of sensible heat, latent heat fluxes, net radiation, ground heat flux and storage. Panel b): Air (from both sonic anemometer and thermohygrometer), soil and surface (with either snow or not) temperatures. Panel c): Wind speed. Panel d): friction velocity.

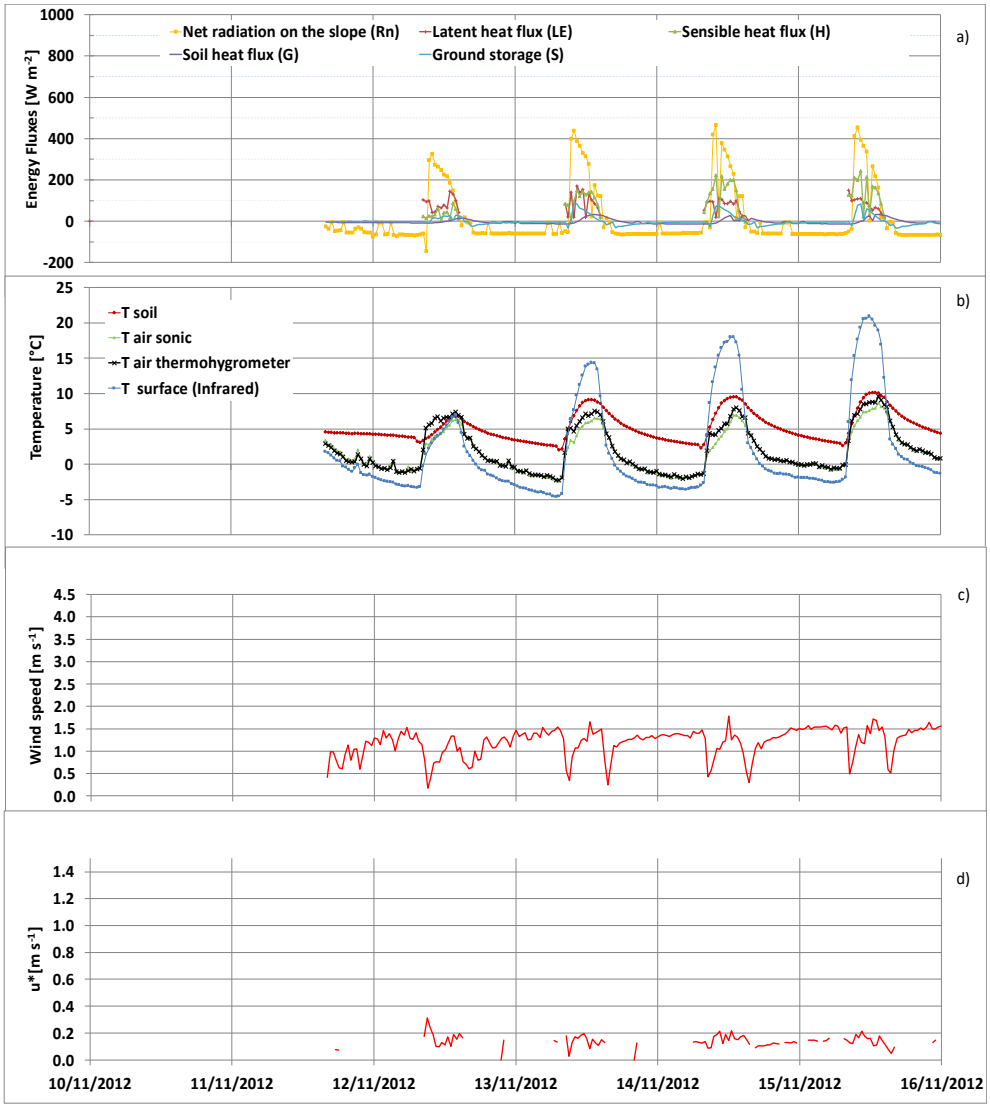

Figure E 3. Event from 10th to 15th November 2012. Panel a): 30-minute values of sensible heat, latent heat fluxes, net radiation, ground heat flux and storage. Panel b): Air, soil and surface temperatures. Panel c): Wind speed. Panel d): friction velocity.

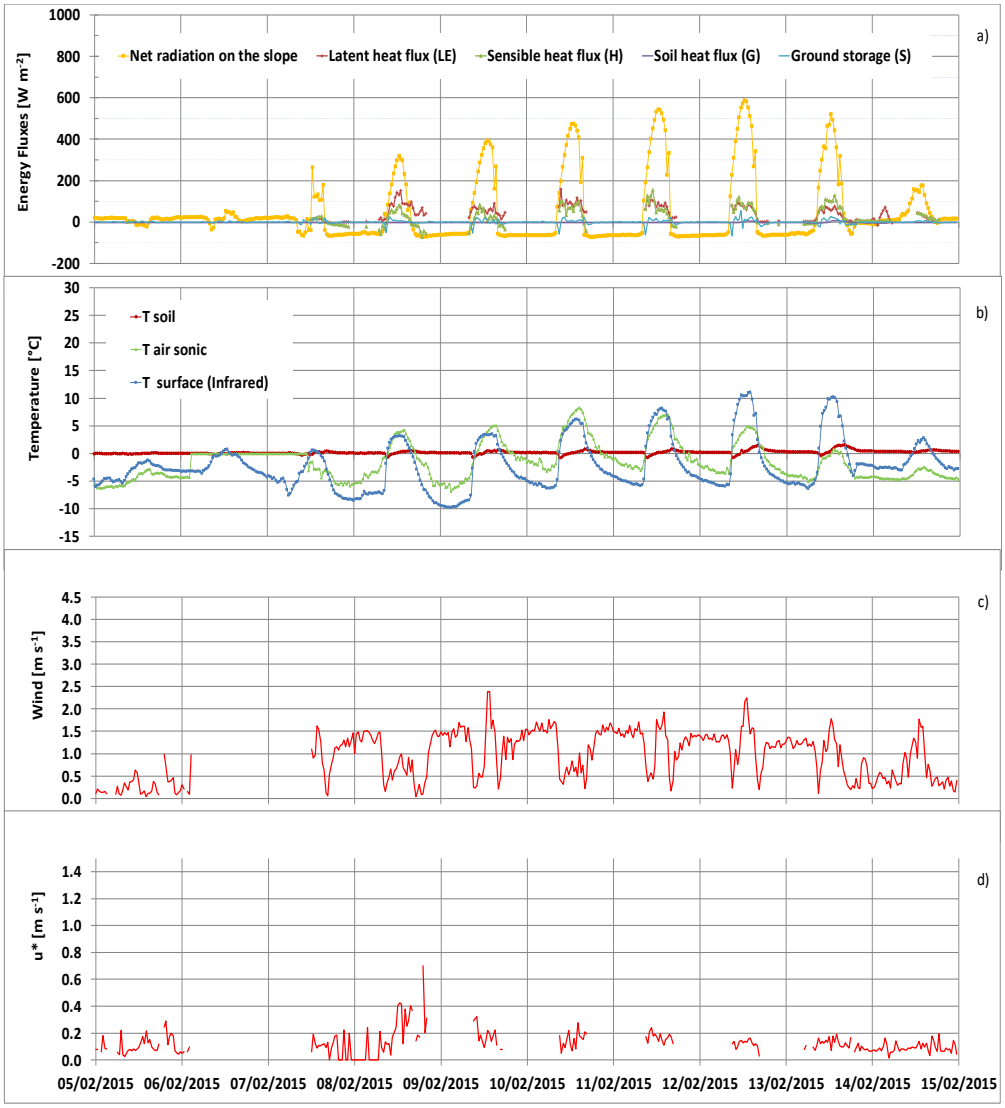

Figure E 4. Event from 7th to 14th February 2015. Panel a): 30-minute values of sensible heat, latent heat fluxes, net radiation, ground heat flux and storage. Panel b): Air (from only the sonic anemometer), soil and surface (with either snow or not) temperatures. Panel c): Wind speed. Panel d): friction velocity.

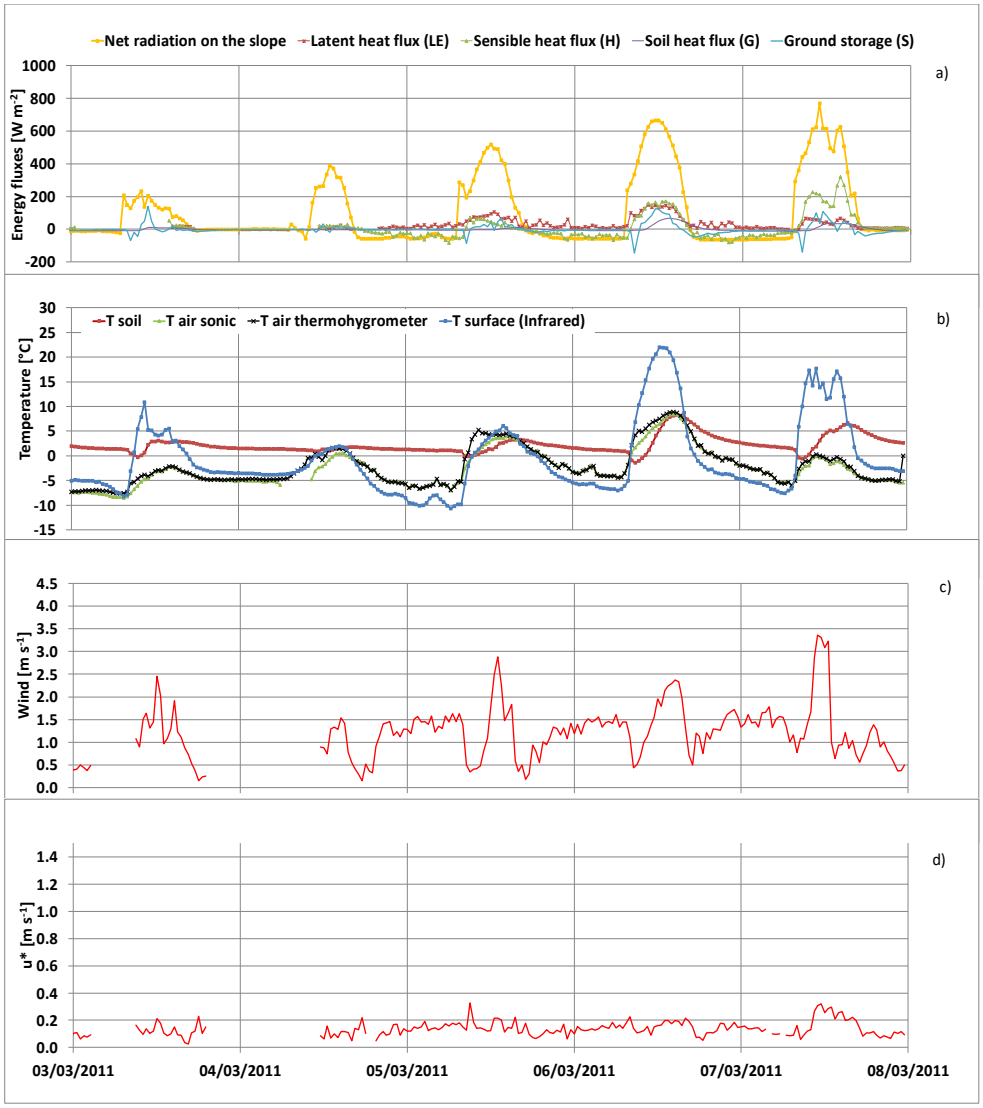

Figure E 5. Event from 3rd to 7th March 2011. Panel a): 30-minute values of sensible heat, latent heat fluxes, net radiation, ground heat flux and storage. Panel b): Air (from both sonic anemometer and thermohygrometer), soil and surface (with either snow or not) temperatures. Panel c): Wind speed. Panel d): friction velocity.

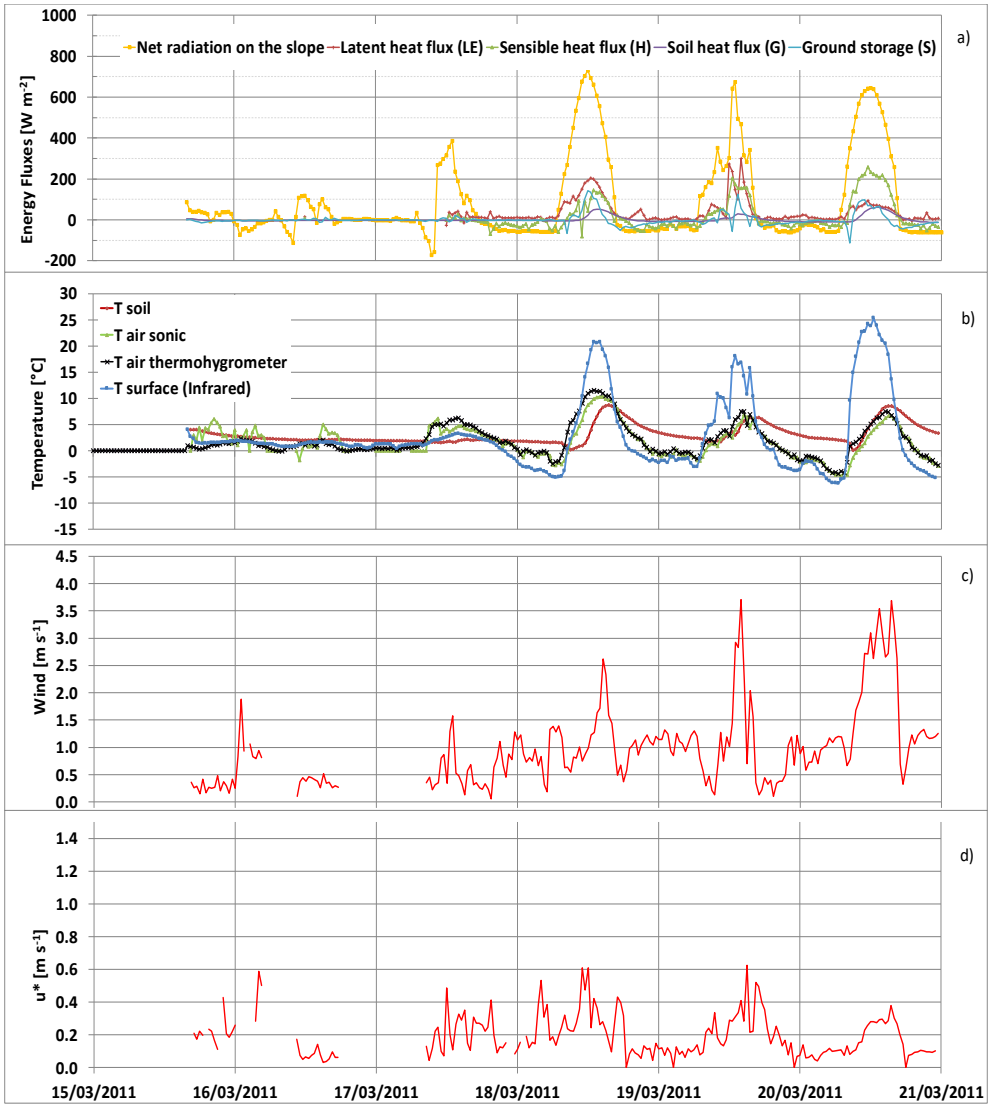

Figure E 6. Event from 15th March to 21st March 2011. Panel a): half hourly values of sensible heat, latent heat fluxes, net radiation, ground heat flux and storage. Panel b): Air (from both sonic anemometer and thermohygrometer), soil and surface (with either snow or not) temperatures. Panel c): Wind speed. Panel d): friction velocity.

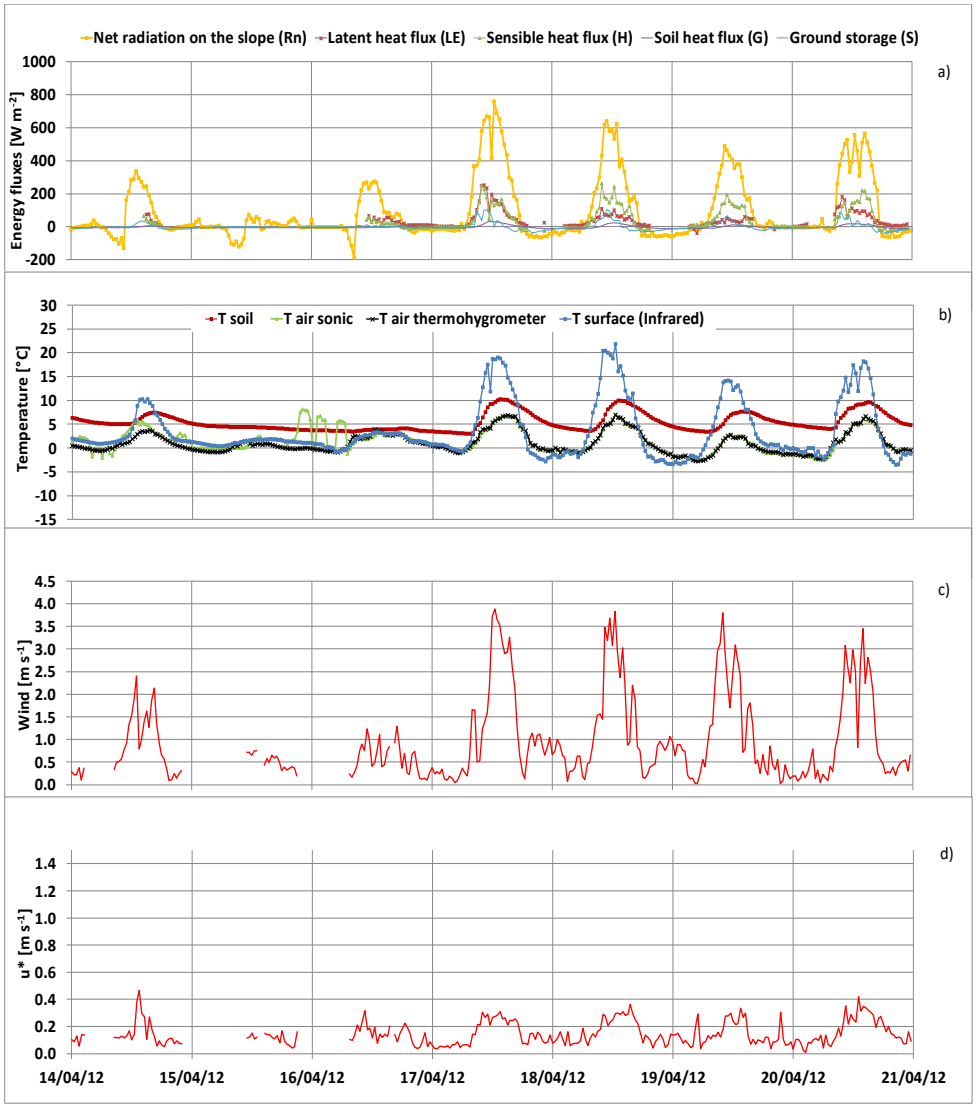

Figure E 7. Event from 14th April to 20th April 2012. Panel a): half hourly values of sensible heat, latent heat fluxes, net radiation, ground heat flux and storage. Panel b): Air (from both sonic anemometer and thermohygrometer), soil and surface (with either snow or not) temperatures. Panel c): Wind speed. Panel d): friction velocity.

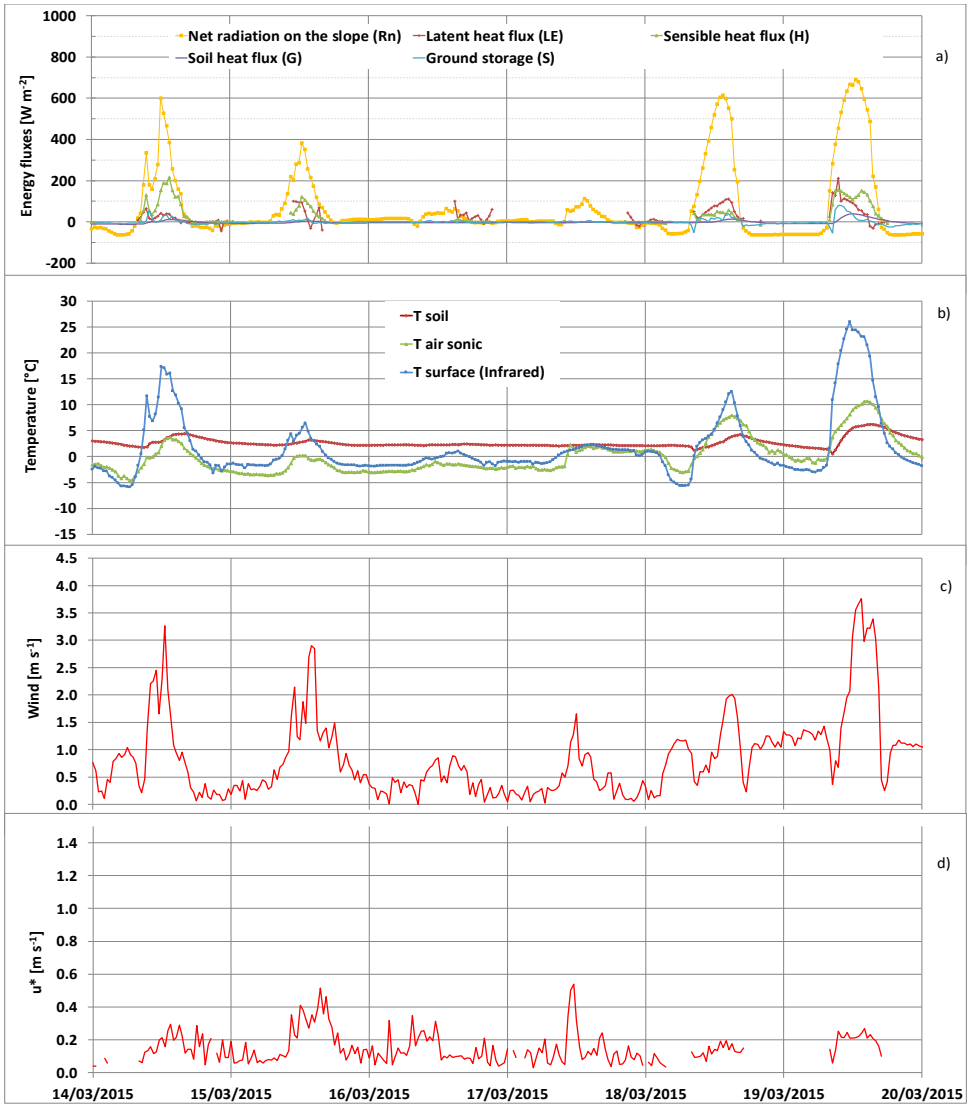

Figure E 8. Event from 15th March to 19th March 2015. Panel a): half hourly values of sensible heat, latent heat fluxes, net radiation, ground heat flux and storage. Panel b): Air (from only the sonic anemometer), soil and surface (with either snow or not) temperatures. Panel c): Wind speed. Panel d): friction velocity.

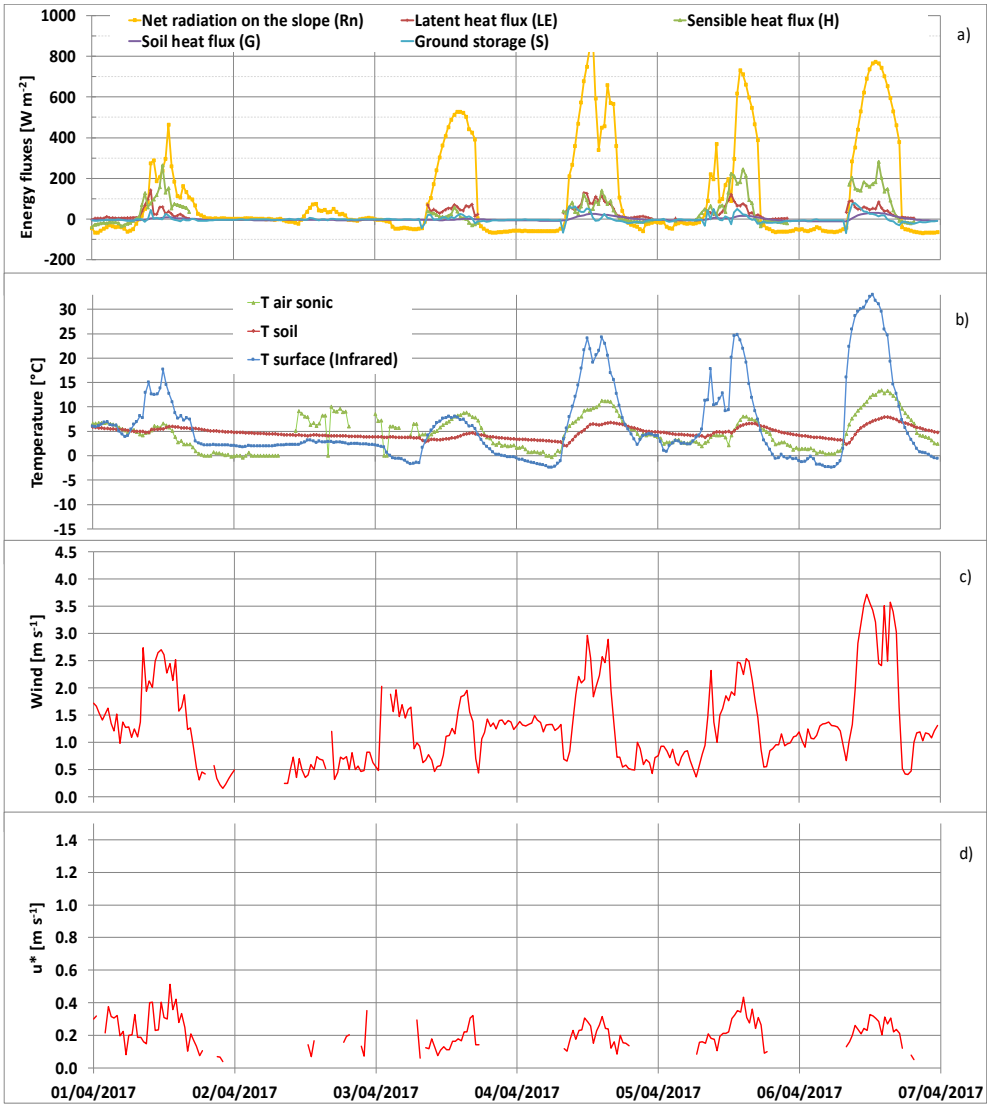

Figure E 9. Event from 1st April to 6th April 2017. Panel a): half hourly values of sensible heat, latent heat fluxes, net radiation, ground heat flux and storage. Panel b): Air (from only the sonic anemometer), soil and surface (with either snow or not) temperatures. Panel c): Wind speed. Panel d): friction velocity.

Appendix F

List of main R packages

List of the main, advanced packages for R software environment used in this Thesis.

ggplot2

It is a package allowing an advanced data representation by means of graphics such as simple plots but with a very good rendering, composite plots with multiple axes, scatter plots, maps, histograms, density and frequency distributions data fitting, contourplots, box plots and signals spectrum.

For further reading and downloading the package:

https://cran.r-project.org/web/packages/ggplot2/ggplot2.pdf
https://cran.r-project.org/web/packages/ggplot2/index.html

hht

It is a package written to provide tools for empirical mode decomposition (EMD) and Hilbert spectral analysis. The main function used to compute EEMD is

EEMD(*signal, tt noise.amp, nimf,trials*)

where *signal* is the time series; *tt* is the sample times of the signal (10 Hz); *noise.amp* is the noise amplitude equal to 0.1 $RMS(signal)$ as in Wu and Huang (2009), where $RMS(signal)$ is the root mean square of the time series; *nimf* is the number of IMFs to record for each trial (13, according to Gao et al., 2017); *trials* is the number of trials (in this Thesis a number of 20 trials was considered appropriate).

For further reading and downloading the package:

https://cran.r-project.org/web/packages/hht/hht.pdf
https://cran.r-project.org/web/packages/hht/index.html

lmodel2

This package computes linear regressions using several techniques. Ordinary least squares (OLS), major axis (MA), standard major axis (SMA) and ranged major axis (RMA) depending on the data set and the required analyses (in this Thesis, lmodel2 package was used selecting the ranged major axis – RMA). The RMA allows to overcome several problems of the ordinary least squares, such as the assumption of no error on the *x* variable (or, in reality, the error of the *y* variable is far greater than that assigned to the *x* variable). Also, the RMA regression solves some issues encountered with MA (e.g. regressions with variables having different units might produce results varying with the scales of the variables) and SMA (the standardisation occurs dividing each variable after the mean subtraction with the standard deviation, and the transformation makes all the variances equal). In addition, RMA is desirable when it is not clear whether a variable is dependent or independent, and when a control on the variables cannot be obtained (i.e. when it is not clear or possible to change one variable value to produce changes in another variable in a controlled way such as in a laboratory). However, the RMA regression requires a control to eliminate outliers.

The RMA is based on the ranging method which normalizes the variables with the following transformation

The steps of the regression are the following:

a) Transform the variables using $y_i' = \frac{y_i - y_{min}}{y_{max} - y_{min}}$ (ranging method)
b) Compute MA regression between the ranged variables. The major axis regression relies on the principal component analysis, in the sense that the regression line is the first principal component of the scatter of points. The objective function to be minimised is the sum of the Euclidean distances between the points and the regression line. The sum is intended over all points.
c) Back-transform the slope and confidence intervals to the original units multiplying them by the ratio of ranges.

The used function is called lmodel2 and it has the following syntax:

lmodel2(*H+LE ~ Rn-G-S, data, range.y="interval", range.x="interval", nperm=10000*)

It requires the formula used to fit the data; the data frame containing the variables of the regression; the parameters for the RMA *("range.y", "range.x"*)

and the number of permutations for the significance of the tests. For the analyses performed in this Thesis, the number of permutations was 10000.

The function yields the results of ordinary least squares, major axis, standard major axis and ranged major axis. The ordinary least squares regression is known, whereas the others are more recent. The significance of the regression slope is computed via a permutation test. The values of the variables are permuted many times and at each step, the regression slope is estimated. The algorithm computes the probability of observing a slope greater or equal to the one of the reference distribution. The less the probability is, the more the slope is statistically significant.

For further reading and downloading the package:

https://cran.r-project.org/web/packages/lmodel2/lmodel2.pdf
https://cran.r-project.org/web/packages/lmodel2/index.html

Metvurst

Metvurst is a package also containing a function which allows to draw color and contourmaps of a scalar quantity together with wind speed and wind direction frequency. This map is a different way of representing wind rose coupled with the value of the scalar variable. Hence, the plot illustrates a sort of "spatial information" around the measurement point. The "windContours" function provides an overview of the wind field climatology plotting wind direction, scalar (such as temperature, water vapour, carbon dioxide) and, in a separate panel, wind speed as a function of the hour of the day. Plus, the wind speed is plotted using a box plot. These approaches allow to identify diurnal flow climatologies. The wind frequencies illustrate the percentage of hours in which the wind flow comes from a certain direction. The scalar is related to wind direction and hour via a contingency table.

The used function syntax is the following:

windContours (*hour,wd,ws = hour, add.var, key.spacing = 10, gapcolor = "grey50", colour = brewer.pal(9, "Greys")*)

The function requires the specification of hour, wind direction (wd), wind speed (ws), add.var=TRUE if the user wants to use a scalar variable, the interval (key.spacing), between two values on the colour scale (as those illustrated in Chapter 4), and instructions on the colour map and wind speed boxplot colours (capcolor, colour)

For further reading and downloading the package functions:
https://metvurst.wordpress.com/2013/03/04/visualising-diurnal-wind-climatologies-2/;

https://github.com/tim-salabim/metvurst/tree/master/R

Openair

Openair is a package which allows the analysis, interpretation and understanding of meteorological and scalar (e.g. pollutant, carbon dioxide, water vapour) dispersion and transport. It allows also the representation of wind roses. In particular, the functions windRose and pollutionRose were used to plot wind roses, that is, wind speed and wind direction are plotted by different intervals.

The windRose function requires a data frame including the wind speed (*ws*) and wind direction (*wd*), the wind speed interval (*ws.int*) and the wind direction bins (*angle*).

The used syntax was

windRose(*data, ws="ws", wd="wd", ws.int=0.5,angle=36*)

The function pollutionRose has the same plot structure as windRose and it was used also to produce more easily understandable wind roses. The used syntax was:

pollutionRose(*data, pollutant="ws", breaks=seq(0,6.5,0.5), max.freq=50*)

"Breaks" is the number of break points for wind speed (or pollutants). Max.freq controls the scaling used by setting the maximum value for radial limits of the wind rose.

For further reading and downloading the package:

https://github.com/tim-salabim/metvurst/tree/master/R;
https://cran.r-project.org/web/packages/openair/openair.pdf

REddyProc

This package implements the standard methods for processing, filtering and filling the gaps of eddy covariance data. The package allows for a friction velocity filtering with the approach suggested by Papale et al. (2006). The friction velocity threshold is estimated in each season binning the records with similar $u*$. The binning is designed to ensure that there is a minimum of records in each bin. For each bin, the average $u*$ and NEE are estimated. The friction velocity threshold is then estimated via a moving point test applied for every bin. Again for each bin, the algorithm checks whether the bin of NEE is higher than 0.95 times the NEE mean of the following 10 bins. If this is true, the $u*$ mean of the bin is classified as "threshold".

The package allows also the gap-filling with approaches similar to the one presented by Falge et al. (2001). An additional feature is implemented: indeed, the covariation of fluxes with other meteorological variables is used, as well as the temporal auto-correlation of fluxes, as suggested by Reichstein et al. (2005). Three conditions are considered:

1) If only flux data are missing, but global radiation, air temperature and VPD are present
2) Also air temperature and VPD are missing, but global radiation is available
3) Also global radiation is missing.

In case 1) look-up tables (LUT) are used, and the missing values are replaced by the average of values found in similar meteorological conditions with a time window of 7 days. If no similar conditions are found in that window, the size is then increased to 14 days.

In case 2), the algorithm considers the same LUT approach. However, similar meteorological conditions are only defined through the global radiation within 7 days of temporal window.

In case 3), the missing flux values are replaced by the average of the values at the same time of the day and a linear interpolation of data available at adjacent hours is performed.

For further reading and downloading the package:
Wutzler et al. (2018);
https://www.bgc.jena.mpg.de/bgi/index.php/Services/REddyProcWebRPackage;
https://www.bgc-jena.mpg.de/bgi/index.php/Services/REddyProcWeb

Stats

The "Stats" package allows the use of basic statistical analyses. It allows the ANOVA analysis, linear models, t-test, Akaike information criterion, loess, linear, generalized linear and nonlinear fitting, autocorrelation functions, Fourier spectra (via Fast Fourier Transform, FFT), statistical momenta, covariances, calculation of Kernel density.

For further reading and downloading the package:
https://stat.ethz.ch/R-manual/R-devel/library/stats/html/00Index.html

Note: All URLs were consulted on 13 September 2021.

References

1. Abera W., Formetta G., Borga M. and Rigon R. (2017). Estimating the water budget components and their variability in a Pre-Alpine basin with JGrass-New AGE. Advences in water resources. doi: 10/1016j.advwatres.2017.03.010.

2. Acevedo O. C., Moraes O.L.L., Degrazia G.A. ; Fitzjarrald, D.R., Manzi, A.O. Campos J. G. (2009). Is friction velocity the most appropriate scale for correcting nocturnal carbon dioxide fluxes?, Agr.For.Met. 149:1-10. doi: 10.1016/j.agrformet.2008.06.014.

3. Anav A., Ruti P.M., Artale V. and Valentini R. (2010). Modelling the effects of land-cover changes on surface climate in the Mediterranean Region. Clim. Res. 41:91-104.

4. Aguilar C., Herrero J. and Polo M. (2010). Topographic effects on solar radiation distribution in mountainous watersheds and their influence on reference evapotranspiration estimates at watershed scale. Hydrol. and Earth Sys. Sci. 14(12): 2479-2494.

5. Alexander J., Diez J. and Levine J. (2015). Novel competitors shape species' responses to climate change. Nature, 525: 515-518. doi: 10.1038/nature14952.

6. Allen R.G., Pereira L.S., Raes D. and Smith M., "Crop evapotranspiration, guidelines for computing crop water requirements*",* FAO irrigation and drainage paper no. 56 (1998). FAO-Food and Agriculture Organization of the United Nations, Rome.

7. Allen R.G., Tasumi M., and Trezza R. (2007). Satellite-based Energy Balance for Mapping Evapotranspiration with Internalized Calibration (METRIC) – Model. J. Irrig. Drain. Eng., 133 (4), 380–394. doi:10.1061/(ASCE)0733-9437(2007)133:4(380).

8. Andreas, E.L., Paulson, C.A., Williams, R.M., Lindsay, R.W., and Businger, J.A., (1979). The turbulent heat flux from Arctic leads. Bound. -Lay. Meteorol. 17, 57–91. doi:10.1007/BF00121937.

9. Anfossi D., Oettl D., Degrazia G. and Goulart A. (2005) An analysis of sonic anemometer observations in low wind speed conditions. Boundary-Layer Meteorology 114: 179–203

10. Appelhans T. (2013). Metvurst: meteorological visualisation utilities using R for science and teaching. R package version 0.0.1.

11. Arck, M. and Scherer, D., 2002. Problems in the determination of sensible heat flux over snow. Geogr. Ann., 84A (3-4), 157-169.

12. Armstrong R.L. and Brun E. (edited by), "Snow and Climate, Physical processes, surface energy exchange and modelling", Cambridge University Press, 222 pp, 2009.

13. Arriga N., Rannic U., Aubinet M., Carrara A., Vesala T. and Papale D., "Experimental validation of footprint models for eddy covariance CO2 flux measurements above grassland by means of natural and artificial tracers", Agr.For.Met.(2017) 242: 75-94.

14. Arya S.P. (1988). Introduction to micrometeorology. Academic Press, 303 pp

15. Asse D., Chuine I., Vitasse Y., Yoccoz N.G., Delpierre N., Badeau V., Delestrade A., Randin C.F. (2018). Warmer winters reduce the advance of tree spring phenology induced by warmer springs in the alps. Agric. For. Meteorol., 252, p. 220–230. doi: 10.1016/j.agrformet.2018.01.030.

16. Auer I., Böhm R., Jurkovic A., Lipa W., Orlik A., Potzmann R. et al. (2007). HISTALP – historical instrumental climatological surface time series of the Greater Alpine Region. Int. J. Climatol. 27: 17-46. doi: 10.1002/joc.1377

17. Aubinet M., Grelle A., Ibrom A., Rannik U., Moncrieff J., Foken T., Kowalski A.S., Martin P.H., Berbigier P., Bernhofer C.H., Clement R., Elbers J., Granier A., Grunwald T., Morgenstern K., Pilegaard K., Rebmann C., Snijders W., Valentini R. and Vesala T., "Estimates of the annual net carbon and water exchange of forests: the EUROFLUX methodology", Advances in ecological research vol. 30, 2000, Academic Press.

18. Aubinet M., Vesala T. and Papale D., (2012). Eddy Covariance, a practical guide to measurement and data analysis. Springer, 2012.

19. Baerentsen J.H. and Berkowicz R. (1984). Monte Carlo simulation of plume dispersion in the convective boundary layer. Atmos. Environ. 18: 701-712. doi: 10/1016/0004-6981(84)90256-7.

20. Baiamonte G., Mercalli L., Cat Berro D., Agnese C. and Ferraris S. (2018). Modelling the frequency distribution of interarrival times from daily precipitation time-series in North-West Italy, Hydr.Res. doi: 10.2166/nh.2019.042.

21. Baldocchi D., Finnigan H., Wilson K., Paw U K.T. and Falge E. (2000). On measuring net ecosystem exchange over tall vegetation on complex terrain. Boundary-Layer Meteorol. 96(1): 257-291. doi: 10.1023/A:1002497616547.

22. Bartelt, P., Lehning, M., (2002). A physical SNOWPACK model for the Swiss Avalanche warning: Part I - numerical model. Cold Reg. Sci. Technol. 35(3), 123-145.

23. Bastiaansen W.G.M., Menenti M., Feddes R.A. and Holtslag A.A.M. (1998). A remote sensing surface energy balance for land (SEBAL). J. hydrol. 212-213,198-212.

24. Bastiaansen W.G.M., Noordman E., Pelgrum H. , Davids G., Thoreson B. and Allen R. (2005). Sebal model with remotely sensed data to improve water-resources management under actual field conditions. J. Irrig. Drain. Eng., 13181): 85-93.

25. Basu, N.B., Rao, P.S.C., Winzeler, H.E., Kumar, S., Owens, P., Merwade, V. (2010). Parsimonious modeling of hydrologic responses in engineered watersheds: structural heterogeneity versus functional homogeneity. Water Resour. Res. 46 (4), W04501. doi:10.1029/2009WR007803.

26. Baudena M., Bevilacqua I., Canone D., Ferraris S., Previati M. and Provenzale A. (2012). Soil water dynamics at a midlatitude test site: field measurements and box modeling approaches. J. Hydrol., 414-415, 329-340. doi: 10.1016/j.hydrol.2011.11.009.

27. Baveye P.C. and Labac M. (2015). Moving away from the geostatistical lamppost: why, where and how does the spatial heterogeneity of soil matter? Ecological Modeling approaches. J. Hydrol. 414-415,329-340.

28. Belusic D. and Güttler I. (2010). Can mesoscale models reproduce meandering motions?, Q. J. R. Meteorol. Soc.136: 553–565.

29. Beniston M. and Rebetez M. (1996). Regional behaviour of minimum temperatures in Switzerland for the period 1979-1993, Theor. Appl. Climatol. 53: 231-243.

30. Beniston M. and Stoffel M. (2014). Assessing the impacts of climate change on mountain water resources. Sci. Total Environ. 493: 1129-1137.

31. Bergström S. (1976). Development and application of a conceptual runoff model for Scandinavian catchments. Norrköping: Swedish Meteorological and Hydrological Institute.

32. Beysens D. (1995). The formation of dew. Atmospheric research 39, 215-237.

33. Blaney H.F. and Criddle W.D. (1950). Determining water requirements in irrigated areas from climatological and irrigation data. USDA Soil Conserv. Serv. SCS-TP96, 44pp.

34. Boehner J., Antonic O. (2009). Land Surface Parameters Specific to Topo-Climatology. in Hengl, T. & Reuter, H.I. [Eds.]: Geomorphometry - Concepts, Software, Applications.

35. Bonan G. (2016). Ecological climatology, concepts and applications, Third Edition. Cambridge University Press, 375 pp.

36. Bottazzi M., Bancheri M., Mobilia M., Bertoldi G., Longobardi A. and Rigon R. (2021). Comparing evapotranspiration estimates from the GEOframe-Prospero model with Penman-Monteith and Priestley-Taylor approaches under different climate conditions. Water, 13, 1221. doi: 10.3390/w13091221.

37. Bouma J. (1989). Using soil survey data for quantitavite land evaluation. In: Stewart B.A. (Ed.). Advances in Soil Sciences, 9. Speinger Verlag, New York, pp. 177-213.

38. Brauchli T., Trujillo E., Huwald H. and Lehning M., "Influence of slope-scale snowmelt on cathment response simulated with the Alpine3D Model", Water Resources Research (2017), 53. DOI: 10.1002/2017WR021279.

39. Brun E., Martin E., Simon V., Gendre C., and Coléou C., (1989). An energy and mass model of snow cover suitable for operational avalanche forecasting. J. Glaciol. 35(121), 333-342.

40. Brutsaert W. (2005). Hydrology: an introduction. Cambridge University Press.

41. Burns S.P., Molotch N., Williams M.W., Knowles J.F., Seok B., Monson R.K., Turnipseed A.A. and Blanken P.D. (2014). Snow temperature changes within a seasonal snowpack and their relationship to turbulent fluxes of sensible and latent heat.J.Hydrometeorol. 15:117-142. doi: 10.1175/JHM-D-13-026.1

42. Cammalleri C., Rallo G., Agnese C., Ciraolo G., Minacapilli M., Provenzano G., "Combined use of eddy covariance and sap flow techniques for partition of ET fluxes and water stress assessment in an irrigated olive orchard", Agricultural Water Management (2013), 120(0):89-97. Soil and Irrigation sustainability practices. DOI: 10.1016/j.agwat.2012.10.003.

43. Campbell, J.L., Mitchell, M.J., Groffman, P.M., Christenson, L.M., Hardy, J.P., 2005. Winter in northeastern North America: A critical period for ecological processes. Front. Ecol. Environ. 3, 314- 322.

44. Campbell Scientific Inc. (2016). Model HFP01 soil heat flux plate, instruction manual.

45. Castelli M., Anderson M.C., Yang Y., Wohlfahrt G., Bertoldi G.,, Niedrist G., Hammerle A., Zhao P., Zeibsch M. and Notarnicola C. (2018). Two-source energy balance modelling of evapotranspiration in Alpine grasslands. Remote Sensing of Environment 209: 327–342. doi: 10.1016/j.rse.2019.02.062 .

46. Ceaglio E., Mitterer C., Maggioni M., Ferraris S., Segor V. and Freppaz M. (2017). The role of soil volumetric liquid water content during snow gliding processes. Cold. Reg. Sci. Technil. 136: 17-29. doi: 10.1016/j.coldregions.2017.01.007.

47. Ceppi P., Scherrer S.C., Fischer A.M. and Appenzeller C. (2010). Revisiting Swiss temperature trends 1959-2008, Int. J. Climatol. 32: 233-251.

48. Chang J.F., Viovy N., Vuichard N., Ciais P., Wang T., Cozic A., Lardy R., Graux A.-I., Klumpp K., Martin R. and Soussana J.F. (2013). Incorporating grassland management in ORCHIDEE: model description and evaluation at 11 eddy-covariance sites in Europe. Geosci. Model. Dec., 6: 2165-2181. doi: 10/5194/gmd-6-2165-2013.

49. Charuchittipan D., Babel W., Mauder M., Leps J-P., and Foken T., "Extension of the Averaging time in eddy-covariance measurements and its effect on the energy balance closure", Boundary-Layer Meteorol. (2014) 152:303, DOI: 10.1007/s10546-014-9922-6.

50. Chen H.S., Shao M..A. and Li Y.Y., (2008). The characteristics of soil water cycle and water balance on steep grassland under natural and simulated rainfall conditions in the Loess Plateau of China Journal of Hydrology, 360 (1–4), pp. 242-251. doi:1016/j.jhydrol.2008.07.037.

51. Chen N.N., Guan D.X., Jin C.J., et al., (2011). Influences of snow event on energy balance over temperate meadow in dormant season based on eddy covariance measurements. J. Hydrol. 399, 100–107. doi: 10.1016/j.hydrol.2010.12.037.

52. Chirouze J., Boulet G., Jarlan L., Fieuzal R. et al. (2013). Inter-comparison of four remote sensing based surface energy balance methods to retrieve ecapotranspiration and water stress of irrigated fields in semi-arid climate. Hydrol. Earth Syst. Sci. Discuss. 10: 895-963. doi: 10.5194/hessd-10-895-2013.

53. Chung U. and Yun, J.I. (2004). Solar irradiance-corrected spatial interpolation of hourly temperature in complex terrain. Agricultural and forest meteorology, 126(1), 129-139, doi: 10.1016/j.agrformet.2004.06.006.

54. Cleugh H.A., Leuning R., Mu Q. and Running S.W. (2007). Regional evaporation estimates from flux tower and MODIS satellite data. Remote Sens. Environ. 106: 285-304. doi: 10.1016/j.rse.2006.07.007.

55. Cleveland W.S., Grosse E. and Shyu W.M. (1992). Local regression models. Chapter 8 of Statistical Models in S. Chambers J.M. and Hastie T.J. Eds, Wadsworth & Brooks/Cole.

56. Cline, D. (1995). Snow surface energy exchanges and snowmelt at a continental alpine site. In Biogeochemistry of Seasonally Snow-covered Catchments, Tonnessen K, Williams MW, Tranter M (eds); IAHS-AIHS Publ. 228. International Association of Hydrological.

57. Conte A., Fares S., Salvati L., Savi F., Matteucci G., Mazzenga F., Spano D., Sirca C., Marras S., Galvagno M., Cremonese E. and Montagnani L. (2019). Ecophysiological responses to rainfall variability in grassland and forests along a latitudinal gradient in Italy. *Front. For. Glob. Change 2:16*. doi: 10.3389/ffgc.2019.00016.

58. Corbari C., Ravazzani G., Galvagno M., Cremonese E. and Mancini M. (2017). Assessing crop coefficients for natural vegetated areas using satellite data and eddy covariance stations. *Sensors* 2017, *17*, 2664. doi:10.3390/s17112664.

59. Crago R. and Brutsaert W. (1996). Daytime evaporation and the self-preservation of the evaporative fraction and the Bowen ratio. J. Hydr. 178:241-255. doi: 10.1016/0022/1694(95)02803-X.

60. Datt P., Srivastava P.K., Negi P.S. and Satyawali P.K. (2008). Surface energy balance of seasonal snow cover for snow-melt estimation in N-W Himalaya. J.Earth Syst. Sci. 117-5: 567-573. doi: 10.1007/s12040-008-0053-7.

61. Davidson P.A., “Turbulence – an introduction for scientists and engineers”, Oxford University Press, 2004, 657 pp.

62. De Groot R.S., Wilson M.A. and Boumans R.M.J., “A typology for the classification, description and valuation of ecosystem functions, goods and services”, Ecological Economics 41 (2002) 393–409.

63. Delpla I., Jung A.V., Baures E., Clement M. and Thomas O. (2009). Impacts of climate change on surface water quality in relation to drinking water production. Environ. Int. 35: 1225-1233. doi: 10.1016/j.envint.2009.07.001.

64. Desiato F., Fioravanti G., Fraschetti P., Perconti W., Piervitali E. and Pavan E. (2018). Gli indicatori del clima in Italia nel 2017. 13th report of the National System for the Environment Protection elaborated by ISPRA (Italian Institute for Environmental Protection and Research.

65. Detto M., Montaldo N., Albertson J.D., Mancini M. and Katul G. (2006). Soil moisture and vegetation controls on evapotranspiration in a heterogeneous mediterranean ecosystem on Sardinia, Italy. Water Resour. Res. 42, W08419. Doi: 10.1029/2005WR004693.

66. Detsch F., Otte I., Appelhans T. and Nauss T. (2017). A glimpse at short-term controls of evapotranspiration along the southern slopes of Kilimanjaro. Environ. Monit. Assess. 189:465. doi: 10.1007/s10661-017-6179-9.

67. Dietrich W.E., Reiss R., Hsu M.L. and Montgomery D.R. (1995). A process-based model for colluvial soil depth and shallow landsliding using digital elevation data. Hydrological processes, 9 (3-4), 383-400. doi: 10.1002/hyp.3360090311.

68. Diffenbaugh, N.S., Pal, J.S., Trapp, R.J., and Giorgi, F. (2005). Fine-scale processes regulate the response of extreme events to global climate change. Proc. Natl. Acad. Sci. USA. 102(44), 15774–15779.

69. D'Odorico P. and Porporato P. (2004). Preferential states in soil moisture and climate dynamics. Proc. Natl. Acad. Sci. USA. 101(24) 8848-8851. doi: 10.1073/pnas.0401428101.

70. Doorenbos, J., Pruitt W.O. (1977). Crop Water Requirements. FAO Irrigation and Drainage Paper 24, Land and Water Development Division, FAO. Rome

71. Easton Z.M., Fuka D.R., White E.D., Collick A.S., Biruk Asharge B., McCartney M., Awulachew S.B., Ahmed A.A. and Steenhuis T.S. (2010).A multi basin SWAT model analysis of runoff and sedimentation in the Blue Nile, Ethiopia. Hydrol. Earth Syst. Sci. Discuss. 7: 3837-3878. doi: 10/5194/hessd-7-3837-2010.

72. Einhorn B., Eckert, N., Chaix, C., Ravanel, L., Deline, P., Gardent, M., Boudières, V., Richard, D., Vengeon, J.-M., Giraud, G., Schoeneich, P. (2015). Climate change and natural hazards in the Alps. Observed and potential impacts on physical and socio-economic systems. Journal of Alpine Research | Revue de géographie alpine, 103-2. DOI:10.4000/rga.2878

73. Eshonkulov R., Poyda A.,Ingwersen J., Pulatov A. and Streck T. (2019a). Improving the energy balance closure over a winter wheat field by accounting for minor storage terms. Agric. For. Met. 264: 283-296. doi:10.1016/j.agrformet.2018.10.012.

74. Eshonkulov R., Poyda A., Ingwersen J., Wizemann H-D., Weber T.K.D., Kremer P., Högy P., Pulatov A. and Streck T. (2019b). Evaluating multi-year, multi-site data on the energy balance closure of eddy-covariance flux measurements at cropland sites in southwestern Germany. Biogeoscoences, 16: 521-540. doi: 10.5194/bg-16-521-2019.

75. Etzold S., Buchmann N. and Eugster W. (2010). Contribution of advection to the carbon budget measured by eddy covariance at a steep slope forest in Switzerland, Biogeosciences, 7, 2461–2475.

76. Eugster W. and Senn W. (1995). A cospectral correction model for measurement of turbulent NO2 flux, Boundary-layer Meteorol. 74:321-340, doi: 10.1007/BF00712375.

77. Evett S.R., Schwartz R.C., Howell T.A., Baumhardt R.L., Copeland K.S. (2012). Can weighting lysimeter ET represent surrounding field ET well enough to test flux station measurements of daily and sub-daily ET? Adv. Water Resour. 50: 79-90. doi: 10.1016/j.advwatres.2012.07.023.

78. Falge E., Baldocchi D.D., Olson R., Anthoni P., Aubinet M., Bernhofer C., Burba G., Ceulemans R., Clement R., Dolman H., Granier A., Gross P., Grunwald T., Hollinger D., Jensen N.O., Katul G., Keronen P., Kowalski A., Ta Lai C., Law B.E., Meyers T., Moncrieff J., Moors E., Munger W.J., Pilegaard K., Rannik Ü., Rebmann C., Suker A., Tenhunen J., Tu K., Verma S., Vesala T., Wilson K and Wofsy S. (2001). Gap filling strategies for defensible annual sums of net ecosystem exchange, Agri.For.Met. 107: 43-69.

79. Falocchi M., Giovannini L., de Franceschi M. and Zardi D. (2018). A refinement of the McMillen (1988) recursive digitl filter for the analysis of atmospheric turbulence, Boundary-Layer Meteorol. 168:517-523, doi:10.1007/s10546-018-355-5.

80. Falocchi, M. PhD Thesis “Analysis of Eddy Covariance measurements in an Alpine valley”, 2013, University of Brescia.

81. Fan S.M., Wofsy S.C., Bakwin P.S., Jacob D.J. and Fitzjarrald D.R. (1990). Atmosphere-biosphere exchange of CO_2 and O_3 in the Central Amazon Forest, Journal of Geophysical Research, 106: 3503-3509.

82. Feigenwinter C., Montagnani L. and Aubinet M. (2010). Plot-scale vertical and horizontal transport of CO2 modified by a persistent slope wind system in and above an Alpine forest. Agric. Forest Meteorol. 150: 665-673. doi: 10.1016/j.agrformet.2009.05.009.

83. Feigenwinter C., Vogt R. and Christen A. (2012). Eddy covariance measurements over urban areas. In M. Aubinet, T.Vesala and D. Papale “a practical guide to measurement and data analysis”, Springer Atmospheric Aciences, Springer Netherlands. DOI: 10.1007/978-94-007-2351-1_16.

84. Finkestein P.L. and Sims P.F. (2001). Sampling error in eddy correlation flux measurements. J. Geophys. Res. 106(D4): 3503-3509. doi: 10.1029/2000JD900731.

85. Fisher J.B., Melton F., Middleton E. et al. (2017). The future of evapotranspiration: global requirements for ecosystem functioning, carbon and climate feedbacks, agricultural management and water resources. Water Resour. Res. 53: 2618-2626. doi: 10.1002/2016WR020175.

86. Foken, T., Skeib, G., Richter, S. H.: 1991, 'Dependence of the integral turbulence characteristics on the stability of stratification and their use for Doppler-Sodar measurements', Z. Meteorol. 41, 311-315.

87. Foken T. and Wichura B. (1996). Tools for quality assessment of surface-based flux measurements, Agri. For. Meteorol. (1996), 78:83–105.

88. Foken T., Jegede O.O., Weisensee U., Richter S. H., Handorf D., Görsdorf U., Vogel G., Schubert U., Kirzel H.-J., Thiermann V. (1997). Results of the LINEX-96/2 Experiment, Deutscher Wetterdienst, Forschung und Entwicklung, Arbeitsergebnisse 48 75 pp.

89. Foken T., 50 years of the Monin-Obukhov Similarity Theory, Boundary-Layer Meteorology (2006) 119: 431–447, DOI: 10.1007/s10546-006-9048-6

90. Foken T., Göckede M., Mauder M., Mahrt L., Amiro B. and Munger W. (2004). Post-field data quality control, in Handbook of Micrometeorology, edited by Lee X., Massman W. and Law B. Kluwer Academic Publishers.

91. Foken, T., Wimmer, F., Mauder, M., Thomas, C., and Liebethal, C., (2006b). Some aspects of the energy balance closure problem. Atmos. Chem. Phys. 6, 4395–4402.

92. Foken T, (2008a) Micrometeorology. Ed. Springer 305 pp.

93. Foken T. (2008b). The energy balance closure problem: an overview. Ecol. Appl. 18(6): 1351-1367.

94. Foken T., Aubinet M., Finnigan J.J., Leclerc M.Y., Mauder M. and Paw U.K.T. (2011). Results of a panel discussion about the energy balance closure correction for trace gases. Bull. Amer. Meteor. Soc. 92 ES13-8.

95. Fratini G., Ibrom A., Arriga N., Burba G. and Papale D. (2012). Relative humidity effects of water vapour fluxes measured with closed-path eddy covariance systems with short sampling lines, Agr.For.Met, 165:53-63.

96. Fratini G. and Mauder M. (2014). Towards a consistent eddy covariance processing: an intercomparison of EddyPro and TK3, Atmos. Meas. Tech., 7, 2273–2281, doi: 10.5194/amt-7-2273-2014.

97. Fridley J. D. (2009), Downscaling climate over complex terrain: high finescale (< 1000 m) spatial variation of near-ground temperatures in a montane forested landscape (great smoky mountains). Journal of Applied Meteorology and Climatology, 48 (5), 1033:1049.

98. Fuhrer J., Smith P. and Gobiet A. (2014). Implications of climate change scenarios for agriculture in Alpine regions – a case study in the Swiss Rhone catchment. Sci. Total Environ. 493: 1232-1241. doi: 10.1016/j.scitotenv.2013.06.038.

99. Galvagno M., Wohlfahrt G., Cremonese E., Filippa G., Migliavacca M., Morra di Cella U. and Van Gorsel E. (2017). Contribution of advection to nighttime ecosystem respiration at a mountain grassland in complex terrain. Agric. For. Meteorol. 237:270-281.

100. Gao Z., Liu H., Katul G.G. and Foken T. (2017). Non-closure of the surface energy balance explained by phase difference between vertical velocity and scalars of large atmospheric eddies. Environ. Res. Lett. 12, 034025. doi:10.1088/1748-9326/aa625b.

101. Gao Z., Liu H., Missik J.E.C., Yao J., Huang M., Chen X., Arntzen E. and Mcfarland D.P. (2019). Mechanistic links between underestimated CO_2 fluxes and non-closure of the surface energy balance in a semi-arid sagebrush ecosystem. Environ. Res. Lett. 14, 044016. doi: 10.1088/1748-9326/ab082d.

102. Gaudard L., Romerio F., Dalla Valle F., Gorret R., Maran S., Ravazzani G. et al. (2014). Climate change impacts on hydropower in the Swiss and Italian Alps. Sci. Tot. Environ. 493:1211-1221. doi: 10.1016/j.scitotenv.2013.10.012.

103. Garratt J. (1992). The atmospheric boundary layer. Cambridge atmospheric and space science series, Cambridge University Press, Cambridge, 416-444.

104. Gayathri K.D., Ganasri B.P. and Dwarakish G.S. (2015). A review on hydrological models. Aquatic Procedia 4. 1001-1007. doi: 10.1016/j.aqpro.2015.02.126.

105. Gehrig-Fasel J., Guisan A. and Zimmermann N.E. (2007). Tree line shifts in the Swiss Alps: climate change or land abandonment?", Journal of Vegetation Science 18: 571-582.

106. Geissbühler P., Siegwolf R. and Eugster W. (2000). Eddy Covariance measurements on mountain slopes: the advantage of surface-normal sensor orientation over a vertical set-up, Boundary-Layer Meteorol. 96: 371-392, doi: 10.1023/A:1002660521017.

107. Gerdel K., Spielmann F.M., Hammerle A. and Wohlfahrt G. (2017). Eddy Covariance carbonyl sulfide flux measurements with a quantum cascade laser absorption spectrometer, Atmos. Meas. Tech., 10, 3525–3537, doi: 10.5194/amt-10-3525-2017.

108. German E.R. (2000). Regional evaluation of evapotranspiration in the Everglades. U.S. Geological Survey – Water Resources Investigations Report 00-4217, 48 pp.

109. Giaccone E., Colombo N., Acquaotta F., Paro L. and Fratianni S. (2015). Climate variations in a high altitude Alpine basin and their effects on a glacial environment (Italian Western Alps). Atmosféra, 28: 117-129.

110. Gibson D.J. (2009). Grasses and grassland ecology. Oxford University Press, 323 pp.

111. Giovannini L., Ferrero E., Karl T., Rotach M.W., Staquet C., Trini Castelli S. and Zardi D. (2020). Atmospheric pollutant dispersion over complex terrain: challenges and needs for improving air quality measurements and modeling. Atmosphere, 11(6), 646. doi: 10.3390/atmos11060646.

112. Gobiet A., Kotlarski S., Beniston M., Heinrich G., Rajczak J. and Stoffel M. (2014). 21st Century climate change in the European Alps – a review. Sci. Tot. Environ. 493: 1138-1151.

113. Goulart A.G.O., Degrazia A., Acevedo O. and Anfossi D. (2007). Theoretical considerations of meandering winds in simplified conditions. Boundary-Layer Meteorol (2007) 125:279–287.

114. Granier A. (1987). Evaluation of transpiration in a Douglas-fir stand by means of sap flow measurements. Tree Physiol. 3:309-320.

115. Gu S., Tang Y., Cui X. et al. (2008). Characterizing evapotranspiration over a meadow ecosystem on the Quinghai-Tibetan Plateau. J. Geophys. Res. 113. doi: 10.1029/2007JD009173.

116. Guo J., Zhou J., Lu J., Zou Q., Zhang H. and Bi s. (2014). Multi-objective optimization of empirical hydrological model for streamflow prediction. Journal of Hydrology 511: 242-253.

117. Gürtz J., Lang H., Verbunt M and Zappa M. (2005). The use of hydrological models for the simulation of climate change impacts on mountain hydrology. In Global change and mountain regions, editors: Huber U.M., Bugmann H.K.M. and Reasoned M.A., Springer.

118. Haeberli W. and Beniston M. (1998). Climate change and its impacts on glaciers and permafrost in the Alps. Ambio, 27, p. 258-265.

119. Halldin S., Gottschalk L., Van de Griend A.A., Gryning S.E., Heikinheimo M., Högstrom U., Jochum A. and Lundin L.C. (1995). Science plan for NOPEX. NOPEX Technical Report No.12. Institute of Earth Sciences, Uppsala University.

120. Ham J.M. Useful Equations in Micrometeorology (Chapter 23). In: Hatfield J.L. and Baker J.M. and Viney M.K., Micrometeorology in agricultural systems. Agronomy, vol 47. 584 pp.

121. Hammerle A., Haslanter A., Schmitt M., Bahn M., Tappeiner U., Cernusca A. and Wohlfahrt G. (2007). Eddy covariance measurements of carbon dioxide, latent and sensible energy fluxes above a meadow on a mountain slope, Boundary Layer Meteorol. 122(2): 397-416, doi: 10.1007/s10546-006-9109-x.

122. Hanks R.J. and Ashcroft G.L. (1980): Applied soil physics: soil water and temperature application, Springer-Verlag, 159 pp.

123. Hanztschel J., Goldberg V. and Bernhofer C. (2007). (2005). GIS-based regionalisation of radiation, temperature and coupling measures in complex terrain for low mountain ranges. Meteorol. Appl. 12, 33-42. doi: 10.1017/S1350482705001489.

124. Harding R.J. (1986). Exchanges of energy and mass associated with a melting snowpack. In Modelling snowmelt induced processes, Morris E.M. (ed.). IAHS Publ. 155. International Association of Hydrological Science. Budapest, pp.3-15.

125. Hargreaves G.H. and Samani Z.A. (1982). Estimating potential evapotranspiration. J.Irrig. Drain. Eng. 108(3): 225-230.

126. Haslinger K. and Blöschl G. (2017). Space-Time Patterns of Meteorological Drought Events in the European Greater Alpine Region Over the Past 210 Years. Water Resources Research, 53: 9807–9823. doi: 10. 1002/2017WR020797.

127. Hayashi, M., Van der Kamp, G., and Schmidt, R., 2003. Focused infiltration of snowmelt water in partially frozen soil under small depressions. J. Hydrol. 270(3-4), 214-229.

128. Heinrich G., Gobiet A., Truhetz H. and Mendlik T. (2013b). Expected climate change and its uncertainty in the Alpine Region: extended uncertainty assessment of the reclip. Century and ENSEMBLES multi-model dataset. Wegener Center Scientific Report 50.

129. Helgason, W.D., and Pomeroy, J.W., (2005). Uncertainties in estimating turbulent fluxes to melting snow in a mountain clearing. Proceedings of the Eastern Snow Conference 62, 129-139.

130. Helgason, W.D., and Pomeroy, J.W., (2012). Problems closing the energy balance over an homogeneous snow cover during midwinter J. Hydrometeor. 13, 557–572.

131. Hemakumara H.M., Chandrapala L. and Arnold M.F. (2003). Evapotranspiration fluxes over mixed vegetation areas measured from large aperture scintillometer. Agric. Water Manage. 58: 109-122. doi: 10.1016/S0378-3774(02)00131-2.

132. Heusinkveld B.G., Jacobs A.F.G., Holtslag A.A.M. and Berkowicz S.M. (2004). Surface energy balance closure in an arid region: role of soil heat flux, Agricultural and Forest Meteorology, (2004)122 (1-2), 21:37. DOI: 10.1016/j.agrformet.2003.09.005.

133. Hicks, B.B., and Martin, H.C., 1972. Atmospheric turbulent fluxes over snow. Bound.-Lay. Meteorol. 2 (4), 496-502.

134. Hiller R., Zeeman M.J. and Eugster W. (2008). Eddy covariance flux measurements in the complex terrain of an Alpine valley in Switzerland, Boundary-Layer Meteorol. 127:449–467, doi: 10.1007/s10546-008-9267-0.

135. Hirschi M., Michel D., Lehner I. and Seneviratne S.I., (2017). A site-level comparison of lysimeter and eddy covariance flux measurements of evapotranspiration, Hydrol. Earth Syst. Sci., 21, 1809-1825.

136. Hiyama T., Strunin M.A., Tanaka H. and Ohta T., 2007. The development of local circulations around the Lena River and their effect on tower-observed energy imbalance. Hydrol. Process., 21, 2038-2048.

137. Hofierka J. and Suri M. (2002). The solar radiation model for Open source GIS: implementation and applications. International GRASS users conference in Trento, Italy, September 2002.

138. Horst T.W. and Weil J.C. (1992). Footprint estimation for scalar flux measurements in the atmospheric surface layer. Bound.-Lay.Meteorol. 59: 279-296.

139. Howell J.F. and Mahrt L., (1997). Multiresolution flux decomposition" Boundary-Layer Meteorology 83: 117–137.

140. Hsieh C.I., Katul G. and Chi T.W. (2000). An approximate analytical model for footprint estimation of scalar fluxes in thermally stratified atmospheric flows, Adv. In Water Resources, 23 (2000) 765-772.

141. Hsieh C.I. and Katul G.G. (2009). The Lagrangian stochastic model for estimating footprint and water vapor fluxes over inhomogeneous surfaces. Int. J. Biometeorol. 53:87-100. doi: 10.1007/s00484-008-0193-0.

142. Hood E., Williams M., and Cline D. (1999). Sublimation from a seasonal snowpack at a continental, mid-latitude alpine site. Hydrol. Process. 13:1781-1797. doi:10.1002/(SICI)1099-1085(199909)13:12/13<1781::AID-HYP860>3.0.CO;2-C

143. Horst T.W. and Weil J.C. (1992). Footprint estimation for scalar flux measurements in the atmospheric surface layer. Boundary-Layer Meteorol. 59: 279-286. doi: 10.1007/BF00119817.

144. Ibanez M., Altimir N., Ribas A., Eugster W. and Sebastià M.T. (2020). Phenology and plant functional type dominance drive CO_2 exchange in seminatural grasslands in the Pyrenees. The Journal of Agricultural Science 1-12. doi: 10.1017/ S0021859620000179.

145. Ibrom A., Dellwik E., Larse S.E. and Pilegaard K. (2007). Strong ow-pass filtering effects on water vapour flux measurements with closed-path eddy correlation systems, Agri.For.Met., 147:140-156.

146. Ionita M., Tallaksen L.M., Kingston D.G., Stagge J.H., Laaha G., Van Lanen H.A.J., Scholz P., Chelchea S.M. and Haslinger K. (2017). The European 2015 drought from a climatological perspective. Hydrol. Earth Syst. Sci. 21: 1397–1419. doi: 10.5194/hess-21-1397-2017.

147. Iqbal M. (1983). An introduction to solar radiation. Academic Press, Toronto, 390 pp.

148. Jacob D., Petersen J., Eggert B. et al. EURO-CORDEX: new high resolution climate change projections for European impact research. Reg. Environ. Change 14: 563-578. doi: 10.1007/s10113-013-0499-2.

149. Jacobs A.F., Heusinkveld B.G., Wichink Kruit R.J. and Berkowicz S.M. (2006). Contribution of dew to the water budget of a grassland area in the Netherlands. Water resources research, 42(3). doi: 10.1029/2005WR004055.

150. Jakeman, A.J., I.G. Littlewood and P.G. Whitehead, 1990. Computation of the instantaneous unit hydrograph and identifiable component flows with application to two small upland catchments. Journal of Hydrology, 117, 275-300.

151. Jepsen, S.M., Molotch, N.P., Williams, M.W., Rittger, K.E., Sickman, J.O., 2012. Interannual variability of snowmelt in the Sierra Nevada and Rocky Mountains, USA: Examples from two alpine watersheds. Water Resour. Res *48(2), W02529*. doi: 10.1029/2011WR011006.

152. Joffre S. and Laurila T. (1988). Standard deviations of wind speed and direction from observations over a smooth surface. J. Appl. Meteorol. 27: 550-551.

153. Johansson C., Smedman A.S., Högström U., Brasseur J.G. and Khanna S. (2001). Critical test of the validity of Monin-Obukhov Similarity during convective conditions, Journal of American Meteorological Society, 1549-1566, DOI: 10.1175/1520-0469.

154. Jones, H.G., Pomeroy, J.W., Walker, D.A., and Hoham, R.W., 2001. Snow Ecology: An Interdisciplinary Examination of Snow-covered Ecosystems. Cambridge University Press, Cambridge, UK. 394 p.

155. Kaimal J.C. and Finnigan J.J. (1994). Atmospheric boundary layer flows, Oxford University Press: Oxford, UK.

156. Kaimal J.C.,Wyngaard J.C., Izumi Y., Coté O.R. (1972). Spectral characteristics of surface-layer turbulence. Q. J. R. Meteorol. Soc.98: 563–589.

157. Kanda M., Inagaki A., Letzel M.O., Raasch S. and Watanabe T. (2004). LES study of the energy imbalance problem with eddy covariance fluxes. Bound. Layer Meteorol. 10:381-404.

158. Karl T., Graus M., Striednig M., Lamprecht C., Hammerle A., Wohlfahrt G., Held A., Von Der Hevden L., Deventer M.J., Krismer A., Haun C., Feichter R. and Lee J. (2017). Urban eddy covariance measurements reveal significant missing NO emissions in Central Europe, Scientific Reports, 7: 2536.

159. Kattelman, R. Elder, K, 1991. Hydrological characteristics and water balance of an alpine basin in the Sierra Nevada. Water Resour. Res. 27, 1553.1562.

160. Keylock C.J.,Hardy R.J., Parsons D.R., Ferguson R.I., Lane S.N. and Richards K.S. (2005). "The theoretical foundations and potential for large-eddy simulation (LES) in fluvial geomorphic and sedimentological research", Communications on Pure and Applied Mathematics, vol. 71, 3-4, Elsevier, pp. 271-304,doi:10.1016/j.earscirev.2005.03.001.

161. Klaasen W. and Sogachev A. (2006). Flux footprint simulation downwind of a forest edge. Bound.-Layer Meteorol. 121:459-473. doi: 10.1007/s10546-006-9078-0.

162. Klein G., Vitasse Y., Rixen C., Marty C. and Rebetez M. (2016). Shorter snow cover duration since 1970 in the Swiss Alps due to earlier snowmelt more than to later snow onset. Climatic Change, 139:637-649, doi: 10.1007/s10584-016-1806-y.

163. Kljun N., Rotach M.W. and Schmid H.P. (2002). A three-dimensional backward Lagrangian footprint model for a wide range of boundary-layer stratifications. Boundary-Layer Meteorol. 103: 205-226. doi: 10.1023/A:1014556300021

164. Kljun N., Kastner-Klein P., Fedorovich E. and Rotach M.W. (2004a). Evaluation of Lagrangian footprint model using data from a wind tunnel convective boundary layer. Afr. For. Meteorol. 127: 189-201. soi: 10.1016/j.agrformet.2004.07.013.

165. Kljun N., Calanca P., Rotach M.W. and Schmid H.P. (2004b). A simple parameterisation for flux footprint predictions. Boundary-Layer Meteorol. 112: 503-523. doi: 10.1023/B:BOUN.0000030653.71031.96.

166. Kondratiev, K.Ja., Pivovarova, Z.I., Fedorova, M.P., 1978: The radiation regime of sloping surfaces. Hydrometeoizdat, 216p.

167. Konings A.G., Williams A.P. and Gentine P. (2017). Sensitivity of grassland productivity to aridity controlled by stomatal and xylem regulation. Nature Geoscience, Vol. 10. doi: 10.1038/NGEO2903.

168. Konzelmann T., Calanca P., Müller G., Menzel L. and Lang A. (1997). Energy Balance and Evapotranspiration in a High Mountain Area during Summer. Journal of Applied Meteorology, 36(7):966-973.

169. Kormann R. and Meixner F.X. (2001). An analytical footprint model for non-neutral stratification, Boundary-Layer Meteorol. 207:224 – 99.

170. Kotlarski S., Lüthi D. and Schär C. (2015). The elevation dependency of 21st century European climate change: an RCM ensemble perspective. Int. J. Climatol. 35:3902-3920. doi: 10.1002/joc.4254.

171. Lang F., Belusic D. and Siems S. (2018). Observations of Wind-Direction Variability in the Nocturnal Boundary Layer. Boundary-Layer Meteorol. 166:51. doi: 10.1007/s10546-017-0296-4 .

172. Leclerc M.Y. and Thurtell G.W. (1990). Footprint predictions of scalar fluxes and concentration profiles using a markovian analysis. Boundary-Layer Meteorol. 52:247-259.

173. Leclerc M.Y., Shen S. and Lamb B. (1997). Observations and large eddy simulation modelling of footprints in the lower convective boundary layer. J. Geophys. Res. 102(D8):9323-9334. doi: 10.1029/96JD03984.

174. Leclerc M.Y. and Foken T. (2014). Footprints in micrometeorology and ecology, Springer Atmospheric Sciences, 239 pp.

175. Lee X. (1998). On micrometeorological observations of surface-air exchange over tall vegetation. Agric. For. Meteorol. 91: 39-50.

176. Lee X., Massman W. And Law B., "Handbook of Micrometeorology", Kluwer Academic Publishers, 2004.

177. Legendre P. lmodel2 package (2018). https://cran.r-project.org/web/packages/lmodel2/lmodel2.pdf

178. Lehning, M., Bartelt, P., Brown, B., and Fierz, C., (2002a). A physical SNOWPACK model for the Swiss avalanche warning: Part III - meteorological forcing, thin layer formation and evaluation. Cold Reg. Sci. Technol. 35(3), 169-184.

179. Lehning, M., Bartelt, P., Brown, B., Fierz, C., and Satyawali, P., (2002b). A physical SNOWPACK model for the Swiss avalanche warning: Part II - Snow microstructure. Cold Reg. Sci. Technol. 35(3), 147-167.

180. Lehning, M., Bartelt, P., Bethke, S., (2004). Review of SNOWPACK and Alpine3D applications. In Snow Engineering, vol. V. (ed. Bartelt, P., E.E. Adams, M. Christen, R.L. Sack, and A. Sato). Leiden: Balkema Pubblishers, pp 299-307.

181. Leitinger G., Ruggenthaler R., Hammerle A., Lavorel S., Schirpke U., Clement J-C., Lamarque P., Obojes N. and Tappeiner U. (2015). Impact of droughts on water provision in managed alpine grasslands in two climatically different regions of the Alps. Ecohydrology. 2015 Dec; 8(8): 1600–1613. doi: 10.1002/eco.1607.

182. Lettenmaier D.P. and Famiglietti J.S. (2006). Hydrology: water from on high. Nature 444: 562-563. doi: 10/1038/444562a.

183. Leuning R., van Gorsel E., Massman W.J., and Isaac P.R., (2012), Reflections on the surface energy imbalance problem. Agr. Forest Meteorol. 156(0), 65-74.

184. Li Z.L., Tang R.L., Wan Z.M., Bi Y.Y., Zhou C.H., Tang B.H., Yan G.J. and Zhang X.Y. (2009). A review of current methodologies for regional evapotranspiration estimation from remotely sensed data. Sensors, 9(5): 3801-3853. doi: 10.1007/s10546-017-0251-4.

185. Lobocki L. (2017). Turbulent mechanical energy budget in stably stratifies baroclinic flows over sloping terrain", Boundary-Layer Meteorol. 164:353–365 DOI 10.1007/s10546-017-0251-4

186. López-Moreno J.I., Revuelto, J., Gilaberte, M., Morán-Tejeda, E., Pons, M., Jover, E., Esteban, P., García, C., Pomeroy, J.W., (2013). The effect of slope aspect on the response of snowpack to climate warming in the Pyrenees. Theor. Appl. Climatol. 117, 207-219.

187. Lowe P.R. (1977). An approximated polynomial for computation of saturation vapor pressure. Journal of Applie Meteorology, 16:100-103.

188. Lumley J.L. and Panofsky A., "The structure of atmospheric turbulence", Interscience Publishers, 1964, 239 pp.

189. MacDonald M.K., Pomeroy J.W. and Pietroniro A. (2010). On the importance of sublimation to an alpine snow mass balance in the Canadian Rocky Mountains. Hydrol. Earth Syst. Sci., 14, 1401–1415, 2010. doi:10.5194/hess-14-1401-2010.

190. Mahrt L. (1991). Eddy asymmetry in the sheared heated boundary layer. Journal of the atmospheric sciences, 48(3).

191. Makkink G.F. (1957). Testing the Penman formula by means of lysimeters. J. Inst. of Water Eng. 11:277-288.

192. Malek E. and Bingham G.E. (1993). Comparison of the Bowen ratio-energy balance and the water balance methods for the measurement of evapotranspiration. J. Hydrol. 146(1-4): 209-220. doi: 10.1016/0022-1694(93)90276-F.

193. Maran S., Volonterio M. and Gaudard L. (2014). Climate change impacts on hydropower in an Alpine catchment. Environ. Sci. Pol. 43: 15-25.

194. Marcolla B., Cescatti A., Manca G., Zorer R., Cavagna M., Fiora A. et al (2011). Climatic controls and ecosystem responses drive the inter-annual variability of the net ecosystem exchange of an alpine meadow. Agric. For. Meteorol. 151(9):1233–1243. doi: 10.1016/j.agrformet.2011.04.015.

195. Martre P., Cochard H. and Durand J-L. (2001). Hydraulic architecture and water flow in growing grass tillers (Festuca arundinacea Screb.). Plant Cell and Environment. 24:65-76. doi: 10.1046/j.1365-3040.2001.00657.x.

196. Marty C. and Philipona R. (2000). The Clear-sky index to separate clear-sky from cloudy-sky situations in climate research. Geophysical Research Letters 27(17), 2649-2652. doi: 10.1029/2000GL011743.

197. Massaro G., Stiperski I., Pospichal B. and Rotach M.W. (2015). Accuracy of retrieving temperature and humifity profiles by ground-based microwave radiometry in truly complex terrain. Atmos. Meas. Tech. 8(8): 3355-3367. doi: 10.5194/amt-8-3355-2015.

198. Masseroni D., Corbari C., Ceppi A., Gandolfi C. and Mancini M. (2013). Operative use of eddy covariance measurements: are high frequency data indispensable?. Procedia Environ. Sci. 19: 293-302. doi: 10.1016/j.proenc.2013.06.034.

199. Masseroni D., Corbari C. and Mancini M. (2014). Limitations and improvements of the energy balance closure with reference to experimental data measured over a maize field. Atmosféra, 27(4), 335-352.

200. Mastrotheodoros T., Pappas C., Molnar P., Burlando P., Manoli G., Parajka J., Rigon R., Szeles B., Bottazzi M., Hadjidoukas P. and Fatichi S. (2020). More green and less blue water in the Alps during warmer summers. Nature climate change 10: 155-161. doi: 10.1038/s41558-019-0676-5.

201. Mauder M., Cuntz M., Drüe C., Graf A., Rebmann C., Schmid H.P., Schmidt M., Steinbrecher R. (2013). A strategy for quality and uncertainty assessment of long-term eddy covariance measurements, Agri. For. Met. 169:122–135, DOI: 10.1016/j.agrformet.2012.09.006.

202. Mauder M. and Foken T. (2004). Carboeurope-IP task 1.2.2.

203. Mauder M., Foken T. and Cuxart J. (2020). Surface energy balance closure over land: a review. Boundary Layer Meteorol. 177:395-426. doi: 10.1007/s10546-020-00529-6

204. McMillen R.T. (1988). An eddy correlation technique with extended applicability to non-simple terrain, Boundary-Layer Meteorol 43(3):231–245.

205. McDonnell J.J., Sivapalan M., Vache K., Dunn S., Grant G., Haggerty R., Hinz C., Hooper R., Kirchner J., Roderick M., Selker I. and Weiler J.M. (2007). Moving beyond heterogeneity and process complexity: a new vision for watershed hydrology. Water Resour. Res. 43, W07301. doi: 10.1029/2006WR005467.

206. Merbold L., Steinlin C. and Hagedorn F. (2013). Winter greenhouse gas fluxes (CO_2, CH_4 and N_2O) from a subalpine grassland. Biogeosciences, 10: 3185–3203.

207. Meyer S., Leifeld J., Bahn M. and Fuhrer J. (2012). Free and protected soil organic carbon dynamics respond differently to abandonment of mountain grassland. Biogeosciences, 9: 853–865. doi: 10.5194/bg-9-853-2012.

208. Michna P., Eugster W., Hiller R.V., Zeeman M.J. and Wanner H. (2013). Topoclimatological case-study of Alpine pastures near the Albula Pass in the eastern Swiss Alps. Geogr. Helv., 68: 249–263. doi: 10.5194/gh-68-249-2013.

209. Minacapilli M., Agnese C., Blanda F., Cammalleri C., Ciraolo G., D'Urso G., Iovino M., Pumo D., Provenzano G. and Rallo G. (2009). Estimation of actual evapotranspiration of Mediterranean perennial crops by means of remote-sensing based surface energy balance models. Hydrol. Earth. Syst. Sci. 13, 1061-1074. doi: 10.1094/hess-13-1061-2009.

210. Moderow U., Grünwald T., Queck R., Spank U. and Bernhofer C. (2021). Energy balance closure and advective fluxes at ADVEX sites. Theor. Appl. Clim. 143: 761-779. doi: 10.1007/s00704-020-03412-z.

211. Moffat A.M., Papale D., Reichstein M., Hollinger D.Y., Richardson A.D., Barr A.G., Beckstein C., Braswell B.H., Churkina G., Desai A.R., Falge E., Gove J.H., Heimann M., Hui D. Jarvis A.J., Kattge J., Noormets A. and Stauch V.J. (2007). Comprehensive comparison of gap-filling techniques for eddy covariance net carbon fluxes, Agric. For. Meteorol. 147: 209-232.

212. Moncrieff J. B., Massheder J.M., de Bruin H., Ebers J., Friborg T., Heusinkveld B., Kabat P., Scott S., Soegaard H. and Verhoef A. (1997). A system to measure surface fluxes of momentum, sensible heat, water vapor and carbon dioxide. Journal of Hydrology 188-189: 589-611.

213. Moncrieff J.B., Clement R., Finnigan J. and Meyers T. (2004). Averaging, detrending and filtering of eddy covariance time series, in Handbook of Micrometeorology, edited by Lee X., Massman W. and Law B., Kluwer Academic Publishers.

214. Monin, A. S. and Obukhov, A. M. (1954). Osnovnye zakonomernosti turbulentnogo peremeshivanija v prizemnom sloe atmosfery (Basic Laws of Turbulent Mixing in the Atmosphere Near the Ground). Trudy geofiz. inst. AN SSSR 24(151). 163–187.

215. Moore R.J. (1985). The probability-distributed principle and runoff production at point and basin scales. Hydrol. Sci. J. 30(2): 273-297. doi: 10.1080/02626668509490989.

216. Moor L.P., Degrazia G.A., Stefanello M.B., Mortarini L., Acevedo O.C., Maldaner S., Szinvelski C.R.P., Roberti D.R., Buligon L. and Anfossi D. (2015). Proposal of a new autocorrelation function in low wind speed conditions. Physica A 438 286–292.

217. Moran M., Clarke T., Inoue Y. and Vidal A. (1994). Estimating cropwater deficit using the relation between surface-air temperature and spectral vegetation index. Remote Sens. Environ. 49: 246-263. doi: 10.1016/0034-4257(94)90020-5.

218. Mortarini L., Ferrero E., Falabino S., Trini Castelli S., Richiardone R. and Anfossi D. (2013). Low-frequency processes and turbulence structure in a perturbed boundary layer. QJR Meteorol. Soc. 139: 1059-1072. doi: 10.1002/qj.2015.

219. Mortarini L. and Anfossi D. (2015). Proposal of an empirical velocity spectrum formula in low-wind speed conditions, Q. J. R. Meteorol. Soc. 141: 85 – 97, doi: 10.1002/qj.2336.

220. Mortarini L., Maldaner S., Moor L.P., Stefanello M.B., Acevedo O., Degrazia G., and Anfossi D. (2016a). Temperature auto-correlation and spectra functions in low-wind meandering conditions. Q. J. R. Meteorol. Soc. 142: 1881-1889.

221. Mortarini L., Stefanello M., Degrazia G., Roberti D., Trini Castelli S., Anfossi D. (2016b). Characterization of wind meandering in low-wind speed conditions. Boundary-Layer Meteorol. 161:165-182. doi: 10.1007/s10546-016-0165-6.

222. Motovilov Y.G., Gottschalk L., Engeland K. and Rodhe A. (1999a). Validation of a distributed hydrological model against spatial observations. Agric. For. Meteorol. 98-99: 257-277. doi: 10.1016/S0168-1923(99)00102-1.

223. Motovilov Y.G., Gottschalk G., Engeland L. and Belorukov A. (1999). ECOMAG a regional model of the hydrological cycle. Application to the NOPEX area. Department of Geophysics, University of Oslo, Institute Report Series, n. 105.

224. Mott, R., Gromke, C., Grünewald, T., and Lehning, M., 2013. Relative importance of advective heat transport and boundary layer decoupling in the melt dynamics of a patchy snow cover. Adv. Water Resour. 55, 88-97.

225. Mountain Research Initiative EDW Working Group, “Elevation-dependent warming in mountain region of the world”, Nature Climate Change, 2015.

226. Nakai, Y., Sakamoto, T., Terajima, T., Kitamura, K., and Shirai, T., 1999. Energy balance above a boreal coniferous forest: a difference in turbulent fluxes between snow-covered and snow-free canopies. Hydrol. Process. 13, 515–529.

227. Nadeau D.F., Pardyjak E.R., Higgins C.W. and Parlange M.B. (2012). Similarity scaling over a steep Alpine slope, Boundary-Layer Meteorol. 147: 401-419, doi: 10.1007/s10546-012-9787-5.

228. Nadeau D.F., Pardyjak E.R., Higgins C.W., Huwald H. and Parlange M.B. (2013). Flow during the evening transition over steep alpine slopes, Q. J. R. Meteorol. Soc. 139: 607 – 624, doi: 10.1002/qj.1985.

229. Norman J.M., Kustas W.P. and Humes K.S. (1995). Source approach for estimating soil and vegetation energy fluxes in observations of directional radiometric surface temperature. Agr. For. Meteorol. 77: 263-293. doi: 10.1016/0168-1923(95)02265-Y.

230. Nourani V., Roughani A. and Gebremichael M. (2011). TOPMODEL capability for rainfall-runoff modelling of the Ammameh watershed at different time scales using different terrain algorithms. Journal of Urban and Environmental Engineering, 5(1), 1:14.

231. Ochoa-Sanchez A., Crespo P., Carrillo-Rojas G., Sucozhanay A. and Celleri R. (2019). Actual evapotranspiration in the High Andean grasslands: a comparison of measurement and estimation methods. Front. Earth Sci. 7:55. doi: 10.3389/feart.2019.00055.

232. Oettl D., Goulart A., Degrazia G. and Anfossi D. (2005). A new hypothesis on meandering atmospheric flows in low wind speed conditions. Atmos. Environ. 39:1739-1749.

233. Oldroyd H.J., Pardyjak E.R., Huwald H. and Parlange M.B. (2016). Adapting tilt corrections and the governing flow equations for steep, fully three-dimensional, mountainous terrain, Boundary-layer Meteorol. 159:539-565, doi: 10.1007/s10546-015-0066-0.

234. Ortega-Farias S.O., Cuenca R.H. and Ek M. (1996). Daytime variation of sensible heat flux by the bulk aerodynamic method over a grass canopy. Agric. For. Meteorol. 81: 131-143.

235. Palazzi E., Filippi L., and Von Hardenberg J. (2017). Insights into elevation dependent warming in the Tibetan Plateau Himalayas from CMIP5 model simulations, Clim. Dyn. 48:3991–4008, DOI 10.1007/s00382-016-3316-z.

236. Palazzi E., Mortarini L., Terzago S. *et al.* Elevation-dependent warming in global climate model simulations at high spatial resolution. Clim Dyn **52,** 2685–2702 (2019). doi: 10.1007/s00382-018-4287-z.

237. Panofsky H.A., Tennekes H., Lenschow D.H. and Wyngaard J.C. (1977)., "The characteristics of turbulent velocity components in the surface layer under convective conditions", Boundary Layer Meteorology 11:3 355-361.

238. Papale D., Reichstein M., Aubinet M., Canfora E., Bernhofer C., Kutsch W., Longdoz B., Rambal S., Valentini R., Vesala T. and Yakir D. (2006). Towards a standardized processing of Net Ecosystem Exchange measured with eddy covariance technique: algorithms and uncertainty estimation, Biogeosciences, 3, 571–583.

239. Penman H.L. (1948). Natural evaporation from open water, bare soil and grass. Proc. Roy. Soc London A (194), S. pp. 120-145.

240. Pepin N., Bradley R., Diaz H. *et al. (2015)*. Elevation-dependent warming in mountain regions of the world. Nature Clim Change **5,** 424–430. doi: 10.1038/nclimate2563.

241. Peters A., Durner W. and Iden S.C. (2017). Modified Feddes type stress reduction function for modeling root water uptake: Accounting for limited aeration and low water potential. Agricultural Water Management 185: 126-136. doi: 10.1016/j.agwat.2017.02.010.

242. Philipona R. (2013). Greenhouse warming and solar brightening in and around the Alps. Int J Climatol, 33: 1530–7.

243. Priestley C.H.B. and Taylor R.J. (1972). On the assessment of the surface heat flux and evaporation using large-scale parameters. Mon. Weather Rev. 100(2): 81-92.

244. Pluss C., and Mazzoni R. (1994). The role of turbulent heat fluxes in the energy balance of high Alpine snow cover. Nordic Hydrology 25:25-38.

245. Plüss C., Pomeroy J. and Ohmura A. (1997). Longwave radiation on snow-covered mountainous surfaces. J.Appl. Meteorol. 36: 818-824. doi: 10.1175/1520-0450-36.6.818.

246. Pomeroy J.W. and Essery R.L.H. (1999). Turbulent fluxes during blowing snow: field tests of model sublimation predictions. Hydrol. Process. 13:2963-2975.

247. Pomeroy J., Toth B., Granger R.J., Hedstrom N.R. and Essery R.L.H. (2003). Variation in surface energetics during snowmelt in a subarctic mountain catchment. J. Hydrometeorol. 4: 702-718. doi: 10.1175/1525-7541(2003)004<0702:VISEDS>2.0.CO;1.

248. Pomeroy J.W., Bewley D.S., Essery R.L.H., Hedstrom N.R., Link T., Granger R.J., Sicart J.E., Ellis C.R. and Janowicz J.R. (2006). Shrub tundra snowmelt. Hydrol. Process. 20: 923-941. doi: 10.1002/hyp.6124.

249. Prabha T.V., Leclerc M. and Baldocchi D. (2008). Comparison of in-canopy flux footprints between large-eddy simulation and the Lagrangian simulation. J. Appl. Meteorol. Climatol. 47(8): 2115-2128. doi: 10.1175/2008JAMC1814.1.

250. Previati M., Godio A. and Ferraris S. (2011). Validation of spatial variability of snowpack thickness and density obtained with GPR and TDR methods. J. Appl. Geophys. 75: 284-293. doi:10.1016/j.appgeo.2011.07.007.

251. Previati M., Canone D., Iurato E., Gisolo D., Ferrari S., Teatini P., Putti M. and Ferraris S. (2020). Thorough wetting and drainage of a peat lysimeter in a climate change scenario. Hydrological Processes. 34(5): 1269-1284. doi: 10.1002/hyp.13675.

252. Priestley C.H.B. and Taylor R.J. (1972). On the assessment of the surface heat flux and evaporation using large-scale parameters. Monthly Weather Review. 100(2):81-92.

253. Raffelli G., Previati M., Canone D., Gisolo D., Bevilacqua I., Capello G., Biddoccu M., Cavallo E., Deiana R., Cassiani G. and Ferraris S. (2017). Local- and plot- scale measurements of soil moisture: time and spatially resolved field techniques in plain, hill and mountain sites. Water 2017, *9*, 706; doi:10.3390/w9090706.

254. Rana G., and Katerji N. (2000). Measurement and estimation of actual evapotranspiration in the field under Mediterranean climate: A review. Eur. J. Agron., 13(2–3), 125– 153. doi:10.1016/S1161-0301(00)00070-8

255. Rangwala I. and Miller J.R. (2012). Climate change in mountains: a review of elevation-dependent warming and its possible causes, Climatic Change 114: 527-547.

256. Rannik Ü.,et al., (2012). "Footprint analysis". In Aubinet M., Vesala T., Papale D., (Eds.), "Eddy covariance: a practical guide to measurement and data analysis. Springer Atmospheric Sciences, Springer; Netherlands.

257. Reba M.L., Link T.E., Marks D., and Pomeroy J. (2009). An assessment of corrections for eddy covariance measured turbulent fluxes over snow in mountain environments. Water Resour. Res. 45, W00D39. doi:10.1029/2008WR007045.

258. Reba M.L., Pomeroy J., Marks D. and Link T.E. (2012). Estimating surface sublimation losses from snowpacks in a mountain catchment using eddy covariance and turbulent transfer calculations. Hydrol. Process. 26: 3699-3711. doi 10.1002/hyp.8372.

259. Rebora, N., Ferraris, L., von Hardenberg, J., and Provenzale, A. (2006). Rainfarm: Rainfall downscaling by a filtered autoregressive model. Journal of Hydrometeorology, 7(4), 724–738., doi: 10.1175/JHM517.1.

260. Reichstein M, Falge E, Baldocchi D et al. (2005). On the separation of net ecosystem exchange into assimilation and ecosystem respiration: review and improved algorithm. Global Change Biology, 11, 1424-1439.

261. Reicosky D.C., Sharratt B.S., Ljungkull J.E. and Baker D.G. (1983). Comparison of alfalfa evapotranspiration measured by a weighting lysimeter and a portable chamber. Agric. Meteorol. 28: 205-211. doi: 10.1016/0002-1571(83)90026-2.

262. Richardson A.D. and Hollinger D.Y. (2005). "Statistical modeling of ecosystem respiration using eddy covariance data: Maximum likelihood parameter estimation, and Monte Carlo simulation of model and parameter uncertainty, applied to three simple models", Agricultural and Forest Meteorology 131:191–209.

263. Richiardone R., Giampiccolo E., Ferrarese S. and Manfrin M. (2008). Detection of flow distortion and systematic errors in sonic anemometry using the planar fit method. Boundary-Layer Meteorol (2008) 128:277–302.

264. Rigon R. and Bertoldi G. (2006). GEOtop: a distributed hydrological model with coupled water and energy budgets. J. Hydrometeorol. 7(3): 371-388. doi:10.1175/JHM497.1.

265. Roerink G., Su Z. and Menenti M. (2000). S-SEBI: a simple remote sensing algorithm to estimate the surface energy balance. Phys. Chem. Earth B., 25: 147-157. doi: 10.1016/S1464-1909(99)00128-8.

266. Rogora M., Frate L., Carranza M.L., Freppaz M et al. (2018). Assessment of climate change effects on mountain ecosystems through across-site analysis in the Alps and Apennines. Sci. Total Environ. 624: 1429-1442.

267. Rogowski A.S. (1972). Watershed physics: soil variability criteria. Water Resour. Res. 8(4): 1015-1023.

268. Romano N., Palladino M. and Chirico G.B. (2011). Parameterization of a bucket model for soil-vegetation-atmosphere modeling under seasonal climatic regimes. Hydrol. Earth Syst. Sci. 15: 3877-3893. doi: 10/5194/hess-15-3877-2011.

269. Rotach M.W., Andretta M., Calanca P., Weigel A.P. and Weiss A. (2008). Boundary layer characteristics and turbulent exchange mechanisms in highly complex terrain. Acta Geophys. 56(1): 194-219. doi: 10.2478/s11600-007-0043-1.

270. Rottler E., Kormann C., Francke T. and Bronstert A. (2018). Elevation-dependent warming in the Swiss Alps 1981–2017: Features, forcings and feedbacks. Int. J. Climatol. 1-13.

271. Russell E.S., Liu H., Gao Z., Finn D. and Lamb B. (2015). Impacts of soil heat flux calculation methods on the surface energy balance closure. Agric. For. Meteorol. 214-215: 189-200. doi: 10.1016/j.agrformet.2015.08.255.

272. Ryu Y., Baldocchi D.D., Ma S. and Hehn T. (2008). Interannual variability of evapotranspiration and energy exchange over an annual grassland in California. Journal of Geophysical Research, 113:D09104. doi: 10.1029/2007JD009263.

273. Saitoh T.M., Tamagawa I., Muraoka H., and Koizumi H., (2011). Energy balance closure over a cool temperate forest in steeply sloping topography during snowfall and snow-free periods. Journal of Agricultural Meteorology 67 (3) 107-116. doi:10.2480/agrmet.67.3.4.

274. Schaap M.G., Feike J.L., van Genuchten M.Th. (2001). ROSETTA: a computer program for estimating soil hydraulic parameters with hierarchical pedotransfer functions. Journal of Hydrology, 251: 163-176. doi: 10.1016/S0022-1694(01)00466-9.

275. Schaefli, B., Hingray, B., Musy, A., 2007. Climate change and hydropower production in the Swiss Alps: quantification of potential impacts and related modeling uncertainties. Hydrol. Earth Syst. Sci. 11, 1191–1205.

276. Schirpke U., Marino D., Marucci A., Palmieri M. and Scolozzi R. (2017). Operationalising ecosystem services for effective management of protected areas: experiences and challenges. Ecosyst. 28(A): 105-114. doi: 10.1016/j.ecoser.2017.10.009.

277. Schmitt M., Bahn M., Wohlfahrt G., Tappeiner U. and Cernusca A. (2010). Land use affects the net ecosystem CO2 exchange and its components in mountain grasslands. Biogeosciences. 7(8): 2297–2309. doi:10.5194/bg-7-2297-2010.

278. Scholz K., Hammerle A., Hiltbrunner E. and Wohlfahrt G. (2018). Analyzing the Effects of Growing Season Length on the Net Ecosystem Production of an Alpine Grassland Using Model–Data Fusion. Ecosystems, 21:982-999. doi: 10.1007/s10021-017-0201-5.

279. Schotanus P., Nieuwstadt F.T.M., and de Bruin H.A.R. (1983). Temperature measurement with a sonic anemometer and its application to heat and moisture fluxes. Boundary-Layer Meteorol. 26:81–93. doi:10.1007/ BF00164332.

280. Schwanghart W. and Scherler D. (2014). TopoToolbox 2 – MATLAB-based software for topographic analysis and modelling in Earth surface sciences. Earth. Surf. Dyn. 2:1-7. doi: 10.5194/esurf-2-1-2014.

281. Sfyri E., Rotach M., Stiperski I., Bosveld F.C., Lehner M. and Obleitner F.M. (2018). Scalar-flux similarity in the layer near the surface over mountainous terrain, Boundary-Layer Meteorol. 169:11-46, doi: 10.1007/s10546-018-0365-3.

282. Sexstone G.A., Clow D.W., Stannard D.I. and Fassnacht S.R. (2016). Comparison of methods for quantifying surface sublimation over seasonally snow-covered terrain. Hydrol. Process. 30: 3373-3389. doi:10.1002/hyp.10864.

283. Sharan M., Modani M. and Yadav A. (2003). Atmospheric dispersion: an overview of mathematical modelling framework. Proc. Indian Natl. Sci. Acad. A 69:725-744.

284. Sicart J.E., Pomeroy J.W., Essery R.L.H. and Bewley D. (2006). Incoming longwave radiation tomelting snow: observations, sensitivity and estimation in northern environments. Hydrol. Process. 20: 3697-3708. doi: 10.1002/hyp.6383.

285. Siebicke L., Hunner M. and Foken T. (2012). Aspects of CO2 advection measurements. Theor. Appl. Climatol. 109(1-2): 109-131. doi: 10.1007/s00704-011-0552-3.

286. Silva Ursulino B., Montenegro S.M.G.L., Coutinho A.P., Coelho V.H.R. *et al.* (2019). Modelling soil water dynamics from soil hydraulic parameters estimated by an alternative method in a tropical experimental basin. Waterm 11, 1007. doi: 10.3390/w11051007.

287. Šimunek J. and van Genuchten M.Th. (2008). Modeling nonequilibrium flow and transport processes using HYDRUS. Vadose Zone K. 7:782-797. doi: 10/2136/vzj2007.0074.

288. Šimunek J., Šejna M., Saito H., Sakai M., and van Genuchten M. Th. (2013). The Hydrus-1D Software Package for Simulating the Movement of Water, Heat, and Multiple Solutes in Variably Saturated Media, Version 4.17, HYDRUS Software Series 3, Department of Environmental Sciences, University of California Riverside, Riverside, California, USA, pp. 342.

289. Sogachev A. and Lloyd J. (2004). Using a one-and-a-half order closure model of atmospheric boundary layer for surface flux footprint estimation. Bound.-Layer Meteorol. 112: 467-502.

290. Sogachev A. and Leclerc M.Y. (2011). On concentration footprints for a tall tower in the presence of a nocturnal low-level jet. Agric. For. Meteorol. 151: 755-764. doi: 10.1016/j.agrformet.2010.10.004.

291. Spinoni J., Vogt J. V., Naumann G., Barbosa P., and Dosio A. (2017). Will drought events become more frequent and severe in Europe? International Journal of Climatology, 38(4), 1718–1736.doi:10.1002/joc.5291.

292. Steinfeld G., Raasch S. and Markkanen T. (2008). Footprints in homogeneously and heterogeneously driven boundary layers derived from a Lagrangian stochastic particle model embedded into large-eddy simulation. Bound.-Layer Meteorol. 129: 225-248. doi: 10.1007/s10546-008-9317-7.

293. Stigter E.E., Steiner J.F., Koch I., Saloranta T.M., Kirkham J.D. and Immerzeel W.W. (2021). Energy and mass balance dynamics of the seasonal snowpack at two high-altitude sites in the Himalaya. Cold. Reg. Sci. Technol. 183: 103233. doi:10.1016/j.coldregions.2021.103233.

294. Stiperski I., Rotach M. and Gohm A. (2012). Boundary layer measurements in complex terrain: Innsbruck-Box. Session AS2.1,Air-Land Interactions, Geophys. Res. Abstracts, EGU2012-8863.

295. Stiperski I. and Rotach M. (2016). On the Measurement of Turbulence Over Complex Mountainous Terrain, Boundary-Layer Meteorol., 159:97–121, doi: 10.1007/s10546-015-0103-z.

296. Stiperski I. and Calaf M. (2017). “Dependence of near-surface similarity scaling on the anisotropy of atmospheric turbulence”, Quarterly Journal of the Royal Meteorological Society. doi: 10.1002/qj.3224.

297. Strasser, U., Bernhardt M., Weber, M., Liston, G.E. and Mauser, W. (2008). Is snow sublimation important in the alpine water balance? The Cryosphere, 2: 53-56. doi:10.5194/tcd-1-303-2007

298. Stössel, F., Guala, M., Fierz, C., Manes, C. and Lehning, M. (2010). Micrometeorological and morphological observations of surface hoar dynamics on a mountain snow cover. Water Resour. Res, 46, W04511. doi:10.1029/2009WR008198

299. Stull R.B. (1988). An introduction to boundary layer meteorology. Kluwer academic publishers, 760 pp.

300. Su Z. (2002). The surface energy balance system (SEBS) for estimation of turbulent heat fluxes. Hydrol. Earth Syst. Sci. 6: 85-100. soi: 10.5194/hess-6-85-2002.

301. Tang Y., Wu X. and Chen Y. (2018). Sap flow characteristics and physiological adjustments of two dominant tree species in pure and mixed plantations in the semi-arid Loess Plateau of China. J. Arid Land. 10(6): 833–849. doi: 10.1007/s40333-018-0027-9.

302. Taylor G.I. (1938). The spectrum of turbulence. Proc. R. Soc.,(1938) A164, 476-490.

303. Tesfa T.K., Tarboton D.G., Chandler D.G. and McNamara J. (2009). Modeling soil depth from topographic and land cover attributes. Water Resour. Res. 45, W10438. doi: 10.1029/2008WR007474.

304. Teuling A., Van Loon A.F., Seneviratne S.I., Lehner I., Aubinet M., Heinesch B., Bernhofer C., Grünwald T., Prasse H. and Spank U. (2013). Evapotranspiration amplifies European summer drought. Geophys. Res. Lett. 40: 2071-2075. doi: 10.1002/grl.50495.

305. Tenhunen J., Geyer R., Adiku S., Reichstein M., Tappeiner U, Bahn M. et al. (2009). Influences of changing land use and CO2 concentration on ecosystem and landscape level carbon and water balances in mountainous terrain of the Stubai Valley, Austria. Global and Planetary Change 67(1):29-43.

306. Teuling A.J., Uijlenhoet R. and Troch P.A. (2005). On bimodality in warm season soil moisture observations. Geophysical Research Letters 32 L13402. doi: 10.1029/2005GL023223.

307. Thomas C., and Foken T. (2002), Re-evaluation of integral turbulence characteristics and their parameterizations, 15th Conference on Turbulence and Boundary Layers, Am. Meteorol. Soc., 129-132.

308. Thornthwaite C.W. (1948). An approach toward a rational classification of climate. Geograph. Rev. 38, pp55.

309. Tramontana G., Migliavacca M., Jung M., Reichstein M., Keenan T.F., Camps-Valls G., Ogee J., Verrelst J. and Papale D. (2020). Partitioning net carbon dioxide fluxes into photosynthesis and respiration using neural networks. Glob. Chang. Biol. 26(9): 5235-5253. doi: 10.1111/gcb.15203.

310. Trini-Castelli S., Falabino S., Mortarini L., Ferrero E., Richiardone R. and Anfossi D., (2014). “Experimental investigation of surface-layer parameters in low wind-speed conditions in a suburban area”. Quart J Roy Meteorol Soc. 140, 2023–2036, DOI 10.1002/qj.2271.

311. Trini-Castelli S. and Falabino S. (2013). Parameterization of the wind velocity fluctuation standard deviations in the surface layer in low-wind conditions. Meteorol. Atmos. Phys. 119:91-107. doi: 10.1007/s00703-012-0219-3.

312. Tromp-van Meerveld H., and McDonnell J. (2006). On the interrelations between topography, soil depth, soil moisture, transpiration rates and species distribution at the hillslope scale, Advances in Water Resources, 29(2), 293–310, doi: 10.1016/j.advwatres.2005.02.016.

313. Turekhanova R. (1995). Root system formation of Hyppophae Rhamnoides L. (seabuckthorn). Acta Phytogeogr. Suec. 81, Uppsala.

314. Turnipseed A.A., Blanken P.D., Anderson D.E., Monson R.K. (2002). Surface energy balance above a high-elevation subalpine forest. Agric. For. Meteorol. 110, 177–201. doi:10.1016/S0168-1923(01(00290-8.

315. Turnipseed A.A., Anderson D.E., Blanken P.D., Baugh W.M. and Monson R.K. (2003). Airflows and turbulent flux measurements in mountainous terrain Part 1. Canopy and local effects. Agri. For. Met. 119:1-21, doi: 10.1016/S0168-1923(03)00136-9.

316. Twidell J. and Weir T. (1986). Renewable energy resources. E&FN Spon, London, UK. pp. 160.

317. Twine, T.E., Kustas, W.P., Norman, J.M., Cook, D.R., Houser, P.R., Meyers, T.P., Prueger, J.H., Starks, P.J., Wesely M.L., (2000). Correcting eddy-covariance flux underestimates over a grassland. Agr. Forest Meteorol. 103(3), 279-300.

318. USGS (2019). Landsat 8 (L8) data users handbook. U.S. Geological survey, Earth resources observation and science (EROS) Center, Sioux Falls, South Dakota, pp.114.

319. Valentini R. and Miglietta M. (Eds) (2015). The greenhouse gas balance of Italy – An insight on managed and natural terrestrial ecosystems. Springer-Verlag, Environmental science and engineering, 211 pp.

320. Van den Bergh T., Körner C. and Hiltbrunner E. (2018). Alnus shrub expansion increases evapotranspiration in the Swiss Alps. Reg. Environ. Change 18: 1375-1385. doi: 10.1007/s10113-017-1246-x.

321. Vanham D. (2012). The Alps under climate change: implications for water management in Europe. J. Water Clim. Chang. 3: 197-206.

322. Van Dijk A., Moene A.F. and De Bruin H.A.R. (2004). The principles of surface flux physics: theory, practice and description of the ECPACK library, Internal Report 2004/1, Meteorology and Air Quality Group, Wageningen University, Wageningen, the Netherlands, 99 pp.

323. Van Lanen H.A.J., Laaha G., Kingston D.G., Gauster T., Ionita M. et al. (2016). Hydrology needed to manage droughts: the 2015 European case. Hydrol. Process. 30:3097-3104. doi: 10.1002/hyp.10839.

324. Van Looy K., Bouma J., Herbst M., Koestel J., Minasny B., Mishra U., Montzka C., Nemes A., Pachepsky Y.A., Padarian J., et al. (2017). Pedotransfer functions in Earth system science: challenges and perspectives. Rev. Geophys. 55, 1199-1256. doi: 10.1002/2017RG000581.

325. Vendrame N., Tezza L. and Pitacco A. (2019). Study of the carbon budget of a temperate-climate vineyard: inter-annual variability of CO2 flux. Am. J. Enol. Vitic. 70:34-41. doi: 10.5344/ajev.2018.18006.

326. Vendrame N., Tezza L. and Pitacco A. (2020). Comparison of sensible heat fluxes by large aperture scintillometry and eddy covariance over two contrasting-climate vineyards. Agric. For. Meteorol. 288-289, 108002. doi: 10.1016/j.agrformet.2020.108002.

327. Venturini V., Islam S. and Rodriguez L. (2007). Estimation of evaporative fraction and evapotranspiration from MODIS products using a complementary based model. Remote Sens. Environ. 112(1): 132-141. doi: 10.1016/j.rse.2007.04.014.

328. Vesala T., Huotari J., Rannik Ü, Suni T., Smolander S., Sogachev A., Launiainen S. and Ojala A. (2006). "Eddy covariance measurements of carbon exchange and latent and sensible heat fluxes over a boreal lake for a full open-water period", J. Geophys. Res.111, D 11101, doi: 10.1029/2005JD006365.

329. Vickers D. and Mahrt L. (1997). Quality control and flux sampling problems for tower and aircraft data", Journal of atmospheric and oceanic technology. American Meteorological Society. 14:512-526, DOI: 10.1175/1520-0426(1997)014<0512:QCAFSP>2.0.CO;2.

330. Vickers D. And Mahrt L. (2003). The cospectral gap and turbulent flux calculations. Journal of Atmospheric and Oceanic Technology. 20: 660-672. doi: 10.1175/1520-0426(2003)20<660:TCGATF>2.0.CO;2

331. Wang K. and Dickinson R.E. (2012). A review of global terrestrial evaporanspiration: observation, climatology and climativ variability. Rev. Geophys. 50, RG2005.

332. Webb E.K., Pearman G.I. and Leuning R. (1980). Correction of flux measurements for density effects due to heat and water vapour transfer, Quart. J. R. Met. Soc. 106, pp. 85-100.

333. Wegehenkel M. and Beyrich F. (2014). Modelling hourly evapotranspiration and soil water content at the grass-covered boundary layer field Falkenberg, Germany. Hydrological Sciences Journal, 59:2, 376-394. doi: 10.1080/02626667.2013.835488.

334. Wever L.A., Flanagan L.B. and Carlson P.J. (2002). Seasonal and interannual variation in evapotranspiration, energy balance and surface conductance in a northern temperate grassland. Agricultural and Forest Meteorology 112: 31–49. doi: 10.1016/S0168-1923(02)00041-2.

335. Wieser G., Hammerle A. and Wohlfahrt G. (2008). The Water Balance of Grassland Ecosystems in the Austrian Alps. Arctic Antarctic and Alpine Research 40(2):439-445. doi: 10.1657/1523-0430(07-039)[WIESER]2.0.CO;2.

336. Wilczak J.M., Oncley S.P. and Stage S.A. (2001). Sonic anemometer tilt correction algorithms. Boundary-Layer Meteorology 99: 127–150.

337. Wilson K., Goldstein A., Falge E., Aubinet M., Baldocchi D., Berbigier P., Bernhofer F. C., Ceulemans R., Dolman H., Field C., Grelle A., Ibrom A., Lawl B.E., Kowalski A., Meyers T., Moncrieff J., Monson R., Oechel W., Tenhunen J., Valentini R., and Verma S. (2002). Energy balance closure at FLUXNET sites. Agri.For.Met. 113:223–243.

338. Wißkirchen K., Tum M., Günther K.P., Niklaus M., Eisfelder C. and Knorr W. (2013). Quantifying the carbon uptake by vegetation for Europe on a 1 km2 resolution using a remote sensing driven vegetation model. Geosci. Model Dev. 6: 1623–1640. doi: 10.5194/gmd-6-1623-2013.

339. Wyngaard J.C. (1973). On surface layer turbulence. In: Haugen D.A. (ed) Workshop on micrometeorology. American Meteorological Society, Boston, pp. 101-150.

340. Wohlfahrt G., Hammerle A., Haslwanter A., Bahn M., Tappeiner U. and Cernusca A. (2008). Seasonal and inter-annual variability of the net ecosystem CO2 exchange of a temperate mountain grassland: effects of weather and management, Journal of Geophys. Res. 113, D08110, doi: 10.1029/2007JD009286.

341. Wohlfahrt G., Hammerle A., Niedrist G., Scholz K., Tomelleri E. and Zhao P. (2016). On the energy balance closure and net radiation in complex terrain. Agric. For. Meteorol. 226-227: 37-49. doi:10.1016/j.agrformet.2016.05.012.

342. Wösten J.H.M., Schuren C.H.J.E., Bouma J. and Stein A. (1990). Functional sensitivity analysis of four methods to generate soil hydraulic functions. Soil Sci. Soc. Am. J. 54: 832-836.

343. Wu Z. and Huamg N.E. (2009). Ensemble empirical mode decomposition: a noise-assisted data analysis method. Adv. Adapt. Data Analysis 01: 1-41.

344. Wu H., Li X-Y., Li J., Zhang C., He B., Zhang S. And Sun W. (2018). Age-related water uptake patterns of alpine plantation shrubs in reforestation region of Qinghai-Tibeta Plateau based on stable isotopes. Ecohydrology, 2019 12:e2049.

345. Wutzler T., Lucas-Moffat A., Migliavacca M., Knauer J., Sickel K., Šigut L., Menzer O. and Reichstein M. (2018). Basic and extensible post-processing of eddy covariance flux data with REddyProc. Biogeosciences, 15, 5015–5030. doi:10.5194/bg-15-5015-2018

346. Xin Y-F., Chen F., Zhao P., Barlage M., Blanken P., Chen Y-L., Chen B., Wang Y-J. (2018). Surface energy balance closure at ten sites over the Tibetan plateau, Agric. For. Met., 259:317-329.

347. Yuan R., Kang M., Park S-B., Hong J., Lee D. and Kim J. (2010). Expansion of the planar-fit method to estimate flux over complex terrain. Meteorol. Atmos. Phys 110:123–133.

348. Zardi D. and Whiteman C.D. (2012). Diurnal mountain wind systems. In: Chow F.K., DeWekker S.F.J. and Snyder B. (eds). Mountain weather research and forecasting, Chapter 2.Springer, pp 289.

349. Zhiyin Y. (2015). Large eddy simulation: Past, present and the future, Chinese Journal of Aeronautics 28:11-24. doi: 10.1016/j.cja.2014.12.007.

350. Zitouna-Chebbi R., Prévot L., Jacob F., Mougou R. and Voltz M. (2012). Assessing the consistency of eddy covariance measurements under conditions of slopig topography within a hilly agricultural catchment. Agric. For. Met. 164: 123-135. doi: 10.1016/j.agrformet.2012.05.010.

351. Zuecco G., Borga M., Penna D., Canone D., Previati M. and Ferraris S. (2013). Towards improved understanding of land use effect on soil moisture variability: analysis and modeling at the plot scale. Procedia Environmental Sciences. 19, 456-464.